Ravipudi Venkata Rao
Samir Khatir
Thanh Cuong-Le *Editors*

Recent Advances in Structural Health Monitoring and Engineering Structures

Select Proceedings of SHM and ES 2022

Springer

Lecture Notes in Mechanical Engineering

Ravipudi Venkata Rao · Samir Khatir ·
Thanh Cuong-Le

Editors

Recent Advances in Structural Health Monitoring and Engineering Structures

Select Proceedings of SHM and ES 2022

Editors
Ravipudi Venkata Rao
Department of Mechanical Engineering
Sardar Vallabhbhai National Institute
of Technology
Surat, India

Samir Khatir
Soete Laboratory, Faculty of Engineering
and Architecture
Ghent University
Ghent, Belgium

Thanh Cuong-Le
Faculty of Civil Engineering
Ho Chi Minh City Open University
Ho Chi Minh City, Vietnam

Contents

About the Editors

Dr. Ravipudi Venkata Rao is currently working as Professor (Higher Administrative Grade) in the Department of Mechanical Engineering, S. V. National Institute of Technology (SVNIT), Surat, India. He has more than 30 years of teaching and research experience, having completed his B.Tech. in 1988, M.Tech. in 1991, Ph.D. in 2002, and D.Sc. in 2017. His research interests include advanced optimization algorithms and their applications to design, thermal and manufacturing engineering. He has more than 350 research papers to his credit, published in national and international journals and conference proceedings, and has received national and international awards for his research efforts. He is on the editorial boards of several international journals. Apart from conducting a number of short-term training programs for faculty members and professionals on advanced engineering optimization techniques, he has handled numerous research projects including the bi-lateral projects with Austria, Russia, and Slovenia. He has authored six books, and all these have been published by Springer.

Dr. Samir Khatir is currently Doctor Researcher at Ghent University Belgium Soete laboratory and Adjunct Doctor Assistant at Ho Chi Minh Open University Vietnam. He received Ph.D. in Civil engineering from Ghent University and another Ph.D. in Mechanical engineering from UMBB Algeria. He improved and created many techniques for damage identification, created and improved a new optimisation technique. He has authored and co-authored of over 100 ISI peer-reviewed articles. His primary research interest is in the areas of civil and mechanical engineering such as FEM, XFEM, Iso-geometric analysis (IGA), extended Iso-geometric analysis (XIGA), dynamic, static, damage identification, fracture mechanics, optimization, inverse problem, wear, friction, laminated composites, delamination, and transmissibility.

Dr. Thanh Cuong-Le is Head of Department of Strength of Material and Engineering Structures at the Faculty of Civil Engineering, Ho Chi Minh City Open University, Vietnam. He received his Ph.D. from Ghent University of Belgium. His research focuses on optimization and structural health monitoring, computational science and engineering, structural stability, dynamic analysis, plates and shells. He published papers in computer methods in applied mechanics and engineering, scientific reports, composite structures, and thin-walled structures.

Weight Optimization of Truss Structures with Different Constraints Using Rao Algorithms and Their Variants

Zinzuvadia Niketkumar Maheshkumar, Ravipudi Venkata Rao, Samir Khatir, and Thanh Cuong-Le

1 Introduction

In structural optimization, designers look for an optimal solution that creates a structure that sustains the loads while satisfying the constraints. Generally, the objective of the structural optimization problem is to optimize the weight and strength while meeting the constraints of displacement at nodes, stress in the bars or natural frequency of the structure. The size, shape and topology optimization are three divisions of structural optimization. If the truss design is considered, then in size optimization, the design variables are the cross-sectional areas of the truss members. In the shape optimization problem, the location of the truss nodes is under study, and in topology optimization, the connectivity of the truss members is under investigation. In the present work, two weight optimization problems of ten bar truss structure are considered. One problem is solved with the natural frequency constraints, and the other is solved with the constraints related to the nodal displacement and the stress in the truss members.

Truss structure optimization has received the interest of researchers because it optimizes the size of the truss resulting in less manufacturing cost and yields better dynamic behavior using natural frequency constraints. In a truss optimization problem, the natural frequency is restricted in a certain range to avoid the phenomenon of resonance. Along with the required dynamic response, engineering

Z. N. Maheshkumar · R. V. Rao (✉)
Department of Mechanical Engineering, Sardar Vallabhbhai National Institute of Technology, Surat, Gujarat, India
e-mail: ravipudirao@gmail.com

S. Khatir
Soete Laboratory, Ghent University, Ghent, Belgium

T. Cuong-Le
Faculty of Civil Engineering, Ho Chi Minh City Open University, Ho Chi Minh City, Vietnam

structures should also be light in weight [1]. The designer can control the frequency of the truss structure in the desired manner to improve the dynamic behavior. The size optimization of truss is a complex problem and consideration of natural frequency as constraints increase the complexity of the problem [2]. Similarly, the truss optimization problem with constraints related to the nodal displacement and the stress in the truss members minimizes the weight of the truss, and it also assures that the truss performs satisfactorily in its application. Researchers have proposed different methods in the past to address the complexity of the truss optimization problem.

Sedaghati et al. [3] solved the frame and truss structure optimization problem with frequency constraints using combined finite element-based technique and sequential quadratic programming. Gholizadeh et al. [4] used genetic algorithm and Salajegheh et al. [5] solved structure optimization problems under multiple natural frequency constraints with a neural network. Gomes [6] optimized the shape and size of the truss structure using particle swarm optimization algorithm. Talatahari et al. [7] developed a material generation algorithm and implemented it for the optimum design of engineering problems, including ten bar truss optimization problem. Yu et al. [8] introduced interior point trust region method to solve the truss structural frequency optimization problems. Lamberti and Pappalettere [9] solved truss structure weight minimization problems using linearization error sequential linear programming. Kaveh and Zolghadr [1] solved truss structures under frequency constraints using the charged system search algorithm and its enhanced version. Eskandar et al. [10] solved the ten bar truss weight optimization problem with displacement and stress constraints using water cycle algorithm. Kaveh and Hassani [11] developed the energy formulation of force method and simultaneously performed optimization of truss structures. Rao et al. [12] solved the truss optimization problem by applying the Rao algorithms, Quasi oppositional Rao algorithms and self-adaptive multi-population Rao algorithms.

Turky and Abdullah [13] introduced a multi-population harmony search algorithm to solve dynamic optimization problems (DOP). In the proposed algorithm, the population of solutions was split into a number of sub-populations for better exploration and exploitation. The proposed algorithm's performance was examined on the moving peak benchmark problems. Feng et al. [14] presented chaos optimization algorithm. The chaotic sequences generated by sixteen chaotic maps were analyzed. The proposed algorithm was applied to test functions to demonstrate its high efficiency and convergence rate. Rao [15] introduced algorithm-specific parameter less Rao algorithms to solve the optimization problems related to different fields. From the literature review, it is observed that the algorithm's performance can be improved by integrating concepts like multi-population, elitism and chaos theory with the basic metaheuristic algorithm. So in the present paper, the self-adaptive multi-population elitist (SAMPE) Rao algorithms and chaotic Rao algorithms are utilized to solve the ten bar truss optimization problem.

The remainder of the paper has the following structure: Sect. 2 describes the Rao, SAMPE Rao and chaotic Rao algorithms. Section 3 describes the two examples of ten bar truss optimization problem. Section 4 discusses the results obtained after

applying the proposed algorithms to the problems. Section 5 presents the conclusions of the present paper.

2 Rao, SAMPE Rao and Chaotic Rao Algorithms

2.1 *Rao Algorithms*

Rao algorithms are recently developed algorithm-specific parameter less optimization algorithms [15]. Rao algorithms use the best and the worst candidate solutions of the population to find an optimal solution during the search process. Rao2 and Rao3 algorithms also use the random interaction between the candidates during the search process. In Rao algorithms, the random population is generated initially, and the value of variables is updated using the following equations.

$$x'_{\text{vn,cn,in}} = x_{\text{vn,cn,in}} + r_{1,\text{vn,in}}(x_{\text{vn,best,in}} - x_{\text{vn,worst,in}}) \tag{1}$$

$$\begin{aligned} x'_{\text{vn,cn,in}} = {}& x_{\text{vn,cn,in}} + r_{1,\text{vn,in}}(x_{\text{vn,best,in}} - x_{\text{vn,worst,in}}) \\ & + r_{2,\text{vn,in}}(|x_{\text{vn,c1,in}} \text{ or } x_{\text{vn,c2,in}}| - |x_{\text{vn,c2,in}} \text{ or } x_{\text{vn,c1,in}}|) \end{aligned} \tag{2}$$

$$\begin{aligned} x'_{\text{vn,cn,in}} = {}& x_{\text{vn,cn,in}} + r_{1,\text{vn,in}}(x_{\text{vn,best,in}} - |x_{\text{vn,worst,in}}|) \\ & + r_{2,\text{vn,in}}(|x_{\text{vn,c1,in}} \text{ or } x_{\text{vn,c2,in}}| - (x_{\text{vn,c2,in}} \text{or} x_{\text{vn,c1,in}})) \end{aligned} \tag{3}$$

where $x_{\text{vn,cn,in}}$ represents the value of variable 'vn' for candidate number 'cn' for iteration number 'in'. $x'_{\text{vn,cn,in}}$ is the updated value of $x_{\text{vn,cn,in}}$. $r_{1,\text{vn,in}}$ and $r_{2,\text{vn,in}}$ are the random numbers between 0 and 1. The random interaction is done between candidate number 'c1' and 'c2'

2.2 *Self-Adaptive Multi Population Elitist (SAMPE) Rao Algorithms*

SAMPE Rao algorithms include the concept of multi-population and elitism to improve the rate of exploration and exploitation of the search mechanism. In SAMPE Rao algorithms, first the elite size (ES), number of variables and the population size (*m*) are initialized. In SAMPE Rao algorithms, the sub-populations are formulated from the whole population. The subgroups are formed according to the quality of the solution. Then, the 'ES' number of worst solutions from the inferior group is replaced with the best solutions of the superior group. Then, the equations of Rao algorithms are used to modify the candidate solutions in each sub-population. Then,
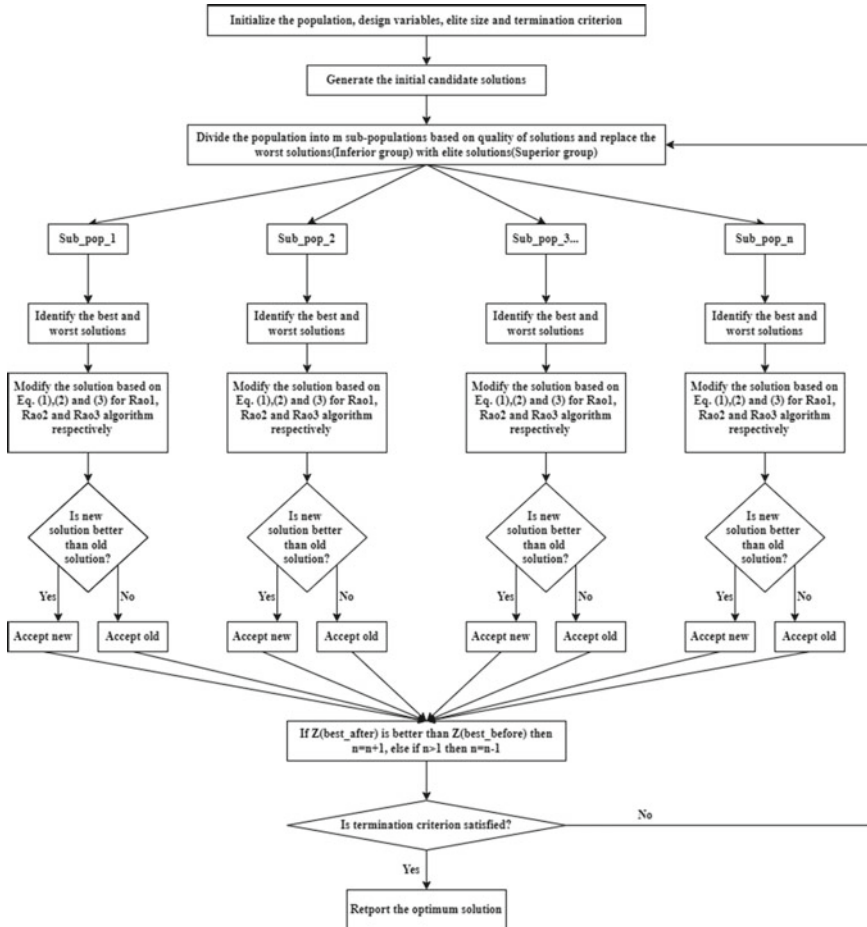
Fig. 1 Flowchart of the SAMPE Rao algorithms

all the sub-populations are merged in a single population. If the current best solution is better than the previous best solution, then the number of sub-population is increased by one for exploration; otherwise, it is decreased by one for exploitation. Figure 1 shows the flowchart of SAMPE Rao algorithms.

2.3 Chaotic Rao Algorithms

The chaotic Rao algorithms integrate the Rao algorithms and the chaos theory. In these algorithms, the random numbers used in the equations of Rao algorithms are replaced with the chaotic numbers. The chaotic numbers are generated using the

mathematical equation of the chaotic map. The researchers have developed different chaotic maps in the past to generate chaotic numbers. Some of the chaotic maps are logistic map, Kent map, Bernoulli shift map, sine map, circle map, Chebyshev map, Gaussian map, etc. The chaotic Rao algorithms help to find a global optimal solution without getting trapped at local optima. The performance of the algorithms is tested using the chaotic numbers generated by different chaotic maps. The algorithms give better results when the Chebyshev map is used to generate the chaotic numbers. The Eq. (4) is used to generate chaotic number when the Chebyshev map is used. Figure 2 shows the flowchart of chaotic Rao algorithms

$$x_{i+1} = |\cos(k \cos^{-1}(x_i))|, \quad x_i \in [0, 1], \ k > 1 \tag{4}$$

where x_{i+1} and x_i are $(i + 1)$th and ith term of a chaotic sequence, respectively.
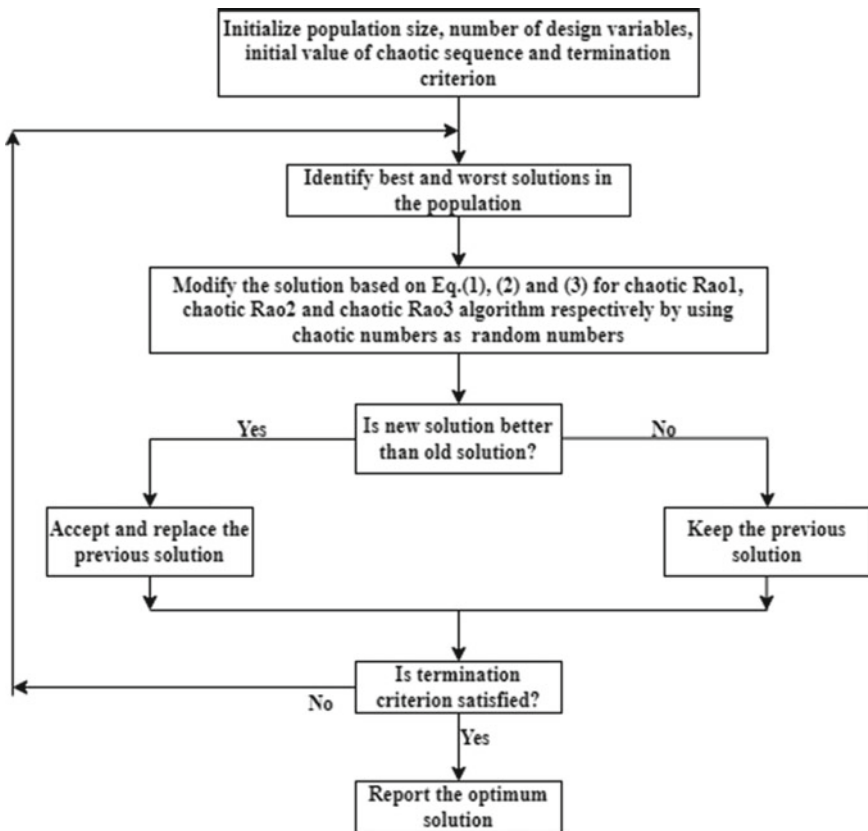
Fig. 2 Flowchart of chaotic Rao algorithms

3   Optimization Problem of Planar Ten Bar Truss

3.1   *Ten Bar Truss Optimization Problem-1*

The weight minimization problem of ten bar truss with frequency constraints was first addressed by Grandhi and Venkayya [16]. In this problem, the cross-sectional area of bars is considered as design variables. The truss material has Young's modulus and density equal to 68.95 GPa and 2767.99 kg/m^3, respectively. Different researches had used different values of Young's modulus in the past for this problem. In this paper, the value of Young's modulus is considered same as it was considered by Grandhi and Venkayya [16]. At each free end of the truss (at node number 2, 3, 4 and 5), a mass of 453.6 kg is attached. The value of natural frequency is calculated using the global stiffness and the global mass matrix. The consistent mass matrix is used to find accurate results of the natural frequency. Figure 3 shows the schematic diagram of ten bar truss for problem-1.

The mathematical model of the ten bar truss optimization problem-1:Design variables:

$$\bar{x} = [A_1, A_2, ..., A_{10}]$$

Objective function:

Minimize,

$$f(\bar{x}) = \rho \sum_{i=1}^{10} L_i(x_i) A_i \tag{5}$$
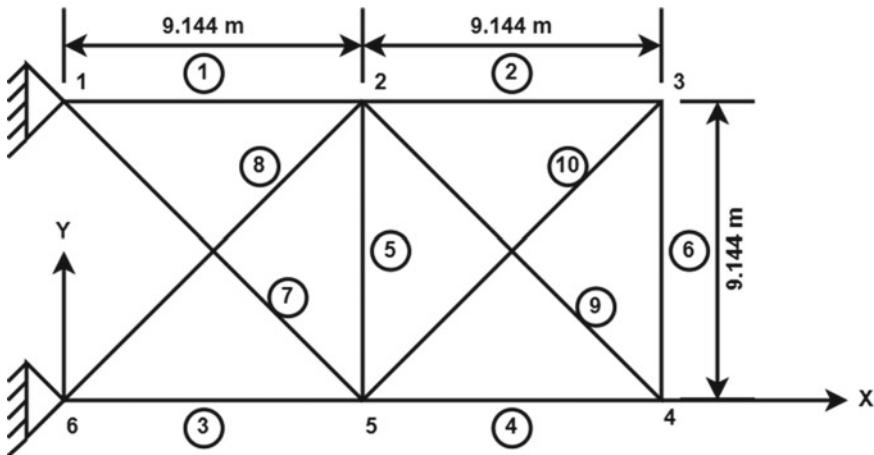
Fig. 3   Ten bar truss for problem-1

Design constraints:

$$C_1(\overline{x}) = \omega_1(\overline{x}) - 7 \geq 0 \tag{6}$$

$$C_2(\overline{x}) = \omega_2(\overline{x}) - 15 \geq 0 \tag{7}$$

$$C_3(\overline{x}) = \omega_3(\overline{x}) - 20 \geq 0 \tag{8}$$

$$6.45 \times 10^{-5} \leq A_i \leq 5 \times 10^{-3} \tag{9}$$

where,

$\rho = \text{Density} = 2767.99 \text{kg/m}^3,$
$L_i(x_i) = \text{Length of the } i\text{th bar (m)}, \quad i = 1, 2, \ldots, 10$
$\omega_1, \ \omega_2 \text{ and} \omega_3 = \text{First three natural frequencies of the truss structure (Hz)},$
$A_i = \text{Cross - sectional area of } i\text{th truss member (m}^2), \quad i = 1, 2, \ldots, 10$

3.2 Ten bar Truss Optimization Problem-2

This problem minimizes the weight of the ten bar truss subjected to constraints associated with the nodal displacement and the stress in the truss members. In this problem, the cross-sectional area of the truss members is the design variables. The truss is made of the material with Young's modulus equal to 10^7 psi and density equal to 0.1 lb/in^3. The maximum allowable displacement at the free nodes is $\pm$ 2, in and the maximum allowable stress in the truss members is $\pm$ 25 ksi. Load $P_1 = 10^5$ lb and $P_2 = 0$ lb are acting at the free nodes as shown in Fig. 4.

The mathematical model of the ten bar truss optimization problem-2:Design variables:

$$\overline{x} = [A_1, A_2, ..., A_{10}]$$

Objective function:
   Minimize,

$$f(\overline{x}) = \rho \sum_{i=1}^{10} L_i(x_i) A_i \tag{10}$$

Design constraints:
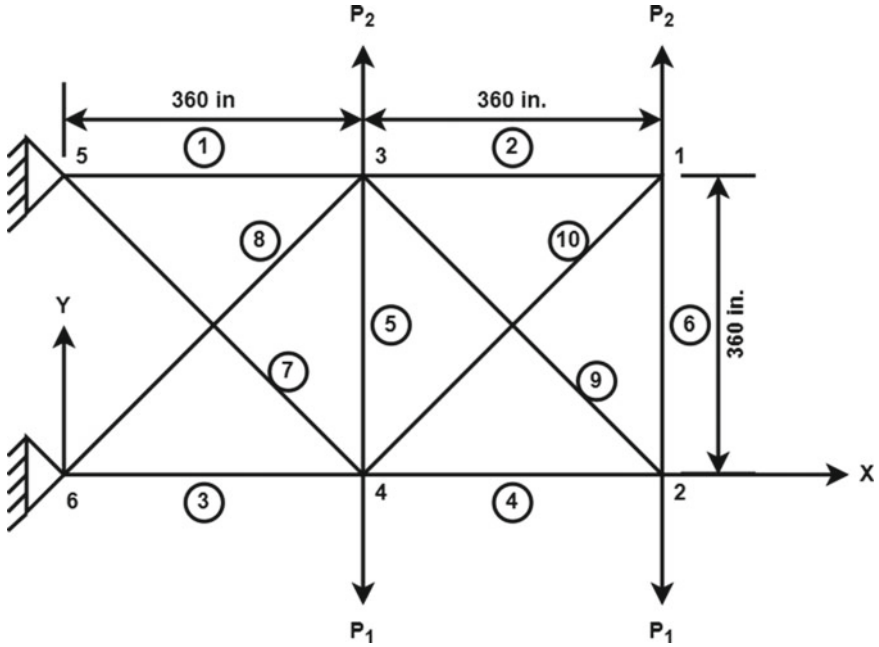
Fig. 4 Ten bar truss for problem-2

$$-2 \leq u_{xi} \leq 2 \tag{11}$$

$$-2 \leq u_{yi} \leq 2 \tag{12}$$

$$-25 \leq \sigma_j \leq 25 \tag{13}$$

$$0.1 \leq A_j \leq 35 \tag{14}$$

where

$\rho =$ Density $= 0.1\text{lb/in}^3$,

$L_i(x_i) =$ Length of the ith bar (in), $\quad i = 1, 2, \ldots, 10$

$u_{xi} =$ Displacement in x direction at ith node (in), $\quad i = 1, 2, 3, 4$

$u_{yi} =$ Displacement in y direction at ith node (in), $\quad i = 1, 2, 3, 4$

$\sigma_j =$ Induced stress in jth truss member (ksi), $\quad j = 1, 2, \ldots, 10$

$A_j =$ Cross - sectional area of jth truss member (in^2), $\quad j = 1, 2, \ldots, 1$

4 Results and Discussion

The optimization results are obtained with the R2019a version of the MATLAB tool. The laptop with the 1.80-GHz Intel Core i7-8550U processor and 8 GB RAM is utilized for computation. The ten bar optimization problem is solved using Rao, SAMPE Rao and chaotic Rao algorithms for 25 times. Various combinations of population size with elite size and initial value of chaotic sequence are tested for SAMPE and chaotic Rao algorithms, respectively, and the combination which gives the best result for different algorithms is also mentioned for both problems. The optimal results achieved using Rao, SAMPE Rao, chaotic Rao algorithms and other advanced optimization algorithms are compared. The bold numbers highlight the improvement in the results from Rao algorithms to modified Rao algorithms.

4.1 Ten Bar Truss Optimization Problem-1

This problem is solved using the presented algorithms with the number of maximum function evaluations equal to 50,000. Table 1 compares the optimal design of ten bar truss obtained using presented algorithms, interior point trust region method (IPTRM), sequential linear programming (SLP), teaching learning-based optimization (TLBO), enhanced charged system search (ECSS) and material generation algorithm (MGA). Table 2 compares the statistical results of the presented algorithms. The optimal results attained using the presented algorithms are better than the same obtained using other algorithms. Figure 5 represents the convergence plot of the Rao, SAMPE Rao and chaotic Rao algorithms for the ten bar truss optimization problem. SAMPE Rao3 algorithm reaches first to its optimal value for this problem.

4.2 Ten Bar Truss Optimization Problem-2

This problem is solved by applying the presented algorithms with the number of maximum function evaluations equal to 50,000. Table 3 compares the optimal design of ten bar truss obtained using presented algorithms, ant colony optimization (ACO), particle swarm optimization (PSO), hybrid genetic algorithm and particle swarm optimization (HGAPSO), water cycle algorithm (WCA), Rao algorithms, quasi-oppositional (QO) Rao algorithms and self-adaptive multi-population (SAMP) Rao algorithms. Table 4 compares the statistical results attained using the SAMPE and chaotic Rao algorithms. The optimal results achieved using the presented algorithms are better than the same achieved using other algorithms. Figure 6 represents the convergence plot of the SAMPE Rao and chaotic Rao algorithms for the ten bar truss optimization problem. chaotic Rao2 algorithm reaches first to its optimal value for this problem.

Table 1 Comparison of optimal results for ten bar problem-1 using different algorithms

Algorithm	f_{min}	A_1	A_2	A_3	A_4	A_5	A_6	A_7	A_8	A_9	A_{10}	C_1	C_2	C_3
IPTRM[a]	544.7	36.38	12.941	35.764	18.314	3.002	5.433	20.989	24.14	9.753	18.102	1.000E−03	3.077E+00	2.500E−02
SLP[a]	534.57	35.148	13.169	37.69	19.556	1.087	4.844	18.314	27.415	12.562	12.106	3.000E−03	1.543E+00	1.540E−01
TLBO[a]	530.76	35.494	14.777	36.203	15.387	0.6451	4.5896	23.211	24.561	12.482	12.324	0.000E+00	1.201E+00	0.000E+00
ECSS[a,b]	529.25	39.569	16.74	34.361	12.994	0.645	4.802	26.182	21.26	11.766	11.392	−1.438E−01	1.115E+00	−2.322E−01
MGA[a,b]	529.1204	36.76416	16.29897	37.94378	16.51087	0.659	4.57489	22.94023	22.63185	10.87892	11.53643	−1.263E−01	1.390E+00	−1.757E−01
Rao1	530.0966	42.480315	6.595627	35.6382	19.92667	1.40975	5.768395	15.05489	28.39336	17.339118	8.239324	1.160E−04	1.294E−02	7.834E−04
Rao2	530.0938	42.459438	6.685081	35.731579	19.82831	1.42142	5.747557	15.025042	28.44203	17.136444	8.383884	2.432E−05	6.012E−02	2.626E−04
Rao3	530.0896	42.386852	6.716022	35.909957	19.7412	1.332839	5.747599	14.87662	28.76973	17.091302	8.276102	3.305E−05	9.102E−03	1.036E−04
SAMPE Rao1	530.0717	42.512825	6.638253	35.771085	19.82477	1.376879	5.698903	14.97328	28.6608	17.212648	8.170349	1.316E−05	1.016E−02	5.850E−04
SAMPE Rao2	530.0751	42.712725	6.603847	35.681113	19.8947	1.422724	5.732315	14.884304	28.47374	17.27057	8.230496	6.679E−06	1.058E−02	2.958E−04
SAMPE Rao3	530.0774	42.516889	6.557441	36.00458	19.72067	1.415428	5.720058	15.049094	28.50076	17.207818	8.181558	1.867E−05	4.381E−03	1.808E−04
Chaotic Rao1	530.0779	42.277734	6.66225	35.779458	19.72491	1.373387	5.716021	14.936021	28.79303	17.276601	8.21746	2.052E−06	1.135E−02	2.971E−04
Chaotic Rao2	530.0896	42.776385	6.595907	35.873518	19.72962	1.405614	5.750094	14.888098	28.57553	17.136128	8.204217	6.317E−06	1.587E−03	6.838E−04
Chaotic Rao3	530.0770	42.586354	6.597214	35.723756	19.84644	1.427229	5.719932	15.013244	28.44623	17.193726	8.310047	1.672E−05	2.130E−02	2.870E−04

[a]The results are taken from [7]
[b]Infeasible solution due to violation of constraints

Table 2 Statistical result comparison for ten bar truss problem-1

Algorithm	B	M	W	SD	MFE	NP, ES/CS$_1$
Rao1	530.0966	530.1672	530.4509	9.091E−02	42,205	20
Rao2	530.0938	530.7118	539.6865	1.887E + 00	44,224	20
Rao3	530.0896	530.4269	533.9654	7.594E−01	42,700	20
SAMPE Rao1	530.0717	530.3919	533.8421	7.495E−01	43,449	20, 2
SAMPE Rao2	530.0751	530.4881	531.3110	3.501E−01	43,120	20, 2
SAMPE Rao3	530.0774	530.5175	531.5239	3.485E−01	40,208	20, 2
Chaotic Rao1	530.0779	530.3403	533.8971	7.697E−01	44,322	20, 0.3
Chaotic Rao2	530.0896	530.4039	531.0919	3.590E−01	43,332	20, 0.3
Chaotic Rao3	530.0770	531.2531	540.5291	2.788E + 00	46,970	20, 0.2

B Best solution, *M* Mean solution, *W* Worst solution, *SD* Standard deviation, *MFE* Mean function evaluations, *NP* Population size, *ES* Elite size, *CS$_1$* Initial value of chaotic sequence
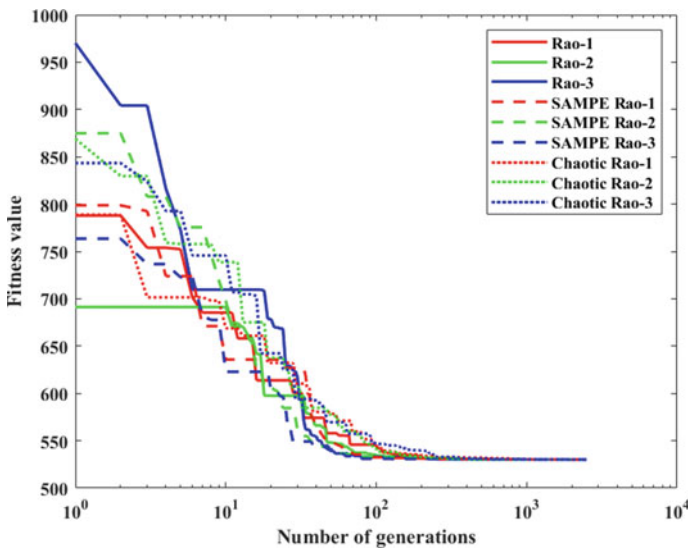
Fig. 5 Convergence plot for the ten bar truss problem-1

5 Conclusions

In this paper, two structural optimization problems of ten bar truss are solved using the Rao algorithms, self-adaptive multi-population elitist (SAMPE) Rao algorithms and chaotic Rao algorithms. The optimal design of the ten bar truss attained using the presented algorithms is compared with the those obtained using other optimization algorithms to show the effectiveness of the presented algorithms. The statistical results of Rao algorithms, SAMPE Rao algorithms and chaotic Rao algorithms are

Table 3 Comparison of optimal design for ten bar problem-2 using different algorithms

Algorithm	f_{min}	A_1	A_2	A_3	A_4	A_5	A_6	A_7	A_8	A_9	A_{10}
ACO[a]	5095.46	30.86	0.1	23.55	0.22	15.01	0.1	7.63	21.65	21.32	0.1
HGAPSO[a]	5061.4	30.63	0.1	23.06	15.01	0.1	0.59	7.49	21.1	21.56	0.1
PSO[a]	5529.5	33.46	0.11	23.17	15.47	3.64	0.11	8.32	23.34	23.01	0.19
WCA[a]	5061.02	30.53	0.1	23.05	15.03	0.1	0.56	7.48	21.12	21.63	0.1
Rao1[a]	5060.9568	30.5227	0.1002	23.2368	15.1605	0.1	0.5661	7.4616	21.0822	21.487	0.1
Rao2[a]	5060.9248	30.4316	0.1003	23.187	15.2439	0.1	0.5556	7.4588	21.0671	21.5524	0.1
Rao3[a]	5060.914809	30.494	0.1	23.1769	15.1519	0.1001	0.5565	7.4655	21.0929	21.5473	0.1
SAMP Rao1[a]	5060.9179	30.4397	0.1	23.2744	15.2244	0.1	0.5673	7.4478	21.0285	21.5401	0.1
SAMP Rao2[a]	5060.8901	30.5175	0.1	23.2595	15.2282	0.1001	0.5422	7.4495	21.0131	21.5238	0.1
SAMP Rao3[a]	5060.9056	30.6059	0.1	23.1606	15.2676	0.1	0.543	7.4659	21.0492	21.4506	0.1
QO-Rao1[a]	5060.9274	30.4877	0.1002	23.1442	15.3299	0.1	0.5624	7.4581	21.0228	21.5225	0.1
QO-Rao2[a]	5060.9113	30.6113	0.1	23.2193	15.1663	0.1	0.5696	7.458	21.0216	21.4938	0.1
QO-Rao3[a]	5060.9136	30.5902	0.1001	23.1012	15.1722	0.1	0.556	7.4675	21.0354	21.5743	0.1
SAMPE Rao1	5060.8908	30.576134	0.100012	23.172501	15.19647	0.1	0.545689	7.458065	21.00616	21.56222	0.1
SAMPE Rao2	5060.8900	30.563172	0.1	23.177081	15.26809	0.1	0.552216	7.453648	20.97761	21.54585	0.1
SAMPE Rao3	5060.8840	30.551849	0.1	23.119761	15.28698	0.1	0.559175	7.460543	21.00636	21.54034	0.1
Chaotic Rao1	5060.9000	30.635388	0.1	23.234186	15.21234	0.1	0.534306	7.457509	21.01874	21.4617	0.1
Chaotic Rao2	5060.8765	30.51544	0.1	23.1954	15.26967	0.100011	0.554081	7.452355	20.99788	21.54496	0.1
Chaotic Rao3	5060.9044	30.508544	0.10003	23.189486	15.27114	0.100006	0.550928	7.452335	20.99723	21.5564	0.1

[a]The results are taken from [12]

Table 4 Statistical result comparison for ten bar truss problem-2

Algorithm	B	M	W	SD	MFE	NP, ES/CS1
SAMPE Rao1	5060.8908	5096.4800	5524.7482	$9.953E + 01$	40,010.0	20, 2
SAMPE Rao2	5060.8900	5089.3144	5409.1376	$7.396E + 01$	43,182.0	20, 2
SAMPE Rao3	5060.8840	5067.5086	5087.1779	$9.239E + 00$	40,679.0	20, 2
Chaotic Rao1	5060.9000	5083.2757	5418.7143	$7.041E + 01$	44,488.0	20, 0.2
Chaotic Rao2	5060.8765	5137.9980	6341.4127	$2.593E + 02$	44,116.0	20, 0.6
Chaotic Rao3	5060.9044	5104.0287	5269.9448	$6.638E + 01$	42,775.0	20, 0.2
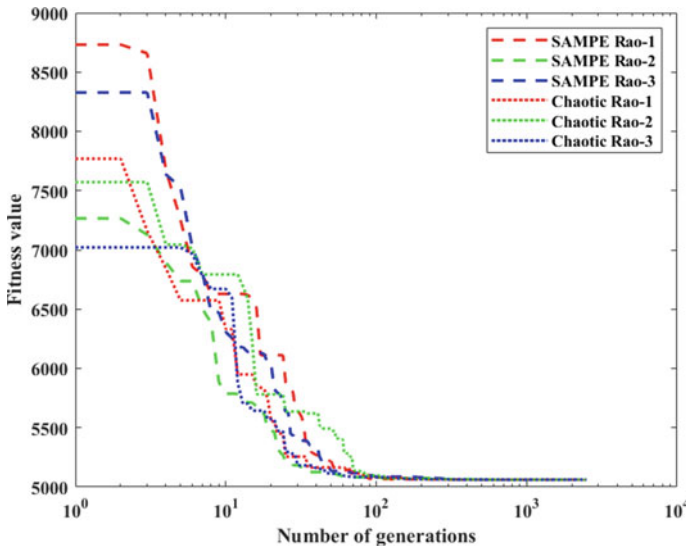
Fig. 6 Convergence plot for the ten bar truss problem-2

also compared. The presented algorithms give better optimal results than the other optimization algorithms for both optimization problems considered.

References

1. Kaveh A, Zolghadr A (2011) Shape and size optimization of truss structures with frequency constraints using enhanced charged system search algorithm. 12(4):487–509
2. Baykasoğlu A, Baykasoğlu C (2021) Weighted superposition attraction-repulsion (WSAR) algorithm for truss optimization with multiple frequency constraints. Structures 30(November 2020):253–264. https://doi.org/10.1016/j.istruc.2021.01.017
3. Sedaghati R, Suleman A, Tabarrok B (2002) Structural optimization with frequency constraints using the finite element force method. AIAA J 40(2):382–388. https://doi.org/10.2514/3.15072
4. Gholizadeh S, Salajegheh E, Torkzadeh P (2008) Structural optimization with frequency

constraints by genetic algorithm using wavelet radial basis function neural network. J Sound Vib 312(1–2):316–331. https://doi.org/10.1016/j.jsv.2007.10.050

5. Salajegheh E, Gholizadeh S, Torkzadeh P (2007) Optimal design of structures with frequency constraints using wavelet back propogation neural. Asian J Civ Eng 8(1):97–111

6. Gomes H (2011) Truss optimization with dynamic constraints using a particle swarm algorithm. Expert Syst Appl 38(1):957–968. https://doi.org/10.1016/j.eswa.2010.07.086

7. Talatahari S, Azizi M, Gandomi A (2021) Material generation algorithm: a novel metaheuristic algorithm for optimization of engineering problems. Processes 9(5):1–35. https://doi.org/10.3390/pr9050859

8. Yu Z, Xu T, Cheng P, Zuo W, Liu X, Yoshino T (2014) Optimal design of truss structures with frequency constraints using interior point trust region method. Proc Rom Acad Ser A Math Phys Tech Sci Inf Sci 15(2):165–173

9. Lamberti L, Pappalettere C (2003) Move limits definition in structural optimization with sequential linear programming. Part I: optimization algorithm. Comput Struct 81(4):197–213. https://doi.org/10.1016/S0045-7949(02)00442-X

10. Eskandar H, Sadollah A, Bahreininejad A, Lumpur K (2013) Weight optimization of truss structures using water cycle algorithm. Int J Optim Civ Eng 3(1):115–129

11. Kaveh A, Hassani M (2009) Simultaneous analysis, dedsign and optimization of structures using force method and ant colony algorithms. Asian J Civ Eng 10(4):381–396

12. Rao RV, Pawar RB, Khatir S, Cuong Le T (2021) Weight optimization of a truss structure using rao algorithms and their variants. In: Lecture notes in civil engineering, vol 148, pp 3–18. https://doi.org/10.1007/978-981-16-0945-9_1

13. Turky A, Abdullah S (2014) A multi-population harmony search algorithm with external archive for dynamic optimization problems. Inf Sci 272:84–95. https://doi.org/10.1016/j.ins.2014.02.084

14. Feng J, Zhang J, Zhu X, Lian W (2017) A novel chaos optimization algorithm. Multimed Tools Appl 76(16):17405–17436. https://doi.org/10.1007/s11042-016-3907-z

15. Rao RV (2020) Rao algorithms: three metaphor-less simple algorithms for solving optimization problems. Int J Ind Eng Comput 11(1):107–130. https://doi.org/10.5267/j.ijiec.2019.6.002

16. Grandhi R (1992) Structural optimization with frequency constraints—a review. In: 4th Symposium of Multidisciplinary Analysis and Optimization, vol 26, no. 7, pp 858–866. https://doi.org/10.2514/6.1992-4813

Crack Identification in Pipe Using Improved Artificial Neural Network

Meriem Seguini, Tawfiq Khatir, Samir Khatir, Djilali Boutchicha, Nedjar Djamel, and Magd Abdel Wahab

1 Introduction

Recently, many new methods have been developed in order to detect the damage of different structures such as beam, pipe, bridge and plates structures. However, the crack identification based on new method, e.g. ANN-PSO, TLBO-PSO-ANN, XFEM, XIGA, IGA and cuckoo search algorithm, etc., has become a very interesting domain and has received significant attention where many researchers work on it. In fact, Gillich et al. [1] studied the free vibration of clamped-free beam and used a new power method to detect the damage on multi modal analysis by taking into account different temperature conditions. The crack identification in beam with multiple cracks has been also studied by Gillich et al. [2], where a simplified method based on the frequency shifts has been used and it has been concluded that when the vibration

M. Seguini · N. Djamel
Faculty of Architecture and Civil Engineering, Department of Civil Engineering, Laboratory of Mechanic of Structures and Stability of Constructions, University of Science and Technology of Oran Mohamed Boudiaf, BP 1505, Oran, Algeria
e-mail: meriem.seguini@univ-usto.dz

T. Khatir
Institute of Science and Technology, Naama University, Naama, Algeria

D. Boutchicha
Laboratory of Applied Mechanics, University of Sciences and Technology of Oran Mohamed Boudiaf, Bp 1505 Elmenouar, Oran, Algeria

S. Khatir (✉) · M. A. Wahab
Faculty of Civil Engineering, Ho Chi Minh City Open University, Ho Chi Minh City, Vietnam
e-mail: Khatir_samir@hotmail.fr

S. Khatir
Soete Laboratory, Faculty of Engineering and Architecture, Ghent University, Technologiepark Zwijnaarde 903, B-9052 Zwijnaarde, Ghent, Belgium

modes were sufficient, the eigenfrequencies were capable of indicating the depth and position of damage. Seguini et al. [3] used the ANN-PSO method to identify also the multiple cracks on two different beams, where the efficiency of the developed models has been proved by making comparison between experimental and numerical results where the percentage of error was very small.

Zhou et al. [4, 5] used the transmissibility and the hierarchical clustering analysis to detect the damage in the structures. In another research, Khatir et al. [6] used the neural network based on the hybrid TLBO and partical swarm optimization (PSO) in order to identify the damage in steel beams. Moreover, several works have been made to investigate the energy approach using on the machine learning concepts in Refs. [7, 8]. Tran et al. [9] used the cuckoo search algorithm combined with neural artificial network (ANN) to detect the damage in bridge and beam-like structures. A novel machine learning method has been also used by the same authors in Ref. [10] to identify the damage in structures by using vectorized data. Different other new methods have been also used to identify the crack in plates using improved ANN technique for solving crack identification based on XFEM, XIGA, PSO and Jaya algorithm [11, 12]. However, the influence of the depth and position of cracks on the response of the pipe has been studied by different researchers [13–17]. In fact, Seguini et al. [14, 15] used the ANN-PSO method in order to identify the crack in the pipes, where numerical and experimental modal analysis have been done and the measured frequencies of cracked and uncracked pipe have been deduced for each depth crack. The obtained results reveal the importance and the efficiency of the ANN-PSO method. The present study focuses on the numerical modal analysis of the cracked pipe by using finite element analysis combined with GA-ANN. However, a new approach has been used in order to identify the crack in the pipe, where many simulations have been generated by using MATLAB software until the convergence is reached. From this analysis, the values of frequencies of three modes shape have been deduced for each depth crack. The noticeable in the present work is that GA-ANN allows us to improve the results and obtain an exact solution in short times instead of inverse analysis.

2 Finite Element Analysis

In this section, 3D finite element model of pipe has been modelled by using ANSYS software, where the mechanical and geometrical properties are presented in Table 1 [14]. A multiples cracks depth has been created in the middle, on the left and right side of the pipe. The cracks have been extended from 2 to 16 mm, and two scenarios have been studied as shown in Figs. 2 and 3. The frequencies of scenarios 1 and 2 are listed in Table 4 (Appendix). The FEM including mesh type is presented in Fig. 1.

However, in order to demonstrate the important effect of multiple cracks on the pipe response, a crack with different depths has been created in the middle and right of the pipe (scenario 1), and another double crack has been created on the middle and left side of the pipe (scenario 2). The natural frequencies of the third modes have

Table 1 Mechanical properties of the pipe [14]

Item	Value
Length Lp (mm)	1000
Diameter Dp (mm)	50
Density ρ (Kg/m^3)	7850
Poisson ratio υp (/)	0.3
Young modulus Ep (MPa)	61950
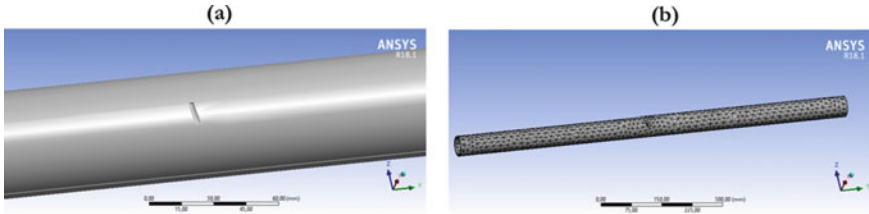
Fig. 1 Cracked pipe: **(a)** Finite Element Model and **(b)** meshed pipe
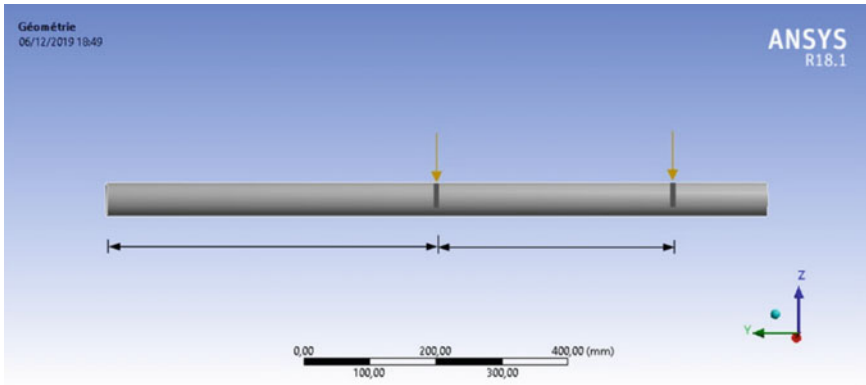
Fig. 2 Pipeline with double notched (scenario 1): middle crack and right crack

been determined for different depths of crack and listed on Table 4 of the Appendix, where some examples have been chosen and illustrated as shown on Figs. 4 and 5. From Table 4, it can be seen that the values of the natural frequencies decrease for the three mode and by comparing the results obtained from the two scenarios, it can be deduced that there is a small difference between the frequencies of the three mode shapes.
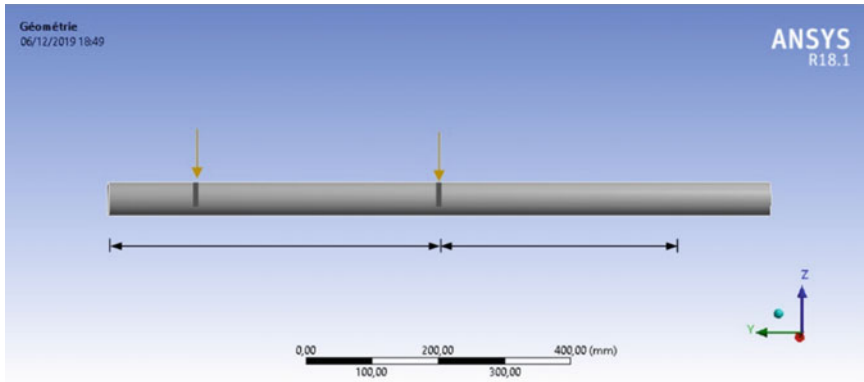
Fig. 3 Pipeline with double notched (scenario 2): middle crack and left crack

3 Results and Discussion

GA is an optimization method based on natural selection and on the class of evolutionary algorithms. The objective of using GA is to find the best solution after combining with ANN. The purpose is to find the best weight and bias during the training process. Through series of damage location tests, the following genetic parameters were chosen precisely in order to obtain an accuracy result: the number of generations of 500, population size of 200. This technique is implemented in MATLAB.

In the first scenario, the regressions of ANN of each hidden layer size ($n = 4, 6$ and 8) are presented in Fig. 6 and the predicted results are resumed in Table 2. It can be deduced that GA provides accurate results for $n = 6$ based on the convergence study and regression value compared with others. Based on the obtained results, we can resume that GA can predict the crack depth 5.5 and 12.5 mm accurately for different hidden layer sizes, where the results are represented by bar graph (Fig. 7). In the second scenario, the same number of hidden layers has been adopted. The regression of GA is presented in Fig. 8, where the obtained results are presented in Table 3. However, the best convergence is found for $n = 4$ compared with others. From the obtained results, we can deduced that GA can predict the crack depth 7.5 and 14.5 mm accurately for different hidden layer sizes, where the results are also represented by bar graph as shown in Fig. 9.

4 Conclusion

Nowadays, great complex problems have been solved by using different numerical methods. However, in our study, GA-ANN was utilized for identifying the damage of multiple cracks on the pipe. However, numerical analysis has been
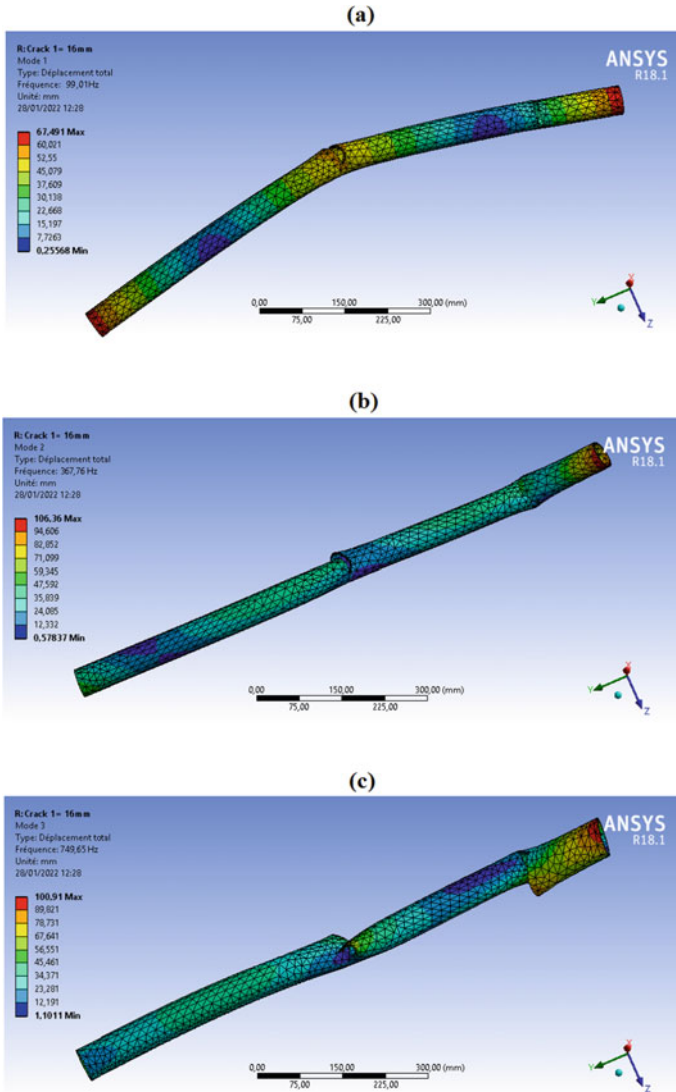
Fig. 4 Natural frequencies for different modes of double notched pipe (scenario 1): **(a)** mode 1, **(b)** mode 2 and **(c)** mode 3 of pipe with cracks of 16 mm

done and two scenarios have been studied. The values of the frequencies of the first three modes have been deduced for each crack depth and position, where the convergence of the results has been proved through the proposed method.

From this work, it has been noted that interesting results have been obtained when a multiple-crack scenario has been considered, and by adopting the GA-ANN method, the accuracy of the results has been proven.
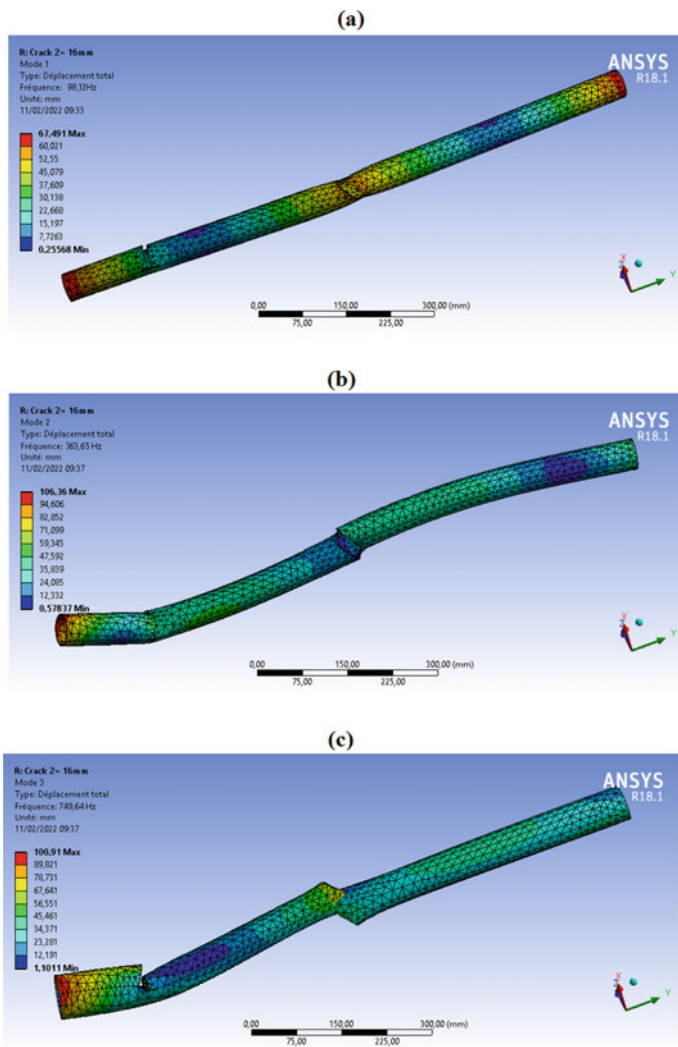
Fig. 5 Natural frequencies for different modes of double notched pipe (scenario 2): **(a)** mode 1 **(b)** mode 2 and **(c)** mode 3 of pipe with cracks of 16 mm
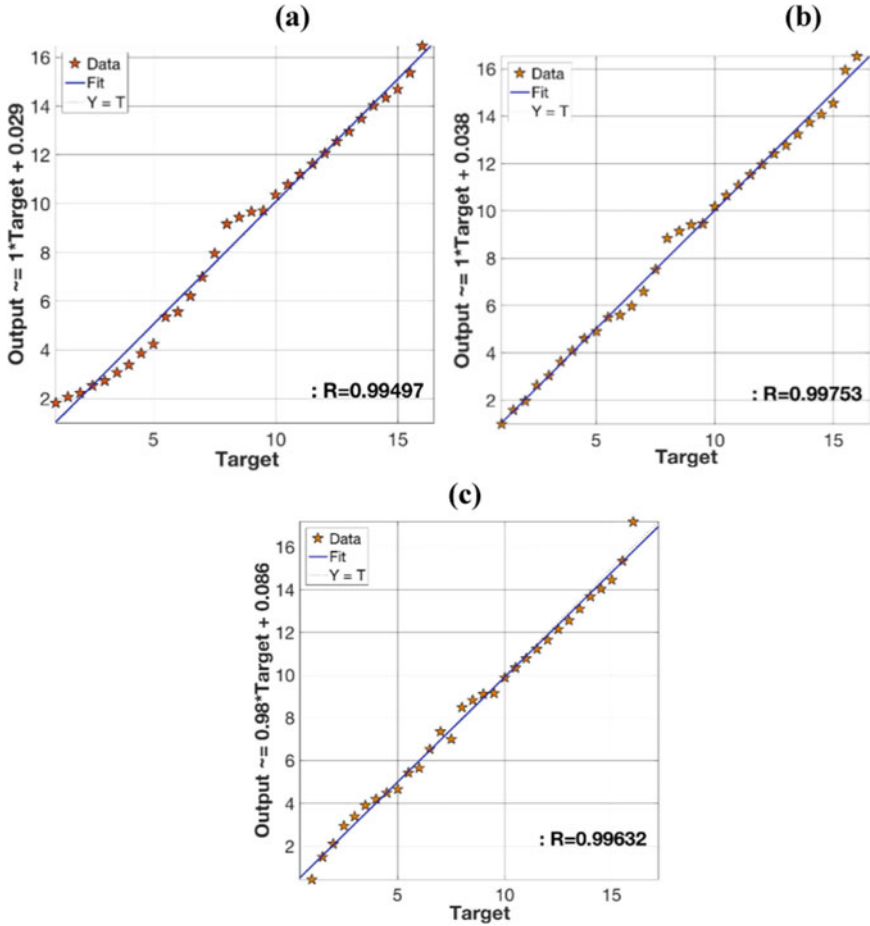
Fig. 6 Regression with different numbers of hidden layer size (scenario 1): (**a**) $n = 4$, (**b**) $n = 6$ and (**c**) $n = 8$

Table 2 Actual crack length (scenario 1)

n	Test	Crack depth (mm)	
		GA-ANN	Real crack depth
4	2	5.35	5.5
6	3	5.49	5.5
8	4	5.42	5.5
A	5	5.42	5.5
4	6	12.55	12.5
6	7	12.42	12.5
8	8	12.15	12.5
A	9	12.37	12.5

Fig. 7 Real and predicted crack depth by using different hidden layer size for scenario 1
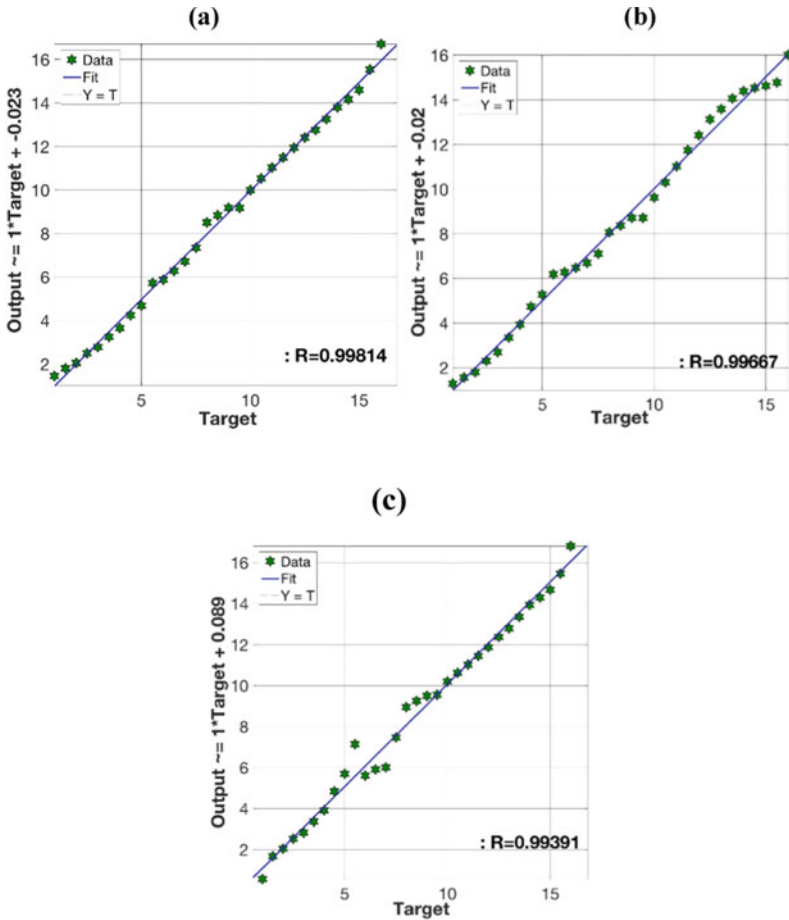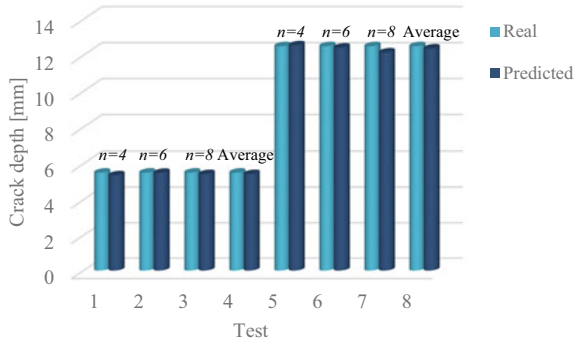
Fig. 8 Regression with different numbers of hidden layer size (scenario 2): (**a**) $n = 4$, (**b**) $n = 6$ and (**c**) $n = 8$

Table 3 Actual crack length (scenario 2)

n	Test	Crack depth (mm)	
		GA-ANN	Real crack depth
4	2	7.16	7.5
6	3	7.11	7.5
8	4	7.46	7.5
A	5	7.24	7.5
4	6	14.49	14.5
6	7	14.13	14.5
8	8	14.30	14.5
A	9	14.31	14.5

Fig. 9 Real and predicted crack depth by using different hidden layer size for scenario 2
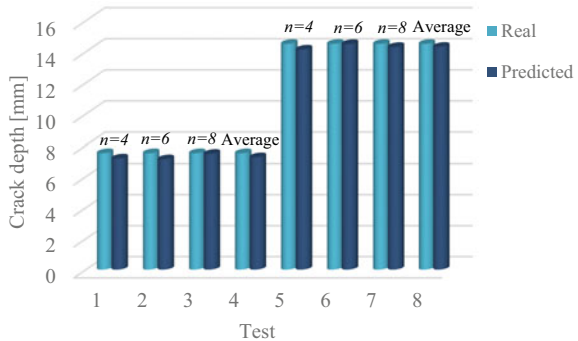
Appendix

See Table 4.

References

1. Gillich GR, Praisach ZI, Abdel Wahab M, Gillich N, Mituletu IC, Nitescu C (2016) Free vibration of a perfectly clamped-free beam with stepwise eccentric distributed masses. J Shock Vib. https://doi.org/10.1155/2016/2086274
2. Gillich GR, Maia MM, Wahab MA, Pop MV (2021) Damage detection on a beam with multiple cracks: a simplified method based on relative frequency shifts. https://doi.org/10.20944/preprints202107.0240.v1
3. Seguini M, Boutchicha D, Khatir S, Nedjar D, Waheb MA (2022) Crack prediction in beam-like structure using ANN based on frequency analysis. Frattura ed Integrità Strutturale 59:18–34. https://doi.org/10.3221/IGF-ESIS.59.02
4. Zhou YL, Maia NM, Sampaio RP, Wahab MA (2017) Structural damage detection using transmissibility together with hierarchical clustering analysis and similarity measure. Struct Health Monit 16:711–731. https://doi.org/10.1177/1475921716680849

Table 4 Frequencies of different cracks depths for scenarios 1 and 2

Crack depth (mm)	Scenario 1			Scenario 2		
	Mode 1	Mode 2	Mode 3	Mode 1	Mode 2	Mode 3
1–1	288.42	774.22	1452	288.418	774.22	1452.1
1.5–1.5	286.20	772.10	1444.9	286.189	773.13	1444.854
2–2	284.59	769.01	1431.19	284.523	765.495	1431.123
2.5–2.5	281.43	765.54	1422.04	281.385	765.513	1422
3–3	279.14	763.34	1407.42	279.123	763.319	1047.391
3.5–3.	275.087	760.98	1397.03	275.015	760.912	1396.98
4–4	271.042	758.60	1385.03	271.016	758.539	1384.982
4.5–4.5	264.251	746.56	1341.87	264.236	746.498	1341.79
5–5	257.989	736.78	1301.08	257.983	736.742	1301.01
5.5–5.5	237.114	712.65	1250.764	237.109	712.596	1250.703
6–6	233.145	680.342	1189.54	233.129	680.328	1189.490
6.5–6.5	220.762	669.041	1106.54	220.759	669.038	1106.501
7–7	208.072	664.23	1089.34	208.072	664.18	1089.29
7.5–7.5	195.321	643.70	1046.56	195.308	643.689	1046.442
8–8	182.09	598.76	1002.12	182.079	598.712	1002.10
8.5–8.5	179.31	574.23	969.76	179.297	542.7293	969.712
9–9	176.97	542.732	941.432	176.5192	542.701	941.381
9.5–9.5	176.521	522.436	921.43	176.5186	522.432	921.392
10–10	170.207	514.34	913.543	170.204	514.281	913.540
10.5–10.5	166.01	500.325	908.239	165.983	500.252	908.178
11–11	161.81	495.87	905.76	161.791	495.854	905.73
11.5–11.5	157.354	469.543	887.654	157.339	469.538	887.947
12–12	152.795	450.765	856.43	152.791	450.760	856.379
12.5–12.5	147.129	430.543	843.87	147.118	430.538	843.80
13–13	142.337	413.965	826.634	142.328	413.942	826.609
13.5–13.5	135.541	407.82	818.04	135.537	407.77	817.98
14–14	128.145	397.052	813.072	128.140	397.01	812.987
14.5–14.5	123.436	382.954	798.0614	123.401	382.938	797.858
15–15	118.297	379.439	787.543	118.289	379.417	787.526
15.5–15.5	108.439	370.03	766.92	108.416	368.43	766.83
16–16	99.01	363.765	749.650	98.12	363.649	749.642

5. Zhou YL, Maia NM, Abdel Wahab M (2018) Damage detection using transmissibility compressed by principal component analysis enhanced with distance measure. J Vib Control 24:2001–2019. https://doi.org/10.1177/1077546316674544

6. Khatir S, Boutchicha D, Le Thanh C et al. (2020) An efficient hybrid TLBO-PSO-ANN for fast damage identification in steel beam structures using IGA. Smart Struct Syst 25:605–617. https://doi.org/10.12989/sss.2020.25.5.605

7. Guo H, Hamdia K, Zhuang X, Rabczuk T (2020) An energy approach to the solution of partial differential equations in computational mechanics via machine learning: concepts, implementation and applications. Comput Methods Appl Mech Eng 362:112790. https://doi.org/10.1016/j.cma.2019.112790

8. Samaniego E, Anitescu C, Goswami S, Nguyen-Thanh VM, Guo H, Hamdia K, Zhuang X, Rabczuk T (2020) An energy approach to the solution of partial differential equations in computational mechanics via machine learning: concepts, implementation and applications. Comput Methods Appl Mech Eng 362:112790. https://doi.org/10.1016/j.cma.2019.112790

9. Tran-Ngoc H, Khatir S, De Roeck G, Bui-Tien T, Wahab MA (2019) An efficient artificial neural network for damage detection in bridges and beam-like structures by improving training parameters using cuckoo search algorithm. Eng Struct 199:109637. https://doi.org/10.1016/j.engstruct.2019.109637

10. Tran-Ngoc H, Khatir S, Le-Xuan T, De Roeck G, Bui-Tien T, Wahab MA (2020) A novel machine-learning based on the global search techniques using vectorized data for damage detection in structures. Int J Eng Sci 157:103376. https://doi.org/10.1016/j.ijengsci.2020.103376

11. Khatir S, Magd AW (2019) A computational approach for crack identification in plate structures using XFEM, XIGA, PSO and Jaya algorithm. Theoret Appl Fract Mech 103:102240. https://doi.org/10.1016/j.tafmec.2019.102240

12. Khatir S, Boutchicha D, Le Thanh C, Tran-Ngoc H, Nguyen TN, Abdel-Wahab M (2020) Improved ANN technique combined with Jaya algorithm for crack identification in plates using XIGA and experimental analysis. Theor Appl Fract Mech 107:102554. https://doi.org/10.1016/j.tafmec.2020.102554

13. Li D, Lu D, Hou J (2017) Pipeline damage identification based on additional virtual masses. Appl Sci 7:1040. https://doi.org/10.3390/app7101040

14. Seguini M, Khatir S, Boutchicha D, Nedjar D, Wahab MA (2021) Crack prediction in pipeline using ANN-PSO based on numerical and experimental modal analysis. Smart Struct Syst 27(3):507–523. https://doi.org/10.12989/sss.2021.27.3.507

15. Seguini M, Khatir S, Boutchicha D, Nedjar D, Waheb MA (2020) Experimental and numerical vibration analyses of healthy and cracked pipes. In: 1st international conference on structural health monitoring and engineering structures (SHM&ES), pp 15–16

16. Dilena M, Dell'Oste MF, Morassi A (2011) Detecting cracks in pipes filled with fluid from changes in natural frequencies. J Mech Syst 25:3186–3197. https://doi.org/10.1016/j.ymssp.2011.04.013

17. Lee JW, Kim SR, Huh YC (2014) Pipe crack identification based on the energy method and committee of neural networks. Int J Steel Struct 14:345–354. https://doi.org/10.1007/s13296-014-2014-0

Evaluating the Remaining Flexural Capacity of a CFRP Composite Beam Having Cracked Cross-Section—A Comparison with ACI 440.2R (2017) for a Case Study

Tham Hong Duong

1 Introduction

Carbon fiber reinforced polymers or plastics (CFRP) are used to strengthen the structure, especially reinforced concrete. They play a role of a supplementary element stuck on the soffit of the beams or around the columns to induce the tensile stress together with the armature. With the low weight but high stiffness of tension, and high strength as well, CPRP is an applicable and efficient solution for increasing the FC of transversal structures. In some specific cases of overloading, the existing structure could have some cracks and the bending moment will be reduced; the structure could deflect more and the demand is to strengthen it. The CFRP is suitable to apply for the structure because of its simple approach and the satisfactory cost, especially for protecting the damaged structures from being attacked by corrosion in reinforcement [1]. The bending bearing capacity together with the stiffness is improved in a certain way. The adhesion between the polymers and structures is the most important factor to ensure the simultaneous working condition between the two kinds of materials. And the failure of such a composite structure occurs when the bond is disappeared or debonding condition (DC). Many previous research works indicated that: the flexural moment will be different according to the stage of.

- No cracks appears
- Crack begins
- Cracked beam with CFRP
- Failure due to debonding.

For the first two stages, ACI 440.2R (2017) regulation assumed there is a perfect bond between the concrete and CFRP, or there is no relative displacement between

T. H. Duong (✉)
Ho Chi Minh City Open University, Ho Chi Minh City, Vietnam
e-mail: tham.dh@ou.edu.vn

the beam and the polymers, and a coefficient is given to take this issue into account [2]; the failure for the beam strengthened by the polymers will fail at the time of debonding, and rupture due to bending occurs simultaneously so that the strain in CFRP will attain the efficient strain ε_{fe} calculated by the regulation; this strain level guarantees the bond of the polymer during appearing the cracks in concrete and not greater than a specified value $k_{\text{m}}\varepsilon_{\text{fu}}$ for a certain kind of polymer [2]. And the main assumption is that at failure, the steel reinforcement will attain the yield stress f_{y} in the debonding condition of the polymers. This assumption is practically acceptable, concerning the linearity of the strain at the cross-section of the structure; besides, several coefficients are applied during the process of locating the neutral axis (N.A), resulting in the nominal flexural moment [2]. As such, the main key for determining the flexural is the location of the N.A. Due to the appearance of cracks with different levels of damage, and CFRP, the position of the N.A changes, resulting in a variation in section properties. The flexural capacity of the structure strengthened by CFRP depends on many factors, including the materials, cracked section before retrofitting, and the stress–strain relationship, etc. The problem is indeed a rather complex one. The normal procedure is that the N.A will be assumed first, then all the strain in all the components of the beam will be formulated, i.e., strain in CFRP and steel rebar, then stress in steel σ_{s}, and coefficients for an equivalent block of the compressive stress in concrete [3, 4]. Finally, the N.A determined by the abovementioned process is compared to the value assumed in the beginning. If the difference in the location of the N.A is less than 0.1 mm, then the N.A is re-determined and the bending moment is calculated using the static equilibrium equations.

Another key point is that the nonlinear stress–strain relationship should be taken into account [4]. During various stages of the structure, different cases could happen: Concrete might be crushed when the steel has not attained the yield stress, or the steel yields then the concrete is crushed; in case, the situation could be that the polymers lose the adhesion (debonding condition attained) before the steel yields and other styles of failure, etc. As such, a problem is that how to assess the flexural moment for the cracked beam, strengthened with the polymer, and all the issues for the analyzing model will be considered rigorously. This study will analyze the different stages of an existing cracked beam, strengthened with CFRP, and the target for the study aims to predict the bending capacity of the structure, i.e., $M_{\text{cr}} < M < M_{\text{u}}$, where M_{u} is the final moment or the ultimate value of the moment of the reinforced structure, then a comparison between the M_{u} to the ultimate bending capacity specified by the ACI 440.2R (2017) is made.

2 Method

2.1 Some Theoretical Points to Be Learned

Material Concrete and steel have the compressive strength f'_c and yield strength f_y, respectively. The stress block in the compressive zone of the cross-section has a rectangular equivalent block, and a (Fig. 1b) or β could be determined by the ACI 440.2R (2017) and by the nonlinear stress–strain relationship as detailed in this study [5, 6].

As a rule, the concrete in the compressive zone of a beam will fail at the ultimate strain $\varepsilon_f = \varepsilon_{cu} = 0.003$; the maximum stress in the concrete is taken as $0.85\,f'_c$. The strain in concrete and steel will be linear as per Bernoulli's assumption [2, 7].

Initial Strain of the Concrete The structure at the beginning time of crack will deflect at M_{cr}. If being strengthened by CFRP, the elongation in the polymers will be

$$\varepsilon_{bi} = \frac{M_{DL}(d - kh)}{I_{cr}E_c} \tag{1}$$

in which M_{DL} is the bending moment due to dead load on the beam, d is the efficient depth of the cross-section, k is the ratio between the height of the N.A and d of the cracked section without the polymers, h is the height of the cross-section, and the denominator is the bending stiffness of the cracked concrete section. The factor k is like below [5]:

$$k = \sqrt{2\left[\rho_s n_s + \rho_f n_f\left(\frac{d_f}{d}\right)\right] + (\rho_s n_s + \rho_f n_f)^2} - (\rho_s n_s + \rho_f n_f) \tag{2}$$

Steel The existing percentage of reinforcement will be prescribed, with or without compression steel. The yield strength is f_y, and the strain will be calculated from the strain of concrete $\varepsilon_c = \varepsilon_{cu}$ with an assumed location c of the N.A (Fig. 1). By installing the CFRP, the strain in the polymer will be taken the initial strain given by Eq. (1) into account, as follows:
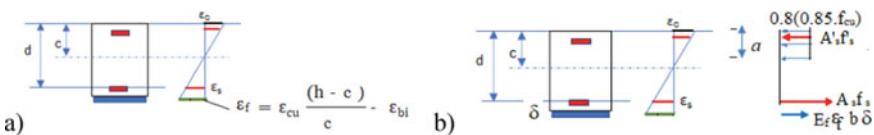
Fig. 1 Cross-section of a cracked beam, strengthened with CFRP and the linear stress–strain relationship. For calculating the stress in polymer, the initial strain ε_{bi} is assumed. (**a**) Strain distribution in a cross-section; (**b**) Stress block diagram in a cross-section

$$\varepsilon_f = \varepsilon_{cu} \frac{(h - c)}{c} - \varepsilon_{bi} \qquad (3)$$

Stress–Strain Relationship as per ACI440.2R (2017) The relationship is linear. Concrete is crushed at the strain $\varepsilon_f = \varepsilon_{cu} = 0.003$, and the maximum stress is 0.8 $(0.85 f_{cu})$ concerning the equivalent compressive force in the concrete. The compressive strength is f_c', or $0.85 f_{cu}$, and the stress is uniformly distributed over a reduced height a that is determined by taking the equilibrium of all the lateral forces applied in the cross-section, as below:

$$\Sigma F_x = 0 \Leftrightarrow 0.8(0.85 f_{cu})a \cdot b + A_s' f_s' = A_s f_s + A_f(E_f \varepsilon_f)b \cdot \delta \qquad (4)$$

in which A_s' is the total area of steel in compression zone; E_f, ε_f, b, and δ are the modulus of elasticity, strain, width, and thickness of the CFRP layer, respectively.

2.2 Flowchart for Determining the N.A of CFRP Reinforced Structures

ACI 440.2R (2017) The neutral axis is assumed first, normally taken as $c = 0.2d$, and the process of calculation depends on the two-step algorithm, the first step is B_1 = appearing the cracks, and the second step is B_2 = debonding or FRP rupture [6]. This algorithm is summarized in the flowchart in Fig. 2.
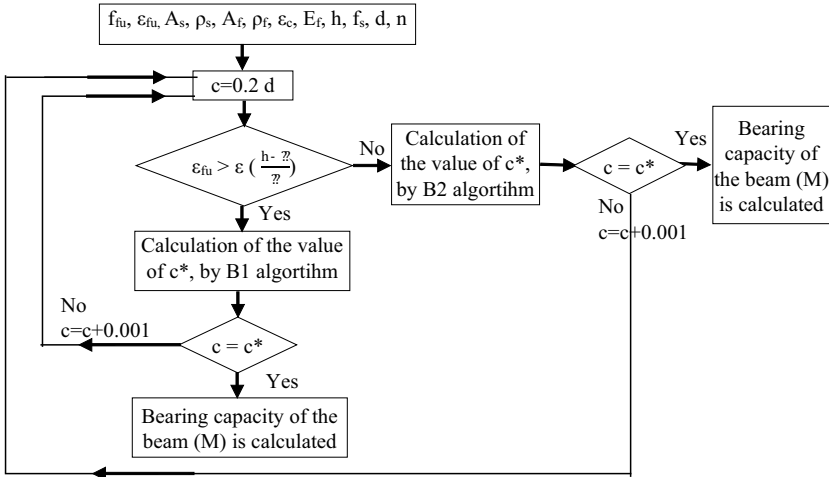
Fig. 2 Calculation algorithm of bending moment capacity of beam cross-section with CFRP

Some characteristic factors in the approach of the ACI 440.2R (2017) are below [5]:

$$\beta_1 = \frac{4\varepsilon_c' - \varepsilon_c}{6\varepsilon_c' - 2\varepsilon_c} \tag{5a}$$

$$\alpha_1 = \frac{3\varepsilon_c'\varepsilon_c - \varepsilon_c^2}{3\beta_1\left(\varepsilon_c'\right)^2} \tag{5b}$$

$$\varepsilon_c' = 1.71\frac{f_c'}{E_c} \tag{5c}$$

in which, ε_c' (Eq. 5c is in units psi) is the maximum value of strain in concrete. The location of the N.A and the factors in the formulas (5a) and (5b) could be determined differently by various authors because the national standards originated from ACI 318–14 and ACI 440.2R (2017) [5, 6].

Analytical Approach The softening concrete results in a nonlinear stress–strain relationship, and the neutral axis at crack appearance is determined by the Eq. (6) [7].

$$x^2\left(\frac{E_{bf}}{(1 + n_\sigma)} + \frac{E_{btu}^{bending}}{(1 + f_t)}\right)b + x\left[E_{cfrp}b\delta + E_s A_s + 2E_{btu}^{bending}bh/(1 + f_t)\right]$$
$$- E_{cfrp}b \cdot \delta h - E_s A_s h_o - E_{btu}^{bending}bh^2/(1 + f_t) = 0 \tag{6}$$

$$n_\sigma = 1 - (1 - f_b)\left(\frac{\sigma_{b,u}}{R_b}\right)^{m_M} \tag{7}$$

$$f_b = \frac{G_{b,u}}{E_b^o} \tag{8}$$

in which n_σ and f_t are factors concerning the shape of the stress diagram, i.e., nonlinear stress–strain relationship; $G_{b,u}$ and E_b^o are respectively the shear modulus at failure condition and initial modulus of deformation. Eq. (5) determined the location of the N.A x from which the bending moment at the time of appearing cracks.

$$M_{cr,f} = \frac{E_{bf}bx^3}{(2 + n_\sigma)}b + \left[E_{cfrp}b\delta(h - x)^2 + E_s A_s(h_o - x)^2\right]$$
$$+ E_{btu}^{bending}b(h - x)^3/(2 + f_t) \tag{9}$$

The above mentioned bending moment will compare to that given by ACI 440.2R (2017) for the stage of crack appearance. For the flexural moment at failure, M_u, with a special notation on the nonlinearity in the stress–strain relationship, the N.A x will be determined by the following equation:

$$\left(\frac{R_{\text{bf}}}{\varepsilon_{\text{bu}}^{\text{bending}}(1+f_{\text{b}})}\right)x^2 + \left[E_{\text{cfrp}}b\delta + E_{\text{s}}A_{\text{s}}\right]x - E_{\text{cfrp}}b \cdot \delta h - E_{\text{s}}A_{\text{s}}h_{\text{o}} = 0 \quad (10)$$

And the moment at failure of a cracked beam strengthened with CFRP is as below:

$$M_{\text{u}} = \left(\frac{R_{\text{b}}bx^2}{(2+f_{\text{b}})}\right) + \varepsilon_{\text{bu}}^{\text{bending}}\left[E_{\text{cfrp}}b\delta(h-x)^2 + E_{\text{s}}A_{\text{s}}(h_{\text{o}}-x)^2\right] \quad (11)$$

2.3 A Specific Example for Illustration

For studying the bending moment or FC (FC) of the cracked beam retrofitting with CFRP, some specified properties are in Table 1. The existing beam for evaluating the FC has the cross-section as in Fig. 3a; the domain of expected moment is shaded in Fig. 3b, i.e., $M_{\text{cr}} < M < M_{\text{u}}$.

A specific reinforced concrete RC beam has the cross-section $b = 0.3$ m and $h = 0.6$ m, and its span is $L = 5.9$ m. The beam is loaded until a crack appears; the moment M_{cr} is predicted. Then, the beam is strengthened by CFRP with specification as in Table 1. It is necessary to predict the remaining FC, both in analytical approach and in the numerical method using SAP2000 [9].

Table 1 Materials used in this study

Material	Modulus of elasticity (MPa)	Strength (MPa)	Ultimate strain	Poisson's ratio
Concrete	3.5e4	17	0.003	0.2
Steel	2.1e5	400	ε_{sy}	0.3
CFRP	1.3e5	100	ε_f	0.2
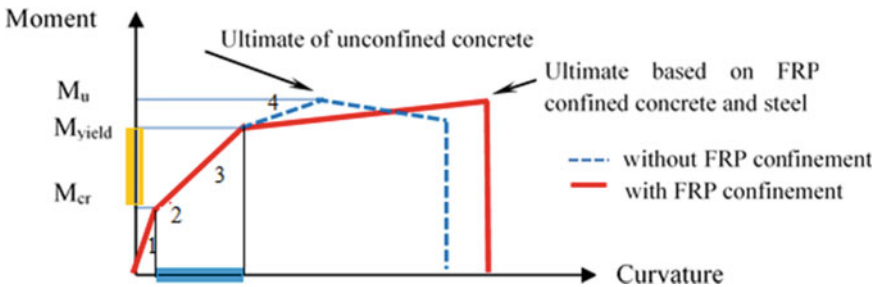
Fig. 3 Remaining FC of beam strengthened CFRP is between M_{cr} and M_{yield} [8]

3　Results

3.1　Model of Planar Frame with Beams Strengthened with CFRP

A specific beam in a 10-story planar frame is analyzed (Fig. 4a). Cross-sections of the main elements with cracks are selected as shown in Table 2. The properties of a cracked beam are calculated with the location of the N.A obtained by the two approaches, not as recommended by ACI or $0.35I_{gr}$ for the appearance of CFRP. The bending moment in the middle of the span for the 1st-story beam is displayed in Fig. 4b, and a part of the beam with positive bending moment is viewed to be a simple support beam with 5.9 m span. The task aims to predict the remaining FC of this beam.

The remaining FC of a 9 m-span reinforced concrete beam with 30×60 in cracked cross-section, retrofitting with CFRP is evaluated. In the conventional case, the maximum positive bending moment is assumed to be approximately $M = 107$ kNm and under the gravity factored load cases (Fig. 4). With a predetermined percentage of tensile reinforcement 1% and the minimum percentage of the compression armature, section 30×60 ($d = 52$ cm) is proved easily to be a cracked one. As recommended by the ACI 318-11 (1999) [5], in which the armature is transformed into an equivalent concrete, the moment at crack appearance is only $M_{cr} = 72$ kNm. At this early stage, the cracks appear, and a measure of using CFRP as a reinforcement is considered.

Fig. 4 Bending moment $M = 107$ kNm in the middle of the beam without CFRP. (**a**) Model of building to be studied; (**b**) Shear diagram and bending moment in the beam under consideration

Table 2 Dimensions of the reinforced concrete frame in this study

Material	Exterior column	Interior column	Beam ($w \times h$)	Span	Properties
1st–4th story	40×60	50×50	30×60	$9 + 2 + 9$	Cracked beams, not columns
4th–7th story	40×50	40×40			
7th–10th story	30×50	30×30			

With CFRP specification as in Table 1, the polymer will be planned to stick under the bottom of the beam, 1 mm in thickness. The main task is to calculate the remaining capacity of the cracked beam after retrofitting CFRP.

3.2 The Calculated Flexural Moment of the Beam Strengthened with CFRP

The process of calculating the FC for a beam of a 2D frame in Fig. 4a is implemented by using the algorithm as mentioned in the flowchart of Fig. 2. The algorithm complies with ACI 440.2R (2017), but its procedure takes two branches of calculation relating the two stages of working in concrete: crushing and debonding.

An alternative to determine the FC of a beam strengthened by CFRP is to take the nonlinear stress–strain relationship of concrete into account. The nonlinearity is represented by parameters n_σ and f_t in Eqs. (7), (8). The strain in the upper edge of compressive concrete is $\varepsilon_{bu}^{bending}$.

A worksheet is developed (see Appendix) to combine all the iteration processes of calculation according to the algorithm in Fig. 2 and compare to the other approach in which the nonlinear distributed stress diagram in Fig. 5 is taken into account. In this worksheet, the vertical blue arrow stands for the two-branch algorithm, or "$B1$ and $B2$ algorithm" [3], and the horizontal one stands for the analytical approach of the nonlinear stress–strain relationship. Both approaches give the same results about the location of the N.A of the cracked beam, $c = 0.203 \pm 0.001$ m. The error between the two values of the N.A is due to the nonlinear parameters n_σ, f_t, and other ones involved in the latter approach. Then, the FC of the beam strengthened with CFRP is calculated to be $M_{yield} = 302$ kNm, or 2.8 times the moment at the time of crack appearance; the analytical approach and finite element model are comparable, and the agreement between the two models confirms the results.
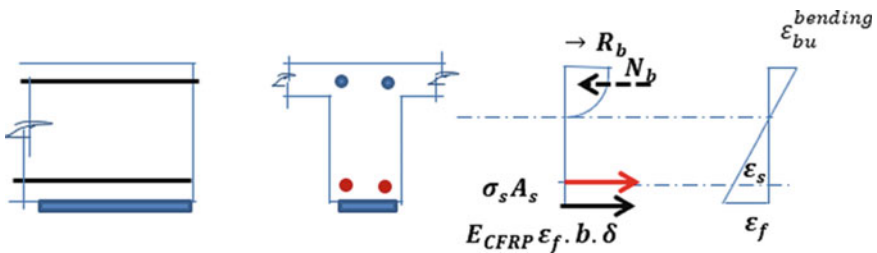
Fig. 5 ACI's diagram of stress and strain in the beam retrofitting with CFRP
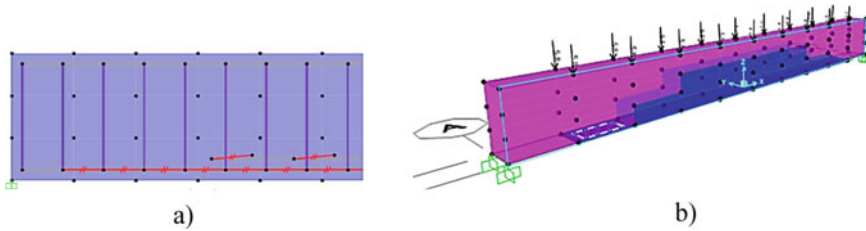
Fig. 6 **a** Beam as a solid element with the bond between rebars and concrete as LINK elements, **b** crushed concrete to be modeled has a very low stiffness and density

3.3 Validation of the Results

Results from ACI's *B*1 and *B*2 algorithm [3] and the analytical approach [7] require some validation. The best validation may come from laboratory tests, using a small scaled model. However, to account for many different factors and save time in real tests, a numerical model should be studied first, as shown in Fig. 6. It is necessary to refer to some prior research work on the procedure to simulate the beam retrofitting CFRP [4, 10, 11]. The stiffness which reduces to zero in crushed concrete is replaced by a very low E material. For a cracked cross-section, the location of the N.A is assumed and modeled as in Fig. 6.

Program of testing includes steps as follows: Assuming the location of the N.A in a model of a simple beam with existing cracks, the vertical loads are applied to the beam. The CFRP sheet is modeled by a very thin element, 1 mm of thickness; the polymer is converted from the solid element, and link element is used to model the bond between the two materials steel and concrete. The existing cracked cross-section with a pre-assumed percentage of reinforcement is loaded in steps until the stress in rebar yields.

This stage recognizes that the stress in compressive concrete is about 6,501e3 kPa, nearly equals the value in worksheet, i.e., $\sigma_c = 6.6$e3 kPa at which the steel yields ($\sigma_s = f_y$). And the stage indicates the strain $\varepsilon_c = 0.000177$, much smaller than that at yielding stage in the steel (in the worksheet, this value is $\varepsilon_s = 0.0021$) (Fig. 7).

Ultimate Moments From the numerical model, some key results are indicated as follows:

- The 5.9 m-span simple beam with load as in the SAP2000 model gives the $\varepsilon_c = 0.000177$ and $\sigma_c = 6.501$e3 kPa; this stage, bending moment would be $M = 91.35$ kNm, far below the values of strain at failure (i.e., stress in steel is $\sigma_s = 4400$ kPa), $M_u = M_{\text{yield}} = 302$ kNm, $\varepsilon_c = 0,00,135$, and $\sigma_c = 6.6$e3 kPa which are confirmed independently by two different approaches (see Appendix).
- While the cracking moment is theoretically between 72 and 77kNm (i.e., cracking moment as per ACI, or M_{cr}), and in SAP2000 model $M = 105$ kNm, but the ultimate moment at failure would be $M_u = 302$ kNm, then the stress in concrete attains $\sigma_c = 18,330$ kPa (crushing concrete, due to $\sigma_c > R_b$), and the σ_s far exceeds
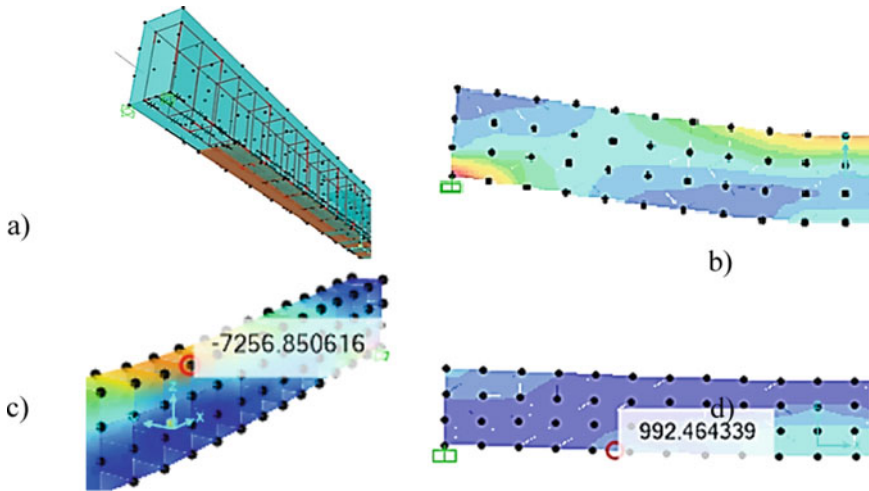
Fig. 7 (**a**) Model of the beam, strengthened with 1mm-thick CFRP sheet; (**b**) Steel yields at strain in concrete $\varepsilon_c = 0.000177$; (**c**) Stress in concrete at yield stress in rebar; (**d**) Cracks appear when maximum principal stress approximates $R_{bt} = 1000$ kPa

the tensile strength f_y. This value is greater than that of the worksheet (i.e., by analytical approach and ACI 440.2R, i.e., 6600 kPa).

- As such, at $M_u = 302$ kNm, not only concrete is crushed, the steel rebar is failed ultimately, and CFRP is coming closer to the tensile strength, or $\sigma_s = 71,110$ kPa. This value could be same as the debonding moment by ACI 440.2R (refer the worksheet in Appendix) as well.

- The small strain in the lower fiber of the beam is from the CFRP. CFRP stress $\sigma_f = 0.000257 (\times 1.3e8) = 33,410$ kPa (cell **B11** in the worksheet of the Appendix) is much smaller than strength $\sigma_{f,u} = 100,000$ kPa. This confirms the efficient role of CFRP in retrofitting the cracked concrete beam. Only when bending moment $M_u = M_{yield} = 302$ kNm, this strain attains 4.92e-4, i.e., stress in CFRP is $\sigma_f = 71,110$ kPa approaching close to the tensile strength (i.e., $R_{CFRP,tensile} = 100$ MPa) when CFRP's failure condition is attained.

- The flexural capacity (FC) given by the SAP2000 model nearly equals that of ACI. There are initial cracks that appeared at the stage where $M = 105$ kNm or $\sigma_c = 7253$ kPa. This confirms the results given by the worksheet (c,f Appendix). And the $M_u = M_{yield} = 302$ kNm. This value is recommended by ACI to be the debonding moment; this is on the safe side.

Stress–Strain Relationship The stress–strain relationship curves for concrete is plotted in Fig. 8. The first plot indicates an increase strain to failure at the stress nearly equal to the ultimate value $\sigma_c = R_b = 17,000$ kPa (i.e., $f_c' = 14,450$ kPa); then, the ultimate strain in concrete is $\varepsilon_{c,u} = 0,000,447$, approximately half to the maximum value in Eq. (5c), i.e., $\varepsilon_c' = 8.1e-4$. This results in a range of the bending moment values of a simply supported beam subjected to a uniformly distributed load,
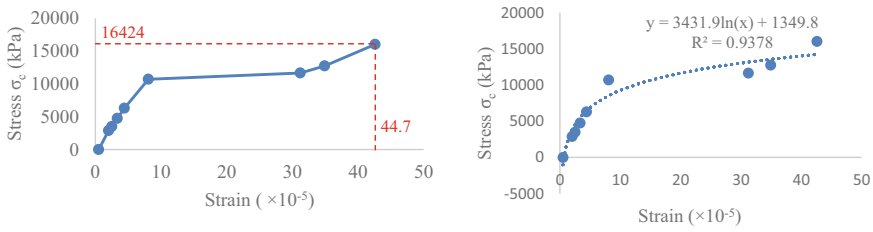
Fig. 8 a Simulated stress–strain relation for concrete, **b** trendline of the stress–strain relationship is compatible with Lam and Teng's model of behavior [12]

from $M = 300$ to 420 kNm, respectively, associated with the uniformly distributed load $q = 68.9$–96 kN/m. This value could be comparative to that of the independent approaches in Sect. 3.2.

4 Discussion

Some main points are listed as follows:

- This study contributes two approaches for determining the remaining FC of an existing cracked beam, strengthened with CFRP. A worksheet shows clearly what are changes in the process of iteration during determining the location of the neutral axis and calculating the bending moment by both the approaches, i.e., ACI's "$B1$ and $B2$" approach and the analytical approach. Two independent approaches give same results which are validated tentatively by SAP2000 model.
- The CFRP sheet in this study is assumed to have a specific specification as shown in Table 1. With a relative low tensile strength $R_f = 100$ MPa, no material angle and confine effect is taken into account.
- The theoretical approaches, including ACI 440.2R (2017) and the analytical solution for determining the location of the neutral axis, give the comparable results. The FC of the previously cracked beam, retrofitting with CFRP is $M = 302$ kNm; this is validated by a numerical model using SAP2000. On the other words, the bending moment at failure is calculated to the condition of yielding the armature in the assumed 1% reinforcement beam. This value is compatible to that of the SAP2000 model. The value $M_{yield} = 302$ kNm is recommended by ACI 440.2R that it occurs at the FRP failure, $B2$ step, or "FRP failure" step in algorithm [6], which is confirmed by the analytical approach (c.f Appendix). This does not exactly reflect in the model, because of the high strength of the polymer, and partially due to the strength of particular material in model.
- The analytical relates the nonlinear stress–strain relationship, and the ACI recommendation uses some coefficients and parameters to account for the relationship. M_{cr} at the beginning stage of crack appearance could be firstly determined by the gross cross-section of the beam, in which the rebar or armature is changed into

Table 3 Comparison between the stress, strain, and bending moment in this study

Results given by	Moment		At failure		Condition	
	M_{cr}	M_{yield}	σ_c	ε_c	σ_{cfrp}	Failure rebar/CFRP
ACI 440.2R	77	301	6600	0.00135	333,970	Yields/debonds
Analytical approach	63.5*	302	6600	0.00135	371,800	Yields/debonds
SAP2000 model	104	294	7253	4.9e-4	76,050	Approaching failure

*At the stress in concrete $\sigma_c = 7253$ kPa, this value would be $M_{cr} = 69.8$ kNm

the equivalent area of concrete. This procedure is based on ACI regulation, but in this study, the analytical procedure gives a result of both M_{cr} and M_u (i.e., Eqs. 9 and 11). The moment at crack appearance is theoretically calculated, $M_{cr} = 77$ kNm, i.e., the value is smaller than that of the latter, M_u. The model indicates $M_{cr} = 105$ kNm, and ACI's method of determining M_{yield} in someway is simpler. Because CFRP is intentionally used to strengthen a cracked beam, M_{cr} is not the target of this study. The results on this moment are rather comparable.

- According to ACI 440.2R (2017), at the level of strain in concrete $\varepsilon_{c,u} = 0,003$, the concrete beam fails with the yielding condition in steel. But this study indicates that the strain attains $\varepsilon_{c,u} = 0,00,135$. This is explained by Eq. (5c), and it could be a good agreement with some prior research works [3]. At this stage, the stress in rebar exceeds the yield stress, and the stress in concrete $\sigma_c = 6600$ kPa in the calculated sheet, or 7253 kPa in the SAP2000 model. Results are in Table 3.

  Stress in CFRP in the Table 3 does not take the adhesive material into account; only the tensile strength of polymer material is reviewed.

- In the numerical model, the tested strain, i.e., $\varepsilon_c^{bending} = 0.000447$, is reaching the half value of the maximum strain (i.e., $\varepsilon_c' = 1,71 \; f_c'/E_c$ or 8.1e-4 in this study), when the concrete is crushed at the ultimate stress, or R_b.

- The range of stress in this study is far below the value of which the nonlinearity in stress–strain relationship could reflect clearly; for instance, stress in confined concrete may attain from 80 to 100 MPa as in Lam and Teng's theories [12].

- For a more rigorous validation, it is necessary to improve the numerical model, especially concerning the bond between the armature and the concrete, and between the polymer and concrete, i.e., bond adhesion, to give more reliable validation [4, 13, 14]. It is beyond the scope of this article and still be studied further.

5   Conclusion

This study uses the approaches to determine the FC of a cracked beam retrofitting CFRP. With an existing condition of material of the cracked beam and CFRP, based on the location of the neutral axis, the FC is calculated by taking the equilibrium equations over all the stress components exerted in the cross-section. ACI 440.2R

(2017) recommends some coefficients to account for the nonlinear stress–strain relationship, and another approach is developed in the forms of analytical equations (i.e., Eqs. 9–11). There is a good agreement between the two approaches of locating the neutral axis, and the bending moments at failure obtained by the two approaches are the same. A finite element model of the beam is developed to validate tentatively the results found. A simply supported beam with a cracked cross-section is modeled by using the SOLID element in SAP2000; rebars with stirrups are modeled as the frame elements. Slip-bond as a LINK element is taken into account for the preliminary validation. The results are that, at the strain of 60.7% out of the maximal strain in concrete ε_c', with the given percentage of steel and the strength of componential materials, i.e., concrete, CFRP, and steel, the stress in concrete attains the ultimate value, and concrete is crushed. With the main properties of the specified material as in the illustrated beam (i.e., for a set of assumed data of materials and cross-section assigned), the remaining FC is predictable by both two approaches and confirmed by the numerical model ranges between $M_u = 302$ and 420 kNm. This result is concluded with particular attention that this FC is merely calculated associated with the specific conditions of the beam (i.e., the cross-section, grade of concrete, percentage of rebar, specification of the CFRP, etc.). Nevertheless, this study has been conducted by three independent approaches, giving comparable results, and gives a practicable approach to predict the FC of a beam, strengthened with CFRP. For any real structure, it might need some laboratory tests or advanced techniques of modeling, especially the cracked cross-section, cracked material, CFRP, and especially the bond between steel rebar and concrete, the adhesion between CFRP and the cracked beam. Furthermore, this study confirms the practicability of the ACI 440.2R (2017) for real construction works and contributes an approach to locate the neutral axis to determine the FC of a beam retrofitting with CFRP.

Appendix

Worksheet for determining the location of the neutral axis c (as in "$B1$ and $B2$ algorithm"), and flexural capacity $M = 302$ kNm for the beam strengthened with CFRP, calculated by two different approaches.
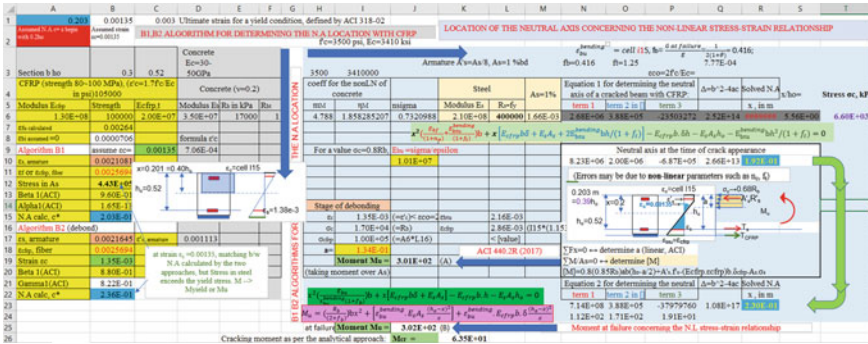
Worksheet for determining the location of the neutral axis and the ultimate flexural capacity of an illustrated beam strengthened with CFRP

References

1. Zabihi-Samani M, Shayanfar M, Safiey A, Najari A (2018) Simulation of the behavior of corrosion damaged reinforced concrete beams with/without CFRP retrofit. Civ Eng J 4(5):2243–2247
2. ACI 440.2R-08 (American Concrete Institute) (2008) Guide for the design and construction of externally bonded FRP systems for strengthening concrete structures. Farmington Hills, MI, USA
3. Gorski M, Krzywon R (2018) Flexural stiffness of RC beam strengthened with FRP. https://www.researchgate.net/publication/324222530
4. Naser MA, Hawileh RA, Abdalla J (2021) Modeling strategies of finite element simulation of reinforced concrete beam strengthened with FRP. J Compos Sci 5:19. https://doi.org/10.3390/jcs5010019
5. Huy TV, Ngon NV, Le Thanh Phong PTH (2018) Comparative study methods for flexural strengthening design of reinforced concrete beam using NSM-FRP material approach ACI 440.2R-08 and ISIS (CANADA). J Sci Technol 11(132). DaNang University. ISSN: 1859–1531
6. Kasimzade A.A, Tuhta S (2014) Analytical, numerical and experimental examination of reinforced composite beams covered with carbon fiber reinforced plastics. J Theor Appl Mech 42(1):55–70. https://www.researchgate.net/publication/258671831
7. Боидареко ВМ, Л. Шагин А (1987) Расчет Эффиективых МногоКопонтных Конструкций- Курсом Ускоренна Научно-Технического Прогресса, Москва Сттройиздат. Moscow Construction, pp 1–174 (in English)
8. Cao VV, Ronagh HR (2014) Reducing the seismic damage of reinforced concrete frames using FRP confinement. Accepted paper in composite structures. https://doi.org/10.1016/j.compstruct.2014.07.038
9. Sap2000 user manual. https://www.civilax.org/sap2000-manual/
10. Danraka MN, Mahmod HM, Oluwatosin OKJ (2017) Strengthening of reinforced concrete beams using FRP technique: a review, research article. Int J Eng Sci Comput 7(6):13199–13213. https://www.researchgate.net/publication/318724420
11. Sakbana A, Masreib M (2020) Finite element analysis of CFRP–reinforced concrete beams (English version). Revista Ingeniería de Construcción 35(2):148–169
12. Lam L, Teng JG (2003) Design-oriented stress-strain model for FRP-confined concrete in rectangular columns. J Reinf Plast Compos 22:1149–1186. https://doi.org/10.1177/0731684403035429

13. Ibrahim AM, Mahmood MS (2009) Finite element modeling of reinforced concrete beams strengthened with FRP laminates. Eur J Sci Res 30(4):526–541, ISSN 1450–216X. https://www.researchgate.net/publication/242163873
14. Jiang S, Yao W, Chen J, Cai T (2018) Finite element Modeling of FRP-strengthened RC beam under sustained load. Research article. Adv Mater Sci Eng 2018. https://doi.org/10.1155/2018/7259424

Reliability Analysis of a System of CFRP Structures on the Piled Raft Foundation Subjected to Earthquakes

Tham Hong Duong and Phuoc Trong Nguyen

1   Introduction

The soil-structure interaction (SSI) always attracts motivation for researchers in geotechnical engineering worldwide. During an earthquake, the waves propagate through the soil medium, and R wave traveling to attack the lower part of the structure upward; the superstructure, in turn, participates in motion and will cause the additional forces, exerting back the soil foundation, and so on. There is a remarkable change in the soil properties during an earthquake, and the response of the structure and foundation in vibration is a vast topic.

Pile raft is normally for high-rising buildings, in which the pile could partially support the load from the structure, and the raft contributes a small part of the total load. In a small raft, the pile could reduce the settlement as well. There are a lot of uncertainties for the topic, both in natural and artificial aspects. The three-component interaction is among three components, i.e., the soil foundation, the raft, and the pile. The raft as a shallow footing always requires a very high stiffness; while the pile as a deep foundation could cause stress for a deeper zone in soil medium.

The abovementioned behavior is more complicated in case the soil is subjected to an earthquake, concerning the non-linearity in the stress–strain relationship in structure when working at a very high level of energy. There are numerous uncertainties in the problem, both in aleatoric and epistemic aspects. They are the configuration and properties of the structures, i.e., the raft-pile system with a dependent distribution of the load that each component would support, the raft-pile-soil interaction, the boundary of the model, and the behavior of the whole system due to dynamic effects of the earthquake, etc. As for the piled raft, there are advanced methods of analysis, in which the variation in stiffness of raft due to pile installation, and the efficiency of

T. H. Duong (✉) · P. T. Nguyen
Ho Chi Minh City Open University, Ho Chi Minh City, Vietnam
e-mail: tham.dh@ou.edu.vn

the pile on the overall bearing capacity are taken carefully into account [1]. However, a question is that, in the case that the lateral excitation is randomly distributed as in an earthquake, is the abovementioned theory still valid? Or what happens if the increasing deformation in structure due to earthquake could cause additional inertia, and distress the foundation, and so on?

Performance-based design concerning the SSI for analyzing the damage in buildings on piled rafts subjected to an earthquake could be generally a soil-foundation-structure interaction (SFSI) [2]. The research indicates a linear elastic analysis causes increasing damping and flexibility from rocking and sliding motion of the foundation, results in a modification of the overall effect of the response; then the non-linearity should be taken into account with special attention on the responsive frequency of the integrated system, and the lifetime for it. Based on such a set of concepts, some performance limits are suggested, including the inter-story drift, the foundation motion together with the level of damage to be assessed [3].

The reliability analysis requires a specific quantification of the abovementioned uncertainties. As for the structure, it requires some data of both variables and parameters that are collected for a long time, to have in hand all the statistically characteristic values of them, i.e., mean value, standard deviation, and the law of distribution. For structure, it is necessary to quantify the load intensity, the materials (strength and stiffness), and its law of distribution; for foundation, the most important is the soil properties, concerning the spatial variability both in vertical depth and in horizontal directions. In earthquake engineering, the most important variable of soil is the shear modulus G. This variable stands for the stiffness of soil against shear stress and is a principal part of the soil impedance. The SSI is intensively studied [3, 4]. According to these research works, there are basically two conceptual trends of studying SSI, the direct approach and the substructure approach. The former integrates the soil and structure into a system and the latter considers the soil flexibility as a dividend part, with damping and velocity [4]. As such, isolated rigid support as in conventional design is not appropriate in an earthquake when no interaction is studied. Spring support is an alternative with a partial consideration for an interaction. The lumped mass model models the soil medium as a SOLID element [3], considers the shear modulus, and the foundation as a mass that connects to the surrounding soil medium with spring and dashpot [5]. For a base mat, the dynamic stiffness in an arbitrary direction of motion, and damping of soil medium as that of a half-space could be calculated from the velocity of shear S-wave V_s and the geometric dimension of the mat [6]. In a piled raft or mat, the piles, disregarding the end bearing or skin friction ones, the stiffness relates strongly to shear modulus G and the configuration and settlement of piles [7]. The non-linearity in the behavior of the system is recognized in the specific case of layered soil medium, resulting in a high level of soil-structure interaction for the system piled raft. Non-linearity in the problem could be of the stress–strain relationship of the structures, of the increasing displacement due to dynamic effects on hinges developed, etc. [8, 9].

Reliability analysis on the piled raft subjected to an earthquake requires a set of relevant input data, including the randomness of the variables, the intensity and time of the earthquake, and the law of logarithm distribution of the responsive amplitude

$S(T)$ in association with the attenuation laws of the displacement of a point in the free domain [10]. In general viewpoint, it is necessary to take into account the uncertainties in:

- The earthquake and its attenuation laws (Peak Ground Acceleration PGA and duration of an earthquake)
- Motion input (design spectrum, time history function, direction of ground motion…)
- Existing conditions of the structure subjected to load in specified combinations.
- Model and strategy of analysis (software, method of analysis…)
- Material stiffness and strength (superstructure, foundation, pile and soil)

This article aims to analyze the reliability of such a complicated relationship between the abovementioned factors for a building on piled raft foundation subjected to an earthquake. The objective for investigation will be an existing planar frame with a cracked beam, strengthened with CFRP, subjected to an earthquake. Because of the vicinity of the site and practical purpose, the Chi-Chi earthquake (Taiwan 1999) will be selected to study.

2 Method

2.1 Solution Strategy

Database for a model: Reliability analysis requires a sufficient amount of input data with possible variations. A flow chart for the analysis is described in Fig. 1:

Input data in this study are of three groups, including the intensity of earthquake, the material of the system of SFSI, the characteristics of the soil medium. The flow chart for studying the reliability is shown in Fig. 1.

For the stronger interaction, in which the stiffness out of the plane of the model is not taken into account, the planar frame is used [3] and structural software is SAP2000; the cracked cross-sections of beam strengthened with CFRP are assumed instead of beams and columns. A unit slice uses the technique of modeling in which the planar structure would reduce the modulus of elasticity instead of re-calculating the cross-section [11].

All the random variables are classified into three groups of which the characteristics are defined statistically with a lognormal law of distribution. For the lognormal distribution, the median and the standard deviation are specifically calculated from data obtained before reliability analysis. A 2D frame of a 10-story building is created for illustration purposes in which the frame and its foundation, i.e., piled raft and soil medium, are modeled with absorbent boundaries (Fig. 2b). In step 6, the time history load case of the Chi-Chi earthquake [12] is used and its results are compared to those of the response spectrum load case. For guaranteeing a sufficient width of wave propagation, dimension A in Fig. 2 should be from 3 to 5 times out of the width
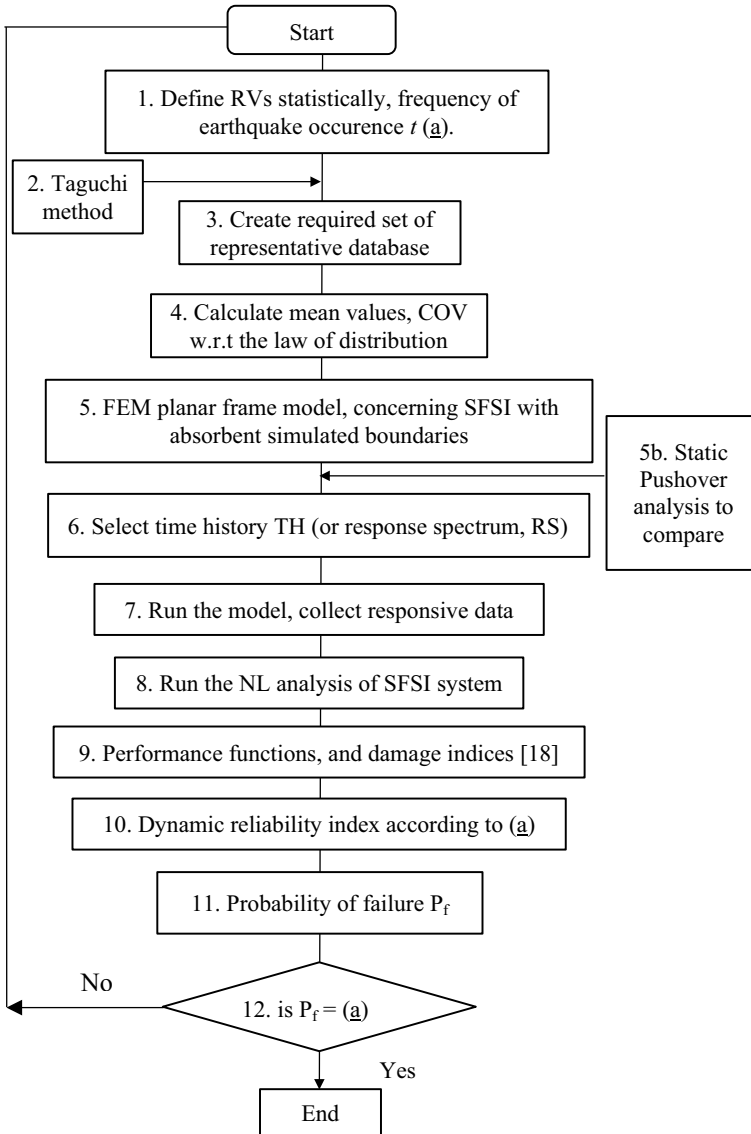
Fig. 1 Steps in reliability analysis for a building on piled raft subjected to earthquake

of structure, and B in the model should be twice the building height or more; such model is more relevant as compared to that in 3D element method using Plaxis [13].

The reliability of the piled raft foundation as a system of combined structures, the reliability index (RI) should be a value which is calculated to those of elements connecting both in series or parallel style in superstructure and parallel of components in substructure, i.e., soil foundation and footings. For the superstructure, performance
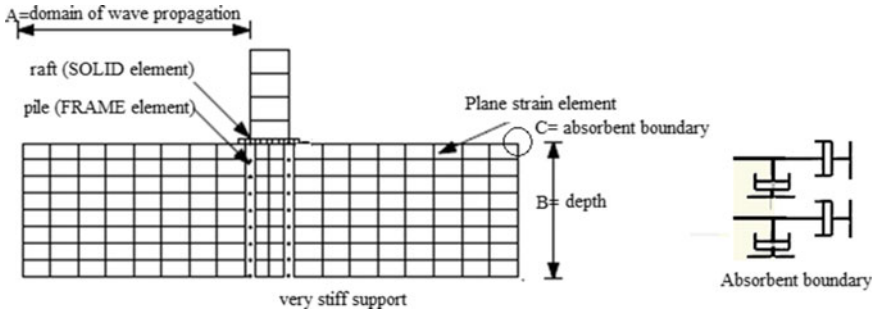
Fig. 2 Planar frame of a building on piled raft subjected to earthquake [4, 11]

Table 1 Cross-section for cracked beams and columns as per ACI 318 [14]

Load condition	Beams	Columns
Factored load condition (FLC)	$0.35I_{gr}$	$0.70I_{gr}$
Service load condition (SLC)	$0.50I_{gr}$	$1.01I_{gr}$

functions are established for the factored load (FLC) and unfactored load (SLC) conditions, and the ACI recommendations for cracked structures are prescribed in Table 1.

It is notable that the cross-section as recommended by ACI 318 in Table 1 is not taken CFRP into account; for cracked beams strengthened with CFRP, the moment of inertia is re-calculated by either the "B_1 and B_2 algorithm" [15] or nonlinear analytical approach [16]. A modifier for inertia around the bending axis will then be obtained from these approaches and is applied to the input data of SAP2000 properties. This would be an attempt to come closer to the strategy for finite element modeling of FRP structure [17]. From an independently conducted study using the concept of material equivalence, the cross-section of a cracked beam, retrofitting 1 mm-thick CFRP has the equivalent $I_{gr} = 0.0363$ m^4 for the 30 × 60 cracked beam with 1% percentage of tensile rebar (i.e., the location of the neutral axis is $c = 0.39h_o$). This could be explained later in the discussion with more details. With five groups of random variables, there are 11 dominant variables as prescribed in Table 2:

The first uncertain variable is the intensity of an earthquake. Due to a few historical records of earthquakes for a specific site (i.e., the location of constructing the building under consideration), and due to lack of knowledge about the intensity of the earthquake, it is necessary to simulate the time history and randomly changeable peak ground acceleration (PGA). Two levels of PGA, i.e., low with 0.129 g (notation "N" case) and high with 0.98 g (notation "V" case), are selected to combine with other varied factors. With just nine two-level factors, there are at least 29 = 512 cases of permutations. This is too difficult to solve all the possible cases for obtaining a sufficient database for analyzing the percentage of contribution and reliability [18, 19]. By using Taguchi's method [20], it is statistically acceptable to solve 12 tasks for collecting a sufficient database to account for all the possible cases with a highly

Table 2 RVs for reliability analysis of structures strengthened with CFRP, s.t an earthquake

List of factors	Level 1	Level 2	Group
$X_1 =$ Earthquake intensity	Low PGA	High PGA	A
$X_2 =$ Time of occurrence	Short	Longer	A
$X_3 =$ Soil amplification factor *	1%	50%	A
$X_4 =$ Cross-section in model	ACI	Calculated	B
$X_5 =$ Thickness of the raft	1.5 m	2.5 m	B
$X_6 =$ Stiffness of foundation (close pile $D =$ 0.35 @ 3 m and $D = 0.28$ @ 2 m, same volume of material)	Low	High	B
$X_7 =$ Strength of CFRP (MPa)	100	900	B
$X_8 =$ Shear modulus of soil	Low G (soft soil)	High G (stiff soil)	C
$X_9 =$ Input mode	Time history	Response spectrum	D
$X_{10} =$ Software and modeling	TD	FD	D
$X_{11} =$ Boundary width (B, the width of the building; <5B; >5B)	<5B	>5B	E

* This factor refers to the possible amplification of amplitude in free domain vibration due to waves propagating through soft soil

representative level. The randomness of the input motion is of intensity, time for the given probability of exceedance (PE), and soil amplification factor. For simplicity, this study keeps the levels of time (X_2), soil amplification factor (X_3), and strength of CFRP (X_7) fixed. It is easy to estimate the PE in a specific average recurrence interval (see Ref. [8]). For concerning the effect of the boundary on the SSI response, two models of boundary width are studied, <5B and >5B.

After all the abovementioned steps are ready, the model will run for 12 combinations for collecting responses, including acceleration, velocity, and displacement. These outcome results may be the internal forces (e.g., bending moment, axial force in pile, etc.) or displacement, both in time domain (TD) and frequency domain (FD). In this study, for 11 two-level factors, the $L_{12}(2^{11})$ orthogonal array is used as follows:

For obtaining more results, 11 factors are tabulated in which X_2, X_3, and X_7 are constant (Fig. 3). In step 5b, a static NL pushover model is conducted as an alternative to compare to results of the time history (TH) method and response spectrum (RS) method [21]. In steps 7 and 8, the frame with beams and columns are considered to be NL elements by defining plastic hinges at both ends of the elements, except for the 1st story and the most upper one [22]. For an NL analysis for a portal frame, the Fast Nonlinear Analysis (FNA) is applied to the structure subjected to a time history load case (i.e., Chi-Chi by PEER Database) with a UX acceleration, and for the specific cracked beams, the moment–curvature curve for a reinforced concrete section with CFRP will be assumed of Lam and Teng's theory [22] as briefly shown in Fig. 4. This relationship could be a base for declaring the NL properties of hinges, PMM for columns, and M3 for beams. In this study, the effective stiffness is calculated from

X1	X2	X3	X4	X5	X6	X7	X8	X9	X10	X11
1	1	1	1	1	1	1	1	1	1	1
1	1	1	1	1	2	2	2	2	2	2
1	1	2	2	2	1	1	1	2	2	2
1	2	1	2	2	1	2	2	1	1	2
1	2	2	1	2	2	1	2	1	2	1
1	2	2	2	1	2	2	1	2	1	1
2	1	2	2	1	1	2	2	1	2	1
2	1	2	1	2	2	2	1	1	1	2
2	1	1	2	2	2	1	2	2	1	1
2	2	2	1	1	1	1	2	2	1	2
2	2	1	2	1	2	1	1	1	2	2
2	2	1	1	2	1	2	1	2	2	1

Fig. 3 $L_{12}(2^{11})$ orthogonal array for obtaining a database of outcome results
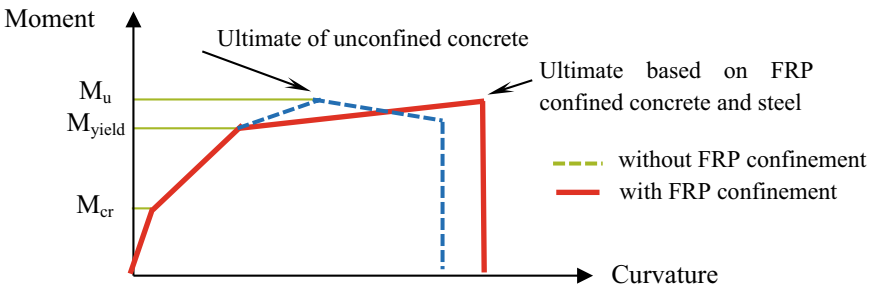
Fig. 4 Moment–curvature curve of an RC beam with/without CFRP [23]

the NA obtained by the two independent procedures [15, 16] and compared to that of ACI standard as in Table 1 [14, 22].

Step 10 is about defining the performance functions. For a 2D frame with cracked sections of beams retrofitting with CFRP on the piled raft and concerning the SSI, it is necessary to obtain enough database of the input data and the responsive data. Twelve combinations of intervening random variables are manipulated as in the table of Fig. 3 to provide data in extended performance functions as shown in Table 3 [18]. Dynamic reliability analysis will be of the second phase of the process, including calculation of the RI for each combination associated with responses of SSI system. The response is taken from the superstructure (i.e., internal forces, displacement in the time domain, for instance, the maximum displacement at the most upper point, or the story drift, vibrational response, etc. for each combination of Table 3; for the foundation, the response will be the force in pile, the bending moment in the raft, the stress in soil mass, settlement, and the lateral displacement, etc.

With database from combinations in the table of Fig. 3, a set of performance functions (also named Limit state function, or LSF) are created and the RIs for each case of risk are computed. The law of distribution is lognormal. In the general case, the performance function has the conceptual equation as below:

Table 3 Performance functions (LSF) used in this study [18]

Load condition	Condition	Performance functions	State
Flexure, beams	Factored load	$G(X) = \frac{M_{\text{yield}}}{M_{\text{max}}} - 1 \geq 0$	ULS
Shear in columns	Factored load	$H(X) = \frac{Q_{\text{max}}}{Q} - 1 \geq 0$	ULS
Horizontal displacement	Service load	$I(X) = \frac{H}{500}/\Delta_{\text{hor}} - 1 \geq 0$	SLS
Deflection	Service load	$J(X) = [f]f - 1 \geq 0$	ULS
Settlement of piled raft	Service load	$K(X) = \frac{\Delta_{\text{vertical}}}{\Delta} - 1 \geq 0$	SLS
Moment in raft	Service load	$M(X) = \frac{[M]}{M_{\text{max PR}}} - 1 \geq 0$	ULS
Axial force in pile	Service load	$N(X) = \frac{N}{R_{c,u}} - 1 \geq 0$	ULS
Vibration			
DI for beams	Service load	$F(X) = \frac{[D.I]}{DI_{\text{beam}}} - 1 \geq 0$	SLS
DI for piled raft	Service load	$P(X) = \frac{0.4}{DI_{\text{PR}}} - 1 \geq 0$	SLS
MFDI for CFRP beam	Service load	$Q(X) = \frac{[\text{MFDI}]}{\text{MFDI}_{\text{beam}}} - 1 \geq 0$	SLS

$$G(\overline{X}) = R_{\text{LIM}}(\mu, \delta) - R(\overline{X}) \tag{1}$$

in which, μ and δ are the median and the coefficient of variation (COV), respectively.

Step 11 is to compute the reliability index. With the outcomes from the PO analysis as limit values, the RI is a time-invariant index and is calculated by using the extreme values of responses.

Peak ground acceleration (PGA) are two-level factors characterizing the seismic intensity (this random variable is denoted X_1 in Table 1). In the analysis using the time history (TH), both the accelerograms recordings utilized are the first of the gradually increased intensity ("V" case), the second is a decreased one ("N" case). With lognormal law of distribution, the statistical values of outcomes should be the median instead of the mean, and the standard deviation, as follows

$$\mu_Y = \ln\left(\frac{\mu_X^2}{\sqrt{\sigma_Y^2 + \mu_X^2}}\right) \tag{2}$$

$$\sigma_Y = \sqrt{\ln\left(\left(\frac{\sigma_X}{\mu_X}\right)^2 + 1\right)} \tag{3}$$

in which X is a set of random variables, having the lognormal law of distribution, the mean value μ_X and standard deviation σ_X. For failure, dynamic effects, it is relevant to apply the lognormal distribution, and the time-invariant RI could be determined by the following formula for a linear limit state function [24] as

$$\beta = \frac{Ln\left(\frac{R_{50}}{Q_{50}}\right)}{\sqrt{\sigma_R^2 + \sigma_Q^2}} = \frac{\mu_R - \mu_Q}{\sqrt{\sigma_R^2 + \sigma_Q^2}} \tag{4}$$

where the term σ_Q^2, the variance of the demands or effects, combines the inheritant variation of the load, excitation, responses in time domain, and σ_R^2 or variance of the resistance, refers to material strength or bearing capacity; the indices 50 stands for median value, i.e., the value of μ_Y in Eq. 2. Performance limits used in this study comply with the threshold in [2], for instance, the limit of the story drift $\theta_{SS,P}$ is 2.5% for a repairable condition [2]. Depends on the structural connection and working conditions of combined structures, the overall RI can be determined to that of the system in series or parallel ones. Statistical values of the prescribed factors are given in Table 4.

Table 4 Statistical values for variables and responses, in case of earthquake [25]

List of variables/responses	Unit	Statistic value		Notes
		Mean	Standard deviation	(for CFRP)
Gravity load (in model) 20%	kPa	25	5	
Internal force:				
Axial force in pile	kN	750	112.5	Lognormal
Bending pos. Moment in beam Bending moment in raft	kNm	107 2000	16.05 200	
Base Shear	kN	220	21.8	
Horizontal displacement, m	M	0.08	0.008	
For ultimate strain ε_c'				
Strength f_c'	MPa	17	2.55	
Stiffness E_c	MPa	32,500	6500	
Settlement (B/20 for dynamic case)	m	0.10	0.01	
Deflection of beam	cm	3.6	0.36	
Frequency	Hz	0.16	0.05	

Finally, step 5b is a pushover analysis (PO). It is a pseudo-static alternative that will calculate the RI for comparison purposes [26]. By assessing the structural performance of the building, the comparison between the capacity and the demand at the various stages of working is conducted, being a good tool for reliability assessment. The different values of the reliability from the pseudo-static PO will compare to those of the other dynamic nonlinear approaches. After all, the performance of the structure could be assessed.

2.2 Characteristic Data of the Chi-Chi Earthquake

The reason for choosing the Chi-Chi earthquake for the study is that the time of quaking lasts very long, its recordings are sufficient, and PGA is not so high as compared to those of worldwide data at the same level of intensity. The time historic recordings obtained by USGS [25, 27] are shown in Fig. 5 as.

At station TAP003 in Luzhou District, the minimum PGA is 127.28 gal or 0.129 g, and the maximum PGA is about 0.98 g (at station TCU129), both in east–west direction [25, 28].

For earthquake input data using the response spectrum (RS), two sets of data as alternatives are applicable for assigning the parameters into the SAP2000 model (Fig. 6). Recorded at different stations, it is notable that the "N" time history tends to gradually decrease the intensity (Fig. 5b), contrary to that of "V" time recordings (Fig. 6d). The assumption to be validated is that each time history may alter the response in some way.

The mean PGA withdrawn from RS curves given by research work [29] is determined to be around 0.5 g as shown in Fig. 6; this value is also the mean value between the recorded time history (0.129 g and 0.98 g). For a high level of factor X_1 in Table 2, the ordinates would be twice those of 0.5 g. This response spectrum is a load case of the input data for the analysis of the possible load case of response spectrum that structure would suffer.
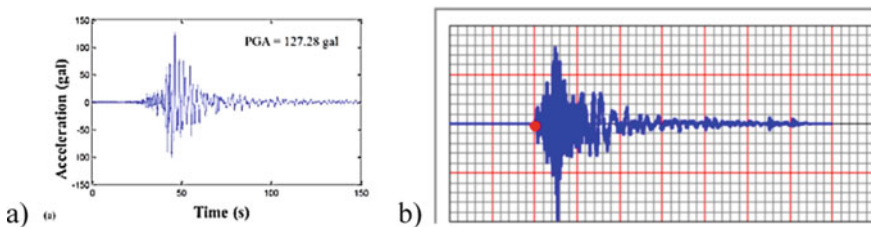
Fig. 5 **a** Chi-Chi recordings at a station, east–west direction [27]; **b** graph in SAP2000 TH function, from accelerogram No. RSN2752_CHICHI.04_CHY101**N**.AT2 (PEER NGA [25])
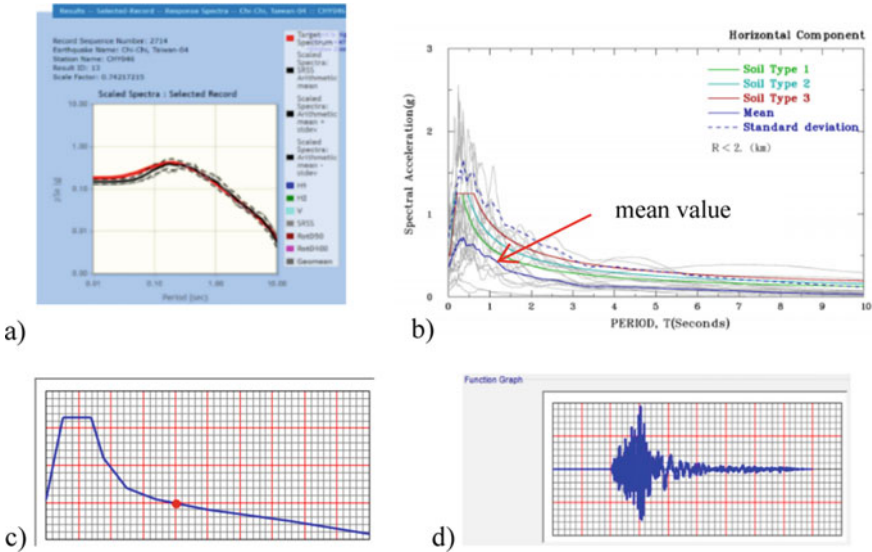
Fig. 6 **a** Chi-Chi response spectrum [25]; **b** RS for different soil type, <2 km at 0.5 g and damping 0.05, in horizontal direction [29]; **c** RS with stronger intensity, PGA = 0.98 g; **d** accelerogram RSN2752_CHICHI.04_CHY101V.AT2 as an increasing intensity

3 Results

3.1 Model Description

A 10-story planar frame of an existing building, 36-m high from the ground level, is developed as in Fig. 7. For ensuring overall stability, the depth of footing is at Ele. −3.5 with a raft 1.5 m of thickness. The boundary will be 60-m outside the edge of the building, and the soil foundation is twice the height of the building, or from Ele. 0.00 to −60.00; all the pile tips are at Ele. −30.00. For the superstructure, all the beams are assumed to be structures having existing cracks, strengthened with CFRP, and the target for this study is to calculate the overall RI, concerning the SSI in the condition of the earthquake. For assessing the reliability, random variables of both two kinds of uncertainties, aleatoric and epistemic uncertainties, are taken into account and quantified with 2- level 11 factors, namely X_1 to X_{11} in Table 2.

Different values of factors imply the possible variation in values of the variables. No uncontrollable factor is assigned; only three out of 11 factors have constant values. The properties of soil layers are listed in Table 5, and the cross-sections in Table 6:

The average value of the bearing capacity could be assumed to be around 900 kN for the 35×35 square pile, and 700 kN for the 28×28 pile. This capacity will be the limit for the axial load for LSF. The COV for the bearing capacity is 0.3 as conventionally given. The moment of inertia for the cracked beam is modified by
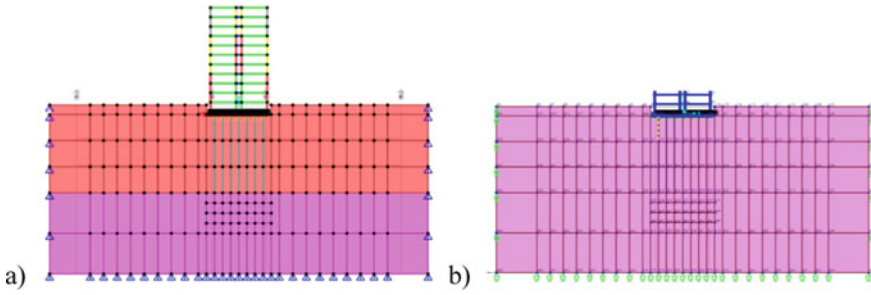
Fig. 7 **a** 2D frame with cracked beams retrofitting CFRP, subjected to earthquake, with rigid support at boundaries; **b** high damping ratio absorbent boundaries ($c = 10\%$)

Table 5 Soil description for layers in the model

List of factors	Layer 1	Layer 2
Classification		
$\gamma_{unsat}/\gamma_{sat}$ (kN/m^3)	17.9	19
Cohesion (kPa)	20	70
Friction angle (degree)	10	16
Modulus of elasticity (kPa)	10,920	32,370
Shear modulus G	4200	12,450

Table 6 Properties for elements in the model

Geometry	Columns		Beams	Raft thickness	D$_{pile}$/spacing
	Outer	Inner			
b × h	40 × 60 40 × 50 30 × 50	50 × 50 40 × 40 30 × 30	30 × 60 (d = 52 mm)	1.5 m or 2.5 m	0.35/3.0 m or 0.28/2.0 m

calculating the neutral axis (NA) and a modifier is applied to the SAP2000 input data. By applying the "B1 and B2 algorithm" [15] or analytical approach [16]. After determining the location of the NA, the moment of inertia is computed. The calculated moment of inertia will be compared to those of ACI recommendation (prescribed in Table 1, no CFRP included). The area of the CFRP polymers is transformed to the equivalent area of concrete, and the revised moment of inertia will be re-determined by conventional calculation with respect to the location of the NA; and the moment of inertia of the cracked beam divided by the gross moment of inertia, a modifier obtained is assigned into a frame property modifier data. The modifier for the moment of inertia about the 3-axis of a cracked beam retrofitting with CFRP is calculated to the location of the neutral axis, the equivalent area of the steel and the polymer, complying with ACI 440.2R [14], being $I_{cr}/I_{gr} = 2.36e-3$ m^4/3.63e-2 m^4 $= 0.065$. For the reason cracked part of concrete contributes no stiffness, together
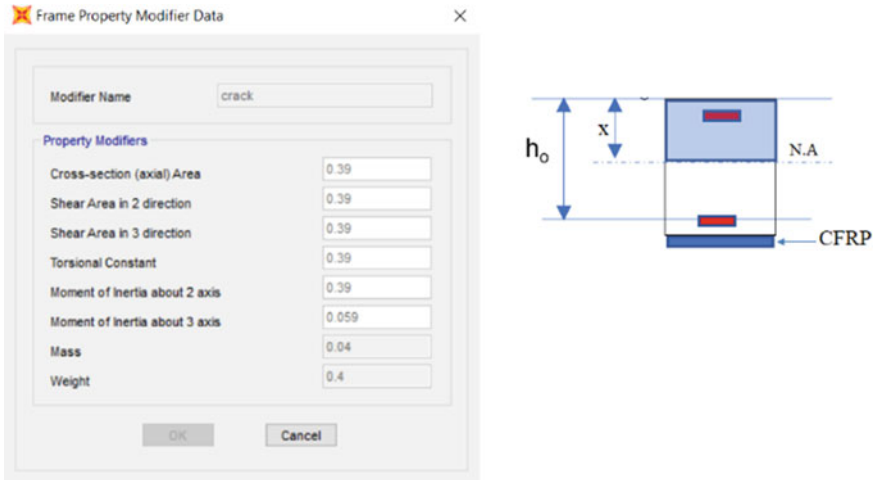
Fig. 8 Modifiers for cracked beams

with using a unit slice for 2D frame without changing the cross-section, this modifier implies the stiffness of the cracked beam with CFRP reduces significantly, resulting in a large deflection. This could be much more practicable than that of using the ACI's recommended reduction factor $0.35I_{gr}$ for cracked beams (without CFRP) as recommended in Table 1.

By scaling down to one-sixth, the modifier for mass and weight are shown in Fig. 8 while the moment of inertia for all the cross-sections is calculated normally.

In a unit-slice frame of planar strain model, all the load and modulus of elasticity would be scaled down by a "One-divided-by-the-bay-distance" factor. In this study, the model has a 6-m bay, so the scaled-down factor will be one-sixth. The nodal concentrated dead load on the unit-slice frame is 22.5 kN and 12.6 kN for the outer and inner columns, respectively; the nodal concentrated live load is 2.83 kN for both outer and inner columns. The uniformly distributed load on 9 m-span beams is 2.17 kN/m/ml (dead load per meter of length, or ml) and 0.7 kN/m/ml (live load). No lateral wind load is applied and combined to the earthquake, because of its conflict with the earthquake in real-world practice. There are four modes to be analyzed, and the most likely response would be obtained using the law SRSS (square root of the sum of squares).

3.2 Model of the 2D-Frames with Cracked Beams Strengthened with CFRP

Frame and piled raft, subjected to different load cases: The frame will be analyzed in three cases: dynamic analyses are TH and RS, and static NL pushover approach

(PO). The response with respect to each combination of levels in Table 2 and the table in Fig. 3, will be the story lateral displacement and drift at the uppermost joint of the building (i.e., joint 48), the deflection of the most sagged cracked beam (i.e., the 1st-story beam), the shear in the columns at the first floor, the bending moment in cracked beams, the settlement of the piled raft foundation, and the axial force in the outer piles (maximum compression in pile) (Table 7). Twelve combinations of different values of input actions stand for all the possible cases of random variables during the earthquake.

For the boundary >5B, the response is given in Table 8:

In the TH load case, the lateral displacement and settlement of the wider model boundary will come earlier with greater values than those of the smaller model boundary. This should be explained by the more accumulation of the strain in the wider boundary, and the energy due to earthquake delivered more to the building. ACI's recommendation that the moment of inertia of a cracked beam with no CFRP is modeled as $0.35I_{gr}$ (I_{gr} is the gross equivalent cross-section) results in a smaller lateral displacement, in both cases of the boundary, and yields greater axial forces in columns and piles; however, the bending moment is cracking moment $M_{cr} = 75.46$ kNm, and the deflection is 0.142 m which exceeds the acceptable deflection in unfactored load condition.

For the pile foundation, an FD analysis would be applied to internal axial force in the heaviest pile, or outer pile, i.e., element #80. The TD response for axial force of the pile is shown in Fig. 9

Pushover analysis: This nonlinear static study method is a good tool for determining the performance level of a building. Its pushover curve shows the base shear versus lateral displacement at each step, indicating the maximum value of the shear base that the building could have enough strength to support the effects during the earthquake. This study uses acceleration in the x-direction as the load that the structure would stand during ground shaking. The plastic hinge which appears in some beams at a specified step is the indicator for the yielding condition. All the responses at the time yielding condition would be considered as the limit of safety for the building. In this study, the load cases of the earthquake are the time history (TH load case) and the response spectrum (RS load case); both are reliable files [28]. For instance, in a particular combination, a Life Safety (LS) limit is attained at step 2, the lateral displacement then being 0.384 m exceeds the limit value H/500 = 0.077 m (see Fig. 10). All the data would collect simultaneously at the time of LS occurrence, disregarding this intermediate stage is coming closer to the collapse prevention (CP) as the response threshold in the PO analysis. The results also show that the broader domain of analysis, the higher displacements, both in x-direction and z-direction. Based on this, for the LSF relating to displacement, the wider boundary should be more appropriate to calculate the LSF (Fig. 11).

The maximum values of the bending moment, lateral displacement, axial forces in columns and piles, and the piled raft settlement, etc. at the step of LS appearance in any hinge, are obtained. The responses of TH and RS load cases with respect

Table 7 Outcome by three methods of analysis, 2D frame with cracked beams retrofitting CFRP—A particular case, with <5B-boundary, ☐35 cm—stiffness of foundation

Method	Axial force in Columns		Δ_{hor} (m) Max	Shear in Columns		Bending moment and deflection (cm)			Pile				Δ_{ver} (m)
	1	2		outer	inner	M+	M−	Q	1	2	3	C	
TH	984	968	0.37	3.26	9.34	25.69	−49.81	31.9	875	532	486	488	0.17
RS	789	792	0.41	5.05	8.45	21.05	−41.47	26.4	721	452	414	422	0.11
PO	1777	1806	0.59 (step 2**)	12.2	9.45	50.91	−88.0	58.5	1.6e3	1e3	905	908	0.4
DL + LL	978	982	0.01	4.28	8.36	25.74	−48.82	31.7	887	537	486	507	0.12

The maximum lateral displacement happens at step 446 or $t = 44.6$ s; *Response frequency $f_1 = 0.208$ Hz, $f_2 = 0.608$ Hz, $f_3 = 0.692$ Hz, $f_4 = 31.50$ Hz, acceleration in x-direction; **In step 2, hinges attain Life Safety (LS) state, SAP2000 hinge results indicate $M = 23.63$ kNm

Table 8 Outcome by three methods of analysis, 2D frame with cracked beams retrofitting CFRP—A particular case, with a >5B-boundary, □35 cm—stiffness of foundation

Method	Axial force in Columns		Δ_{hor} (m) Max	Shear in Columns		Bending moment and deflection (cm)			Pile				Δ_{ver} (m)
	1	2		outer	inner	M+	M−	Q	1	2	3	C	
TH	976	977	0.39	5.64	9.73	25.68	−49.56	31.8	888	469	428	494	0.24
RS	790	793	0.46	6.39	5.66	21.04	−41.4	26.3	723	449	402	415	0.21
PO	1767	1765	0.58 (step 2**)	9.32	33.0	46.78	−91.51	58.4	1.6e3	980	874	879	0.24
DL + LL	978	978	0.01	4.33	8.34	28.4	−47.36	31.9	888	526	471	494	0.24

The maximum lateral displacement happens at step 436 or $t = 43.6$ s; *Response frequency $f_1 = 0.262$ Hz, $f_2 = 0.432$ Hz, $f_3 = 0.612$ Hz, $f_4 = 27.119$ Hz, acceleration in x-direction; **In step 2, hinges attain Life Safety (LS) state, SAP2000 hinge results indicate $M = 23.59$ kNm

to those of PO load case at different steps are used to calculate the time-invariant reliability index.

The results indicate that the beam is weaker than the column, the building vibrates at a higher frequency in the z-direction, and the dimension of the boundary affects the response of the structure, both in dynamic and pseudo-static analysis. The wider boundary of the model (e.g., boundary >5B), the smaller fundamental frequency of responsive might be (Table 9); for cracked beam, it depends on the simulation of the cracked cross-section with CFRP reinforcement.

The SSI is clearly recognized in higher frequencies (i.e. mode 4) while characteristics of displacement with larger mass alter three first modes frequency, and the responsive frequencies of the individual structure are different (Fig. 9c–e). This is explained by the different stiffness of the individual structure.

Results from combination: Twelve sets of responses as outcomes are collected, and the value of the performance functions are calculated at the step of failure occurrence (Table 10). This would supply a sufficiently big data set for analyzing the reliability. For illustrating purpose, seven following performance functions LSFs in 12 combinations of level values are selected as below:

- ULS with flexural moment;
- ULS with bending moment in raft;
- ULS with axial force in outer pile (or element #80);
- ULS with base shear in the outer column;
- SLS with horizontal displacement at the most upper joint 48, and deflection at mid-span of the most sagged beam element #46 (obtained at the time step when the beam plastic hinge appears first);
- SLS with the settlement at the central pile tip (this should be the settlement of the piled raft as well).
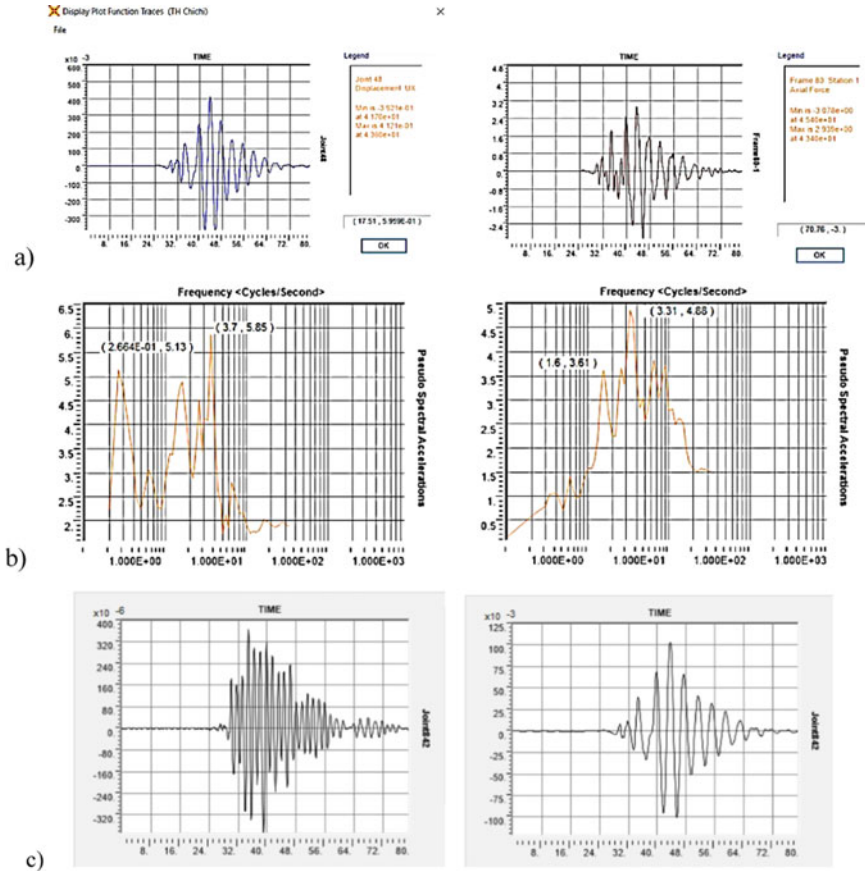
Fig. 9 a TD Response of joint 48 (left, superstructure), and axial force in the outer pile, element #80 (right, subground structure) and; **b** FD response for lateral displacement at the upper point (Ux, No 12) and the pile tip (Ux, No 737); **c** TD displacement in vertical direction and horizontal direction of joint #842 at mid-span of the most sagged beam; **d** FD displacement at the mid-span joint of beam in z-direction ($f = 0.617$ Hz) and in x-direction ($f = 0.268$ Hz); **e** FD pseudo-spectral acceleration of a point #307 at the bottom of the raft

The values of RIs for various limit state conditions are given in the last column of Table 11, with notation of calculating the statistical parameters in lognormal distribution (μ_Y, σ_Y in formula 2, 3). This value is calculated by the general formula (1) and functions in Table 3; a single negative value in Table 11 (with asterisk symbol) is physically meaningless. This occurs when the factor of safety for this LSF is much less than 1; this may be viewed as an outlier value. The reliability indices for different LSFs would be used to compute the reliability index for the overall system, concerning the SSI (Table 12).

d)

e)
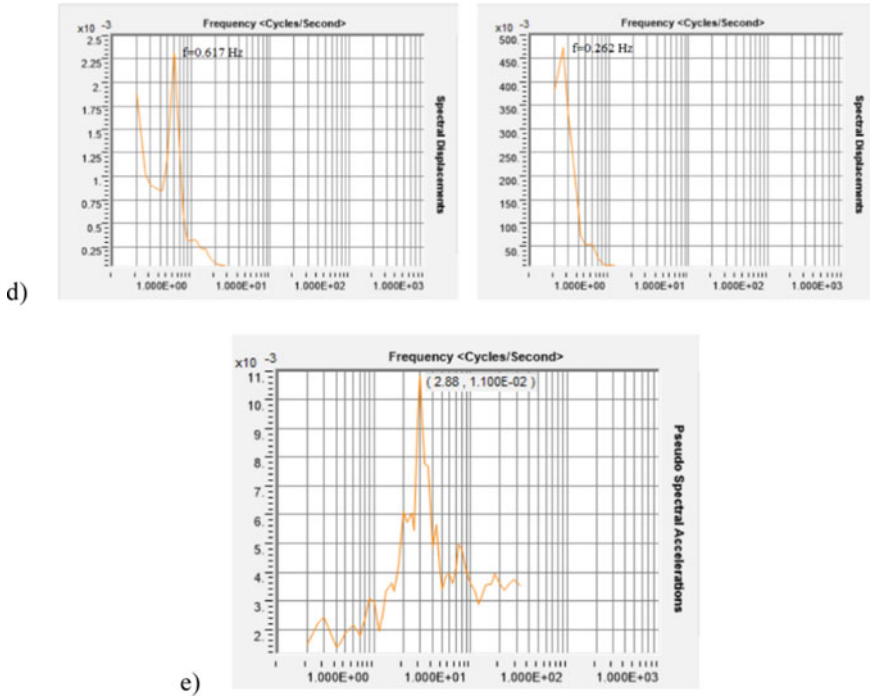
Fig. 9 (continued)

The overall RI for SSI system of structures: Beams and columns are connected in series, and the piles and raft are in parallel; the superstructure including beams and columns in turn is in series with the piled raft. The diagram for this system is in Fig. 12. RI of each structure is taken as the lowest RI among actions and responses for that structure. For instance, RI of a beam is the lowest value among different βs having the response such as the deflection of the SLS and bending ULS, $J(X)$ and $G(X)$, being 1.29. For the column, a $\beta = 0.64$ for lateral displacement $I(X)$ and base shear in columns $G(X)$, being 0.74.

For n_i parallel components having reliability indices R_i, the product law of unreliabilities is applied. The reliability for this parallel sub-system is

$$R_p = 1 - \prod_{i=1}^{n}(1 - R_i) \tag{5}$$

For m components in series, the system reliability will be

$$R_S = \prod_{i=1}^{m} R_i \tag{6}$$
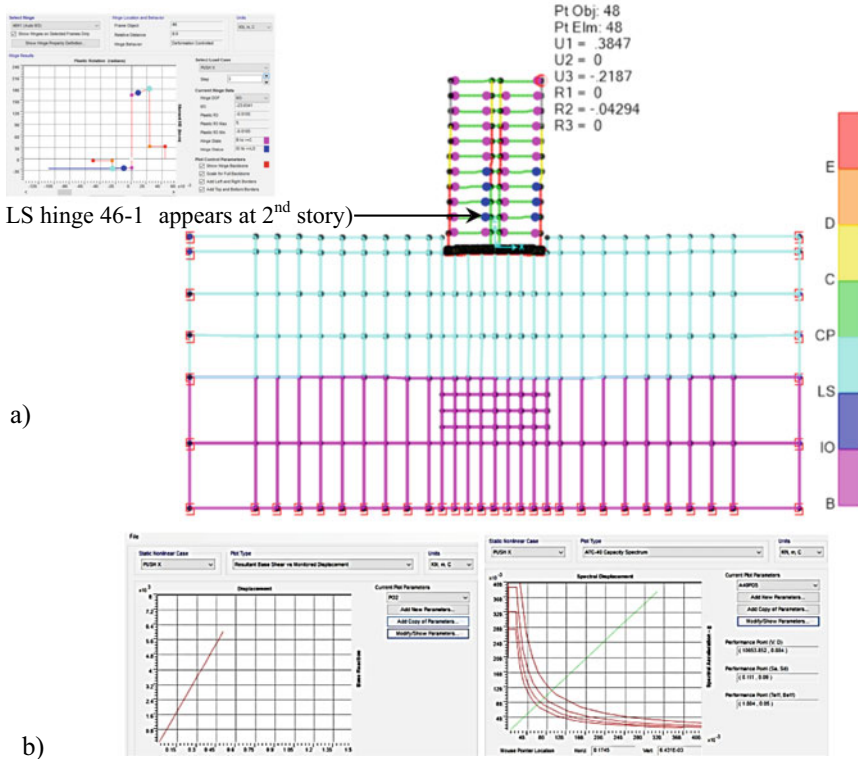
Fig. 10 **a** The performance at step 2 out of 9 with LS state in beams (e.g., No 46), <5B; **b** base shear versus displacement curve, and ATC-40 Capacity spectrum in PO load case, high shear modulus soil, and boundary <5B

For series–parallel system in which there are n-series stages, each with n_i parallel components

$$R_{sp} = \prod_{i=1}^{n}[1 - (1 - R_i)]^{ni} \tag{7}$$

By accepting that once one element in a parallel sub-system fails, the sub-system fails accordingly, and for easier controlling the system of n-parallel components, the failure probability P_f is used; the P_f for a block in parallel is

$$P_{f,sys} = 1 - \prod_{i=1}^{n}(1 - P_{f,i}) \tag{8}$$

P_f for beam failure, lateral displacement, pile capacity, and raft in bending are $0.0985, 0.23, 0.00104$, and 0.171, respectively; in turn, all the abovementioned system

LS hinge 46-1 appears at 2nd story

a)

b)
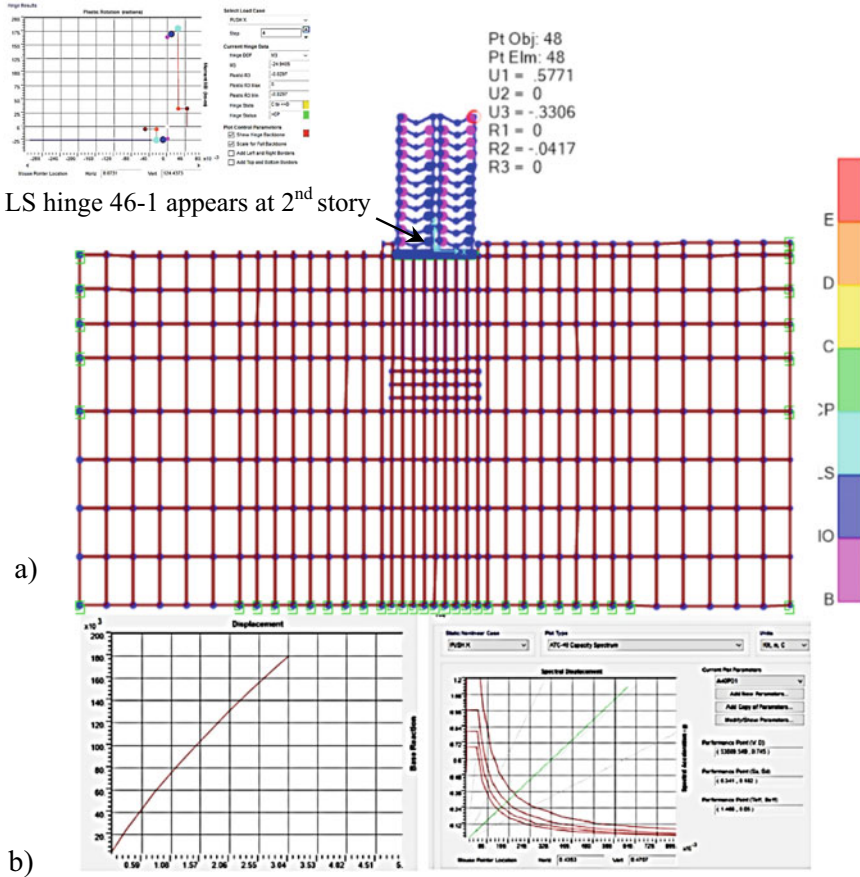
Fig. 11 **a** The performance at step 2 out of 9 with LS state in beams (e.g., No 46), >5B; **b** base shear versus displacement curve, and ATC-40 Capacity spectrum in PO load case, high shear modulus soil, and boundary >5B

Table 9 Responsive frequency of the building, x-direction

Mode	Frequency (Hz)				State of stiffness of piled raft foundation
	1	2	3	4	
Boundary <5B	0.388	0.534	0.855	26.45	11 □28 cm piles @2 m
Boundary >5B	0.268	0.446	0.609	27.83	7 □35 cm piles @3 m

is connected in series, the probability of failure for the overall system is calculated by formula 8:

$$P_{f,\,\mathrm{sys}} = 1 - (1 - P_{f,\,\mathrm{beam}}) \cdot (1 - P_{f,\,\mathrm{col}}) \cdot (1 - P_{f,\,\mathrm{pile}}) \cdot (1 - P_{f,\,\mathrm{raft}}) = 1 -$$
$$(1 - 0.0985)]_{\mathrm{beam}} \times (1 - 0.23)_{\mathrm{col}} \times (1 - 0.00104)_{\mathrm{pile}} \times (1 - 0.171)_{\mathrm{raft}} = 0.425,\ \mathrm{or}$$

Table 10 Responses of the system, at a time step which LS limit in PO analysis is attained, in comparison with the maximum value in TH load case/RS load cases

Response	Flexure beams	Base shear	Drift Δ_{hor} cm	Deflection Δ_{beam}	Settlement s_{max} (cm)	Moment in piled raft	Axial force in pile
LSF Combins	$G(X)$	$H(X)$	$I(X)$	$J(X)$	$K(X)$	$M(X)$	$N(X)$
1	48.7 26.65/21.7	29.3 17.7/14.8	39.6 18.6/21.8	0.83 0.46/0.37	23.3 12.5/10.8	846 461/384	1607 884/731
2	46.8 25.7/21.1	29.3 17.6/14.9	54.7 39.2/51.5	3.25 1.78/1.47	39.9 21/18.8	846 475/392	1420 781/643
3	46.8 25.7/21.0	26.2 15.5/5.93	47.9 20.9/42.4	3.52 1.92/1.59	66.7 35.2/31.4	369 204/171	1280 677/606
4	46.8 25.7/21.6	27.1 16.6/14	39.0 30/51	1.91 1.57/1.89	43.1 14.1/22.6	313 168/131	1452 789/767
5	46.8 25.7/21.0	26.7 16.4/14.1	49.5 37.7/49.5	3.29 1.81/1.51	42.9 22.5/20.4	383 211/174	1416 773/647
6	46.8 25.6/20.9	29.8 17.7/14.9	55.2 39/43	3.32 1.82/1.51	45.4 24/21.4	860 476/391	1612 891/739
7	46.8 25.7/21.1	29.6 15.7/16.3	28.9 51/90	3.48 1.91/1.58	40.2 21.1/13.7	1009 506/533	1507 706/825
8	46.78 25.7/21.1	26.8 15.4/14.1	49.5 20/49.5	3.29 1.79/1.48	42.9 22.5/20.4	387 209/172	1416 772/628
9	46.7 28.7/21.0	25.8 15.2/13.6	28.6 21/52	3.47 1.9/1.58	42.7 22.4/20	290 160/136	955 520/438
10	49.1 26.7/21.8	28.6 16.2/15.6	29.6 28.9/46.1	1.05 0.54/0.47	40.2 21.2/19.2	1039 599/523	1505 825/707
11	46.8 25.7/21.1	31 17.5/12.2	28.8 38.9/64	3.13 1.89/0.512	36.9 22.8/20.7	304 165/134	1107 603/607
12	46.8 25.7/21.1	29.9 17.8/14.9	55.3 39.4/42	3.33 1.82/1.5	45.4 24/21.3	854 480/391	1610 891/730

Note Underlined numbers are values at LS state (failure or limit attained) in static NL pushover analysis. Values with slash are of TH and RS, respectively

42.5% then the reliability index is $\beta_{sys} = 0.19$. The system with the $\beta = 0.19$ is too hazardous to survive during the earthquake.

Probability of exceedance P_e: During analyzing the structure subjected to response spectra, the probability of exceedance (PE) is the percentage of occurrence at least one or more times in given years. This probability is computed by Eq. 9:

$$P_e = 1 - \left(1 - \frac{1}{\tau}\right)^t \tag{9}$$

Table 11 FORM reliability indices

Load condition	Limit state functions	μ_X	σ_X	μ_Y	σ_Y	β
Flexure, beams	$G(X) =$ $\frac{M_{\text{yield}}}{M_{\text{max}}} - 1 \geq 0$	26.1 21.2	0.8637 0.2928	3.2615 3.0543	0.0330 0.0138	15.94 36.73
Shear in columns	$H(X) =$ $\frac{Q_{\text{max}}}{Q} - 1 \geq 0$	16.6083 13.7775	0.96993 2.56370	2.80820 2.60601	0.05835 0.18449	6.48 3.80
x-dir displacement	$I(X) =$ $\frac{H}{500}/\Delta_{hor} - 1 \geq 0$	32.05 50.233	9.90812 15.2323	3.42165 3.87269	0.30211 0.29658	0.74 -0.41*
z-dir deflection	$J(X) =$ $[f]/f - 1 \geq 0$	1.575 1.31433	0.49807 0.51303	0.40659 0.20242	0.30873 0.37658	1.29 1.57
Settlement	$K(X) =$ $\frac{\Delta_{\text{vertical}}}{\Delta} - 1 \geq 0$	21.9416 20.0583	5.31200 4.72183	3.05990 2.97167	0.23865 0.23223	2.07 2.38
Moment in raft	$M(X) =$ $\frac{[M]}{M_{\text{max PR}}} - 1 \geq 0$	342.83 294.33	160.833 149.339	5.73778 5.57017	0.44600 0.47861	0.95 1.18
Axial force in pile	$N(X) =$ $\frac{N}{R_{c,u}} - 1 \geq 0$	759.33 672.333	110.892 96.4929	6.62188 6.50056	0.14527 0.14278	3.08 3.72

Table 12 RI with respect to different LSFs

Response	Flexure beams	Base shear in column	Drift Δ_{hor} cm	Deflection Δbeam	Settlement s_{max} (cm)	Moment in piled raft	Axial force in pile
LSF	$G(X)$	$H(X)$	$I(X)$	$J(X)$	$K(X)$	$M(X)$	$N(X)$
β (TH)	15.94	6.48	0.74	1.29	2.07	0.95	3.08
β (RS)	36.73	3.8	0	1.57	2.38	1.18	3.72
β_{normal}	17.95	6.12	0.70	1.17	1.93	0.85	2.89

TH = Time history analysis; RS = Response analysis. β_{normal} is the reliability index (RI) when random variables are normally distributed
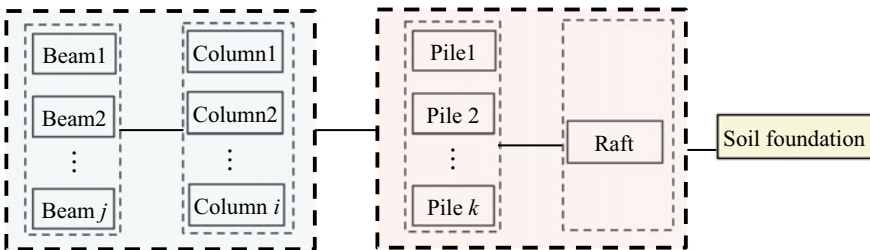
Fig. 12 System of superstructure, piled raft footing, and soil foundation

in which τ is the average recurrence interval, i.e., the time between occurrences of failure for a random variable X exceeding the threshold value x_T. For a 19% probability of exceedance as abovementioned calculation, PE in 50 years is $P_e = 1 - \left(1 - \frac{1}{19}\right)^{50} = 0.933$, or 93,3%. This is quite unacceptable.

4　Discussion

There are many ways of collecting data for reliability analysis as follows.

- Input data in this study uses both V and N recordings. These are recordings for EW direction at different stations. For another than NS direction, the assumed building would rotate 90 degrees to be subject to EW quake. As such, two accelerogram recordings are brought into the analysis. This may be viewed as uncertainty in direction of ground motion, instead of taking the base motion of a symmetrically shaped building into account.
- The time of occurrence for the maximum lateral displacement is at step 393, or $t = 39.3$ s. This time is earlier than other results in the configuration of less pile model. As such, the smaller number of piles, the lower frequencies are, and it is predictable that the lateral displacement would be greater. The larger response would be brought into reliability analysis.
- Cracked beam with CFRP which is modeled as per ACI recommendation and converts the CFRP to the equivalent concrete area should be carefully concerned. Nevertheless, it is logically acceptable viewing CFRP as a reinforcement to calculate the equivalent cross-section in addition to the cracked cross-section. In the SAP2000 model, by calculating iteratively to determine the location of the neutral axis in a separate study, the moment of inertia for the cracked beam with a specific CFRP and beam reinforcement is computed with a modifier of 0.06 for the moment of inertia. This process is more rigorous than using the ACI's cracked cross-section.
- Two situations are considered: the first group of 7 square 35 cm-piles, and the second one is 11 square 28 cm-piles, symmetrically distributed under the raft. This is intentionally modeled to study the effects of the pile intensity on the response of the superstructure and the possibility of settlement reduction, together with validating the assumption the closer pile spacing, the smaller displacement, and settlement, especially for small size of rafts [1]. Alternatively, the pile spacing reflects the uncertainty of modeling the foundation in SSI. The high frequency of the fourth mode of response implies SSI is remarkably significant. By investigating a small boundary, with the same volume of the piles, the frequencies of the overall system increase because of the higher stiffness.
- The outer pile supports more load than the inner one. This working characteristic is well agreed with the real response of the pile foundation in cohesive soil. For piles in sand, it is predictable the contrary trend, in which the inner piles would support more load than outer ones.

- For a cracked beam strengthened with CFRP, it is rather difficult to model numerically the structure for a dynamic analysis concerning the SSI of a piled raft foundation. Nevertheless, the rigor for this reliability analysis is tentatively ensured when various kinds of uncertainties are concerned and quantified, the results obtained by TH and RS are accordingly correlated, and the values of responses are reasonable as the moment of inertia of cross-sections is calculated by two independent algorithms [15, 16].
- Although nine factors are studied, there might be some dominant factors governing the reliability by applying an analysis of variance (ANOVA) [19].
- It is necessary to examine the resistance of each random variable used in this study. The variable of soil depends on the load during the soil-structure interaction. In the other words, the exact value of the soil properties, i.e., strength parameters by which the bearing capacity for pile and raft is determined depends on the load-settlement curves. This issue may be overcome by using the "square root of the sum of the square" law or SRSS, as

$$\mu_R = \mu_S + \beta \cdot \sigma_z = \mu_S + \beta \cdot \sqrt{\sigma_S^2 + \sigma_{\text{pile}}^2 + \sigma_{\text{raft}}^2} \tag{10}$$

in which $\mu_S \ \sigma_S$ is the mean value of the load, respectively; σ_{pile} is the standard deviation of the pile resistance and the same σ_{raft} for the raft resistance.

- This study takes the response at LS condition in pushover analysis to be the threshold values, and the envelope values, i.e., maximum and minimum values of the response are taken into account. The threshold values should be somewhat that is obtained by the regulation, or at least as prescribed in Table 3 instead.
- The time-variant reliability could be analyzed by considering the response in ranges of time steps and applying the moving average techniques [30],

$$\beta_{\text{dyn}} = \frac{E(\text{FS}) - 1}{\sigma(\text{FS})} \tag{11}$$

in which FS would be the safety factor for a specific limit state, i.e., the ratio of the capacity divided by the demand; $E(\text{FS})$ and $\sigma(\text{FS})$ are the mean value and the standard deviation of the SF, respectively. This would be a further study in the future.

5 Conclusion

This reliability analysis takes various conditions of uncertainties into account. Five categories of random variables are of the earthquake intensity (i.e., the duration of the quake and the intensity, group A, three variables), the materials of the superstructure and piled raft, together with their stiffness (group B, four variables), the soil (group C, shear modulus), epistemic uncertainty or mode of analysis (group D, two variables),

and boundary for analyzing (group E). A numerical 2D model that combines a 10-story frame to a piled raft foundation with absorbent boundaries is developed. For the superstructure, a modifier of the moment of inertia for a cracked cross-section of CFRP-strengthened beams (with a reference to ACI recommendation as in Table 1), and a reduced modulus E for simulating the unit-slice model for the planar frame of the building; for the sub-ground foundation, solid element for raft and frame element for piles are modeled. The two techniques of modeling the superstructure ensure an acceptable rigorousness in obtaining the proper response of the structure. TH and RS load cases in 12 combinations would supply the database for calculating the reliability index considering all the possible values of the variables involved. Limit safety LS level of performance for beam in the displacement-control PO analysis is chosen as the ultimate state for calculating the safety factor, and the value of LSFs in the earthquake. All the TH, RS, and PO use the acceleration in x-direction as the load exerting on the structure. A lot of data obtained could be useful for a reasonable analysis of reliability. Results indicate a broader domain of foundation basically yields the larger values in displacement and fundamental frequency of the SSI system.

For time-invariant reliability, the maximum and the minimum values are considered. This index would be for strength LSFs with the factored load condition. Although the "weak beam, strong column" concept is intentionally applied to this problem, the frame with cracked beams strengthened with CFRP, resting on a piled raft foundation, subjected to an earthquake with soil-structure interaction has very low reliability, largely for lacking the relevant measure of energy dissipation such as base isolation, or tuned dampers. Such a further study should be conducted in the future.

References

1. Katzenbach R, Arslan U, Moormann C, Reul O (1998) Piled raft foundation—interaction between piles and raft. In: International conference on soil-structure interaction in urban civil engineering, damstadt geotechnics 4:279–296
2. Millen MDL, Pampanin S, Cubrinovski M, Carr A (2014) Integrating soil structure interaction within performance based design. In: Proceedings of 2014 conference NZSEE, New Zealand
3. Zubair M, Shilpa BR (2016) A parametric study of soil structure interaction of raft foundation by using dynamic analysis. Int J Eng Sci Invent Res Dev III(I):68–76, e-ISSN: 2349–6185
4. Khatibinia M, Gharenhbaghi S, Moustafa A (2015) Seismic reliability-based design optimization of reinforced concrete structures including soil-structure interaction effects. Chapter 11, IntechOpen, https://doi.org/10.5772/59641
5. Lysmer J, Kuhlemeyer R (1969) Finite element model for infinite media. J Eng Mech ASCE 95:859–877
6. Gazetas (2016) Formulas and charts for impedance of the surface and embedded foundations. J Geotech Eng 117(9):1363–1381, https://www.researchgate.net/publication/248878272, Uploaded 1 July
7. Song MJ (2018) Development of an approximate nonlinear analysis of piled raft foundation, https://fdocuments.in/document/development-of-an-approximate-nonlinear-analysis-of-piled-raft-foundations.html. Last Accessed 14 April 2018

8. Pinto PE, Giannini R, Franchin P (2004) Seismic reliability analysis of structures. IUSS Press Publisher, 1st edn., Amazon.com
9. Wolf JP, Song C (2002) Some cornerstones of dynamic soil-structure interaction. J Eng Struct 24:13–28
10. Datta TK (2010) Seismic analysis of structures. John Wiley & Son Asia Pte Ltd Publications
11. Edger L, Sanayei M, Alonge JL (2016) Modeling the effects of soil-structure interaction on a tall building bearing on a mat foundation. Arti Civil Eng Pract 51–68. https://www.researchgate.net/publication/258671831. Uploaded 1 July
12. Lin C-C, Lin P-Y, Chang T-M, Lin T-K, Weng Y-T, Chang K-C, Tsa K-C (2012) Development of on-site earthquake early warning system for Taiwan. Chapter 13, IntechOpen, https://doi.org/10.5772/28056
13. Susila1 E, Anggrain N (2018) Soil-structure interaction of a piled raft foundation in clay—a 3D numerical study. J Eng Technol Sci 48(4):388–407. https://doi.org/10.1155/2018/7259424
14. ACI 318–14 (American Concrete Institute), Building Code Requirements for Structural Concrete (ACI 318–14)—Commentary on Building Code Requirements for Structural Concrete (ACI 318R-14). Copyright © 2014, American Concrete Institute. The First Printing September 2014, ISBN: 978–0–87031–930–3. University of Texas Revised Sub Account/5620001114 (2014)
15. Kasimzade AA, Tuhta S (2014) Analytical, numerical and experimental examination of reinforced composite beams covered with carbon fiber reinforced plastics. J Theor Appl Mech, Sofia 42(1):55–70. https://www.researchgate.net/publication/258671831. Uploaded 2 Sept 2014
16. Боидареко ВМ, Шагин АЛ (1987) Расчет Эффиективых МногоКопонтных Конструкций- Курсом Ускорениа Научно-Технического Прогресса, Москва Стрройиздат (in English: Moscow Construction) 1–174
17. Fallahl AA, Moghadam AS, Mohammadzadeh S (2009) Reliability index for reinforced concrete frames using nonlinear pushover and dynamic analysis. Int J Adv Struct Eng 1(2):135–151, 2(5)
18. Duong TH (2021) Reliability index of a multi-story building considering the uncertainties of monitoring system. In: Lecture notes in civil engineering, vol 148. Springer Singapore, pp 281–300. https://doi.org/10.1007/978-981-16-0945-9_24
19. Duong TH (2021) The group efficiency of soil-cement columns in comparison with the group factor of piles. In: Computational intelligence methods for green technology and sustainable development, proceedings of the international conference GTSD2020. Springer, pp 351–363. https://doi.org/10.1007/978-3-030-62324-1_30
20. Tan O, Sahin Zaimoglu A, Hinislioglu S, Altun S (2005) Taguchi approach for optimization of the bleeding on the cement-based grouts. Int J Tunnell Undergr Space Eng 20:167–173
21. Liu L, Gou W, Bi L, Li Y, Wu Y (2012) Analysis of elastio-plastic soil-structure interaction system using pushover method. In: 15th international proceedings on world conference on earthquake engineering, Lisbon, Portugal
22. Inel M, Ozmen HB (2006) Effects of plastic hinge properties in nonlinear analysis of reinforced concrete buildings. J Eng Struct 28:1494–1502. https://doi.org/10.1016/j.engstruct.2006.01.017
23. Cao VV, Ronagh HR (2014) Reducing the seismic damage of reinforced concrete frames using FRP confinement. Accepted paper in composite structures. https://doi.org/10.1016/j.compstruct.2014.07.038
24. Mousavi S, Noorzad A (2019) Dynamic reliability analysis of earth dam's slope stability. In: Proceedings of the international conference on sustainable and safe dams around the world—Tournier, Bennett and Bibeau (Eds), Canadian Dam Association, ISBN 978–0–367–33422–2
25. PEER Ground Motion Database. https://ngawest2.berkeley.edu/site/documentation. Pacific Earthquake Engineering Research Center. Last Accessed 9 June 2021
26. Nowak AS, Collins KR (2000) Reliability of structures. McGraw Hill International Editions
27. Gu Q (2014) Performance and risk assessment of soil-structure interaction systems based on finite element reliability method. J Math Prob Eng 16. https://doi.org/10.1155/2014/704804

28. Lin S-Y, Hung H-H, Yang JP, Yang YB (2017) Seismic analysis of twin tunnels by a finite/infinite element approach. Int J Geomech 17(9). https://doi.org/10.1061/(ASCE)GM.1943-5622.0000940
29. Tsai Y-B, Huang M-W (2000) Strong ground motion characteristics of the Chi-Chi TaiWan earthquake of September 21, 1999. Earthq Eng Eng Seismol 2(1):1–21
30. Saleh F, Supriyadi B, Suhendro B, Tran D (2016) Damage detection in non-prismatic reinforced concrete beams using curvature mode shapes. J Struct Integr Fract. https://www.researchgate.net/publication/37617255. Uploaded by Bambang Suhendro 29 Jan 2016

Research on Crack Extension Resistance and Remaining Strength of High-Strength Concrete Using Nano-silica

Thi Cam Nhung Nguyen [ID], **Van Thuc Ngo** [ID], **Tien Thanh Bui** [ID], and **Viet Hung Tran** [ID]

1 Introduction

The cracking of concrete is one of the topics that are focused on research. Materials and structures made from concrete are prone to cracking due to various reasons. According to Van Mier [1], cracking in concrete is due to the disconnection of aggregate particles and cement mortar or broken aggregate itself. In the curing process, there will inevitably be internal micro-cracks, which will grow and be connected to form some distinct cracks because of the change in temperature and load during extraction. With the propagation of cracks, fractures can occur on concrete structures. In order to analyze the fracture mechanism and crack behavior of concrete, assuming that the concrete is intact while working in the elastic behavior, the concrete material is homogeneous. The fracture of concrete begins with the appearance of micro-cracks dispersed in adverse bearing areas, as the load continues to increase, these micro-cracks tend to concentrate on creating large cracks that may be observed.

The crack extension resistance is considered a vital characteristic to describe the crack propagation of concrete. Many authors have studied that the crack extension resistance curve in concrete from the crack starts to appear until it is ultimately damage. Examples are the studies Hilsdorf and Brameshuber [2], Karihaloo [3], Mai [4], Bazant and Jirasek [5], Planas et al. [6], Xu and Reinhart [7, 8], Kumar and Barai [9], Dong et al. [10]. Among them, the proposed method to evaluate according to the K_R curve was performed by Xu and Reinhardt used very common. According to the research of Reinhardt and Xu, the essential relationship is between the cohesive forces operating in the cohesive cracks and the K_R crack curves for the complete fracture

T. C. N. Nguyen · T. T. Bui · V. H. Tran
University of Transport and Communications, Hanoi, Vietnam

V. T. Ngo (✉)
Mien Tay Construction University, 20B Pho Co Dieu Street, Ward 3, Vinh Long, Vietnam
e-mail: nvthuc34@gmail.com

in concrete when considering cohesion forces along the region. Cohesive cracking is regarded as a significant factor. In this method, the crack extension resistance K_R is obtained by a combination of the initial crack toughness K_{Ic}^{ini}, which is the inherent toughness of the material against the occurrence of a propagation crack and K_I^C is cohesion toughness as a result of the contribution of cohesive stress along the length of the cracking process.

Besides, according to Wu's research [11], the existence of a crack with a specific length in concrete can still indicate the working state of a structure. An analytical method to predict the remaining strength of the HSC structure using NS post-crack using the fracture working method is based on previous research approach by Hiroshi Tada [12] and Wu [11]. According to Wu, the remaining strength of any cracked concrete structure component will be proportional to the U_R/U_T ratio and the ratio of the crack length to the height of beam a/D, or the non-cracked part of the beam height $(D-a)/D$. Therefore, it is possible to predict the remaining strength of cracked concrete structures by using the work of fracture and the ratio of the crack propagation length of the structure.

Currently, NS is widely used for research, along with the reduction of industrial production costs, the use of NS materials has received a special attraction for researching concrete and HSC [13]. The use of nano-silica (NS) in concrete has been well documented, which can significantly improve the mechanical properties and durability of concrete [14–18]. The incorporation of NS materials into the mix concrete to improve mechanical properties has become a promising field of research. The silica nanoparticles are characterized by a large surface area ratio and high activity potential. Nanometer-sized silica particles help activate the hydration reactions of cement and the removal of less durable components in concrete $Ca(OH)_2$ producing better performance pozzolans gel products. This process makes the concrete structure consistency, develops early strength, increases compressive strength, tensile strength, water anti-permeability, chloride permeability [16]. Besides, the fracture characteristics of concrete using mineral components such as fly ash, silica fume, and nano-silica in high-strength concrete have paid much attention to research [19, 20]. The fracture of structures designed with high-strength concrete is characterized by high brittleness, so the presence of ultrafine material will significantly change the behavior of cracking of concrete. The increased toughness of concrete is explained by bridging higher cracked surfaces in the presence of ultrafine particles. The study used analytical methods of fracture models in concrete to determine the effect of NS on the crack extension resistance and the remaining strength of the post-crack of HSC.

2 Experimental Fracture Characteristics of HSC Using NS

2.1 Preparing for Experimental

- **Materials**

  Materials include cement with PC40, coarse aggregates are basalt with D_{max} of 12.5 mm, fine aggregates are sand with a module greater than 2.7, superplasticizer (Viscocrete 3000-20 M), silica fume (sikacrete PP1), and nano-silica. Investigate the use of NS with dimensions ranging from 5 to 50 nm and a typical surface area of 200 ± 25 m^2/g (Fig. 1).

  The results of SEM analysis to analyze the size and shape of nano-silica are shown in Fig. 2. The nanoparticles are spherical in shape and have an average size of about 13 nm.

- **Mix Proportions**

Fig.1 Materials for experimental
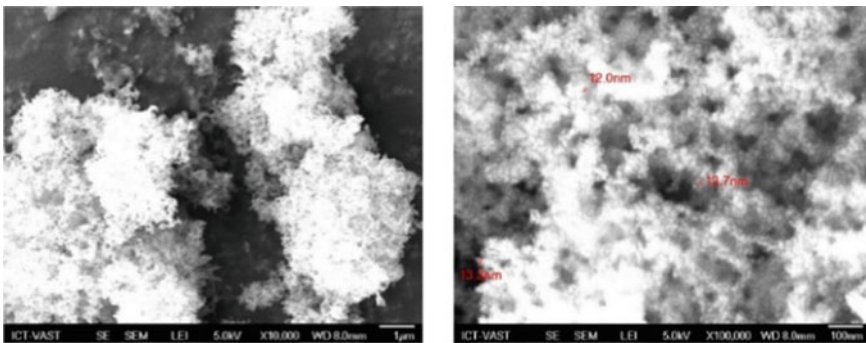
Fig. 2 Results of SEM analysis

Table 1 Material composition of HSC using NS

Mix code	Material compositions (kg/m³)							
	PC	CA	FA	SF	NS	SP (liter)	W	W/B
NS0.0	544.2	1049	674.6	28.60	0.00	5.44	154	0.27
NS0.5	541.3	1049	673.6	28.60	2.86	6.53	154	0.27
NS1.5	535.6	1049	671.6	28.60	8.59	7.62	154	0.27

PC Portland cement, *CA* coarse aggregate, *FA* fine aggregate, *SF* silica fume, *NS* nano-silica, *SP* superplasticizer, *W* water, *B* binder
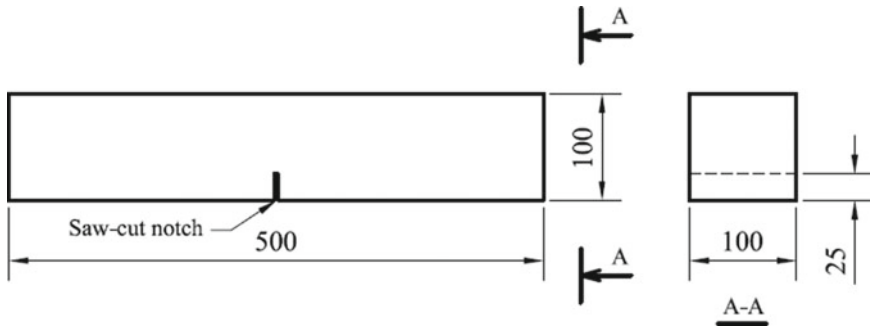
Fig. 3 Sample of three-point bending with a notch used in the experimental

HSC with NS is designed with a typical compressive strength of 70 MPa calculated using the ACI method. For the fracture characterization test, HSCs with 0, 0.5, and 1.5% NS were used. The results of three compositions are shown in Table 1.

- **Preparing for Sample**

  The beam specimen used in the three-point bending test is a prism with size of 500 × 100 × 100 mm and a notch width of 2 mm and depth of 25 mm (Fig. 3).

  During casting, notches are performed on a surface that are rectangular to the top of the sample. According to Rilem [21], test beams after 28 days, the notch should be performed on the 21st day. cc. Each mix proportion was prepared with six samples for testing.

2.2 Experimental Results

During the test, crack mouth open displacement, deflection in the middle of the beam, and the corresponding load were recorded until the beam was utterly damage. Samples of HSC beams have cracks developed in a relatively narrow vertical plane. Cracks are formed from the notch and width upon the sample of the test beam.

Observed from the experiment, it was found that it took a short time (about 1 min) to reach the peak load. However, it took a long time after the load reaches its peak until complete fracture, caused by the control of CMOD in the test process.

The load–deflection and load-CMOD curves are measured for all mix proportion with silica nano-ratios varying from 0 to 1.5%. Experimental results are averaged over six samples for each corresponding mix. The results showed that the difference of the P-CMOD curves corresponding to the beam specimens cured up to 28 days using nano-silica with ratios of 0, 0.5, and 1.5%, as in Fig. 5. After reaching the peak (Pmax), the P-CMOD curve of HSC without NS has a steep slope. When the CMOD is very small, the force value decreases quickly. When added to concrete with the ratio of 0.5 and 1.5% NS, the result is that the P-CMOD curve has a significant change, especially with 1.5%NS. The curves tend to grow the same in the early stages when the concrete is still in the elasticity limit, and the difference begins to appear when the curve is about to peak.

In the post-peak period, the curve of HSC using NS has a slope of less than HSC control. Figure 4 shows that the force value decreases with the growth of the slower CMOD when comparing the same value of CMOD. The load valuation of specimens using NS was maintained higher than the non-NS specimens.

The load–deflection relationship curves (P-δ) of HSC using NS are shown in Fig. 5. For HSC using NS, P-δ curve will be thicker, the curve's nonlinear period is longer, and the load slowly decreases. Observation P-δ curves on Fig. 5 show that the area under the curve (work of fracture-W_F) of the graph varies with the NS ratio. To calculate the area under the P-δ curves, use the integral method. W_F increased by 21.4% when the NS ratio was 0.5% and by 58.71% when the NS ratio was 1.5%.

Fig. 4 Effect of nano-silica in P-CMOD
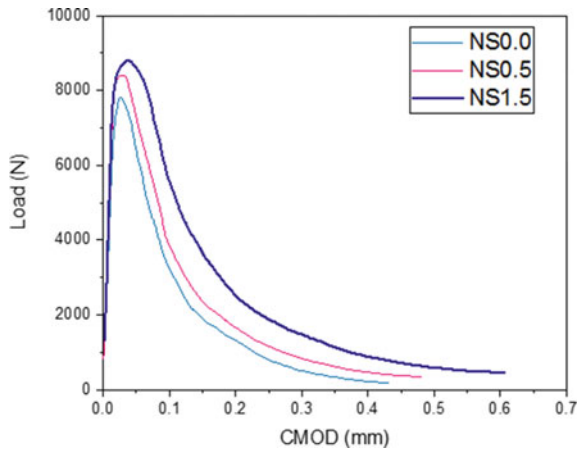
Fig. 5 Effect of nano-silica on *P*-deflection
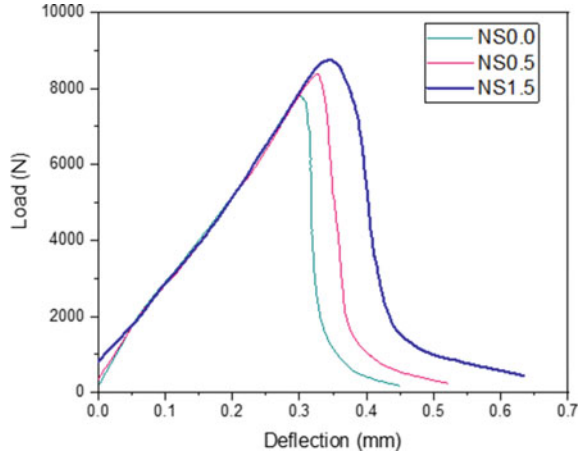
3   Calculation of Crack Extension Resistance HSC Using NS

To assess the effect of nano-silica on the crack extension resistance of concrete, the $K_R(\Delta a)$ evaluation method based on the bilinear softening law of Xu et al. will be applicated [22]. The K_R crack propagation resistance is obtained in this method by combining K_{Ic}^{ini}, which is the available toughness of the material counteract the occurrence of cracks, with cohesive toughness K_I^C as a result of the contribution of cohesive stress along the crack length.

$$K_R = K_{Ic}^{ini} + K_I^C \tag{1}$$

According to Xu and Reinhardt [23], the general formula for calculating the cohesion strength for three-point bending tests of beams is as follows:

$$K_I^C(\Delta a) = \int_{a_0}^{a} 2\sigma(x) F_1\left(\frac{x}{a}, \frac{a}{D}\right) / \sqrt{\pi a} \, \mathrm{d}x \tag{2}$$

$$F_1\left(\frac{x}{a}, \frac{a}{D}\right) = \frac{3.52(1 - x/a)}{(1 - a/D)^{3/2}} - \frac{4.35 - 5.28x/a}{(1 - a/D)^{1/2}}$$
$$+ \left\{ \frac{1.30 - 0.30(x/a)^{3/2}}{\sqrt{1 - (x/a)^2}} + 0.83 - 1.76\frac{x}{a} \right\} \left\{ 1 - \left(1 - \frac{x}{a}\right)\frac{a}{D} \right\} \tag{3}$$

Four distinct crack propagation sites characterize the fracture stages [23]. The first station is $a = a_0$, the second is $a_0 \leq a \leq a_c$, the third is $a_c \leq a \leq a_{w0}$, and the final station is $a > a_{w0}$.

Table 2 Results of calculation the initial crack toughness

Mix code	β_c	U_e	$K_{Ic}^C\,(\mathrm{MPa}\cdot\sqrt{m})$	$K_{Ic}^{un}\,(\mathrm{MPa}\cdot\sqrt{m})$	$K_{Ic}^{ini}\,(\mathrm{MPa}\cdot\sqrt{m})$
NS0.0	0.116	0.914	0.432	1.607	1.175
NS0.5	0.114	0.904	0.514	1.787	1.273
NS1.5	0.105	0.877	0.755	2.075	1.320

Fig. 6 Effect of NS on HSC's crack extension resistance
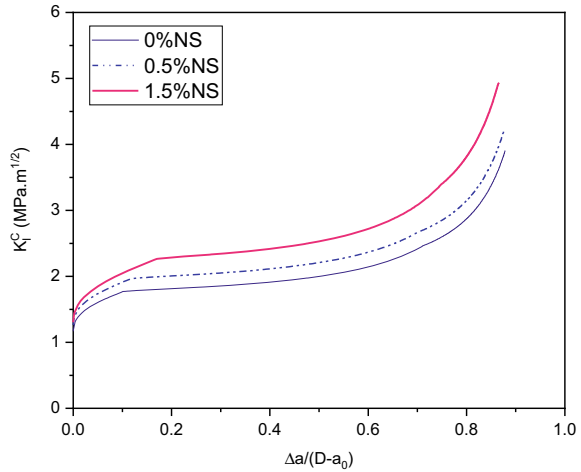
The initial toughness is calculated based on a simplified method of Xu and Reinhardt [23]. The results are shown in Table 2. The combined initial toughness and cohesive toughness result in crack extension resistance.

The formulations are set in a series programmed by Mathcad software to calculate crack extension resistance. The experiment's fracture parameters and the *P*-CMOD relationship curve of high-strength concrete using NS will be used in the calculation. The results are shown in Fig. 6.

Figure 6 shows the effect of NS on crack extension resistance as a function of load and crack propagation length. The crack extension resistance curve for HSC with 1.5% NS has a greater beginning point than the other combination, and the values along the crack are also much higher. The crack resistance curve results were very similar to other results estimated by previous authors [10, 22, 24].

4 The Post-cracking Remaining Strength

The total amount of work of fracture absorbed by the beam can be determined by Eq. (4):

$$U_T = W_F = \int_0^\delta P\,d\delta \tag{4}$$

where: U_T is the total of work of fracture (N.mm); P is the load (N); δ is the deflection obtained from a three-point bending test (mm).

At a point i on the curve P-δ, the corresponding load P_i, deflection, and crack development length δ_i, a_i. The amount of work of fracture be used to create a crack length a_i designated U_L, in which the remaining work of fracture corresponds to the undamaged beam, is called U_R. When the crack continues to propagate, the amount of remaining work will be reduced, and the uncracked height is calculated by the difference of the height of the beam D and the crack development length a.

Calculation results of the post-cracking remaining strength U_R (%) of HSC beam structure using NS are shown in Figs. 7 and 8. Results are shown in tables corresponding to HSC with 0 and 1.5% NS in which $U_L(\Delta a)$ is the consumed strength by the development of cracks, and the $U_L(\Delta a)$ results are converted to percent by total absorbed amount of work of fracture.

Relationship of crack propagation length and remaining strength of HSC with 0% NS.

Based on the results of calculating the remaining strength U_R according to the crack propagation length Δa in Fig. 7, the relationship between U_R-Δa of HSC without NS was built like the following Eq. 5:

$$U_{\text{RNS0.0}} = -8.519\ln(\Delta a) + 41.296 \tag{5}$$

Relationship of crack propagation length and remaining strength HSC use 1.5% NS.

Based on the results of calculating the remaining strength according to the crack propagation length Δa in Fig. 8, the relationship between U_R-Δa of HSC using 1.5%
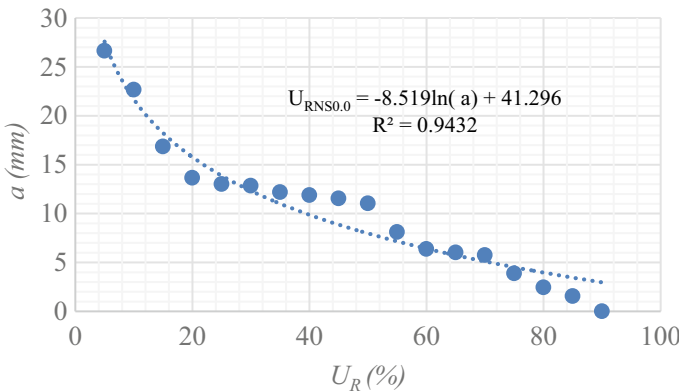
Fig. 7 Relationship of remaining strength and crack propagation length of HSC with 0%
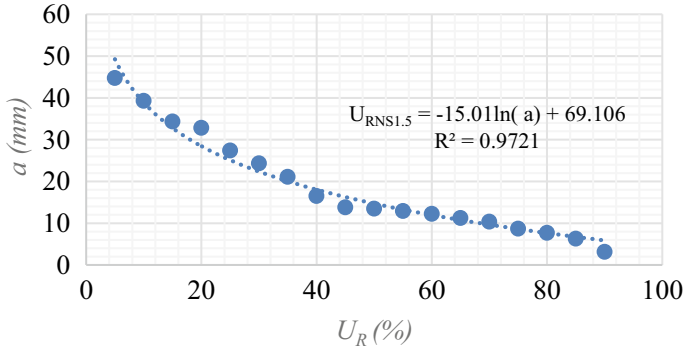
Fig. 8 Relationship of remaining strength and crack propagation length of HSC with 1.5% NS

NS was built like the following equation:

$$U_{RNS1.5} = -15.01 \ln(\Delta a) + 69.106 \tag{6}$$

The post-cracking remaining strength is calculated based on the method of using the fracture work corresponding to the crack propagation length. The results calculated based on Figs. 7 and 8 have a tendency the same. The remaining strength decreases at each crack development stage.

In the calculation results, the post-cracking remaining strength for the same crack development length, the calculation result of the HSC using NS was higher than the unused type. This can explain the ability to help maintain the strength after the crack appears of NS particles by improving the quality of the mortar and interface transition zone of aggregate with mortar. In addition, NS particles can increase HSC's crack extension resistance as mentioned through the above analysis.

5   Conclusion

Based on results of this study, some conclusions could be drawn as follows:

- This research determined characteristics of HSC. The characteristics of HSC using NS were determined through experiment and analysis, such as relationships between *P*-CMOD, relationships between *P*-deflection, work of fracture.
- The crack extension resistance $K_R(\Delta a)$ of HSC using NS was calculated based on the result of three-point bending tests notch beams. The formulas were established based on the bilinear softening law. The results showed that initial toughness K_{Ic}^{ini} and cohesive toughness K_I^C of HSC using nano-silica were increased when compared to the control mixture (0% NS). Thereby, it is possible to show the ability to resist the occurrence of propagation cracks of high-strength concrete using NS than the non-use type. In addition, the degree of influence of NS to

cohesive toughness along the cracking is also a significant contribution to the ability to resist crack propagation in HSC.

- The post-cracking remaining strength is assessed by the method of using the absorbing during the fracture process. The result is the values corresponding to the bearing capacity of the remaining load corresponding to the propagation length Δa. Through the calculation results, it can comment that the remaining strength of the HSC beam structure is reduced when the crack starts to develop when using NS in the HSC mixture can significantly improve the remaining strength of post-cracking compared to unused types.

References

1. Van Mier J (1997) Concrete fracture: a multiscale approach. CRC Press, New York
2. Hilsdorf K, Brameshuber W (1984) Size effects in the experimental determination of fracture mechanics parameters. In: Shah SP (ed.) Application of fracture mechanics to cementitious composites. NATO-ARW, pp 361–397
3. Karihaloo L (1987) Do plain and fibre-reinforced concretes have an R-curve behaviour? In: Shah SP, Swartz SE (eds.) Fractures of concrete and rock. Springer±Verlag, pp 96–105
4. Mai W (1984) Fracture measurements of cementitious composites. In: Shah SP (ed.) Application of fracture mechanics to cementitious composites. NATO-ARW, pp 399–429
5. Bazant P, Jirasek MR (1993) curve modeling of rate and size effects in quasibrittle fracture. Int J Fract 62:355–373
6. Planas J, Elices M, Ruiz G (1993) The equivalent elastic crack: 2. X-Y equivalences and asymptoticanalysis. J Fract 61:231–246
7. Reinhardt W, Cornelissen W, Hordijk D (1986) Tensile tests and failure analysis of concrete. J Struct Eng ASCE 112:2462–2477
8. Xu S, Reinhardt W (1999) Determination of double-K criterion for crack propagation in quasi-brittle materials-part II: analytically evaluating and practically measuring methods for three-point bending notched beams. Int J Fract 98:151–177
9. Kumar S, Barai S (2008) Influence of specimen geometry and size-effect on the KR-curve based on the cohesive stress in concrete. Int J Fract 152(2):127–148
10. Dong W, Wu M, Zhou M (2013) Calculating crack extension resistance of concrete based on a new crack propagation criterion. Constr Build Mater 38(2):879–889
11. Wu X (2006) Prediction of service load of concrete structures after cracking. New Jersey Institute of Technology, Newark
12. Hiroshi T, Paul C, Irwin R (2000) The stress analysis of cracks handbook. Wiley, New York
13. Ngo T, Lam K, Do D, Nguyen C (2020) Increased plasticity of nano concrete with steel fibers. Mag Civ Eng 93(1):27–34
14. Nazerigivi A, Nejati H, Ghazvinian A, Najigivi A (2018) Effects of SiO_2 nanoparticles dispersion on concrete fracture toughness. Constr Build Mater 171:672–679
15. Sanchez F, Sobolev K (2010) Nanotechnology in concrete: a review. Constr Build Mater 24(11):2060–2071
16. Zhang P, Zhao Y, Li Q, Zhang T, Wang P (2014) Mechanical properties of fly ash concrete composite reinforced with nano-SiO_2 and steel fiber. Curr Sci 106:1529–1537

17. Chithra S, Kumar R, Chinnaraju K (2016) The effect of Colloidal Nano-silica on workability, mechanical and durability properties of High Performance Concrete with Copper slag as partial fine aggregate. Constr Build Mater 113:794–804
18. Qing Y, Zenan Z, Li S, Rongshen C (2008) A comparative study on the pozzolanic activity between nano-SiO_2 and silica fume. J Wuhan Univ Technol Mater Sci 21:153–157
19. Van Mier J (2013) Concrete fracture: a multiscale approach. CRC Press, New York
20. Zhang P, Wan J, Wang K, Li Q (2017) Influence of nano-SiO_2 on properties of fresh and hardened high performance concrete: a state-of-the-art review. Constr Build Mater 148:648–658
21. RILEM (1985) Determination of the fracture energy of mortar and concrete by means of three-point bend tests on notched beams. Mater Struct 18:285–290. Committee FMC 50
22. Xu S, Reinhardt W (1998) Crack extension resistance and fracture properties of quasi-brittle softening materials like concrete based on the complete process of fracture. Int J Fract 92:71–99
23. Xu S, Reinhardr H (2000) A simplified method for determining double-K fracture parameters for three-point bending tests. Int J Fract 104:181–209
24. Reinhardt W, Xu S (1999) Crack extension resistance based on the cohesive force in concrete. Eng Fract Mech 64:563–587

Evaluate the Safe Working Capacity of the Driven Pile Deviated the Designed Position: A Case Study in Vietnam

Bac An Hoang

1 Introduction

Vietnam is now a country with a developing economy. According to the increasing urbanization level, more and more high-rise buildings, supermarkets, apartments are built. For many large-scale construction projects in poor geological conditions, the pile foundation solution is popular. During the construction of such deep foundations, there are often pile problems. The most common problem is the horizontal displacement of the pile head compared to the original design position. The Vietnamese standard [1] already has regulations as the pile's tolerance is not more than 0.2D for the side pile and not more than 0.3D for the middle pile when arranging tape piles or groups of 2 and 3 rows. In fact, in many projects, after installing piles, there is a phenomenon that the pile head has deviated beyond the allowed range. Therefore, the designer has to recalculate the load capacity of the pile, which is very complicated, leading to an increase in cost and progress of construction [2–5]. There are cases where the position deviation of the pile is within the allowable range but still endangers the working of the pile.

There are not many studies on the deflection of piles affecting the bearing capacity of piles, as Budi and Wijaya [6] studied the precision of pile foundation position compared to its original predetermined location. Huang [7] studied the acceptable tolerance of driven piles with position deviation. Silva et al. [8] used order statistics when predicting pile foundation failure probability. Amir and Ahmad [9] is carried out to design and reanalyze the pile cap due to eccentricity. In Vietnam, there are many studies on piles. Still, the primary studies on pile load capacity as Vo [10] studied the bearing capacity of piles taking into account the influence of the surrounding ground

B. A. Hoang (✉)
University of Architecture Ho Chi Minh City (UAH), 196 Pasteur, District 3, Ho Chi Minh City, Vietnam
e-mail: an.hoangbac@uah.edu.vn

displacement. Nguyen and Pham [11] recommended the method to determine the reliability of pile foundations in construction. Trinh [12] studied the prediction of the load-settlement relationship of piles from the results of static compression of piles. Also, studies on the influence of position tolerance on pile load capacity are not yet available. Therefore, this study proposes a method of evaluating the safe working of piles, considering the influence of pile axis deviation and other factors, thereby making recommendations to designers and builders. The reliability theory is applied to simulate the state function with random parameters, thereby determining the pile's bearing capacity reliability.

2   Theoretical Method

2.1   Calculation Load Per Pile

According to [13], consider the foundation as a frame structure, under axial load, shear force, and bending moments. For a foundation with vertical piles, the calculated load N_j per jth pile shall be admissible to be determined as per the formula:

$$N_j = \frac{N}{n} + \frac{M_x y_j}{\sum_{i=1}^{n} y_i^2} + \frac{M_y x_j}{\sum_{i=1}^{n} x_i^2}, \tag{1}$$

where:

N	the calculated axial force;
M_x, M_y	the calculated bending moments, concerning the main central axes x, y of the pile layout in the flatness of the footing of the foundation grillage;
n	the number of piles in the foundation;
x_i, y_i	the distances from the main axes to the axis of each ith pile;
x_j, y_j	the distances from the main axes to the axis of each jth pile, for which is calculated.

2.2   Limit State Function and Reliability Analysis

The single pile in the foundation's structure and beyond its boundaries, for the load-bearing capacity of the base soil, the equilibrium equation to be satisfied in the ultimate limit state design of axially loaded piles in compression is:

$$N_{c,d} \leq R_{c,d} \tag{2}$$

where:

$N_{c,d}$	the calculated load to be transferred to the pile;

$R_{c,d} = R_{c,k} \cdot \gamma_0 / (\gamma_k \cdot \gamma_n)$ the calculated load-bearing capacity of the pile;

$R_{c,k}$ the standard bearing capacity of the pile;

γ_0 the coefficient of working conditions;

γ_n the confidence coefficient of the importance of the building;

γ_k the soil reliability coefficient is taken according to [13].

Assuming the occurrence of the failure of the pile when condition (2) is not satisfied, therefore, a hypothetical boundary distinguishing between the safety and failure states (so-called limit state function) of the pile is given by the following equation:

$$R_{c,d} - N_{c,d} = 0 \tag{3}$$

Both $N_{c,d}$ and $R_{c,d}$ are generally random variables, and the validity of inequality (2) cannot be guaranteed, i.e., with the probability equal to 1. The essential objective of reliability theory is to assess the probability of failure p_f and find the necessary conditions for its limited magnitude. Thus, the probability of failure can be formulated as:

$$p_f = P(N_{c,d} > R_{c,d}), \tag{4}$$

Assumed that variables $N_{c,d}$ and $R_{c,d}$ are random variables. Then, the difference M (called the reliability margin) has a normal distribution:

$$M = R_{c,d} - N_{c,d} \tag{5}$$

Distribution of M has mean $\mu_M = \mu_{R_{c,d}} - \mu_{N_{c,d}}$, standard deviation (σ_M), and probability density $(f(m))$.

When $N_{c,d}$ and $R_{c,d}$ are independent random variables, we have:

$$f(m) = \int_{-\infty}^{\infty} g(m + n_{c,d}) f(n_{c,d}) dn_{c,d}, \tag{6}$$

With $g(m + n_{c,d})$—probability density of pile's load capacity, the variable is $m + n_{c,d}$; $f(n_{c,d})$—probability density of load per pile.

Reliability of structure:

$$R = P(M > 0) = \int_0^{\infty} f(m) dm = \int_0^{\infty} \int_0^{\infty} g(m + n_{c,d}) f(n_{c,d}) dn_{c,d} dm, \tag{7}$$

Thus, the probability of failure is given:

$$P_f = P(M < 0) = 1 - R = \int\limits_{-\infty}^{0} f(m)\mathrm{d}m, \tag{8}$$

In practice, there is often not enough statistical data to determine the specific density function of each variable. To obtain an analysis of the probability of failure or safety determined by expressions (7 and 8), using FORM [14] can approximate reliability.

2.2.1 FORM Method [14]

If the safety interval M is nonlinear for the variables X_i, it can be linearized by keeping only the linear terms using the Taylor series expansion at the point $(X_1, \ldots, X_n) = (\mu_{X1}, .., \mu_{Xn})$:

$$M = f(\overline{X}) = f(\mu_{X1}, .., \mu_{Xn}) + \sum_{i=1}^{n} \frac{\partial f}{\partial X_i}(X_i - \mu_{xi}), \tag{9}$$

In which: $\partial f / \partial X_i$ is calculated at the mean $(\mu_{X1}, .., \mu_{Xn})$.

From this expression, with the variables being uncorrelated, the approximate values of the expectation and the variance of M are

$$\mu_M \approx f(\mu_{X1}, .., \mu_{Xn}) \tag{10}$$

$$\sigma_M^2 \approx \sum_{i=1}^{n} \left(\frac{\partial f}{\partial X_i}\right)^2 .\sigma_{X_i}^2 \tag{11}$$

Then, the β index [14] can be calculated

$$\beta = \frac{\mu_M}{\sigma_M} \tag{12}$$

If the variables X_i have a normal distribution, then there is a relationship between the probability of failure and the β index, with:

$$P_f = \Phi(-\beta) \Leftrightarrow \beta = -\Phi - 1(P_f) \tag{13}$$

Considering the pile cap as shown in Fig. 1, the pile at the boundary has maximum compressive force.

Determine the state function from (2) for pile number 1 in Fig. 1 is:

$$N_1 \le R_{c, d} \rightarrow M = R_{c, d} - N_1 \tag{14}$$
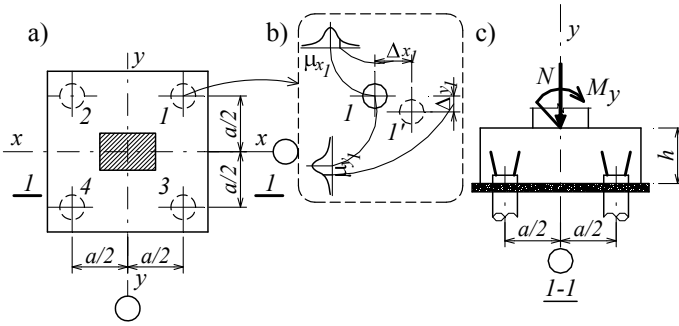
Fig. 1 Pile cap

which: N_1 force on the pile $N^0 1$;

From (14), consider a foundation with n piles, whose coordinates are random quantities, we can determine the mean and standard deviation of M as follows:

$$\mu_M = \mu_{R_{c,d}} - \mu_{N_1} = \frac{N}{n} + \frac{M_x \mu_{y_1}}{\sum_{i=1}^n \mu_{y_i}^2} + \frac{M_y \mu_{x_1}}{\sum_{i=1}^n \mu_{x_i}^2} \tag{15}$$

$$\sigma_M = \left(\begin{array}{l} \sigma_{x1}^2 \left(\dfrac{M_y}{\sum_{i=1}^n x_i^2} - 2M_y \dfrac{x_1^2}{\left(\sum_{i=1}^n x_i^2\right)^2} \right)^2 + 4M_y^2 x_1^2 \dfrac{\sum_{i=2}^n \sigma_{xi}^2 x_i^2}{\left(\sum_{i=1}^n x_i^2\right)^4} \\[4mm] + \sigma_{y1}^2 \left(\dfrac{M_x}{\sum_{i=1}^n y_i^2} - 2M_x \dfrac{y_1^2}{\left(\sum_{i=1}^n y_i^2\right)^2} \right)^2 + 4M_x^2 y_1^2 \dfrac{\sum_{i=2}^n \sigma_{yi}^2 y_i^2}{\left(\sum_{i=1}^n y_i^2\right)^4} \end{array} \right)^{\frac{1}{2}} \tag{16}$$

However, the disadvantage of this method is the complex state function when the number of variables is many. In that case, the Monte Carlo simulation method has the advantage of being an accurate and powerful technique to analyze this problem.

2.2.2 Monte Carlo Method

$N_{c,d}$ and $R_{c,d}$ often do not know in advance or have no explicit mathematical expressions, or maybe they are not independent variables. In that case, it is best to represent the essential variables x_i, $i = 1, 2, \ldots, n$, which are statistically independent and have known distribution functions. The Monte Carlo method creates a set of values for different representations of x_i for each primary variable and thereby determines the corresponding values of the safety margin [14].

$$m = f(x_1, \ldots x_n) = f(\overline{x}), \tag{17}$$

Fig. 2 Flowchart of Monte
Carlo simulation
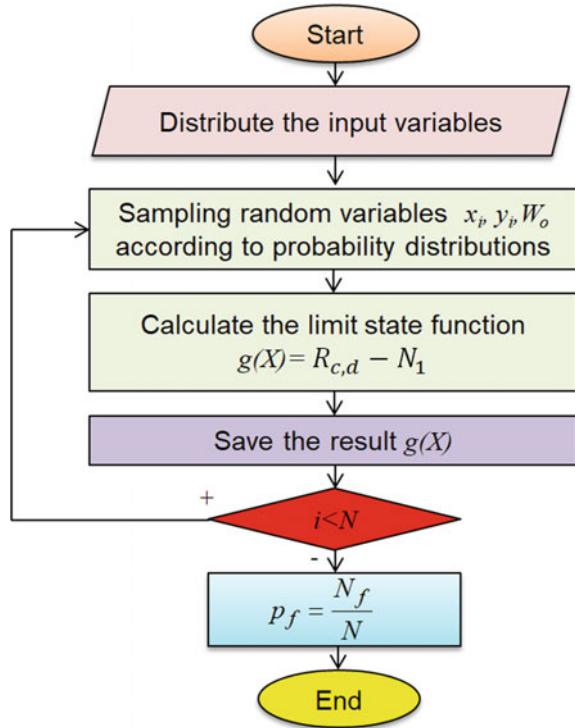
By generating random numbers, this process is repeated many times to create a
large set of n values, simulated the probability distribution of the quantity M. So,
the probability of failure is formulated as:

$$P_{\mathrm{f}} = P(M \le 0) = \lim_{n \to \infty} \frac{k}{n} \tag{18}$$

In which: n—the total number of tests, k—the number of trials with $f(x) \le 0$
(Fig. 2).

3 Numerical Example

3.1 Example Description

Consider a typical building, and the structure consists of concrete reinforced (Fig. 3),
built-in Ho Chi Minh city. The building is located in the wind region II-A. Impact
load: self-weight of structure and equipment. According to [15], the standard value
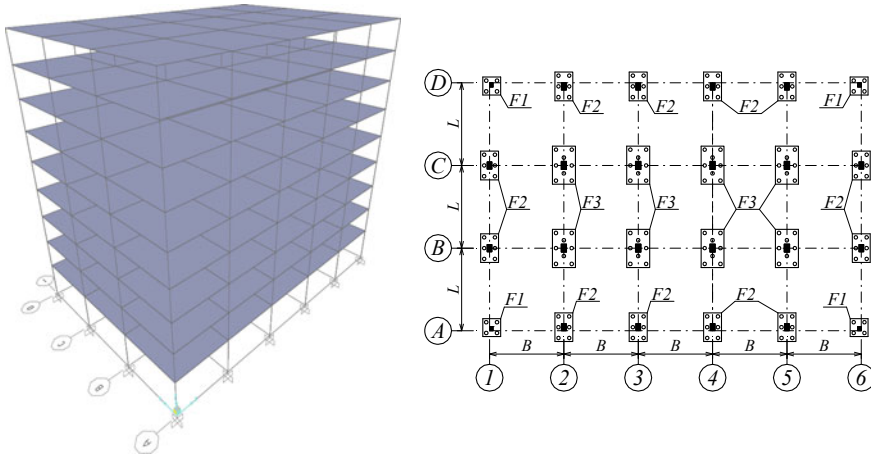
Fig. 3 3D model of building structure and foundation plan (pile layout)

Table 1 Input parameters

Pile cap	Design load						
	N (kN)	M_x (kNm)	Q_y (kN)	M_y (kNm)	Q_x (kN)	N_1 (kN)	$R_{c,d}$ (kN)
Pile cap F_1	−2297.4	−130	−47.3	212.62	68	746.2	900
Pile cap F_2	−3606	−122.8	−39.7	309	100	718	900
Pile cap F_3	−5701.2	−191.29	−57.9	441.5	123	818	900

of wind pressure is determined as $W_0 = 0.83$ kN/m^2. Analysis results indicated that the dangerous combination of internal forces at the base of the column to calculate the foundation (Table 1). Diameter of pile $D = 0.5$ m, pile spacing: $a = 0.75$ m; $c = 1.1$ m; $d = 1.1$ m (Fig. 4).

3.2 Statistic Properties of Random Variables

The random variable is used for reliability analysis as follows (Table 2):

- Tolerance of the pile axis expressed through the standard deviation coordinates of the pile axis in two directions is σ_{x_i}, $\sigma_{y_i} = (0.15–0.6)D$; the correlation coefficient is CV_{x_i}, $CV_{y_i} = 0.15–0.6$;
- In [16, 17], it was shown that, due to climate change, the variation and maximum wind speed in Vietnam tend to increase gradually. So in this study, the author has included wind load as a random factor in the reliability analysis. Wind load causes significant lateral force in buildings. It increases the moment, the shear force at the column foot, and increases the axial force at the boundary columns of
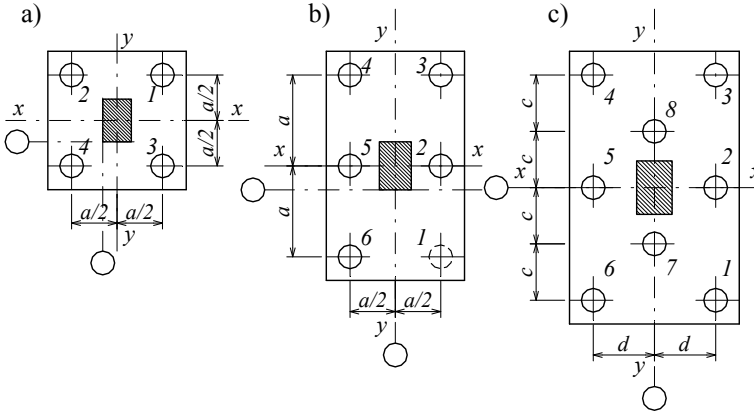
Fig. 4 Pile cap: **a** F_1—4 pile cap, **b** F_2—6 pile cap, **c** F_3—8 pile cap

Table 2 Statistic parameters of random variables

S. no.	Property	Random variables	Mean, μ	Std. deviation, σ	CV	Probability distribution
1	Coordinates	x_i, y_i	μ_{x_i}, μ_{y_i}	$(0.15–0.6).D$	0.15–0.6	Normal [19]
2	Wind pressure, $\mathrm{daN}/\mathrm{m}^2$	W_0	μ_{Wo}	$(0.05–0.3).\mu_{Wo}$	0.05–0.3	Gumbel [18, 19]
3	Bearing capacity of pile	$R_{c,d}$	$\mu_{R_{c,d}}$	$0.05.\mu_{R_{c,d}}$	0.05	Normal [19]

the building. The variations in wind loads significantly affect the load per pile in the foundation; with the mean value of wind speed is $V_0 = 36.8$ m/s, the standard deviation of wind speed is $\sigma_{Vo} = 0.9$–6.1 m/s, then $CV_{Vo} = 0.024$–0.166 and correspondingly $CV_{Wo} = 0.05$–0.3 [18].

- According to [10], if considering the influence of the surrounding ground displacement, the bearing capacity of piles is not significantly different from the static pile load test results (from 4.6 to 4.8%). Therefore, the author uses the standard deviation of the pile bearing capacity of 5% in the survey cases in this study.

3.3 Structural Design Case and Reliability Estimation

Analyzing the reliability of the capacity of the boundary piles when considering the influence of the random factors in the following cases (Table 3):

Case 1: due to the deviation of coordinates of the pile axis (σ_x, σ_y);
Case 2: due to variation of wind load (σ_{Wo}).

Table 3 Cases of analysis

S. no.	Survey cases		Coefficient of variation, CV	
			CV_{x_i}, CV_{y_i}	CV_{W_0}
1	Case 1	$g_1 \approx 0.05$	0.15, 0.2, 0.25, 0.3, 0.4, 0.45, 0.5, 0.55, 0.6	
		$g_2 \approx 0.10$	0.15, 0.2, 0.25, 0.3, 0.4, 0.45, 0.5, 0.55, 0.6	
		$g_3 \approx 0.15$	0.15, 0.2, 0.25, 0.3, 0.4, 0.45, 0.5, 0.55, 0.6	
		$g_4 \approx 0.20$	0.15, 0.2, 0.25, 0.3, 0.4, 0.45, 0.5, 0.55, 0.6	
2	Case 2	$g_1 \approx 0.05$		0.05, 0.1, 0.15, 0.2, 0.25, 0.3
		$g_2 \approx 0.10$		0.05, 0.1, 0.15, 0.2, 0.25, 0.3
		$g_3 \approx 0.15$		0.05, 0.1, 0.15, 0.2, 0.25, 0.3
		$g_4 \approx 0.20$		0.05, 0.1, 0.15, 0.2, 0.25, 0.3
3	Case 3	$g_1 \approx 0.05$	0.2	0.05, 0.1, 0.15, 0.2, 0.25, 0.3
		$g_2 \approx 0.10$	0.2	0.05, 0.1, 0.15, 0.2, 0.25, 0.3
		$g_3 \approx 0.15$	0.2	0.05, 0.1, 0.15, 0.2, 0.25, 0.3
		$g_4 \approx 0.20$	0.2	0.05, 0.1, 0.15, 0.2, 0.25, 0.3

Case 3: consider the simultaneous effect of wind load (σ_{W_0}) and pile axis deviation (σ_x, $\sigma_y = 0.2D$);

Each case is surveyed with g_i (which varies with different M values), where $g_i = \left(\mu_{M_i} / \mu_{R_{c,d}} . \gamma_0 / \gamma_n \right)$ is the ratio between the mean of M and mean of $R_{c,d}$, where $i = 1, 2, 3, 4$ is the sequence number for the value of M_i which has changes (Table 3).

Use the MATLAB program to assess the reliability of the capacity of the pile by implementing Monte Carlo simulation, with $N = 10^5$ samples (Fig. 3).

4   Result and Discussion

To estimate the reliability of the structure, refer to [20] for buildings and offices with lifetime $t = 50$ years; the recommended value is index $\beta = 3.8$ (reliability level RC2). The analysis results for three foundations F_1, F_2, F_3 have the density of coordinates x_1, y_1, load per pile N_1, safety margin M, reliability P_s, probability of failure P_f, and reliability index β. Figures 5 and 6 presented the density of random variables for piles in foundation F_1 with coordinate deviation $\sigma_x = \sigma_y = 0.2D$, $g_2 = 0.1$ (Fig. 7).

Figure 8 and Tables 4 and 5 show the relationship between reliability (P_s) and standard deviation of pile coordinates with three values of safety margins for foundation F_1, F_2, F_3. Considering the influence of pile coordinate deviation, the larger
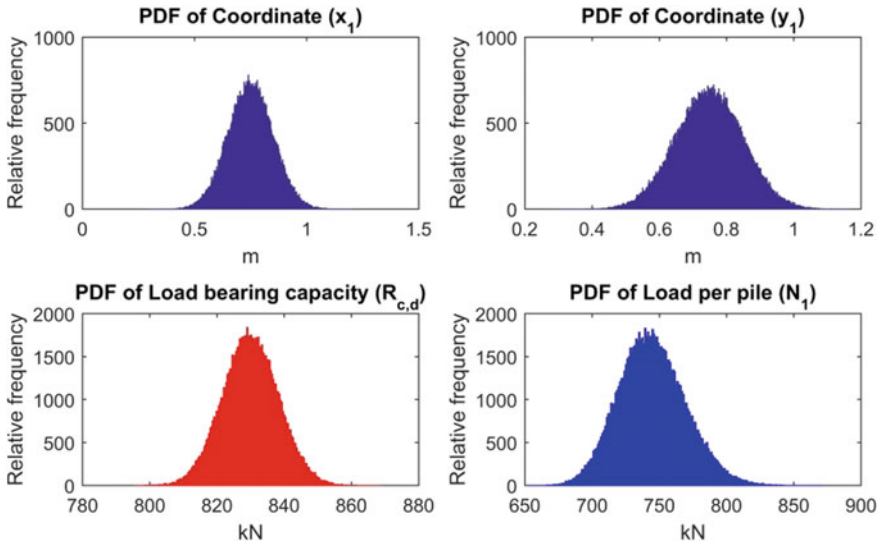
Fig. 5 Probability density function (PDF) of coordinate (x_1, y_1), pile load-bearing capacity $(R_{c,d})$, load per pile (N_1)
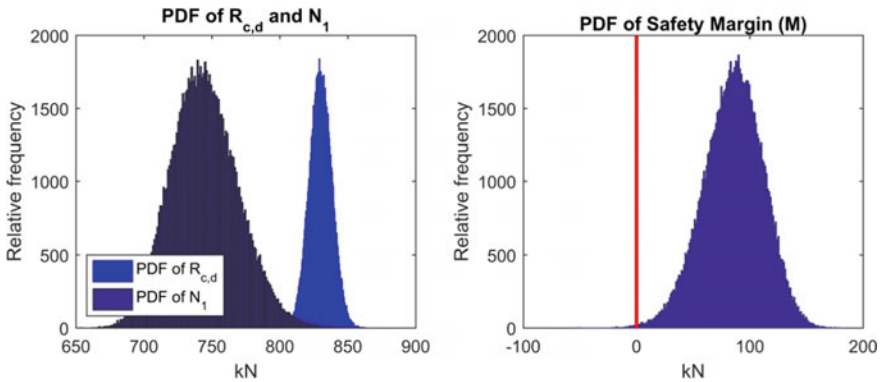
Fig. 6 PDF of pile load-bearing capacity $(R_{c,d})$ and load per pile (N_1); PDF of safety margin (M)

the safety margin (M), that the more reliable the pile's load-bearing capacity; a foundation with a large number of piles $(F_3$ has eight piles, F_2 has six piles) has higher reliability of pile bearing capacity than a foundation with a small number of piles $(F_1$ has four piles);

- Ratio $g_1 \approx 0.05$: deviation pile coordinates σ_x, $\sigma_y = 0.15D$, foundation F_1 has low pile reliability with $\beta = 2.78$, $P_s = 0.9973$ at σ_x, σ_y from 0.2D has $\beta = 2.13$ and $P_s = 0.983$; with foundation F_2, σ_x, σ_y from 0.2D, the reliability of the pile
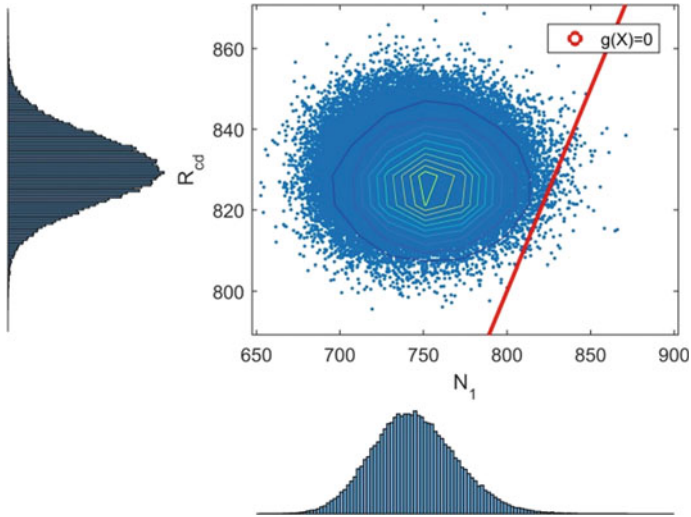
Fig. 7 Representation of the failure zone of the pile with a margin of safety $g(X) = 0$
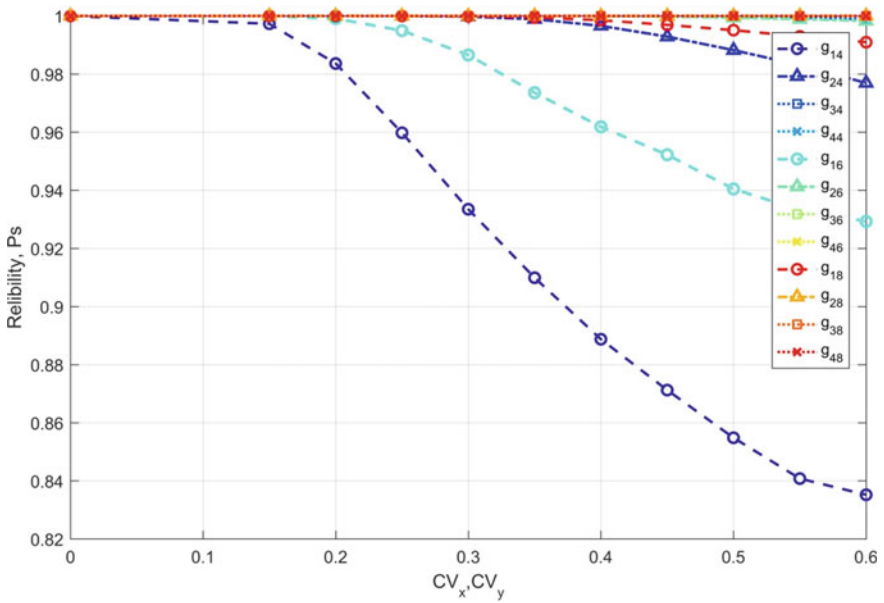
Fig. 8 Analyze the reliability of the structure according to the variations CV_x, CV_y

Table 4 Characteristics of reliability of cases with a standard deviation σ_x, σ_y

S. no.	Characteristic reliability		Variable coefficients of pile coordinate, CV_x, CV_y				
			0.15	0.2	0.25	0.3	0.35
1	$g_{14} \approx 0.05$	P_s	0.997303	0.983628	0.95978	0.933479	0.909901
		β	2.782479	2.135211	1.74819	1.502213	1.340146
	$g_{24} \approx 0.10$	P_s	1.00	1.00	0.99999	0.999782	0.998905
		β	> 5.2	5.167055	4.1756	3.517305	3.063221
	$g_{34} \approx 0.15$	P_s	1.00	1.00	1.00	1.00	0.999999
		β	> 5.2	> 5.2	> 5.2	> 5.2	4.80228
	$g_{44} \approx 0.20$	P_s	1.00	1.00	1.00	1.00	1.00
		β	> 5.2	> 5.2	> 5.2	> 5.2	> 5.2
2	$g_{16} \approx 0.05$	P_s	0.999978	0.999087	0.99495	0.986571	0.973586
		β	4.085917	3.117233	2.57251	2.213578	1.936327
	$g_{26} \approx 0.10$	P_s	1.00	1.00	1.00	0.999999	0.999988
		β	> 5.2	> 5.2	> 5.2	4.808175	4.21757
	$g_{36} \approx 0.15$	P_s	1.00	1.00	1.00	1.00	1.00
		β	> 5.2	> 5.2	> 5.2	> 5.2	> 5.2
3	$g_{18} \approx 0.05$	P_s	1.00	1.00	0.99999	0.999893	0.999454
		β	> 5.2	> 5.2	4.28177	3.702274	3.265626
	$g_{28} \approx 0.10$	P_s	1.00	1.00	1.00	1.00	1.00
		β	> 5.2	> 5.2	> 5.2	> 5.2	> 5.2
	$g_{38} \approx 0.15$	P_s	1.00	1.00	1.00	1.00	1.00
		β	> 5.2	> 5.2	> 5.2	> 5.2	> 5.2

is low with $\beta = 3.11$, $P_s = 0.9949$; in the foundation F_3 when σ_x, σ_y from 0.3D, the reliability of pile $\beta = 3.7$, $P_s = 0.9998$, is quite low;

- Ratio $g_2 \approx 0.1$: deviation pile coordinates σ_x, σ_y from 0.3D for F_1 foundation, then pile has reliability with $\beta = 3.51$ and $P_s = 0.99978$ after that P_s decreases to a low level; in the foundation $F_2$, σ_x, σ_y from 0.4D, the reliability of the pile is $\beta = 3.78$, $P_s = 0.99992$; pile in the foundation F_3 has the reliability which is guaranteed although σ_x, σ_y increased to 0.6D with $\beta = 4.79$, $P_s = 0.1$;
- Ratio g_3 is 0.15: pile coordinate deviation from 0.45D for F_1 foundation, pile reliability is $\beta = 3.83$, $P_s = 0.9999$ and then decreases to unsafe; for foundations F_2 and F_3, the piles have high reliability with $\beta \geq 4.72$, $P_s = 0.999999$ although σ_x, σ_y increases to 0.6D;
- Ratio g_4 is 0.2, piles in foundations are safe with $\beta \geq 4.03$ $P_s = 0.9999$ although σ_x, σ_y increases to 0.6D.

Table 6 and Fig. 9 investigate the pile reliability when the deviation of wind pressure is $CV_{W_0} = 0.05$–0.3 with different values of safety margins of pile load

Table 5 Characteristics of reliability of cases with a standard deviation σ_x, σ_y

S. no.	Characteristic reliability		Variable coefficients of pile coordinate, CV_x, CV_y				
			0.4	0.45	0.5	0.55	0.6
1	$g_{14} \approx 0.05$	P_s	0.888738	0.871231	0.854818	0.840782	0.835207
		β	1.219846	1.132231	1.057323	0.997679	0.974947
	$g_{24} \approx 0.10$	P_s	0.996592	0.992879	0.988233	0.983074	0.976943
		β	2.705747	2.451109	2.264646	2.121828	1.99435
	$g_{34} \approx 0.15$	P_s	0.999989	0.999936	0.999774	0.999449	0.998837
		β	4.241452	3.831733	3.507248	3.263166	3.045186
	$g_{44} \approx 0.20$	P_s	1.00	1.00	0.999999	0.999994	0.999973
		β	> 5.2	5.196132	4.735199	4.363326	4.039917
2	$g_{16} \approx 0.05$	P_s	0.961847	0.952228	0.940449	0.933272	0.929281
		β	1.772536	1.666852	1.558552	1.500611	1.470455
	$g_{26} \approx 0.10$	P_s	0.999921	0.999738	0.999368	0.998899	0.998295
		β	3.778335	3.467932	3.224069	3.061534	2.928207
	$g_{36} \approx 0.15$	P_s	1.00	1.00	1.00	1.00	0.999999
		β	> 5.2	> 5.2	> 5.2	4.969539	4.726657
	$g_{46} \approx 0.20$	P_s	1.00	1.00	1.00	1.00	1.00
		β	> 5.2	> 5.2	> 5.2	> 5.2	> 5.2
3	$g_{18} \approx 0.05$	P_s	0.99853	0.996922	0.995099	0.992949	0.990964
		β	2.974042	2.739402	2.582747	2.45463	2.36414
	$g_{28} \approx 0.10$	P_s	1.00	1.00	1.00	1.00	0.999999
		β	> 5.2	> 5.2	> 5.2	5.010314	4.79482
	$g_{38} \approx 0.15$	P_s	1.00	1.00	1.00	1.00	1.00
		β	> 5.2	> 5.2	> 5.2	> 5.2	> 5.2

Notes g_{ij}—i=1, 2, 3, 4 for g_1, g_2, g_3, g_4; j=4, 6, 8 corresponds to the foundation F_1 (4 piles), F_2 (6 piles), F_3 (8 piles); from $\beta = 5.2$, then $P_s = 0.9999999 \approx 1$

capacity. It is shown that the larger the safety margin and the foundation have more piles, the safer the working piles, as follow:

- Ratio $g_1 = 0.05$: piles in the foundation F_1, F_2 are only safe when $CV_{W_0} = 0.05$ with $\beta = 4.78, 5.35$ and $P_s = 1$, after that reliability of piles decreases to a low level; In the F_3 foundation, with $CV_{W_0} = 0.15$, the reliability of the pile is $\beta = 3.18$ and $P_s = 0.99928$, then decreases rapidly;
- Ratio $g_2 = 0.1$: deviation of wind pressure CV_{W_0} from 0.2, piles in the foundation F_1, F_2 have low reliability, respectively, $\beta = 2.67, 3.33$ and $P_s = 0.996, 0.9995$; piles in foundation F_3 have low reliability when the deviation of wind pressure CV_{W_0} from 0.25 with $\beta = 3.36$ and $P_s = 0.99961$;

Table 6 Characteristics of reliability of cases with variable CV_{W_0}

S. no.	Characteristic reliability		Variable coefficients of wind pressure, CV_{W_0}					
			0.05	0.1	0.15	0.2	0.25	0.3
1	$g_{14} \approx 0.05$	P_s	1.00	0.9945	0.94393	0.86004	0.81571	0.77111
		β	4.7861	2.542	1.58865	1.0805	0.89912	0.74249
	$g_{24} \approx 0.10$	P_s	1.00	1.00	0.99996	0.99624	0.98621	0.96554
		β	> 5.2	> 5.2	3.96363	2.6727	2.2033	1.8189
	$g_{34} \approx 0.15$	P_s	1.00	1.00	1.00	0.99999	0.99978	0.99816
		β	> 5.2	> 5.2	> 5.2	4.3024	3.5176	2.9036
	$g_{44} \approx 0.20$	P_s	1.00	1.00	1.00	1.00	1.00	0.99997
		β	> 5.2	> 5.2	> 5.2	> 5.2	4.7998	4.0198
2	$g_{16} \approx 0.05$	P_s	1.00	0.99935	0.98918	0.92829	0.8665	0.83309
		β	5.3501	3.2153	2.29678	1.46318	1.10999	0.96644
	$g_{26} \approx 0.10$	P_s	1.00	1.00	1.00	0.99957	0.99371	0.98523
		β	> 5.2	> 5.2	5.20752	3.3354	2.4953	2.1762
	$g_{36} \approx 0.15$	P_s	1.00	1.00	1.00	1.00	0.99999	0.99989
		β	> 5.2	> 5.2	> 5.2	> 5.2	4.2250	3.6840
	$g_{46} \approx 0.20$	P_s	1.00	1.00	1.00	1.00	1.00	1.00
		β	> 5.2	> 5.2	> 5.2	> 5.2	> 5.2	> 5.2
3	$g_{18} \approx 0.05$	P_s	1.00	1.00	0.99928	0.97232	0.93668	0.90364
		β	> 5.2	4.86997	3.18687	1.916	1.5274	1.3025
	$g_{28} \approx 0.10$	P_s	1.00	1.00	1.00	0.99999	0.99961	0.99785
		β	> 5.2	> 5.2	> 5.2	4.1869	3.3624	2.8549
	$g_{38} \approx 0.15$	P_s	1.00	1.00	1.00	1.00	1.00	0.99999
		β	> 5.2	> 5.2	> 5.2	> 5.2	5.1864	4.414
	$g_{48} \approx 0.20$	P_s	1.00	1.00	1.00	1.00	1.00	1.00
		β	> 5.2	> 5.2	> 5.2	> 5.2	> 5.2	> 5.2

- Ratio $g_3 = 0.15$: the piles in foundations F_3, F_2 are safe; pile in the foundation F_1 has low reliability when wind pressure deviation $CV_{W_0} = 0.25$, $\beta = 3.517$ and $P_s = 0.99978$;
- With $g_4 = 0.2$, the piles in all three surveyed foundations are safe with quite a significant deviation of wind pressure of 0.3;

Next, analyzing the reliability of the pile when considering the pile coordinates deviation CV_x, $CV_y = 0.2$, and the variation of wind pressure, the results are shown in Table 7 and Fig. 10:

- The ratio $g_1 = 0.05$, the piles in the foundation F_1, F_2 have very low reliability $\beta = 1.94$, 2.88 and $P_s = 0.97406$, 0.99804; foundation F_3, when CV_{W_0} from 0.1 has $\beta = 3.62$ and $P_s = 0.99986$, pile is unsafe risk;
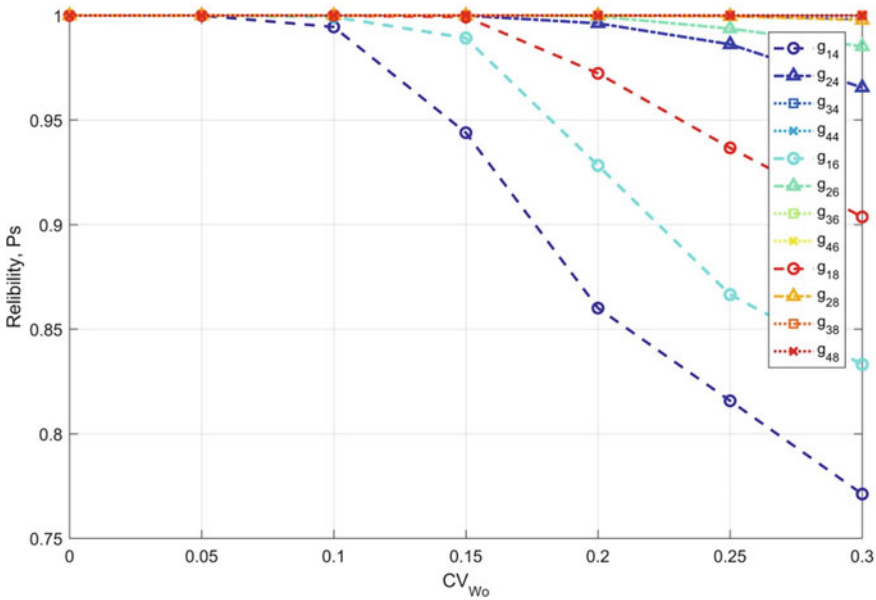
Fig. 9 Analyze the reliability of the structure according to the variations CV_{W_0}

- With ratio $g_2 = 0.1$, pile in foundation F_1, F_2 is unsafe when CV_{W_0} from 0.15 with $\beta = 3.49$, 4.17 and $P_s = 0.99976$, 0.99999 and then degree the reliability of the pile rapidly decreases; foundation F_3, when CV_{W_0} from 0.2 with $\beta = 3.95$ and $P_s = 0.9996$, the pile is unsafe;
- With the ratio $g_3 = 0.15$, the pile in the foundation F_1 is unsafe when CV_{W_0} is from 0.25 with $\beta = 3.39$ and $P_s = 0.99966$; for the foundation F_2, F_3, the pile has guaranteed reliability;
- Ratio $g_4 = 0.2$, piles in foundations F_1, F_2, F_3 are considered safe with β from 3.78, $P_s = 0.99992$.

From the analysis results, it can be said that the choice of safety margin has a significant influence on the reliability of the pile in the foundation. The larger the safety margin, the safer the pile's load capacity. With conventional foundation design, the margin of safety is usually 0.1–0.15. Still, when considering the randomness of the calculated quantities, it is necessary to choose the appropriate margin of safety, considering the economic factor.

5 Conclusion

This study has evaluated the safety level of the pile's bearing capacity under the influence of random factors such as pile coordinates and pile load-bearing capacity.

Table 7 Characteristics of reliability of cases with variable CV_{W_0} and $CV_D = 0.2D$

S. no.	Characteristic reliability		Variable coefficients of wind pressure, CV_{W_0}					
			0.05	0.1	0.15	0.2	0.25	0.3
1	$g_{14} \approx 0.05$	P_s	0.97406	0.95669	0.92653	0.85494	0.81424	0.76516
		β	1.94411	1.71355	1.45041	1.05785	0.89363	0.723
	$g_{24} \approx 0.10$	P_s	1.00	0.99998	0.99976	0.99441	0.98348	0.95953
		β	4.73235	4.15515	3.49487	2.537	2.13169	1.74529
	$g_{34} \approx 0.15$	P_s	1.00	1.00	1.00	0.99997	0.99966	0.99714
		β	> 5.2	> 5.2	> 5.2	4.0501	3.39411	2.76306
	$g_{44} \approx 0.20$	P_s	1.00	1.00	1.00	1.00	1.00	0.99992
		β	> 5.2	> 5.2	> 5.2	> 5.2	4.6283	3.78694
2	$g_{16} \approx 0.05$	P_s	0.99804	0.9883	0.97008	0.89582	0.8575	0.82636
		β	2.8851	2.26675	1.88202	1.25811	1.06914	0.93989
	$g_{26} \approx 0.10$	P_s	1.00	1.00	0.99999	0.99725	0.9908	0.98207
		β	> 5.2	5.0395	4.17799	2.77607	2.3573	2.09842
	$g_{36} \approx 0.15$	P_s	1.00	1.00	1.00	1.00	0.99997	0.99978
		β	> 5.2	> 5.2	> 5.2	4.66483	3.9934	3.51463
	$g_{46} \approx 0.20$	P_s	1.00	1.00	1.00	1.00	1.00	1.00
		β	> 5.2	> 5.2	> 5.2	> 5.2	> 5.2	5.25133
3	$g_{18} \approx 0.05$	P_s	1.00	0.99986	0.99729	0.96552	0.934	0.90242
		β	4.61614	3.6281	2.78042	1.8187	1.50628	1.29546
	$g_{28} \approx 0.10$	P_s	1.00	1.00	1.00	0.99996	0.99948	0.99743
		β	0	7.84229	6.01517	3.95257	3.2793	2.79775
	$g_{38} \approx 0.15$	P_s	1.00	1.00	1.00	1.00	1.00	0.99999
		β	> 5.2	> 5.2	> 5.2	> 5.2	5.02791	4.31651
	$g_{48} \approx 0.20$	P_s	1.00	1.00	1.00	1.00	1.00	1.00
		β	> 5.2	> 5.2	> 5.2	> 5.2	> 5.2	> 5.2

Statistical results of the characteristics of these parameters are developed in Sects. 3 and 4.

Monte Carlo simulation was used to analyze the reliability with the state function as the pile load capacity condition, analyzing the relationship between the random variables and different levels of safety margin.

In standard [1], there is a regulation on the allowable deviation of the pile axis. In some cases, even though the pile coordinate tolerance is within the permissible range, the pile can still be potentially dangerous. In addition, the safety margin has a significant influence on the workability of the pile. With conventional foundation design, the margin of safety is usually 0.1–0.2. The higher the safety margin, the safer the pile's load-carrying capacity. Therefore, in structural calculations, the designer
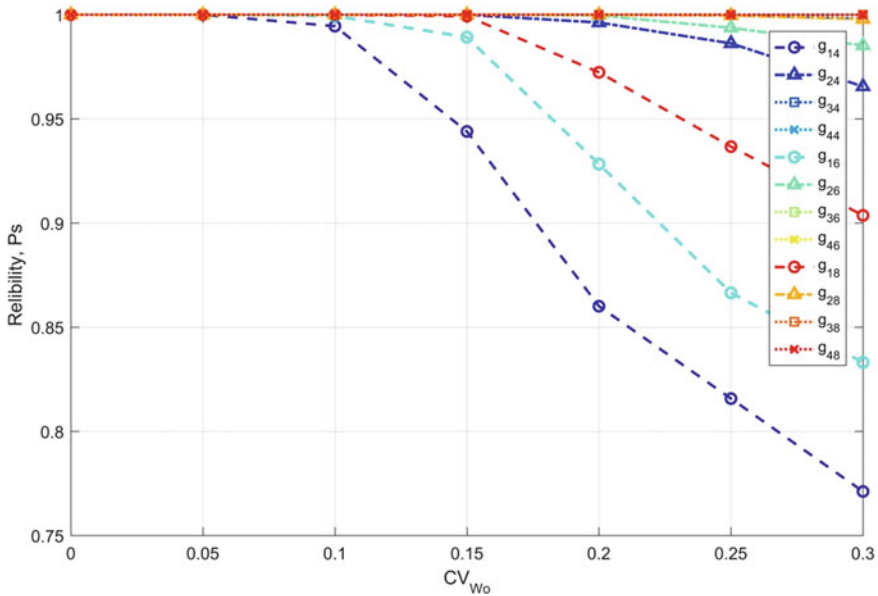
Fig. 10 Reliability of pile when considering the simultaneous effects of wind load and pile axis tolerance

needs to carefully consider the number of piles in the foundation and choose an appropriate safety margin, paying attention to economic factors.

In addition, analysis of other random effects such as the inclination of the pile, the load-bearing capacity of the pile (according to the condition of the material, ground soil, etc.), the type of load (the dynamic component of the wind, due to the ground settlement, etc.), and pile size factors (section, length, etc.) continue in further studies.

References

1. National Standard (2012) TCVN 9394:2012. Pile driving and static jacking work-construction, check and acceptance
2. Ngoc TD (2013) Accident of deflection piles at Thang long cement grinding station—causes and prevention measures. Collect Rep 50th Anniv Conf Inst Build Sci Technol 1-Geotec
3. Hien Q (2006) Waiting for load test. Working people [Online]. Available: https://nld.com.vn/thoi-su-trong-nuoc/phai-cho-thu-tai-160405.htm
4. Nam K (2016) Tilt the foundation, suspending construction of the hospital 3000 billion VND. Youth newspaper [Online]. Available: https://tuoitre.vn/nghieng-tru-mong-tam-ngung-thi-cong-benh-vien-3000-ti-dong-1055290.htm
5. Duy T (2017) The hundred billion project is tilted due to wrong design. Vietnamese culture [Online]. Available: https://nongnghiep.vn/cong-trinh-tram-ty-bi-nghieng-do-sai-thiet-ke-d217900.html

6. Budi GS, Wijaya HC (2015) Deviation of position of piles foundation from its original designed location
7. Huang K (2018) A research for deviation estimation analysis for driven piles foundation: a case of Penang Second Marine Bridge
8. Silva J, Aoki N, Franco Y (2017) Use of the order statistics when predicting pile foundation failure probability. DYNA 84:247–252
9. Amir A, Ahmad A (2016) Design and reanalysis of pile cap under eccentricity
10. Vo P (2012) Studying the bearing capacity of piles taking into account the influence of the surrounding ground displacement. J Sci Ho Chi Minh City Open Univ 7
11. Nguyen DT, Pham VT (2009) The reliability determination method of low stage pile foundations in construction. Marit Sci Technol 19
12. Trinh VC (2016) Prediction of the load-settlement relationship of piles from the results of static compression of piles of reduced cross-section. J Constr Sci Technol 1
13. National Standard (2014) TCVN 10304: 2014. Pile nail—design standard
14. Rayzer VD (2010) Reliability theory of structures. Izd-vo ASV, Moscow
15. TCVN, Vietnam Standard (1995) TCVN 2737-1995, Loads and effects—design standard. Construction Publishing House
16. Dai Minh N (2014) Experience of the Philippines in dealing with Super Typhoon Haiyan and storm prevention solutions for low-rise buildings in our country. Sci Technol Mag 2
17. Huong CT (2010) Variations and trend of maximum wind speed in Vietnam during 1961–2007 (in Vietnamese). J Sci Univ Nat Technol 3
18. Hoang BA (2021) Safety evaluation of billboards when considering the random effects of design parameters in the Southern Region of Vietnam. In: Structural health monitoring and engineering structures, pp 313–329
19. Rzhanitsyn A (1978) Theory of design of reliable structures. Stroyizdat, Moscow
20. E. Standard (2002) Eurocode 0-basis of structural design. Eurocode 0

Notch Depth Identification in CFRP Composite Beams Based on Modal Analysis Using Artificial Neural Network

A. Zara, I. Belaidi, A. Oulad Brahim, S. Khatir, R. Capozucca, and M. Abdel Wahab

1 Introduction

The development of composite materials remains a topical issue, given the complexity of damage mechanisms of mechanical, physical, or environmental origin. To ensure correct performance in different areas of use, it is necessary to consider the resistance to damage over a long period (durability). Thus, the optimal use of these substances requires better knowledge and careful study of the damage mechanisms that control their behavior. These materials often suffer from a variety of hard-to-detect damage that reduces their structural integrity. Therefore, it is necessary to find methods to detect the location and size of damage at an early stage to prevent disasters. Recently, researchers have focused on the development of new analytical techniques to detect damage in composite materials [1, 2]. Among the experimental methods available to analyze these materials, we find, on the one hand, that acoustic emission signals represent a technique for evaluating damage mechanisms [3, 4]. On the other hand, vibration analysis is a practical method to assess damage in composite structures based on natural frequencies. Dynamic experimental tests have been developed

A. Zara · I. Belaidi · A. Oulad Brahim
LEMI Laboratory, Department of Mechanical Engineering, University M'hamed Bougara Boumerdes, 35000 Boumerdes, Algeria
e-mail: a.zara@univ-boumerdes.dz

S. Khatir (✉)
Faculty of Civil Engineering, Ho Chi Minh City Open University, Ho Chi Minh City, Vietnam
e-mail: Khatir_samir@hotmail.fr

R. Capozucca
DICEA, Structural Section, Polytechnic University of Marche, Ancona, Italy

M. A. Wahab
Soete Laboratory, Faculty of Engineering and Architecture, Ghent University, Technologiepark Zwijnaarde 903, B-9052 Zwijnaarde, Belgium

on damaged composite material structures, relating their dynamic properties to the size and position of the damage [5]. Numerical techniques have been used for flexible shear plates based on modal analysis [6, 7]. An experimental study on four models of RC beams with circular rods NSM Carbon-FRP has been presented in [8]. Esfahani et al. [9] performed dynamic tests by vibration analysis on a polymer composite reinforced with CFRP carbon fibers. Damage affects the vibratory properties and the bending stiffness of structures due to different section reductions. Bendada et al. [10] carried out an experimental and numerical study based on modal analysis, to characterize and model epoxy sheets based on wooden reinforcements. Capozucca [11] carried out experimental and theoretical studies on undamaged and damaged carbon fiber reinforced polymer (CFRP) beams using vibration analysis. Then, an experimental method was used to reinforce damaged reinforced concrete beams with carbon fiber reinforced polymers (NSM-CFRP), the latter has been provided in Ref. [12], and has proven its effectiveness in practice. Over the past three decades, several researchers have proposed new methods for the identification of damage based on data extracted from experimental and numerical measurements of different damage configurations, which means the position and size of the damage. Two optimization methods, namely bat algorithm (BA) and genetic algorithm (GA), were used to identify the location and severity of damage on structures modeled using the finite element method (FEM), these were presented in Ref. [13]. Dinh-Cong et al. [14] used an efficient optimization approach to minimize computational cost and detect damage in a laminated composite plate. In some papers, the artificial neural network-based optimization algorithm has been developed and applied to identify damage [15, 16]. A powerful and rapid application relying on artificial intelligence with particle swarm optimization (ANNPSO) has been used to discover the location and level of damage in a laminated composite plate, it has been reported in [17]. The comparison between two optimization methods genetic algorithm (GA) and particle swarm optimization (PSO) were proposed using experimental and numerical data, for the detection and localization of damage in composites, this comparison has been presented by [18, 19], and more another study in Ref [20]. We also mention that the application of artificial neural networks (ANN) in structural health monitoring is improved using the Jaya algorithm [21, 22]. Therefore, this technique is more accurate in identifying the position, size, and orientation of damage. Tran-Ngoc et al. [23] proposed a method for the detection of damage in structures, based on a combination between the artificial neural network (ANN) and cuckoo search (CS) algorithm. They proved that the proposed method (ANN-CS) was more precise than (ANN) for the identification of damage.

In this work, an artificial neural network (ANN) optimization technique is studied to estimate damage in composite structures after adapting the influential parameters of neural networks. In a first step, the finite element models are developed using the ABAQUS software and the results obtained are compared with the experimental ones. In the second step, a numerical simulation is developed for several cases of the damage that we have proposed on (CFRP) specimens by focusing on several parameters such as: position, width, and depth. In the third step, after extracting the numerical data we give them to the artificial neural network (ANN) to train and

validate the results. Finally, we end with a conclusion in which the results obtained are discussed.

2   Experimental Analysis

Four CFRP specimens undamaged and damaged were manufactured and a vibration analysis test was performed to obtain the natural frequencies. Fixed free beam was considered as boundary condition. Next, the damaged case including double notches crack. The configuration of the vibration test of a sample of CFRP cantilever beam with accelerometer and impact hammer accompanied with a data acquisition system is shown in Fig. 1.

Table 1 shows the geometric and mechanical parameters of carbon fiber reinforced polymer laminate composite [11]

Regarding the experimental tests, a CFRP cantilever specimen was excited at point (M), which is at 20 mm from the fixed end, by an impact hammer (Brüel & Kjær Impact Hammer Type 8202), while the accelerometer is used to measure the response in several points a_i with $i = 1…, 4$.

The natural frequencies of undamaged and damaged CFRP laminates near the fixed end have been determined experimentally and theoretically. The position of the
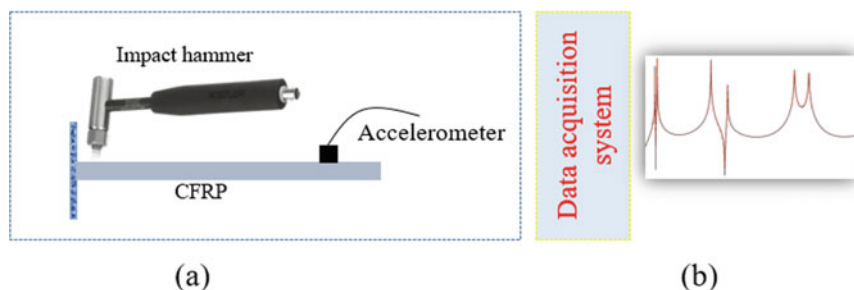

Fig. 1   Set up the vibration test of the CFRP specimen: **a** accelerometer and impact hammer; **b** a data acquisition system

Table 1 Geometric and mechanical parameters of CFRP laminate [11]	Geometric and mechanical parameters	Value
	Length L [mm]	200
	Width b [mm]	20.253
	Thickness h [mm]	1.7
	Young's modulus E $\left[\text{kN}/\text{mm}^2\right]$	91.65
	Density ρ $\left[\text{Ns}^2/\text{mm}^4\right]$	$1.376 * 10^{-9}$
	Moment of inertia I [mm4]	8.29

Fig.2 Damages Di, $i =$ 1…,3 of CFRP cantilever beam; accelerometer positions a_i, $i = 1$…,4 and point M for the impulse by an impact hammer
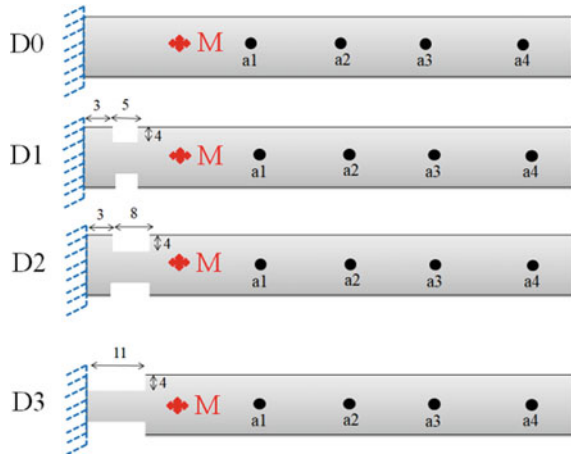

Table 2 Theoretical and experimental first three frequencies of undamaged and damaged CFRP beam for $D0$, $D1$, $D2$, and $D3$ [11]

Undamaged and damaged CFRP beam	Natural frequency values [Hz]	f_1 [Hz]	f_2 [Hz]	f_3 [Hz]
$D0$	Theoretical	67.49	423.00	1184.53
	Experimental	47.50	309.50	858.50
$D1$ Depth $= 4$ mm Width $= 5$ mm	Theoretical	65.34	410.19	1150.20
	Experimental	43	291.75	834
$D2$ Depth $= 4$ mm Width $= 8$ mm	Theoretical	64.14	403.65	1134
	Experimental	41	287.75	824.5
$D3$ Depth $= 4$ mm Width $= 11$ mm	Theoretical	63.01	397.8	1120.2
	Experimental	41	281.25	821.50

damage, excitation point M, and the accelerometer are shown in Fig. 2. Table 2 shows the results of the experimental and theoretical frequencies of the modal analysis.

Theoretical and experimental of the first three modes in the case of undamaged ($D0$) and damaged ($D1$, $D2$, and $D3$) CFRP beams have been presented in Table 2.

3 Finite Element Method (FEM) Analysis

ABAQUS software was used to validate the results of experimental testing of CFRP specimens. The geometries of undamaged and damaged specimens are first created with dimensions of 200 mm in length, 20.253 mm in width, and 1.7 mm in thickness. The properties of the material of the test specimen are then introduced. Then, one end of the sample beam was clamped. Then, a fine mesh of type (C3D8R: 8-node

Table 3 FEM frequency values of undamaged and damaged CFRP specimens

Natural frequency values of FEM	f_1 [Hz]	f_2 [Hz]	f_3 [Hz]
D0	48.9	306.35	857.95
D1 Depth = 4 mm Width = 5 mm	46.40	294.50	832.15
D2 Depth = 4 mm Width = 8 mm	45.69	292.26	829.15
D3 Depth = 4 mm Width = 11 mm	45.47	291.04	826.11

linear brick, reduced integration, and hourglass control) was used to mesh the beam, in which the total number of elements is 6552. Finally, the first three natural frequencies were obtained from FEM as shown in Table 3.

Figure 3 shows the first three mode shapes of an undamaged beam D0, and Fig. 4a–c shows the mode shapes of damaged beams, D1, D2, D3, respectively.
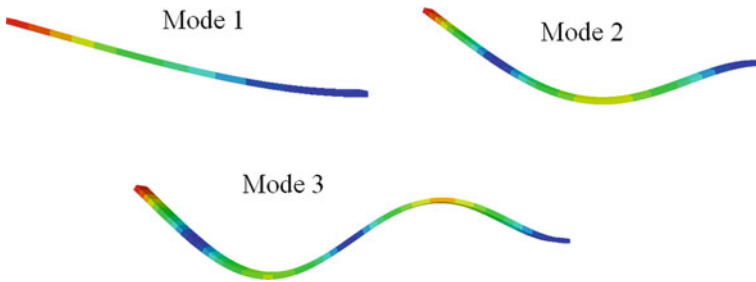

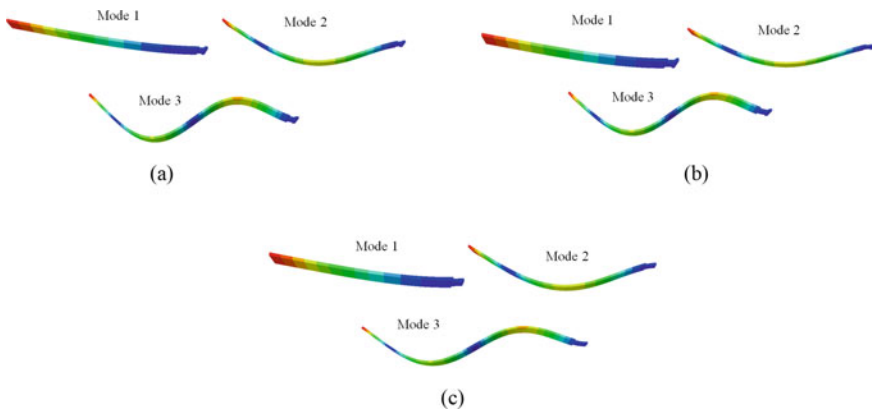**Fig. 3** Mode shapes of undamaged beam D0

Fig. 4 **a** Mode shapes of damaged beam D1. **b** Mode shapes of damaged beam D2. **c** Mode shapes of damaged beam D3

Table 4 Comparison between experimental and FE results

Damage degree	Natural frequencies	f_1 [Hz]	f_2 [Hz]	f_3 [Hz]
$D0$	Experimental	47.50	309.50	858.50
	FEM	48.9	306.35	857.95
	Error %	2.95	1.02	0.06
$D1$	Experimental	43	291.75	834
	FEM	46.4	294.5	832.15
	Error %	7.9	0.9	0.22
$D2$	Experimental	41	287.75	824.5
	FEM	45.69	292.26	829.15
	Error %	8.8	1.56	0.56
$D3$	Experimental	41	281.25	821.50
	FEM	45.47	291.04	826.11
	Error %	10.9	3.48	0.56

3.1   Comparison Between Experimental and FEM Results

The first three natural frequencies of undamaged ($D0$) and damaged ($D1$, $D2$, and $D3$) specimens are obtained by the FEM. They were compared with the frequencies obtained from the experimental methods as indicated in Table 4.

From the obtained results, we can see a minimal decrease in frequencies with increasing damage length, and the error between FEM and experimental results is very low for the second and third mode. Thus, the results show good agreement with the numerical values obtained by FEM and the experimental.

3.2   FEM Data for training

In this study, we have introduced other cases of damage to CFRP specimens by focusing on several parameters such as: position, width, and depth. Figure 5 shows the different locations of the proposed positions for the notches. So, for the identification of specimen damage (CFRP) using artificial neural network, we can extract the data from natural frequencies by FEM at different positions of notches and use it for training of the neural network.

4   Neural Network Modeling

The data provided in Table 5 are used for ANN and 80% of the data is for training and 20% is for testing and validating networks. In MATLAB, the desired inputs

Fig. 5 The location of different positions with depth and width of notches; **C1** next to the fixed side, **C2 in the** middle, **C3** in the free side
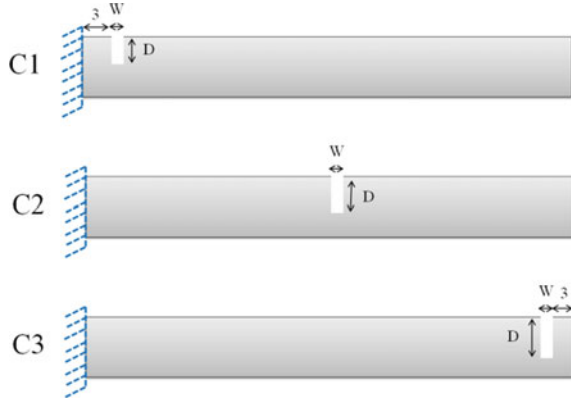

Table 5 Input parameters for training

Parameter	Minimum	Maximum	Number of collected data
Target			
Position	Three positions		–
Notch width	Fixed		–
Notch depth	0.5	19.5	39
Input			
f_1 [Hz]	49.009	49.496	39
f_2 [Hz]	306.960	309.530	39
f_3 [Hz]	859.810	865.070	39

and outputs or targets are imported into the workspace and using the "nntool", the network is created using inputs and targets. ANN model has a multi-layered structure that is connected by nodes with three main layers, namely, the input layer (3), the hidden layer (s) (10 neurons), and the output layer (notch depth) see Fig. 6. The ANN architecture is shown in Fig. 7.

The notches depth are taken as an output parameter; frequencies (f_1, f_2, f_3) are selected as inputs parameters for each study. The input parameters required for data training are provided in Table 5.
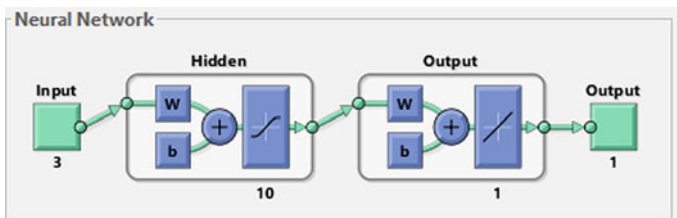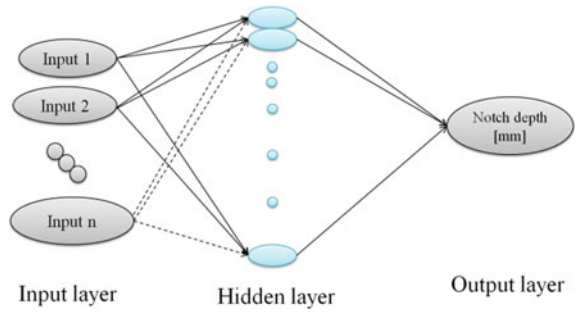

Fig. 6 Neural network model

Fig. 7 ANN architecture

4.1 Results and Discussion

The regression and the best validation performance are shown in Figs. 8 and 9, respectively, to predict the notch depth based on the frequencies (f_1, f_2, f_3) using 39 collected data.

Inputs are considered the first three modes frequency (f_1, f_2, f_3) to predict different notch depth. The provided results are plotted in Fig. 10. The errors between exact and predicted notch depth for three scenarios using ANN method are shown in Fig. 11.

Tables 6, 7, and 8 summarize the results of three inputs (different positions), and compared with the exact notch depth. Next, the errors are computed for each scenario to study the effectiveness of ANN.

Based on the provided results in Tables 6, 7, and 8, we can conclude that ANN can detect the notch depth with high accuracy.
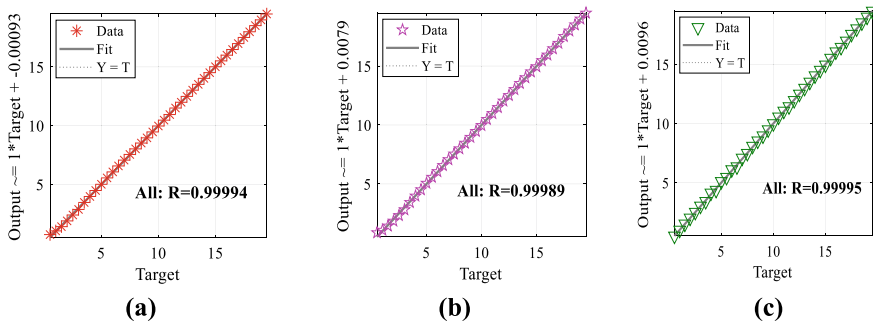

Fig. 8 Regression analysis of ANN: **a** next to fixed side (C1), **b** in the middle (C2), **c** in the free side (C3)
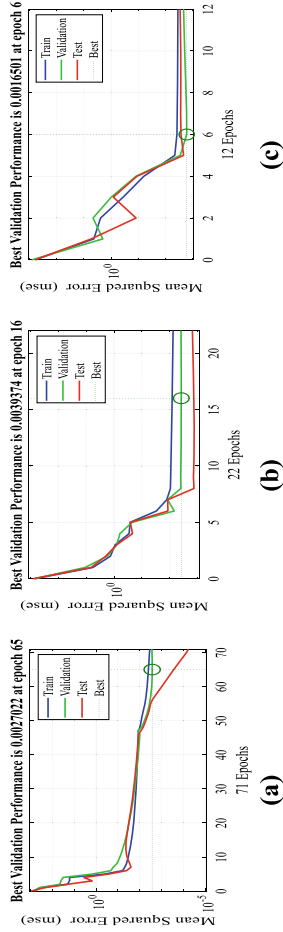
Fig. 9 Performance analysis of ANN: **a** next to the fixed side (C1), **b** in the middle (C2), **c** in the free side (C3)
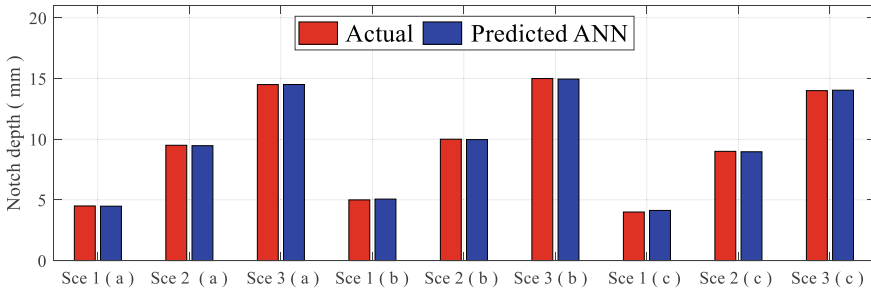
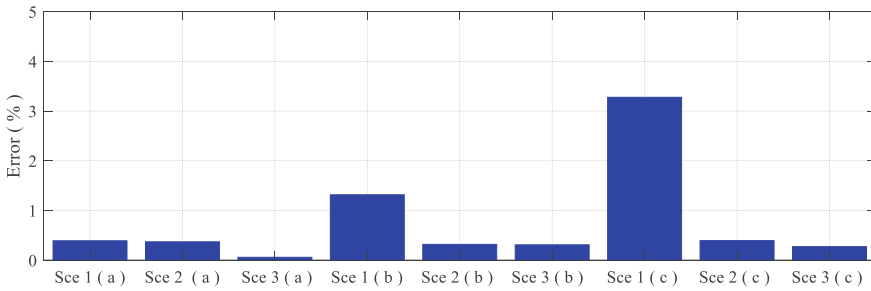**Fig. 10** Predicted notch depth using 39 collected data

Fig. 11 Error of predicted notch depth using 39 collected data

Table 6 Result for the first position (C1)

Scenario	f_1 [Hz]	f_2 [Hz]	f_3 [Hz]	Actual notch depth [mm]	Predicted ANN [mm]	Error %
1	48.242	302.84	849.19	4.5	4.482	0.400
2	46.131	292.6	821.48	9.5	9.465	0.368
3	42.043	275.45	764.43	14.5	14.508	0.055

Table 7 Result for the second position (C2)

Scenario	f_1 [Hz]	f_2 [Hz]	f_3 [Hz]	Actual notch depth [mm]	Predicted ANN [mm]	Error %
1	48.905	303.76	859.48	5	5.066	1.32
2	48.521	294.47	853.79	10	9.968	0.32
3	47.633	276.44	809.9	15	14.954	0.307

Table 8 Result for the third position (C3)

Scenario	f_1 [Hz]	f_2 [Hz]	f_3 [Hz]	Actual notch depth [mm]	Predicted ANN [mm]	Error %
1	49.13	307.63	861.45	4	4.131	3.275
2	49.243	308.27	862.93	9	8.965	0.389
3	49.364	308.93	864.38	14	14.038	0.271

5   Conclusion

In this work, we presented an approach focused on artificial neural networks to identify notch depth in CFRP beam based on modal analysis. First, the experimental tests of damaged and undamaged CFRP specimens were validated when a numerical simulation was performed based on FEM using ABAQUS software.

From this study, we proposed three damage scenarios in CFRP specimens by focusing on several parameters such as: position, width, and depth. Then, based on the numerical data extracted by the FEM using ABAQUS software from the three proposed positions, we used a novel approach to the artificial neural network for the identification of notch depth in CFRP specimens with different positions.

In this work, the main results are presented below:

- The experimental and numerical analysis values show good agreement with a low percentage of error especially the second and the third mode.
- The presence of damage in structures causes a decrease in natural frequencies. Thus, the rigidity of the structure decreases.
- The values of natural frequencies obtained by FEM from the three proposed positions are used for training in the artificial neural network (ANN) for the notch depth identification in CFRP specimens with different positions. Thus, the maximum error percentage between predicted (ANN) and actual (FEM) outputs is less than 3.3%, indicating that the ANN can detect notch depth with high accuracy.

References

1. Ammar MMA et al (2021) An approach for damage initiation and propagation in metal and carbon fiber hybrid composites manufactured by robotic fiber placement. Compos Struct 268:113976. https://doi.org/10.1016/j.compstruct.2021.113976
2. Dang H et al (2020) A new analytical method for progressive failure analysis of two-dimensional triaxially braided composites. Compos Sci Technol 186:107936. https://doi.org/10.1016/j.compscitech.2019.107936
3. Kelkel B, Popow V, Gurka M (2020) Inline quantification and localization of transverse matrix cracking in cross-ply CFRP during quasi-static tensile testing by a joint event-based evaluation of acoustic emission and passive IR thermography. Compos Sci Technol 190:108013. https://doi.org/10.1016/j.compscitech.2020.108013
4. Yue JG, Kunnath SK, Xiao Y (2020) Uniaxial concrete tension damage evolution using acoustic emission monitoring. Constr Build Mater 232:117281. https://doi.org/10.1016/j.conbuildmat.2019.117281
5. Capozucca R, Bonci B (2015) Notched CFRP laminates under vibration. Compos Struct 122:367–375. https://doi.org/10.1016/j.compstruct.2014.11.062
6. Laura PAA, Gutierrez RH (1993) Analysis of vibrating Timoshenko beams using the method of differential quadrature. Shock Vib 1:89–93. https://doi.org/10.3233/SAV-1993-1111
7. Liew KM, Han JB, Xiao ZM (1997) Vibration analysis of circular Mindlin plates using the differential quadrature method. J Sound Vib 205(5):617–630. https://doi.org/10.1006/jsvi.1997.1035

8. Capozucca R, Magagnini E (2016) Vibration of RC beams with NSM CFRP with unbonded/notched circular rod damage. Compos Struct 144:108–130. https://doi.org/10.1016/j.compstruct.2016.02.027

9. Esfahani M et al (2021) Experimental investigation of residual flexural capacity of damaged reinforced concrete beams exposed to elevated temperatures. Eng Struct 240:112388. https://doi.org/10.1016/j.engstruct.2021.112388

10. Bendada A et al (2020) Mechanical characterization of an epoxy panel reinforced by date palm petiole particle. Steel Compos Struct 35(5):627–634

11. Capozucca R (2014) Vibration of CFRP cantilever beam with damage. Compos Struct 116:211–222. https://doi.org/10.1016/j.compstruct.2014.04.027

12. Capozucca R, Domizi J, Magagnini E (2016) Damaged RC beams strengthened with NSM CFRP rectangular rods under vibration in different constrain conditions. Compos Struct 154:660–683. https://doi.org/10.1016/j.compstruct.2016.07.044

13. Zenzen R et al (2018) A damage identification technique for beam-like and truss structures based on FRF and bat algorithm. Comptes Rendus Mécanique 346(12):1253–1266. https://doi.org/10.1016/j.crme.2018.09.003

14. Dinh-Cong D et al (2017) An efficient multi-stage optimization approach for damage detection in plate structures. Adv Eng Softw 112:76–87. https://doi.org/10.1016/j.advengsoft.2017.06.015

15. Khatir S et al (2021) An improved artificial neural network using arithmetic optimization algorithm for damage assessment in FGM composite plates. Compos Struct 273:114287. https://doi.org/10.1016/j.compstruct.2021.114287

16. Zenzen R et al (2020) A modified transmissibility indicator and artificial neural network for damage identification and quantification in laminated composite structures. Compos Struct 248:112497. https://doi.org/10.1016/j.compstruct.2020.112497

17. Khatir S et al (2019) Damage assessment in composite laminates using ANN-PSO-IGA and Cornwell indicator. Compos Struct 230:111509. https://doi.org/10.1016/j.compstruct.2019.111509

18. Khatir S et al (2017) Multiple damage detection in composite beams using particle swarm optimization and genetic algorithm. Mechanics 23(4):514–521

19. Tiachacht S et al (2018) Damage assessment in structures using combination of a modified Cornwell indicator and genetic algorithm. Eng Struct 177:421–430

20. Ouladbrahim A et al (2022) Experimental crack identification of API X70 steel pipeline using improved artificial neural networks based on whale optimization algorithm. Mech Mater 166:104200. https://doi.org/10.1016/j.mechmat.2021.104200

21. Khatir S et al (2020) Improved ANN technique combined with Jaya algorithm for crack identification in plates using XIGA and experimental analysis. Theoret Appl Fract Mech 107:102554. https://doi.org/10.1016/j.tafmec.2020.102554

22. Nguyen T, Vu A (2021) Evaluating structural safety of trusses using machine learning. Frattura ed Integrità Strutturale 15(58):308–318

23. Tran-Ngoc H et al (2019) An efficient artificial neural network for damage detection in bridges and beam-like structures by improving training parameters using cuckoo search algorithm. Eng Struct 199:109637. https://doi.org/10.1016/j.engstruct.2019.109637

Characteristics of Sea Surface Temperature Fronts Along Vietnamese Coast

Tu Tran Anh, Cuong Nguyen Kim, Ha Tran Thu, and T. Vu-Huu

1 Introduction

The oceanfront is one of the essential elements in oceanography. Ocean fronts are sharp boundaries between different water masses and different types of vertical structure (stratification) that are usually accompanied by enhanced horizontal gradients of temperature, salinity, density, nutrients, and other properties [1, 2, 4, 5]. Sea surface temperature front is the most basic form of oceanfront. There is always a difference in temperature in all oceans and seas in separate areas. This difference may be due to the non-uniform distribution of the solar radiation field, the infiltration of water masses, the water transport of circulation, or the difference in physical and nutritional factors. Thus, research on sea surface temperature front can help identify the distinction on physical conditions in large water areas. It is possible to determine the boundaries of water masses or the boundaries of significant flows [11, 21, 22].

Sea surface temperature data (SST) obtained from satellites has been used to study Pacific fronts since the 1970s [16]. Previous studies have focused on fronts associated with western boundary flows, such as the Kuroshio [19] and the East Australia flow [18]. The fronts associated with eastern boundary flows and coastal upwelling areas

T. T. Anh
Institute of Marine Environment and Resources (IMER-VAST), Haiphong City 18000, Vietnam

C. N. Kim
VNU University of Science, Hanoi 100000, Vietnam

H. T. Thu
Quangninh Department of Natural Resources and Environment, Quangninh Province 01100, Vietnam

T. Vu-Huu (✉)
Faculty of Civil Engineering, Vietnam Maritime University, 484 Lach Tray Str., Hai Phong, Vietnam
e-mail: truongvh.ctt@vimaru.edu.vn

[10] have been studied in areas such as the California flow [23, 24] and the Peru-Chile flow [6, 13].

In the East Vietnam Sea (internationally known as the South China Sea), the SST front in the west of Luzon in the heat field coincides with the bloom of phytoplankton mainly occurred with upwelling water phenomena [25] or relates to the steady swirl in offshore of the northwest of Luzon [20]. This front and the front strip offshore of the east of Vietnam coincides with three vital dynamic areas that can be monitored from the sea level data TOPEX/Poseidon [14]. Through the TOPEX/Poseidon data, it has been proved that the SST in the coastal area of Vietnam is close to narrow strips, and their seasonal change is remarkable with the immense maximum value [29]. Jing et al. [15] pointed out that fronts occur around Hainan Island in the northwestern South China Sea and persist through the summer upwelling season where thermal gradients are generally more than 0.1 °C/km. Zeng et al. [33] detected upwelling fronts for a similar study area and found that the maximum gradient is about 0.5 °C/km. In the winter, the SST fronts are mainly located along the offshore continental slopes of the South China Sea and across the entrance of Thailand Gulf and the northwestern of Luzon. In the Gulf of Thailand, SST fronts occurred from December to February through AVHRR data and from March to April through navigational data when the horizontal temperature variable was biggest. This front separates the freshwater mass in the Gulf and the water masses of the South China Sea. The SST front of the Gulf of Thailand disappeared entirely in May. In June, the navigational data indicated no SST front [30–32].

In this paper, the distribution of fronts SST was computed during 25 years (from 1985 to 2009) to provide assessments of seasonal location fluctuations in the year and the corresponding location fluctuations during the flood season (September) and dry season (April) for the Vietnamese coast.

2 Data and Methodology

2.1 Data

The project is based on acquiring a 4-km high-resolution satellite image using the Pathfinder 5 algorithm (Pathfinder 5). It is a new analysis of a high-resolution satellite image (AVHRR) developed by the Rosenstiel School of Marine and Atmospheric Science (RSMAS) and the National Oceanographic Data Center (NODC) NOAA. With many years of implementation and development of the previous Pathfinder datasets, NASA's Physical Oceanography Distributed ActiveArchive Center—(PO.DAAC) has joined to implement this project. This project was expected to expand the global sea surface temperature recording (SST) system with that development.

The oceanographic Pathfinder program with the high-resolution image (AVHRR) of NOAA/NASA has been developed for global ocean surface temperature with a

resolution of 9.28 km since the early 1990s. The result is a data set Version 4.x (V4). Despite some successes, the dataset also has limitations, such as considerable deviations from one area affected by atmospheric aerosols. Moreover, the relatively rough soil separation capability is significant for coastal area applications. It limits information about the non-existence of sea ice in the use of high latitude data. With three years of development, RSMAS/NODC with a new preprocessor algorithm has solved the limitations of version 4.x and introduced a more accurate ocean surface temperature data set with higher resolutions.

Satellite data preprocessing uses an enhanced version of the Pathfinder algorithm and processing steps to produce two global oceanic surface temperature images of a day. Related parameters have been started since 1985. With a resolution of approximately 4 km, this dataset is considered the highest possible resolution for high-resolution (AVHRR) data globally. Not only that, but this data set also includes the average datasets for 5-days, 7-days, 8-days, month, and year. Compared to Pathfinder Ocean surface temperature data sets with resolution 9-km, this data set has more advances with greater accuracy, better soil resolution, higher resolutions, and include information on sea ice.

2.2 Methodology for Determining Sea Surface Temperature Fronts from Satellite Images

The pioneers who carried this basic idea are Cayula et al. [7–9]; Ullman et al. [26–28]. During 1985–2009, fronts were obtained from the SST Pathfinder NOAA/NASA fields analysis. These fields are derived from high-resolution global data (AVHRR) (two fields with a resolution of 9.28 km per day) available from the Jet Propulsion Laboratory. In addition, surface temperature fronts are derived from sea surface temperatures removing clouds with the multi-images boundary separation algorithm [9, 26–28].

- Divides panoramas into windows of a given size
- Each window will be processed independently
- The windows need to design overlap so that it can link the boundaries that defined on different windows
- The window size can be selected by: 16 × 16, 32 × 32, etc. It depends on the size of the boundary and the resolution of the image, noise, etc.
- The boundary is defined as the boundary of the two regions $\omega 1$ and $\omega 2$ with almost homogeneous temperatures.

Histogram chart analysis (Histogram)

- In histogram analysis, it is necessary to find the threshold value for separating two domains of water temperate with remarkable distinction.
- In the case of two distinct domains of water temperature, a statistic method should be used to identify (classify) them.

Cohesion algorithm

- Used in the case of taking account to the spatial distribution of data.
- Assume: $\omega1'$ and $\omega2'$ are two defined domains; X is the point on the specified image; $t(x)$ is the corresponding temperature value, and τopt is the optimum threshold value divides two domains $\omega1'$ and $\omega2'$.
- The link coefficients for $\omega1'$ and $\omega2'$ for the whole defined domain are determined as follows:

$$C1 = \frac{R1}{T1}; \ C2 = \frac{R2}{T2}; \ C = \frac{R1 + R2}{T1 + T2} \tag{1}$$

in which, $C1$ and $C2$ are the cohension cofficients relating to $\omega1'$ và $\omega2'$.

$T1$, $T2$ are the validated points of temperature in $X \in \omega1'$ $X \in \omega2'$ and to the other regions, respectively.

$R1$, $R2$ are the validated points of temperature surrounding $X \in \omega1'$ $X \in \omega2'$ and to the other regions, respectively.

As the ideal cases, the domain is almost homogeneous, the linking coefficient:

$$C = 0.9; \ C1 = 0.92 \ C2 = 0.92 \tag{2}$$

Location of boundaries: After defining boundaries for each window, the next step is to identify and confirm the fronts. Front images are represented as pixels without front that will receive a value of 0. Next, define boundaries using multiple sea surface temperature (SST) images. Algorithm defining the boundary using multiple images is a combination of algorithms including:

- Identify clouds in a single image
- Define clouds in multiple images
- Define boundary using a single image
- Define boundaries.

The order of implementation is as follows

- Use the method for defining boundary in a single image [7] and apply it to multiple single images.
- Link boundaries by each image
- Minimize the width of boundary (handle to boundary only exists on 1 point)
- Combine defined boundaries with the original image to identify weak boundaries
- Set up a mask for the cloud cover area.

Computation of gradient

- Gradient computation using calculating gradient matrices with general formula as follows:

$$GX = \{GX \text{ dimension, direction } (+) \ 0 \ GX \text{ dimension, direction } (-)\} \tag{3}$$

$$GY = \{GY \text{ dimension, direction } (+) \ 0 \ GY \text{ dimension, direction}(-)\} \quad (4)$$

in which, dimension is the size of calculating gradient matrix, e.g., 3×3, 5×5, etc.; direction is the direction of gradient calculating, which can be two or more directions.

Computation procedure of sea surface temperature front with the method of Cayula&Cornillon (1992): The above computation procedures are carried out with MGET software (Marine Geology and Environment Tools). It is a set of more than 150 valuable tools with many different functions. MGET's specific tools include converting oceanographic data to the format of ArcGIS software, defining fronts by sea surface temperature images or statistical programs, etc. It is a package of open-source programs written by Python code and developed by Duke University, U.S., for GIS analysts and marine researchers.

MGET is acted based on ArcGIS as a tool of ArcToolbox. The implementation steps are as follows:

- Step 1: Convert HDF files to ArcGIS Rasters
- Step 2: Calculate the sea surface temperature values from infrared values
- Step 3: Remove clouds
- Step 4: Calculate the distribution of the sea surface temperature front
- Step 5: Convert these files to ASCII format
- Step 6: Calculate the occurrence frequency of SST and convert the ASCII file to an ArcGIS Raster file to display the data.

3 Results

The front of the Red River estuary and surrounding areas mainly have gradient values in the range of 0.125 °C/4 km and have different gradient intensities, alternating. Gradient intensity is more remarkable in winter than in summer (Fig. 1). In the winter, the fronts mainly involved the phenomenon of deep penetrating of the cold tongue into the South, forming the frontal areas mainly: West Philippine, Taiwan Strait, East of Hainan Island, Gulf of Tonkin, South Central of Vietnam, and the entrance of Thailand Gulf. The front mainly appears in Taiwan Strait in the summer, around Hainan Island and South Central of Vietnam. Front derived from upwelling water occurs in the South-Central region lasting five days to more than ten days. The fronts appear in the north of the East Sea simultaneously in the winter, while they do not appear in the south part except at the mouth of Thailand Gulf. The Gulf of Thailand is where fronts of seasonal continental slopes strong developed from January to February. The West Luzon Front (WLF) is observed in the west of Luzon Island (expanding to deep water masses) in winter (from October to May). This front expands to the north in the seasonal order to Bashi Strait and disappears in summer

(from May to October). The fronts offshore of Northwest of Boneo appear in the spring, summer and fall and disappear in the winter.

In April, front SST usually existed far from shore and extended continuously. From the North of Khanh Hoa province to the South of Binh Thuan province, there was a front strip stretched and far from shore 70 km. There was an arched front offshore of the Mekong River mouth (270 km from the shore), from Vung Tau to Tra Vinh (Fig. 2). In the downstream of the Mekong River system, in some years (1986; 2001), there was an SST front occurring nearby river mouths. In addition, there existed another front strip extending from Binh Dinh down to Bac Lieu. The more down to the South, the closer to the shore. In the flood season (September), the intensity and scope of the SST front appeared as not clear as they do in the dry
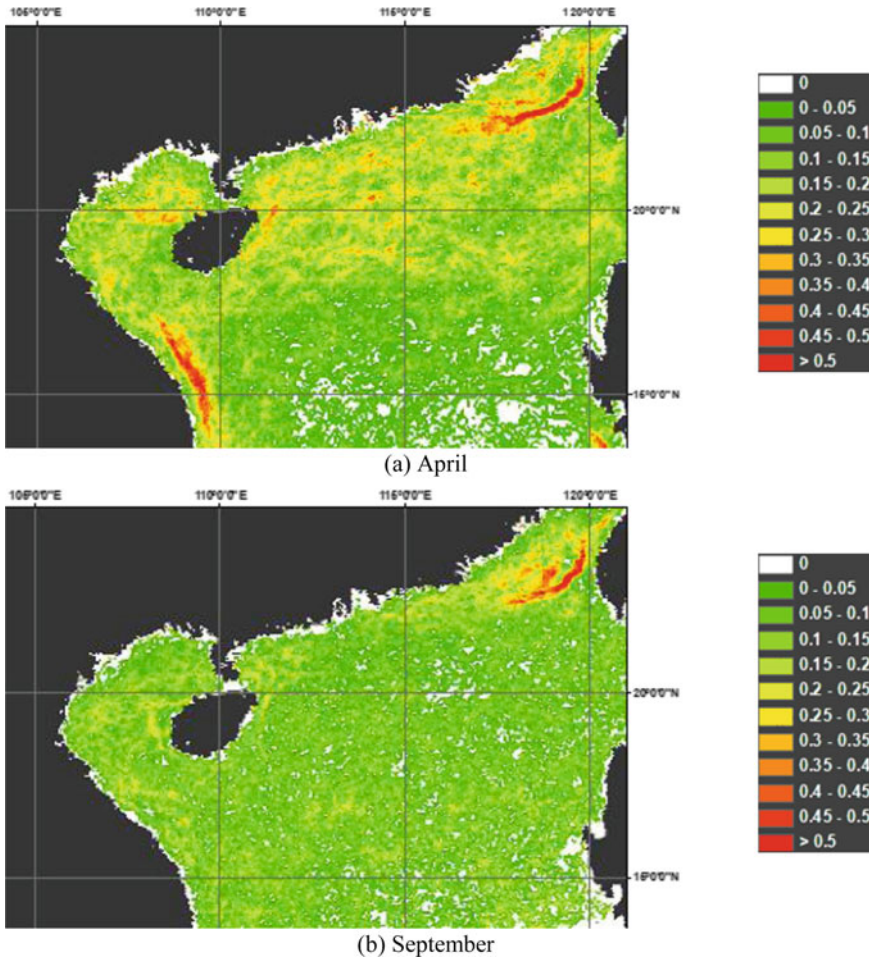

Fig. 1 Distribution frequency of occurrence of front SST in the Red River estuary
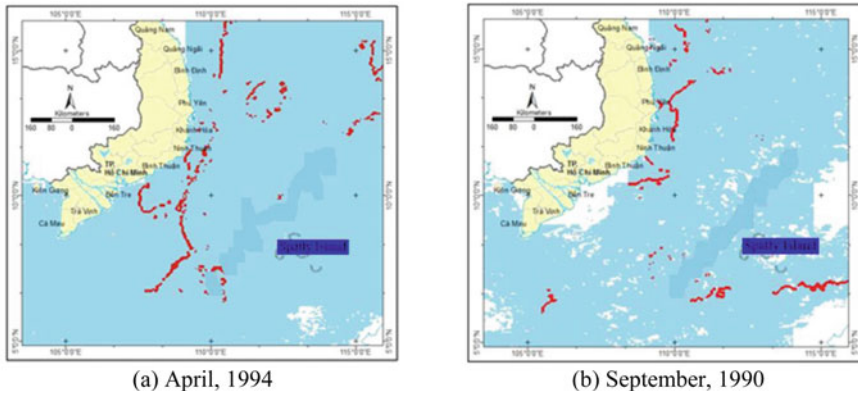
(a) April, 1994   (b) September, 1990

Fig. 2 Distribution frequency of occurrence of front SST in the Mekong River estuary

season. SST front was not found in some years (1988, 1991, 1996, 1999, 2003). In the upwelling water area, there was usually occur a strip of SST front that extended parallel to the shoreline in the years 1990 and 1994 (Fig. 2). In the downstream area of the Me Kong River, during the calculation period, the SST front appeared only in 1987, and its location was quite far from shore. In areas adjacent to the river mouths, the SST front was only found at the Tran De mouth (100 km from the shore), and there was no found SST front in other river mouths.

In winter and summer, the study area is affected by the northeast monsoon and southwest monsoon. In winter, the temperature field of the area is featured by the infiltration of cold-water mass from the north. In contrast, the summer is characterized by upwelling water phenomena in the South-Central region.

During the year, in the offshore area of Khanh Hoa-Binh Thuan, there always existed SST front strip in both dry and flood season, this front strip squeezed closely to the shoreline, and the location changed seasonally. However, in the dry season (April), the front strip was still influenced by the infiltration of cold-water mass from North to South (Fig. 3a). Offshore, there exist many areas with local fronts—where the interaction of water masses. Meanwhile, in the southern part of the Ca Mau Cape, a front strip often appears running across the gate of Thailand Gulf (Fig. 3a). This result is similar to some previously studied authors [3].

In the flood season (September), discrete front strips far 240 km from shore occur. It is clear that, during this period, the central axis of the front had changed compared to that in April. In the Khanh Hoa-Binh Thuan area, front trips with the east–west axis were dominant. It could be the consequence of two main ocean flows' interaction that creates the flow divider in this area (Fig. 3b). In the flood season, the interaction between freshwater from the Mekong River and seawater happens relatively near shore (within a few tens of kilometres). These fronts are unclear and un-continuous because the temperature field at this time was relatively uniform. To assess the accuracy location where the interaction of river-sea occurs, the image of the turbidity field will be more precise and more accurate. In the offshore of the
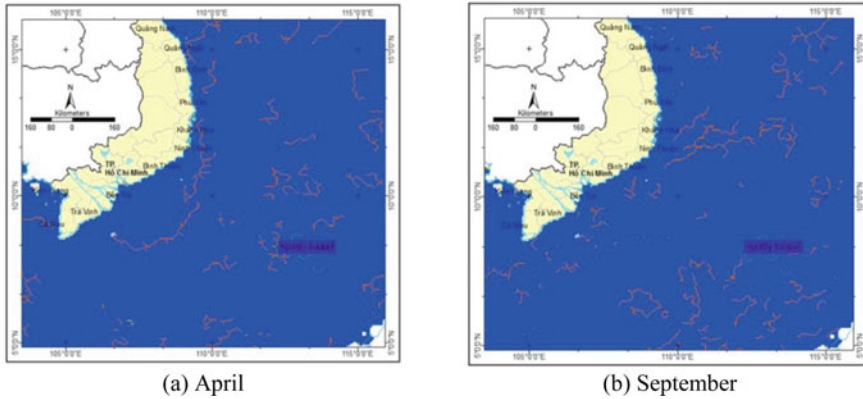
(a) April   (b) September

Fig. 3 Synthesis of distribution of front SST in the Mekong River estuary

southern part, the fronts of local water masses are larger and more seamless than in April. It shows that the water masses in this area were more extensive and more stable. Research on the fluctuation of flows the downstream of Mekong River shows that the average annual flow has decreased by about 10% since 2001. The level of decline inflow in the dry season is more significant than that in the flood season. It is one of the main reasons for the displacement of the SST front in the study area.

4 Conclusions

The locations of the sea surface temperature fronts along the Vietnamese coast were not fixed and fluctuated with the characteristics of meteorological and hydrodynamic fields. In the dry season, the fronts usually appear at both the continental shelf and the continental shelf border and are influenced by the cold water mass infiltrating to the South. They are also influenced by season characteristics with the interaction and dividing of local water masses. In the flood season, the impact of freshwater from the Mekong River is not clear in the distribution of front SST. During this period, there always existed a continuous and stable front strip due to the dispersion of North–South flow in the Khanh Hoa-Binh Thuan area. Although the results of this study are qualitative assessments concerning river flow, they also partially make clear the general mechanism of the front in the study area. Due to the limitation on the resolution of the satellite images, detailed studies using a 3-dimensional numerical model of the front structure's temperature field structure concerning the river flow is essential and should be implemented in the future.

References

1. Belkin IM, Cornillon PC (2003) SST fronts of the Pacific coastal and marginal seas. Pac Oceanogr 1(2):90–113
2. Belkin IM, Cornillon PC (2004) Surface thermal fronts of the Okhotsk Sea. Pac Oceanogr 2(1–2):6–19
3. Belkin IM, Cornillon PC, Sherman K (2005) Fronts in large marine ecosystem of the wold ocean. Progress in Oceanography
4. Belkin IM, Cornillon PC (2014) Fronts, fish and predators. Deep-Sea Research Part II 107:95
5. Belkin IM, Helber RW (2015) Physical oceanography of fronts: an editorial. Deep-sea Res 119:1–2
6. Brink KH, Halpern D, Huyer A, Smith RL (1983) The physical environment of the Peruvian upwelling system. Progr Oceanogr 12(3):285–305
7. Cayula J-F, Cornillon P (1992) Edge detection algorithm for SST images. J Atmos Oceanic Tech 9:67–80
8. Cayula J-F, Cornillon P (1995) Multi-image edge detection for SST images. J Atmos Oceanic Technol 12
9. Cayula J-F, Cornillon P (1996) Cloud detection from a sequence of SST images. Remote Sens Environ 55(1):80–88
10. Chen C, Lai Z, Beardsley RC, Xu Q, Lin H, Viet TV (2012) Current separation and upwelling over the southeast shelf of Vietnam in the South China Sea. J Geophys Res 117:C03033
11. Cuong NK (2009) Determination of sea surface temperature front using satellite images of South Central region. Master thesis, VNU University of Science, p 74
12. Wang D, Liu Y, Qi Y, Shi P (2001) Seasonal variability of thermal fronts in the Northern South China Sea from satellite data. Geophys Res Lett 28(20):3963–3966
13. Fonseca T (1989) An overview of the pole ward undercurrent and upwelling along the Chilean coast. In: Neshyba SJ, Mooers CNK, Smith RL, Barber RT (eds) Poleward flows along eastern ocean boundaries. Springer-Verlag, New York etc, pp 203–228
14. Ho C-R, Kuo N-J, Zheng Q, Soong YS (2000) Dynamically active areas in the South China Sea detected from TOPEX/POSEIDON satellite altimeter data. Remote Sens Environ 71(3):320–328
15. Jing Z, Qi Y, Du Y, Zhang S, Xie L (2015) Summer upwelling and thermal fronts in the northwestern South China Sea: observational analysis of two mesoscale mapping surveys. J Geophys Res 120:1993–2006
16. Legeckis R (1978) A survey of worldwide sea surface temperature fronts detected by environmental satellites. J Geophys Res 83(C9):4501–4522
17. MGET website: http://code.env.duke.edu/projects/mget
18. Nilsson CS, Cresswell GR (1980) The formation and evolution of East Australian Current warm-core eddies. Progr Oceanogr 9(3):133–183
19. Qiu B, Toda T, Imasato N (1990) On Kuroshio front fluctuations in the East China Sea using satellite and in situ observational data. J Geophys Res 95(10):18191–18204
20. Qu T (2000) Upper-layer circulation in the South China Sea. J Phys Oceanogr 30(6):1450–1460
21. Shi R, Guo X, Wang D, Zeng L, Chen J (2015) Seasonal variability in coastal fronts and its influence on sea surface wind in the Northern South China Sea. Deep-Sea Res 119:30–39
22. Shi R, Chen J, Guo X, Zeng L, Li J, Xie Q, Wang X, Wang D (2017) Ship observations and numerical simulation of the marine atmospheric boundary layer over the spring oceanic front in the northwestern South China Sea. J Geophys Res 122(7):3733–3753
23. Strub PT, Kosro PM, Huyer A, CTZ collaborators (1991) The nature of the cold filaments in the California current system. J Geophys Res 96(C8):14743–14768
24. Strub PT, James C (1995) The large-scale summer circulation of the California Current. Geophys Res Lett 22(3):207–210
25. Tang D-L, Ni I-H, Kester DR, Müller-Karger FE (1999) Remote sensing observations of winter phytoplankton blooms southwest of the Luzon Strait in the South China Sea. Mar Ecol Prog Ser 191:43–51

26. Ullman DS, Cornillon PC (1999) Surface temperature fronts off the East Coast of North America from AVHRR imagery. J Geophys Res 104(C10):23459–23478
27. Ullman DS, Cornillon PC (2000) Evaluation of front detection methods for satellite-derived SST data using in situ observations. J Atmos Oceanic Tech 17(12):1667–1675
28. Ullman DS, Cornillon PC (2001) Continental shelf surface thermal fronts in winter off the northeast U.S. coast. Cont Shelf Res 21(11–12):1139–1156
29. Wang L, Koblinsky CJ, Howden S (2000) Mesoscale variability in the South China Sea from the TOPEX/Poseidon altimetry data. Deep-Sea Res I 47(4):681–708
30. Wattayakorn G, King B, Wolanski E, Suthanaruk P (1998) Seasonal dispersion of petroleum contaminants in the Gulf of Thailand. Cont Shelf Res 18(6):641–659
31. Yanagi T, Takao T (1998) Seasonal variation of three-dimensional circulations in the Gulf of Thailand. La Mer 36(2):43–55
32. Yanagi T, Sachoemar SI, Takao T, Fujiwara S (2001) Seasonal variation of stratification in the Gulf of Thailand. J Oceanogr 57(4):461–470
33. Zeng X, Belkin IM, Peng S, Li Y (2014) East Hainan upwelling fronts detected by remote sensing and modeled in summer. Int J Remote Sens 35:4441–4451

An Eaton Lens Design to Reduce of Earthquake Impact

Sy Pham-Van, Q.-Hoan Pham, Thi-Le Le, and T. Vu-Huu

1 Introduction

An earthquake is a sudden release of energy in the ground that causes shaking of the ground. This release is usually caused by geological activities within and on the earth's surface. The occur of an earthquake produces an energy wave, known as a seismic wave. The seismic wave consists of two waveforms; they are the primary wave, named P-wave and secondary wave, called S-wave. P-wave is formed immediately after forming a geological process in the earth. It is a longitudinal wave propagating quickly inside the earth. Its speed can reach 330 m/s in air, 1450 m/s in water and 5000 m/s in rock [1]. The following wave is the S-wave, making particles vibrate perpendicularly to the wave propagation. This wave has a speed of about 60% of the P-wave; it only travels in solids and liquids.

Earthquakes cause many enormous casualties, i.e. destroy buildings, infrastructure, society and economy. Since 2000, it has recorded many severe earthquakes causing severe damage to people. For example, on 26 January 2001, the earthquake in Bhui, India, killed 13,481 people. In 2004, an earthquake with a magnitude of 9.1 caused a tsunami in the Indian Ocean that killed 225,841 people. Then, a magnitude 7.8 earthquake occurred in the city of Gorkha in Nepal, killing 8831 people [2].

Generally, the Eaton lens is a gradient refractive index lens (GRIN) as the Luneburg, Maxwell fisheye. However, the Eaton lens cannot make the wave converge at a point on the edge of the lens like the Lunburg or a point in the centre of the lens like a Maxwell. The main feature of the Eaton lens is the bending capacity of the propagation direction in any direction. These lenses have been extensively studied for the electromagnetic fields using homogeneous material. In addition, lenses have also been studied for minimising the effect of tsunami [3, 4]. For this problem, a

S. Pham-Van · Q.-H. Pham · T.-L. Le · T. Vu-Huu (✉)
Faculty of Civil Engineering, Vietnam Maritime University, Haiphong, Vietnam
e-mail: truongvh.ctt@vimaru.edu.vn

large cylinder is placed at the lens' centre to create reflections against the incident waves.

This paper is set up as follows: Sect. 2 presents the Eaton lens. Then, Sect. 3 briefly shows the proposed Eaton lens of cylinder cells to minimise the impact of an earthquake. Finally, Sect. 4 presents the conclusions and future works.

2 Eaton Lens

Eaton lens adapts the refraction index continuously, uniformly and directionally, known as GRIN lens. The distinguishing feature is bending the incident wave in any direction. Generally, the equation presenting the diffraction index is [3]:

$$n^{\pi/\theta} = \frac{R}{nr} + \sqrt{\left(\frac{R}{nr}\right)^2 - 1}$$ (1)

in which, θ is the central angle showing the bent direction of waves; R is the lens radius; r is the distance between wave direction to the lens centre. Generally, Eaton lenses are often applied for special bends (i.e. 90 and 180°). Therefore, mathematical tools are created to calculate the diffraction index for the particular bending incident wave propagation. Remarkably, the formulation to define the refraction index of 180° is shown as follows [3]:

$$n^2 = \frac{1}{nr} + \sqrt{\left(\frac{1}{nr}\right)^2 - 1}$$ (2)

Then, for the 90° Eaton lens, the refraction index is expressed as:

$$n = \sqrt{\frac{2R}{r} - 1}$$ (3)

Due to the varying refraction index, waves are bent in different directions by Eaton lenses. The index of refraction is a non-dimensional value describing the propagation path of waves in a material. Mainly, it is determined by the following formulation:

$$n = \frac{c}{v}$$ (4)

where c is the light speed in space; v is the light speed in the medium.

Thus, the index of refraction is directly proportional to the wave velocity in the incident medium and inversely proportional to the wave velocity in the refracting medium. The elastic wave velocity in any medium is expressed as the ratio of the elastic strain modulus to the density of that medium, see Eq. (4) [4].
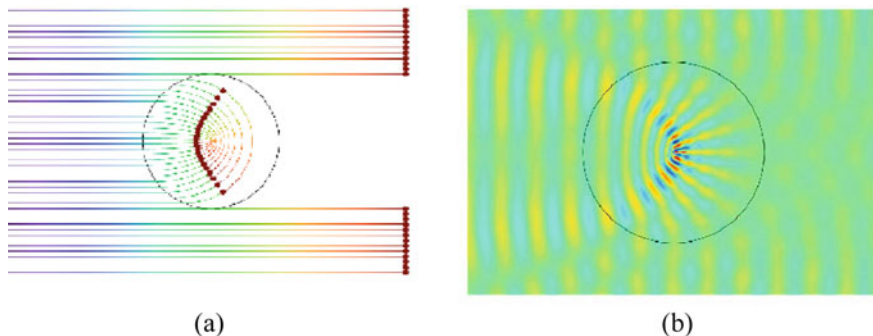
Fig. 1 Numerical result of the beam through **a** the homogenous lens and **b** the 180° Eaton lens

$$v = \sqrt{\frac{B}{\rho}} \tag{5}$$

in which, B is the elastic modulus, ρ is the density of the medium. Thus, the formulation describing the refractive index is expressed as (Figs. 1 and 2):

$$n = \sqrt{\frac{B_0}{\rho_0} \cdot \frac{\rho_1}{B_1}} \tag{6}$$

where B_0 and B_1 are the elastic modulus of the medium and the lens' material, respectively; ρ_0 and ρ_1 are the density of the medium and lens' material, respectively. Assume the elastic modulus of the initial and the refracting medium is similar, Eq. (6) is rewritten as follows [5, 6]:

$$n = \sqrt{\frac{\rho_1}{\rho_0}} \tag{7}$$

3 Eaton Lens Modelling

For a homogeneous Eaton lens, the equation representing the refractive index is a continuous function of the lens's density and radius [7]. They are assuming that the elastic coefficiencies of the incident and refractive medium are similar and constant. Making and applying a homogeneous Eaton lens is not easy.

Therefore, dividing the lens into small cells of equal size, see Fig. 3. The interval cylinder (green circle, see Fig. 3) is constructed by a specific material [5, 6]. The general medium sets the outside of the circle. A refraction index is generally defined by Eq. (1) for each cell. It depends on the distance from the cell centre to the lens
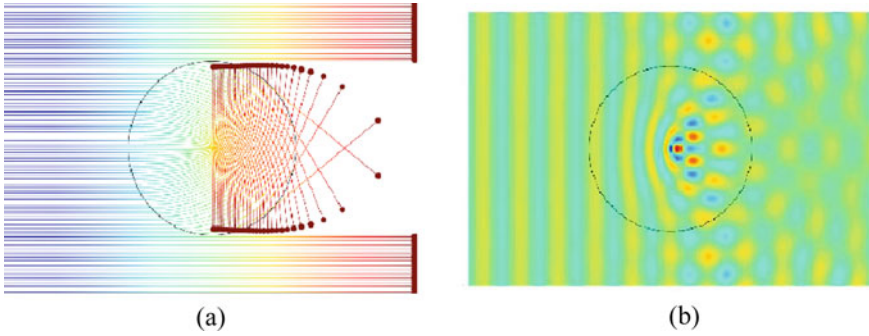
Fig. 2 Numerical result of the beam through **a** the homogenous lens and **b** the 90° Eaton lens

one. Then, for the case of 90° and 180° Eaton lenses, Eqs. (2) and (3) are deployed to define the refraction index, respectively. Deploy Eq. (7) to Eq. (2) and Eq. (3) for 90° and 180° Eaton lenses, respectively, to define the diameter of the lens [4].

Moreover, it is evident that the refraction index approaches infinity when the distance from the cell to the lens centre reaches zero, see Fig. 4a. In this case, it is not able to find the cylinder diameter of such cells. To deal with this problem, the cell properties are set similar to nearby cells so that the refractive index value at the centre of the lens will be constant, see Fig. 4b.

Based on the numerical results of the model and the analytical solution, they prove that the lens formed by cylinders successfully bends the direction of the wave. Moreover, as the diameter of the cylindrical lens is much larger than the wavelength, no reflection wave is caused by these cylinders (Fig. 5).

As the solution of the model on the frequency domain of many different frequency values, the proposed Eaton lens successfully bends the particular wave frequencies. Remarkably, the proposed Eaton lens presents good bending for frequencies below 1500 Hz. On the contrary, if the frequency is higher than 1500 Hz, the result of the

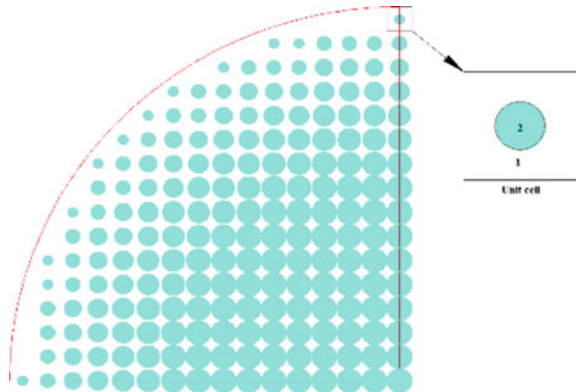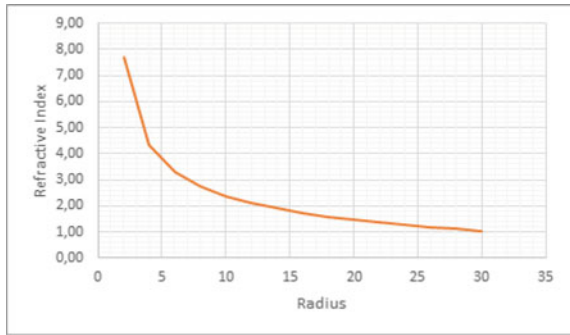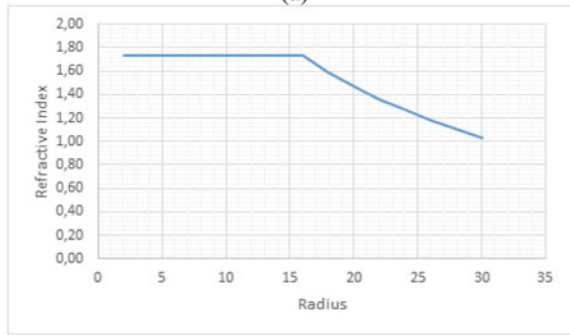**Fig. 3** Proposed Eaton lens was designed by cylinder cells

Fig. 4 Refraction index of **a** idealisation material lens and **b** the cylindric-cell lens
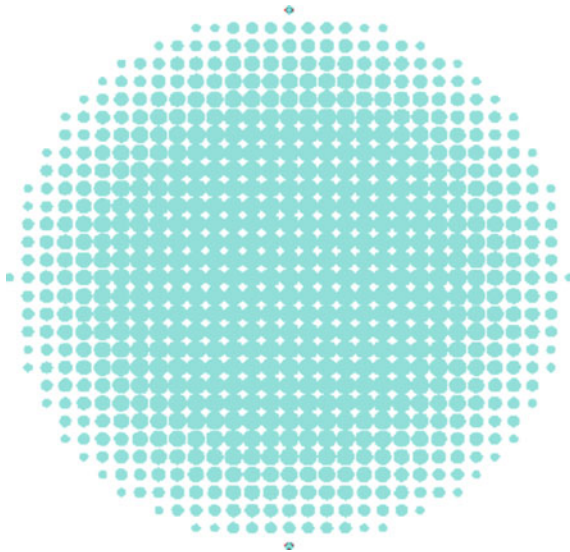

(a)

(b)

Fig. 5 Prototype of a cylindric-cell lens

wave bending is not good. It means that the proposed lens works well with large wavelengths (Figs. 6 and 7).

According to the above simulation results, the proposed Eaton lens has worked well with elastic waves (i.e. acoustic, seismic, etc.). Besides, earthquakes cause seismic waves, a type of elastic wave. It means that applying the Eaton lens in minimising the damages of earthquakes is high practicability. In this case, the cylinder cells of the Eaton lens are constructed by the concrete piles of the foundations. Then, all foundation piles are calculated and organised as a particular system of an Eaton
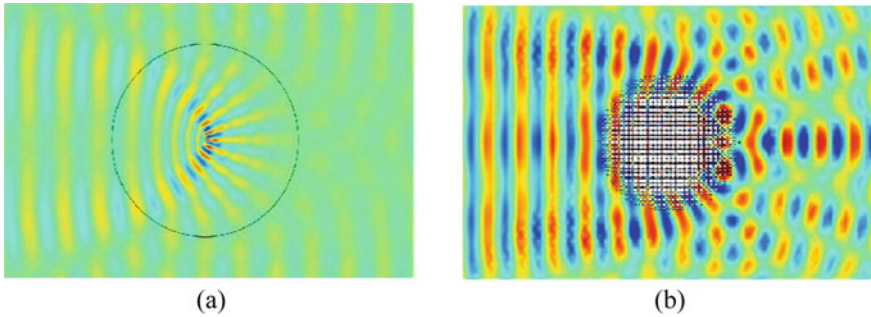

Fig. 6 Numerical results of 180° Eaton lenses: **a** homogeneous material; **b** cylindric-cell lens
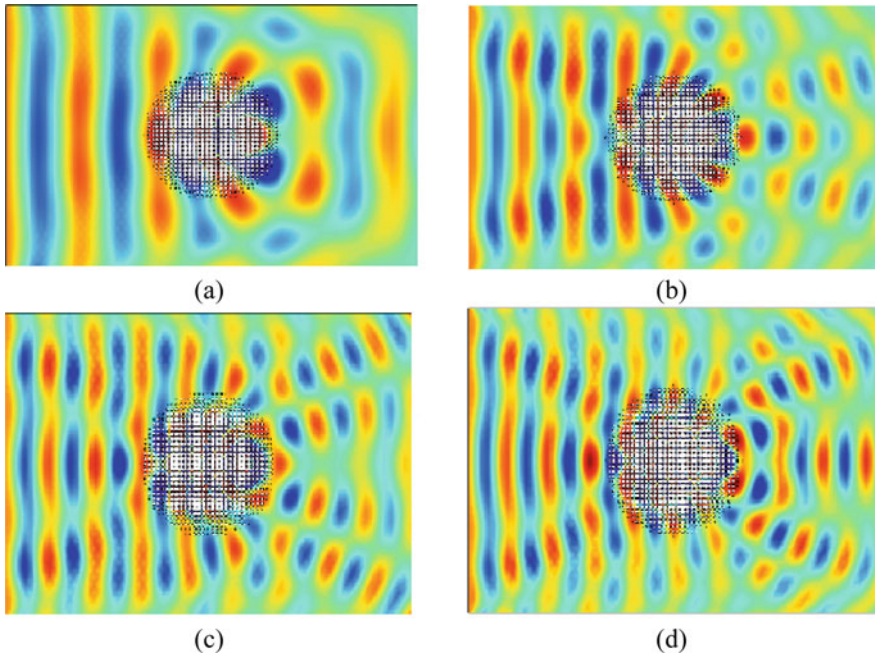

Fig. 7 Results of 180° Eaton lens with: **a** $f = 1500$; **b** $f = 1700$; **c** $f = 1900$; and **d** $f = 2000$ Hz

lens. This application of the Eaton lens becomes more practical due to the increasing popularity of pile foundations instead of shallow foundations as before. Significantly, the foundations of the skyscraper, the exceptional infrastructures, i.e. nuclear power plants, hydroelectric dams, etc. It means that the regular pile foundation becomes an Eaton lens to minimise the damages of earthquakes. Thus, the foundation can support the building and prevent seismic earthquake waves.

4 Conclusions

This paper successfully introduces a novel cylindric-cells design of an Eaton lens in bending the elastic waves (i.e. acoustic, seismic, etc.), which earthquakes could cause. The numerical results in this paper prove that the proposed cylindric-cells Eaton lens similarly performs to an Eaton lens entirely made by homogenous material. It is the key to turning the idea of the cylindric-cells Eaton lens into reality. This proposed design poses two significant benefits. First, the design is simple and has high applicability. Second, the lens's cylindric cells could be constructed by the standard and popular material, especially concrete or steel.

References

1. Alsadi HN (2017) Seismic hydrocarbon exploration, 1st edn, Springer
2. Spence R, So E, (2021) Why do buildings collapse in earthquakes?: Building for safety in seismic areas, 1st edn, Wiley-Blackwell
3. Kim S-H (2021) Analytic solution of the generalised Eaton lens. J Mod Opt 68(3):143–145
4. Kim S-H, Sy P-V, Das MP (2017) Acoustic Eaton lens array and its fluid application. Mod Phys Lett 31(08):1750081
5. Zentgraf T, Liu Y, Mikkelsen MH, Valentine J, ZhangA X (2011) Plasmonic Luneburg and Eaton lenses. Nat Nanotechnol 6:151–155
6. Zeng Y, Werner DH (2012) Two-dimensional inside-out Eaton Lens: design technique and TM-polarized wave properties. Opt Express 20(3):2335–2345
7. Yin M, Tiana XY, Wu LL, Li DC (2014) All-dielectric three-dimensional broadband Eaton lens with large refractive index range. Appl Phys Lett

Regression Method-Based Structural Condition Assessment for Bridge Health Monitoring

Tam Nguyen-Nhat ⓘ**, Nhi Ngo-Kieu** ⓘ**, Toan Pham-Bao** ⓘ**,
Luan Vuong-Cong** ⓘ**, and Hung Nguyen-Quoc** ⓘ

1 Introduction

It is worth considering that every structure over time has a change in the mechanical properties of both the structure and the material. Surveys in terms of structural changes have been carried out a lot around the world. However, the mechanical properties of the materials have not been really focused on assessment. In fact, in order for structural damage changes (cracks, breakage, etc.) to occur, changes in materials must have occurred before.

The structure is subjected to many ambient influences such as impact loads, weather, and chemicals. These agents gradually cause changes in the structure with respect to appear changes in the mechanical properties of the material. Mechanical properties of materials include elasticity and viscosity. The change in elasticity coincides with changes in the overall stiffness of the structure. Consequently, this change can be discerned through the change in stiffness. Theoretical formulas to model the deteriorating process of the mechanical system have been presented in many studies in structural health monitoring (SHM) since many decades ago, mainly on the reduction of structural stiffness, typically cracks [1]. Structural cracks are generally classified into open, closed, and breathing (opening and closing) cracks. Open cracks are commonly used in most of the research on crack modeling. They are classified into three main groups: finite element (stress concentration) models applying linear cracking mechanics [2], either a continuous model using a reduction in stiffness (elastic modulus reduction model) [3], or a continuous-discrete model using a spring of equivalent stiffness [4]. The structural deteriorating modeling equations

T. Nguyen-Nhat · N. Ngo-Kieu · T. Pham-Bao (✉) · L. Vuong-Cong · H. Nguyen-Quoc
Laboratory of Applied Mechanics (LAM), Ho Chi Minh City University of Technology
(HCMUT), 268 Ly Thuong Kiet Street, District 10, Ho Chi Minh City, Vietnam
e-mail: baotoanbk@hcmut.edu.vn

Vietnam National University Ho Chi Minh City, Ho Chi Minh City, Vietnam

have been proven by many experimental tools and are applied in engineering calculations [5–7] to support SHM. A good point of SHM is the early identification of damage by using vibration [8]. In recent years, vibration signal-based methods for SHM have become universal [9, 10]. These models are necessary for the calculation of structural vibrations, but they are unable to provide complete information about the entire deteriorating phenomenon of the structure. In addition, current structural analysis methods capability is not relatively high enough to detect the change in viscosity.

With a view to solving the problem of identifying changes in viscosity of the material, this research proposes a new method through the change of the distribution of loss factor with respect to the value of frequency and amplitude vibration. The article investigates a model of flat horizontal bending beams, but in order for the results to be consistent with reality, the study randomizes the distributed force values. From the random force spectrum obtained from the above process, a corresponding response spectrum will be derived. Many researchers have successfully used power spectral density (PSD) to detect damage in bridges [11, 12]. This paper uses a viscoelastic material model to inversely extract the loss factor value from the response spectrum characteristics. The viscoelastic model involves both the elasticity and viscosity of material [13–15]. In theory, the random excitation is usually modeled as a white noise signal with the same spectral amplitudes over the entire frequency domain. However, in practice, the values of the spectral amplitude of force are randomly distributed without inherently contant. Consequently, the proportional relationships between the amplitudes of the response spectrum are also randomly distributed. When the mechanical properties of the material change, thereby affecting the above distribution, so the article proposes to use the regression method to retrieve the distribution plane of the loss factor. Furthermore, intending to observe the trend of changing the mechanical properties of materials that the article focuses on viscosity, we investigate the change of the regression surface area where the boundary limit is the maximum of the characteristics of the response spectrum. The survey is based on the known change in mechanical properties proposed by the article.

2 Theoretical Rationale

2.1 Viscoelastic Model of Material and Loss Factor

Viscoelastic model

The viscoelastic model is an extended model compared to Hooke's model, including the influence of the modulus of elasticity E and the viscosity C_0 of the material, according to Voigt's law:

$$\sigma = E\varepsilon + C_0 \frac{\mathrm{d}\varepsilon}{\mathrm{d}t} \tag{1}$$

where E—elastic modulus; C_0—viscous coefficient; ε—strain; σ—normal stress.

Equation (1) is an extension of Hooke's law, which contains only the first term on the right-hand side, $\sigma = E\varepsilon$. From the point of view of Hooke's law, the relationship between stress and strain is linear, also known as the absolute elastic model. The parameter E (elastic modulus) represents the elasticity of the material used in the structure. The second term on the right-hand side of Eq. (1) $\left(C_0 \frac{d\varepsilon}{dt}\right)$ represents the stress σ proportional to the rate of change of strain, i.e., $\frac{d\varepsilon}{dt}$. Thus, with the proposal of this study, Eq. (1) shows both the elasticity and viscosity of the material; we call it the viscoelastic model of the material. According to this viscoelastic model, the mechanical properties of the material are determined by two parameters: E, C_0.

Loss factor

For viscoelastic materials, the maximum strain potential energy of the structure will have a value that is linearly proportional to the square of the initial strain value ε_0 according to Eq. (2). However, the strain potential energy will be dissipated by a definite amount of D in each vibration period, according to Eq. (3). And the ratio between the dissipated energy and the original strain potential is called the loss factor η.

$$\prod = \frac{1}{2} E \varepsilon_0^2 \tag{2}$$

$$D = \pi C_0 \omega \varepsilon_0^2 \tag{3}$$

$$\eta = \frac{D}{2\pi \prod} = \frac{C_0 \omega}{E} \tag{4}$$

The loss factor purely depends on the basic parameters of the material, such as viscous coefficient C_0, elastic modulus E, and vibration frequency. The loss factor can therefore be used to assess the overall condition of the material.

2.2 Bending Vibration of Beam

Suppose, the inertial force caused by the rotation of the sections is disregarded. In that case, the governing equation of the cross section at longitudinal x positions on the beam is expressed by the differential equation:

$$EJ\frac{\partial^4 w(x,t)}{\partial x^4} + C_0 J\frac{\partial^5 w(x,t)}{\partial x^4 \partial t} + \rho A\frac{\partial^2 w(x,t)}{\partial t^2} = f(x,t) \tag{5}$$

where J—area moment of inertia of cross section; ρ—mass density per unit length; A—area of cross section; $w(x, t)$—transverse displacement.

The function $w(x, t)$ is found in the form:

$$w(x, t) = \sum_{r=1}^{n} X_r(x) T_r(t) \tag{6}$$

According to Eq. (6), the function $w(x, t)$ is found in the form of two separate functions: $X_r(x)$ and $T_r(t)$, where the function $X_r(x)$ involves only the variable representing the position, and the function $T_r(t)$ involves only the variable representing the time. Substituting Eq. (6) into Eq. (5), we derive the following two differential equations:

$$X_r^{(4)} - p_r^2 \frac{\rho A}{EJ} X_r = 0 \tag{7}$$

$$\ddot{T}_r + p_r^2 \frac{C_0}{E} \dot{T}_r + p_r^2 T_r = f_r(t) \tag{8}$$

where p_r is the natural frequency, $f_r(t)$ is the generalized force function of the rth vibration mode, and p_r is determined from the results of solving Eq. (7) with the boundary condition of the simply supported beam.

$$p_r = \frac{r^2 \pi^2}{l^2} \sqrt{\frac{EJ}{\rho A}} \quad r = 1, 2, ..., n \tag{9}$$

Then, the function $X_r(x)$ has the form:

$$X_r(x) = \sin\left(r\pi \frac{x}{l}\right) \tag{10}$$

From Eq. (8), with input forced spectrum $F(\omega)$, the amplitude of vibration spectrum $T_r(\omega)$ at each vibration mode of the structure during the vibration is expressed:

$$T_r(\omega) = \frac{F(\omega)/p_r^2}{\sqrt{\left[1 - \left(\frac{\omega}{p_r}\right)^2\right]^2 + \left(\frac{c_o \omega}{E}\right)^2}} \tag{11}$$

In order to be suitable for the process of collecting and processing acceleration signals, we need to convert $T_r(\omega)$ from Eq. (11) to the amplitude of the acceleration power spectral density (PSD) according to Eq. (12). Therefore, we calculate the PSD of acceleration S_r and the PSD of force S_{fr} according to Eq. (12), from which we determine the formula for calculating loss factor according to Eq. (13) considering Eq. (11):

$$S_r(\omega) = \left(\omega^2 T_r(\omega)\right)^2 = \omega^4 \cdot T_r^2(\omega)$$
$$S_{fr}(\omega) = (F(\omega))^2 \tag{12}$$

$$(\eta)^2 = \left(\frac{C_0\omega}{E}\right)^2 = \frac{\frac{S_{fr}(p_r)}{S_{fr}(\omega)}\left(1 - \left(\frac{\omega}{p_r}\right)^2\right)^2}{\left(\frac{\max(S_r)}{S_r(\omega)}\right) \cdot \left(\frac{\omega^2}{p_r^2}\right) - \frac{S_{fr}(p_r)}{S_{fr}(\omega)}} \tag{13}$$

In practice, the derived bridge vibration signal is usually in two primary forms: the free vibration state and the forced vibration state by artificial or natural excitation sources [16]. Methods of artificially forced stimulation generally use electronic vibration devices or shock hammers. Vibrators can be used to create different types of force excitation both vertically and horizontally on the structure. The artificially forced excitation measures have the advantage that we can predefine and manage the force functions acting on the structure. This excitation usually uses input–output methods using the relationship between the input load signal (e.g., the power spectrum of force S_{fr}) and output response (e.g., the power spectrum of the response S_r). From there, we can quickly determine the necessary parameters (e.g., loss factor η). However, this stimulation method has two limitations: firstly, it is usually applied to simple structures; secondly, it has to pause the operating during the excitation process, which increases the cost per test [17]. Intending to overcome the above limitation, we propose an idea of using the natural load source of the structure itself. However, the disadvantage of using natural excitation is the randomness of amplitude, time, direction, and frequency level, so it is laborious to precisely determine the excitation source. This measure belongs to the output type of defect identification methods (using only the vibration signal of the structure itself and ignoring the properties of the excitation source). Theoretically, the random excitation source usually has the form of white noise with constant power spectral amplitude value ($S_{fr} \sim$ const). The loss factor calculation formula in Eq. (13) becomes the loss factor function in Eq. (14), depending only on the response power spectrum.

$$\eta(S_r, \omega) = \frac{\left(1 - \left(\frac{\omega}{p_r}\right)^2\right)^2}{\left(\frac{\max(S_r)}{S_r(\omega)}\right) \cdot \left(\frac{\omega^2}{p_r^2}\right) - 1} \tag{14}$$

3 Results and Discussion

3.1 Regression Procedure

The paper proposes a regression method to generate the feature surface representing the distribution of loss factor values concerning frequency and PSD according to Eq. (14). In the real world, bridges operating under moving load, environmental impact, and errors may occur during measurement. Consequently, we use signal
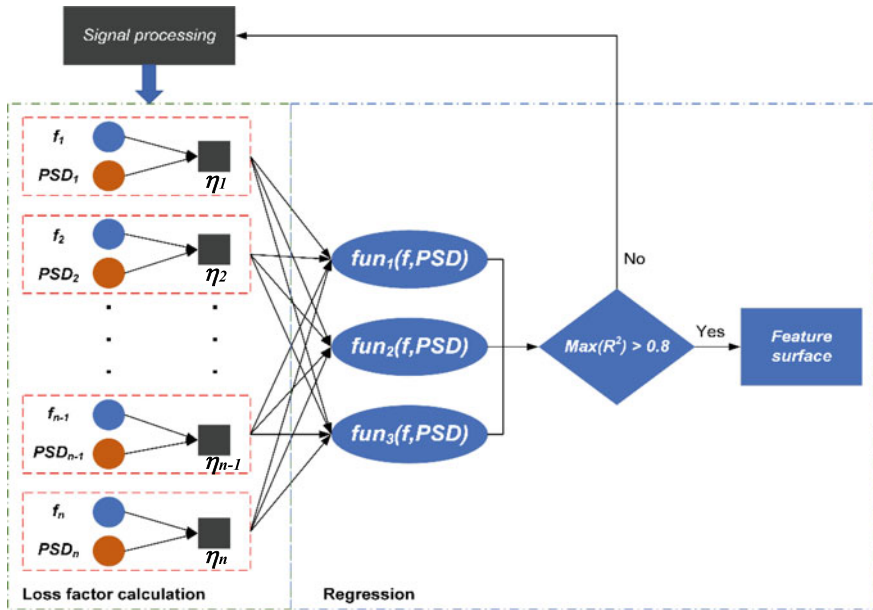
Fig. 1 Regression procedure of proposal

processing to refine and filter noise for acceleration signals. This signal processing uses to remove outliers, filter signal interference using wavelet transform. The proposed procedure is illustrated as shown in Fig. 1.

The loss factor values are calculated from the power spectrum (frequency, PSD) of the measured acceleration signal. A power spectrum consists of n values of frequency f and n values of PSD, so the calculation will derive n corresponding values of loss factor. Subsequently, these sets of frequency, PSD, and loss factor values considered as the sets of x, y, and z values are put into three functions for regression. The three mentioned functions have the following expressions:

$$\mathrm{fun}_1(x, y) = p_{00} + p_{10}x + p_{01}y \tag{15}$$

$$\mathrm{fun}_2(x, y) = p_{00} + p_{10}x + p_{01}y + p_{20}x^2 + p_{11}xy + p_{02}y^2 \tag{16}$$

$$\mathrm{fun}_3(x, y) = a + b\sin(m\pi xy) + ce^{(-(wy)^2)} \tag{17}$$

The most optimal surface is selected from the regression surfaces of three functions based on the squared correlation coefficient R^2 with the initial set of values. The selected surface has the most significant squared correlation coefficient, and this value must be greater than 0.8. Suppose the surface has the largest squared correlation coefficient not greater than 0.8. In that case, the procedure goes back to

signal processing with the higher resolution wavelet filter and duplicates the above process. Eventually, the proposed procedure derives the feature surface representing the distribution, and the assessment parameter will be the area of this feature surface.

3.2 Numerical Simulation

Intending to assess the trend of change in the assessment parameter concerning changes in mechanical properties of the material, we perform a simulation for material deterioration. This process simulated a reinforced concrete beam considered a viscoelastic beam consisting of two essential parameters: elastic modulus and viscous coefficient. This simulated beam has been structured by concrete with a compression strength of 40Mpa and has dimensions of $24.7 \times 20.6 \times 1.3$ m (length $\times$ width $\times$ thickness). The deterioration process is simulated with six mechanical scenarios of material as described in Table 1. The simulation process is illustrated in Fig. 2.

The simulation is performed according to a proposed process based on vibration theory. For each level of six levels mentioned in Table 1, the beam is subjected to random excitation, a normally distributed random vector with a mean value of 1 kN and a standard deviation value of 0.5 kN. Moreover, the power spectrum of force is

Table 1 Description of mechanical scenarios of material

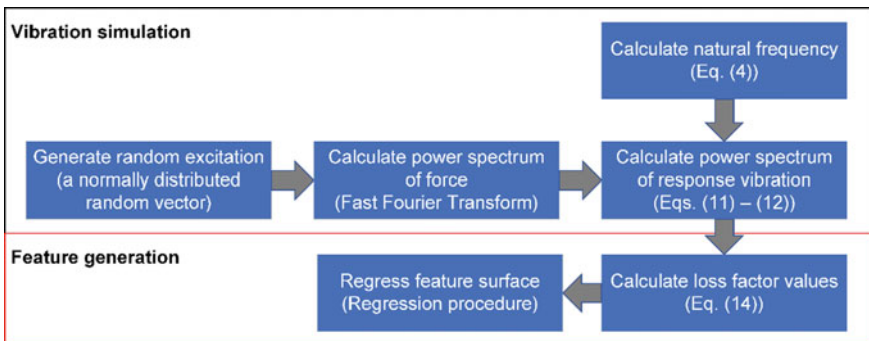| Deterioration level	Elastic modulus (E)	Viscous coefficient (C0)
0	E0 = 33.9 GPa	C00 = 0.35 GPa·s
1	E1 = 0.95 E0	C01 = 1.1 C00
2	E2 = 0.90 E0	C02 = 1.2 C00
3	E3 = 0.85 E0	C03 = 1.3 C00
4	E4 = 0.80 E0	C04 = 1.4 C00
5	E5 = 0.75 E0	C05 = 1.5 C00

Fig. 2 Simulation process for simply supported beam

derived by using fast Fourier transform (FFT) for random excitation then square it. The natural frequencies of simulation scenarios are calculated based on boundary conditions of the simply supported beam based on Eq. (4). Subsequently, we incorporate natural frequency and power spectrum of force to derive the power spectrum of vibration response according to Eqs. (11), (12). Lastly, we perform the proposed regression procedure to generate feature surfaces of mechanical condition scenarios of the material. The results of six deterioration levels of mechanical properties are shown in Fig. 3. Also, the trend of change in the area of feature surfaces concerning material deterioration is shown in Fig. 4.

Thus, by simulating material deterioration, we can observe that the area of regression surface gradually decreases when the material is deteriorating. In Fig. 4, from deterioration level 0 to level 5, the area is changed 25%. Although the step from level 3 to level 4 showed that the area is increased, it was insignificant.

3.3   Actual Bridges Investigation

According to the previous sub-section, the assessment parameter tends to decrease concerning material deterioration. To validate the variation rule of the set of loss factor values, we investigate the vibration signal received from three different types of bridge spans: Phu My bridge, Saigon bridge, and Cong Dap Rach Chiec bridge. Traffic levels, as well as environmental factors of the three bridges, are considered to be the same. The bridge is a complex structure, so this technique is applied for bridge span. The acceleration signal directly measured from span vibration under moving load is the input of the proposed approach. Figures 5, 6 and 7 show the power spectrum from signal processing and loss factor values of a span of three bridges.

By processing and setting up the set of loss factor values, the transformation of this set can be observed. However, this processing is not transparent enough in terms of images to determine the change rule. Loss factor values are determined based on two main characteristics: amplitude and frequency. Because amplitude characteristic has many inflection points in the resonance region, leading to changes in the distribution of these values.

The Phu My bridge was built in 2005 and opened in 2009 with the prestressed concrete girder structure. Next, the Saigon bridge was significantly upgraded in 2000 with a prestressed concrete girder structure. Lastly, the Cong Dap Rach Chiec bridge was built and opened in 1990 with a precast concrete girder structure. Based on the operating time, structure type of these bridges, and mechanical parameters at present, the structural conditions of the Phu My bridge, the Saigon bridge, and the Cong Dap Rach Chiec bridge are classified as good, medium, and weak, respectively. The proposed procedure is applied to one span of these bridges and derived corresponding feature surface as shown in Fig. 8. And the trend of difference between the three bridges is shown in Fig. 9.
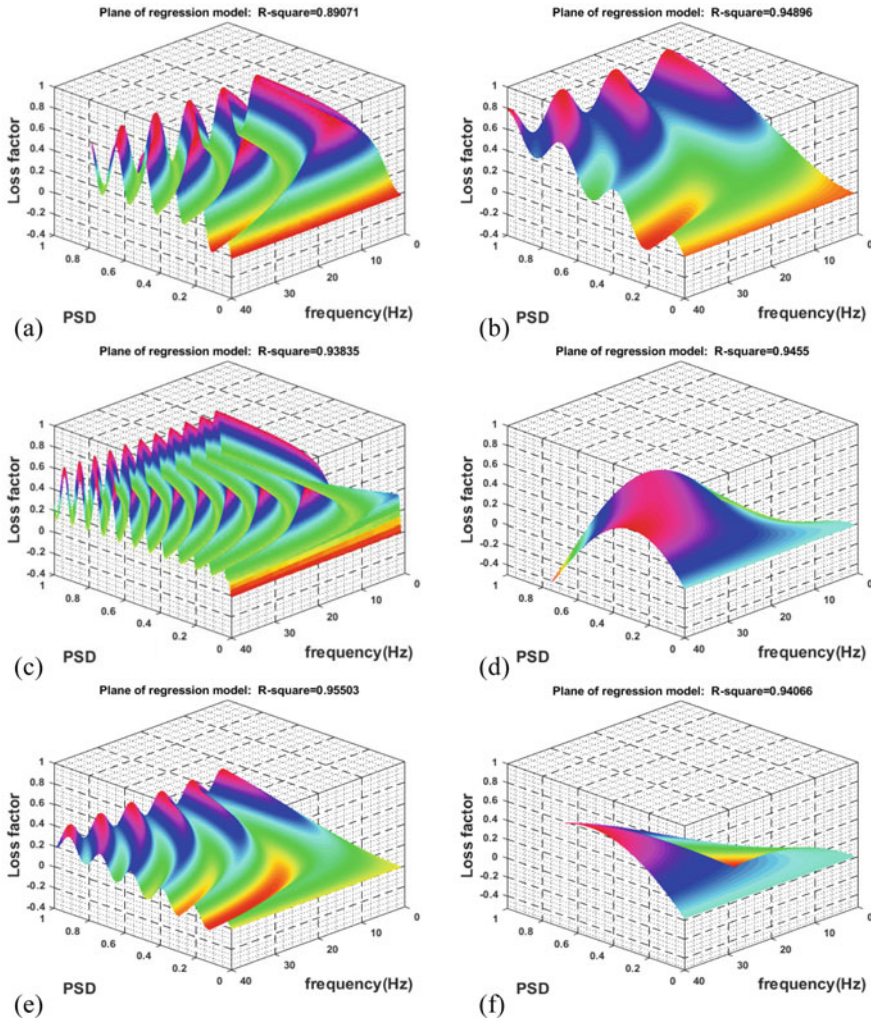
Fig. 3 Feature surfaces of deterioration scenarios: **a** level 0, **b** level 1, **c** level 2, **d** level 3, **e** level 4, **f** level 5

The result of the proposed method shows a high degree of conformity with reality. The area values of feature surfaces tend to decrease concerning good to weak structural conditions progressively.
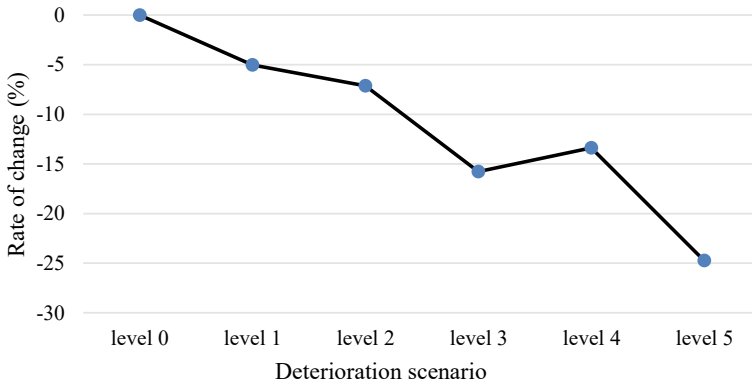
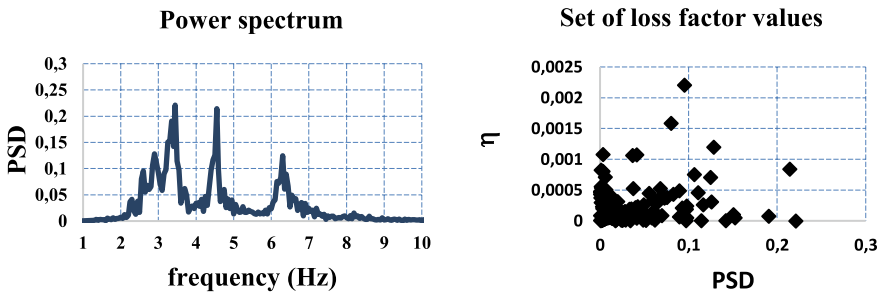**Fig. 4** Change of the area of feature surface with respect to material deterioration

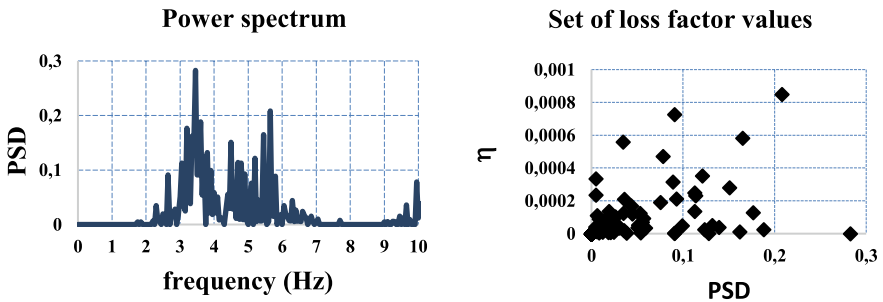**Fig. 5** Power spectrum and loss factor values of Phu My bridge

Fig. 6 Power spectrum and loss factor values of Saigon bridge

Power spectrum   **Set of loss factor values**
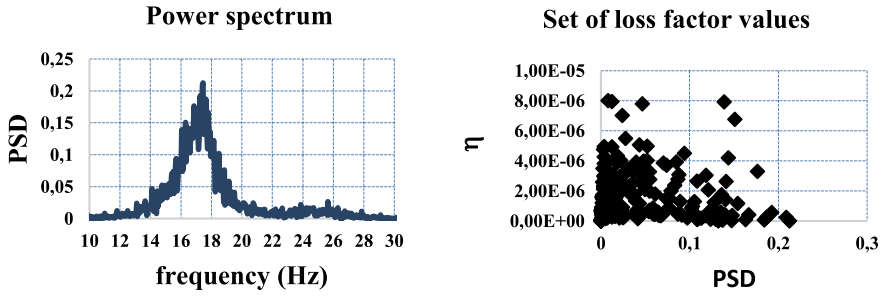
Fig. 7 Power spectrum and loss factor values of Cong Dap Rach Chiec bridge
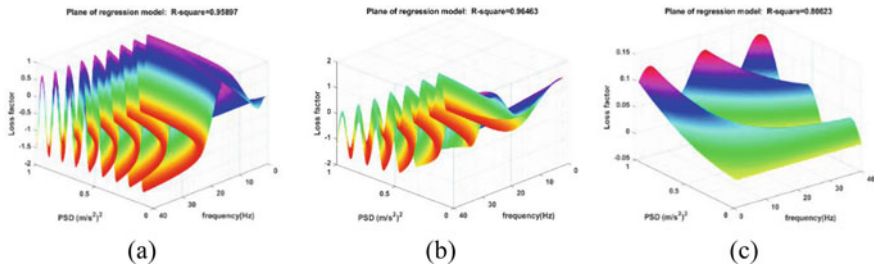
Fig. 8 Feature surface of bridges: **a** Phu My, **b** Saigon, **c** Cong Dap Rach Chiec
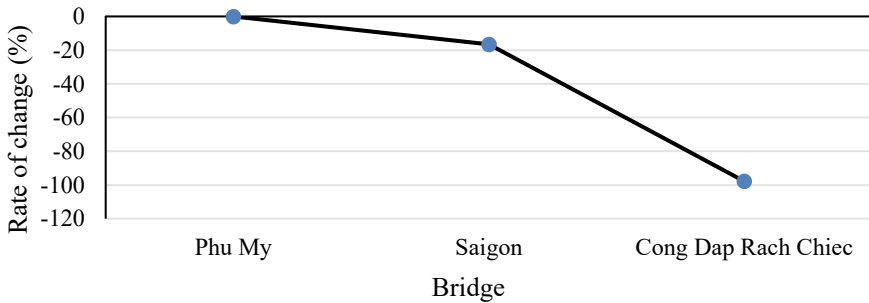
Fig. 9 Trend of difference between the three bridges

4 Conclusion

This article proposes a regression method for structural condition assessment with high practical applicability. The area of the feature surface from the regression is a suitable parameter to assess the mechanical conditions of the material.

With a view to assessing the mechanical properties of the material in bridge span, the results observed that the area of surface representing the loss factor distribution decreases when the material has deteriorated.

The proposed method is easy to apply with the purely automatic procedure. In addition, the used signals are vibration signals which are easily measured from actual bridges.

Eventually, the efficiency and economy of using the real random load of the structure itself as the excitation source are high.

The proposed method will be further developed to produce an adequate procedure and improve the accuracy of bridge health monitoring.

References

1. Friswell MI, Penny JE (2002) Crack modeling for structural health monitoring. Struct Health Monit 1(2):139–148
2. Lee Y-S, Chung M-J (2001) A study on crack detection using eigen frequency test data. Comput Struct 77(3):327–342
3. Christides S, Barr A (1984) One dimensional theory of cracked bernoulli-euler beams. Int J Mech Sci 26(11–12):639–648
4. Ostachowicz W, Krawczuk M (1991) Analysis of the effect of cracks on the natural frequencies of a cantilever beam. J Sound Vib 150(2):191–201
5. Wahab MA, De Roeck G, Peeters B (1999) Parameterization of damage in reinforced concrete structures using model updating. J Sound Vib 228(4):717–730
6. Law S, Zhu X (2004) Dynamic behavior of damaged concrete bridge structures under moving vehicular loads. Eng Struct 26(9):1279–1293
7. Ariaei A, Ziaei-Rad S, Ghayour M (2010) Repair of a cracked Timoshenko beam subjected to a moving mass using piezoelectric patches. Int J Mech Sci 52(8):1074–1091
8. Arangio S, Bontempi F (2015) Structural health monitoring of a cable-stayed bridge with Bayesian neural networks. Struct Infrastruct Eng 11(4):575–587
9. Li Y, Zhao W, Li Q, Wang T, Wang G (2019) In-situ monitoring and diagnosing for fused filament fabrication process based on vibration sensors. Sensors 19(11):2589
10. Spanos NA, Sakellariou JS, Fassois SD (2020) Vibration-response-only statistical time series structural health monitoring methods: a comprehensive assessment via a scale jacket structure. Struct Health Monit 19(3):736–750
11. Nguyen TQ, Doan HC, Vuong LC, Nguyen-Xuan H, Ngo NK (2020) Fretting fatigue damage nucleation and propagation lifetime using a central point movement of power spectral density. Shock Vib 2020:4985134
12. Bayat1a M, Ahmadi HR, Mahdavi N (2019) Application of power spectral density function for damage diagnosis of bridge piers. Struct Eng Mech 71(1):57–63
13. Ngo-Kieu N, Nguyen-Da T, Pham-Bao T, Nguyen-Nhat T, Nguyen-Xuan H (2021) Deep learning-based signal processing for evaluating energy dispersal in bridge structures. J Zhejiang Univ-Sci A 22(8):672–680
14. Nguyen TD, Nguyen TQ, Nhat TN, Nguyen-Xuan H, Ngo NK (2020) A novel approach based on viscoelastic parameters for bridge health monitoring: a case study of Saigon bridge in Ho Chi Minh City-Vietnam. Mech Syst Signal Process 141:106728
15. Nguyen TD, Nguyen HQ, Pham TB, Ngo NK (2021) A novel proposal in using viscoelastic model for bridge condition assessment. In: Structural health monitoring and engineering structures. Springer, pp 331–341

16. Ren W-X, Zong Z-H (2004) Output-only modal parameter identification of civil engineering structures. Struct Eng Mech 17(3–4):429–444
17. Hsieh KH, Halling MW, Barr PJ (2006) Overview of vibrational structural health monitoring with representative case studies. J Bridg Eng 11(6):707–715

An Optical Embedded MEMS-Based System for Real-Time Structural Health Monitoring

Abdelhakim Latoui and Mohamed El Hossine Daachi

1 Introduction

Structural health monitoring (SHM) is a very multidisciplinary research area, which involves many different branches of engineering such as computer science, seismology and civil engineering, in order to enhance reliability and performance of such systems [15, 21]. The aim of SHM for civil structures is not only to identify possible existing damages but also to evaluate their performance under operational conditions or under some particular environmental issues such as landslides or earthquakes. Furthermore, maintaining safe and reliable civil infrastructures for daily use is important to the well-being of all of us [5, 25]. Indeed, monitoring the health of a structure provides the ability to anticipate structural failures to protect both the health and safety of buildings occupants, which is a major concern in buildings especially those of public services. However, many factors [19] can affect the state of the health of a structure. For example, an empirical study in east China [13] has shown that in fact about 30 impact factors can affect healthy building. These factors are, for instance, humidity, heavy loads on the structures, mistakes in the construction, chemical reactions, environmental impacts like wind loads, temperature changes and natural hazards like landslides and earthquakes [3]. Thus, obtaining information from such systems in real time could be useful [20], for example, in rapid evaluation of conditions of damaged structures after a landslide or an earthquake [9].

A. Latoui (✉)
Department of Electronics, Faculty of Sciences and Technology, Mohamed El Bachir El Ibrahimi University, 34030 Bordj Bou Arreridj, Algeria
e-mail: a.latoui@univ-bba.dz

M. E. H. Daachi
ETA Laboratory, Department of Electronics, Faculty of Sciences and Technology, Mohamed El Bachir El Ibrahimi University, 34030 Bordj Bou Arreridj, Algeria
e-mail: mohamed.daachi@univ-bba.dz

Therefore, a large number of methods and techniques for SHM have been proposed, in order to assess the health state of a civil engineering construction [4, 6, 16, 20]. Roughly speaking, the monitoring system is primarily responsible for collecting data from multiple sensors installed on structures in order to process and extract useful information about current state of the structure [2]. However, wireless sensors and sensor networks are emerging as alternative sensing paradigms for traditional tethered monitoring systems [12]. Indeed, among the many possible applications of wireless sensor networks, SHM is considered as a typical area of such applications [24]. Furthermore, smart sensors offer new opportunities for SHM due to their, among others, wireless communication capabilities. Indeed, they reduce drastically the costs associated with the installation and maintenance of SHM systems, since they do not require any power or communication cable [17]. In fact, there are many possibilities for embedding intelligence in a hardware design. A digital signal processor (DSP) is one concrete example among others choices, where programs can be embedded in it [16]. Thus, the data gathered from smart sensors can be saved locally, and desired computations are then performed in order to make decisions and to send results quickly, etc. On the other hand, recently there has been a growing interest in using micro-electromechanical systems (MEMS) accelerometers sensors in SHM [22].

In the present paper, a new SHM system based on these types of sensors is proposed. In addition to the smart sensor, an optical built-in logic block observation (OBILBO) [10] is considered in the DSP architecture in order to carry out data responses during its normal operating, to be sent to remote system and without affecting its normal functioning. In others words, the OBILBO register, configured in its parallel load mode, permits to send, remotely to a distant system, optical beams corresponding to its outputs logic states. Hence, with the use of simple PIN diodes and after an analog/digital conversion, the received data can be compared to those pre-stored of a reference model, in order to perform an online anomaly detection to decide on the anomaly in the SHM data.

The remainder of the paper is organized as follows. In Sect. 2, the principle of functioning of the proposed SHM system is described. In Sect. 3, a motivating example is presented, whereas some simulation results are discussed in Sect. 4. Section 5 concludes the paper.

2 Functional Principles

The data acquisition portion of the SHM process involves hardware as well as software aspects: selecting the excitation methods, the sensor types, number and locations and the data acquisition/storage/transmittal hardware [6]. In fact, contrary to a wireless system, a large-scale wired data acquisition system requires, usually, more time to be installed, and it is more expensive [18, 23]. Indeed, a wireless system has many advantages: flexibility of deployment with low costs, ease of maintenance, etc. We recall that the goal of SHM research is to develop a monitoring methodology that is capable of detecting and identifying, with minimal human intervention,

various damage types during the service life of the structure [7]. In the following, we describe the new proposed SHM system that relies on inexpensive sensors which allows data acquisition. These latter are then transmitted online to a distant system. The basic idea developed in this work consists of using low-cost devices such as DSP and accelerometer and exploiting the optical beams produced by an optical BILBO, integrated in the DSP structure, to carry out data response concurrently. Thus, the optical beams are then transmitted to remote system for comparison with pre-stored ones. These data can be then analyzed in real time to perform anomaly detection, which is an important task in SHM applications. Indeed, this task allows detecting and locating anomalies. Thus, any abnormal structural behaviors or sensor faults can be easily identified [8]. Furthermore, thanks to the OBILBO integrate in its structure, the integrity of the DSP can be also checked without affecting its normal functioning.

The overall SHM system proposed is illustrated in Fig. 1, which can be divided into two main parts: the first part (Emitter) that is the set of the sensors and the digital signal processing unit DSP and the second part (Receiver) which consists
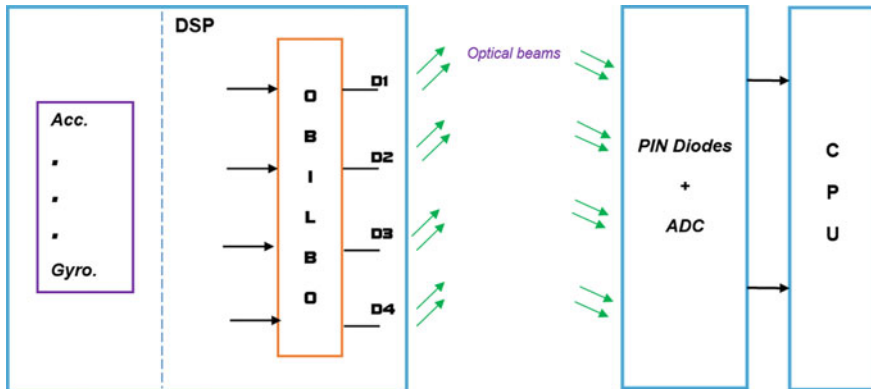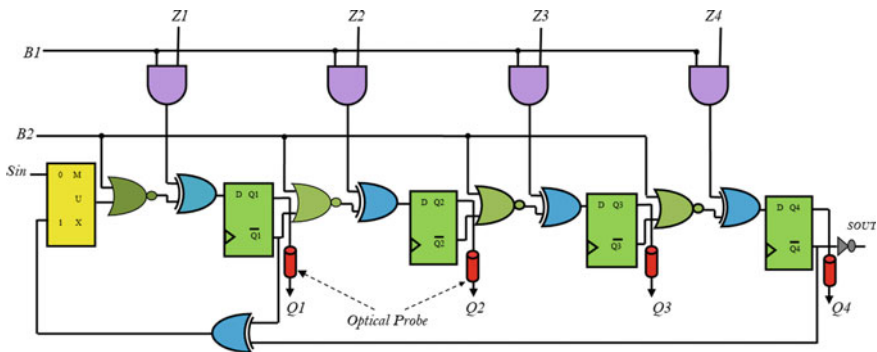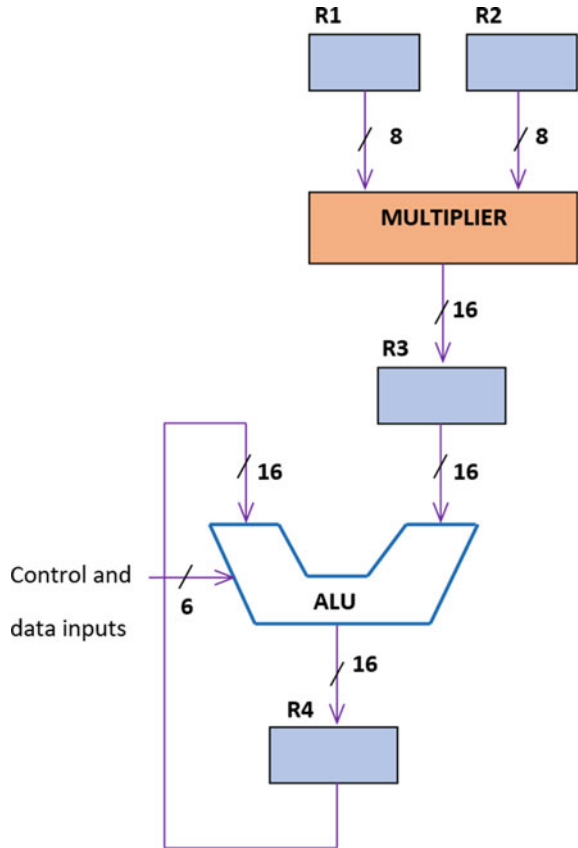

Fig. 1 Proposed SHM system

Fig. 2 Logic diagram of OBILBO [10]

Fig. 3 Portion of the
TMS32010 signal processing
chip [1]

of remote system that receives data from the emitter. The set of sensors consists
of accelerometers and gyroscopes which can be now easily integrated on chip and
widely used in many applications. For the sake of argument, accelerometer integrated
in modern smartphones is used for monitoring transient displacements when such
devices are attached to a structure [14]. In our case, these sensors are used in the
same manner. The sampled data from these sensors are then passed through the DSP
for local treatment such as filtering noise, fusion of the different data collected from
the sensors and managing different tasks in order to reduce power consumption of
the sensors. It is worth noting that this first part is now equipped by optical emitter
(OE) that acts as snapshot of the output's responses of the DSP. In fact, the OE is the
OBILBO, integrated in the DSP structure, which is briefly described here and more
details can be found in [10].

An OBILBO register is simply a BILBO [1] where optical probes (OP) are inte-
grated in its architecture [10]. Indeed, the OBILBO, lighted up by a laser source,
will reflect optical signals corresponding to the values present on its outputs. The
different probes inserted on different electrical lines of the outputs of the OBILBO
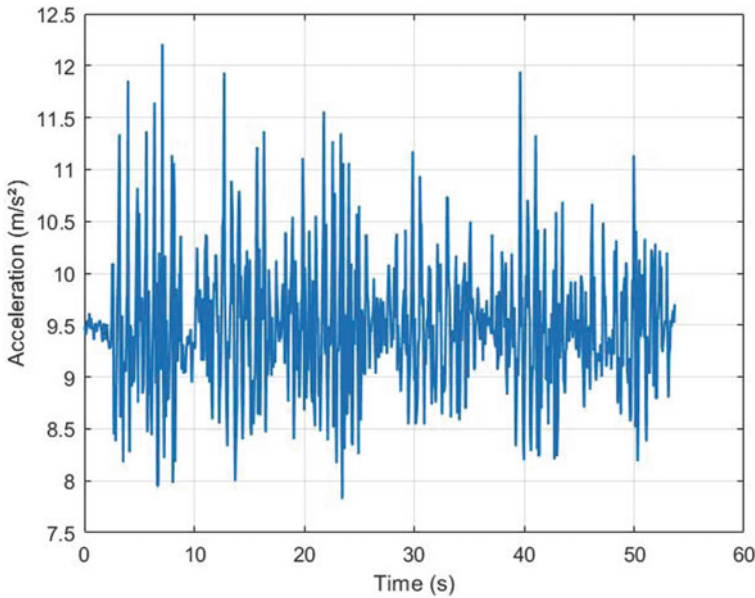
Fig. 4 Acceleration (Z-axis) collected after shaking periodically a smartphone

(see Fig. 2), according to the voltage of the line, will reflect a low or a high optical intensity. The reflected beams will be deflected and collimated on optical detector (PIN diodes) of the receiver (part two) distant from the emitter. Hence, the delivered signals by the PIN diodes undergo an analog/digital conversion, to be compared with a pre-stored reference data. Thus, the CPU generates the corresponding graphs for visualization and activates alarm if certain thresholds are exceeded. The next section presents an example modeled with the VHDL-AMS tool.

3   An Example

Environmental and operating condition variability presents significant challenges to the building monitoring application. Hence, the need for online monitoring should be reinforced to avoid possible hazards due to the damage of a building or bridges. Furthermore, detecting damage at remote system can save many human lives. To reach this goal, several techniques have been proposed in the literature (see for example: [4, 6, 11, 14, 16]), where the main idea is how to monitor structural health in a continuous basis, diagnose any structural problem early and deal with it appropriately while keeping the cost of the implementation of such schemes in reasonable limits. So, we will prove, through the following example, that our scheme is more efficient in terms of error latency, and it can be easily deployed anywhere, according to our
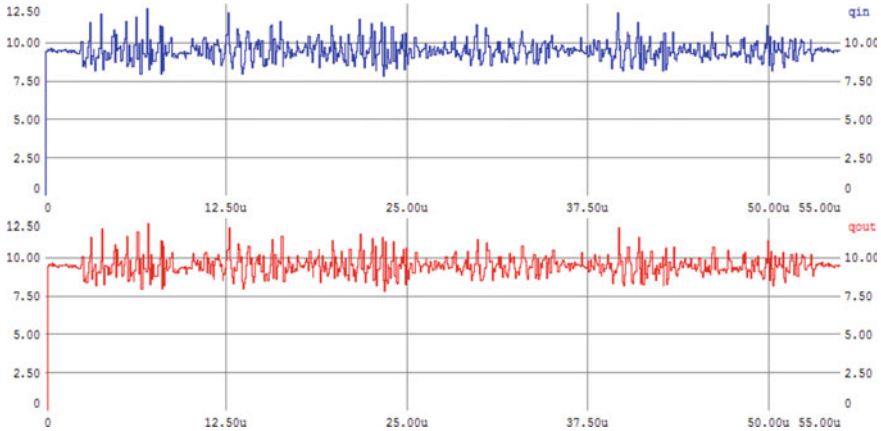
Fig. 5 Response (q_{out}) of the proposed SHM system to the input (q_{in})

specific need, without permanent installation in infrastructure systems. To do so, let us focus now on the famous of the TMS32010 signal processing (see Fig. 3; [1]), where some registers (R1, R2, R3 and R4) are considered now as BILBO ones, to allow testing ALU and the multiplier. By assuming the BILBO registers are now OBILBO and according to SHM system depicted in Fig. 1, we will show that, for example, the data collected from the accelerometer can be treated by the CPU and visualized in real time. In order to simulate this model, a smartphone (Galaxy S3) is used to collect data from the accelerometer integrated within it. Figure 4 shows the response of the accelerometer (Z-axis) after shaking the smartphone periodically. The VHDL-AMS model of the SHM system developed in this work is not presented here. We should note that the collected data from the accelerometer are injected at the inputs of the DSP. Thus, the corresponding response data are collected from the outputs of the OBILBO and are transmitted in real time to the receiver. For the sake of simplicity, no treatment (filtering) of the data has realized here by the DSP.

4 Simulation Results

Simulation results are reported in the following figures. Figure 5 represents the corresponding response "q_{out}", at the remote system (receiver), to the input data "q_{in}" (data delivered by the accelerometer). The digital signals d_1, d_2, d_3 and d_4, corresponding to the quantity "q_{out}", are represented in Fig. 6, whereas their corresponding optical beams, transmitted by the OBILBO ql_1, ql_2, ql_3 and ql_4 respectively, are represented in Figs. 7 and 8. We can see from these figures that the collected data from the accelerometer are transmitted by the OBILBO in real time and without any delay. Hence, a comparison of these data to the pre-stored ones of reference model can be done in real time. This enables us to perform anomaly detection and thus to be
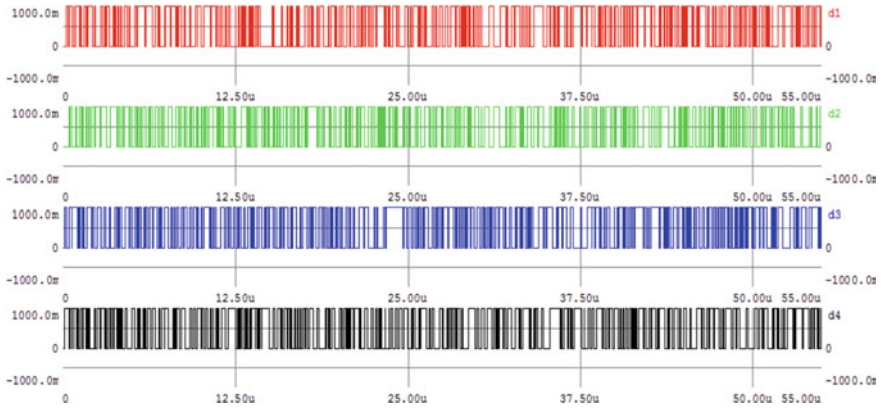
Fig. 6 Digital outputs response of the OBILBO
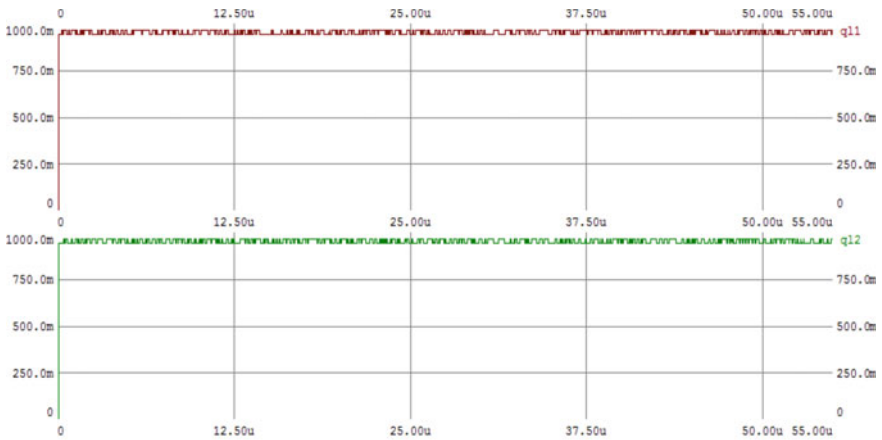
Fig. 7 Optical beams transmitted (lines D1 and D2)

warned whether the vibration response is of damaged or healthy structure, in order to take the appropriate actions.

Moreover, the OBILBO can be configured in built-in self-test (BIST) mode which allows testing the DSP itself to diagnose faults and checking its integrity. This is highly appreciated for embedded systems which are not necessarily designed with high performance since they are low-cost products and integrates hundreds of millions of transistors in their structure. Furthermore, the OBILBO produces an optical signature which can be analyzed at remote system. We note that the signature is a data compression technique that allows reducing the amount of the stored data. It is worth noting that to carry out an online testing, for example, of the multiplier (Fig. 3), the transmitted optical beams corresponding to the outputs of R1 and R2 will be used as inputs for the reference model of the multiplier at the receiver, which delivers a
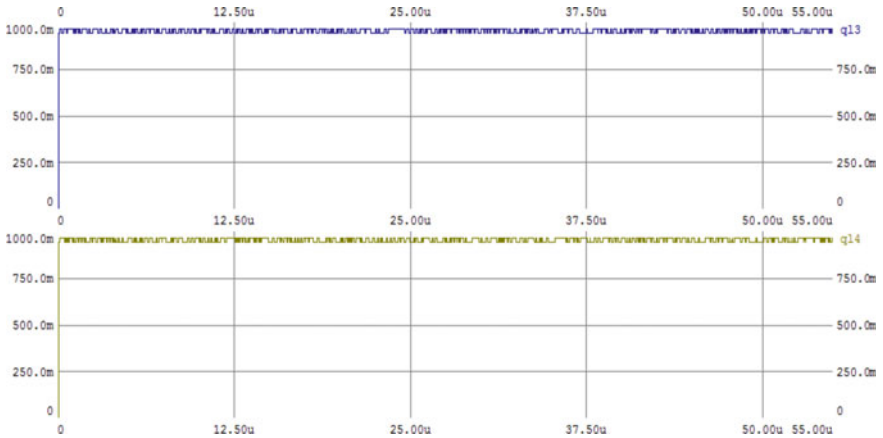
Fig. 8 Optical beams transmitted (lines D3 and D4)

corresponding response. This latter is compared to the response of the multiplier via the transmitted signals by the R3 register. Hence, thanks to the optical probes considered, if an error occurs in the multiplier, it will be detected in real time and without affecting its normal functioning.

5 Conclusion

In this work, a new remote online monitoring system of building and structure health based on optical embedded MEMS sensor is proposed. Our system is useful in remotely monitoring buildings to detect vibrations due, for example, to an earthquake. The proposed system is in fact composed mainly of low-cost embedded devices: a MEMS accelerometer sensor and a digital signal processing unit where its built-in logic block observation (BILBO) registers integrate optical probes, thus forming optical BILBO registers (OBILBOs). Therefore, each formed OBILBO register, configured in its parallel load mode, permits to send, remotely to a distant system, optical beams corresponding to the logic states of its outputs. Hence, the received data can be compared to those of a reference model, in order to perform an online anomaly detection to judge whether there is anomaly in the SHM data. All this enables us to assess in real time the structural health conditions in order to ensure safe exploitation of, for example, public or historical building. Simulation results have been shown that detecting vibrations in a building can be accomplished by our SHM system in real-time way and obviously without any delay thanks to the optical sensors integrated in the BILBO registers. In addition, the proposed SHM system not only requires a permanent installation in infrastructure systems but it can also be deployed anywhere according to our specific need.

References

1. Abramovici M, Breuer MA, Friedman AD (1994) Digital systems testing revised. Wiley, New York
2. Arcadius Tokognon C, Gao B, Tian GY, Yan Y (2017) Structural health monitoring framework based on internet of things: a survey. IEEE Internet Things J 4(3):619–635. https://doi.org/10.1109/JIOT.2017.2664072
3. Brownjohn J (2006) Structural health monitoring of civil infrastructure. Philos Trans Royal Soc Math Phys Eng Sci 365(1851):589–622 https://doi.org/10.1098/rsta.2006.1925
4. Chang FK, Markmiller JF, Yang J, Kim Y (2011) Structural health monitoring. System health management: with aerospace applications, pp 419–428
5. Chang PC, Flatau A, Liu S (2003) Health monitoring of civil infrastructure. Struct Health Monit 2(3):257–267. https://doi.org/10.1177/1475921703036169
6. Farrar CR, Worden K (2006) An introduction to structural health monitoring. Philos Trans Roy Soc A Math Phys Eng Sci 365(1851):303–315. https://doi.org/10.1098/rsta.2006.1928
7. Giurgiutiu V, Santoni-Bottai G (2011) Structural health monitoring of composite structures with piezoelectric-wafer active sensors. AIAA J 49(3):565–581
8. Huang HB, Yi TH, Li HN (2020) Anomaly identification of structural health monitoring data using dynamic independent component analysis. J Comput Civ Eng 34(5):04020025. https://doi.org/10.1061/(asce)cp.1943-5487.0000905
9. Kanwar VS, Kwatra N, Aggarwal P, Gambir M (2008) Health monitoring of RCC building model experimentally and its analytical validation. Eng Comput 25(7):677–693. https://doi.org/10.1108/02644400810899960
10. Latoui A, Djahli F (2013) An optical BILBO for online testing of embedded systems. IEEE Des Test 30(3):34–48. https://doi.org/10.1109/mdt.2012.2204398
11. Lopez-Higuera JM, Cobo LR, Incera AQ, Cobo A (2011) Fiber optic sensors in structural health monitoring. J Lightw Technol 29(4):587–608. https://doi.org/10.1109/jlt.2011.2106479
12. Lynch JP, Loh KJ (2006) A summary review of wireless sensors and sensor networks for structural health monitoring. Shock Vib Dig 38(2):91–130
13. Mao P, Qi J, Tan Y, Li J (2017) An examination of factors affecting healthy building: an empirical study in east China. J Clean Product 162:1266–1274. https://doi.org/10.1016/j.jclepro.2017.06.165
14. Morgenthal G, Höpfner H (2012) The application of smartphones to measuring transient structural displacements. J Civ Struct Health Monit 2(3–4):149–161
15. Muttillo M, Stornelli V, Alaggio R, Paolucci R, Battista LD, de Rubeis T, Ferri G (2020) Structural health monitoring: an IoT sensor system for structural damage indicator evaluation. Sensors 20(17):4908. https://doi.org/10.3390/s20174908
16. Nagayama T, Spencer BF Jr (2007) Structural health monitoring using smart sensors. Technical report. Newmark Structural Engineering Laboratory. University of Illinois at Urbana
17. Noel AB, Abdaoui A, Elfouly T, Ahmed MH, Badawy A, Shehata MS (2017) Structural health monitoring using wireless sensor networks: A comprehensive survey. IEEE Commun Surv Tutor 19(3):1403–1423. https://doi.org/10.1109/comst.2017.2691551
18. Paek J, Chintalapudi K, Govindan R, Caffrey J, Masri S (2005) A wireless sensor network for structural health monitoring: performance and experience. In: The second IEEE workshop on embedded networked sensors, 2005. EmNetS-II. IEEE, pp 1–9
19. Pentaris F, Makris J, Stonham J, Vallianatos F (2012) Principles in wireless building health monitoring systems. In: EGU general assembly conference abstracts, p 13239
20. Rainieri C, Dey A, Laorenza C, Fabbrocino G, de Magistris FS (2011) Ambient vibration based modal identification of a flexible retaining wall. In: Civil engineering topics, vol 4. Springer, New York, pp 349–356. https://doi.org/10.1007/978-1-4419-9316-8_33
21. Rainieri C, Fabbrocino G, Cosenza E (2010) Structural health monitoring through automated OMA techniques in operation and during seismic events. In: The 14th European conference on earthquake engineering-14th ECEE, pp 5315–5322

22. Sabato A, Niezrecki C, Fortino G (2017) Wireless MEMS-based accelerometer sensor boards for structural vibration monitoring: a review. IEEE Sens J 17(2):226–235. https://doi.org/10.1109/jsen.2016.2630008

23. Szewczyk R, Mainwaring A, Polastre J, Anderson J, Culler D (2004) An analysis of a large scale habitat monitoring application. In: Proceedings of the 2nd international conference on embedded networked sensor systems, pp 214–226

24. Wang P, Yan Y, Tian GY, Bouzid O, Ding Z (2012) Investigation of wireless sensor networks for structural health monitoring. J Sens 2012:1–7. https://doi.org/10.1155/2012/156329

25. Zonzini F, Aguzzi C, Gigli L, Sciullo L, Testoni N, Marchi LD, Felice MD, Cinotti TS, Mennuti C, Marzani A (2020) Structural health monitoring and prognostic of industrial plants and civil structures: a sensor to cloud architecture. IEEE Instrum Meas Mag 23(9):21–27. https://doi.org/10.1109/mim.2020.9289069

Friction Damper Performance on Stay Cable Bridges in Vietnam, Solution Prediction, and In-Situ Testing

Nguyen Phuong Duy and Tran Duc Lan

1   Introduction

Stay cable structures, with the architectural and structural advantages, have become a widespread solution for medium to long-span bridges over the past several decades. In parallel, with the structural slenderness and excitation sensibility, the serviceability problems with large amplitude vibrations of cables stay due to environmental conditions have been observed. The term "rain/wind vibration" [1] for example was familiar to specify the large amplitude vibration occurred under a certain condition of rain and wind combination. On another hand, large amplitude vibrations at high wind speeds have also been reported as possible in the literature [2] without specific rain conditions and known as "galloping of dry inclined cables". An amount of theoretical and experimental research on this subject had been conducted by worldwide researchers and stay cable specialist contractors. With this understanding, mitigation measures such as various cable surface modifications as well as external/internal dampers and/or cable cross-ties have been proposed and tested with the development of stay cable technology. Those technics are aimed to disrupt the water rivulet interaction with the wind flow considering as the root cause of the rain/wind vibration or to dissipate the cable vibrations energy by adding damping to the cables' stay.

Since the inauguration in 2000 of My Thuan bridge, the first stay cable bridge built in the territory of Vietnam, large amplitude vibration mitigation measures were adopted in several types such as hydraulic external dampers in My Thuan bridge,

N. P. Duy (✉)
University of Transport and Communications, No. 3 Cau Giay, Hanoi, Vietnam
e-mail: npduy@utc.edu.vn

T. D. Lan
VSL Vietnam Ltd., 44, Le Ngoc Han, Hai Ba Trung District, Hanoi, Vietnam

hollow cable surface modification in Can Tho bridge and Nhat Tan bridge, double-helix cable surface modification and friction dampers in Tran Thi Ly and Vam Cong bridges …

The lack of standardized criteria and local design guidelines have made the consistent practical design and application of the mitigation measures difficult. Furthermore, the cable damping characteristics depend on many parameters of cable system nature but also environmental conditions and the accurate value is difficult to predict. Testing field is generally considered as the most effective solution to evaluate and/or verifying the damping characteristics. However, not much local research, field-testing report, or publication on those issues have been recorded.

This paper presents an assessment of the large amplitude vibration possibility on two stay cable bridges recently completed in Vietnam in considering the vibration mitigation measures using friction dampers system. The results were then confronting with the field damper test to confirm the theoretical prediction and evaluate the performance of the friction damper system.

2 Stay Cables Vibration

2.1 Direct Excitations

Based on the existing world-wise research data, wake galloping, galloping of dry inclined cable, and rain/wind combination excitations mechanisms appear to be the biggest concerns for vibration mitigation.

Wake galloping is caused by variations in drag and cross-wind forces leading to elliptical movement of the cables in the wake of other elements (towers or other cables). The phenomenon characterizes by large amplitude oscillations at high wind speeds. That could theoretically be the cause of possible fatigue on the stay cable bridges. Even if wake galloping is generally not a major design concern for normal cable arrangement conditions, it's recommended to pay some attention in the unusual cases. The cable shall be stable up to a higher wind velocity by increasing the Scruton number or natural frequency (Eq. 1).

Galloping of Dry Inclined Cables defines the phenomenon of possible large amplitude vibrations of single cable-stayed occur at high wind speeds which is not normal to the cable axis. For inclined cable, wind acts on the cable cross-section of elliptical form defined by the cable inclination. When the cable structural damping is very low, galloping instability is then possible.

Rain/Wind induced vibrations have been observed worldwide on many stay cable bridges and researched in detail. The phenomenon specifying as cable vibrations with high amplitude at low frequencies causes by a combination of rain and moderate wind speeds. Experimental researches [1, 3] have shown that raining water rivulets running in the upper and lower surface of the cable cross-section under perturbed

wind condition is the essential component of the phenomenon. Under that condition, the effective shape of the cable is changed when the cable oscillates causing cyclic changes in the aerodynamic forces leading to the oscillation.

2.2 Design Criteria

Regarding the wake galloping effect, an approximate equation for the minimum wind velocity U_{crit} based on an important parameter, the Scruton number (S_c), has been proposed by Irwin [4] and Cooper [5] and adopted by PTI [6] as a critical wind speed above which, instability due to wake galloping can be expected.

$$U_{\text{crit}} = c\, f D \sqrt{S_c} \tag{1}$$

In the equation, c is a constant depending on the clear spacing between cable ($c = 25$ for closely spaced and $c = 80$ for normally spaced). D and f are the cable diameter and natural frequency, respectively.

On another hand, inclined dry cable galloping is generally not a common phenomenon in completed bridges during service. Saito [2] suggested however an instability criterion based on a series of wind tunnel experimental. The equation was given in a different form from the Eq. (1) with $c = 40$.

$$(U/f D)_{\text{crit}} = 40\sqrt{S_c} \tag{2}$$

Rain-wind oscillation excitation is suggested by PTI to be reduced to a harmless level using a criteria for Scruton number based on the Saito's rig test data [2] and the wind tunnel test performed by other researchers [1, 5].

$$S_c = \frac{m\xi}{\rho D^2} \geq 10 \tag{3}$$

Based on limited tests on cable with double-helix surface modification, Larose et al. [7] have suggested that $S_c > 5$ may be acceptable. PTI also suggested that a value of 5 could be proposed in lieu of the higher limit of 10 for special helix or dimpled stay pipes with special testing to verify this value [6]. This criterion can be used to specify the amount of damping that must be added to the cable to mitigate rain/wind vibrations.

FIB (International Federation for Structural Concrete) on another hand suggested that an effective damping of $\delta = 3$–4% has often been found to be sufficient to control wind-/rain-induced stay cable vibrations in practice [8]. Those values are quite in line with the recommendation by CIP (French International Commission on Prestressing) for a logarithmic decrement (damping) of the cable greater than 3% for cable of more than 80 m in length to avoid rain and wind instability [9].

3 Friction Damper

3.1 *Energy Dissipation and the Threshold Amplitude*

The principle of the friction damper system is to dissipate the maximum of mechanical energy through the interface contact between the friction elements. The key point of system design is to keep the threshold vibration amplitude below a specific value considering as structural and user comfort acceptable. Figure 1 shows the on-site assembling of friction damper in Vam Cong bridge (Dong Thap, Vietnam).

The mechanical energy dissipation is mobilized in the relative movement at the prestressed contact between two specific friction patterns. It consists of a first pattern connected to the moving cable and another one connected to the support assuming to be fixed. As consequence, the movements are damped to a certain threshold amplitude of vibration.

3.2 *Damping Behavior*

Figure 2 presents a typical relationship of vibration amplitude dependent on damping ratio (ξ) provided by friction damper. It shows that at a level of less than a hundred millimeters, the cable vibration amplitude cannot induce a deviation force sufficiently important to overcome the friction force and make the cable move at the external damper installed location. Once the threshold vibration amplitude is exceeded, the friction force is activated and provides sufficient damping to the cable to dissipate external excitation energy. The cable movements are quickly stabilized to a level of amplitude defined by the specific demanded damping ratio of 0.5% (see Fig. 2).

The damper remains activated after the excitation stops until the vibration amplitude decreases to a certain level lower than the initial threshold [10].
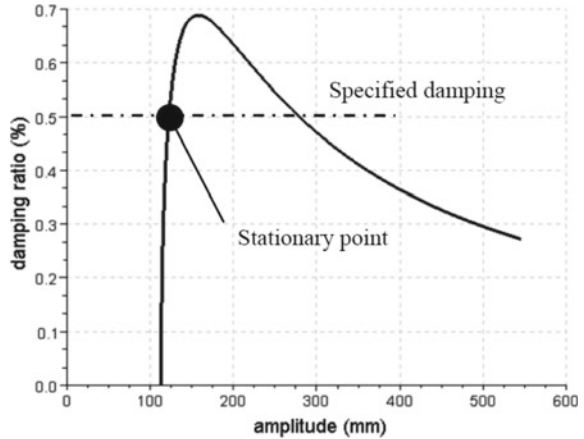
4   Field-Testing Performance

4.1   Field-Testing

We present in the following the damping test results performed on two stay cable bridges recently built in Vietnam. They are Tran Thi Ly bridge (2015) and Vam Cong bridge (2020). The testing campaigns were performed in post-evaluation of the wind-induced vibration assessment to confirm the theoretical damping values and the performance of the mitigation friction dampers solution.

The damping of the cable and the friction damper performance were measured during the assumed free response of the stay cable to an impulse excitation. The testing procedure had been repeated to acquire the vibration data for three first mode of cable vibrations.

4.2   Friction Damper Solution

For the studied stay cable bridges, the excessed wind vibration assessment is evaluated based on the criteria specified by PTI [6] and FIB [8] with regard to the Scruton Number (Eq. 3), the critical wind velocity (Eq. 2), and the intrinsic damping.

Figure 4 presents the relationship between the critical wind velocities and the cable length for the interested bridges. If considering a very common design wind speed of 20 m/s, we can observe that additional damping is required for nearly all the cables to eliminate completely the risk of vortex vibration on all the three stay cable bridges. It should be noted however that the approach is considering as very conservative in practice without considering the aerodynamic damping which increases with wind speed [9].

Even the determination of the exact intrinsic damping for cable-stayed is very difficult, in practice, it is common to consider that the value is in proportional with the cable-free length (L):

$$\delta_{\text{int}} = 2\pi(0.24 - 6 \times 10^{-4}L) \tag{4}$$

The estimation of intrinsic damping however needs to be confirmed by an adequate testing campaign as per presented in the following. Figure 5 shows the relationship between the evaluated value of Scruton Number (S_c) and the first mode of cable natural frequency on the bridges. We can notice that most of the estimated values of (S_c) are even lower than 3 and all of them are lower than the critical value specified by PTI [6].

In the three studied bridges, in combining with double helical surface treatment for cable pipe the external friction dampers have been proposed to mitigate the wind vibration excitation on the in-risk cables stayed.

4.3 Field-Testing and Results

Due to the important amount of time-consuming, the field test was performed only on selected cables representatives for each bridge. Table 1 presents the characteristic of testing cables performed on Tran Thi Ly (TTL) bridge and Vam Cong (VC) bridge, respectively.

The objectives of the tests were to confirm the intrinsic damper evaluated values and the need for additional external damping but also to prove the performance of the proposed friction damper solution.

It's to be highlighted that the measurement data was acceptable if the environment conditions, the wind and dynamic loads excitation on the deck level were controllable and then their effects could be removed from the measured data. The portable accelerometers were used for the data collection which were installed on the cable

Table 1 Testing cables characteristics

Cable No./Bridge name	Cable length (m)	Num. of strands	Cable incl. (deg.)	Cable outer dia (mm)	Cable mass (kg/m)	1st mode theo. freq. (Hz)	Tension force (kN)
301/TTL	275.09	95	26.80	250	123.5	0.50	9014
308/TTL	230.06	78	28.89	225	101.4	0.62	7901
316/TTL	179.45	66	32.72	210	85.8	0.81	6857
106/TTL	218.46	54	32.38	180	70.2	0.65	5340
C1S8/VC	119.21	41	36.82	200	53.3	1.15	4059
C1C11/VC	150.85	46	29.95	200	59.8	0.88	4245
C1C18/VC	234.06	61	24.14	2.25	79.3	0.58	5519

at specified height from deck (see Fig. 3) individually for each cable in considering each of the first three modes of vibration (*i*th). A correction factor (α) was added to correct the error on the measurement location (L_s) and the maximum displacement location on the cable-free length (L_c).

$$\alpha = \left(\sin \frac{L_s i \pi}{L_c} \right)^{-1} \tag{5}$$

At first, the friction damper has been disconnected for cable intrinsic damping measurement. The operations have been executed by distressing the friction pads in assuring the free movement of the cables. The additional damping was then measured

Fig. 3 Installation of the accelerometers for damping test on the Tran Thi Ly stay cable bridge (photo provided by VSL Vietnam)
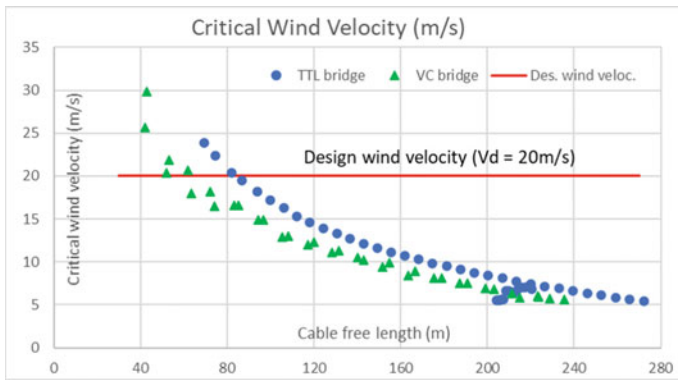

Fig. 4 Critical wind velocity evaluated in regard to the cable length
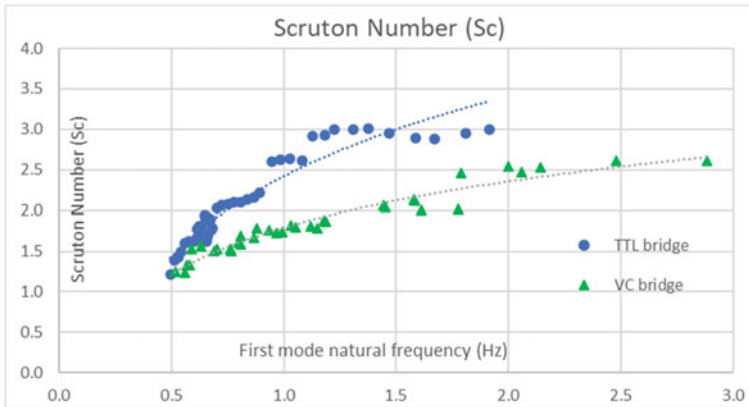
Fig. 5 Scruton Number and the cables' first mode natural frequency

by engaging the friction pads by stressing patterns. A post-measurement data treatment was performed to eliminate the measured values which had been affected by environment excitation conduiting to exaggerated damping value.

Rigorously, the cable movements were extracted from the measured acceleration signal by a double integration process. However, to eliminate the noise and measurement error that could lead to the unsuitable signal, the integration process was performed over the frequency domain. The logarithmic decrement (damping) was obtained from the envelope of displacement signal with the below formula in which (f) is the frequency of the harmonic signal [10].

$$\delta(t) = -\frac{1}{f}\frac{A'(t)}{A(t)} \tag{6}$$

Figure 6 presents a comparison between the measurement intrinsic damping and the theoretical evaluation in regard to the 1st mode natural frequency of the cables. We observe that the measured intrinsic damping values are comparable to those given in most of the International Standard [6, 8, 9] and quite in line with the theoretically evaluated ones.

Figure 7 shows the respective logarithmic decrement with the friction damper engaging in comparing to the measured intrinsic cable damping in Tran Thi Ly (TTL) and Vam Cong (VC) bridges. We observe a net increase of cable damping values proving the performance of the installed friction damper solution.

The average addition damping due to the friction damper system could reach a minimum of 4%.
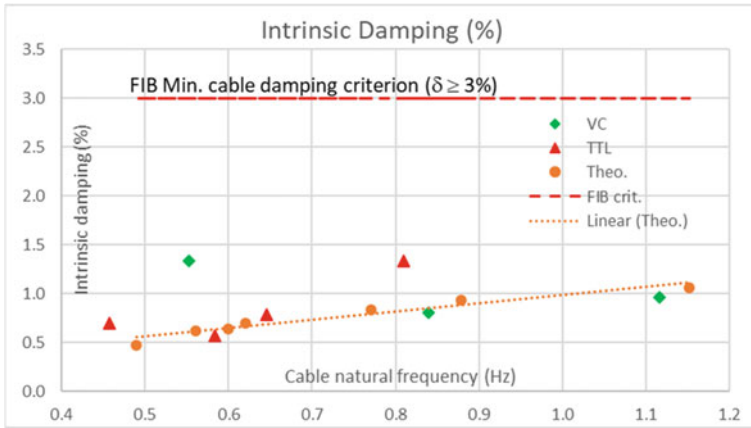
Fig. 6 Theoretical and measured Intrinsic Damping cable confrontation
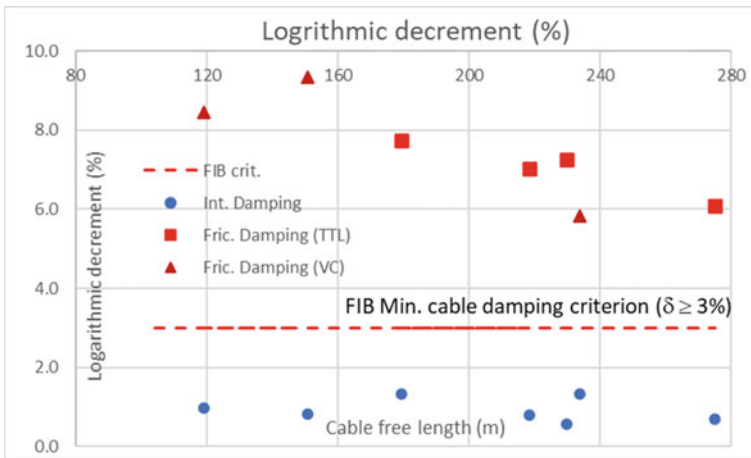
Fig. 7 Measured additional damping with friction damper engaged (Friction damping)

5   Conclusions and Discussion

The evaluation process of the possibility of excessive wind-induced vibration seems to be too conservative based on the approach by PTI recommendation. Furthermore, the evaluation of intrinsic damping is difficult to be accurate. The stay cable damping estimation needs to be confirmed by a suitable testing campaign for determining the cable logarithmic decrement.

The damping test process, correlation, and data treatment processes were presented for reference and future works.

The testing results show that the measured intrinsic damping of cables were in line with the evaluated ones and the values specified in the current International Standards and Specifications.

The performance of the friction damper system installed on the bridges had been also proved through the experimental data by increasing the cable logarithmic decrement by more than 4%.

References

1. Hikami Y, Shiraishi N (1988) Rain-wind induced vibrations of cables in cable stayed bridges. J Wind Eng Ind Aerodyn 29:409–418
2. Saito T, Matsumoto M, Kitazawa M (1994) Rain-wind excitation of cables on cable-stayed Higashi-Kobe bridge and cable vibration control. In: Proceedings of conference on cable stayed and suspension bridges, pp 507–514
3. Matsumoto M, Shiraishi N, Shirato H (1989) Inclined cable aerodynamics. In: Structural design, analysis and testing proceedings, proceedings of the ASCE structures congress, San Francisco
4. Irwin PA (1977) Wind vibrations of cables on cable-stayed bridges. In: Proceedings of structural congress XV. Portland, Oregon, pp 383–387
5. Cooper KR (1985) A note on the wind induced vibrations of bundled bridge stay cables. National Research Council of Canada, Note provided to RWDI
6. PTI (2001) Recommendations for stay cable design, testing and installation, 4th Edn. Post Tensioning Institute—Committee on Cable-Stayed Bridge, USA
7. Larose GL, Smitt LW (1999) Rain/wind induced vibrations of parallel stay cables. In: Proceedings of IABSE conference, Malmö
8. FIB (2005) Acceptance of stay cable system using prestressing steels. International Federation for Structural Concrete (FIB), Lausanne, Switzerland
9. CIP (2002) Recommendations on cable stays. In: French international commission on prestressing, Setra, Bagneux, France
10. Annan R, Guile M, Shim B, Ahn SS, Yang JH (2010) Friction dampers on Incheon bridge, performance prediction and in situ test. In: 3rd FIB international congress, Washington, USA

Numerical Study on Bending Resistance of Composite Beam Containing Conventional Concrete and HPFRC

Duy-Liem Nguyen and H. T. Tai Nguyen

1 Introduction

Strengthening a reinforced concrete (RC) beam members by using a better concrete has been a common technique [1–3]. During service life, RC beams may significantly degrade under mechanical and environmental load, and thus require a repairing/strengthening work to resist the initial design load. High-performance fiber-reinforced concrete (HPFRC) could be appropriately used as a strengthening material because HPFRC has been characterized by significantly greater mechanical properties than conventional concrete (CC). The great mechanical properties of HPFRC included high strengths in both compression and tension, high energy absorption capacity, and high cracking resistance [4–7]. Nonetheless, the cost of HPFRC is comparatively higher than that of CC [8], this issue has really been limited the practical application of HPFRC. In previous experimental study [9], the authors proposed to use HPFRC at extreme compression/tension fiber zone of RC beam to enhance its load-bearing capacity. The composite beam with CC-HPFRC experimentally performed the great enhancement of load bearing capacity in comparison to the control RC beam.

In addition to experimental approach, numerical approach has been widely used in civil engineering for performing the damaged behavior as well as mechanical resistance of materials or structural members. The advantages of numerical simulation techniques are to quickly provide various future outcomes based on experimentally historical data and to consequently save much cost and time for testing. Therefore, the main objective of this paper is to show the potential of a numerical model approach for providing fitting flexural response curves of the composite CC-HPFRC beams. The

D.-L. Nguyen · H. T. T. Nguyen (✉)

Faculty of Civil Engineering, Ho Chi Minh City University of Technology and Education, Ho Chi Minh City, Vietnam

e-mail: tainht@hcmute.edu.vn

finite element software ATENA is employed for the numerical analysis. The behaviors of the composite beams from this simulation will be compared with those from experimental test in [9]. Besides, the analytical result of the composite CC-HPFRC beam based on cross-section analysis was also compared and discussed.

2 Materials and Beam Design

Figure 1 shows the beam detail and bending test setup. Two thicknesses of HPFRC layer on beam top were studied as follows: $t = 50$ mm (beam 1) and $t = 75$ mm (beam 2). The size of the beams was $150 \times 150 \times 600$ mm^3 (width $\times$ depth $\times$ length) with its span of 450 mm. The beams were reinforced using $2 \times D$ 6 mm and $2 \times D$ 12 mm in the compressive and tensile zone, respectively, stirrups of D 6 mm were spaced at 120 mm. The compositions of CC and HPFRC regarding weight proportions were shown in Table 1 [2]. The fibers used in the HPFRC was a hybrid system, containing 1.0 vol.% long hooked and 0.5 vol.% short smooth fibers. The properties of the used fibers were presented in Table 2 [2]. Table 3 provides the direct tensile and compressive resistances of HPFCR and CC [9]. It was observed that the tensile and compressive resistances of HPFRC were much higher than those of CC. The yield strengths of longitudinal rebars and stirrups were 400 MPa and 240 MPa, respectively.
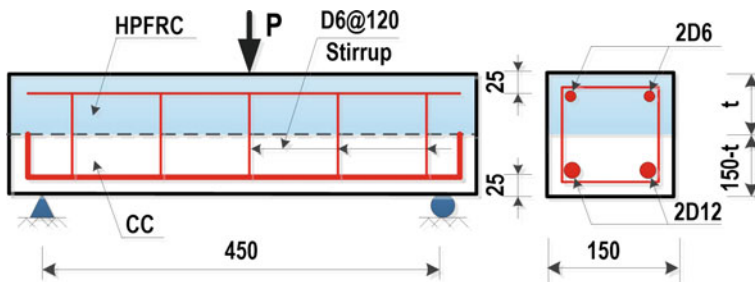

Fig. 1 Beam detail and bending test setup

Table 1 Composition of mortar matrix of CC and HPFRC [2]

Mortar matrix	Cement (INSSE PC40)	Silica fume	Silica sand	Fly ash	Superplas-ticizer	Coarse aggregate	Water
CC	1.00	–	2.23	–	–	4.62	0.63
HPFRC	0.80	0.25	1.10	0.20	0.04	–	0.26

Table 2 Properties of the hybrid fibers used [2]

Fiber type	Diameter (mm)	Length (mm)	Aspect ratio	Tensile strength (MPa)	Cross section
Long hooked	0.5	35	70	>1200	Circular
Short smooth	0.2	13	65	>2500	Circular

Table 3 Direct tensile and compressive resistances of CC and HPFRC

Property | Material	CC	HPFRC
Compressive strength (f'_{cu}, MPa)	20.2	79.6
Strain at ultimate strength (ε'_{cu}, %)	0.2	0.35
Tensile strength (f'_{tu}, MPa)	2.0	9.81
Strain at ultimate strength (ε'_{cu}, %)	–	0.36

3 Numerical Modeling of Composite Beams Made of CC and HPFRC

3.1 Modeling the Concrete Behavior and Failure Laws

The behavior and failure of CC and HPFRC was modeled using the SBeta Material and 3D Nonlinear Cementitious 2 User predefined in ATENA software [10], which were developed based on fracture plastic theory and are summarized as follows. In the following paragraphs, the Einstein summation convention is used thoroughly for the sake of brevity unless otherwise stated. Let $\boldsymbol{\varepsilon}$ be the strain tensor in the material, which can be decomposed into three parts: elastic, plastic, and fracture ones:

$$\boldsymbol{\varepsilon} = \boldsymbol{\varepsilon}^e + \boldsymbol{\varepsilon}^p + \boldsymbol{\varepsilon}^f. \tag{1}$$

The stress tensor in the material is related to the elastic strain via the Hook's law:

$$\boldsymbol{\sigma} = \frac{E}{(1+\nu)}\boldsymbol{\varepsilon}^e + \frac{E\nu}{(1+\nu)(1-2\nu)}\mathrm{tr}(\boldsymbol{\varepsilon}^e).\boldsymbol{I} \tag{2}$$

where E, ν are the initial elastic modulus and Poisson ratio, $\mathrm{tr}(\boldsymbol{\varepsilon}^e)$ is the trace of the elastic strain tensor, and $\boldsymbol{I}$ is the second order tensor of unity.

Rankine criterion is used in ATENA to model the concrete cracking behavior:

$$f^f(\boldsymbol{\sigma}) = \sigma'_{ii} - f'_{t_i} \leq 0 \tag{3}$$

where σ'_{ii} (no summation) is the trial stress and f'_{t_i} is the tensile strength in the material direction i. In ATENA, the material directions are defined by the actual principal directions or the principal directions at the onset of cracking.

The hardening/softening Menétrey-Willam yield surface is used to model the concrete crushing behavior:

$$f(\boldsymbol{\sigma}) = \left(\sqrt{1.5}\frac{\rho}{f_c'}\right)^2 + m\left[\frac{\rho}{\sqrt{6}.f_c'}r(\theta, e) + \frac{\xi}{\sqrt{3}.f_c'}\right] - c \tag{4}$$

where f_c' is the compressive strength; ρ, ξ, θ are defined as:

$$\xi = I_1/\sqrt{3}; I_1 = \sigma_{ii}; \tag{5}$$

$$\rho = \sqrt{2J_2}; J_2 = \frac{1}{2}s_{ij}s_{ij}; \tag{6}$$

$$\cos(3\theta) = \frac{3\sqrt{3}}{2}\frac{J_3}{J_2^{3/2}}; J_3 = \frac{1}{3}s_{ij}s_{jk}s_{ki}; \tag{7}$$

and $m, r(\theta, e)$ are related to the tensile, compressive strength and the roundness of the yield surface controlled by a parameter e:

$$m = 3\frac{f_c'^2 - f_t'^2}{f_c'f_t'^2}\frac{e}{e+1}; \tag{8}$$

$$r(\theta, e) = \frac{4(1 - e^2)\cos^2(\theta) + (2e - 1)^2}{2(1 - e^2)\cos(\theta) + (2e - 1)\left[4(1 - e^2)\cos^2(\theta) + 5e^2 - 4e\right]^{\frac{1}{2}}}. \tag{9}$$

In Eq. (4), the parameter $c = f_c'(\varepsilon_{eq}^p)/f_c'$ is to define the yielding/hardening process, in which ε_{eq}^p is a scalar representing the equivalent plastic strain and the function $f_c'(\varepsilon_{eq}^p)$ defines the hardening/softening law of the material in uniaxial compression.

The plastic flow obeys the non-associated flow rule in Eq. (10):

$$\dot{\boldsymbol{\varepsilon}}^p = \dot{\lambda}\frac{\partial g(\boldsymbol{\sigma})}{\partial \boldsymbol{\sigma}}; \ g(\boldsymbol{\sigma}) = \beta\frac{1}{\sqrt{3}}I_1 + \sqrt{2J_2} \tag{10}$$

where $\dot{\lambda}$ is the plastic multiplier representing the rate of plastic strain and β is a parameter defining the return direction of the stress.

The illustration of the uniaxial tensile and compressive behavior of concrete is shown in Fig. 2a while the admissible zone for stress in two principal directions is presented in Fig. 2b.

a) Stress-strain law   b) Biaxial failure law
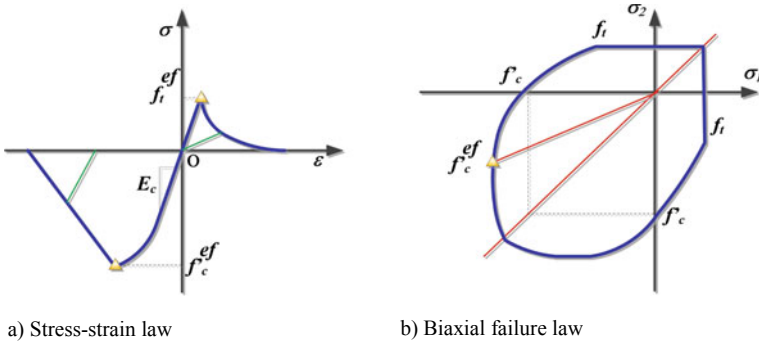
Fig. 2 Illustration of concrete behavior and failure laws

3.2 Determination of Material Parameters

The determination of material parameters is performed based on the tensile and compressive tests as well as their numerical simulation. The mechanical problems of the direct tensile and compressive tests were solved in ATENA 2D for both CC and HPFRC to calibrate the model parameters. After trial-and-error process, the best-fit model parameters were determined and are reported in Table 4.

The best-fit behavior and failure of HPFRC obtained with ATENA are also presented in Fig. 3, where a good fitting between numerical and experimental results can be observed.

Table 4 Best-fit parameters of the fracture plastic model for NC and HPFRC

Parameter | Material	NC	HPFRC
Elastic modulus (E, MPa)	24,200	24,200
Poisson ratio	0.2	0.2
Localized strain ε'_{cu}	–	0.0035
Localized strain ε'_{tu}	–	0.0036
Stress–strain law in compression		
Yield strain (%) | Stress (MPa)		
(0,72.59); (0.03, 80.65); (0.05, 74.04); (0.07, 65.33); (0.09, 61.70); (0.3, 47.18); (5, 0.32)		
Stress–strain law in tension		
Yield strain (%) | Stress (MPa)		
(0, 1.79); (0.36, 9.81); (1, 1.58)		

a) Under uniaxial compression   b) Under uniaxial tension
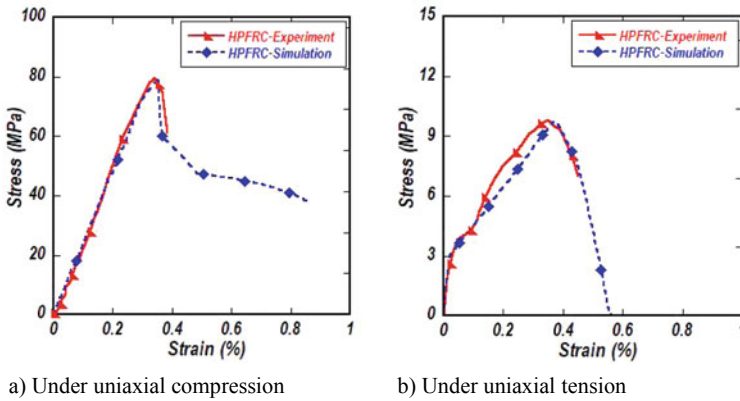
Fig. 3 Numerical and experimental stress–strain responses of HPFRC

3.3 Finite Element Simulation of Three-Point Bending Test of Composite Beams

The finite element models of composite beams made of CC and HPFRC were displayed in Fig. 4. Owing to symmetry, only one-half of the beam was considered to reduce the computing time. 2D triangle solid elements were used to discretize the beam geometry while truss elements were used to model the steel reinforcement. In this study, the element sizes were chosen small enough for numerical convergence—namely, the maximal size of element is 0.02 m for the beam and the steel support. It is worth mentioning that the number of elements is restricted to be smaller than 300 in Demo mode, which prevents us to proceed with finer meshes. The predefined materials in ATENA with the parameters previously determined were used to define the behavior and failure of CC and HPFRC. The elastic perfect plastic model was used to model the behavior of rebars.

The boundary conditions were as follows. The displacements of all nodes along the symmetric axis was fixed along the horizontal direction and the displacement at the

a) Composite beam 1   b) Composite beam 2

Fig. 4 Finite element modeling of composite beams

Fig. 5 Flexural responses according to test and simulation results

middle node at the bottom of the steel support was fixed along the vertical direction. The loading applied to the beam was a prescribed displacement 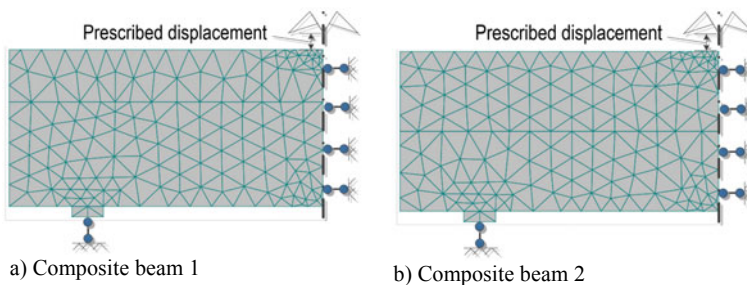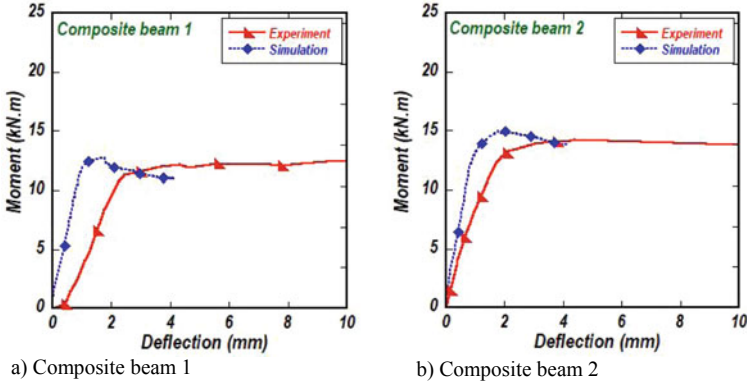of increment of 5.08×10^{-2} mm applied to the nodes near the symmetric axis as illustrated in Fig. 5. The interaction between CC and HPFRC and between the concrete and steel rebar were assumed perfect connection.

Since the problem is nonlinear, Newton Raphson method was used for equation resolution. The tolerance of convergence was 0.01 for the displacement, residual, and absolute residual error and 0.0001 for the energy error. The maximal iteration per increment was chosen to be 40. The calculation results will be presented in the next section.

4   Numerical Results

4.1   Flexural Response Curves of the Composite Beams

Figure 6 plots the flexural response curves of the composite beams. As can be seen in the figure, there is a critical point in the curves based on which the behavior of the beam can be divided into two principal phases. In the first phase, the bending moment increases with an increase of the prescribed mid-span deflection, i.e., the beam is still capable to carry the increasing load. In the second phase, after the bending moment has reached its maximal value, the bending moment gradually decreases with increasing prescribed mid-span deflection, i.e., the beam is in failure and the load-carrying capacity of the beam is reduced. The bending moment at critical point is the maximal load-carrying capacity of the beam, noted M_{MOR}, and the corresponding deflection was noted as δ_{MOR}. Summary of M_{MOR} and δ_{MOR} obtained from FE modeling is presented in Table 5. For comparison purposes, the results obtained from experiment and cross-section analysis are also shown in the table. It

a) Composite beam 1

b) Composite beam 2
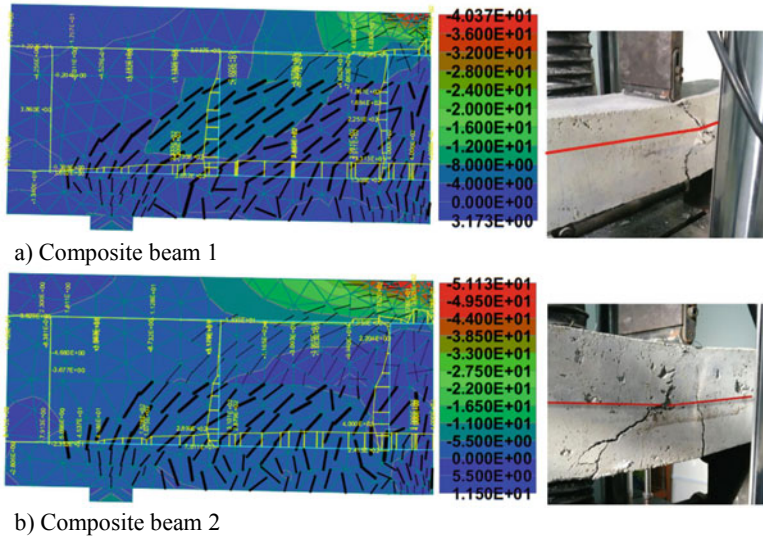
Fig. 6 Crack patterns obtained from numerical analysis and experiment [9]

Table 5 Results of experiment and numerical simulation

Specimen	Moment resistance					
	Experiment [9]		Simulation		Difference	
	M_{MOR} (kN.m)	δ_{MOR}(mm)	M_{MOR} (kN)	δ_{MOR}(mm)	M_{MOR} (%)	δ_{MOR}(%)
Beam 1	13.22	4.27	12.69	1.78	4.0	58.3
Beam 2	14.21	4.37	14.90	1.98	4.9	54.7

can be seen that the predicted M_{MOR} match relatively well with the experimental ones. The relative error between the M_{MOR} obtained from numerical simulation and the experimental M_{MOR} is lower than 4.9%. However, the simulated δ_{MOR} is much smaller than that from experiment. The large difference between the simulated and experimental δ_{MOR} is likely to stem from the fact that the deflections measured during testing are in fact the deflections of the platens of the UTM, in which excess deformations due to local failures of the materials at supports and at the location of the applied load are also included.

4.2 Crack Pattern and Failure Mode

Figure 6 displays the crack patterns of the composite beams obtained from FE modeling. It can be seen in the figure that both beams exhibit mainly shear flexural failures in the CC layer—namely, the computed maximal crack width in the

CC layer is 0.362 mm while the computed maximal crack width in the HPFRC is only 0.14 mm at the corresponding deflection of 1.83 mm. Based on experiment, the observed cracks consist of vertical and diagonal cracks in both the CC and HPFRC layers while the FE simulation only predicts cracks in the CC layer. The mismatch between prediction and experiment is likely to reside in the material model and element type used in the simulation. Since the cracks initiated from the CC layer and propagated through the HPFRC layers, appropriate finite element that allows crack propagation should be used to well capture the observed phenomenon.

The tensile stress in the steel reinforcing bars at the mid-span section in both composite beams attain their yield strength while the compressive stress does not exceed the crushing strength of HPFRC. In addition, based on the bending moment – deflection curves, the numerical bending moment slightly decreases with an increase of deflection after the critical point. Therefore, the failure mode of the beams is predicted to be of ductile failure. In effect, experimental results show that both beams present ductility. Therefore, the FE simulation predicts well the failure mode of the composite beams—and so does the analysis of sectional stress state at ultimate limit.

5 Conclusion

The load-carrying capacity of composite beams comprised of conventional concrete at the bottom layer and HPFRC at the top layer was successfully investigated using finite element method with the aid of ATENA software. The numerical simulation predicts well the moment resistance and the failure mode of the composite beams while the deflection and crack pattern were not very well predicted, which will be deeply studied in future works. By performing rigorous material characterization and using appropriate material models and element types, the behavior and failure of composite beams and composite structures comprised of conventional concrete and HPFRC can be predicted with high accuracy without conducting expensive and time-consuming experiments.

References

1. Hussein L, Amleh L (2015) Structural behavior of ultra-high performance fiber reinforced concrete-normal strength concrete or high strength concrete composite members. Constr Build Mater 93:1105–1116
2. Nguyen DL, Tran VT, Tran NT, Ngo TT, Nguyen MT (2021) Evaluating load-carrying capacity of short composite beam using strain-hardening HPFRC. KSCE J Civ Eng 25:1410–1423.https://doi.org/10.1007/s12205-021-1327-8

3. Martinola G, Meda A, Plizzari GA, Rinaldi Z (2010) Strengthening and repair of RC beams with fiber reinforced concrete. Cem Concr Compos 32(9):731–739
4. Nguyen DL, Song J, Manathamsombat C, Kim DJ (2015) Comparative electromechanical damage-sensing behavior of six strain-hardening steel-fiber-reinforced cementitious composites under direct tension. Compos: Part B 69:159–168
5. Song J, Nguyen DL, Manathamsombat C, Kim DJ (2015) Effect of fiber volume content on electromechanical behavior of strain-hardening steel-fiber-reinforced cementitious composites. J Compos Mater. https://doi.org/10.1177/0021998314568169
6. Nguyen DL, Thai DK, Ngo TT, Tran TK, Nguyen TT (2019) Weibull modulus from size effect of high-performance fiber-reinforced concrete under compression and flexure. Constr Build Mater 226:743–758
7. Nguyen DL, Lam MN-T, Kim DJ, Song J (2020) Direct tensile self-sensing and fracture energy of steel-fiber-reinforced concretes. Compos B 183(107714):1–19. https://doi.org/10.1016/j.compositesb.2019.107714
8. Špak M, Kozlovská M, Struková Z, Bašková R (2016) Comparison of conventional and advanced concrete technologies in terms of construction efficiency. Adv Mater Sci Eng 2016:6. Article ID 1903729. http://dx.doi.org/10.1155/2016/1903729
9. Nguyen DL, Thai DK, Nguyen HTT, Nguyen TQ, Le-Trung K (2021) Responses of composite beams with high-performance fiber-reinforced concrete. Constr Build Mater 270:121814. https://doi.org/10.1016/j.conbuildmat.2020.121814
10. Červenka Consulting (2021) ATENA program documentation—Part 1: theory. Retrieved from https://www.cervenka.cz/ on July 2021

Multi-scale Modelling of the Ballistic Impact of One Single Kevlar Yarn

Q. Hoan Pham, C. Ha-Minh, T. Long Chu, T. Kanit, and A. Imad

1 Introduction

Kevlar fibre plays an important role in many applications, especially in lightweight composite material for ballistic armour. The ballistic behaviour of Kevlar fabric has been studied by many authors using experimental and numerical approaches [1]. However, numerical modelling is dominant due to the high cost and complex structure of the material.

Generally, numerical models can be classified into three scales: macroscopic, mesoscopic, and microscopic. Within the macroscopic (fabric) scale, the fabric was assumed to be a homogeneous plate; thus, only global behaviours of the material, such as the perforation process or the evolution of deformation pyramid, were predicted [2, 3]. In the case of mesoscopic or yarn scale, each yarn was considered as orthotropic material [4, 5]. Then, many important mechanisms were studied, e.g. yarn damage mechanisms, yarn–yarn, fabric-projectile contact, yarn pull-out and sliding, and effects of friction, shape of the impactor, boundary conditions as well.

At the scale of microscopic, some numerical models have been conducted. In 2004, Zhou et al. [6] performed model of the fabric at the fibre scale using "digital element method". One frictionless pin-connected rod element chain was used to represent one fibre. Then, Grujicic et al. [7] developed this approach for predicting

Q. H. Pham (✉)
Faculty of Civil Engineering, Vietnam Maritime University, Haiphong City, Vietnam
e-mail: hoanpq.ctt@vimaru.edu.vn

T. Kanit · A. Imad
Université de Lille, EA 7512—UML—Unité de Mécanique de Lille, F-59000 Lille, France

C. Ha-Minh
LMT, Université Paris-Saclay, Cachan Cedex, France

T. L. Chu
Thuyloi University, Hanoi, Vietnam

microscopic mechanisms of Kevlar KM2 fibre. However, only a sub-yarn model in these models, in which one ÷ thirty digital fibres depicted the yarn rather than 400 fibres, was performed. The digital element is not able to describe the deformation of fibres. Thus, many important phenomena cannot be captured.

One straight yarn was first fully modelled by Nilakantan [8]. The straight yarn colliding with a hemicylindrical projectile was simulated. Two cases, including wall constrained and unconstrained, were investigated. Yarn cross section was depicted by hexagonal packing of fibres with a fibre volume fraction of 0.907. Besides, three fibres were put around the edge of the yarn to get a cross section with exactly 400 fibres. The deformation, wide-spreading, and redistribution of fibres were observed. It clearly showed the independence of the propagation of transverse displacement wave, projectile velocity, and yarn energy to the constraint. The effect of the friction factor between fibres or the transverse and shear modulus on the transverse wave displacement was also independent of this condition. However, the arrangement of fibres is not the same as this of yarn in fabric. Thus, the behaviour of the yarn was not thoroughly investigated.

Sockalingam et al. [9] also conducted a microscopic scale model of a single Kevlar KM2 yarn. The transverse impact was studied to investigate the dynamic sort time behaviour of each individual fibre. Four hundred fibres were arranged to be an elliptical cross section as in real fabric. Fibre damage criteria, as well as fibre–fibre, fibre-projectile interaction, were predicted. The modelling also can depict the stress wave propagation, absorbed energy, and fibre deformation. However, the process of de-crimping of the yarn was not predicted as it was straight.

In 2021, a microscopic model of fabric was conducted by Yang et al. [10]. Fibre failure, fibre–fibre interaction, and the evolution of fabric energy were investigated. However, to gain computation time, 400 fibres were represented by only 17 equivalent fibres. In addition, its cross section was discreted by only two elements. Thus, the behaviour of the fabric was still not fully predicted. In our previous work [11], a microscopic model of fabric was also introduced. 98 equivalent fibres were used to represent 400 fibres. Fibre failure and fibre–fibre interactions have been predicted. However, the computation time was quite high, and this needs to be reduced.

In this paper, a multi-scale model of one single crimped Kevlar yarn under ballistic impact is developed. In order to gain the computation time, the yarn is divided into two parts. While, the impact zone is modelled on the microscopic scale, and the other is on the mesoscopic one. The model is validated by the results from the microscopic model in the literature [11]. The computation time is also compared. This multi-scale model allows developing a meso-microscopic multi-scale model of a fabric with a reasonable computation cost in further works.

Table 1 Properties of Kevlar KM2 fibre [12]

ρ (T/m^3)	D (μm)	E_1 (GPa)	$E_2 = E_3$ (GPa)	G_{12} (GPa)	ν_{12}	ν_{32}
1.44	12.0	84.62	1.34	24.40	0.60	0.24

2 Numerical Model

2.1 Material Properties

In this paper, Kevlar KM2 material is studied. Properties of Kevlar KM2 fibre are listed as follows (Table 1).

The material is assumed to be transversely orthotropic [12]. G, E, and ν denote shear, Young's modulus, and Poisson's ratio. As Kevlar fibres show a linear elastic behaviour until 90% of ultimate stress, it is assumed that the material is in the linear elastic domain until failure [13]. Additionally, the crush and transverse shear strength are still unknown. Thus, only failure by axial tension is considered in the failure mode. The tensile strength is set to be 3.88 GPa [12].

2.2 Multi-Scale Model

In this paper, the 3D numerical model of one single yarn under ballistic impact has been performed using the commercial finite element code HyperWork Radioss. A 50.6 mm length yarn is subjected to a spherical impactor. The diameter of the impactor is 533 μm, and its mass is 625 mg. The selected initial impact velocity is 245 m/s. As the configuration is symmetric, only a quarter of the finite element model is conducted, shown in Fig. 1.

In this study, 400 fibres of 12 μ diameters are represented by 98 equivalent fibres of 24 μ diameters. Details of this concept have been discussed in our previous works [11]. Moreover, in order to minimize the number of elements, the model of a hybrid yarn is conducted. Only the impact zone is modelled in the scale of microscopic. The rest of the yarn is modelled as a mesoscopic one (Fig. 2). As Hashin failure criterion, which used stress to evaluate, is utilized, a so-called "without failure" zone to connect the microscopic and mesoscopic parts is proposed to avoid the concentration of stress.

In this model, the solid element is used. The connection of the mesoscopic and microscopic is computed so that the acoustic impedance is constant by considering the formula in the work of Nilakantan [14], as follows:

$$Z = A\sqrt{E\rho} \tag{1}$$

Here, A is the area of the considered cross section, E is Young's modulus, and ρ denotes the material density.
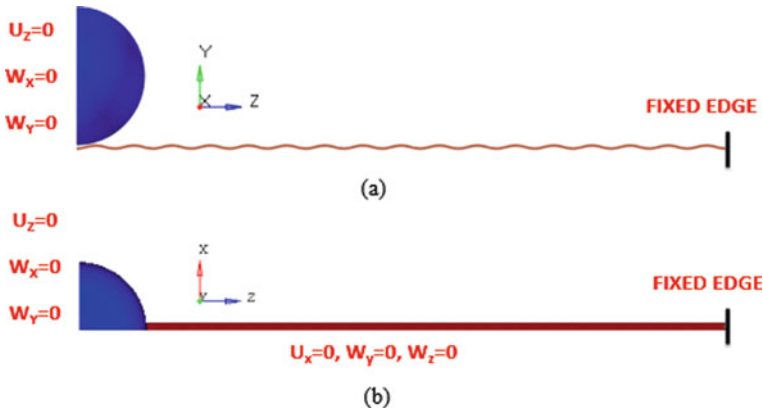
Fig. 1 Quarter FE model
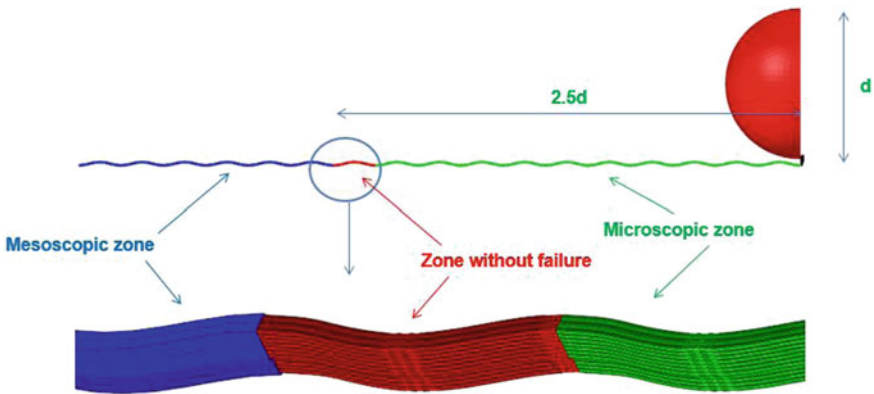
Fig. 2 Hybrid yarn

3 Results and Discussion

The results of the multi-scale model are analyzed in this section. In order to validate and evaluate the model, results are compared with these of the microscopic model in the literature [11]. Figure 3 displays the evolution of projectile velocity versus time. The curves clearly show two different phases: (i) de-crimping and (ii) tension. There is an insignificant difference (244.19 and 244.21 m/s). The de-crimping process (from 0 to 12 μs) is almost the same. In the case of microscopic yarn, the projectile escapes the fabric at 25 μs, later than in the case of the hybrid yarn (24 μs).

Model total energies are compared in Fig. 4. The results of both models are almost the same. Also, a slight difference is observed at about 24 μs. Thus, the model is validated, and the precision of this model is reliable.

Fig. 3 Evolution of
projectile velocity
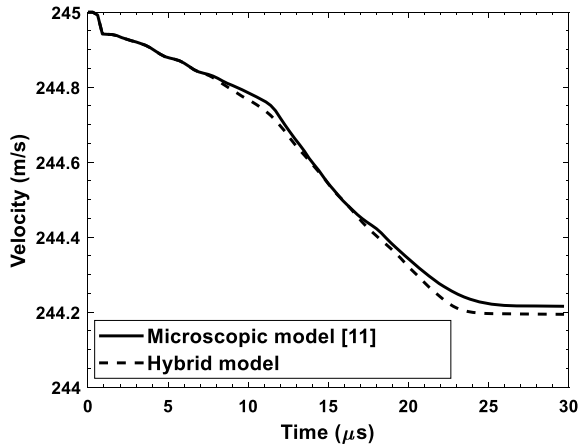
Fig. 4 Total energy of the
two models
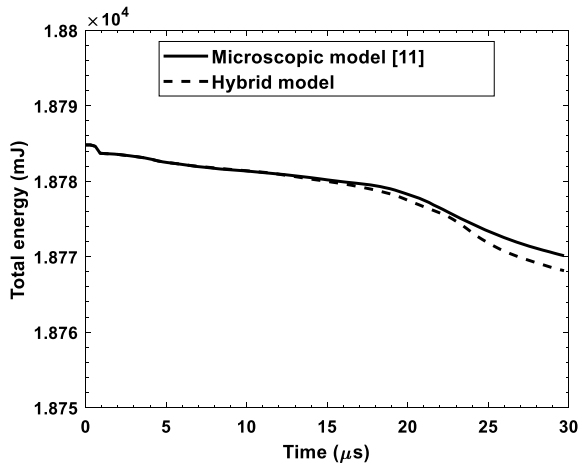
The deformation of the yarns at 24 µs is shown in Fig. 5. The same pyramids
and fibre failure are observed. However, the failure of the part outside the pyramid
is different. In the microscopic yarn, some fibres fail near the edge, while the meso-
scopic part of the multi-scale cannot simulate this phenomenon. Therefore, the curves
of the two models are slightly different from this moment.

The evolution of yarn's energy, including kinetic, internal, and friction energies,
is shown in Fig. 6. In general, the total energies of the two models are mostly the
same. Critical failure of the microscopic and multi-scale yarns are observed at 20
and 21 µs. It can be explained by the effect of the mesoscopic part. This part is
not damaged, while some fibres near the fixed edge of the microscopic yarn are
damaged (Fig. 6). After the total failure of the yarn (24 µs), kinetic energies are
almost constant, while the friction one keeps increasing due to the vibration of the
whole yarn and the contact between the fibres.
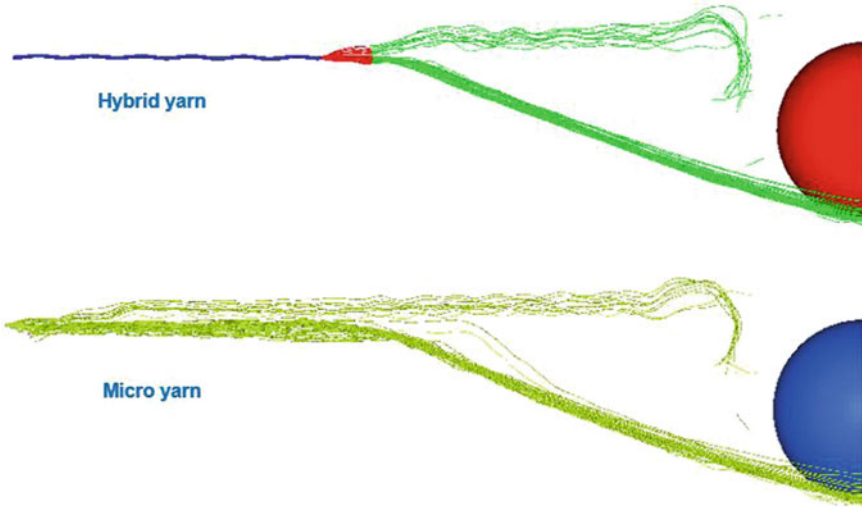
Fig. 5 Deformation and fibre failure
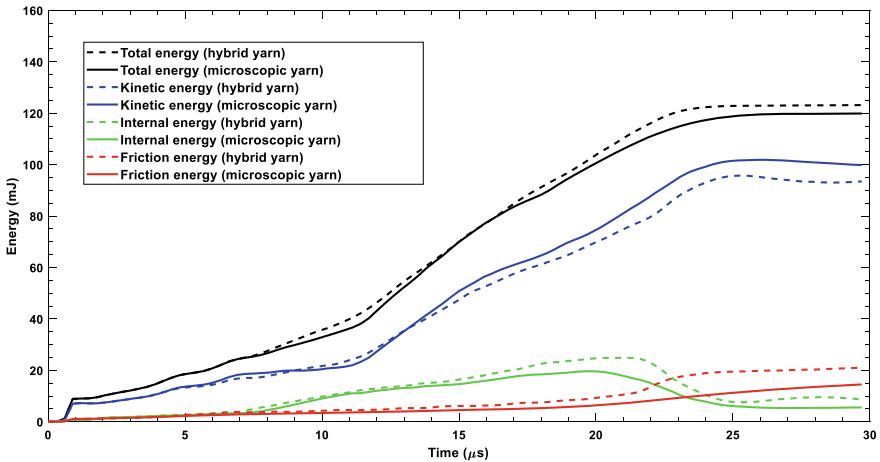
Fig. 6 Evolution of hybrid yarn's energy in comparison with microscopic ones

Figure 7 shows the computation time of the two models. It is observed that the calculation time is reduced by about 16%. This reduction is because the mesoscopic part of the multi-scale uses a coarse mesh, and there are only two elements through the thickness of the yarn. Thus, a considerable number of elements are reduced. In addition, failure and contact do not occur in this zone. Then, the calculation time is reduced.

Fig. 7 Computation time (hours)
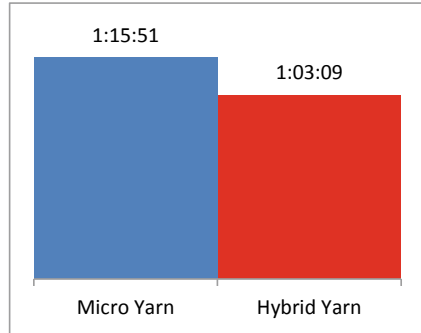
4 Conclusion

A single Kevlar yarn has been modelled by micro-mesoscopic multi-scale model in which the zone under impact is modelled at the microscopic scale while the other is at the mesoscopic one. The model was evaluated by comparing it with the microscopic one in terms of the residual velocity of the impactor, model's total energy, and the energy of the yarn. Results show that the differences between the residual velocity of the projectile and the total energy of the two models are insignificant. In general, the behaviour of the material, including the evolution of yarn energy, the formation of the impact pyramid and fibre failure, is the same. However, due to the mesoscopic part, after the total failure of the yarn, there are slight differences, especially in the case of frictional energy. In conclusion, the multi-scale model can predict the important phenomena during the ballistic impact event. Additionally, 16% of calculation time is saved. Furthermore, in the case of fabric mesoscopic and microscopic models, fibre failure occurs only in the impact zone; the micro-mesoscopic multi-scale reduces the number of elements and the interaction outside this zone. Therefore, the multi-scale hybrid yarn can be applied for the fibre scale model of the fabric in the future work with a reasonable computation cost.

References

1. Cheeseman BA, Bogetti TA (2003) Ballistic impact into fabric and compliant composite laminates. Compos Struct 61(1):161–173
2. Roylance D, Wilde A, Tocci G (1973) Ballistic impact of textile structures. Text Res J 43(1):34–41
3. Ha-Minh C, Kanit T, Boussu F, Imad A (2011) Numerical multi-scale modeling for textile woven fabric against ballistic impact. Comput Mater Sci 50(7):2172–2184
4. Rao MP, Nilakantan G, Keefe M, Powers BM, Bogetti TA (2009) Global/local modeling of ballistic impact onto woven fabrics. J Compos Mater 43(5):445–467
5. Ha-Minh C, Imad A, Kanit T, Boussu F (2013) Numerical analysis of a ballistic impact on textile fabric. Int J Mech Sci 69:32–39

6. Zhou G, Sun X, Wang Y (2004) Multi-chain digital element analysis in textile mechanics. Compos Sci Technol 64(2):239–244
7. Grujicic AHM, Pandurangan B, Yen CF, Cheeseman BA, Wang Y, Miao Y, Zheng JQ (2012) Fiber-level modeling of dynamic strength of Kevlar® KM2 ballistic fabric. J Mater Eng Perform 21:1107–1119
8. Nilakantan G (2013) Filament-level modeling of Kevlar KM2 yarns for ballistic impact studies. Compos Struct 104:1–13
9. Sockalingam S, Gillespie JW, Keefe M (2016) Modeling the fiber length-scale response of Kevlar KM2 yarn during transverse impact. Text Res J 87(18):2242–2254
10. Yang Y, Liu Y, Xue S, Sun X (2021) Multi-scale finite element modeling of ballistic impact onto woven fabric involving fiber bundles. Compos Struct 267:113856
11. Pham QH (2021) Analyse des réponses balistiques des fibres d'un matériau tissé à l'échelle microscopique basée sur l'homogénéisation numérique. PhD Thesis, UML, University of Lille. http://www.theses.fr/2021LILUI008/document
12. Cheng M, Chen W, Weerasooriya T (2005) Mechanical properties of Kevlar® KM2 single fiber. J Eng Mater Technol 127(2):197–203
13. Duan Y, Keefe M, Bogetti TA, Cheeseman BA (2005) Modeling friction effects on the ballistic impact behavior of a single-ply high-strength fabric. Int J Impact Eng 31(8):996–1012
14. Nilakantan G, Keefe M, Gillespie Jr JW, Bogetti TA (2008) Novel multi-scale modeling of woven fabric composites for use in impact studies. In: 10th international LS-DYNA users conference, 2008

Defect Detection and Identification on an Embedded Beam Using Modal Deformation Parameters and the Dempster–Shafer Data Fusion Technique

Rachid Azzi and Farid Asma

1 Introduction

Engineering structures such as bridges, offshore platforms, wind turbines, etc., and rotating machinery components such as rotating shafts, blades, bearings, etc., accumulate defects during their use or operation.

The presence of a local structural defect in a structure traditionally results in a change in the geometric (moment of inertia I) or material (Young's modulus E) characteristics of the damaged element or section of the structure that obviously affects the performance, safety, reliability, and operational life of the structure in a negative way. The early detection of these structural defects helps to take appropriate actions for an economical maintenance and avoid a possible failure of the structure.

Defect identification methods based on vibration characteristics have attracted much research interest due to their non-destructive local and global defect detection nature, their potential to automatically detect defects, their high reliability and accessibility, lower cost of measuring instruments and also by the presence of a rich literature in the field of structural health monitoring.

However, parametric methods developed using modal data have dominated the state of the art of vibration-based fault identification, in particular those based on eigenfrequencies, mode shapes, and their derivatives. The modal parameters (eigenfrequencies, mode shapes, and their derivatives such as curvature, slope, modal strain energy, etc.) are physically interpreted (resonances, spatial description of the structure at resonance, etc.), while the methods based on the time and frequency domains

R. Azzi
Mouloud Mammeri University of Tizi-Ouzou, BP 17 RP 15000, Tizi Ouzou, Algeria

F. Asma (✉)
Professor, Mouloud Mammeri University of Tizi-Ouzou, BP 17 RP 15000, Tizi Ouzou, Algeria
e-mail: asma-farid@ummto.dz

are based on analytical formulas. According to the modal parameters used in defect identification, the so-called parametric methods are classified into:

- Methods based on natural frequencies;
- Methods based on the mode shape;
- Methods based on mode shape curvature/mode shape deformation;
- Other methods based on modal parameters.

These different methods are discussed in [1–4], and their practical applications and their advantages and disadvantages are discussed.

In this study, we develop a fault detection method applied to an embedded beam. We used an embedded beam model for two main reasons:

(1) The majority of civil and mechanical structures or their components can be modeled by an embedded beam;
(2) The ability and efficiency of a method to identify a particular fault can be evaluated and considered as a reference on a simple beam structure model that is easy to verify experimentally.

2   Embedded Beam Model

Numerical simulations are performed on an embedded beam of length 1006 mm and Section 5×46 mm presented in the following figure. The defects are modeled by the reduction of Young's modulus of the damaged element by the formula (αE) with $0 < \alpha < 1$.

The material properties of the beam are: Young's modulus $E = 2.2 \ 10^5$ Mpa, Poisson coefficient $\nu = 0.3$, and the material density is $\rho = 7.896 \ 10^{-6}$ kg/mm^3. The beam is discretized into finite elements of size $5 \times 23 \times 10.06$ mm^3 as shown in Fig. 1.

The defect is inserted on the finite element model of the embedded beam as a reduction of Young's modulus of the damaged element of the model. During this parametric study, the defect takes several levels of severity and at different locations of the beam. In the presentation of the results, only three levels of fault severity,
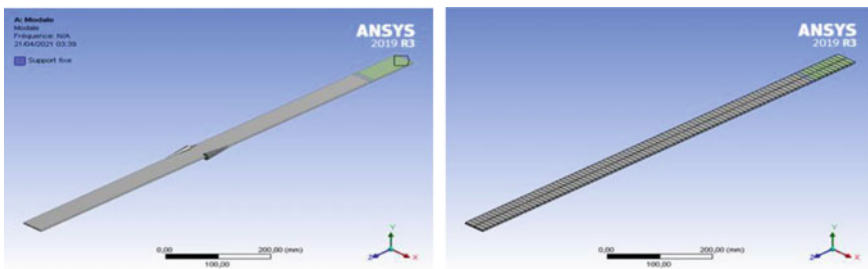

Fig. 1   Finite element model of a cantilever beam

0.3 E, 0.5 E, and 0.7 E, and a single fault position at $Z = [60.36–70.42\ \text{mm}]$ are considered.

Modal and harmonic analyses were performed on Ansys software, the strain energy is calculated for each element, for the two states are undamaged and damaged.

3 Finite Element Analysis

The matrix form of the vibration equation of the structure subjected to a dynamic load is:

$$[M]\{\ddot{x}\} + [C]\{\dot{x}\} + [K]\{x\} = \{F(t)\} \tag{1}$$

where $\{\ddot{x}\}$, $\{\dot{x}\}$ and $\{x\}$ are, respectively, the acceleration, velocity, and displacement of the structure $[M]$, $[C]$, and $[K]$ are, respectively, matrices of mass, damping, and stiffness of the structure. $\{F(t)\}$ is the external excitation force applied to the structure. The displacement transfer function at point k due to the excitation at point p is obtained by application of the Fourier transform to the (Eq. (1)) [5]:

$$H_{km}(\omega) = X_k(\omega)/F_m(\omega) \tag{2}$$

where $H(\omega)$ is the frequency response function. $X(\omega)$ and $F(\omega)$ are the displacement and excitation forces in the frequency domain, respectively.

According to Ref. [6], the vibration equation in eigenvalues of an intact structure can be written as:

$$[K]\{\varphi_i\} = \omega_i[M]\{\varphi_i\} \tag{3}$$

with $i = 1, …, n$—the number of considered vibration modes, ω_i—the eigenvalue, and $\{\varphi_i\}$—the ith mode shape of the structure.

For damaged structure, Eq. (3) can be rewritten as:

$$[K^d]\{\varphi_i^d\} = \omega_i^d[M]\{\varphi_i^d\} \tag{4}$$

where $[K^d]$ the stiffness matrix of the damaged structure, ω_i^d and $\{\varphi_i^d\}$ are, respectively, the eigenvalue and the mode shape of the damaged structure.

4 Modal Strain Energy Change Method

This method uses the modal strain energy change in each element of the structure before and after the defect occurrence. The modal strain energy change of the

damaged element is very high, however, it is very low for the undamaged elements that are far from the damaged element. However, the elements corresponding to the nodal points of the mode shape have exceptionally small values, which does not allow their identification. The use of modal strain energy change for multiple modes overcomes this problem. Shi and Law [7] applied the modal strain energy on an embedded beam and a two-story, single-span portal frame steel structure. The results show that this method is simple and reliable for locating single or multiple damages in a structure. This method is originally developed for a beam structure characterized by one-dimensional curvature. Cornwell et al. [8] generalized the modal strain energy method to a two-dimensional plate structure. From their numerical and experimental results, the strain energy-based method was found to be effective in locating cracks with stiffness reductions as small as 10% using relatively few mode shapes.

Thus, the **m**odal **s**train **e**nergy **c**hange **r**atio (MSECR) could be a significant indicator of defect location defined

$$\text{MSECR}_n^i = \left| \gamma_{n,i}^* - \gamma_{n,i} \right| / \gamma_{n,i} \tag{5}$$

where n and i denote the element number and mode number, respectively. If the MSEs for multiple modes are considered together, the MSECR_n of the nth element is defined as the average of the summation of MSECR_n^i for all modes normalized to the largest value $\text{MSECR}_{\text{max}}^i$ of each mode.

$$\text{MSECR}_n = \frac{1}{N_m} \sum_{i=1}^{N_m} \frac{\text{MSECR}_n^i}{\text{MSECR}_{\text{max}}^i} \tag{6}$$

Figure 2 shows the ratio of modal strain energy change along the length of the embedded beam for each of the first three vibration modes. We observe a sharp peak in the graphs, of modal strain energy change ratio, of first and third vibration modes. The peak is at the position $Z = [60.36–70.42 \text{ mm}]$ which corresponds to the position of the damaged element. Another important remark that can be made from this figure is that the amplitude of MSECR_3 at the position of the damaged element is higher than that of MSECR_1, this can be explained by the position of the damaged element in relation to the vibration mode node, the farther the damaged element is from the mode node the higher the amplitude of MSECR is. The modal strain energy change ratio for the second mode shows two more sharp peaks in addition to the one presented at the fault position.

This leads to a false indication of the fault position and can be explained by the fact that the MSECRs of the mesh elements corresponding to the mode nodal points have large or small values. To avoid a false indication of the damaged element, it is better to calculate the MSECR for a few first vibration modes.

Figure 3 shows the MSECR for the first three vibration modes. A sharp peak is noticed at the fault position $Z = [60.36–70.42 \text{ mm}]$. Another peak was noticed at the position $Z = [230–240 \text{ mm}]$ of the beam length due to the second mode as explained before, it can be said that it is important to calculate the ratio of change of modal

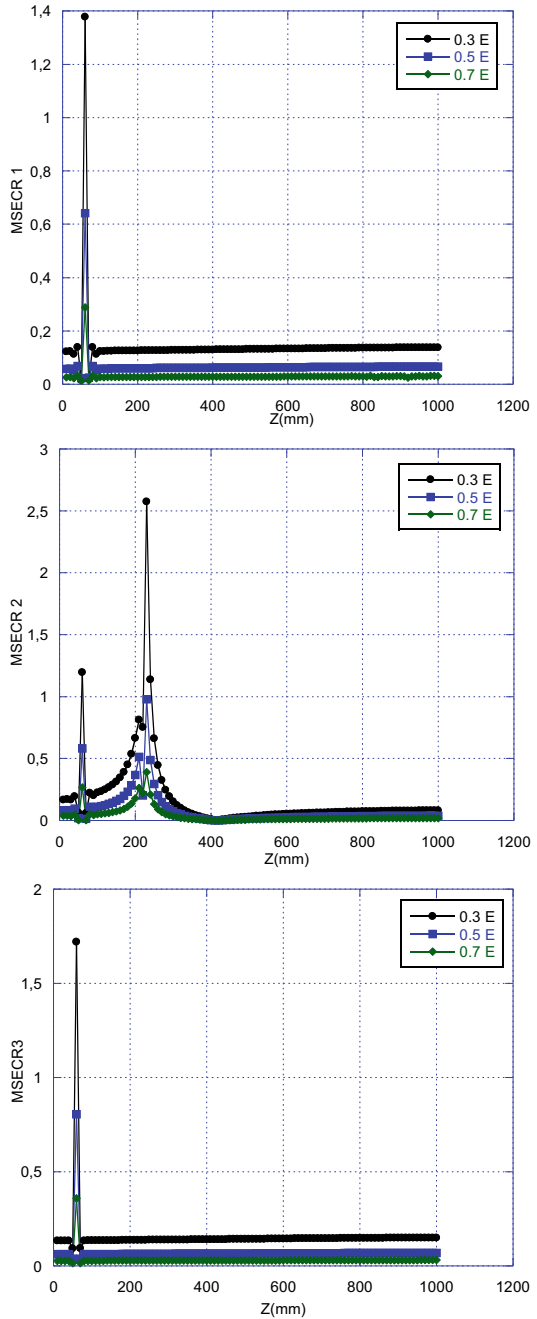**Fig. 2** MSECR$_{ij}$ along the length beam for various damage levels, damage position at $Z =$ [60.36–70.42 mm]

Fig. 3 MSECR$_j$ for first three mode along the length beam, damage position at Z = [60.36–70.42 mm]
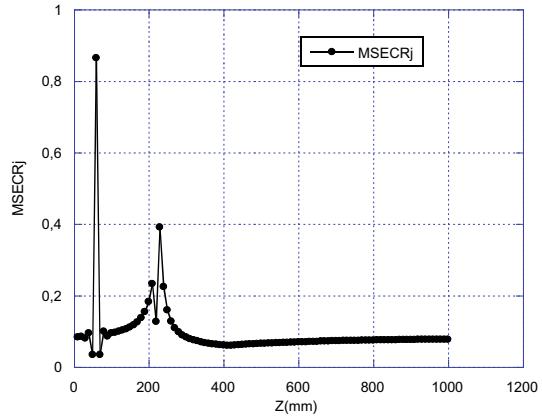
strain energy for each of the first three modes and for all three modes to have a clear view on the fault position.

The fault identification method based on modal strain change is improved by introducing the modal strain energy change ratios (MSECR) into an optimization algorithm, and this helps to specify the fault position and quantify its severity [9].

On the other hand, the modal strain energy change ratio (MSECR) is very high over a long distance, at the fault position and also at the neighborhood positions, which decreases the efficiency of the method in localizations. In order to limit the fault position and remove the neighborhood effect, Grande and Imbimbo [10] used the Dempster–Shafer data fusion technique to combine the fault localization indices of several modes, and thus the efficiency and accuracy of the MSECR method are significantly improved. The authors applied the same technique in a paper [11] to improve the defect localization based on the flexibility change index. In the following section, we will present and apply the Dempster–Shafer technique to the results of the MSECR method.

5 Dempster–Shafer Data Fusion Technique

Consider a set Θ of finite elements of the model of the beam to be identified if they are damaged or not:

$$\Theta = \{\text{el}_1, \text{el}_2, \ldots, \text{el}_N\} \tag{7}$$

with $\text{el}_i \, (i = 1, \ldots, N)$ represent the finite elements of the beam. If one of the beam elements $\{\text{el}_i\}$ is affected by a fault, then the beam is damaged. If all the elements of the beam are intact, then the state of the beam is intact and one represents it by an empty set $\emptyset$. Then, the power set 2^θ is defined as:

$$2^{\Theta} = \{\emptyset, \{el_1\}, \{el_2\}, \ldots, \{el_N\}\} \tag{8}$$

The application of the Dempster–Shafer theory on each subset X of 2^{θ} allows the basic probability assignment or the local decision $m(X)$.

The local decision $m(X)$ is defined as:

$$m : 2^{\theta} \rightarrow [0, 1] \tag{9}$$

$$\text{With } m(\emptyset) = 0 \text{ and } \sum_{X \subset \theta} m(X) = 1$$

The rules of Dempster combines the different local decision from different sources to obtain a global decision. Let two sources of information S_1 and S_2, $m_1 (S_1)$ and $m_2 (S_2)$ be the two local decisions provided by both sources, the merged decision is given by:

$$m_1(\overline{S}_1) = \frac{\sum_{S_1 \cap S_2 = \overline{S}_1} m_1(S_1) * m_2(S_2)}{1 - K} \tag{10}$$

where * is the scalar product operation and K is the degree of conflict between the two sources, given by:

$$K = \sum_{S_1 \cap S_2 = \emptyset} m_1(S_1) * m_2(S_2) \tag{11}$$

5.1 Proposed Method

In this section, we present the different steps of the application of the Dempster–Shafer method to detect the damaged element of the beam. The identification of defects is done on a fixed beam discretized in 100 elements of length 10.06 mm. The objective of this study is to identify if one of the 100 elements constituting the beam is damaged or healthy. Then we define a set of propositions Ω, the set of possible prepositions at the Dempster–Shafer theory, which constitute the beam model elements that must be identified whether they are damaged, or not.

$$\Omega = \{el_1; el_2; el_3; \ldots; el_{100}\} \tag{12}$$

Then, the power set 2^{Ω} is defined as:

$$2^{\Omega} = \{\emptyset_1, \{el_1\}, \{el_2\}, \{el_3\}, \ldots \{el_{100}\}\} \tag{13}$$

The intact state of the beam is represented on the power set by an empty set (i.e.{∅}) and the damaged state of the beam, where one of the model elements is affected by a decrease in the modulus of elasticity is represented by (i.e.{el_i}).

Consider the first three vibration modes of the beam for both cases, before and after the defect insertion on the model of the beam. A group of three information sources S_i with $i = 1, 2, 3$ is formed based on a pair intact/damaged of mode shapes $\overline{\Phi}_i = (\varphi_i, \varphi_i^d)$ according to the scheme shown in Fig. 4. For each source, the local decisions are obtained using MSECR_j (see Eq. 5).

The modal strain energy change ratio for the jth element, $\text{MSECR}_j^{[S_i]}$, is evaluated, by Eq. (4), considering the mode pairs of the source S_i. This results in:

$$\text{MSECR}_j^{[S_i]} = \frac{1}{n_{S_i}} \sum_{i=1}^{n_{S_i}} \frac{\text{MSECR}_{ij}}{\max_j(\text{MSECR}_{ij})} \tag{14}$$

where n_{S_i} denotes the number of damaged and undamaged mode pairs for the source S_i. The local decision $m_i(S_i)$ associated with the ith first-level source S_i is then obtained by converting each $\text{MSECR}_j^{[S_i]}$ value as follows:
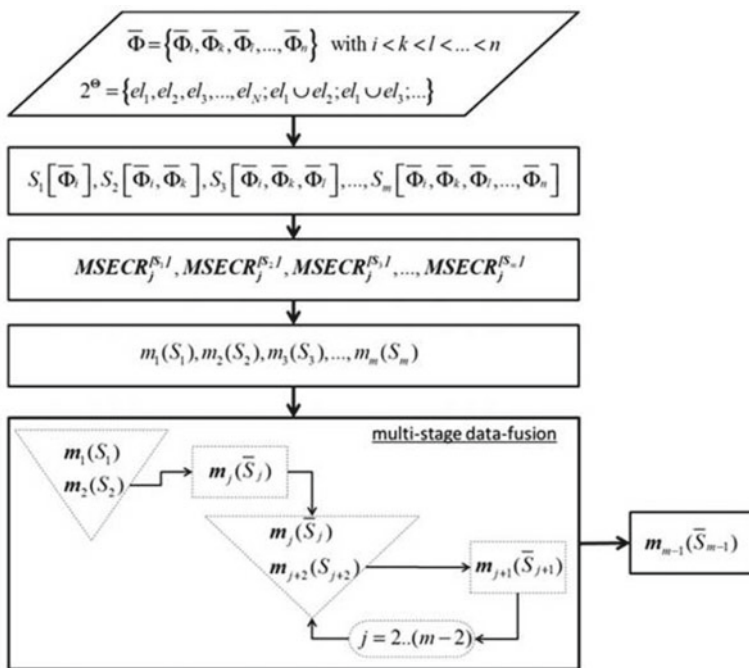

Fig. 4 Chart of the fusion approach [8]

$$m_i(S_i) = \left(\frac{\text{MSECR}_j^{[S_i]}}{\sum_{j=1}^N \text{MSECR}_j^{[S_i]}} \right)_{j=1...N} \tag{15}$$

$m_i(s_i)$ is a vector of order N ($N = 100$ in our case study) which contains information on the position and the severity of the damaged element.

A second group of sources of level $n - 1$, denoted $\overline{S}_i$, is introduced and, for each $\overline{S}_i$, the corresponding local decision $m_i(\overline{S}_i)$ is obtained from subsequent data fusion operations according to the scheme shown in Fig. 4.

Therefore, the derivation of the second-level sources is based on the fusion of pairs of local decisions. Starting from the first two sources, S_1 and S_2, where the corresponding local decisions are evaluated as:

$$m_1(S_1) = \left(\frac{\text{MSECR}_j^{[s_1]}}{\sum_{j=1}^N \text{MSECR}_j^{[s_1]}} \right)_{j=1...N} \tag{16}$$

$$m_2(s_2) = \left(\frac{\text{MSECR}_j^{[S_2]}}{\sum_{j=1}^N \text{MSECR}_j^{[S_2]}} \right)_{j=1...N} \tag{17}$$

$$\text{MSECR}_j^{[S_1]} = \frac{\text{MSECR}_{1,j}}{\max_j(\text{MSECR}_{1,j})} = \frac{\frac{\left| \text{MSE}_{1j}^d - \text{MSE}_{1j} \right|}{\text{MSE}_{1j}}}{\max_j \left(\frac{\left| \text{MSE}_{1j}^d - \text{MSE}_{1j} \right|}{\text{MSE}} \right)} \tag{18}$$

$$\text{MSECR}_j^{[S_2]} = \frac{1}{2} \sum_{k=1}^2 \frac{\text{MSECR}_{k,j}}{\max_j(\text{MSECR}_{k,j})}$$

$$= \frac{1}{2} \left[\frac{\frac{\left| \text{MSE}_{1j}^d - \text{MSE}_{1j} \right|}{\text{MSE}_{1j}}}{\max_j \left(\frac{\left| \text{MSE}_{1j}^d - \text{MSE}_{1j} \right|}{\text{MSE}_{1j}} \right)} + \frac{\frac{\left| \text{MSE}_{2j}^d - \text{MSE}_{2j} \right|}{\text{MSE}_{2J}}}{\max_j \left(\frac{\left| \text{MSE}_{1j}^d - \text{MSE}_{1j} \right|}{\text{MSE}_{1j}} \right)} \right] \tag{19}$$

After having calculated the $\text{MSECR}_j^{[S_1]}$ and $\text{MSECR}_j^{[S_2]}$ by Eqs. (18) and (19), we apply the Dempster–Shafer rule to obtain the local decision $m_1(\overline{s}_1)$ associated to the source $\overline{s}_1$:

$$m_1(\overline{S}_1) = \frac{\sum_{s_1 \cap s_2 = \overline{s}_1} m_1(S_1) * m_2(S_2)}{1 - \sum_{s_1 \cap s_2 = \emptyset} m_1(S_1) * m_2(S_2)} \tag{20}$$

In the same way and according to the diagram of Fig. 4, the local decision $m_2(\overline{s}_2)$ associated with the source $\overline{s}_2$ is defined by:

$$m_2(\overline{S}_2) = \frac{\sum_{\overline{S}_1 \cap S_3 = \overline{S}_2} m_1(\overline{S}_1) * m_3(S_3)}{1 - \sum_{\overline{S}_1 \cap S_3 = \emptyset} m_1(\overline{S}_1) * m_3(S_3)} \tag{21}$$

According to the Dempster–Shafer approach, the vector of local decision $m_2(\overline{s}_2)$ associated to the last source of the second level $\overline{s}_2$ is the vector taken into account to obtain information about the damaged element of the beam. The higher components of this vector indicate the damaged element.

5.2 Application of the Dempster–Fisher Technique on the Beam Model

During the application of this technique, three sources of information are considered: $S_1 = [\overline{\phi}_1]$, $S_2 = [\overline{\phi}_1, \overline{\phi}_2]$, $S_3 = [\overline{\phi}_1, \overline{\phi}_2, \overline{\phi}_3]$, where $\overline{\phi}_1 = [\varphi_1, \varphi_1^d]$, $\overline{\phi}_2 = [\varphi_2, \varphi_2^d]$, $\overline{\phi}_3 = [\varphi_3, \varphi_3^d]$. With $\varphi_1, \varphi_2, \varphi_3$ are the mode shapes of the beam without defected element and $\varphi_1^d, \varphi_2^d, \varphi_3^d$ the mode shapes of the beam with one defected element.

For each source S_i, the corresponding $\mathrm{MSECR}_j^{[S_i]}$ were evaluated by Eq. (14) obtaining: $\mathrm{MSECR}_j^{[S_1]}$, $\mathrm{MSECR}_j^{[S_2]}$, $\mathrm{MSECR}_j^{[S_3]}$, and then each $\mathrm{MSECR}_j^{[S_i]}$ is converted using Eq. (15) to obtain the basic probability assignment: $m_1(S_1)$; $m_2(S_2)$; $m_3(S_3)$.

Dempster's rule was applied according to the procedure illustrated in Fig. 4, then the vector of local decisions corresponding to the last step of the procedure Eq. (21):

$$m_2(\overline{S}_2) = \frac{\sum_{\overline{S}_1 \cap S_3 = \overline{S}_2} m_1(\overline{S}_1) * m_3(S_3)}{1 - \sum_{\overline{S}_1 \cap S_3 = \emptyset} m_1(\overline{S}_1) * m_3(S_3)} \tag{22}$$

This vector $m_2(\overline{s}_2)$ was then used in the data fusion approach for defect identification. A higher value at a position along the beam indicates the fault location.

Therefore, the Fig. 5 shows the position $Z = [60.36\text{–}70.42 \text{ mm}]$ as the fault location. The result provided by the Dempster–Shafer approach seems to be more obvious.

6 Conclusion

The results of numerical simulation via Ansys Workbench on a model of embedded beam showed that the modal strain parameter and modal strain energy is very sensitive to the structural defect and their monitoring allows to identify the position of the defect and quantify its size. The damage position is identified by a sharp peak of the modal strain energy change ratio of the damaged element and neighboring elements. The fault severity can be also identified by monitoring the amplitude of the modal

Fig. 5 Multiple data fusion
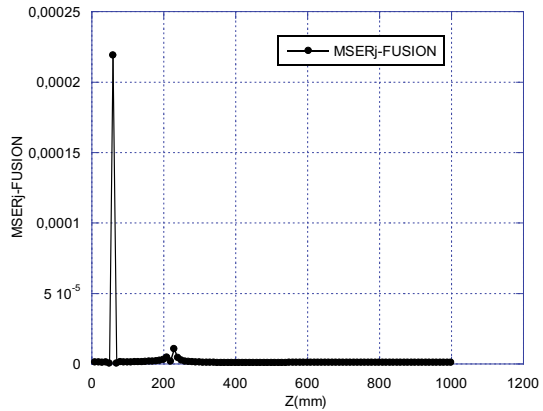
strain energy change ratio, the greater the fault severity the higher the amplitude of MSECR.

The change of modal strain energy allows to locate the defect and to estimate its severity, we observed that the difference is very high even at positions close to the defect, we propose to apply the data fusion method on the change of the modal strain energy ratio in order to limit the defect position only to the length of the damaged element.

The modal strain energy-based defect detection method presented in this paper using the strain energy change ratio has shown its effectiveness in identifying structural defects. The application of the data fusion method (Dempster–Shafer) on the modal strain energy change ratio removes any ambiguity in the defect location. The results of the proposed method show remarkable efficiency.

References

1. Fan W, Qiao P (2011) Vibration-based damage identification methods: a review and comparative study. Struct Health Monit 10(1):83–111
2. Sinou J-J (2009) A review of damage detection and health monitoring of mechanical systems from changes in the measurement of linear and non-linear vibrations. Robert C. Sapri. Mechanical vibrations: measurement, effects and control. Nova Science Publishers, Inc., pp 643–702. 978-1-60692-037-4. ffhal-00779322
3. Carden EP, Fanning P (2004) Vibration based condition monitoring: a review. Struct Health Monit 3(4):355–377. https://doi.org/10.1177/1475921704047500
4. Doebling SW, Farrar CR, Prime MB, Shevitz DW (1996) Damage identification and health monitoring of structural and mechanical systems from changes in their vibration characteristics: a literature review. Los Alamos National Laboratory report (LA-13070-MS)
5. Swamidas ASJ, Chen Y (1995) Monitoring crack growth through change of modal parameters. J Sound Vib 186(2):325–343
6. Gomes GF et al (2020) An inverse damage location problem applied to AS-350 rotor blades using bat optimization algorithm and multiaxial vibration data. Mech Syst Sig Process 145(2020):106932

7. Shi ZY, Law SS (1998) Structural damage localization from change of modal strain energy. J Sound Vib 218(5):825–844. https://doi.org/10.1006/jsvi.1998.1878

8. Cornwell P, Doebling SW, Farrar CR (1999) Application of the strain energy damage detection method to plate-like structures. J Sound Vib 224(2):359–374

9. Srinivas V, Ramanjaneyulu K, Jeyasehar CA (2011) Multi-stage approach for structural damage identification using modal strain energy and evolutionary optimization techniques. Struct Health Monit 10(2):219–230. https://doi.org/10.1177/1475921710373291

10. Grande E, Imbimbo M (2014) A multi-stage data-fusion procedure for damage detection of linear systems based on modal strain energy. J Civ Struct Heal Monit 4:107–118. https://doi.org/10.1007/s13349-013-0070-3

11. Grande E, Imbimbo M (2016) A multi-stage approach for damage detection in structural systems based on flexibility. Mech Syst Signal Process 76–77:455–475

Impact Resistance of Cement Material Partial Replaced by Silica Fume Under the Charpy Test

Thac-Quang Nguyen, Duy-Liem Nguyen [ID], Tri N. M. Nguyen [ID], and Tien Thanh Bui

1 Introduction

Concrete has long been viewed as an important material in the construction field. During their life service, concrete structures have been subjected to many types of loading that causing fracture, especially impact load. There are numerous investigations indicate that impact resistance is affected by many factors such as storage condition, mixture design, the surface properties of aggregate, and the bond between binder and coarse material. In 1964, Green indicated that the energy absorption capacity is higher when curing in dry condition [1]. In addition, the work of Neville showed that the impact strength of concrete will be increased when the surface of aggregate is rough, because of the better mechanical interlocking, and this capacity would be also affected by the insufficient bond between aggregate and binder or the interfacial transition zone properties [2]. In general, concrete is considered as a two-phase composite material: cement paste and aggregate. The fracture can be occurred by the broken of cement paste, of the aggregate, as well as of the bond

T.-Q. Nguyen · T. N. M. Nguyen (✉)
Campus in Ho Chi Minh City, University of Transport and Communications, 450-451 Le Van Viet Street, Tang Nhon Phu A Ward, Thu Duc City, Ho Chi Minh City, Vietnam
e-mail: trinnm_ph@utc.edu.vn

T.-Q. Nguyen
e-mail: quangnt_ph@utc.edu.vn

D.-L. Nguyen
Faculty of Civil Engineering, Ho Chi Minh City University of Technology and Education, 01 Vo Van Ngan Street, Thu Duc City, Ho Chi Minh City, Vietnam
e-mail: liemnd@hcmute.edu.vn

T. T. Bui
University of Transport and Communications, 3 Cau Giay Street, Lang Thuong Ward, Dong Da District, Hanoi, Vietnam
e-mail: btthanh@utc.edu.vn

between cement paste and aggregate (the interfacial transition zone) or any complex combination of these mechanisms [3, 4]. However, the matrix zone has seen to be the weakest one in concrete [5, 6]. Although there are many investigations have been conducted on the impact resistance of concrete with and without mineral admixtures, there is still less study related to this characteristic of cement paste, which is an important phase in this composite material [7–11]. Recently, silica fume (SF) has shown its advantage in improving cement characteristics. The work of Zhang et al. [12] showed that SF can increase the hydration degree, as well as the compressive strength of the hardened cement pastes. The work of Rao [13] reported the increase of some cement paste characteristics like normal consistency, soundness, and drying shrinkage complied with the increase of SF content. In addition, other characteristics of cement pastes containing SF like hydration, rheology, and porous structure were pointed out by Flores et al. [14]. They concluded the effect of SF in accelerating the cement hydration process, compacting the matrix structure, and also increasing the compressive strength of the cement paste due to their role on heterogeneous nucleation and pozzolanic reaction. The above literature review showed the influence of SF on numerous characteristics of cement paste. However, the influence of SF on the impact resistance of hardened cement paste has still not declared.

In another perspective, there are various experimental methods to obtain the impact resistance of cement-based materials such as drop-weight test, projectile impact test, explosive test, Charpy and Izod test [15–20]. The principle of these methods is based on the theorem of potential and kinetic energy. Among them, the Charpy V-notch impact test is still the most reasonable, inexpensive and suitable experiment for determining the impact resistance of materials. Basically, the principle of Charpy test is based on the potential energy of a single pendulum that breaks the sample at high strain rates to determine the energy absorption capacity or the shear resistance of the sample. Applied in the early twentieth century so far, the Charpy pendulum test has been conducted on a variety of materials, not only metals [21–23] but also plastics or polymers [24–26]. Particularly, there were some works measure the impact resistance of cement composite materials like nano-cement mixture [27], cement-mesh mixture [28], high strength concrete [29], and so on. However, current standards are only limited for plastic materials [30, 31] or metal [32, 33]. Although many studies were utilized the Charpy pendulum test for measuring the impact resistance of cement-based materials as mentioned above, there are no comprehensive standards or specification to recommend the application of Charpy pendulum test for this brittle material. Therefore, it is leading to inconsistency in the test parameters as well as the comparing results between studies. This present work focuses on the examination of the impact resistance of silica fume blended cementitious materials. The finding from this work can contribute to the literature of Charpy impact test for cement-based material, expand the comparing data as well as experimental parameters for this field.

Above all, the objective of this present work is investigating the influence of silica fume on the impact resistance of hardened cement pastes and proposing the relationship between compressive strength and impact resistance of these modified hardened cement pastes at the age of 28 days.

Table 1 Properties of silica fume

SiO$_2$ (%)	Retention on 45 µm sieve (%)	H$_2$O (when packed) (%)	Bulk density (U) (Kg/m^3)
>90	<1.5	<1.0	200–350

Table 2 Mixture designs

Samples	SF00	SF05	SF08	SF10	SF12	SF15	SF18	SF20
OPC	1	0.95	0.92	0.9	0.88	0.85	0.82	0.8
SF	0	0.05	0.08	0.1	0.12	0.15	0.18	0.2
Water	0.5	0.5	0.5	0.5	0.5	0.5	0.5	0.5

2 Experimental Programs

2.1 Materials

This present work used ordinary Portland cement and silica fume. Ordinary Portland cement (Type I) complies with ASTM C150/150M [34], the density of 3.14 g/cm^3, and the specific surface area of 2800/cm^2. The properties of silica fume, the key material in this present work, are summarized in Table 1.

2.2 Mixture Designs

In this study, OPC was partly replaced by the additions of SF to obtain the composite binders. Follow that manner, the proportions of SF were chosen of 0, 5, 8, 10, 12, 15, 18, and 20% by weight of the binder. The mixture designs were presented in Table 2. Where, the water–binder ratio was used constantly of 0.5, and names of the sample were marked from SF00 to SF20 in that order for the proportion of SF from 0 to 20%.

2.3 Mixing Procedure and Samples Molding

The mixing works were conducted by the power-driven revolving pan mixer with different speed and mixing time compliance with ASTM C305 [35]. First of all, the mixture of water and SF was placed into the dry standard bowl. It is worth mentioning that, due to the high area surface feature of SF particles, they are able to cause the agglomeration phenomenon in the mix, leading to decrease their performance in the final products [36]. Therefore, an ultrasonication process was conducted for
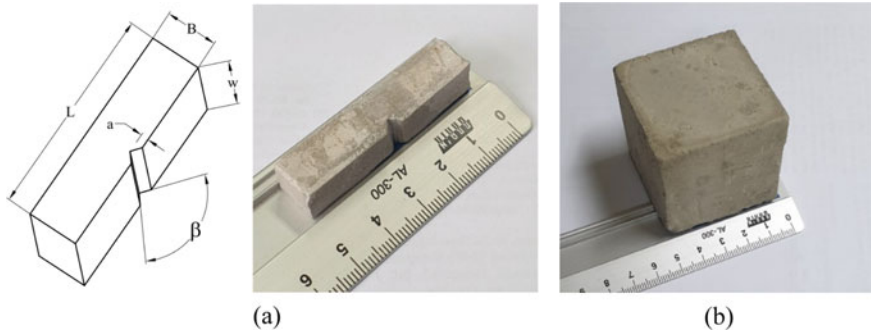
Fig. 1 a V-notched sample; **b** the cube sample

obtaining the homogeneous aqueous mixture [37–39]. The ultrasonication processes were applied in 35 min for each mixture design. Then, OPC was added into the obtained aqueous mixture, relaxed for 30 s for the absorption process. Finally, the mixing job was conducted under low- and high-speed conditions, complied with the specification in ASTM C305. The mixtures were poured into the same serial molds prepared with a thin oil layer cover, $10 \times 10 \times 50$-mm-prism and $50 \times 50 \times 50$-mm-cube molds which were used for the Charpy impact test and compression test, respectively. The samples were cured in water under normal room conditions (20 ± 20 °C, $50 \pm 5\%$ R.H), demolding after 24 h. For the Charpy impact test, 15 samples were prepared for each mixture design and tested at the ages of 7, 14, and 28 days, respectively. Besides, three cube samples were also prepared for each mixture and tested after 28 days to obtain the compressive strength of the hardened cement pastes.

Due to the complexity of the matrix microstructure as well as the spontaneous cracking that occurs during the curing time, the samples for cement pastes are designed in small size normally. According to ASTM C 109/109M [40] about the compressive strength test of hardened cement paste, the sample dimensions are specified as a $50 \times 50 \times 50$-mm-cube. In contrast, as above presented, there is no standard or specification for conducting the Charpy test for hardened cement paste. Therefore, based on the ASTM E23 [33] for impact testing of metallic materials as well as the capacity of the testing apparatus, the Charpy sample dimension was proposed as a $10 \times 10 \times 50$ mm V-notched bar. Figure 1a presents the Charpy sample dimension, where $\beta = 450$, $a = 2$ mm, $w = B = 10$ mm, and $L = 50$ mm.

2.4 Testing Methods

The impact experiment was conducted at the same velocity (2.92 m/s) by the digital Charpy impact instrument MT-333, the hammer mass of 0.7 kg, initial height of 0.435 m (see Fig. 2a), which was fully functional equipped, so that this instrument could calculate automatically compensate for windage and friction. Therefore, the
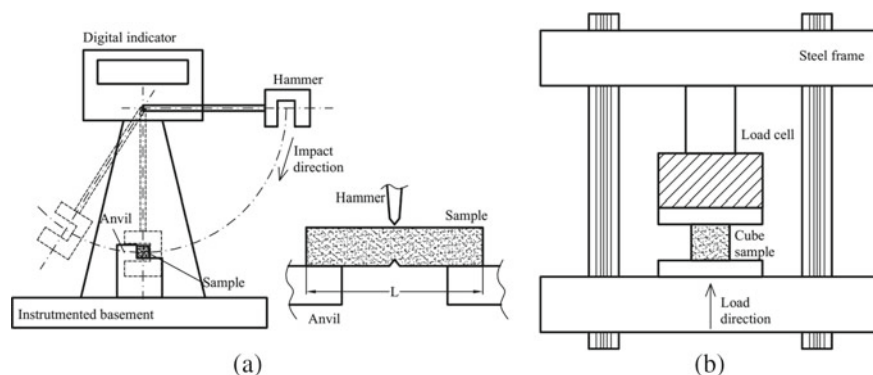
Fig. 2 The testing apparatus. **a** The Charpy impact instrument; **b** the UTM

result of energy absorption or net breaking energy by the V-notch sample can be reliable. The impact resistance (J/m^2) was obtained by the energy absorption per average breaking area [41–43].

Setting up the experiment, a V-notched bar was laid freely on the anvil stake as a horizontal simple beam, and the notched was set opposite to the impact interface. At the initiation state, the hammer was kept in position by the hold–release mechanism. The maximum potential energy at the highest position of hammer (2.986 J) was showed in the digital screen. The hold–release mechanism played a significant role that keeping the hammer stably at the initiation state. Therefore, the testing procedure was conducted without any vibration or imparting acceleration. Consequently, a high accuracy result would be obtained. The experiment was started easily by pushing the handgrip of release mechanism, and the result would be accepted if the sample was broken completely. For each mixture design, the samples were prepared at same source as well as the curing conditions, and five samples were used for testing per time at 7, 14, and 28 days old.

The uniaxial compression test was done by means of a 1000 kN-hydraulic universal testing machine compliance with ASTM C109/109M [40] (see Fig. 2b), using the cube samples at 28 days old. All the experiment was done at the room temperature and relative humidity.

3 Result and Discussion

3.1 Compressive Strength

Figure 3 shows the compressive strength of the hardened silica fume blended cement pastes at 28 days. Overall, the result shows an increasing tendency of the compressive strength with the increase of SF content. As can be seen from Fig. 3, with the content
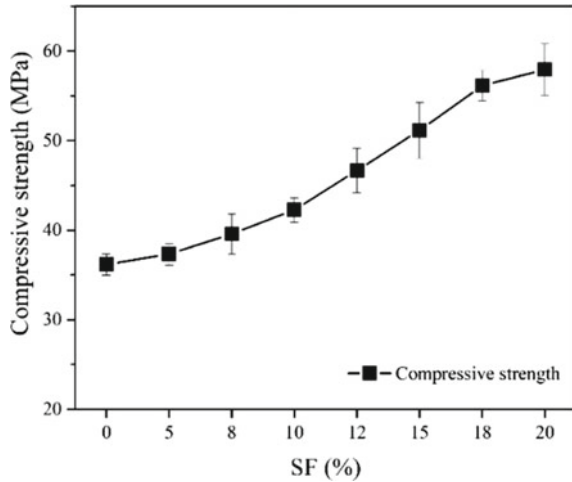
of silica fume less than 10 wt%, the increase was not significant. In contrast, with the replacement content of over 10 wt%, the compressive strength of the pastes rose remarkably. For instance, the increases in compressive strength were observed of 17%, 29%, 41%, 55%, and 60% when replacing cement by silica fume with the proportion of 10%, 12%, 15%, 18%, and 20%, respectively. This result also met with the finding from the work of Yajun and Cahyadi [44], that investigated the effects of densified SF on microstructure and compressive strength of blended cement pastes. Similar results can be found from literature with the studies concern with the effect of SF on the strength and durability characteristics of concrete [45–47].

3.2 Impact Resistance

It is worth noting that the Charpy test result would be accepted if the sample was broken completely after impaction. Figure 4 shows the impact resistance results of the hardened silica fume blended cement pastes at the ages of 7, 14, and 28 days. As a general trend, there was an increase of impact resistance of the hardened pastes as the increase of curing time (Fig. 4a) and/or the increase of silica fume's content (Fig. 4b). From Fig. 4a, the increase of impact resistance from the samples at the age of 14 days to that at 7 days was observed around 15 to 20%. However, that parameter was shown lower of around 7 to 13% when comparing the increase of impact resistance from the samples at the age of 28 days to that at 14 days. The higher in increasing trend at the early age was consistent with the observations in the literature which were concerned with the effect of SF in accelerating the pozzolanic reaction, as well as consuming the generated calcium hydroxide (CH) from the hydration of cement. As a result, increase the performance of the hardened pastes at the early ages [14, 44, 48]. From another perspective, Fig. 4b shows the influence of the different proportions of SF

on the impact resistance of hardened cement pastes. As observed from Fig. 4b, the increase of impact resistance complied with the increase of SF proportion. From the scope of the study, the impact resistance of the hardened cement pastes blended with 20% SF showed the highest value. For instance, at 28 days, the impact resistance of the 20% SF blended cement pastes was 23,000 J/m^2. For comparison, at 28 days, there were increases of 20, 31, 31, 53, 62, 73, and 77% in that order when replacing cement with 5, 8, 10, 12, 15, 18, and 20% of SF. Follow that manner, the replacement of 20% of SF can be considered as the optimum proportion of SF from the scope of this study.

Continuous the strategy of investigating the effect of SF on the impact resistance of hardened cement pastes, Fig. 5 shows the linear relationship between the SF content and the impact resistance by regression analysis, where I means the impact resistance in J/m^2 and SF means the SF content in %. The R^2 value was 0.9794.

Fig. 4 Effect of silica fume to the impact resistance of cement paste. **a** Based on the curing time; **b** based on the content of silica fume
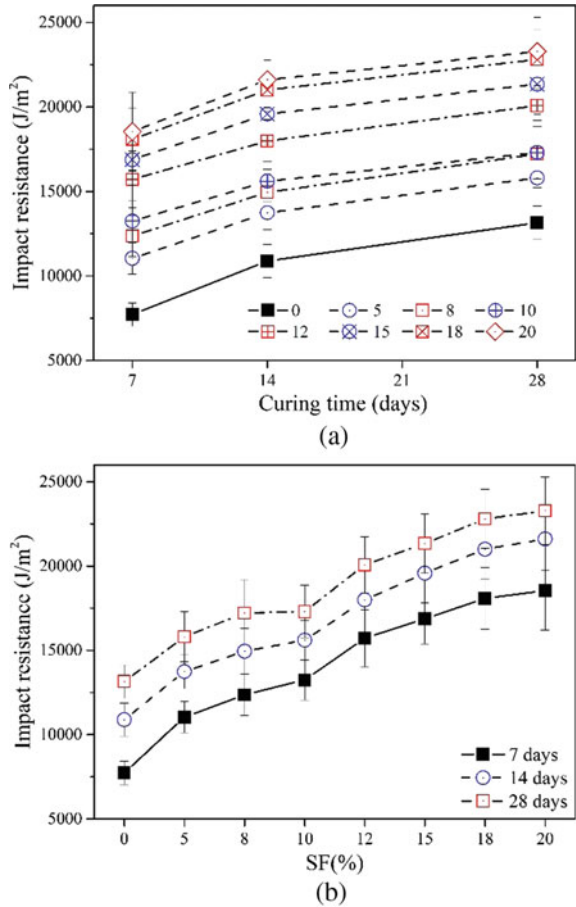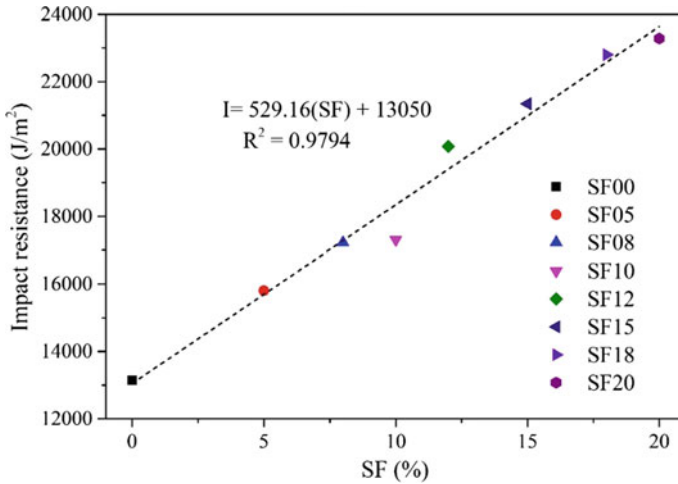
Fig. 5 Relationship between SF content and impact resistance

3.3 Relationship Between Compressive Strength and Impact Resistance

As can be observed from the above results, there is a correlation between compressive strength and impact resistance of the hardened cement pastes at the age of 28 days. For instance, the increase in compressive strength is consistent with the increase in impact resistance complied with the increase in SF content (see Figs. 3 and 4a). That result was also met with the conclusion of previous authors, i.e., a material with high strength and high ductility will have more impact resistance capacity than the lower one [49–51]. Hence, it can be said that there is a relationship between the compression strength and the impact resistance at the age of 28 days. Numerous types of functions such as exponential, linear, logarithmic, power, and polynomial were carried out to find the best R^2. Among them, the best curve with the highest R^2 of 0.9669 was obtained by using a polynomial function with the equation as below:

$$I = -12.476 f_c'^2 + 1584.1 f_c' - 26,779,$$

where I means the impact resistance in J/m^2; f_c' means the compressive strength at the age of 28 days in MPa (see Fig. 6).

Above all, regardless of the SF content, the derived relationship between compressive strength and impact resistance can provide a clear reference for estimating the impact resistance of hardened cement pastes based on their compressive strength.
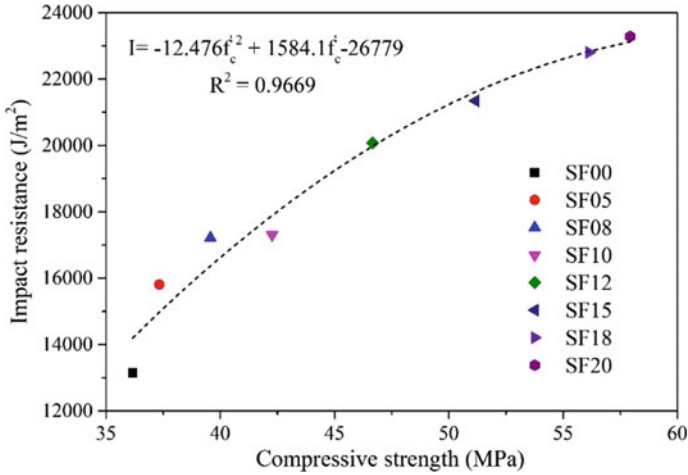
Fig. 6 Relationship between compressive strength and impact resistance

4 Conclusion

The experiment study figured out the influence of silica fume on impact resistance of cement pastes. The following conclusions can be drawn from the results of this study:

- Silica fume showed an important role in increasing the impact resistance of hardened cement pastes. The optimum proportion of SF of 20% was observed within the scope of this study. Based on the results in this study, at 28 days, there were an increase of 77% in impact resistance and 60% in compressive strength compared with those of the plain pastes when replacing cement by 20% SF.
- The Charpy impact instrument is useful for determining the impact resistance of brittle material like cement pastes. The ultrasonication process shows a good effect on dispersing SF in an aqueous solution.
- The relationship between the replaced silica fume proportion and impact resistance was pointed out as reference for predicting the impact resistance based on the SF proportion.
- The relationship between the compressive strength and impact resistance at 28 days was pointed out, as a reference for predicting the impact resistance based on the compressive strength of SF blended cement pastes regardless the SF proportion.
- The finding from this study can be a good reference for the works concerned with the effects of silica fume, as well as have an overview of its optimum percentage when dealing with the impact resistance of cement.

References

1. Green H (1964) Impact strength of concrete. Proc Inst Civ Eng 28(3):383–396
2. Neville AM (2011) Properties of concrete, 5th edn. Pearson Education Limited, UK
3. Scrivener KL, Crumbie AK, Laugesen P (2004) The interfacial transition zone (ITZ) between cement paste and aggregate in concrete. Interface Sci 12:411–421
4. Naus DJ (1973) Fracture mechanics applicability to Portland cement concretes. Army Construction Engineering Research
5. Su Z, Bijen JMJM, Larbi JA (1991) Influence of polymer modification on the hydration of Portland cement. Cem Concr Res 21(2–3):242–250
6. Rossignolo JA (2007) Effect of silica fume and SBR latex on the paste aggregate interfacial transition zone. Mater Res 10(1):83–86
7. Farooqi MU, Ali M (2019) Effect of pre-treatment and content of wheat straw on energy absorption capability of concrete. Constr Build Mater 224:572–583
8. Saxena R, Siddique S, Gupta T, Sharma RK, Chaudhary S (2018) Impact resistance and energy absorption capacity of concrete containing plastic waste. Constr Build Mater 176:415–421
9. Kumar V, Iqbal MA, Mittal AK (2018) Study of induced prestress on deformation and energy absorption characteristics of concrete slabs under drop impact loading. Constr Build Mater 188:656–675
10. Kumar V, Iqbal MA, Mittal AK (2017) Energy absorption capacity of prestressed and reinforced concrete slabs subjected to multiple impacts. Proc Struct Integrity 6:11–18
11. Maho B, Jamnam S, Sukontasukkul P, Fujikake K, Banthia N (2017) Preliminary study on multilayer bulletproof concrete panel: impact energy absorption and failure pattern of fibre reinforced concrete, para-rubber and Styrofoam sheets. Proc Eng 210:369–376
12. Zhang Z, Zhang B, Yan P (2016) Comparative study of effect of raw and densified silica fume in the paste, mortar and concrete. Constr Build Mater 105:82–93
13. Rao GA (2003) Investigations on the performance of silica fume-incorporated cement pastes and mortars. Cem Concr Res 33(11):1765–1770
14. Flores YC, Cordeiro GC, Filho RDT, Tavares LM (2017) Performance of Portland cement pastes containing nano-silica and different types of silica. Constr Build Mater 146:524–530
15. Badr A, Ashour AF (2005) Modified ACI drop-weight impact test for concrete. ACI Mater J 102(4):249–255
16. Mohammadhosseini H, Awal ASMA, Yatim JBM (2017) The impact resistance and mechanical properties of concrete reinforced with waste polypropylene carpet fibres. Constr Build Mater 143:147–157
17. Yu R, Beers LV, Spiesz P, Brouwers HJH (2016) Impact resistance of a sustainable ultra-high performance fibre reinforced concrete (UHPFRC) under pendulum impact loadings. Constr Build Mater 107:203–215
18. Vallens K, Bescher E, Mackenzie JD, Rice E (2001) A new technique for the measurement of the impact resistance of wall coatings. Cem Concr Res 31(6):965–968
19. Francois D, Pineau A (2002) From Charpy to present impact testing, vol 30, 1st edn. Elsevier Science
20. Tahmasebinia F (2008) Finite element simulation of reinforced concrete structures under impact accident. Struct Surv 26(5):445–454
21. Cabrilo A, Geric K (2018) Fracture mechanic and Charpy impact properties of a crack in weld metal, HAZ and base metal of welded armor steel. Proc Struct Integrity 13:2059–2064

22. Cao R, Chan ZS, Yuan JJ, Han CY, Xiao ZG, Zhang XB, Yan YJ, Chena JH (2018) The effects of Silicon and Copper on microstructures, tensile and Charpy properties of weld metals by refined X120 wire. Mater Sci Eng, A 718:350–362
23. Cao Y, Zhen Y, Song M, Yi H, Li F, Li X (2020) Determination of Johnson–Cook parameters and evaluation of Charpy impact test performance for X80 pipeline steel. Int J Mech Sci 179
24. Lenkey GB, Major Z (2002) Application of electric emission technique for determining the dynamic fracture toughness of polymers. Eur Struct Integrity Soc 30:129–136
25. Major Z, Lang RW (2002) Determination of rate dependent fracture toughness of plastics using precracked Charpy specimens. Eur Struct Integrity Soc 30:137–144
26. Grellmann W, Lach R, Seidler S (2002) Determination of geometry-independent fracture mechanics values of polymers. Eur Struct Integrity Soc 30:145–154
27. Hakamy A, Shaikh FUA, Low IM (2014) Thermal and mechanical properties of hemp fabric-reinforced nanoclay–cement nanocomposites. J Mater Sci 49:1684–1694
28. Liu Z, Cui Q, Li Q (2015) Properties of GRC modified by emulsion. Presented at the GRCA 2015 Congress, Dubai, United Arab Emirates, April 19–21, 2015, International Glassfibre Reinforced Concrete Association, Hampton, UK, 14p, 2015
29. Yu R, Spiesz P, Brouwers HJH (2014) Static properties and impact resistance of a green ultra-high performance hybrid fibre reinforced concrete (UHPHFRC): experiments and modeling. Constr Build Mater 68:158–171
30. ISO 179-1:2010 (2010) Plastics—determination of Charpy impact properties. International Organization for Standardization, Geneva, Switzerland
31. ASTM D6110-18 (2018) Standard test method for determining the Charpy impact resistance of notched specimens of plastics. ASTM International, West Conshohocken, PA
32. ISO 148-1:2016 (2009) Metallic materials—Charpy pendulum impact test. International Organization for Standardization, Geneva, Switzerland
33. ASTM E23-18 (2018) Standard test methods for notched bar impact testing of metallic materials. ASTM International, West Conshohocken, PA
34. ASTM C150/C150M-20 (2020) Standard specification for Portland cement. ASTM International, West Conshohocken, PA
35. ASTM C305-20 (2020) Standard practice for mechanical mixing of hydraulic cement pastes and mortars of plastic consistency. ASTM International, West Conshohocken, PA
36. Yajun J, Cahyadi JH (2003) Effects of densified silica fume on microstructure and compressive strength of blended cement pastes. Cem Concr Res 33(10):1543–1548
37. Janca M, Siler P, Opravil T, Kotrla J (2019) Improving the dispersion of silica fume in cement pastes and mortars. In: International conference building materials, products and technologies
38. Rodríguez ED, Bernal SA, Provis JL, Payá J, Monzó JM, Borrachero MV (2012) Structure of portland cement pastes blended with sonicated silica fume. J Mater Civ Eng 24(10):1295–1304
39. Fraga YSB, da Silva Rêgo JH, Capuzzo VMS (2020) Ultrasonication effect of silica fume on compressive strength of cement pastes. In: Proceedings of the international conference of sustainable production and use of cement and concrete, pp 149–155
40. ASTM C109/C109M-20b (2020) Standard test method for compressive strength of hydraulic cement mortars (using 2-in. or [50 mm] Cube Specimens), ASTM International, West Conshohocken, PA
41. Nguyen TNM, Kim JJ (2021) Energy absorption capacity of SBR latex-modified ordinary portland cement by Charpy impact test. Materials 14:2544
42. Nguyen TNM, Lim NH, Kang YS, Kim JJ (2018) Investigation of impact resistance for latex modified hardened cement pastes. Int J Railway 11(1):10–14
43. Nguyen TNM, Kim JJ (2018) Impact resistance evaluation of cement pastes including admixtures by Charpy impact tests. J Korean Soc Hazard Mitigation 18(6):229–233
44. Yajun J, Cahyadi JH (2003) Effects of densified silica fume on microstructure and compressive strength of blended cement pastes. Cem Concr Res 33:1543–1548
45. Amudhavalli NK, Mathew J (2012) Effect of silica fume on strength and durability parameters of concrete. Int J Eng Sci Emerg Technol 3(1):28–35

46. Michal Ž, Tomáš V, Lenka L (2016) Dosage of silica fume in high performance concrete. Key Eng Mater 677:98–102
47. Imam A, Kumar V, Srivastava V (2018) Review study towards effect of silica fume on the fresh and hardened properties of concrete. Adv Concr Constr 6(2):145–157
48. Maagi MT, Jun G (2020) Effect of the particle size of nanosilica on early age compressive strength in oil-well cement paste. Constr Build Mater 259:120393
49. Mosaberpanah MA, Eren O (2016) Relationship between 28-days compressive strength and compression toughness factor of ultra high performance concrete using design of experiments. Procedia Eng 145:1565–1571
50. Murali G, Santhi AS, Ganesh GM (2014) Empirical relationship between the impact energy and compressive strength for fiber reinforced concrete. J Scien Ind Res 73:469–473
51. Marar K, Eren Ö, Çelik T (2001) Relationship between impact energy and compression toughness energy of high-strength fiber-reinforced concrete. Mater Lett 47(4–5):297–304

Damage Detection of the Beam Under Moving Load by Using a Variation of Power Spectrum Density

Vien Le-Ngoc, Luan Vuong-Cong ⓘ**, Toan Pham-Bao** ⓘ**, and Nhi Ngo-Kieu** ⓘ

1 Introduction

The rate of deterioration of the bridge structure with respect to time is increasing due to external influences such as large traffic, storms, and waves, etc. Stemming from the fact that the world has formed measurement and data collection systems fixed on the structure to collect data continuously over time, called structural health monitoring (SHM) system [1]. SHM systems are often used in the important structures of cable-stayed bridges, large-span concrete beam to ensure safety, accuracy, and predictability of works in construction field. The SHM system can diagnose and confirm the workability of the designed structure during each stage of construction [2, 3].

Today, SHM has been recognized as an important technology to assist in assessing the performance of bridges. The SHM system was designed for the purpose of using the vibration response to monitor and evaluate the structural condition. This system has introduced a new approach by using the vibration measurement signal for structural condition assessment. This research approach aims to provide measures to assess the overall structural condition, also known as the vibration-based damage identification (VBDI) method [4].

The damage identification on structures is a significant problem that has been exploited in recent studies. Many parameters are given to identify the change of structure under the effect of defects. The natural frequency is one of the most popular parameters in the studies on assessing the bearing capacity in the structure [5]. It is

V. Le-Ngoc · L. Vuong-Cong · T. Pham-Bao (✉) · N. Ngo-Kieu
Laboratory of Applied Mechanics (LAM), Ho Chi Minh City University of Technology
(HCMUT), 268 Ly Thuong Kiet Street, District 10, Ho Chi Minh City, Vietnam
e-mail: baotoanbk@hcmut.edu.vn

Vietnam National University Ho Chi Minh City, Linh Trung Ward, Thu Duc City, Ho Chi Minh
City, Vietnam

the most representative parameter for the ability to show the total stiffness modal of the system through the equation $\omega \approx \sqrt{EJ_x}$. However, many studies show that natural frequency is still not a sensitive enough to apply in reality [6, 7]. Therefore, many worldwide studies have used other features to compensate for the shortcomings of natural frequencies, such as damping coefficient or mode shape. In addition, many studies have combined many different algorithms to increase the sensitivity of features in damage detection, such as wavelet transform [8], statistical [9] or correlation algorithms [10].

In practice, basic features such as mode shape, natural frequency, and damping are only applied to each suitable vibration mode to detect structural damage. However, the structure's vibration by the actual load is a state that multiple various vibration modes, forming a stochastic process. Therefore, each of the above features is suitable for assessing structural weakness if simple vibration modes are merely used. A random vibration's power spectral density (PSD) depends on the natural frequency, damping, and mode shape. Therefore, many studies uesd the shape change of PSD to help us diagnose defects in general. In research by Kumar et al. [11], the experimental results of concrete beams confirmed the effect of the amplitude changes of the peaks in the PSD before and after creating a crack as an indication for locating and monitoring the structural damage. Besides, some researchers also use the derived value from PSD as the shape curve of PSD [12]; the results show that this method improves more than using the PSD value itself. Besides some studies using the PSD value of displacement response, some studies switch to using PSD of acceleration response [13], strain energy [14], and a bending moment of the structure [15]. However, the random excitations are all white noise generated by the oscillator, which is always fixed at one position on the structure. The actual excitations randomly changed in amplitude and location for a bridge structure as traffic load, thereby leading to significant effects of the above methods. To investigating the influence of random moving loads on the vibration spectrum, the article proposes a combination of the spectral moment feature of the PSD and the correlation coefficient to evaluate the shape change of the PSD when the structure has deteriorated. This study is based on the experiment vibration data of the steel beam structure and some bridge spans under moving load to test the proposed method.

2 Theoretical

With a signal $x(t)$ obtained, performed by integral in the infinite domain, we are allowed to transform Fourier:

$$X(\omega) = \int_{-\infty}^{\infty} x(t) e^{-i\omega t} dt \tag{1}$$

Fig. 1 Fourier transform

where $X(\omega)$ is the amplitude of the harmonics of frequency ω, and i is the complex number ($i = \sqrt{-1}$) (Fig. 1).

The measuring signal $x(t)$ is usually within a particular time interval T. Then, the Fourier transform of a finite signal $x(t)$ with period T has the form:

$$X(\omega) = \int_0^T x(t)e^{-i\omega t}\,dt \tag{2}$$

The autocorrelation function R_w measures the correlation between two vibration states of a random signal at two different times. Where N being the number of sample points and τ being the time variable ($\tau = n\Delta t$) and $E[x]$ being the mathematical expectation of the random signal variable $x(t)$, the autocorrelation function is calculated as follows:

$$R_w(\tau) = E[x(t)x(t + \tau)] \tag{3}$$

The PSD S_x of a simple stochastic process is determined from the Fourier transform of the corresponding autocorrelation function R_x. The PSD and the correlation function are pairs of Fourier transforms (known as the Wiener–Khintchine theorem):

$$S_x(\omega) = \frac{1}{2\pi} \int_{-\infty}^{\infty} R_x(\tau)e^{-i\omega t}\,d\tau$$

$$\Leftrightarrow R_x(\tau) = \int_{-\infty}^{\infty} S_x(\omega)e^{i\omega t}\,d\omega \tag{4}$$

In the frequency domain, the PSD represents the energy distribution. In mathematics, the moment is a quantity that describes the shape of a set of points. The moment can also be understood as a property representing a distribution. Therefore, the concept of the spectral moment is proposed to investigate the change of spectral shape or energy distribution of the response signal in frequency domain.

For a continuous signal, the moment is calculated using the following general formula:

$$SM_{(n)} = \int_{-\infty}^{\infty} |\omega - \omega_0|^n S_x(\omega) d\omega \tag{5}$$

where $SM_{(n)}$ is the nth order spectral moment of the PSD $S_x(\omega)$

ω_0 is the frequency to choose the vertical axis for the calculation of the spectral moment.

For a one-degree-of-freedom system, we have the following equation:

$$m\ddot{x} + c\dot{x} + ky = f(t) \tag{6}$$

where m is mass, k is stiffness, and c is damping coefficient.

According to Eq. (6), the natural frequency ω_n and damping ratio ξ calculated using the formula:

$$\omega_n^2 = \frac{k}{m}, \quad 2\xi\omega_n = \frac{c}{m} \tag{7}$$

From Eq. (7), then Eq. (6) can be rewritten as:

$$\ddot{x} + 2\xi\omega_n\dot{x} + \omega_n^2 y = \frac{f(t)}{m} \tag{8}$$

Now, the frequency response function (FRF) has the form [16]:

$$H(\omega) = \frac{X(\omega)}{F(\omega)} = \frac{1}{m} \cdot \frac{1}{-\omega^2 + 2i\xi\omega_n\omega + \omega_n^2} \tag{9}$$

Then, the PSD $S_x(\omega)$ of the input responses is calculated through the FRF and the PSD of the same force function $S_f(\omega)$ as follows:

$$S_x(\omega) = |H(\omega)|^2 S_f(\omega) \tag{10}$$

From the FRF at each mode, we have the FRF of the system at position i caused by the excitation source at position j as follows:

$$H_{ij}(\omega) = \sum_{r=1}^{\infty} \phi_{ir}\phi_{jr} H(\omega) \tag{11}$$

From Eqs. (5), (10), and (11), we get the equation:

$$SM_{(n)} = \int_{-\infty}^{\infty} |\omega - \omega_0|^n S_f(\omega) \left| \sum_{r=1}^{\infty} \frac{\phi_{ir}\phi_{jr}}{(\omega_r^2 - \omega^2) + 2i\xi_r\omega_r\omega} \right|^2 d\omega \qquad (12)$$

where ϕ_r is mode shapes

ω_r is the natural frequency of the rth mode.

3 Experimental Model

The experimental model was held at the Laboratory of Applied Mechanics of the Ho Chi Minh City University of Technology. The system includes steel beam, vehicle, vehicle transmission system, inverter, signal receiver box, DC power supply, signal amplifier circuit, multi-channel receiver circuit, and computer. The experimental organization model is described in Fig. 2. Then, proceed to create damage for the beam model with cuts.

Specifically, the beam demensions are length of 1.2 m, width of 0.1 m, and thickness of 0.003 m. The load is modeled by a vehicle whose direction of travel is from B to A. Where K1, K2, K3, and K4 are the sensors and their placement for data collection. There are seven scenarios S1 → S7 of the first cut (the first cut is located right at the K4 sensor). Subsequently, the following scenarios S8 → S9 of the second cut (the second cut is situated right at the K2 sensor) are created, established in Table 1. The second cut is made after the completion of seven amounts of the first cut.

The beams are subject to moving loads (vehicle models) with varying speeds for damage scenarios. The accelerometer will receive the signal at each measurement
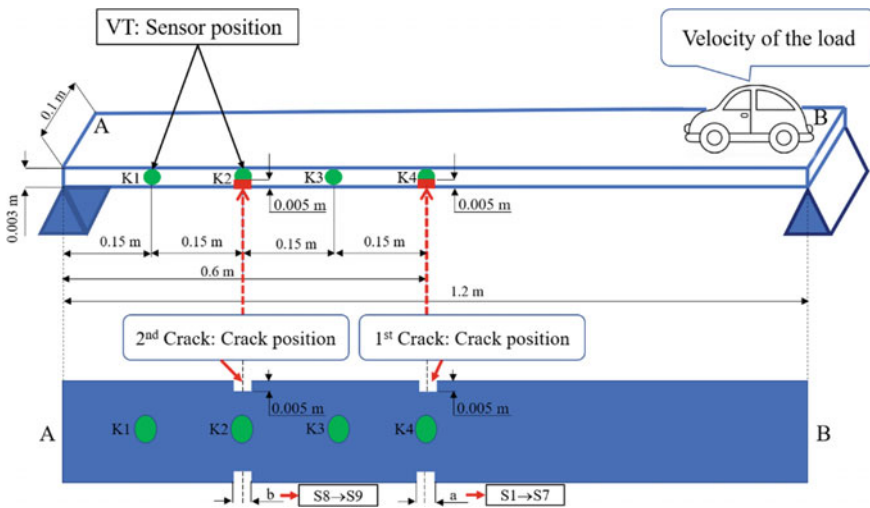

Fig. 2 Experimental model, sensor positions, and cuts

Table 1 Experimental parameters

Sign	Dimension of cuts width (mm) × depth (mm)	Beam status
S0	0.000 × 0.000	Intact
S1	0.004 × 0.005	One cut
S2	0.008 × 0.005	
S3	0.012 × 0.005	
S4	0.016 × 0.005	
S5	0.020 × 0.005	
S6	0.024 × 0.005	
S7	0.028 × 0.005	
S8	0.010 × 0.005 & 0.028 × 0.005	Two cuts
S9	0.020 × 0.005 & 0.028 × 0.005	

thanks to four sensors placed in positions such as Fig. 2. From the signal received from the sensors, conduct spectrum analysis and survey simultaneously the process of changing the mechanical behavior through the PSD. The transform from the original signal to the PSD is shown in Fig. 3.

Depending on the number of peaks displayed on the spectrum, we divide it into regions as Fig. 4.

More clearly, Table 2 shows the borders between regions. The spectrum of K1, K3, and K4 has 14 regions, and the spectrum of K2 has 17 regions.

In this paper, the applied spectral moment is the second-order spectral moment. The moment value is calculated relative to the axis passing through frequency 0
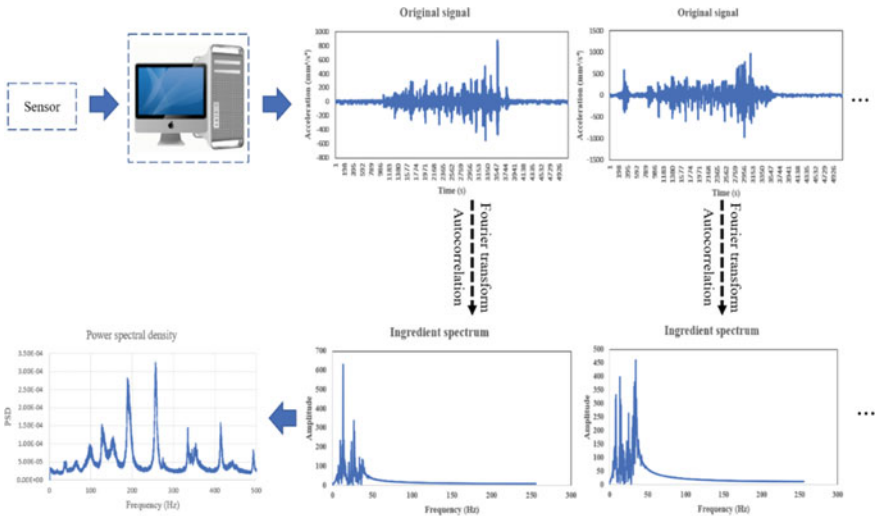
Fig. 3 Diagram of the conversion of an vibration signal to a power spectral density (PSD)
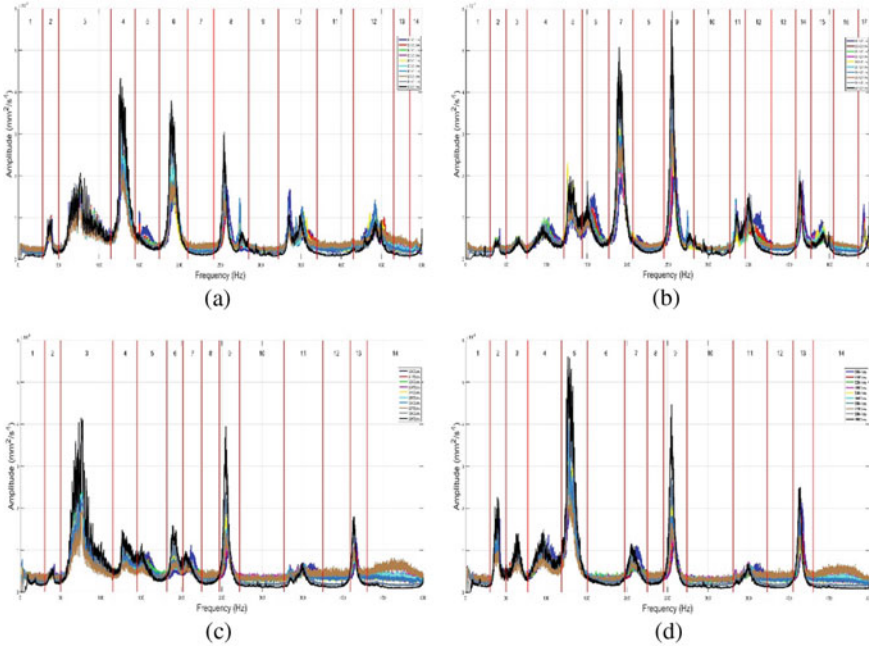
Fig. 4 Spectrum regions through the cuts from S0 → S9. **a** First sensor (K1); **b** second sensor (K2); **c** third sensor (K3); **d** fourth sensor (K4)

($\omega_0 = 0$). Thus, Eq. (5) becomes:

$$SM_{(2)} = \int_{-\infty}^{\infty} |\omega|^2 S_x(\omega) d\omega \tag{13}$$

Applying formula (13) to calculate the moment value of each region of the separated PSD, we get the results in Table 3.

Similarly, the other sensors also give the results of calculating the spectral moment value in each region. From those results, we apply the correlation coefficient for that set of numbers with the equation:

$$r = \frac{\sum (a_i - \bar{a}) \times (b_i - \bar{b})}{\sqrt{\sum (a_i - \bar{a})^2 \sum (b_i - \bar{b})^2}} \tag{14}$$

where a_i, b_i are the ith values of the correlation set, respectively.

$\bar{a}$, $\bar{b}$ are the mean values of the set of correlation numbers, respectively.

In this study, we use the correlation coefficient by comparing the shape change of cPSD across different cutting states with the initial state. From there, we have the following result (Fig. 5).

Table 2 Frequency regions of the spectrum of K1 to K4

No	Frequency region (Hz)			
	K1	K2	K3	K4
1	0–30	0–30	0–30	0–30
2	30–50	30–50	30–50	30–50
3	50–115	50–77	50–115	50–77
4	115–145	77–121	115–145	77–118
5	145–175	121–144	145–182	118–151
6	175–210	144–177	182–202	151–197
7	210–242	177–207	202–225	197–225
8	242–285	207–245	225–247	225–245
9	285–322	245–282	247–272	245–274
10	322–370	282–327	272–327	274–331
11	370–415	327–346	327–375	331–373
12	415–465	346–378	375–409	373–405
13	465–485	378–408	409–430	405–430
14	485–500	408–427	430–500	430–500
15		427–455		
16		455–486		
17		486–500		

Table 3 Some moment values for each region of the power spectrum at the first sensor (K1)

| Region	Moment value through the levels of the cut						
	S0K1	S1K1	S2K1	…	S7K1	S8K1	S9K1
1	5.3	5.6	6.5	**…**	8.5	4.1	2.7
2	48.5	49.6	48.1		46.2	47.4	45.4
3	1517.0	1452.6	1375.0		1173.7	1594.5	1503.5
4	2433.4	2572.0	2618.0		2170.3	3276.3	3496.9
5	1639.5	1278.2	1248.7		1113.1	1218.8	1091.4
6	3671.7	3870.5	4150.1		4143.7	5510.7	6001.1
7	1399.7	1270.5	1586.4		2046.3	985.3	806.2
8	5774.7	5350.6	6007.4		6122.9	6138.7	7435.3
9	2482.2	2851.3	3107.4		3569.7	2271.8	1852.2
10	12,342.2	10,965.6	10,681.4		10,222.4	9803.3	9758.8
11	6128.4	7478.7	7338.7		9602.8	3970.5	3174.9
12	19,894.4	20,958.5	17,743.1		20,316.0	15,038.8	14,104.8
13	3597.0	3791.5	4495.4		7690.0	2332.2	1737.3
14	2613.7	3146.8	3471.2		5083.2	2319.0	2242.8
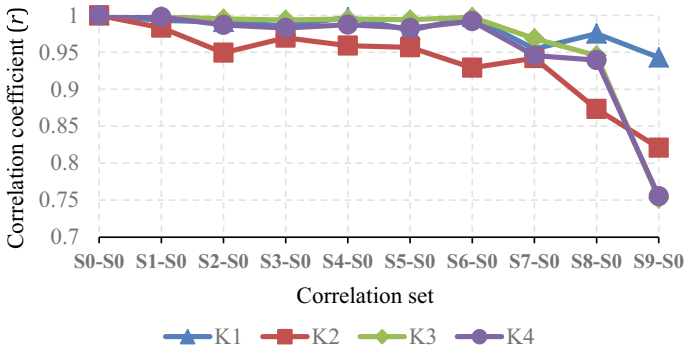
Fig. 5 Correlation coefficient of the cuts compared to the initial state

The results show that the correlation coefficient r tends to decrease with the degree of cutting. Specifically, when the first cut appears, the correlation coefficient will fall, and the correlation coefficient will decrease much faster when there is a second cut.

4 Test on the Actual Bridge

To compare with the results obtained from the experiment, we collected data on Saigon 1 bridge and applied the same method to review the obtained results. However, for the span of the Saigon Bridge, it is not possible to create damage, so we will instead rely on the weakening of the Saigon Bridge over time. Therefore, we will use the data obtained in four different periods to show the weakening of the bridge structure, specifically as follows: first in 2012, followed by 2013, 2015, and 2017. All data were collected on bridge spans 29, 30, 31, and 32 (Fig. 6). On bridge spans, 29, 30, 31, and 32 acceleration sensors are placed at the midpoint of those spans to collect the signal (Fig. 7).

For the convenience of representing on the graph, we sign the spans and measurement times in Table 4.
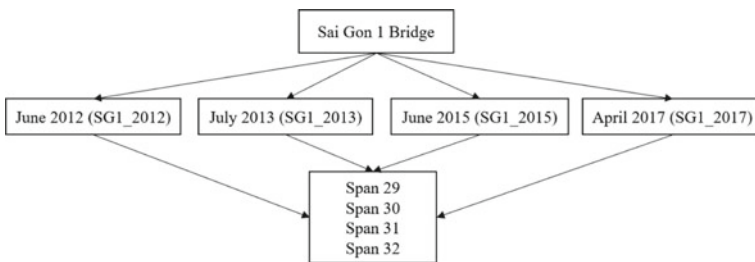

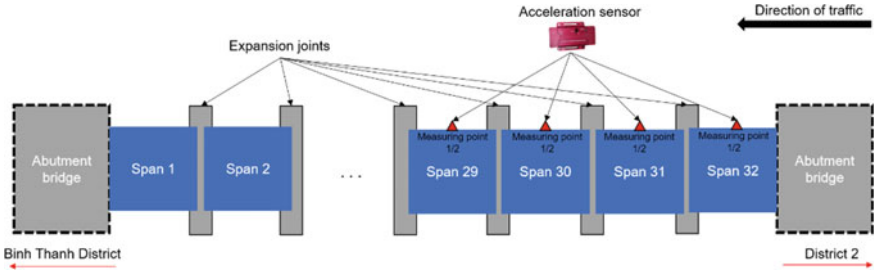**Fig. 6** Time and spans of the bridge taken with the oscillation signal

Fig. 7 Location of the acceleration sensor during data collection at Saigon 1 Bridge

Table 4 Span and measurement time of Saigon 1 Bridge

Span	Measurement time (year)			
	T1 (2012)	T2 (2013)	T3 (2015)	T4 (2017)
S29	S29T1	S29T2	S29T3	S29T4
S30	S30T1	S30T2	S30T3	S30T4
S31	S31T1	S31T2	S31T3	S31T4
S32	S32T1	S32T2	S32T3	S32T4

After collecting the actual data, we proceed to process the data into the PSD. The processing is similar to that described in Sect. 3 (Fig. 3). The PSD and frequency region are shown in Fig. 8.

Table 5 shows the border between the spectrum regions of the span 29, 30, 31, and 32. Due to the similar structure, the number of peaks shown on the spectrum is also relatively similar. Therefore, the regions are similar (8 regions).

Similar to Sect. 3, applying Eq. (13), we can calculate the spectral moment value of each region of the PSD. The results are given in Table 6.

Similarly, we also have the results of the spectral moment values of each region at spans 30, 31, and 32. Then, apply the correlation method to calculate the correlation coefficient value for the sets of spectral moment values of each region as Sect. 3 gets the following results (Fig. 9).

Ti1 is the correlation coefficient between the *i*nd and the *1*st survey (2012). From the initial period of T1 to T4 (2012–2017), the results show that the correlation coefficient tends to decrease over time.

5 Conclusion

The study has performed experimental research tasks, including building models, providing experimental procedures, and data collection and processing on steel beams. Besides, together with the data obtained from the actual bridge (Saigon 1
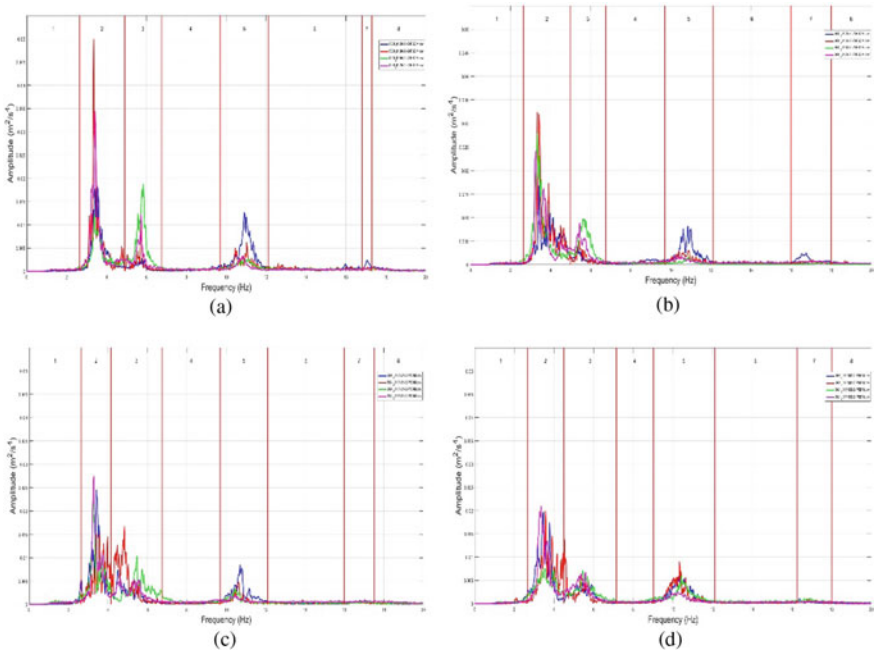
Fig. 8 Power spectrum division over different measurements from 2012 → 2017. **a** Span 29 of Saigon 1 Bridge (S29); **b** Span 30 of Saigon 1 Bridge (S30); **c** Span 31 of Saigon 1 Bridge (S31); **d** Span 32 of Saigon 1 Bridge (S32)

Table 5 Frequency regions of the spectrum of S29 to S32

Region	Frequency region (Hz)			
	S29	S30	S31	S32
1	0.00–2.65	0.00–2.65	0.00–2.65	0.00–2.65
2	2.65–4.90	2.65–5.00	2.65–4.15	2.65–4.50
3	4.90–6.75	5.00–6.75	4.15–6.75	4.50–7.15
4	6.75–9.70	6.75–9.70	6.75–9.70	7.15–9.00
5	9.70–12.10	9.70–12.10	9.70–12.10	9.00–12.10
6	12.10–16.80	12.10–16.00	12.10–16.00	12.10–16.25
7	16.80–17.30	16.00–18.00	16.00–17.50	16.25–18.00
8	17.30–20.00	18.00–20.00	17.50–20.00	18.00–20.00

bridge), we use the value of the spectral moment to survey and evaluate the structural condition, explicitly using the correlation coefficient for sets of spectral moment values are calculated when separating the PSD.

The results show that the correlation coefficient for the set of spectral moment values in both experiment and actual bridge cases show a decreasing trend with the

Table 6 The moment value of each region of the power spectrum at span 29 of Saigon 1 Bridge

Region	Moment value over different times			
	S29T1	S29T2	S29T3	S29T4
1	0.0343	0.0800	0.1079	0.0941
2	5.2006	6.7632	4.1490	6.6437
3	2.0759	3.5693	12.2758	6.1493
4	3.1233	3.2257	3.7166	3.6535
5	41.9089	18.8725	14.7017	11.4405
6	20.2567	20.0960	18.0995	15.3660
7	8.1234	3.1075	3.5460	3.6950
8	10.6644	10.4697	11.4909	13.3714
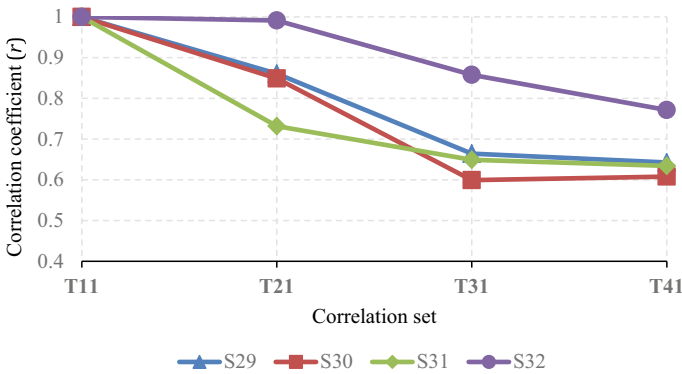
Fig. 9 Correlation coefficient of spectral moments between measurements

deterioration of the structure. The trend of the proposed modal parameter in the experiment coincides with reality, thereby demonstrating the high applicability of the proposed method.

References

1. Sohn H, Farrar CR, Hemez FM, Shunk DD, Stinemates DW, Nadler BR, Czarnecki JJ (2003) A review of structural health monitoring literature: 1996–2001. Los Alamos National Lab USA 1:1–7
2. Ciang CC, Lee J-R, Bang H-J (2008) Structural health monitoring for a wind turbine system: a review of damage detection methods. Measur Sci Technol 19:122001

3. Magalhães F, Cunha Á, Caetano E (2012) Vibration based structural health monitoring of an arch bridge: from automated OMA to damage detection. Mech Syst Signal Process 28:212–228
4. Fan W, Qiao P (2011) Vibration-based damage identification methods: a review and comparative study. Struct Health Monit 10:83–111
5. Javanmardi A, Abadi R, Marsono AK, Md Tap M, Ibrahim Z, Ahmad A. Correlation of stiffness and natural frequency of precast frame system. In: Applied mechanics and materials, pp 141–144 (Trans Tech Publ (Year))
6. Khiem NT, Tran HT (2014) A procedure for multiple crack identification in beam-like structures from natural vibration mode. J Vibr Control 20:1417–1427
7. Salawu O (1997) Detection of structural damage through changes in frequency: a review. Eng Struct 19:718–723
8. Ülker-Kaustell M, Karoumi R (2011) Application of the continuous wavelet transform on the free vibrations of a steel–concrete composite railway bridge. Eng Struct 33:911–919
9. Basöz NI, Kiremidjian AS, King SA, Law KH (1999) Statistical analysis of bridge damage data from the 1994 Northridge, CA, earthquake. Earthq Spectra 15:25–54
10. Koh B, Dyke S (2007) Structural health monitoring for flexible bridge structures using correlation and sensitivity of modal data. Comput Struct 85:117–130
11. Kumar RP, Oshima T, Mikami S, Miyamori Y, Yamazaki T (2012) Damage identification in a lightly reinforced concrete beam based on changes in the power spectral density. Struct Infrastruct Eng 8:715–727
12. Beskhyroun S, Oshima T, Mikami S, Yamazaki T (2005) A numerical study of structural damage dectection using changes in the curvature of power spectral density. J Struct Eng 51A:38–49
13. Beskhyroun S, Oshima T, Mikami S, Tsubota Y (2005) Structural damage identification algorithm based on changes in power spectral density. J Appl Mech 8:73–84
14. Bayissa W, Haritos N (2007) Structural damage identification in plates using spectral strain energy analysis. J Sound Vibr 307:226–249
15. Bayissa W, Haritos N (2007) Damage identification in plate-like structures using bending moment response power spectral density. Struct Health Monit 6:5–24
16. Newland DE (2012) An introduction to random vibrations, spectral & wavelet analysis, 3rd edn. Courier Corporation, New York

Gear Fault Detection, Identification and Classification Using MLP Neural Network

Afia Adel, Ouelmokhtar Hand, Gougam Fawzi, Touzout Walid, Rahmoune Chemseddine, and Benazzouz Djamel

1 Introduction

Gears are small units having a large transmission rate. For example, gears are often used in many mechanical systems, including vehicles, tools and other machinery. As a result, unexpected gear failures can directly impact the entire mechanism's performance, leading to potentially catastrophic breakdowns or massive financial costs. Therefore, gear fault diagnosis is now a critical factor in avoiding major incidents and ensuring the smooth running of industrial machinery addition operators' safety. Vibration analysis is being intensively studied in order to detect early failure. Vibration signals contain significant dynamic information regarding gearbox condition. Therefore, fault features may be gathered by analyzing these signals.

Currently, several decomposition methods gained the attention in several investigators. Empirical mode decomposition (EMD), which is a self-adaptive decomposition technique, decomposes the data to a number of intrinsic mode functions (IMFs) [1, 2]. However, EMD suffers from two main disadvantages: end effect, leading to inaccurate instantaneous values on the ends of the decomposed data and mode mixing, whereby waves with same frequency are associated with other IMFs [3–8]. Local mean decomposition (LMD) recently developed by Smith [9] to exceed these limitations. Data signal is decomposed to an amount of product functions (PFs) [8–18]. In contrast to EMD, LMD exhibits a reduced iteration decomposition

A. Adel (✉)
Department of Mechanical Construction and Production Engineering, Houari Boumediene University of Science and Technology, Bab Ezzouar, Algeria
e-mail: adel.afia@usthb.edu.dz

A. Adel · O. Hand · G. Fawzi · T. Walid · R. Chemseddine · B. Djamel
Solid Mechanics and Systems Laboratory (LMSS), Department of Mechanical Engineering, University M'hamed Bougara, Boumerdès, Algeria

number and is able to produce the instantaneous frequency and instantaneous amplitude directly avoiding the use of Hilbert transform (HT) [9–18]. However, LMD suffers from the same limits with EMD, namely the end effect and mode mixing [16–18], and DWT has been a popular preferred decomposition method for many works [19–24]. DWT decomposes the signal with a both temporal and frequency bandpass filter into a collection of signals with a particular frequency band [19–22]. Yet, the dyadic step in the subsampling procedure acts as the biggest problem for DWT. Maximal overlap discrete wavelet transform (MODWT) is an enhanced implementation of DWT in order to avoid the undersampling process but still has poor frequency resolution [25–27]. Maximal overlap discrete wavelet packet transform (MODWPT) takes over DWT and MODWT [25–27]. MODWPT decomposes the data signal to multiple simple components and provides the circular shift equivariance property [25–27]. MODWPT offers a uniform frequency bandwidth, overcoming the time-varying transformation [25–27].

Presently, for classification phase, intelligent techniques like artificial neural networks ANN [27, 28], fuzzy logic systems [29, 30], neuro-fuzzy systems [31–33] are the most common methods used. Therefore, the aim of this work is to offer an intelligent automatic new technique using MODWPT, entropy and MLP neural network for detecting and distinguishing various kinds of faults under several loads and speeds.

2 Theoretical Background

2.1 MODWPT

MODWPT is a further development of DWT and MODWT [27]. Similar to Mallat's algorithm, MODWPT also utilizes quadrature mirror filters [27]. Assume that $\tilde{g}_l$ and $\tilde{h}_l$ are a low-pass and a high-pass filter, respectively, while L stands for their length (L is even). Filters are designed as follows [27]:

$$\left\{ \begin{array}{l} \sum_{l=0}^{L-1} \tilde{h}_l^2 = \frac{1}{2} \\ \sum_{l=0}^{L-1-2k} \tilde{h}_l \tilde{h}_{l+2k} = 0, \quad k = 1, 2, \ldots, \frac{1}{2}(L-2) \\ \tilde{g}_l = (-1)^{l+1} \tilde{h}_{L-l-1}, \quad l = 0, 1, \ldots, L-1 \end{array} \right\} \tag{1}$$

Contrary to Mallat's algorithm that uses a 2-base decimation operation, MODWPT uses an interpolation. In particular, at MODWPT level, $2^{j-1}-1$ zeros are provided between two consecutive adjacent coefficients of $\tilde{g}_l$ and $\tilde{h}_l$ to assure that the produced wavelet coefficients (WTs) for every wavelet sub-band have the same length as the original signal.

For a discrete time sequence $\{x(t), t = 0,1,\ldots,N-1\}$, WTs $\{W_{j,n,t}\}$ of the nth sub-band at level j are computed by

$$W_{j,n,t} = \sum_{l=0}^{L-1} \tilde{f}_{n,l} W_{j-1,[n/2],(t-2^{j-1}l) \bmod N}, \quad t = 0, 1, \ldots, N-1 \tag{2}$$

With $n = 0, 1.\ldots,2^j - 1$, $W_{0,0,t} = x(t)$

$$\tilde{f}_{n,l} = \begin{cases} \tilde{g}_l, & if\ n \bmod 4 = 0\ or\ 3 \\ \tilde{h}_l, & if\ n \bmod 4 = 1\ or\ 2 \end{cases} \tag{3}$$

2.2 MLP Neural Network

MLP neural network is built with one input, one output and several hidden layers of computational nodes called "neurons", where nodes number in the output and input layers is equal to the number of targets and inputs, respectively [34].

Figure 1 illustrates a typical MLP architecture with $x_1, x_2,\ldots, x_i$ and $y_1, y_2,\ldots, y_k$ being the input and output nodes, respectively.

u_j is the jth node output in the hidden layer and is given as follows:

$$u_j = \varphi_1 \left(\sum_{i=1}^{N} w_{i,j}^1 x_i + b_j^1 \right) \tag{4}$$

φ_1 being the activation function, $w_{i,j}^1$ is the weight of the connection between the ith input and the jth node in the hidden layer, while b_j^1 represent the bias [34].
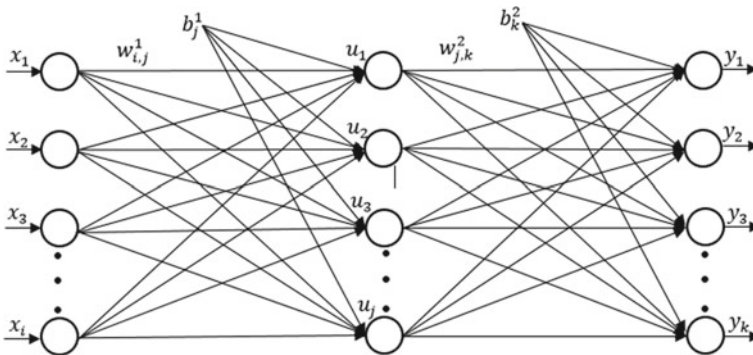

Fig. 1 Three-layer multilayer perceptron (MLP) neural network

Finally, the output y_k is achieved by a 2nd activation function φ_2 at the output layer. y_k is expressed in [34]:

$$y_k = \varphi_2 \left(\sum_{l=1}^{N} w_{j,k}^2 u_j + b_k^2 \right) \tag{5}$$

where superscript 1 in Eq. (4) refers to the first connection between the input and hidden layers, and superscript 2 in Eq. (5) refers to the second connection between the hidden and output layer neurons. There are different forms for the activation functions such as logistic function, hyperbolic tangent and piecewise linear function, respectively, given as below [34]:

$$\varphi(v) = \frac{1}{1 + e^{-v}} \tag{6}$$

$$\varphi(v) = \frac{1 - e^{-2v}}{1 + e^{-2v}} = \frac{2}{1 + e^{-2v}} - 1 \tag{7}$$

$$\varphi(v) = v \tag{8}$$

3 Experimental Study

Experimental data sets were delivered by INSA laboratory Lyon, France [27, 28]. A gearbox with 25/56 gear ratio is taken as a test rig. The movement through the 2 shafts is created by a DC electric motor having 3600 r/min nominal speed. The torque is transferred to the gearbox by the coupling, wherever multiple gear defect patterns are mounted. Output shaft is coupled to a magnetic power brake to produce several resistive torques.

Six gears with various health states are employed to evaluate the efficiency of our proposed method. One is a defect-free pinion (good). The rest exhibit different types of defects. (Missing tooth, chipped tooth in width, tooth root crack, general surface wear and chipped tooth in length).

Three gears are placed simultaneously on the gearbox input shaft. The engagement of every of gears is carried out by an axial motion of the output shaft wheel.

Two accelerometers with a sensitivity of 100 mV/g have been employed to get the vibration data, one fixed horizontally other vertically on the bearing housing. The sampling frequency is 125 kHz, anti-aliasing filter cut-off frequency is 27 kHz, and acquisition time is 30 s.

Table 1 presents the vibration signals gathered from the accelerometers under various working conditions, loads and rotational speeds.

Table 1 Works conditions

Gear state	Speed (RPM)	Speed (RPM)
Good (G)	900, 1200, 1500, 1800, 2400	0, 8, 11
Missing tooth (MT)	900, 1200, 1500, 1800, 2400	0, 8, 11
Tooth root crack (TRC)	900, 1200, 1500, 1800, 2400	0, 8, 11
General surface wear (GSW)	900, 1200, 1500, 1800, 2400	0, 8, 11
Chipped tooth in width (CTW)	900, 1200, 1500, 1800, 2400	0, 8, 11
Chipped tooth in length (CTL)	900, 1200, 1500, 1800, 2400	0, 8, 11

Figure 2 displays the vibration data measured by the gears with diverse conditions with an operation speed of 1200 RPM and 11 Nm as load. Figure 2 makes it obvious that all five defects have no significant influence on the vibration data. No important rise in the signal energy is found.

4 Experimental Results

4.1 Comparison

The comparative study is performed in order to justify why MODWPT performs significantly better even under varying operating conditions. The comparative study is made between LMD-entropy and MODWPT-entropy for four working modes.

MODWPT decomposes the vibration signals into six levels to obtain 64 wavelet coefficients, while LMD decomposes the vibration data into ten sets of FPs. Each wavelet coefficient and PF are picked to conduct the entropy indicator and build the feature vectors. Both methods are applied to the same vibration signals with 6 gear conditions.

The entropy indicator trajectories of each approach are given from Figs. 3, 4, 5 and 6 for the LMD-entropy and MODWPT-entropy, respectively.

From Figs. 3, 4, 5 and 6, even for four operating conditions, most of PFs overlap in nearly all points, approving the limits of LMD for identifying and classifying fault features.

However, for our proposed algorithm (MODWPT-entropy), practically, no intersecting between the several gear conditions is observed. These results are found to be superior to those obtained by the above approach (LMD-entropy). Experimental results confirmed the fact that our suggested decomposition approach is able to distinguish and classify various types of gear faults.

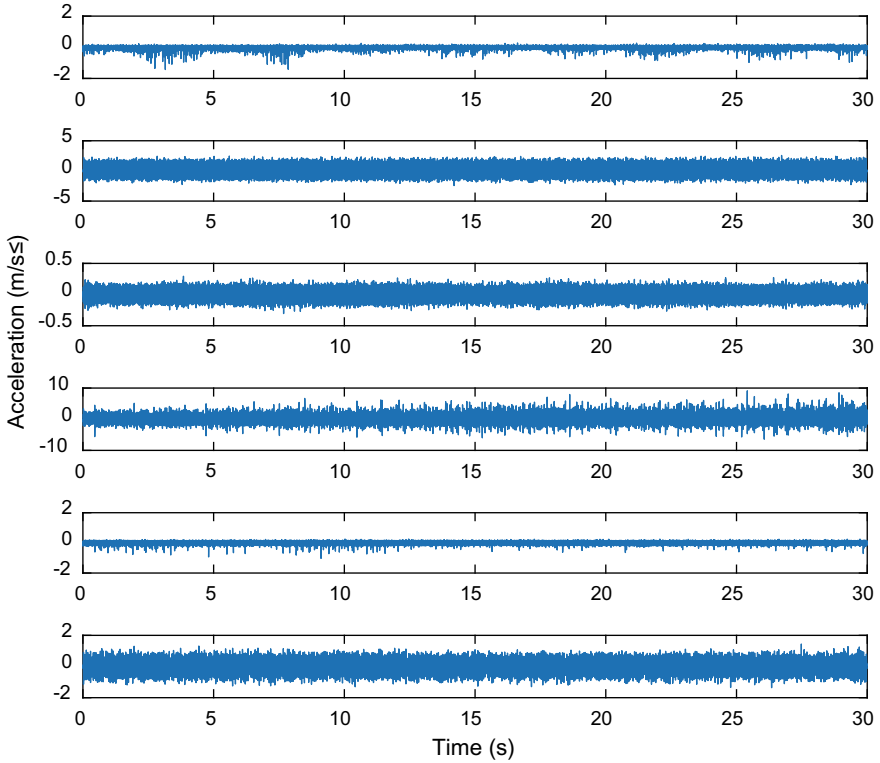**Fig. 2** Vibration data of several gear defect (1200 RPM, 11 Nm): G (**a**), TRC (**b**), CTL (**c**), CTW (**d**), MT (**e**), GSW (**f**)

Fig. 3 Entropy values for every WT computed using MODWPT (**b**) and PF computed by LMD (**a**) under (8 N.m, 900 RPM)
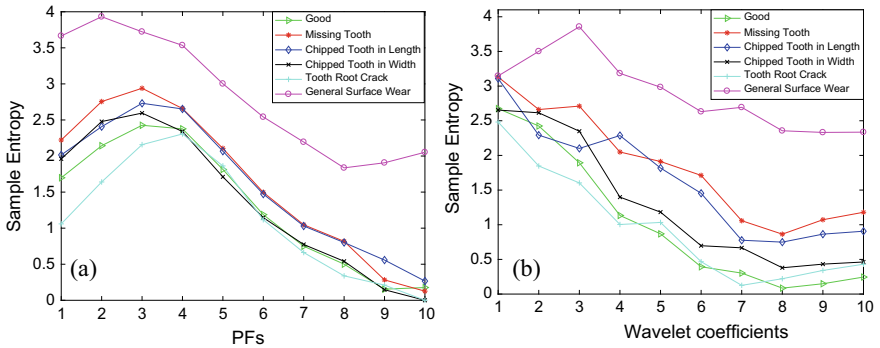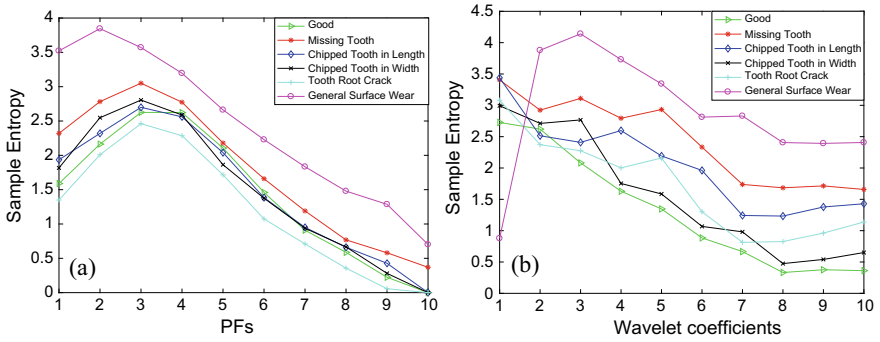
Fig. 4 Entropy values for every WT computed using MODWPT (**b**) and PF computed by LMD (**a**) under (11 N.m, 900 RPM)
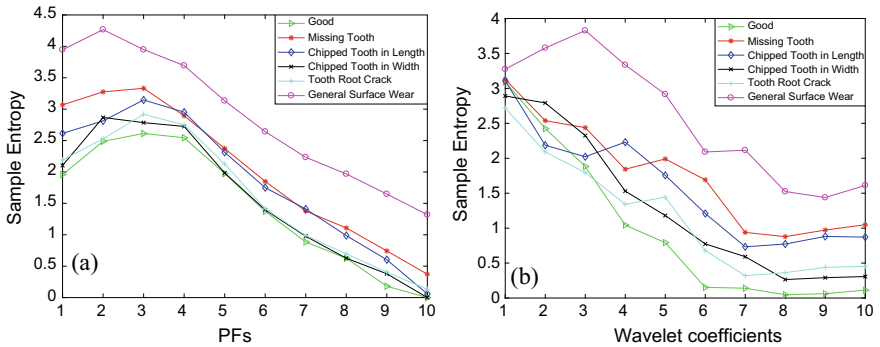

Fig. 5 Entropy values for every WT computed using MODWPT (**b**) and PF computed by LMD (**a**) under (11 N.m, 1200 RPM)
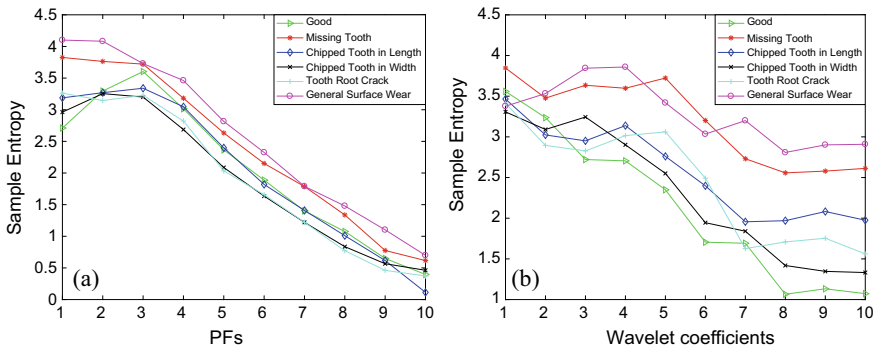

Fig. 6 Entropy values for every WT computed using MODWPT (**b**) and PF computed by LMD (**a**) under (11 N.m, 1800 RPM)

4.2 Instigating MODWPT, Entropy Indicator and the MLP

Within this section, fault feature matrixes derived by MODWPT-entropy are employed to identify and classify the gear health conditions using the MLPNN. The suggested algorithm is evaluated in fifteen different operating modes with six unique gear conditions. Every vibration data is divided into 20 data sets and further decomposed by MODWPT by six levels. Afterward, entropy is implemented to each level of the decomposed signal to get the feature matrix for every health condition.

4.2.1 Experiment Parameters

- *MODWPT Decomposition and Entropy*

  Since MATLAB has built functions to use the MODWPT and entropy, it is as simple as calling the function on the processed data, and the rest is handled by computation when running the script. First, the MODWPT decomposition begins. It is followed by feature extraction (use of entropy algorithm). Finally, the output is a feature matrix for each signal with its respective work condition. The step follow this one is initiating the training of the neural network (See Fig. 7).

- *The Neural Network*

  After the feature matrices are generated, the part of the neural networks comes in. The NN was picked as a set of 3 layers, with 10, 10 and 6 nodes, respectively (See Fig. 8). We used three in this case to get excellent resolution, and so that the data is well interpreted by the model with higher precision.

  The first two layers operate based on the hyperbolic tangent sigmoid transfer function, or in MATLAB, referred to with the function "tansig". This was picked as it is often a suitable trade-off for neural networks, in which speed is critical but the precise transfer function form is not.
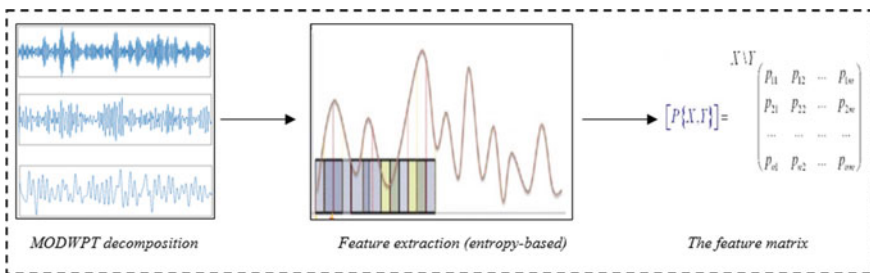

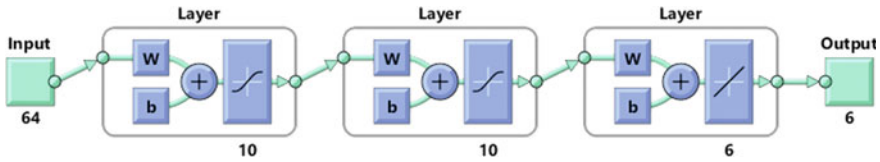**Fig. 7** Flowchart explaining the decomposition and feature extraction

Fig. 8 Constructed neural network model viewed by MATLAB

Sigmoid and linear output neurons are frequently employed for pattern recognition and for function fitting tasks, respectively. In this case, the two types are used, to harness the advantages of both sigmoid output neurons and linear output neurons.

- *Algorithms*

The training algorithm that was picked is that which uses the Levenberg–Marquardt backpropagation, or also known as the damped least-squares method. In MATLAB, it is referred to as "trainlm". This is a built-in network training function which updates the weight and bias values in accordance with the Levenberg–Marquardt optimization. "trainlm" is highly recommended as the supervised algorithm since it is frequently referred to as the fastest backpropagation algorithm in the toolbox, despite the fact that it requires more memory than the other algorithms. Which explains why it was our choice for this experiment.

In summary, MLP employed in this experiment consists of four layers: an input layer, two hidden layers and an output layer. Nodes in the input layer stand for the extracted feature matrixes, with six output nodes, standing for each health condition. Every hidden layer is composed of ten hidden nodes to achieve the highest resolution. Finally, a tan-sigmoid is utilized as the activation function for the hidden layers and linear functions that are implemented for every output layer. The MLP was trained several times to decrease the gap between the network outputs and the matching target values. Input data is split to two groups. A learning set and a training set representing 70% and 30%, respectively. This is very important, as without a training set, the model would be less accurate, and has no way to test its classification system. This
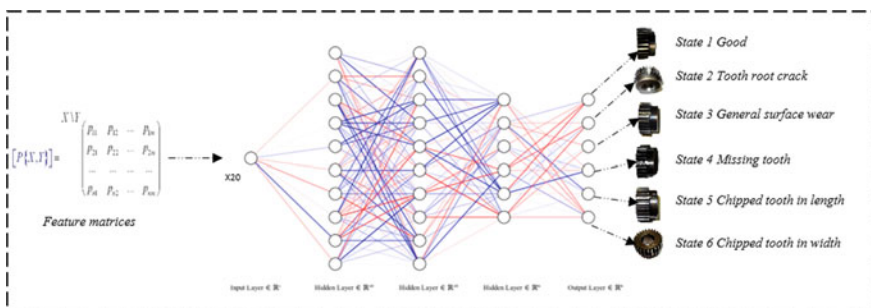

Fig. 9 Flowchart of the neural network architecture schematic and its operation of training

facilities the process by allowing the model to train based on what it has learned and further optimize the neural networks, further reinforcing the bounds between the nodes in an indicative manner.

4.2.2 Running the Experiment and Its Results:

Running the script quickly starts the "nntraintool" MATLAB window, which will use the parameters we explained earlier and launch the training operation. It takes roughly 5 min for the performance to reach the optimal value based on a goal that was manually set. After that the training is finished, before the number of iteration is concluded (See Fig. 10).

Viewing the performance plot displays the trend of the mean squared error (MSE) versus the number of epochs, or simply iterations that the training has undertaken.

Figure 11 demonstrates that our algorithm considerably increases the convergence of the network, showing a performance of 9.9343e-18 using only 186 iterations.

The obtained results given in Fig. 11 show the feasibility and efficiency of the suggested approach. Figure 12 also shows the evolution of important parameters such as the gradient, the Mu and the validation checks.

5 Conclusion

Neural classification is a revolutionary approach to solving one of the oldest issues in engineering. As parts breakdown, systems become unstable and often result in catastrophic failures, which is costly both to lives and capital. Instead of resorting to old methods, neural classification has proven to be efficient, accurate and fast enough to out-shadow any other competing approach.

For the case of gears, often representing crucial parts of machines, it is evident that feature classification is the optimal solution, yet not without its challenges. Since the main difficulty of machine learning is presented in decomposition and feature extraction, having that right algorithm at hand can make a notable difference in the performance of the generated neural network model.

In the case of our selected method, a combination of the revolutionary MODWPT and entropy, the features were shown to be extracted much more accurately for the MLP to train the model in a better precision. The model could classify entropy vectors unknown to it, which it was not trained by, showing that the model was deployable and fully functional. Attempting a comparison with a different decomposition method using the LMD has not yielded satisfactory results, further reinforcing the superiority of MODWPT for this scenario.
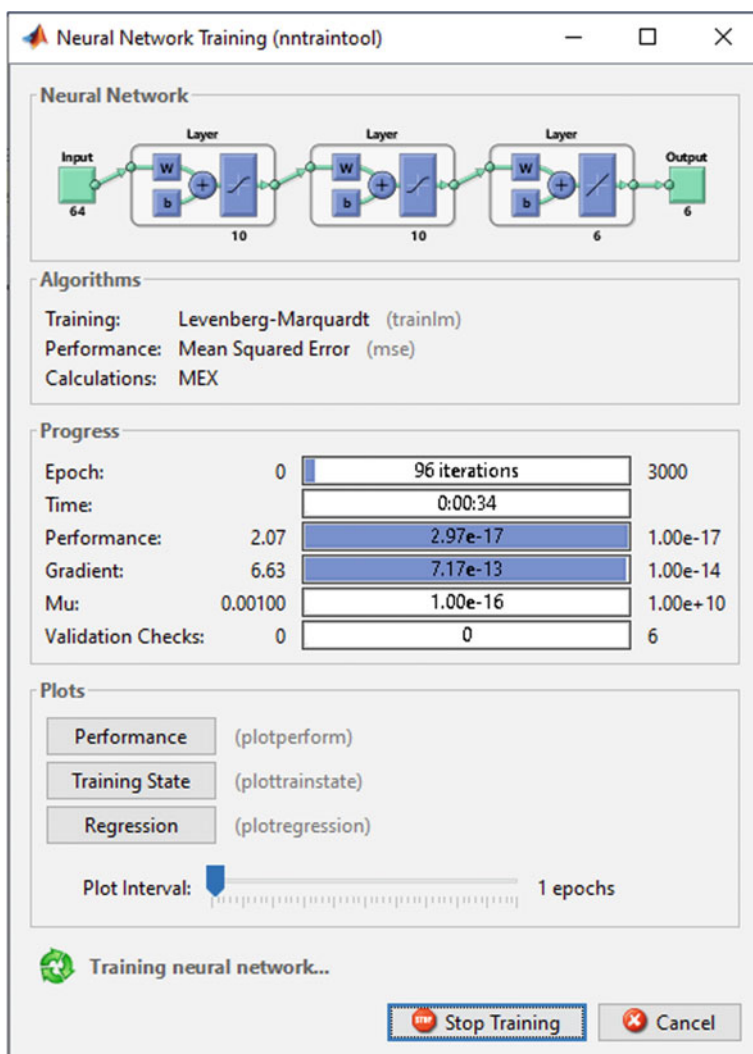
Fig. 10 "nntraintool" training the neural network model
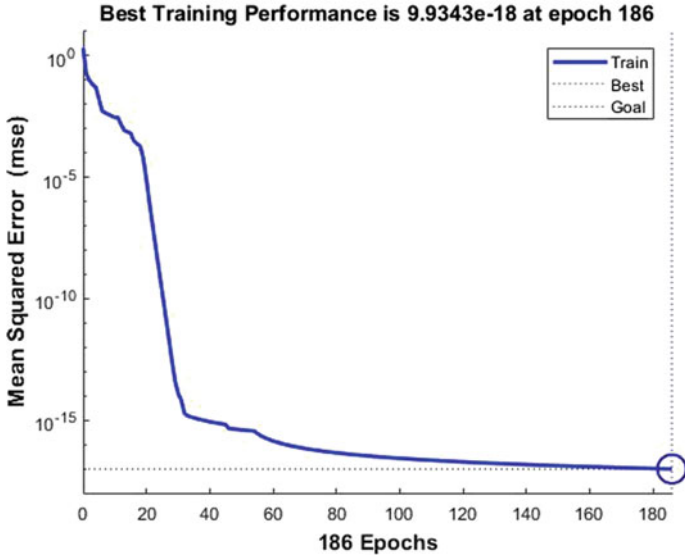
Fig. 11 Performance evaluation of suggested algorithm
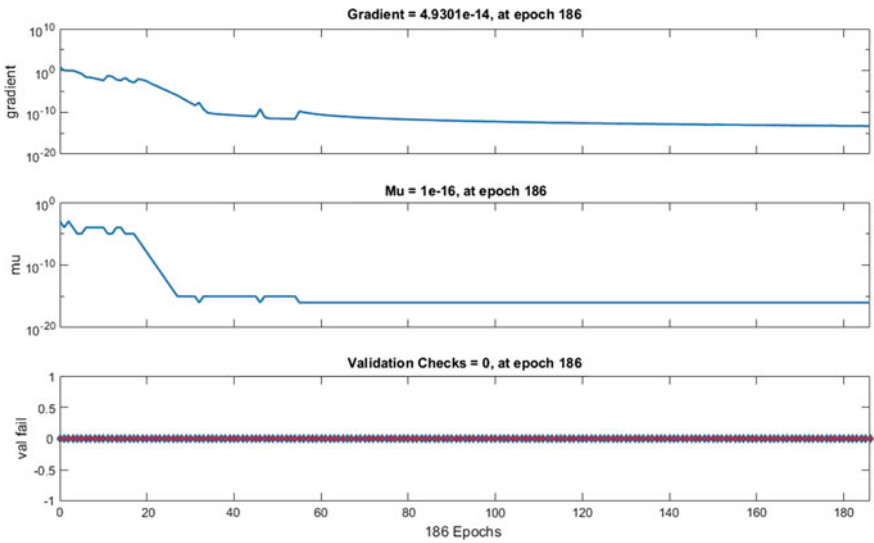

Fig. 12 Evolution of the gradient, the Mu and validation check across 186 epochs or iterations

References

1. Huang NE, Shen Z, Long SR, Wu MC, Shih HH, Zheng Q, Yen N-C, Tung CC, Liu HH (1998) The empirical mode decomposition and the Hilbert spectrum for nonlinear and non-stationary time series analysis. Proc Royal Soc A 454(1971):903–995. https://doi.org/10.1098/rspa.1998.0193
2. Yang Y, He Y, Cheng J, Yu D (2009) A gear fault diagnosis using Hilbert spectrum based on MODWPT and a comparison with EMD approach. Measurement 42(4):542–551. https://doi.org/10.1016/j.measurement.2008.09.011
3. Wu Z, Huang NE (2009) Ensemble empirical mode decomposition: a noise-assisted data analysis method. Adv Adapt Data Anal 1(1):1–41. https://doi.org/10.1142/S1793536909000047
4. Lei Y, He Z, Zi Y (2009) Application of the EEMD method to rotor fault diagnosis of rotating machinery. Mech Syst Signal Process 23(4):1327–1338. https://doi.org/10.1016/j.ymssp.2008.11.005
5. Zhou Y, Tao T, Mei X, Jiang G, Sun N (2011) Feed-axis gearbox condition monitoring using built-in position sensors and EEMD method. Robot Comput-Integr Manuf 27(4):785–793. https://doi.org/10.1016/j.rcim.2010.12.001
6. Mahgoun H, Bekka RE, Felkaoui A (2012) Gearbox fault diagnosis using ensemble empirical mode decomposition (EEMD) and residual signal. Mech Ind 13(1):33–44. https://doi.org/10.1051/meca/2011150
7. Amarnath M, Krishna IRP (2013) Detection and diagnosis of surface wear failure in a spur geared system using EEMD based vibration signal analysis. Tribol Int 61:224–234. triboint.2013.01.001
8. Yang CY, Wu TY (2015) Diagnostics of gear deterioration using EEMD approach and PCA process. Measurement 61:75–87
9. Smith JS (2005) The local mean decomposition and its application to EEG perception data. J R Soc Interface 2(5):443–454. https://doi.org/10.1098/rsif.2005.0058
10. Chen B, He Z, Chen X, Cao H, Cai G, Zi Y (2011) A demodulating approach based on local mean decomposition and its applications in mechanical fault diagnosis. Meas Sci Technol 22(5):055704. https://doi.org/10.1088/0957-0233/22/5/055704
11. Cheng J, Zhang K, Yang Y (2012) An order tracking technique for the gear fault diagnosis using local mean decomposition method. Mech Mac Theor 55:67–76. mechmachtheory.2012.04.008
12. Cheng J, Yang Y, Yang Y (2012) A rotating machinery fault diagnosis method based on local mean decomposition. Dig Signal Process 22(2):356–366. https://doi.org/10.1016/j.dsp.2011.09.008
13. Liu WY, Zhang WH, Han JG, Wang GF (2012) A new wind turbine fault diagnosis method based on the local mean decomposition. Renew Energy 48:411–415. https://doi.org/10.1016/j.renene.2012.05.018
14. Kidar T, Thomas M, Guilbault R, El Badaoui M (2013) Comparison between the efficiency of L.M.D and E.M.D algorithms for early detection of gear defects. Mech Ind 14(2):121–127. https://doi.org/10.1051/meca/2012037
15. Liu H, Han M (2014) A fault diagnosis method based on local mean decomposition and multi-scale entropy for roller bearings. Mech Mach Theory 75:67–78. https://doi.org/10.1016/j.mechmachtheory.2014.01.011
16. Liu Z, Jin Y, Zuo MJ (2016) Time-frequency representation based on robust local mean decomposition. In: ASME international mechanical engineering congress and exposition. American Society of Mechanical Engineers, New York, 8. https://doi.org/10.1115/IMECE2016-65184
17. Liu Z, Jin Y, Zuo MJ, Feng Z (2017) Time-frequency representation based on robust local mean decomposition for multicomponent AM-FM signal analysis. Mech Syst Signal Process 95:468–487
18. Afia A, Rahmoune C, Benazzouz D. An early gear fault diagnosis method based on RLMD, Hilbert transform and cepstrum analysis

19. Li Z, Ma Z, Liu Y, Teng W, Jiang R (2015) Crack fault detection for a gearbox using discrete wavelet transform and an adaptive resonance theory neural network. J Mech Eng 61(1):63–73. https://doi.org/10.5545/sv-jme.2014.1769

20. Heydarzadeh M, Kia SH, Nourani M, Henao H, Capolino G-A (2016) Gear fault diagnosis using discrete wavelet transform and deep neural networks. In: IECON, 42nd annual conference of the IEEE industrial electronics society. Institute of Electrical and Electronics Engineers, Piscataway, NJ, pp 1494–1500. 7793549

21. Er-raoudi M, Diany M, Aissaoui H, Mabrouki M (2016) Gear fault detection using artificial neural networks with discrete wavelet transform and principal component analysis. J Mech Eng Sci 10(2):2016–2029. https://doi.org/10.15282/jmes.10.2.2016.6.0190

22. Sanz J, Perera R, Huerta C (2012) Gear dynamics monitoring using discrete wavelet transformation and multi-layer perceptron neural networks. Appl Soft Comput 12(9):2867–2878. asoc.2012.04.003

23. Bajric R, Zuber N, Skrimpas GA, Mijatovic N (2015) Feature extraction using discrete wavelet transform for gear fault diagnosis of wind turbine gearbox. Shock Vib 2016:6748469. 1155/2016/6748469

24. Wu J-D, Hsu C-C (2009) Fault gear identification using vibration signal with discrete wavelet transform technique and fuzzy–logic inference. Expert Syst Appl 36(2):3785–3794. 1016/j.eswa.2008.02.026

25. Shan P-W, Li M (2010) Nonlinear time-varying spectral analysis: HHT and MODWPT. Math Probl Eng 2010:618231

26. Afia A, Rahmoune C, Benazzouz D (2018) Gear fault diagnosis using autogram analysis. Adv Mech Eng 10(12):1–11

27. Afia A, Rahmoune C, Benazzouz D, Merainani B, Fedala S (2020) New intelligent gear fault diagnosis method based on Autogram and radial basis function neural network. Adv Mech Eng 12(5):1687814020916593

28. Afia A, Rahmoune C, Benazzouz D, Merainani B, Fedala S (2019) New gear fault diagnosis method based on modwpt and neural network for feature extraction and classification. J Test Eval 49(2):1064–1085

29. Gougam F, Rahmoune C, Benazzouz D, Afia A, Zair M (2020) Bearing faults classification under various operation modes using time domain features, singular value decomposition, and fuzzy logic system. Adv Mech Eng 12(10):1687814020967874

30. Gougam F, Rahmoune C, Benazzouz D, Merainani B (2019) Bearing fault diagnosis based on feature extraction of empirical wavelet transform (EWT) and fuzzy logic system (FLS) under variable operating conditions. J Vibroeng 21(6):1636–1650

31. Touzout W, Benazzouz D, Gougam F, Afia A, Rahmoune C (2020) Hybridization of time synchronous averaging, singular value decomposition, and adaptive neuro fuzzy inference system for multi-fault bearing diagnosis. Adv Mech Eng 12(12):1687814020980569

32. Gougam F, Chemseddine R, Benazzouz D, Benaggoune K, Zerhouni N (2020) Fault prognostics of rolling element bearing based on feature extraction and supervised machine learning: Application to shaft wind turbine gearbox using vibration signal. Proc Inst Mech Eng C J Mech Eng Sci 6:0954406220976154

33. Gougam F, Rahmoune C, Benazzouz D, Varnier C, Nicod JM (2020) Health monitoring approach of bearing: application of adaptive neuro fuzzy inference system (ANFIS) for RUL-estimation and Autogram analysis for fault-localization. In: 2020 prognostics and health management conference (PHM-Besançon), 4 May 2020, pp 200–206. IEEE

34. Samanta B (2004) Gear fault detection using artificial neural networks and support vector machines with genetic algorithms. Mech Syst Signal Process 18(3):625–644. https://doi.org/10.1016/S0888-3270(03)00020-7

Monitoring the Change in Vibration Characteristics for Reinforced Concrete Frames Under Various Loadings

Chi-Thien Nguyen, Manh-Hung Tran, Minh-Nhan Pham, Huu-Phuong Nguyen, Tran-De-Nhat Truong, and Duc-Duy Ho

1 Introduction

Structural health monitoring (SHM) plays an important role in civil structures [1]. It helps to detect early abnormalities in the structures, creates favorable conditions for timely repair or replacement of damaged components, assesses the remaining life of the building, and minimizes possible consequences. In addition, non-destructive testing methods are becoming increasingly popular due to benefits such as flexible measurement capabilities and low cost. Vibration-based SHM methods, in particular, have emerged as one of the most indirect and effective ways for detecting and diagnosing structural health. Structural damages cause changes in vibration characteristics such as natural frequencies, mode shapes [2–4]. Based on the change of vibration responses, damages can be detected, both in terms of location and extent.

Nowadays, reinforced concrete (RC) frames are widely used in civil structures. The RC frames serve as the primary bearing structure and ensure overall rigidity and stability of the buildings. Many different causes can affect and damage the building, particularly the main load-bearing structures, directly affecting the building's function and life. As a result, SHM in RC frames is critical in order to determine the damage's location and extent, as well as the bearing capacity. The detection and treatment of potential damages as soon as possible will ensure usability and extend the life of the frame structures.

From inheriting previous studies and practical needs, the objective of this study is to evaluate the change of natural frequencies and mode shapes for reinforced concrete frames under various loads. A reinforced concrete frame is modeled by

C.-T. Nguyen · M.-H. Tran · M.-N. Pham · H.-P. Nguyen · T.-D.-N. Truong · D.-D. Ho (✉)
Faculty of Civil Engineering, Ho Chi Minh City University of Technology (HCMUT), Ho Chi Minh City, Vietnam
e-mail: hoducduy@hcmut.edu.vn

Vietnam National University Ho Chi Minh City, Ho Chi Minh City, Vietnam

the finite element (FE) method using ANSYS software. In the model, the frame's damages are considered corresponding to different load levels. The reliability and feasibility of simulation results is verified by comparing them with experimental ones. Finally, the results are analyzed and assessed to conclude the damage states in the reinforced concrete frame.

2 Vibration-Based SHM Methods

2.1 Natural Frequency Change-Based SHM Method

One of the simple and effective methods in monitoring the overall health of structures has been using natural frequency changes to alarm the occurrence of damages [3–6]. For structures, whether damaged or not, the natural frequency is obtained when performing vibration measurement and analysis. Once damage occurs in the structure, the natural frequency tends to decrease in proportion to the decrease in the stiffness of the structure. Based on the change of the natural frequency, the structure's damage level is evaluated. The degree of change in natural frequency is expressed as follows:

$$\Delta f = \frac{|f - f*|}{f} \times 100\% \tag{1}$$

where Δf is the percentage change in natural frequency, f is the undamaged state's natural frequency, and $f*$ is the damaged state's natural frequency. The Δf result of each mode is considered. If there is any structural damage, Δf will be non-zero, and vice versa.

2.2 Mode Shape Change-Based SHM Method

Structural damage detection based on the changes in mode shapes has been introduced and developed through many studies, in which the MAC (Modal Assurance Criterion), a statistical indicator of mode shape similarity, is commonly used [7–9]. MAC index accepts numbers in the range [0;1]. The value of 0 indicates that there is no consistent correspondence; and 1 represents a consistent correspondence in mode shapes. The formula for evaluating the similarity of the mode shape between the undamaged state and the damaged state is given as follows:

$$\text{MAC}(X, X*) = \frac{\left|\sum_{i=1}^{n} \{\phi_X\}_i \{\phi_{X*}\}_i\right|^2}{\left(\sum_{i=1}^{n} \{\phi_X\}_i\right)^2 \left(\sum_{i=1}^{n} \{\phi_{X*}\}_i\right)^2} \tag{2}$$

where *X*, *X** are two states of the structure, *X* represents the initial state when no damage has occurred in the structures and *X** represents the damaged state under the applied load, *n* is the number of data in mode shape under consideration. MAC index evaluates the correspondence of mode shapes between two states. Therefore, the appearance of damage in the structures is warned.

3 Numerical Simulation for Reinforced Concrete Frame

3.1 Numerical Simulation

A reinforced concrete frame under vertical and horizontal loads was selected for simulation in this study, in which, the frame has a height of 2.15 m, a span of 4.05 m, beam sections are 0.2×0.35 m and column sections are 0.25×0.3 m. For beams, the longitudinal rebar consists of $3\phi16$ for tension and compression, the stirrup is sufficiently provided and consists of $\phi8@100/200$. For columns, longitudinal rebar is arranged of $6\phi16$, and $\phi8@100/200$ is used for stirrup according to the diagram of the bearing frame in the plane (Fig. 1). The material properties of concrete and rebar are summarized in Tables 1 and 2. The vertical load on the frame was presented by three concrete blocks of size $1 \times 1.2 \times 1.2$ m for each block. The horizontal load applied to the frame was carried out through a hydraulic jack [10].

A FE model of the RC frame is simulated by using ANSYS APDL (Fig. 2). The types of elements used for this model are shown in Table 3. In this study, seven load levels, listed in Table 4, are selected to investigate the change in vibration characteristics of the frame. From there, the natural frequencies and mode shapes are analyzed for each load level.

3.2 Numerical Results

From the FE model, the results of damaged areas are analyzed and compared with experimental ones in [10]. The damages in particular cases are described in Fig. 3. These indicate that the cracks in the frame are mainly perpendicular. This demonstrates that cracking is caused primarily by bending moments. Besides, at the beam-column joints and the body of columns exhibit inclined cracks at 45° as a result of shear force caused by horizontal loads. The formation and growth of crack zones tend to be the same at these joints. In comparison to the experimental crack results shown in Fig. 4 [10], the cracked regions analyzed using the ANSYS model produce extremely consistent results in terms of crack shapes, locations, and the development of the crack zone. Moreover, the horizontal displacement in the FE model, at the position in Fig. 2 with the load of $P = 322$ kN is 43.74 mm. The corresponding
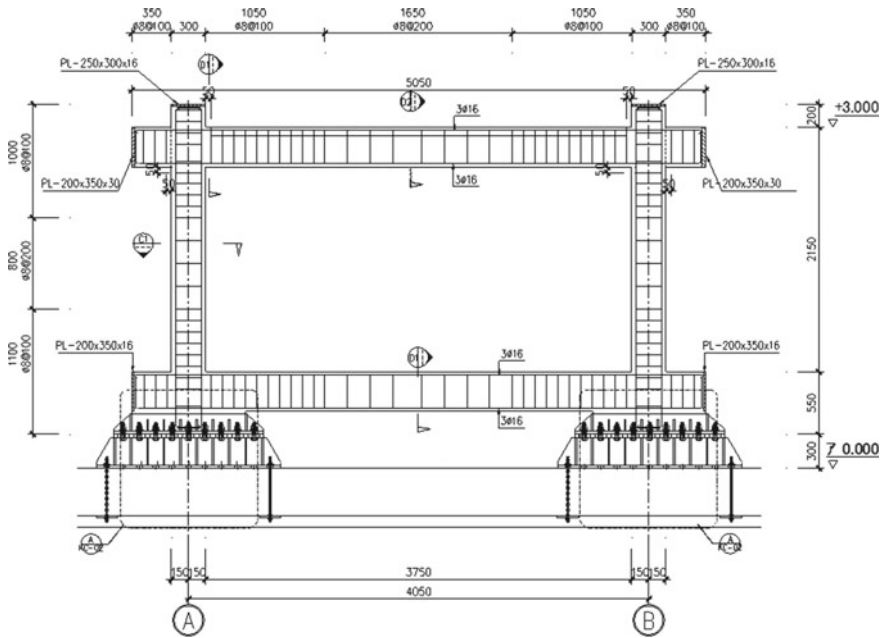
Fig. 1 Reinforced concrete frame

Table 1 Properties of concrete [10]

Property	Value
Compression strength	33 MPa
Tensile strength	2.9 MPa
Elastic modulus	32,500 MPa
Mass of density	2450 kg/m^3
Poisson ratio	0.2
Ultimate strain	0.0035

Table 2 Properties of rebar [10]

Property	Longitudinal rebar	Stirrup
Elastic modulus	210,000 MPa	210,000 MPa
Yield strength	400 MPa	240 MPa
Poisson ratio	0.3	0.3

experimental horizontal displacement at the same position is 43.08 mm [10]. As a consequence, the difference between two results is only 1.5%.

Furthermore, natural frequencies are analyzed and compared to experimental ones [11] to verify the reliability of the numerical simulation. The natural frequencies for the first mode of frame are shown in Table 5 with two states $P = 0$ kN (none of
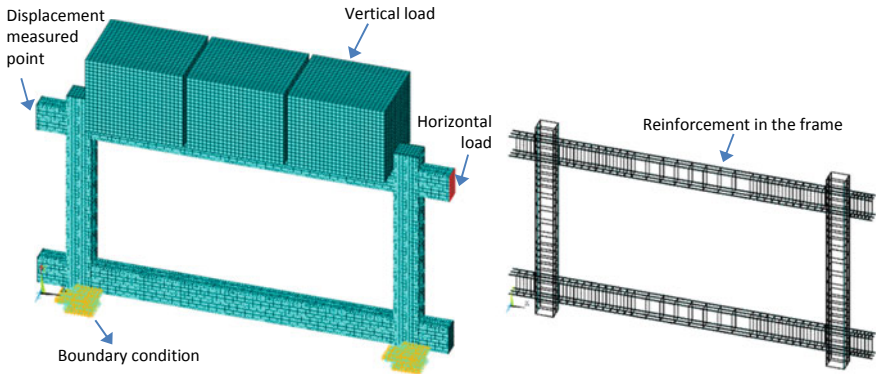
Fig. 2 Finite element model of reinforced concrete frame

Table 3 Types of element in FE model

Material	Element
Concrete	SOLID65
Longitudinal rebar	BEAM188
Stirrup	BEAM188
Steel plate	SOLID185

Table 4 Investigated load levels

Horizontal load P (kN)	Note
ORG	Initial state, none of vertical load
0	With only vertical load, none of horizontal load
98	
147	
224	Yield state of longitudinal rebar
301	
322	Maximum experimental load

horizontal load) and $P = 322$ kN (maximum horizontal load), respectively. The values of natural frequency decrease when damages occur due to reduction of stiffness in the frame. The results between numerical simulation and experiment are good agreement for both load levels, the difference in their range is from 3.6 to 8.5%.

The above-mentioned discussions on the static behavior analysis of crack regions and the dynamic analysis of natural frequency have demonstrated that numerical simulation of the RC frame produces reliable results. This is the foundation for using the analysis results from FE model in SHM of the RC frame by vibration characteristics.

(a) ORG   (b) P = 0 kN

(c) P = 224 kN   (d) P = 322 kN
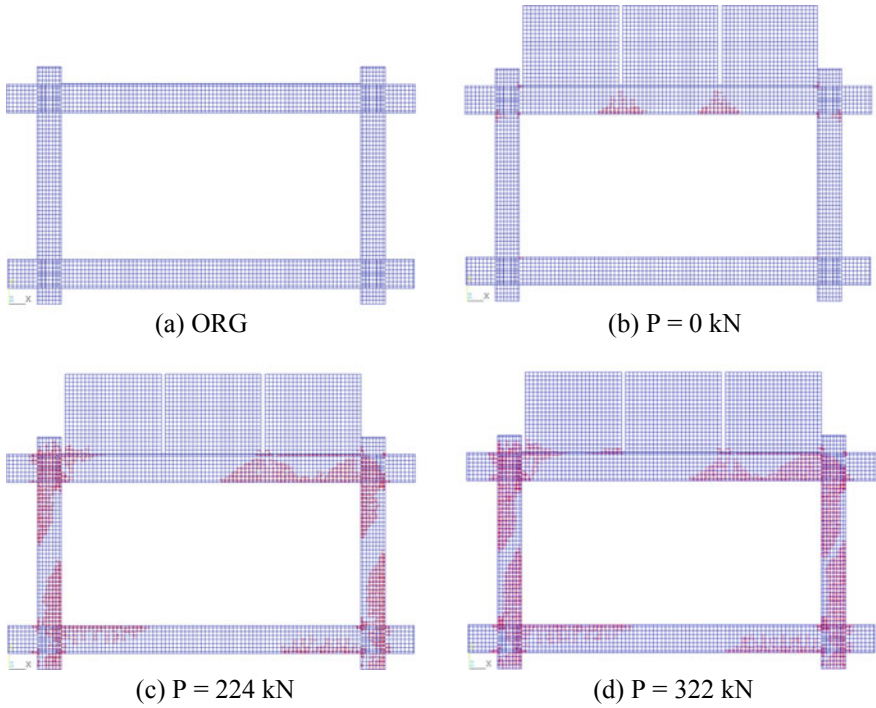
Fig. 3 Cracks in reinforced concrete frame model

(a) Top-left corner   (b) Top-right corner   (c) Bottom-left corner (d) Bottom-right corner

Fig. 4 Cracks in the experiment [10]

Table 5 The first natural frequency

State	Numerical frequency (Hz)	Experimental frequency (Hz)	Different (%)
$P = 0$	8.322	7.617	8.5
$P = 322$ kN	5.420	5.615	3.6

4 Analysis of Change in Vibration Characteristics

4.1 Evaluation the Change in Natural Frequencies

Based on numerical results, the frame's natural frequencies corresponding to the four bending modes for each load level are listed in Table 6 and the variation of natural frequencies is calculated according to Eq. (1) and summarized in Table 7. It is clear that damage regions appeared in the upper beam (Fig. 3b) when vertical loading was applied. This significantly reduces the overall stiffness of the frame; the natural frequencies are reduced by 31.4–71.1% compared to the original state (ORG). In this case, the second mode has the greatest reduction of natural frequency (up to 71.1%); it points out the stiffness of the upper beam contributing significantly to the overall stiffness of the frame, which corresponds to the second mode of the frame.

When applying lateral load to the frame, the higher the load level, the wider the crack areas; and the greater the stiffness decreases, resulting in a much reduced natural frequency. At the load of 224 kN, which occurs plasticity of the reinforcement in the frame, the natural frequency has increased slightly but not significantly. This can be explained by the fact that the frame is changing state at this time, causing a redistribution of stiffness and mass in the structure. The natural frequencies fluctuate at loads greater than 300 kN (closer to frame failure), but they still follow a decreasing trend. At the maximum load ($P = 322$ kN), the value of natural frequencies is reduced by 45.7–75.1% compared to initial state (ORG), and from 2% to 53.5% in the case of only vertical load ($P = 0$ kN). For the frame, the first two bending modes have the most sensitive natural frequency, with more reduction in the change in natural frequencies than the two others.

Table 6 Natural frequencies corresponding to load levels

Load	ORG	0 kN	98 kN	147 kN	224 kN	301 kN	322 kN
f_1 (Hz)	20.684	8.322	5.780	5.559	5.528	5.460	5.420
f_2 (Hz)	54.036	15.601	13.958	13.486	13.715	13.619	13.441
f_3 (Hz)	64.981	36.013	40.164	39.344	38.357	35.911	35.309
f_4 (Hz)	121.500	83.313	67.703	62.595	60.847	57.706	56.499

Table 7 Change in natural frequencies corresponding to load levels

Load	ORG	0 kN	98 kN	147 kN	224 kN	301 kN	322 kN
Δf_1 (%)	0.000	59.766	72.056	73.124	73.274	73.603	73.796
Δf_2 (%)	0.000	71.129	74.169	75.043	74.619	74.796	75.126
Δf_3 (%)	0.000	44.579	38.191	39.453	40.972	44.736	45.663
Δf_4 (%)	0.000	31.430	44.277	48.481	49.920	52.505	53.499

In general, it is a simple and effective method to alarm the occurrence of damage for the RC frame under various loads. As the severity of the damage grows, so does the natural frequency variation in the structure. However, this method only provides accurate results for modes that are extremely sensitive to damage. The change in lower sensitive modes is very minor, so it is difficult to give a precise outcome. Furthermore, damage identification based on change in vibration frequency is incapable of determining the location of the crack zone in the frame.

4.2 Evaluation of the Change in Mode Shapes

The mode shapes of the frame in different states and load levels are extracted from the modal analysis in ANSYS software. Figures 5 and 6 show the four bending modes in two cases, which are the initial state (without considering vertical load) and the first load state (only considering vertical load). The mode shapes under various load levels are investigated and compared to them in the initial state. MAC index, according to Eq. (2) is used to evaluate the change in mode shapes. The values of MAC for upper beam (UB), lower beam (LB), left column (LC) and right column (RC) for each load level is summarized in Table 8.
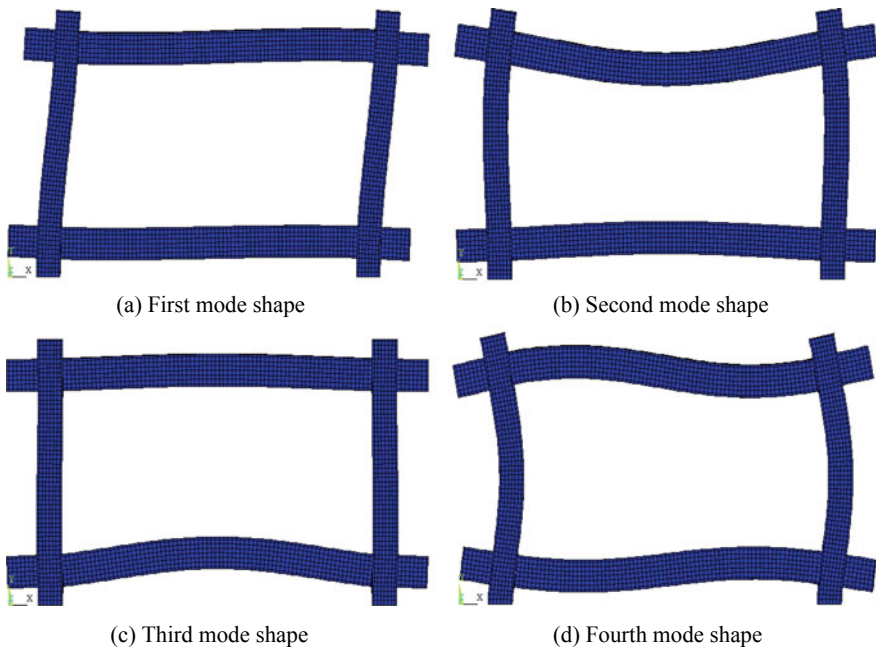

(a) First mode shape

(b) Second mode shape

(c) Third mode shape

(d) Fourth mode shape

Fig. 5 Mode shapes of the frame in initial state

(a) First mode shape

(b) Second mode shape

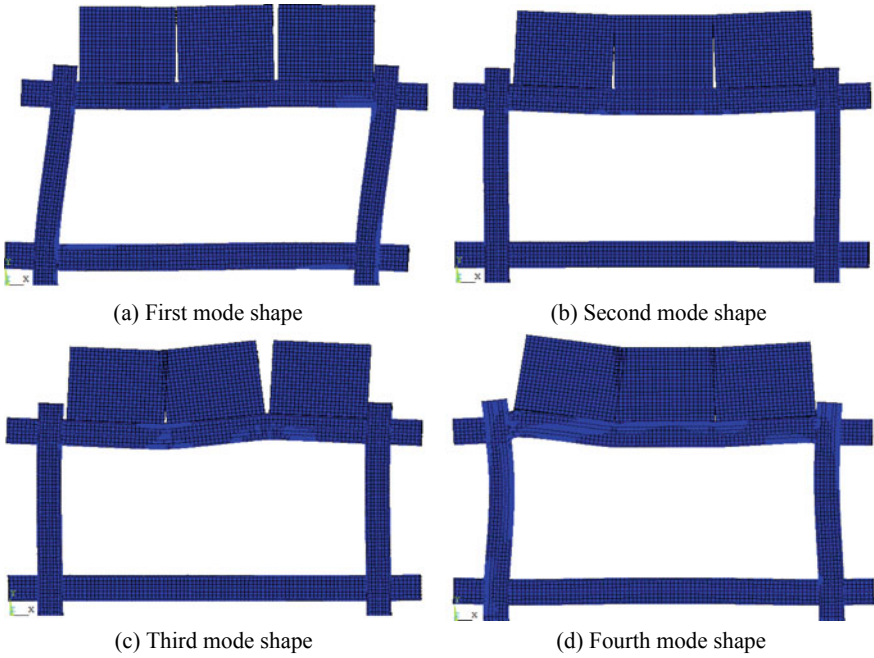(c) Third mode shape

(d) Fourth mode shape

Fig. 6 Mode shapes of the frame in the case of $P = 0$ kN

Table 8 Change in mode shapes corresponding to load levels

Component	Mode shape	ORG	0 kN	98 kN	147 kN	224 kN	301 kN	322 kN
UB	Mode 1	1.000	0.975	0.339	0.259	0.227	0.213	0.216
UB	Mode 2	1.000	0.999	0.973	0.969	0.973	0.978	0.977
UB	Mode 3	1.000	0.000	0.052	0.056	0.038	0.016	0.014
UB	Mode 4	1.000	0.037	0.000	0.001	0.000	0.008	0.008
LB	Mode 1	1.000	0.998	0.834	0.805	0.802	0.796	0.788
LB	Mode 2	1.000	0.966	0.909	0.889	0.878	0.871	0.870
LB	Mode 3	1.000	0.001	0.777	0.838	0.830	0.827	0.846
LB	Mode 4	1.000	0.005	0.173	0.199	0.142	0.053	0.063
LC	Mode 1	1.000	1.000	0.999	0.999	0.999	0.999	0.999
LC	Mode 2	1.000	0.922	0.843	0.822	0.822	0.823	0.822
LC	Mode 3	1.000	0.394	0.401	0.460	0.456	0.452	0.452
LC	Mode 4	1.000	0.803	0.902	0.899	0.922	0.938	0.917
RC	Mode 1	1.000	1.000	1.000	1.000	1.000	1.000	1.000
RC	Mode 2	1.000	0.901	0.944	0.945	0.949	0.951	0.953
RC	Mode 3	1.000	0.389	0.336	0.301	0.290	0.286	0.284
RC	Mode 4	1.000	0.471	0.445	0.404	0.373	0.337	0.352

As shown in Table 8, the MAC value of the upper beam tends to decrease significantly in the first mode shape of the frame. The MAC, after loading, has a value of 0.207 (with 79.3% reduction compared to the initial state). For the second mode shape, MAC index decreases as well, but with a slight change. The value of MAC after loading, in this case, is 0.979 (only declined by 2.1%). Similar to the lower beam, the MAC index in the first two bending mode shapes is 0.793 (reduce by 20.7%) and 0.868 (reduce by 13.2%), respectively. Meanwhile, there are arbitrariness changes in MAC value for remaining mode shape in beams.

The analysis in MAC results shows that each individual member in the RC frame is significantly affected by one or more specific mode shapes. Therefore, it is a different change in different members, depending on the investigated mode shape. In this study, beam members are primarily impacted by the change of the first and the second mode shapes. Also, the left column is primarily represented by the second and the third mode shapes, while the right column is mainly affected by the third and the fourth mode shapes of the frame. In the main mode shape of each member, as the load increases, more damage occurs, the MAC value tends to decrease. The reduction of MAC index indicates the existence and development of damage in the RC frame as the increment of load.

5   Conclusions

In this study, the occurrence and development of damages in an RC frame under various loads are successfully warned based on the change of natural frequencies and mode shapes. The FE model of the RC frame was highly reliable. The numerical results have good accuracy compared to experimental ones for both the static and dynamic analysis. The change in natural frequencies alarmed the occurrence of damage in the RC frame. The variation of natural frequency had different sensitivity depending on the investigated mode. In which, the first and the second modes gave the most significant variation in natural frequency according to damage rate in the structure. These natural frequencies tend to decrease gradually as the damage increases in the frame. Moreover, the change in mode shapes were investigated with good results. In particular, for the main mode shapes of each respective member, the change of them between the damage state and initial state were presented by MAC index. As the load level increased, the damage area expanded, MAC gradually declined and became smaller than 1. Then, the occurrence and development of damage areas in each load level was successfully alerted by the difference in the states. The simultaneous use of two methods will improve the reliability of SHM results. However, these two methods only can evaluate the existence of damage as well as overall development in damaged areas, rather than detecting the location and the extent of damages in the frame. Therefore, these two simple methods are appropriate for the general assessment of structural health.

References

1. Das S, Saha P, Patro SK (2016) Vibration-based damage detection techniques used for health monitoring of structures: a review. J Civ Struct Heal Monit 6(3):477–507
2. Kim JT, Ryu YS, Choi HM, Stubbs N (2003) Damage identification in beam-type structures: frequency-based method vs mode-shape-based method. Eng Struct 25(1):57–67
3. Adams RD, Cawley P, Pye CJ, Stone BJ (1978) A vibration technique for non-destructively assessing the integrity of structures. J Mech Eng Sci 20(2):93–100
4. Cawley P, Adams RD (1979) The location of defects in structures from measurements of natural frequencies. J Strain Anal 14(2):49–57
5. Sato H (1983) Free vibration of beams with abrupt changes of cross section. J Sound Vib 89(1):59–64
6. Yuen MM (1985) A numerical study of the eigenparameters of a damaged cantilever. J Sound Vib 103(3):301–310
7. Allemang RJ (2003) The modal assurance criterion—twenty years of use and abuse. Sound Vib 37(8):14–23
8. Pastor M, Binda M, Harcarik T (2012) Modal assurance criterion. Proc Eng 48:543–548
9. Yan YJ, Cheng L, Wu ZY, Yam LH (2007) Development in vibration-based structural damage detection technique. Mech Syst Signal Process 21(5):198–221
10. Vuong HT (2019) Experimental study on the behavior of reinforced concrete frames strengthening with FRP under vertical and horizontal loads. Master thesis, Ho Chi Minh City University of Technology (HCMUT)
11. RECTIE (2018) Vibration testing of reinforced concrete frames. Report, Faculty of Civil Engineering, Ho Chi Minh City University of Technology (HCMUT)

Development of Modal Strain Energy Method Combined with Multi-phase Genetic Algorithm for Structural Damage Detection in Plates

Thanh-Cao Le, Van-Sy Bach, Thanh-Son Vo, Ngoc-Lan Pham, Thanh-Canh Huynh, and Duc-Duy Ho

1 Introduction

Numerous researchers have been interested in developing methods for detecting structural damage via vibration throughout the last three decades. Additionally, vibration-based damage detection technologies have been widely applied in fields like mechanics, aerospace, and civil construction. The modal strain energy (MSE) approach, in particular, has been demonstrated as one of the most efficient tools for identifying structural damage [1]. Recently, many two-step MSE-based damage detection procedures have been proposed to identify the position and the extent of damaged areas in the plate structures. Fu et al. [2] developed a two-step approach for detecting damage in plate structures made of isotropic homogeneous material by combining MSE with response sensitivity analysis. Vo-Duy et al. [3] described a two-step strategy for detecting damage in laminated composite structures based on the MSE method and an enhanced differential evolution methodology. Dinh-Cong et al. [4] developed an effective two-stage technique for assessing damage in plate-type structures based on MSE variation and the Jaya algorithm. Le and Ho [5] proposed a two-step process combining normalized MSE-based damage index and genetic

T.-C. Le · V.-S. Bach · T.-S. Vo · N.-L. Pham · D.-D. Ho (✉)
Faculty of Civil Engineering, Ho Chi Minh City University of Technology (HCMUT), Ho Chi Minh City, Vietnam
e-mail: hoducduy@hcmut.edu.vn

Vietnam National University Ho Chi Minh City, Ho Chi Minh City, Vietnam

T.-C. Le · V.-S. Bach
Faculty of Civil Engineering, Nha Trang University, Nha Trang, Vietnam

T.-C. Huynh
Faculty of Civil Engineering, Duy Tan University, Da Nang City, Vietnam

Center for Construction, Mechanics and Materials, Institute of Research and Development, Duy Tan University, Da Nang City, Vietnam

247

algorithm (GA) for damage identification in plates, using only the vertical displacement component of the mode shape. Gomes and Giovani [6] displayed an efficient two-step method for identifying damage in laminated composite plates by employing mode shape curvature and a novel metaheuristic Sunflower Optimization method. Fan [7] proposed a two-stage damage identification method based on cross-model modal strain energy and simultaneous optimization to reduce the effect of noise and modal incompleteness.

The above-mentioned methods can detect both the location and the extent of damage in some particular damaged scenarios. However, these methods are ineffective in more complex damage scenarios, such as the minimal damage (less than 10%), adjacent damaged elements, and multiple damages with different locations and damage rates. In such scenarios, the first step located preliminary damaged areas with some wrong detected elements. Therefore, the objective function value with variables dependent on the first step result is hard to converge, and the damage extent identification results will be inaccurate.

To overcome the research gaps mentioned above, this study proposed an enhanced two-stage procedure based on MSE change and an iterative genetic algorithm. The idea of this improvement is that the GA procedure is deployed in many phases to eliminate gradually wrong detected elements. As a result, the size of the variable of the GA procedure will be reduced after every phase. Therefore, the objective function value in the present phase will be more accessible to convergence than in the previous phase, and the extent of the damaged elements will be estimated more and more accurately. Two numerical examples are conducted on a rectangular concrete plate with single and multiple damages to demonstrate the efficiency of the suggested approach.

2 Damage Detection Technology Based on Modal Strain Energy Method Change and Multi-phase Genetic Algorithm

2.1 The Drawback of the Two-Stage Damage Detection Procedure in a Particular Damaged Case

A 300×200 mm rectangular plate with a thickness of 4 mm is simply supported on all four sides, as shown in Fig. 1. The plate is made of aluminum with the material properties given in Table 1. The plate's finite element (FE) model is divided into a mesh 15×10 of nine-node isometric quadrilateral elements in the x and y-direction to guarantee the convergent condition. The parameters for the damage scenario are identical to those in Kumar's study [8], as shown in Table 1. Specifically, the 83rd element is examined with a stiffness decrease of 5%. In the first phase, the MSE technique [5] is applied to the entire plate in order to locate the preliminary damaged regions. Next, the MSE procedure is deployed in this local damaged area to eliminate
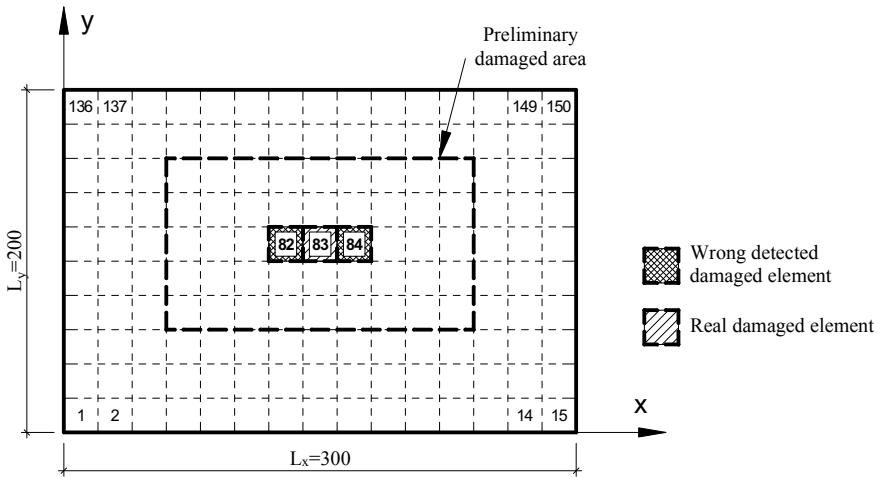
Fig. 1 The preliminary damaged area was detected from the first step

Table 1 Properties of the aluminum material

Properties	Value	Unit
Young's modulus	68.9	GPa
Mass density	2710	kg/m^3
Poisson's ratio	0.33	

more wrong alarms. At the end of the first step, three elements are detected as damaged ones, as illustrated in Fig. 1. In the second step, the GA with the objective function based on MSE change [5] is used as the optimum tool to identify the damaged extent. The damaged ratio identification results in Fig. 2 show that even after 50 generations, the GA cannot identify precisely the extent of elements. The error of the 83rd element is considerable at 25%, and the remaining undamaged elements are diagnosed as damaged ones. Moreover, the fitness value is also significant at 0.17. So, many wrong alarms in the first step dramatically affected the damage extent identification capability of the next step.

Although the original GA [5] cannot identify the damage ratio of the plate after 50 iterations, the damage extents of the 82nd and 83rd elements decrease and converge very quickly. Figure 3 below shows that after 20 iterations, the diagnosed damage extent of the 82nd element is smaller than the 83rd element's one and 0.01.

2.2 Multi-phase Genetic Algorithm

As mentioned in Sect. 2.1, the original two-stage damage detection procedure [5] has some drawbacks. Therefore, this study proposes an improvement to remove
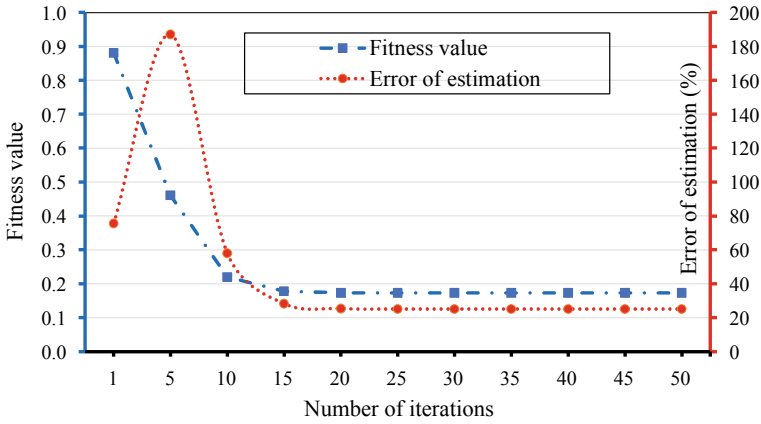
Fig. 2 Fitness value and error of damaged extent estimation using original GA
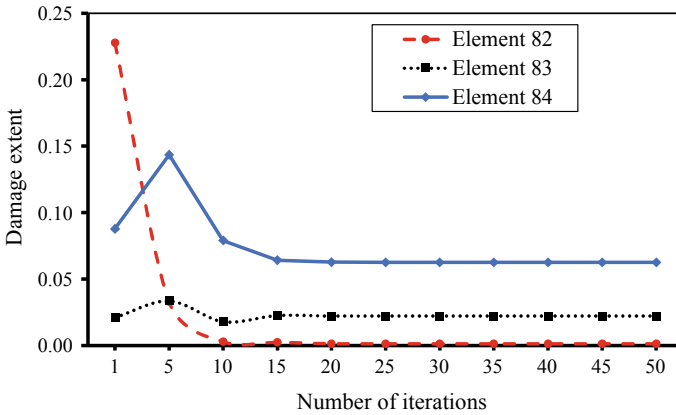

Fig. 3 Damage extent of three damaged elements located from the first step

the misidentified elements from the preliminary damaged area and rerun the GA algorithm. From there, it may gradually remove damaged elements that were falsely warned in the first step. This new method, namely the multi-phase GA algorithm, has many phases, and each stage will filter out a false alarm damaged using a damaged threshold. The threshold is suggested as 1% to investigate the new method's effectiveness because damage less than 1% is trivial and can be neglected. After 50 iterations, if no element has a damaged extent of less than 1%, the element with the most minor damage extent is chosen for elimination. This enhancement is combined with the GA algorithm to increase the diagnostic effectiveness of the two-step procedure first presented by Le and Ho [5]. Figure 4 illustrates a two-stage damage detection procedure that employs the MSE method in conjunction with a multi-phase genetic algorithm.
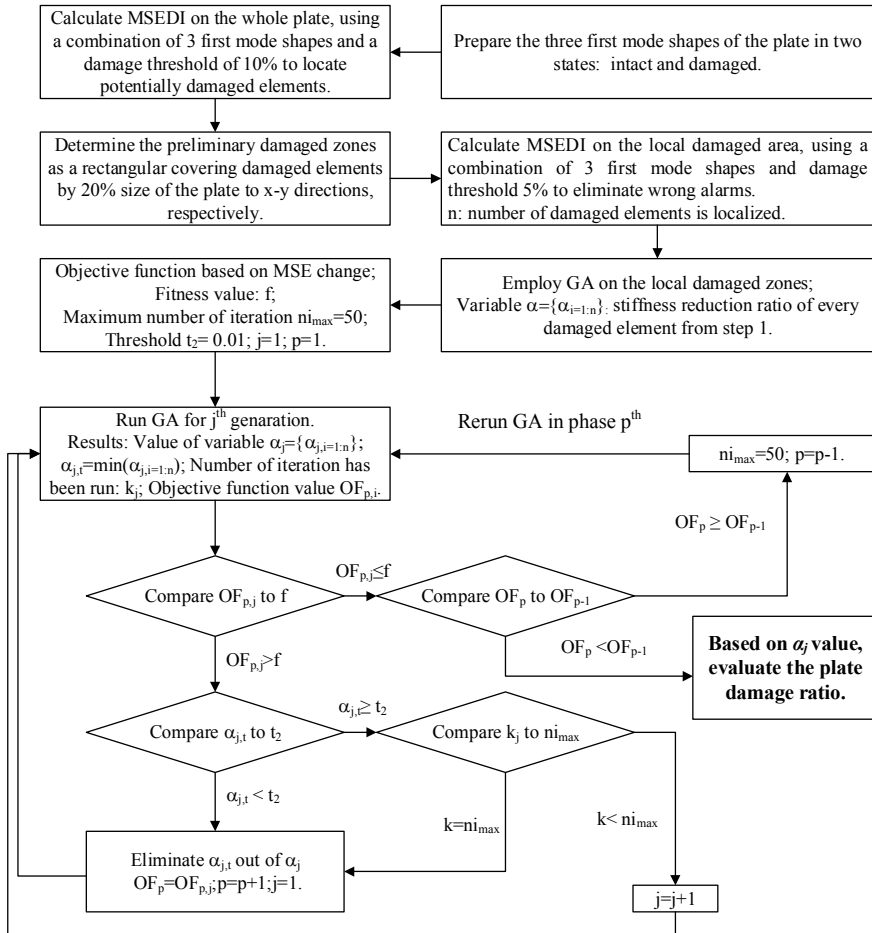
Fig. 4 Workflow of the proposed procedure

2.3 Damage Extent Identification Results

By applying the workflow as presented in Fig. 4, Table 2 shows that the proposed damage identification procedure gives the accurate damage extent after 3 phases. The first phase removed the 82nd element of the damage extent variable after 20 iterations because its extent is convergent and smaller than 0.01. Then, the 84th element is eliminated after nine iterations in the second phase, with the damaged extent nearly equal to zero. Finally, the third phase only gives the exact damaged extent of the 83rd element at 5% after three iterations.

Table 2 Damage extent identification results using multi-phase GA

Phase of GA	Number of iterations	The minimum value of damage extent	Index of denoized element	Fitness function
Damaged elements at 1st phase: 82nd, 83rd, 84th	20	1.4E-03	82nd	1.73E-01
Damaged elements at 2nd phase: 83rd, 84th	9	6.7E-06	84th	4.15E-04
Damaged elements at 3rd phase: 83rd	3	5.0E-02		2.20E-04

Table 3 Detail of damage scenario

Damaged element	Damaged extent (%)
7	5
8	10

3 Further Numerical Verification

3.1 Details of Damaged Scenario

In this further verification, the aluminum plate with the sizes and material properties described in Sect. 2.1 is investigated in a more complex damage scenario. Two adjacent damaged elements at the long edge of the plate are assumedly reduced stiffness with different ratios. The detail of the two damaged elements is shown in Table 3.

3.2 Damage Location Identification Results

The combination of the first three modes is used to improve the accuracy of the damaged locations. Besides, the damaged threshold of 5% is applied for both global and local steps not to miss the damaged elements. As a result, the global MSE detected six damaged elements, including two actual damaged elements and four wrong detected elements, as shown in Fig. 5a. The preliminary damaged area that covers these damaged elements is depicted in Fig. 6. Then, the local MSE is applied to this area to eliminate more wrong detected elements from the global MSE, as presented in Fig. 5b.
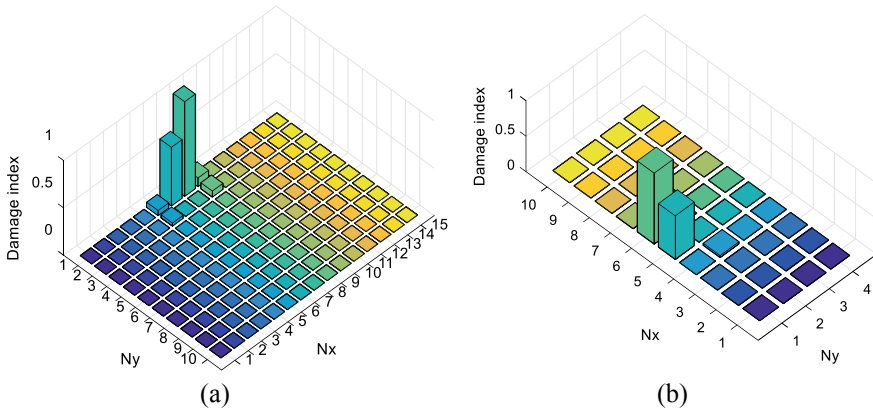
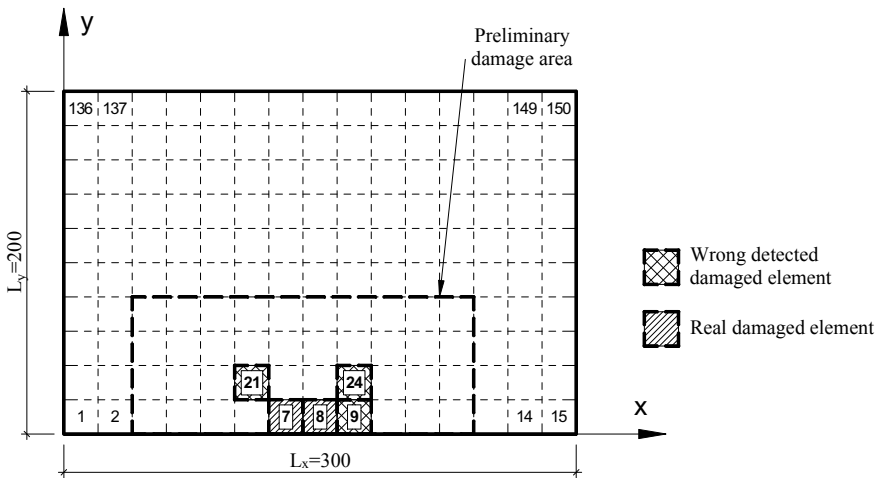**Fig. 5** Damage location identification results: **a** Global MSE; **b** Local MSE

Fig. 6 The preliminary damaged area was detected from the first step

3.3 Damage Severity Estimation Results of the Plate

At the end of the first step, five potentially damaged elements were detected from the local MSE, including the 7th, 8th, 9th, 21st, and 24th elements. Then, the multi-phase GA is applied to the preliminary damaged area to eliminate more wrong alarms. As shown in Table 4, the three first phases of four phase GA removed the 24th, 21st, and 9th elements step-by-step, using a threshold of 0.01. Finally, after four phases, the extent of existing element damage is estimated to be 5% for the 7th element and 10% for the 8th element.

Table 4 Damage extent identification results using multi-phase GA

Phase of GA	Number of iterations	The minimum value of damage extent	Index of eliminated element	Fitness function
Damaged elements at 1st phase: 7th, 8th, 9th, 21st, 24th	45	8.5E-03	24th	5.03E-01
Damaged elements in 2nd phase: 7th, 8th, 9th, 21st	40	3.2E-02	21st	3.59E-01
Damaged elements in 3rd phase: 7th, 8th, 9th	16	2.4E-04	9th	9.78E-04
Damaged elements in 4th phase: 7th, 8th	15	7: 0.049 8: 0.100		9.35E-04

4   Remarkable Conclusions

This study successfully developed a two-stage procedure based on the modal strain energy method and the multi-phase genetic algorithm to improve damage identification effectiveness in plate-type structures. The multi-phase genetic algorithm can eliminate wrong detected damage elements after every phase. Furthermore, reducing the variable size helps the genetic algorithm converge faster and gives a more accurate damaged extent identification result. In addition, the proposed procedure can detect both single and multiple damages in different locations, both inside the plate and at the boundary of the plate. Despite this, the implementation of the suggested procedure needs more research to handle more complex damage cases and eliminate the effect of the damage threshold and environmental noise.

References

1. Das S, Saha P, Patro SK (2016) Vibration-based damage detection techniques used for health monitoring of structures: a review. J Civ Struct Heal Monit 6(3):477–507
2. Fu Y, Liu J, Wei Z, Lu Z (2014) A two-step approach for damage identification in plates. J Vib Control 22(13):3018–3031
3. Vo-Duy T, Ho-Huu V, Dang-Trung H, Nguyen-Thoi T (2016) A two-step approach for damage detection in laminated composite structures using modal strain energy method and an improved differential evolution algorithm. Compos Struct 147:42–53

4. Dinh-Cong D, Vo-Duy T, Ho-Huu V, Nguyen-Thoi T (2018) Damage assessment in plate-like structures using a two-stage method based on modal strain energy change and Jaya algorithm. Inverse Prob Sci Eng 27(2):166–189
5. Le TC, Ho DD (2021) Structural damage identification of plates using two-stage approach combining modal strain energy method and genetic algorithm. Lect Notes Mech Eng 2021:1004–1017
6. Gomes GF, Giovani RS (2020) An efficient two-step damage identification method using sunflower optimization algorithm and mode shape curvature (MSDBI–SFO). Eng Comput
7. Fan Q (2021) A two-step damage identification based on cross-model modal strain energy and simultaneous optimization. In: IOP conference series: earth and environmental science, vol 643, p 012145
8. Kumar KA, Reddy DM (2016) Application of frequency response curvature method for damage detection in beam and plate like structures. In: IOP conference series: materials science and engineering, vol 149, p 012160

Study on Determining the Length of the Cracked Zone of Reinforced Concrete Beams Under Load Using Deformed Shape Curvature Method

Tuan Minh Ha, Quang-Phu Nguyen, Phan-Nhat-Trung Nguyen, Thanh-Duy Tran, Duc-Duy Ho, and Saiji Fukada

1 Introduction

In recent decades, studies on structural health monitoring (SHM) have become popular in all fields to detect damage at an early stage. This assists in detecting structural abnormalities early, creating favorable conditions for timely repair or replacement of damaged components, assessing the remaining life of the building and minimizing the consequences that may occur. When the construction industry is overcrowded, developed countries should rely on monitoring, diagnosis, maintenance and component replacement.

The reinforced concrete structure is a main structure in construction today, appearing in most civil engineering projects. The reinforced concrete beam is the primary bearing structure, ensuring the rigidity and stability of the entire building. Many different causes can affect and damage the building, especially the main load-bearing components, directly affecting the building's use, function and life. Therefore, damage diagnosis to determine the location and extent of the damaged area to

---

T. M. Ha (✉) · Q.-P. Nguyen · P.-N.-T. Nguyen
Faculty of Civil Engineering, HUTECH University, Ho Chi Minh City, Vietnam
e-mail: hm.tuan@hutech.edu.vn

T.-D. Tran · D.-D. Ho
Faculty of Civil Engineering, Ho Chi Minh City University of Technology (HCMUT), Ho Chi Minh City, Vietnam

Vietnam National University Ho Chi Minh City, Linh Trung Ward, Thu Duc District, Ho Chi Minh City, Vietnam

T.-D. Tran
T.Y.Lin International Vietnam Co., Ltd, Ho Chi Minh City, Vietnam

S. Fukada
Faculty of Geosciences and Engineering, Kanazawa University, Kanazawa City, Japan

assess the bearing capacity of existing structures (especially high-rise buildings) is very necessary.

Several methods for diagnosing structural damage to beams based on vibrational and static characteristics have been researched and developed up to this point. Since the 1970s, researchers have been studying the use of structural vibration characteristics (frequency and mode shape) for failure diagnosis, which is now widely used in SHM [1–3]. However, determining the dynamic characteristics of structures frequently necessitates the use of sophisticated analytical equipment and methods. In addition to dynamic features, many current studies investigate the applicability of static features, which can be determined with simpler devices to diagnose damage within structures.

Chen et al. [4] established in 2005 that defects in a beam model may be identified by computing the Gray relational coefficient (GRC) using displacement data at the periods of sound and degradation. Furthermore, Lee and Eun [5] developed an analytical approach for detecting damage by employing displacement curvature and expanding all static deflection data from collected deflection data. Their technique may identify defects in basic cantilever beams, detecting both single and multiple damages based on an accurate displacement measurement. Abdo [6] performed a parametric study for localizing damage using displacement curvature in 2012. The findings demonstrated that changes in displacement curvature might be employed as a useful indicator even when stiffness loss is minimal. Another study examined the efficacy of using displacement curvature obtained from static response data to show the location and extent of damage in Euler–Bernoulli beams [7]. According to numerical results, the displacement curvature obtained from static reactions is sensitive to stiffness reductions. In 2017, Ha and Fukada investigated the use of only direct displacement data to diagnose damage inside a prestressed girder [8]. The authors proposed two indicators: the index of detecting the occurrence of damage and the index of locating the location of the damage. Then, Ono et al. [9] suggested the usage of the displacement-based index (DBI) and gray relation coefficient (GRC) in 2019 in which displacement influence lines of deck slabs are utilized as input into the assessment procedure.

Prior research is frequently conducted for beam structures to be simulated into homogenous bars. The diagnosis was restricted to analyzing the site of one or a few single fractures caused by removing or decreasing the stiffness of the matching element at that place. As a result, it is required to improve the application of this approach for reinforced concrete beam constructions, taking into consideration the joint functioning of concrete and reinforcement. The primary objective of this study is to provide a method for determining the length of the fracture zone in reinforced concrete beams based on the change in deformed shape curvature with different damage levels. A reinforced concrete beam is modeled using the finite element technique and the ANSYS APDL program, taking into consideration the nonlinear behavior of the concrete and reinforcement. The beam is then loaded with varied load levels to see how it behaves and cracks appear. The findings of the study of the curvature of the beam's deformed shape corresponding to each condition are used to locate and diagnose the length of the fracture zone. To assess the accuracy of the

diagnostic technique for reinforced concrete beams, suitable damage thresholds and novel diagnostic signs are proposed.

2 Deformed Shape Curvature Method

2.1 Method Introduction

Pandey et al. proposed a technique for detecting structural damage based on the difference in mode shapes between damaged and healthy structures in 1991 [2]. The current study offers a novel technique based on the curvature difference of deformed shapes based on the suggested mode shape curvature method. When there is a failure inside the structure, the curvature of the deformed shape changes. The displacement curvature is determined by the displacement vector's second derivative. The displacement values of the case before and after failure are determined by studying the nonlinear behavior of the beam model using a finite element software. The curvature of the deformed shape is given by the following equation in this study:

$$u_i^{''} = \frac{u_{i+1} - 2 \times u_i + u_{i-1}}{h^2},$$
(1)

where $u_i^{''}$ is the second derivative of the ith displacement vector, u_i is the displacement at the ith position, u_{i+1} is the displacement at the ith $+ 1$ position, u_{i-1} is the displacement at the ith $- 1$ position and h is the element's length. However, the data of node $i - 1$ is not accessible for the left boundary node, and the data of node $i + 1$ is not available for the right boundary node for the nodes at the two ends of the beam. As a result, the extrapolation method is used to estimate the displacement value at these two nodes. The boundary node is not restricted to the rotation displacement under the circumstances of the pin and roller supports (free rotation). The following two values are proposed to be calculated using the symmetry principle:

$$u_{i-1} = -u_{i+1},$$
(2)

$$u_{i+1} = -u_{i-1}.$$
(3)

2.2 Displacement Curvature Difference Index

Deformed shapes are gathered through studying the nonlinear behavior of the reinforced concrete beam model using ANSYS APDL software at different load levels of the case before and after failure. The difference (Z_i) in the curvature of the two

deformed shapes will be calculated based on the absolute difference in values at each position after having the displacement curvature in a loaded state but no fractures and in the damaged state (state to be diagnosed).

$$Z_i = \left| \left| u_{si}'' \right| - \left| u_{di}'' \right| \right|, \tag{4}$$

where Z_i is the curvature difference at the ith location; u_{si}'' and u_{di}'' are the displacement curvature at position i of the beam in a loaded condition but without cracking and in the state to be diagnosed, respectively. After standardizing the curvature difference (Z_i), , the displacement curvature difference index (DCDI) was calculated using the following equation:

$$\text{DCDI}_i = \max\left[0, \frac{Z_i - \mu}{\sigma} \right], \tag{5}$$

where μ and σ represent the mean and standard deviation of Z_i, respectively. Then, based on the positive side of the curve that represents the relationship between the standardized curvature difference and the element location, the locations where the curve changes significantly are the damaged region of the beam.

2.3   Accuracy Assessment Method

The failure zone of beams is unknown in practice. However, in order to evaluate the diagnostic method's accuracy, the actual crack zone length (as determined by ANSYS simulation) was collected and compared to the result diagnosed using the deformed shape curvature method, thereby determining the method's accuracy. For the aforementioned reasons, this study proposes the damage threshold Z_0 and three evaluation indices A, B and C for a more comprehensive and appropriate evaluation of diagnostic work. To diagnose the location and extent of the damaged area in the problems examined in this study, the threshold $\text{DCDI}_0 = 30\%\text{DCDI}_{\max}$ is proposed to be used (with $\text{DCDI}_{\max}$ being the maximum value of the calculated damage index). The following definitions apply to the accuracy of cracked zone, non-cracked zone and the overall accuracy of A, B and C.

A is the ratio of the length of the diagnostic cracked zone located within the actual cracked zone to the length of the actual cracked zone calculated using Eq. 6. In which case, the diagnostic crack area is the projection of the chart DCDI with $\text{DCDI}_i \geq \text{DCDI}_0$ on the beam axis at mid-span. This index is used to determine the method's accuracy in estimating the extent of cracking in beams.

$$A = \frac{L_{\text{pred}}}{L_{\text{crack}}} \times 100\%, \tag{6}$$

where L_{pred} is the length of the diagnostic cracked zone located within the actual cracked zone and L_{crack} is the length of the actual cracked zone. Accuracy of the non-cracked zone B is the ratio of the length of the diagnostic non-cracked zone to the actual length of the non-cracked zone as determined by Eq. 7.

$$B = \frac{L_{0,pred}}{L_{0,crack}} \times 100\%, \tag{7}$$

where $L_{0,pred}$ is the diagnostic crack-free zone's length (with the diagnostic crack excluded from the actual crack range) is calculated as follows:

$$L_{0,pred} = L_{0,crack} - L_{pred,out}, \tag{8}$$

$L_{0,crack}$ is the actual length of the uncracked zone, as determined by the following equation:

$$L_{0,crack} = L - L_{crack}, \tag{9}$$

$L_{pred,out}$ is the diagnostic cracked zone located outside the actual cracked zone.

The method's accuracy under load changes has not been evaluated using the two diagnostic accuracy indexes for cracked and non-cracked zones, as these indexes are dependent on the magnitude of the crack zone at each load level. Thus, the overall accuracy C is proposed to be calculated as the sum of the diagnostic accuracy of cracked and uncracked areas multiplied by the weights assigned to each region. The weight of each zone (cracked or uncracked) is equal to the ratio of the actual length of the cracked or uncracked zone to the total length of the beam, Eq. 10. Under ideal conditions, the diagnostic accuracy of the cracked zone (A) and the non-cracked zone (B) will be 100%, resulting in accurate diagnosis for the entire beam. Overall accuracy will be used to determine the diagnostic method's reliability over the entire beam length with any load level.

$$C = A \times \frac{L_{crack}}{L} + B \times \frac{L_{0,crack}}{L}, \tag{10}$$

3 Application Problem

The simulated reinforced concrete beam has a length of $L = 4$ m and two fixed connection ends. The rectangular cross-section is $b \times h = 0.2 \times 0.6$ m in size. On the top of the beam, the beam is loaded uniformly with $q = 300\,\text{kN/m}^2$. The simulated concrete material is a linear elastic material with an elasticity modulus of $E = 2.4 \times 10^7$ kN/m^2, a Poisson coefficient of $v = 0.2$, a density of $p = 2.4028$ T/m^3, a uniaxial tensile strength of $f_t = 1400$ kN/m^2, a uniaxial compressive strength of f_c

$= 28{,}000$ kN/m^2, a force transmission coefficient (when the crack is open) of $\alpha = 0.3$ and a force transmission (when the crack is closed) of $\beta = 0.5$.

4 Results of Analysis and Diagnostics

The result of increasing the applied load indicates that the beam's cracking load is 157 kN and its fracture load is 373 kN. The crack patterns in Figs. 1 and 2 correspond to 157 kN and 373 kN load levels, respectively. Additionally, the crack zone in the middle of the span was determined to be 0.2 m wide, corresponding to a load level of 157 kN. The cracked zone length gradually increases with increasing applied load and reaches its maximum value at the 1 m mid-span.

The positive difference in displacement curvature between the 50 kN load level (when no cracks appear) and the data obtained from the loads with cracks are shown in Fig. 3. The damage threshold proposed in this study was 30% of the maximum diagnosed positive difference between each pair of diagnostic data. According to Fig. 3a and 3b, the 30% threshold that crosses the standardized curvature difference is 0.28 m and 0.71 m, while the ANSYS model predicted a cracked zone length of 0.2 m and 0.6 m, respectively. For a load level of 315 kN, the method diagnosed a cracked zone length of 1.05 m at mid-span when the actual length was 1 m, Fig. 3c. Additionally, when considering Fig. 3d, the diagnostic chart shows a rise at the location of the two mount ends, which accurately reflects the location of the crack area on the top surface of the beam at the two mount ends. The accuracy of the diagnostic
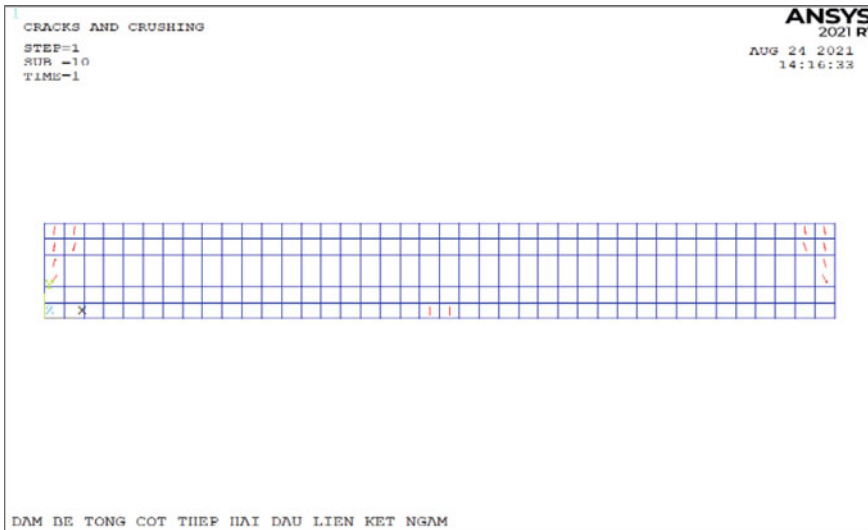

Fig. 1 Crack in the middle of span and two ends of the beam (load level 157 kN)
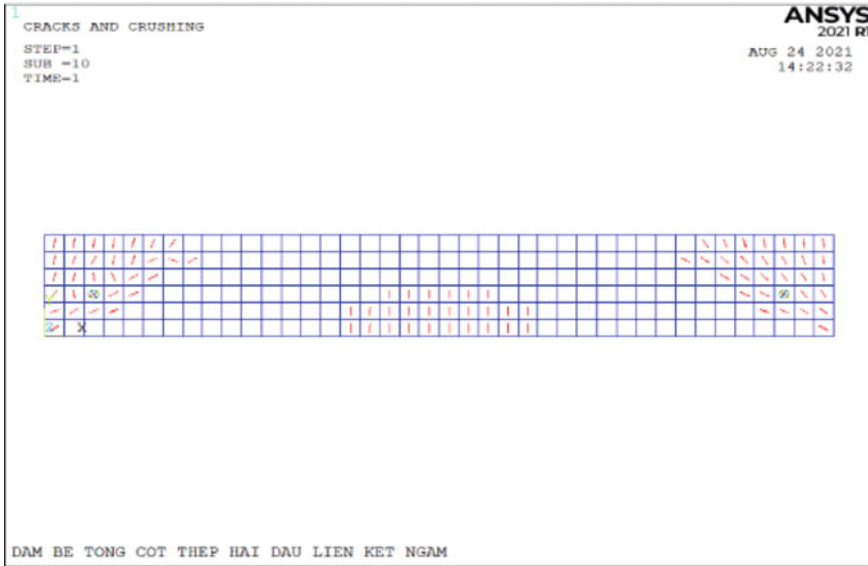
Fig. 2 Crack in the middle of span and two ends of the beam (load level 373 kN)

method is given in Table 1. According to Table 1, the method's overall accuracy in diagnosing cracked zone length is greater than 95% for each load level. Thus, it can be seen that the displacement curvature can be used to accurately determine the length of the cracked zone at the beam's mid-span.

5   Conclusions

The purpose of this study is to propose a method for diagnosing the location and length of the crack area in reinforced concrete beams using only the curvature of the deformed shape as input data. The diagnostic method accepts as input only two states of deformed shapes (uncracked and cracked). From the actual external displacement, this data can be analyzed. Additionally, damage thresholds and three accuracy measures are introduced. The following conclusions were drawn from the study.

The research findings demonstrate that the deformed shape curvature method is capable of accurately diagnosing the location and length of the crack zone in reinforced concrete beams with varying degrees of damage, corresponding to varying loads. According to the results of the accuracy analysis based on the evaluation indexes *A*, *B* and *C*, the deformed shape curvature method can diagnose the cracked zone length with the lowest overall accuracy of 95% for the load level investigated in this study. This enables the method to be used in practice for inspecting
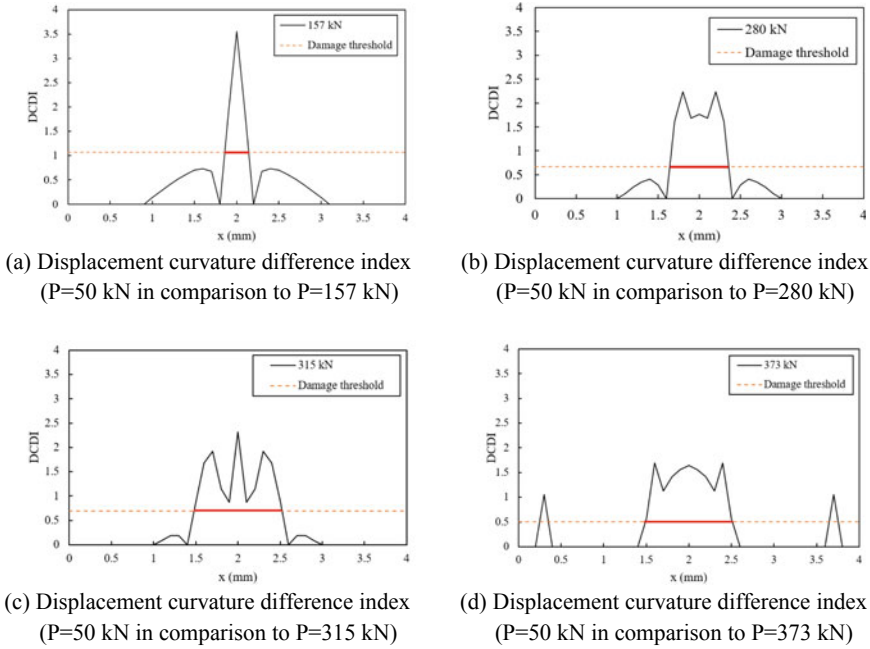
(a) Displacement curvature difference index
(P=50 kN in comparison to P=157 kN)

(b) Displacement curvature difference index
(P=50 kN in comparison to P=280 kN)

(c) Displacement curvature difference index
(P=50 kN in comparison to P=315 kN)

(d) Displacement curvature difference index
(P=50 kN in comparison to P=373 kN)

Fig. 3 Diagram illustrating the cracked zone's diagnosis. **a** Displacement curvature difference index ($P = 50$ kN in comparison with $P = 157$ kN). **b** Displacement curvature difference index ($P = 50$ kN in comparison with $P = 280$ kN). **c** Displacement curvature difference index ($P = 50$ kN in comparison with $P = 315$ kN). **d** Displacement curvature difference index ($P = 50$ kN in comparison with $P = 373$ kN)

Table 1 Accuracy of the diagnostic method

Load level	L (m)	L_{crack} (m)	L_{pred} (m)	A (%)	$L_{pred,out}$ (m)	$L_{0,crack}$ (m)	$L_{0,pred}$ (m)	B (%)	C (%)
373 kN	4	1	1.05	95	0.05	3	2.95	98	98
350 kN	4	0.8	0.91	88	0.11	3.2	3.09	97	95
315 kN	4	1	1.05	95	0.05	3	2.95	98	98
280 kN	4	0.6	0.71	85	0.11	3.4	3.29	97	95
245 kN	4	0.6	0.71	85	0.11	3.4	3.29	97	95
210 kN	4	0.6	0.71	85	0.11	3.4	3.29	97	95
175 kN	4	0.2	0.31	65	0.11	3.8	3.69	97	95
157 kN	4	0.2	0.28	71	0.08	3.8	3.72	98	96

and diagnosing reinforced concrete beam damage, and it can be extended to other members.

The deformed shape curvature method is used exclusively in this study to diagnose ideal two-support reinforced concrete beams. The displacement curvature method should be investigated further in the future with beams with varying boundary conditions, particularly beams in a reinforced concrete frame.

References

1. Stubbs N, Osegueda R (1990) Global nondestructive damage evaluation in solids. Anal Exp Modal Anal 5(2):67–79
2. Pandey AK, Biswas M, Samman MM (1991) Damage detection from changes in curvature mode shape. J Sound Vib 145(2):321–332
3. Doebling SW, Farrar CR, Prime MB (1998) A summary review of vibration-based damage identification methods. Shock Vib Dig 30(2):91–105
4. Chen X, Zhu H, Chen C (2005) Structural damage identification using test static data based on grey system theory. J Zhejiang Univ A 6A:790–796
5. Lee ET, Eun HC (2008) Damage detection of damaged beam by constrained displacement curvature. J Mech Sci Technol 22:1111–1120
6. Abdo MA-B (2012) Parametric study of using only static response in structural damage detection. Eng Struct 34:124–131
7. Yazdanpanah O, Seyedpoor SM (2013) A crack localization method for beams via an efficient static data based indicator. Comp Meth Civil Eng 4:43–63
8. Ha TM, Fukada S (2017) Nondestructive damage detection in deteriorated girders using changes in nodal displacement. J Civ Struct Heal Monit 7:385–403
9. Ono R, Ha TM, Fukada S (2019) Analytical study on damage detection method using displacement influence lines of road bridge slab. J Civ Struct Heal Monit 9(4):565–577

Seismic Response of a Reinforced Concrete Frame with Reduced Stiffness

Huu Anh Tuan Nguyen, Trong Tinh Le, and Dinh Nhan Dao

1 Introduction

The stiffness of reinforced concrete members depends on the cracked state and loading history of the members as well as the elastic–plastic properties of concrete and steel reinforcement. Factors affecting the effective stiffness of reinforced concrete members may also include transverse reinforcement, longitudinal reinforcement ratio, concrete strength, cross-section shape, and cross-section aspect ratio [1]. Analysis of reinforced concrete structures using the full elastic stiffness may be inappropriate because the structural stiffness could be reduced following the formation and development of concrete cracks. This reduction occurs even when the building is subjected to static loads under normal operating conditions and becomes more concerned when strong impacts such as seismic loads have to be dealt with. A reduction in stiffness would have a negative effect on the over strength, displacement ductility, and collapse limit states of a building under seismic actions [2]. Using the full elastic stiffness in seismic analysis of a concrete building could underestimate the building response in terms of interstory drift and overestimate the performance level relating to plastic rotations [3]. Although nonlinear dynamic analysis could yield a comprehensive insight into the seismic response of structures, it requires complex modeling and designers in depth knowledge of advanced structural dynamics and earthquake engineering [4]. A much simpler approach to partially improve the conventional linear elastic analysis is introducing stiffness reduction factors to reinforced concrete members.

A very first formula for calculating effective moment of inertia of cracked flexural members was proposed by Branson in 1963 [5]. Several improved forms of this formula have been incorporated into concrete design standards of some countries

H. A. T. Nguyen (✉) · T. T. Le · D. N. Dao
University of Architecture Ho Chi Minh City, HCMC, Ho Chi Minh City, Vietnam
e-mail: tuan.nguyenhuuanh@uah.edu.vn

Table 1 Stiffness reduction factor for modeling RC elements [11, 12]

FEMA 356-2000			TS 500-2000		
Beam	Column		Beam	Column	
α	n	α	α	n	A
	<0.3	0.5		<0.1	0.4
0.5	0.3-0.5	0.6	0.4	0.1-0.4	0.4-0.8
	>0.5	0.7		>0.4	0.8

in which the effective moment of inertia is a function of the ratio of the cracking moment and applied moment [6–9]. The European seismic design standard Eurocode 8 states that if a more accurate analysis of the cracked elements is not performed, the elastic flexural and shear stiffness properties of concrete elements are permitted to be taken as one-half of the corresponding stiffness of uncracked elements [10]. Both American and Canadian concrete standards take a stiffness reduction factor of 0.35 for conventional beams and 0.7 for columns regardless of the axial compression ratio [6, 7]. A number of design guides and standards consider the stiffness reduction factor for beams to be constant while that for columns vary linearly with the axial compression ratio of the columns. For instance, provisions for reinforced concrete beams and columns as per the FEMA 356 guideline and Turkisk standard TS 500 are summarized in Table 1 in which n and α are the axial compression ratio and stiffness reduction factor, respectively [11, 12].

The paper proposes a method to find the effective nonlinear stiffness of reinforced concrete beams and columns. A case study frame subjected to seismic loading is investigated in which the stiffness reduction factor for each frame member is calculated via pushover analysis with input parameters including geometrical dimensions, reinforcement area, axial compression force of the member, and the nonlinear stress–strain relationship of concrete and reinforcing steel. The frame response based on the full elastic stiffness is compared with that considering stiffness reduction factors.

2 Methods

2.1 Proposal of a Method for Determination of Nonlinear Stiffness

Pushover Models for Beam and Column Elements. Consider a typical frame panel consisting of span-length beams and story height columns of a rigid frame with moment-resisting joints. Figure 1 presents the deflected shape and bending moment diagram of the panel due to lateral loads applied to the frame, which would be obtained from a conventional static analysis. It can be seen that the bending moments at two ends of a member are more or less the same. The column bends in double curvature
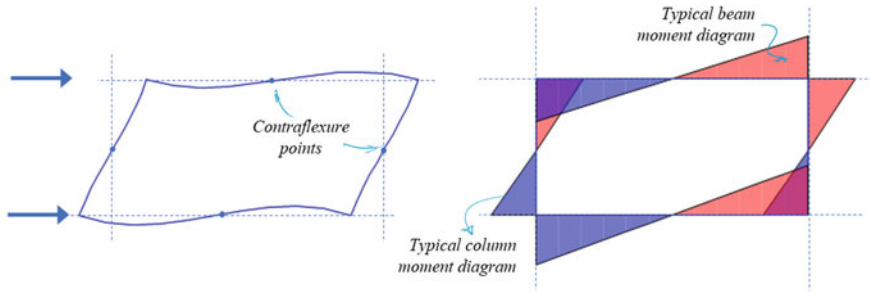
Fig. 1 Deformation and bending moment of a typical frame panel

with contraflexure points at approximately column height. The beams also bend in double curvature with contraflexure points at approximately midspan.

From an observation of Fig. 1, the nonlinear pushover analysis models for a beam element and a column element are proposed as shown in Figs. 2 and 3, respectively. These models are developed in OpenSees, an open-source simulation software [13], using nonlinear stress–strain relationships of concrete and reinforcement (Fig. 4) together with the geometrical dimensions and reinforcement areas of the members. For the beam analysis model, M and θ are the average values of the bending moment and the rotation angle at the two ends of the beam, respectively. A pushover curve that shows the relationship between the bending moment and rotation angle at the ends of the beam as the rotation angle increases monotonically is to be calculated (Fig. 2).

For the column analysis model, M is the average bending moment at the two ends of the column, and u is the relative lateral displacement between two floor levels. A pushover curve is to be constructed for each column element, which shows the variation of the lateral load Q against the displacement u as u increases monotonically, and the column's axial force P (due to gravity loads) is kept constant (Fig. 3).

Material Models. Figure 4a depicts the stress–strain behavior of concrete in uniaxial compression according to a constitutive model developed by Scott et al. [14], which
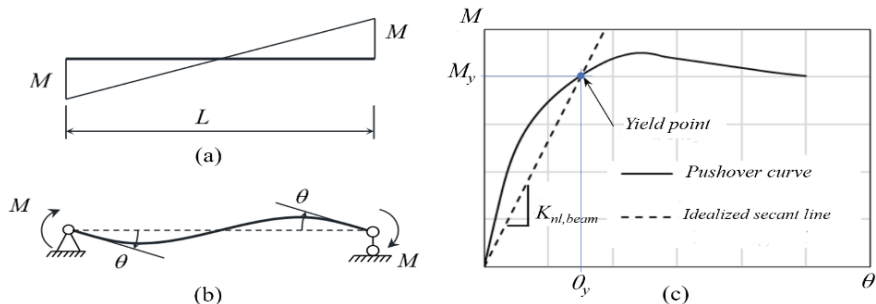

Fig. 2 Beam: **a** moment diagram, **b** loads and deflected shape, and **c** pushover curve
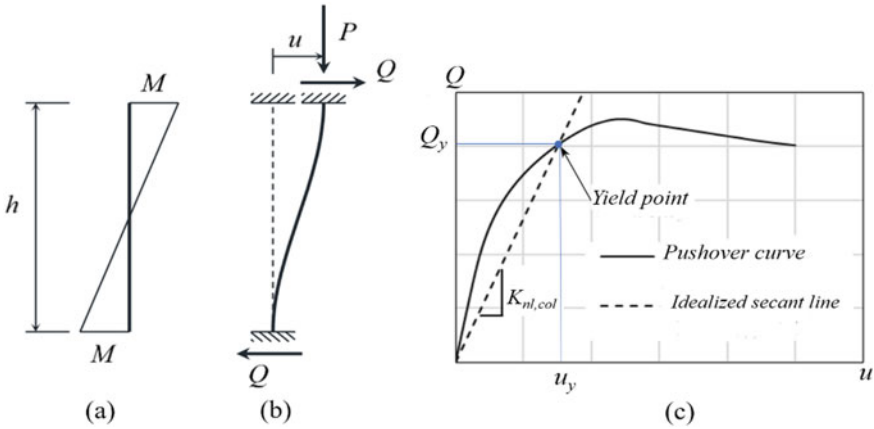
Fig. 3 Column: **a** moment diagram, **b** loads and deflected shape, and **c** pushover curve
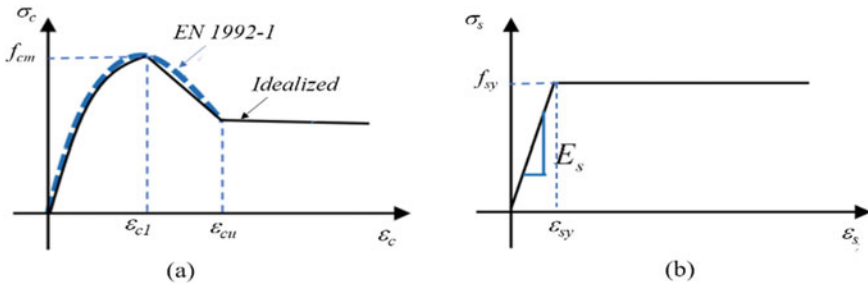

Fig. 4 Stress–strain curves for **a** concrete and **b** steel reinforcement

is available in OpenSees and was utilized in this research for pushover analysis of beams and columns. The concrete model as per EN 1992-1 [15], drawn with thick dashed lines in Fig. 4a, is quite consistent with Scott's model. The main parameters that define this model include compressive strength of concrete, f_{cm}, strain corresponding to compressive strength, ε_{c1}, and strain when concrete begins to crush, ε_{cu}. The behavior of reinforcing steel is assumed to be ideal elastic–plastic with key parameters including yield strength, f_{sy}, and elastic modulus, E_s, as shown in Fig. 4b. The steel yield strain can be computed from these two parameters as $\varepsilon_{sy} = f_{sy}/E_s$.

Calculation of Stiffness Reduction Factor. It is possible to determine the yield point in the pushover curve corresponding to when the reinforcement reaches the yield strain [14, 15]. The effective nonlinear stiffness of the beam, $K_{nl,beam}$, and column, $K_{nl,col}$, can be taken as the slope of the secant line joining the origin of the pushover curve to the yield point:

$$K_{nl,beam} = M_y/\theta_y \tag{1}$$

$$K_{\text{nl,col}} = Q_y / u_y \qquad (2)$$

In which M_y and θ_y are the moment and rotation angle corresponding to the yield point of the beam (Fig. 2c), Q_y and u_y are the lateral force and displacement corresponding to the yield point of the column, respectively (Fig. 3c).

From basic principles of structural analysis [16], the elastic stiffness $K_{\text{el,beam}}$ and $K_{\text{el,col}}$ of the beam element of Fig. 2b and column element of Fig. 3b, respectively, can be expressed as

$$K_{\text{el,beam}} = 6E_c I_g / L \qquad (3)$$

$$K_{\text{el,col}} = 12 E_c I_g / h^3 \qquad (4)$$

where E_c is the modulus of elasticity of concrete, I_g is the gross moment of inertia of the uncracked section, L and H are the length of the beam and column, respectively. The stiffness reduction factor can be computed as the ratio of the effective nonlinear stiffness to the corresponding elastic stiffness.

2.2   Case Study Frame Description

The case study frame is a ten-story reinforced concrete structure shown in Fig. 5a. The cross sections of the 6.3-m-span and 7.9-m-span beams are 250×450 mm and 250×550 mm, respectively. The cross sections of the edge columns are 400×700, 400×600, and 300×450 mm, and of the middle columns are 500×750, 400×650, 400×400 mm with larger columns at lower stories. The concrete's properties are $f_{\text{cm}} = 28$ MPa, $E_c = 30$ GPa, $\varepsilon_{c1} = 0.002$, and $\varepsilon_{cu} = 0.0035$. The steel reinforcement has $f_{\text{sy}} = 400$ MPa and $E_s = 200$ GPa. The total gravity load per story amounts to 1500–1910 kN. For seismic loading, the design response spectrum for type D ground, behavior factor $q = 3.9$, and DCM ductility class (medium ductility) as per Eurocode 8 (EC8) was used. The building is classified as importance class II, and the peak ground acceleration is $a_g = 0.0856\,g$ with g being the acceleration of gravity. A preliminary finite element (FE) model of the frame using elastic rigidity $E_c I_g$ of uncracked gross sections was created in SAP2000 software [17]. Figure 1 illustrates the first two mode shapes with natural periods of $T_1 = 3.32$ and $T_2 = 1.13$ s as acquired from the frame modal analysis. The response to earthquake loading was computed using modal response spectrum analysis where modal responses were combined via the SRSS rule [10, 17]. In the modal response spectrum analysis, 12 modes of vibration were taken into account with the sum of the effective modal masses being 98% of the total mass of the structure.
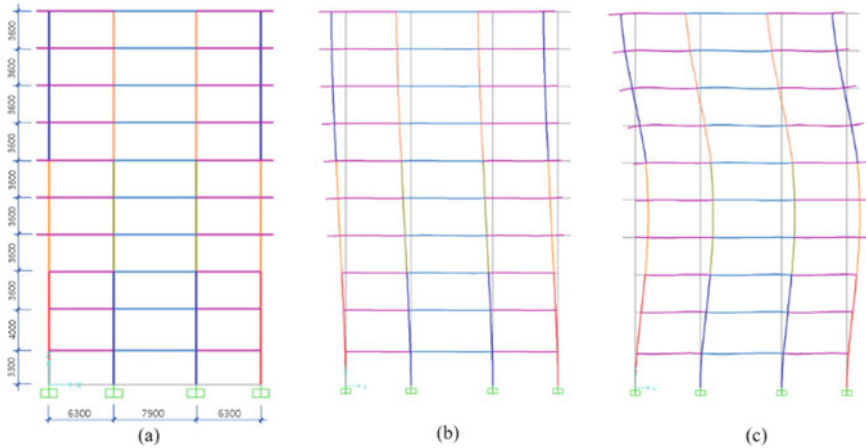
Fig. 5 Case study frame: **a** geometry, **b** mode shape 1, and **c** mode shape 2

3 Results and Discussion

3.1 Stiffness Reduction Factor

Using the internal forces resulted from frame analysis with elastic stiffness, reinforcement calculation was performed in accordance with Eurocode 2 [15]. The area of longitudinal reinforcement obtained for each frame member was then utilized in the determination of nonlinear effective stiffness of the member.

Beams. A comparison of the stiffness reduction factor for beam elements calculated by different methods is presented in Fig. 6a. While design standards consider the stiffness reduction factor for beams to be constant, the proposed method revealed that this factor depended on many parameters including the internal forces, reinforcement, and cross-sectional size of the member. The stiffness reduction factor as per the proposed method was found to fluctuate from 0.314 to 0.523 with an average value of 0.414 which was closest to the value suggested by the Turkish standard TS 500. Moreover, the 10-th percentile stiffness reduction factor calculated using the proposed method was 0.344 which closely matched the value of 0.35 recommended by the ACI 318 and CSA A23 standards. The 10-th percentile value can be considered as a reasonable and conservative value for design as 90% of the stiffness reduction factor values would be above the 10-th percentile value.

Columns. Let $n = P/A_c f_{cm}$ be the axial compression ratio where P and A_g are, respectively, the axial force and cross-sectional area of a column. For the case study frame, the axial compression ratio was in the range 0.14–0.64. The variation of the stiffness reduction factor against the axial compression ratio is shown in Fig. 6b. It can be seen that the EC8-based effective stiffness, which was independent of any factors,
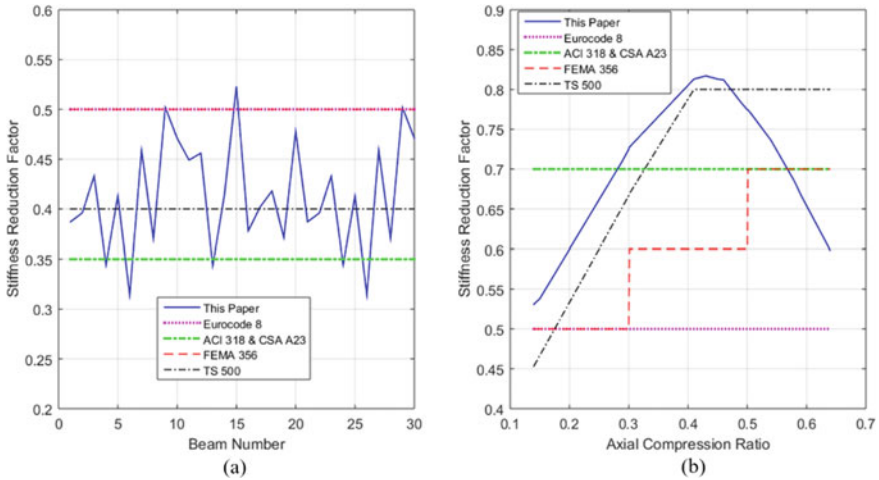
Fig. 6 Stiffness reduction factor for: **a** beam and **b** column

was lowest for almost all columns of the frame, thus being the most conservative value. The stiffness reduction factor recommended by the FEMA 356 and TS 500, which depended only on the axial compression ratio, increased with increase in the compression force then remained constant. The stiffness reduction factor resulted from the proposed method varied from 0.531 to 0.817 depending on many factors including the axial force, member dimensions, and area of provided reinforcement. The 10-th percentile stiffness reduction factor acquired from the proposed method was 0.592. This value agreed well with the experimental data of Haselton et al. [18] which revealed that for a typical column, the elastic stiffness was about 1.7 times the secant stiffness to yield, i.e., the stiffness reduction factor was approximately 0.588. The average stiffness reduction factor as per the proposed method was 0.697, matching the value of 0.7 given by the ACI 318 and CSA A23 standards for all axial compression ratios.

Unlike the FEMA 356 and TS 500, the variation of the stiffness reduction factor found from the proposed method had both increasing and decreasing segments (Fig. 6b), which can be explained as follows. When the compression force was small enough, the tensile stress from the bending moment caused cracks over the column section, hence small effective stiffness of the column. Increasing the compression force could reduce concrete cracks and increase the column effective stiffness factor. For the columns of the investigated frame, the effective stiffness got highest values when the axial compression ratio was in the range 0.40–0.48. However, when the compression force was further increased beyond this limit, the compressive strain in concrete (due to compression force and bending moment) was found to exceed the ε_{c1} value, putting the compressive concrete zone into the softening region of the stress–strain curve of Fig. 4a. As a result, a lower effective stiffness was obtained.

Table 2 Natural periods and base shear ratio

	Elastic	This paper	EC8	ACI 318, CSA A23	FEMA 356	TS 500
Natural period T_1 (s)	3.32	4.40	4.22	4.60	4.06	4.32
Natural period T_2 (s)	1.13	1.46	1.47	1.53	1.41	1.45
Base shear ratio (%)	1.58	1.56	1.56	1.55	1.56	1.55

3.2 Seismic Response of Frame with and Without Stiffness Reduction

The stiffness reduction factor identified previously was applied to the linear elastic FE model of the frame as a multiplier of the full elastic rigidity $E_c I_g$ of the frame member. The modal analysis was reconducted to get the updated natural periods and mode shapes. The same design spectrum was used for calculating the earthquake action and frame response according to EC8 for each scenario of stiffness reduction.

Natural Periods and Base Shear Force. Table 2 presents the first two natural periods T_1, T_2 and the base shear ratio which was the base shear force normalized by the total building weight. Although the natural mode shapes of the frame with and without stiffness reduction were almost the same, the reduction in stiffness increased the natural periods by 22–39% for the first mode and 25–35% for the second mode. Interestingly, the base shear force associated with the original frame (i.e., without stiffness reduction) and the base shear forces following various stiffness reduction methods were approximately the same. This is because the T_1 values from all investigated cases fell into the long period range of the EC8 design spectrum where the spectral acceleration was constant and equal to the lower bound of $0.2a_g$. Since the first mode contributed the most to the overall response, the difference in total base shear among investigated cases would be minimal. The story shear force distributing along the building height was also similar across the original frame and the frames with reduced stiffness.

Displacement and Drift. There are a number of reasons for lateral displacement in tall buildings to be of interest. These may include rigidity requirement, limitation of stress in structural members, comfort of occupants on upper floors, estimation of required gap between building blocks to avoid pounding, etc. Compared with the elastic stiffness case, the stiffness reduction cases increased the peak lateral displacement of the investigated frame by 52–92% with the largest increase pertained to the ACI 318 and CSA A23. The displacement predicted by the proposed method, which was 76% greater than that based on the elastic stiffness, was more conservative than the results from the EC8, FEMA 356, and TS 500 (see Table 3 and Fig. 7a).

Figure 7b demonstrates the distribution of seismic-induced interstory drift ratio (IDR), defined as the relative lateral displacement between two consecutive floors divided by the story height, along the building elevation. It should be noted that the IDR is an important indicator of structural performance [10, 11, 19]. The maximum values of IDR estimated by the model using the full elastic stiffness and the models

Table 3 Displacement and interstory drift ratio

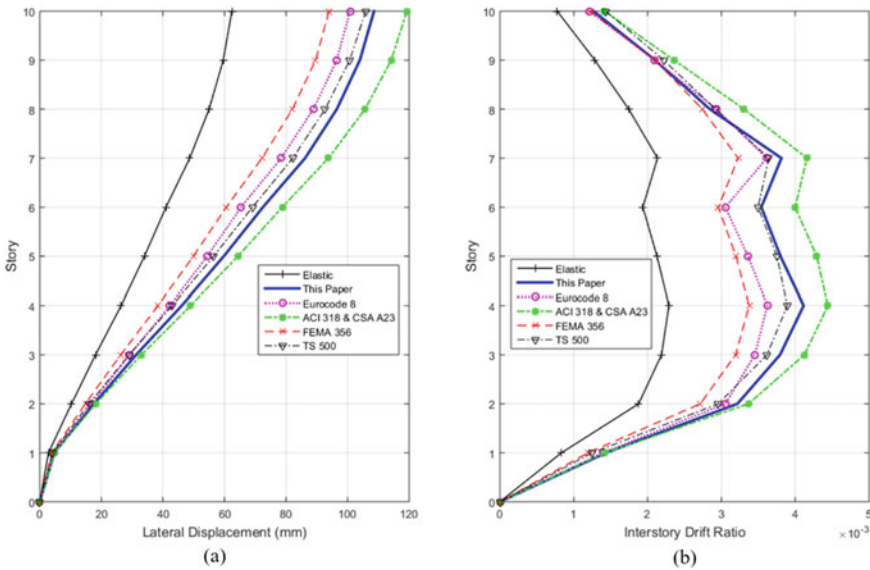|	Elastic	This paper	EC8	ACI 318, CSA A23	FEMA 356	TS 500
Peak displacement (mm)	62	109	101	119	94	106
Peak IDR (%)	0.23	0.41	0.36	0.44	0.34	0.39

Fig. 7 **a** Lateral displacement and **b** interstory drift ratio

using the reduced stiffness can be seen from Table 3. Using the stiffness reduction factor in the linear elastic analysis model could increase the peak interstory drift ratio by 48–91%. Among the investigated stiffness reduction methods, the proposed method resulted in the second largest IDR. Prediction based on the ACI 318 or CSA A23 seemed to be most conservative for the frame under consideration.

Damage Limitations. Interstory drift thresholds have been introduced in building codes to limit damage to non-structural components. Sensitivity of structures to second-order effects (P-Delta) is also dependent on the drift index [10]. In order to satisfy the damage limitation requirement as per EC8, the IDR multiplied by the behavior factor q shall not exceed β/ν in which β is taken as 0.005 for buildings having brittle non-structural elements attached to the structure, 0.0075 for ductile non-structural elements, and 0.010 for non-structural elements not interfering with the structure or without non-structural elements. The factor ν is taken as 0.5 for buildings with class II importance and the corresponding β/ν values amount to 1.0, 1.5, and 2.0%. For the case study frame, the peak q(IDR) associated with the elastic stiffness, proposed method, EC8, ACI 318, FEMA 356, and TS 500 was 0.89%,

Table 4 Check damage limitations

Type of non-structural elements	Acceptability of frame using stiffness values from					
	Elastic	This paper	EC8	ACI 318, CSA A23	FEMA 356	TS 500
Brittle materials	Yes	No	No	No	No	No
Ductile materials	Yes	No	Yes	No	Yes	No
Not interfering, without	Yes	Yes	Yes	Yes	Yes	Yes

1.60%, 1.40%, 1.72%, 1.33%, and 1.52%, respectively. When evaluated using the elastic stiffness, the building frame would be deemed suitable for all types of non-structural elements. By contrast, when the stiffness reduction as per the proposed method, ACI 318, CSA A23, and TS 500 was taken into account, the frame could not satisfy the damage limitation state for non-structural elements of either brittle or ductile materials (see Table 4).

4 Conclusion

In this research, a pushover analysis-based approach was proposed to determine the effective nonlinear stiffness for each element of a reinforced concrete frame. Depending on many parameters including the member's internal forces and reinforcement details, the stiffness reduction factor varied across the frame members. It was revealed that the stiffness reduction factor for columns did not always increase with increase in the axial compression ratio. The 10-th percentile value of the stiffness reduction factor, which was found to be 0.34 for beams and 0.59 for columns, can be used for all elements to simplify the design. The range of values of the stiffness reduction factor acquired from the proposed method was in good agreement with contemporary design standards.

For the case study frame, the ACI 318 and CSA A23 produced the most conservative prediction about the interstory drift, followed by the proposed method. The use of full elastic stiffness in structural analysis could lead to unrealistic estimates of earthquake response. Applying the stiffness reduction factor to the linear elastic analysis model of the frame was found to increase the interstory drift ratio by up to 91% and alter the evaluation of frame acceptability in terms of damage limitation. On the other hand, since the base shear force corresponding to various stiffness reduction methods was practically the same, the EC8-based stiffness reduction constant, due to its simplicity, could be used in strength design of reinforced concrete members.

References

1. Godínez-Domínguez EA, Tena-Colunga A, Velázquez-Gutiérrez I, Silvestre-Pascacio RE (2021) Parametric study of the bending stiffness of RC cracked building beams. Eng Struct 243:112695
2. Cando MA, Hube MA, Parra PF, Arteta CA (2020) Effect of stiffness on the seismic performance of code-conforming reinforced concrete shear wall buildings. Eng Struct 219:110724
3. Das S, Choudhury S (2019) Influence of effective stiffness on the performance of RC frame buildings designed using displacement-based method and evaluation of column effective stiffness using ANN. Eng Struct 197:109354
4. Dao ND, Nguyen-Van H, Nguyen TH, Chung AB (2020) A new statistical equation for predicting nonlinear time history displacement of seismic isolation systems. Structures 25:177–190
5. Branson DE (1963) Instantaneous and time-dependent deflections of simple and continuous reinforced concrete beam. HPR Publication No.7, Part 1, AHD, U.S.B of Public Road
6. ACI 318-19 (2019) Building code requirements for structural concrete and commentary. American Concrete Institute, Farmington Hills, MI
7. CSA A23.3 (2014) Design of concrete structures. Canadian Standards Association, Rexdale
8. AS 3600:2018 (2018) Concrete structures. Standards Australia, Sydney
9. NZS 3101:2006 (2006) Concrete structures standard. Part 1—the design of concrete structures. Standards New Zealand, Wellington
10. EN 1998 Eurocode 8 (2004) Design of structures for earthquake resistance. European Committee for Standardization, Brussels, Belgium
11. FEMA 356 (2000) Prestandard and commentary for seismic rehabilitation of buildings. Federal Emergency Management Agency, Washington, D.C.
12. TS 500-2000 (2000) Requirements for design and construction of reinforced concrete structures. Turkish Standard Institute, Bakanliklar, Ankara
13. OpenSees Homepage. http://opensees.berkeley.edu. Last accessed 20 July 2021
14. Scott BD, Park R, Priestley MJN (1982) Stress-strain behavior of concrete confined by overlapping hoops at low and high strain rates. ACI J Proc 79(1):13–27
15. EN 1992-1-2 Eurocode 2 (2004) Design of concrete structures, part 1-1: general rules and rules for buildings. European Committee for Standardization, Brussels, Belgium
16. Hibbeler RC (2017) Structural analysis, 10th edn. Pearson Prentice Hall, Upper Saddle River, NJ
17. CSI (2017) Analysis reference manual for SAP2000, ETABS, SAFE and CSiBridge. Computers and Structures, Inc., Berkeley, CA
18. Haselton CB, Liel AB, Taylor-Lange SC, Deierlein GG (2016) Calibration of model to simulate response of reinforced concrete beam-columns to collapse. ACI Struct J 113(6):1141–1152
19. Rastegarian S, Sharifi A (2018) An investigation on the correlation of inter-story drift and performance objectives in conventional RC frames. Emerg Sci J 2(3):140–147

Investigation of Potential Alkali–Silica Reaction of Different Types of Aggregate in Mortar with and Without Fly Ash

Nguyen Thi Bich Thuy and Nguyen Trong Lam

1 Introduction

Alkali-aggregate reaction (AAR) is a reaction in concrete, which is classified into alkali–silica reaction (ASR) and alkali–carbonate reaction (ACR). ASR is more widespread than ACR. ASR is a chemical reaction between the alkali hydroxides in concrete pore solution and silica in activate aggregate. Normally, the alkali hydroxide was derived from the alkalis present in the used cement. The reactive silica in aggregate usually exists as amorphous or poorly crystallized structures. The product of the action is alkali–silica gel composed of Na, K, Ca, and Si. The alkali–silica gel is hydrophilic and around and within the aggregate particles. After absorbed moisture, its volume increases significantly. Thus, it generates a pressure to disrupt the fabric of concrete [1]. The mechanism of the ASR in concrete is presented in Fig. 1. Generally, ASR occurs in the long-term stage of concrete. Therefore, the consequences that it brings are very large and difficult to maintain.

There are three main factors affected on the alkali–silica reaction in concrete: the alkali requirement in ASR or total alkalis present in concrete, the reactive silica component on the aggregate, and the presence of moisture in concrete structure. The sodium equivalent is calculated by using a following equation [1]:

$$Na_2O_{eq} = \%Na_2O + 0.658\%K_2O \tag{1}$$

where the 0.658 is the ratio between the molecular weight of Na_2O and K_2O.

N. T. B. Thuy (✉)
Ho Chi Minh City Open University, Ho Chi Minh City, Vietnam
e-mail: thuy.ntbich@ou.edu.vn

N. T. Lam
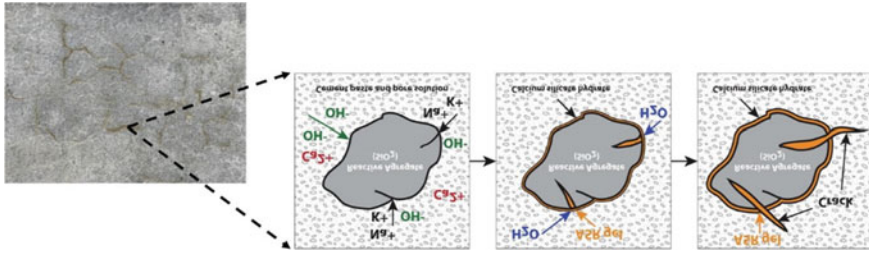Hanoi University of Civil Engineering, Hanoi, Vietnam

Fig. 1 Schematic representation of the mechanism of the ASR in concrete [2]

In order to inhibit the ASR, the properties of materials should be concerned. Generally, mineral admixtures, such as fly ash, slag, and natural pozzolans were used in concrete [3, 4] and the sodium equivalent of used cement exceeds 0.6%, according ASTM C150 [5]. However, the active silica content in aggregate cannot be changed. Therefore, the potential ASR of aggregate needs to investigate before using in concrete.

This study investigates the potential ASR of four types of aggregate. The influence of fly ash on the expansion due to ASR of mortar bar containing different aggregates also is examined. The test results provide an information and show a potential risk of ASR in concrete using tested aggregates.

2   Experimental Details

2.1   Materials and Mixture Proportions

Binders including Portland cement type I (OPC) and low CaO fly ash (FA) were used in this study. Chemical compositions of cement and fly ash are given in Table 1. The sodium equivalent values (Na_2O_{eq}) of cement and fly ash are 0.42% and 1.71%, respectively. Blaine fineness of cement and fly ash are 3700 cm^2/g and 3300 cm^2/g, respectively.

Four aggregate types were investigated the potential ASR in this study, namely limestone (L), andesite (A), rhyolite (R), and sandstone (S). The chemical compositions of aggregates are given in Table 1. It can be seen that andesite, rhyolite, and sandstone are rich in silica.

Two series mortars, non-FA mortar and FA mortar, were examined in this study. Fly ash replaced (FA/b) 30% by weight of cement. Water to binder (w/b) and aggregate to binder (A/b) ratios are 0.45 and 2.75, respectively. In each series, w/b, A/b, and amount of aggregates with different size were same. Aggregate ratios of #8, #16, #30, #50, and #100 were 10, 25, 25.25, and 15, respectively. The mix proportions of mortar are presented in Table 2.

Table 1 Chemical compositions of binder and aggregates

Chemical compositions (% by weight)	Binders			Aggregates			
	OPC	FA	Limestone (S)	Andesite (A)	Rhyolite (R)	Sandstone (S)	
SiO_2	19.34	62.10	17.31	55.82	56.32	58.13	
Al_2O_3	4.89	19.87	1.23	17.54	17.14	14.02	
Fe_2O_3	3.54	5.15	0.25	7.78	6.35	6.10	
CaO	65.13	2.21	44.02	6.98	8.68	6.87	
MgO	1.12	1.34	1.43	3.32	3.14	2.56	
Na_2O	0.15	0.77	0.27	3.43	2.89	3.11	
K_2O	0.42	1.43	0.41	1.78	4.12	1.21	
LOI	2.05	5.86	–	–	–	–	

Table 2 Mix proportions of mortar

Series	FA/b	w/b	A/b	Aggregate (g)	Aggregate with different sizes (%)				
					#8	#16	#30	#50	#100
Non-FA mortar	0	0.45	2.75	1320	10	25	25	25	15
FA mortar	30	0.45	2.75	1320	10	25	25	25	15

2.2 Test Methods

To investigate the potential ASR, four aggregate types were tested by the accelerated mortar bar test, according to ASTM C1260 [6]. This method was measured the expansion of mortar bar containing aggregate exposed in the sodium solution at 80 °C during 14 days. Because the specimens were submerged in the sodium solution, the alkali content of cement and fly ash was not a significant factor in affecting expansion.

Specimen dimension was $25 \times 25 \times 285$ mm. After mixing 1 day, specimens were demoulded, submerged in water at 80 °C for 24 h, and measure an initial reading. The mortar bar continually exposed to the 1 N NaOH solution at 80 °C and conducted subsequent comparator readings periodically for 14 days. Based on the expansion of specimens at 14 days in the sodium solution, the potential alkali of aggregate was classified to 3 cases. The first, the expansions of more than 0.20%, the aggregate indicative of potentially deleterious expansion. The second, the expansions between 0.10 and 0.20% that are known to be innocuous and deleterious in some cases. And the third, the aggregate is innocuous behavior when the expansions are less than 0.1%.

3   Results and Discussion

3.1   Expansions of Mortar bar Containing Different Aggregate Types

The results of the expansion of mortar bar containing four types of aggregate are shown in Fig. 2. It can be seen that the expansion of mortar used sandstone and rhyolite are higher than the limited expansion at 14 days, corroding ASTM C1260. Sandstone and rhyolite are classified to potential of the risk of ASR in Portland cement mortar. The expansion of specimens used andesite at 14 days is between 0.10% and 0.20%. It is innocuous and deleterious of ASR in Portland cement mortar in some cases. And, the expansion of specimens containing limestone at 14 days is less than 0.10%. It is deleterious of ASR in Portland cement. Based on the chemical compositions of four aggregates, the rich silica aggregates lead to a higher potential in ASR when compared to the low silica aggregate (limestone).

It is noted that the ranges of chemical compositions of the rich silica aggregate are equivalent, but their silica reactions are different. When considered aggregate type in potential of ASR, it should be focused on the type and quantity of reactive mineral in rock [1]. Future investigation is still need to clarify the effect of mineral component in rock on the ASR of mortar.
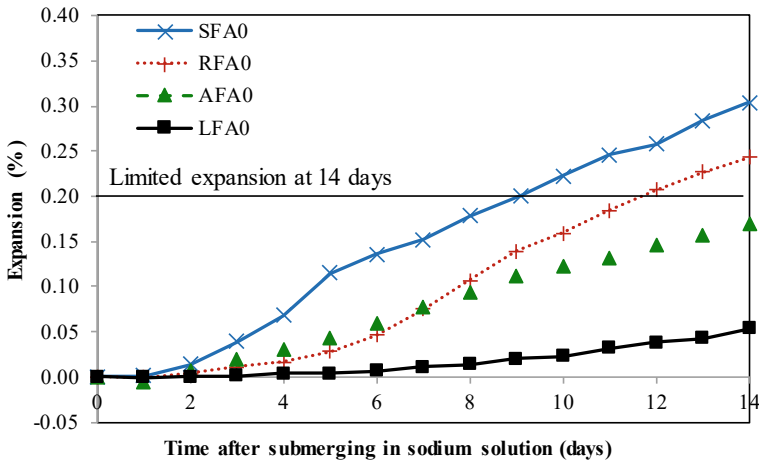
Fig. 2 Expansion of non-FA mortar bar
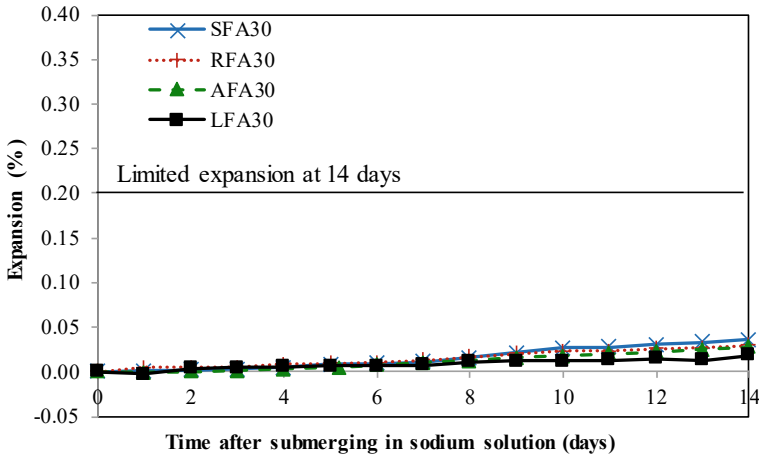
Fig. 3 Expansion of fly ash mortar bar

3.2 Effect of Fly Ash on the Expansion of Mortar Due to ASR

Figure 3 shows the expansion due to ASR of fly ash mortar series. All mixtures have the expansion at 14 days after submerging in sodium solution less than 0.05%. When compared to the classified potential of ASR in ASTM C1260, the risk of ASR of mortar containing reactive aggregates becomes innocuous. The reducing expansion ratio of mortar due to ASR by using fly ash is the percentage between the expansion of non-FA mortar and that of fly ash mortar, as shown in Eq. (2).

$$R_E = \frac{E_{Non-FA} - E_{FA}}{E_{Non-FA}} \times 100\% \qquad (2)$$

where R_E is the reducing expansion ratio, E_{Non-FA} and E_{FA} are expansion at 14 days of non-FA mortar and FA mortar, respectively.

The expansions due to ASR of mortar are significantly reduced by using fly ash, seen in Fig. 4. The reducing expansion ratios of mortar used rich silica aggregates are higher than that of mortar used limestone. The using fly ash to suppress expansion due to ASR is proposed by three mechanisms [7]. First, the alkali content in mortar containing fly ash is lower when compared to that in mortar used cement-only. Second, some of the alkalis from the pore solution are removed by binding into the low C/S ratio hydration products. And third, the permeability and diffusivity of concrete are reduced due to the pozzolanic reaction and filling effect of fly ash. In this study, the mortar specimens were exposed to the sodium solution. Therefore, the alkali content in mortar is not a major factor.
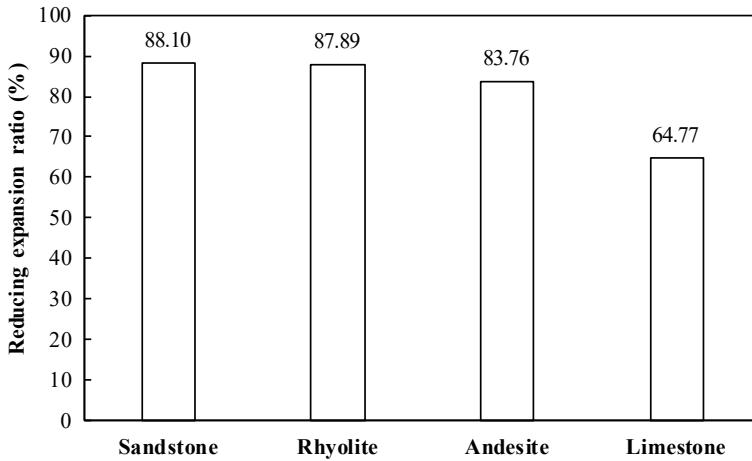
Fig. 4 Effect of fly ash on the reducing expansion ratio of mortar bar

4 Conclusions

The following conclusions can be drawn:

1. The rich silica aggregates lead to a higher potential of ASR in mortar when compared to low silica aggregate such as limestone.
2. The aggregates with similar range of chemical compositions have different alkali–silica reaction. Therefore, the chemical compositions of studied aggregates are not strongly effect on the ASR in mortar.
3. The expansion of mortar due to ASR is suppressed by using fly ash as replacing cement material. By using ASTM C1260 to investigate the potential of ASR of aggregate, the mechanism of the effect of fly ash mainly due to the pozzolanic reaction of fly ash.

5 Future Study

In order to investigate the effect of different types of aggregates on the ASR in mortar, the mineral component and structure of aggregate should be examined deeply. The mineral components of aggregate should be considered both type and content of reactive silica mineral.

References

1. Glasser FP (1992) Chemistry of alkali-aggregate reaction, the alkali-silica reaction in concrete. Van Nostrand Reinhold, New York, pp 30–35
2. Figueira RB et al (2019) Alkali-silica reaction in concrete: mechanisms, mitigation and test methods. Constr Build Mater 222:903–931
3. Monteiro PJM (1997) Influence of mineral admixtures on the alkali-aggregate reaction. Cem Concr Res 27:1899–1909
4. Haifeng W, Dingan W, Zhen M (2019) Effect of fly ash and limestone powder on inhibiting alkali aggregate reaction of concrete. Constr Build Mater 210:620–626
5. ASTM C150 (2003) Standard specification for Portland cement. Annual Book of ASTM Standards. ASTM International, West Conshohocken, PA
6. ASTM C1260 (2008) Standard test method for potential alkali reactivity of aggregate (mortar-bar method). Annual Book of ASTM Standards. ASTM International, West Conshohocken, PA
7. Rachel D (1997) The role of fly ash composition in reducing alkali-silica reaction. Portland Cement Association

A Novel Proposal in Applying Big Data for the Bridge Management System

Nhi Ngo-Kieu , **Thao D. Nguyen, Lam Q. Tran, Canh M. Le,**
Luan Vuong-Cong , **Hung Nguyen-Quoc** , **and Toan Pham-Bao**

1 Introduction

Ho Chi Minh City is region with thousands of bridges because the city's topography is divided by many rivers and canals. Bridges facilitate traffic between different parts of the city, as well as between the city and other localities in the region.

The role of bridges is closely linked to all economic, social, and security activities and closely related to the lives of all people in the city. Therefore, making sure they are "healthy" is a very heavy task. There are two activities to ensure healthy bridges: (1) monitoring and detecting deterioration due to damage and (2) maintenance.

This article focuses on the first activity. According to national regulations in Vietnam, health monitoring is carried out by two measures: patrol and inspection.

Patrol measures carried out by patrol teams. The patrol mission is to detect structural damage and phenomena that can affect the bridge structure. The method of implementation is visual observation. Patrols are carried out on a daily basis, and as a result, surface damage is detected in a timely manner. The disadvantage of this method is that it does not allow access to places that are hidden from sight. And the biggest disadvantage is that it does not allow the assessment of factors related to bearing capacity.

N. Ngo-Kieu · T. D. Nguyen · L. Q. Tran · C. M. Le · L. Vuong-Cong · H. Nguyen-Quoc ·
T. Pham-Bao (✉)
Laboratory of Applied Mechanics (LAM), Ho Chi Minh City University of Technology
(HCMUT), 268 Ly Thuong Kiet Street, District 10, Ho Chi Minh City, Vietnam
e-mail: baotoanbk@hcmut.edu.vn

Vietnam National University Ho Chi Minh City, Linh Trung Ward, Thu Duc City, Ho Chi Minh
City, Vietnam

T. D. Nguyen · L. Q. Tran
Ho Chi Minh City Department of Transportation, District 1, Ho Chi Minh City, Vietnam
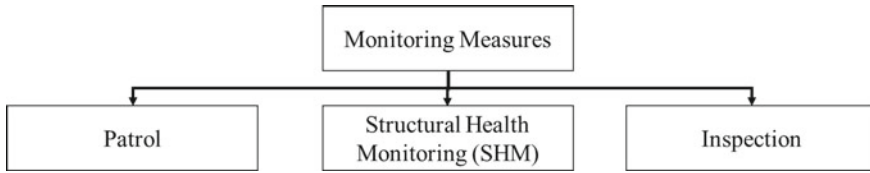
Fig. 1 Current bridge monitoring measures around the world

The inspection is organized with given loads of position and magnitude. Behavioral parameters such as deflection and deformation are measured. Thus, the bearing capacity of the bridge can be assessed. This measure allows to evaluate the bearing capacity of the structure. The main disadvantage of this method is the high cost of performance. The performance of inspection often requires stopping traffic, thus affecting the activities of society. Therefore, the State Regulations require the inspection cycle of bridges from 3 to 5 years [1], but it is limited due to restricted budget. Therefore, the inspection is only applied for priority bridges such as Saigon Bridge when absolutely necessary. This situation makes the second task, the decision to "cure" the bridge difficult.

In the last decade, an additional intermediate method was carried out, which is to monitor the bridge's fluctuations during actual operation and is called the structural health monitoring (SHM). This measure in the world is currently only implemented with cable-stayed bridges or key bridges. The actual vibration signal is mainly picked up by the accelerometers. Thus, there are 3 measures in the world today (Fig. 1).

The inspection process mainly consists of static tests. Dynamic tests only use free decay vibration caused by pulses. Theoretically, the properties obtained from the dynamic state provide more information about the structural situation than the static state. Vibration signals will give more parameters of the structure if the signals contain many different load states. Therefore, the vibration data obtained by the SHM form will be of better quality than the signal obtained only in the damped state. In addition, the vibration signal under real traffic makes inspection less expensive than other measures.

Due to the difficulties in monitoring the bridge system, and the advantages of the measure using actual vibration data, laboratory of applied mechanics (LAM) began to research the data collection and the characteristics of the bridge system in Ho Chi Minh city. From 2006 to 2009, we carried out a research project to install a continuous automatic strain measurement system on 100 measuring points at Saigon Bridge. The strain measurement signals are collected to a center station at the bridge, then transmitted via the Internet to the management units. The system has worked well and continuously for 2 years of implementing the project. Figure 2 is the screen to monitor the traffic image synchronization signal.

This is the first work of SHM system in the approach of big data. Following the above research work, with the support and cooperation of the Ho Chi Minh City Department of Transport, LAM has continued to conduct 2 pilot projects in 2011 and 2019 to generate big data on actual oscillate of nearly 40 bridges. The biggest
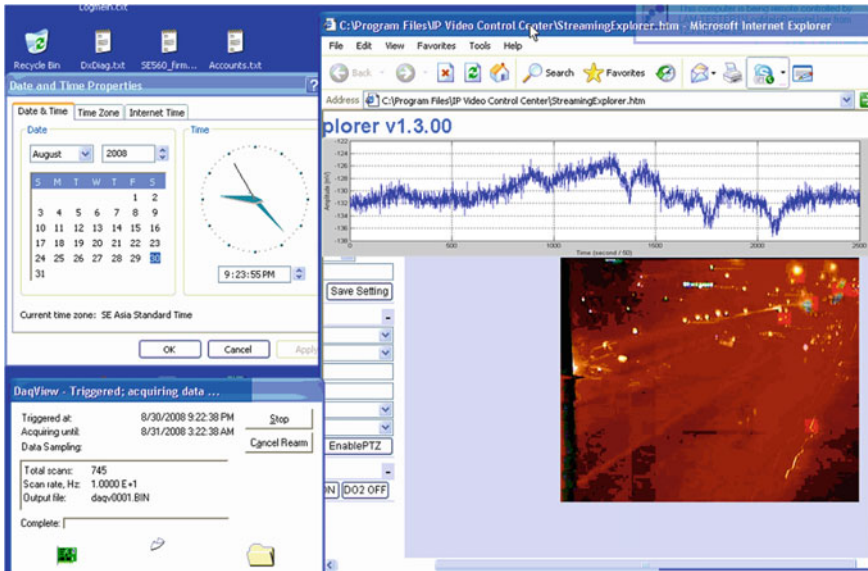
Fig. 2 Traffic image synchronization signal monitor screen

difference between our bridge health monitoring program and the world' currently operating is taking a long time and performing the monitoring for the majority of the bridges instead of focus on each bridge as in the world. With the reality of limited finance, our method will have to be completely different. Instead of a sensor system fixed on the bridge and collected continuously 24/24, we organize the form of portable sensors, which is a semi-manual method of data collection. The signal is recorded at selected times. Table 1 show the characteristics of vibration signal recorded between SHM and the study, for the comparison of the measuring method between the fixed systems of SHM and the proposal of the LAM.

Table 1 Characteristics of signal recorded between SHM and the proposal of the LAM

Method	Sensor status	Signal record time	Number of observed bridges	Number of observed spans	Number of observed pillar	Number of measuring points per span	Bridge structure type
Current SHM system	Fixed install	24/24	1	2–3	2–3	All	Cable stayed and suspension bridge
This study	Portable install	Finite time to choose	>30	All	All	3	All types

Although less than one-tenth of the total bridges under management of the Ho Chi Minh City Department of Transport is implemented, these are already the first big data source to be developed for bridge at the present time. This data is used for the artificial intelligence program (AI) which is being developed for transport management in the Ho Chi Minh city.

In parallel with studying how to organize data collection covering the entire bridge network, LAM also conducts research on fundamental problems in the field of machine learning (ML), looking for specific features, and investigates their sensitivity [2–5] apply deep learning such as wavelet [6] and CNN [7].

2   The Organization of Data Collection

The following is a presentation of the projects (Table 2) in phase 1 (2011–2012) and phase 2 (2019–2020) that the research team implemented with the approval and cooperation of the Ho Chi Minh City Department of Transport. Location of measuring points on the bridge is shown in Fig. 3.

Direct collection system includes sensor and computer (Fig. 4). The signals obtained from the sensor after measuring at each point in bridge (Fig. 5) will be saved in the computer.

Table 2 Size of measurement organization

Phase	Number of bridges	Locality (ward)	Bridge structure type	Number of measuring batch	Measurement parameters	Structure
1	38	2, 9, Thu Duc Districts	Simple supported beam, continuous box girder	4	Acceleration	Span, pillar, abutment
2	34	2, 9, Thu Duc, Binh Chanh Districts	Simple supported beam, continuous box girder	4	Acceleration	Span

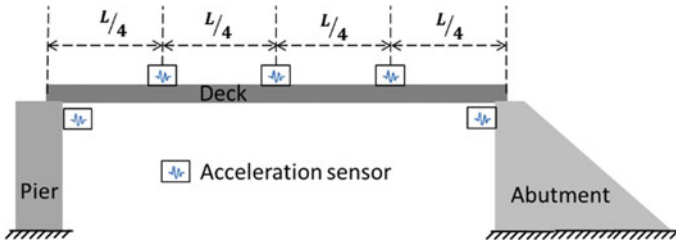| Phase	Number of measuring points			Number of measuring directions			Number of samples at 1 point in 1 direction each measurement
	Span	Pillar	Abutment	Span	Pillar	Abutment	
1	1	1	1	3	3	3	60,000 samples
2	3	1	1	3	3	3	200,000 samples

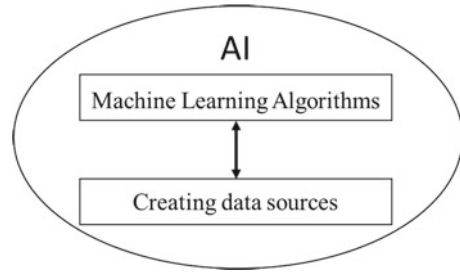**Fig. 3** Vibration measurement on bridges of the project

Fig. 4 Acceleration sensor (left) and data acquisition computer (right)

Fig. 5 Data collection (deck, pier, and abutment)

Fig. 6 Two main tasks of AI
implementation content

3 Applying AI in Bridge System Management

3.1 Orientation and Tasks

With more than 500 bridges under direct management and many others indirectly managed, the Ho Chi Minh City Department of Transport quickly brought up the idea of using information technology and together with LAM of Ho Chi Minh City University of Technology took initial steps in applying AI techniques to bridge system management. A simply way, the content of artificial intelligence, includes two tasks (Fig. 6).

To be able to create artificial intelligence in the management system, two tasks must be performed:

- Creating data sources which are big, rich, and time-spanning. This data source allows the AI system to recognize and learn from experience.
- Researching the identification techniques for the system to recognize, then make a decision. These algorithms are called machine learning algorithms (ML). In the recognition math part, the core task is to study to find the features. The problem of finding the features is a very difficult one. This feature may be relevant in one case, but completely impotent in another.

3.2 Results

3.2.1 Big Data Creation

From Table 1, the actual vibration data to date of bridges covers the following characteristics:

- Bridge structure
- Operating time
- Element types
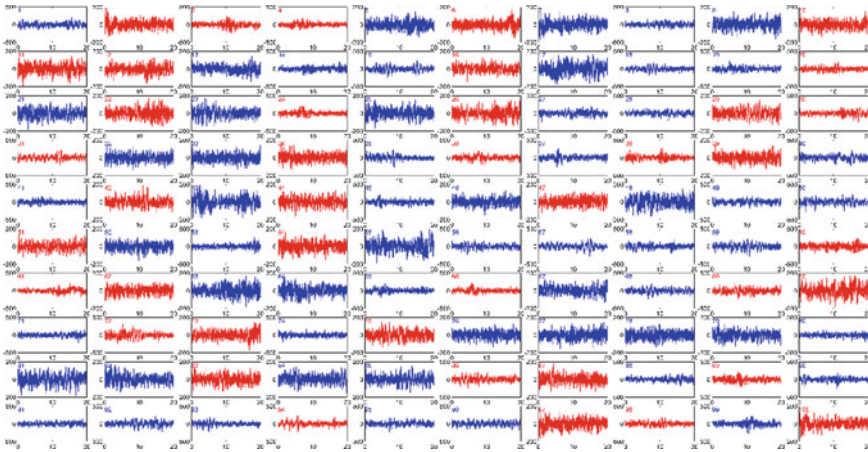- Positions on span
- Direction of oscillation

Fig. 7 Non-stationary signals with red representation

- Signal recording history (already 8 times in 10 year period)
- The number of samples at 1 measuring point is up to 200,000 samples with 100 signals.

The data must be checked for stationarity and roughly processed by filters for noise cancelation, clarified before becoming input to the following processes (Fig. 7). The above rich features meet the quality for the performance of task 2 (Fig. 6), that is, performing the study of machine learning algorithms (ML).

3.2.2 Researching on Recognition Techniques (ML)

The study of recognition techniques can be divided into two problems: foundation of matching features and identification algorithms.

In the above two types of problems, the research problem of finding suitable identification features is the (basic) premise problem. If the features do not match, then the second problem (i.e., the identification algorithm) will not be able to give the correct result, and in many cases, it will not give the result. Until now, the most commonly used features are the natural frequency, the mode shape.

Our actual data studies show that these characteristics do not reflect the deterioration of the bridge structure. We have tried to study other characteristics such as spectral moment [8], correlation [5, 9], energy dissipation [2, 4], wavelets [6, 10, 11], … For the second problem, besides the traditional methods, we have studied using ANN neural networks [10–12] and recently using deep learning neural networks (DNNs) [7].

Table 3 Structural damage limits and inspection limits

Region	Structural damage limits [13]	Inspection limits
I	No damage	No inspection
II	Possible small damage (plaster cracks) and no effect to load-bearing structural parts	No inspection or inspection on specified period
III	Probable damage to load-bearing structural parts	Inspection on right time
IV	Damage to load-bearing parts	Early inspection
IV+	Destruction	Instant inspection

3.2.3 Practical Application

One of the constraints of implementing our bridge measurement projects is to come up with a method of preliminary assessment of the bridge. As shown in Fig. 1, the actual vibration measure often has the goal of assisting in the implementation of the inspection procedure. The conclusions on assessing the condition and bearing capacity of the bridge structure by inspection have high reliability and are recognized by compliance with the State Regulations. However, the inspection methods due to more expense and difficulty not suitable for tight budgets of developing country. The solution is not to apply the measure to all bridges and to follow a specified period (from 3 to 5 years) in the standard. The proposed solution is a test measure with conditional execution based on many factors. The most important factor is that the healthy condition of bridge.

In order to advise for the Ho Chi Minh City Department of Transport on inspecting bridge, we have proposed to classify a inspection limits of bridge (Table 3) based on structural damage limits [13].

The measurement results and calculation of the vibration parameters: natural frequency, damping coefficient, impact factor.

The disadvantage of the damage limits is that the concepts are not quantified. This makes direct use difficult because it depends on the classification view of experts, difficult to apply to the AI process. To quantify the inspection limits in Table 3, based on vibration parameters (features), we have proposed the following:

- Using Features

In order for the regulator to be able to apply the classification process (Table 4), we have to comply with the following 3 things:

- Using the features specified in the State Regulation [1], specifically for oscillations: first natural frequency (f_z and f_x are vertical and horizontal frequency, respectively), impact factor (IF), damping ratio (ξ).
- The limit value of each feature is subject to the State Regulations.
- The inspection limits of bridge are raised depending on the number of different features reaching the limit value.

Table 4 Proposed method to classify bridge span

Level	Prestressed concrete	Reinforced concrete—steel beam
I	$f_z > 6$ Hz	$f_z > 15$ Hz
II	$4 < f_z \leq 6$ Hz	$10 < f_z \leq 15$ Hz
III	$3 < f_z \leq 4$ Hz	$8 < f_z \leq 10$ Hz
IV	$2.5 < f_z \leq 3$ Hz	$7.5 < f_z \leq 8$ Hz
IV +	$f_z \leq 2,5$ Hz	$f_z \leq 7,5$ Hz
Increase 1 level	$f_x = n f_z$ (n: positive integer)	
	IF > 1.25	
	$\xi > 0.01$	

- Classification results of project are shown in Table 5.

4 Conclusions

This article presents the research on damage and condition identification of bridge structures over the 10 years from 2010 to 2021 by the laboratory of applied mechanics. The results of study create the premise to allow the application of AI and big data in management for bridge system in the Ho Chi Minh City. Specifically, the studies have yielded the following positive results:

- Introduced portable signal collection process, no need to build fixed sensor systems. From here, it is possible to perform regular healthy monitoring for the bridge system of the city.
- Introduced new monitoring method as a supplement to bridge monitoring process.

The result of applying the above two things is

- Changed the bridge inspection and maintenance from periodic mode to conditional mode. The benefits of the conditional mode are to repair and maintain the right objects, in a timely manner, effectively improve the safety of the bridge system, and allocate financial resources reasonably, to the right objects and save the national budget.
- To proposal to the classification of bridge spans based on structural damage limits with an improved contribution by quantifying the concepts of inspection limits. With the introduction of this quantification, the classification work can be automated and introduced into the program using AI in the management of the bridge system.
- To initially build a storage of actual vibration data, as big data for positively performing AI in management of the bridge system.

Table 5 Number of classified span in project of phase 2

STT	Bridge	Number of measured spans	Inspection limits				
			I	II	III	IV	IV+
01	Ca Tre 1	3		3			
02	Giong Ong To 1	5		5			
03	Giong Ong To 2	16		8	6	2	
04	Giong Ong To 3	13		5	5	2	1
05	My Thuy 2	5		3	2		
06	Ong Hoa	1		1			
07	Sai Gon 1	32			31	1	
08	Sai Gon 2	21		27	4		
09	Ben Noc	3		3			
10	Chum Chup	2		2			
11	Go Cong	3		2	1		
12	Ong Tan	1		1			
13	Trao Trao	3		2	1		
14	Huyen Thanh	1			1		
15	Kinh	2			2		
16	Rach Ham	1			1		
17	Bui Dinh Tuy	2			2		
18	Son	1		1			
19	Dinh Bo Linh	2		2			
20	Phu An	2		2			
21	Van Khanh 1	2		2			
22	Van Khanh 2	2		2			
23	Nguyen Huu Canh Overpass	14	10	3	1		
24	Bay Nhao	2		2			
25	Binh Phu	3	2	1			
26	Vinh Binh	17	12	5			
27	Linh Xuan Overpass	6		4	1	1	
28	Binh Phuoc 1 Overpass	6		5	1		
29	Binh Phuoc 2 Overpass	6		3	3		
30	Song Than 1 Overpass	6		1	4	1	
31	Song Than 2 Overpass	6		1	3	1	1
32	Thu Duc 1 Overpass	8		5	2	1	
33	Thu Duc 2 Overpass	8		5	2	1	
34	Ba Cua	7		7			
	Project	212	24	103	73	10	2

- To novel research on machine learning platforms (feature selection, algorithm selection) for monitoring the health status of bridge structures.

References

1. Nguyen VT (2010) Diagnosing bridge. Construction Publishing House, Ha Noi
2. Nguyen TD, Nguyen HQ, Pham TB, Ngo NK (2021) A novel proposal in using viscoelastic model for bridge condition assessment. In: Structural health monitoring and engineering structures. Lecture notes in civil engineering, vol 148. Springer, Singapore, pp. 331–341
3. Nguyen TQ, Nguyen TD, Tran LQ, Ngo NK (2020) A new insight to vibration characteristics of spans under random moving load: case study of 38 bridges in Ho Chi Minh City, Vietnam. Shock Vibr 1547568
4. Nguyen TD, Nguyen TQ, Nguyen TN, Nguyen-Xuan H, Ngo NK (2020) A novel approach based on viscoelastic parameters for bridge health monitoring: a case study of Saigon bridge in Ho Chi Minh City–Vietnam. Mech Syst Sig Process 141:106728
5. Ngo NK, Nguyen TQ, Vu TV, Nguyen-Xuan H (2020) An fast Fourier transform–based correlation coefficient approach for structural damage diagnosis. Struct Health Monit 1475921720949561
6. Nguyen TQ, Vuong LC, Le CM, Ngo NK, Nguyen-Xuan H (2020) A data-driven approach based on wavelet analysis and deep learning for identification of multiple-cracked beam structures under moving load. Measurement 162:107862
7. Ngo-Kieu N, Nguyen-Da T, Pham-Bao T, Nguyen-Nhat T, Nguyen-Xuan H (2021) Deep learning-based signal processing for evaluating energy dispersal in bridge structures. J Zhejiang Univ-Sci A 22(8):672–680
8. Nguyen TQ, Doan HC, Vuong LC, Nguyen-Xuan H, Ngo NK (2020) Fretting fatigue damage nucleation and propagation lifetime using a central point movement of power spectral density. Shock Vibr 4985134
9. Nguyen TQ, Nguyen TD, Nguyen-Xuan H, Ngo NK (2019) A correlation coefficient approach for evaluation of stiffness degradation of beams under moving load. CMC-Comput Mater Continua 61(1):27–53
10. Nguyen DS, Nguyen HQ, Ngo NK (2015) Identifying undamaged-beam status based on singular spectrum analysis and wavelet neural networks. J Comput Sci Cybern 31(4):341–355
11. Nguyen SD, Ngo KN, Tran QT, Choi SB (2013) A new method for beam-damage-diagnosis using adaptive fuzzy neural structure and wavelet analysis. Mech Syst Sig Process 39(1–2):181–194
12. Tran QT, Ngo KN, Nguyen SD (2021) Fault diagnosis of rolling bearings using singular spectrum analysis and artificial neural networks. Vietnam J Mech 43(2):183–196
13. Beards CE (1996) Structural vibration: analysis and damping. Butterworth-Heinemann

Enhanced Vibration Serviceability of Multi-bay Floors Using Tuned Mass Dampers

Huu Anh Tuan Nguyen, Emad F. Gad, John L. Wilson, and Nicholas Haritos

1 Introduction

Long-span composite floors comprised of hot-rolled steel beams and concrete slab on metal decking have several advantages over traditional reinforced concrete floors in terms of erection speed, strength-to-weight ratio, and construction cost. The low stiffness and damping of composite floors may, however, increase their vulnerability to vibrations caused by various human activities including walking excitation. It has been found that the fundamental frequency of most composite floors can be in resonance with a multiple of the pace frequency and the natural frequencies of human body organs [1–3]. Limiting the level of vibration to the specific acceptance criteria is hence crucial for ensuring the comfort of occupants or the functionality of floor-mounted equipment. Several design guides for human-induced floor vibrations have been introduced, which discuss the characterization of the excitation force, the methodology to estimate the floor response and the maximum vibration limits. Contemporary guidelines on floor vibrations normally specify acceptable vibration levels for human comfort in terms of acceleration or velocity. The vibration criteria are based on either peak, root-mean-square (RMS), or root-mean-quad (vibration dose) values. Furthermore, these limits vary with the individual, the person's activity and orientation, the surrounding environment and the characteristics of the excitation source [1, 3, 4]. Since human comfort is a complex phenomenon, a level of vibration may be tolerable for certain persons but unacceptable for others. The relationship and degree of consistency among vibration quantifiers have also been investigated [2, 5, 6].

H. A. T. Nguyen (✉)
University of Architecture Ho Chi Minh City, HCMC, Ho Chi Minh City, Vietnam
e-mail: tuan.nguyenhuuanh@uah.edu.vn

E. F. Gad · J. L. Wilson · N. Haritos
Swinburne University of Technology, Melbourne, Australia

There are several known remedial measures for mitigating structural vibrations including stiffening methods, utilization of non-structural elements and relocation. The structural stiffness can be increased by adding posts with or without damping elements, increasing slab thickness or beam depth, providing a queen post hanger to the bottom flange of a beam. Floor vibrations can be improved by increasing the damping of the floor system with non-structural elements such as furnishings and interstory full-height partitions. Relocation of the vibration source or sensitive occupants can sometimes be useful [1, 7, 8]. In spite of being able to treat new floors in the design stage, the above-mentioned methods might be unfavorable when applied to existing floors. For example, adding columns or full-height partitions would reverse the original architectural idea of an open-plan office layout. Stiffening structural members would be intrusive when requiring the members to be jacked up prior to adding the new materials.

Another vibration rectification measure is using tuned mass damper (TMDs). A conventional TMD is comprised of a mass attached to the primary structure through a spring and damping device. TMDs have been proved to be effective in controlling horizontal motion of tall buildings under wind gust loadings and earthquake excitations [9]. Formulas for optimum TMD parameters have been introduced in the relevant literature, aiming at minimizing the displacement or acceleration response of the primary structure [10–12]. Several types of TMD have also been explored for human-induced floor vibration applications with some degree of success. A TMD in the form of a concrete filled steel box and steel plates suspended by springs and viscous dampers was used to alleviate the vibration of a cantilevered ballroom floor [13]. A pendulum TMD successfully controlled excessive vibrations of a laboratory test floor [14]. An active damper system has been explored to reduce high levels of vibrations caused by crowds of people jumping during concert events [15]. A large multiple TMD system with each TMD weighing up to two tons was installed on a gymnasium floor in order to lessen the vibrations caused by crowd-induced rhythmic vibrations [16].

A conventional TMD with a mechanical spring and dashpot is, however, not practically suitable for office floors where the vibration level that can cause human discomfort is too small. A new TMD in the form of a cantilever sandwich beam, which is more sensitive to low levels of vibrations, has been developed specifically for office floor applications. The new damper system was installed on a single bay of an actual office floor and performed well in a series of onsite tests [17]. In this paper, the sandwich beam TMD concept is extended to control multiple bays of a long-span office floor of steel–concrete composite construction. In addition, the effect of several tuning options for the TMD system on the response level and acceptability of the case study floor is numerically investigated.

2   Materials and Methods

2.1   Finite Element Model of Case Study Floor

Floor Description. Figure 1 illustrates the framing layout of a floor in an existing office building. The floor structure is comprised of concrete-metal decking slab spanning 2.7 m between secondary steel beams with span of up to 16.2 m. The secondary beams are in turn supported by steel girders spanning between the columns which are intermittently braced around the perimeter of the building. The floor zone of interest consists of six bays located within gridlines 1-7-B-C, where vibration levels due to normal walking need to be minimized in order to ensure comfort of the floor occupants in a premium office environment. These bays, denoted as (1)–(6) in Fig. 1, are those considered to be critical. Each of the investigated bays has a middle corridor virtually constituting a walking path along the bay span and crossing the bay center.

A finite element (FE) model of the floor as shown in Fig. 2 was built using SAP2000 software [18]. The model considered the stiffness differences in the two directions of the orthotropic composite slab, the steel beam offsets, and the reduced weight of the slab with ribs compared with a solid slab, etc. The columns attached to the floor were assumed to be fixed one story below and above the floor under consideration. The gravity load constituting the mass used in the modal analysis was taken as the dead load plus a representative live load of 0.4 kPa as recommended by design guides for office floors. Also, a damping ratio of 2% can be assumed for an open-plan electronic office [1, 3].
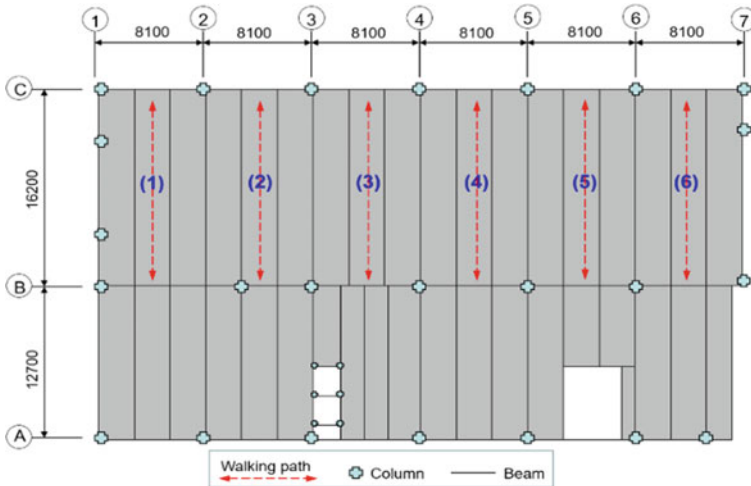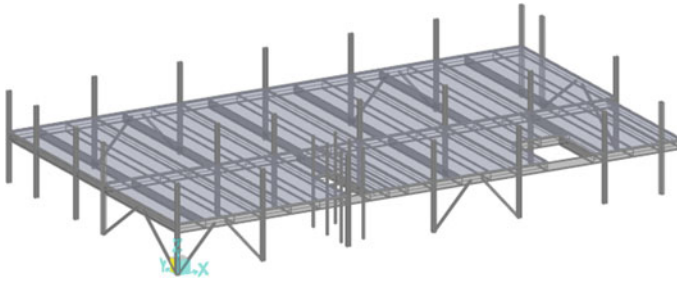

Fig. 1   Framing plan of case study floor

Fig. 2 FE model of floor system

Table 1 Dynamic load factors and phase angles [3]

i	α_i	ϕ_i
1	$0.436(if_p - 0.95)$	0
2	$0.006(if_p + 12.3)$	$-\pi/2$
3	$0.007(if_p + 5.2)$	π
4	$0.007(if_p + 2.0)$	$\pi/2$

Modeling of Walking Excitation. Contemporary guidelines [1, 3, 4] suggest using a Fourier series to represent the vertical dynamic force produced by successive steps of a person walking:

$$F(t) = Q\left[1 + \sum_{i=1}^{4} \alpha_i \sin(2\pi i f_p t + \phi_i)\right] \tag{1}$$

where Q is the static weight of the pedestrian, f_p is the step frequency, α_i and ϕ_i are the dynamic load factor and phase angle of the ith harmonic component, respectively. In this paper, a standard pedestrian weight of 760 N and the α_i and ϕ_i values given in Table 1 were used as recommended by the SCI P354 design guide [3].

Since the forcing function (1) is for a stationary walk, i.e., walking on the same spot, enhancement was needed to take into account the translation of the excitation force from one end of the floor span to the other end during a walking event. This was done by incorporating a half-sine function, which was a simplified representation of the fundamental modal displacements along the span, into the stationary force. The half-sine function was in the form of $u(x) = \sin(\pi x/L)$ where $u(x)$ was the unity normalized amplitude at position x from one end of the span and L was the span length. Let v_p be the walking speed then x can be replaced by $v_p t$ and u became a function of time. The modified walking force can therefore be written as:

$$F(t) = Q\sum_{i=1}^{4} \alpha_i \sin(2\pi i f_p t + \phi_i)\sin(\pi v_p t/L) \tag{2}$$

in which v_p can be computed from f_p using the following relationship [3]:

$$v_p = 1.67 f_p^2 - 4.83 f_p + 4.5 \tag{3}$$

It should be noted that the static component was already subtracted from (2) so that only the dynamic variation of the force was used in the time history analysis. The forcing function (2), which represents a walking event, can be applied to the center point of the floor bay as a time-varying concentrated force.

2.2 Modeling of Tuned Mass Dampers

The cantilever sandwich beam TMD concept developed by the authors in a previous project [17] was extended and tried on this case study floor. Figure 3a shows a schematic diagram of a four-arm TMD of which each arm is a sandwich beam having a rubber core constrained between two steel plates and a concentrated mass at the tip. The TMD can be installed within the limited space of about 150 mm of the raised floor without causing any architectural or structural intrusions. For structural analysis convenience, the TMD can be simplified as a single-degree-of-freedom system with a mass m_d, frequency f_d and damping ratio ζ_d, see Fig. 3b. The material properties and dimensions of the damper's components can be selected so that the expected values of m_d, f_d and ζ_d can be obtained [17]. However, a detailed discussion on the construction of the damper is outside the scope of this paper which focusses on numerical investigation of damper's tuning strategies for the multi-bay floor.

For the case study floor, it was proposed that a multi tuned mass damper system be installed within the raised floor space on six bays on the basis of retaining an open-plan office environment. Three four-arm dampers with twelve sandwich beams were provided for each bay of the investigated floor zone (Fig. 4). The damper with parameters m_d, f_d, and ζ_d was modeled in SAP2000 as a linear damper element. The assignment of damper parameters for various tuning options is presented in Sect. 3.2.
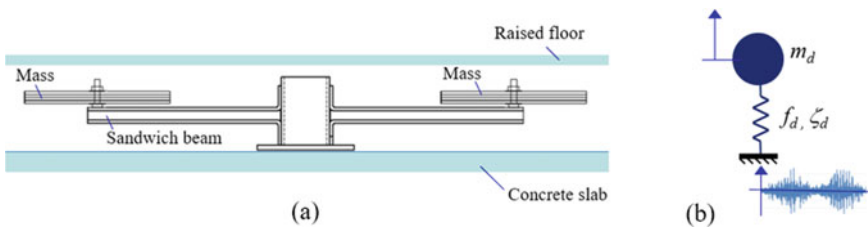

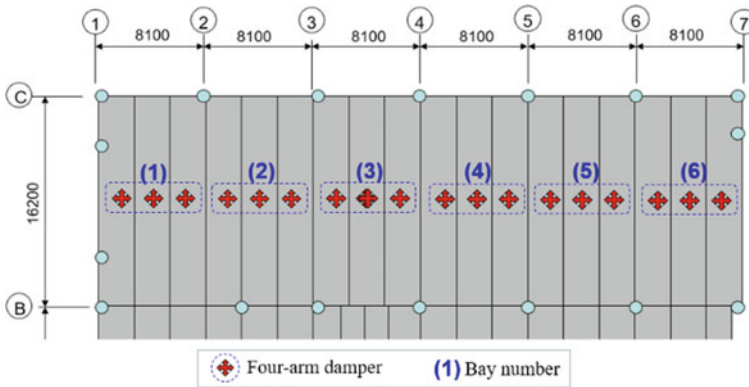**Fig. 3** A typical TMD (two transverse arms not shown for clarity)

Fig. 4 Distribution of dampers on floor plan

3 Results and Discussions

3.1 Floor Modal Properties

An observation of various mode shapes obtained from the FE modal analysis could assist in recognizing the vibration mode that would be most critical to the bay of interest. For the floor without dampers, Fig. 5 shows the modal displacement contours of some natural modes with maximum modal displacements located around the central area of the investigated bays. The dominant frequencies can be identified as 5.12 Hz (mode 2) for the first bay, 6.09 Hz (mode 8) for the second bay, 5.56 Hz (mode 5) for the third bay, 5.17 and 5.32 Hz (modes 3 and 4) for the fourth bay, 5.17 Hz (mode 3) for the fifth bay and 5.85 Hz (mode 7) for the sixth bay. Since these critical natural frequencies were less than 9 Hz, the case study floor can be classified as a low-frequency floor which might experience a resonant build-up response due to walking excitation [1, 3]. In the context of footfall-induced vibrations, the term "resonant" refers to when a harmonic or an integer multiple of the step frequency matches the floor natural frequency.

3.2 Damper Configurations

From an observation of the floor natural frequencies and mode shapes, three options of configuring the damper system as presented in Table 2 were proposed. The first option involved tuning the dampers on the six bays to four frequencies ranging from 5.17 to 6.09 Hz which closely matched the dominant frequencies of the bays. For the second tuning option, dampers of 5.17 and 6.09 Hz frequency were utilized. The
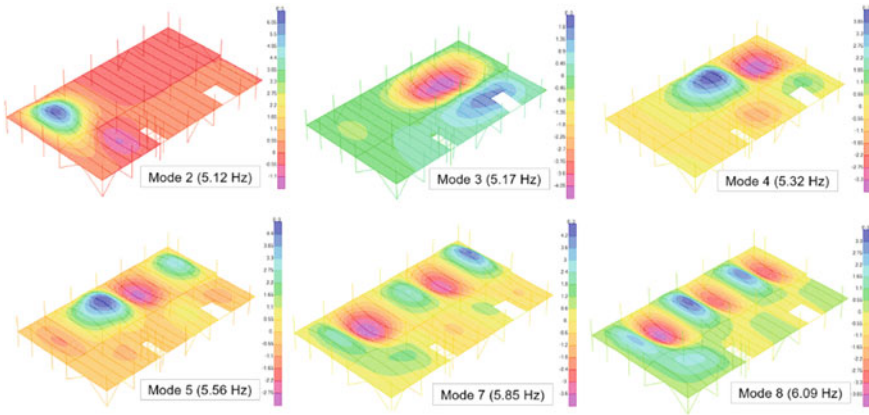
Fig. 5 Natural mode shapes and frequencies

Table 2 Frequency of TMDs

TMDs option	f_d (Hz) of dampers installed on					
	Bay 1	Bay 2	Bay 3	Bay 4	Bay 5	Bay 6
1	5.17	6.09	5.56	5.17	5.17	5.85
2	5.17	6.09	6.09	5.17	5.17	6.09
3	5.56	5.56	5.56	5.56	5.56	5.56

third tuning option, which was the simplest one, related to the use of only 5.56 Hz dampers in all six bays.

For simplicity in damper construction, the TMD's frequency can be adjusted by changing the amount of mass at the tip of the sandwich beams whereas other dimensions of the damper were unchanged in different tuning options. The equivalent mass m_d of each four-arm damper was estimated at 128 kg, 110 kg, 100 kg, and 92 kg associated with the damper frequency f_d of 5.17 Hz, 5.56 Hz, 5.85 Hz, and 6.09 Hz, respectively. The equivalent viscous damping ratio ζ_d of the TMD was taken as 4.5%, which was based on the authors' experience in testing off-the-shelf rubber for dampers in previous projects [17]. It should be noted that this damping level was lower than the otherwise suggested optimum values [10–12] due to restrictions in the inherent damping of the rubber used. The whole damper system weighs about 2060 kg for the first option, and 1980 kg for either the second or the third option. The total weight of the TMD system is equivalent to an additional uniformly distributed load of about 0.026 kN/m^2 that the investigated floor zone has to bear. This additional load is minimal considering safety factors have been used in strength design of the floor.

3.3 Response to Walking

For the floor model either with or without dampers, time history analysis was performed for a large number of load cases in which the step frequency f_p varied from 1.50 to 2.20 in 0.05 Hz increments. The investigated range of step frequencies covered the pacing rates commonly found in practice [1, 3]. The response at the center of the floor bay, i.e., the midpoint of the walking path, was collected for each analysis case. For instance, Fig. 6a shows the acceleration time history of the center of the first bay without dampers due to walking at 1.70 Hz pacing rate whose third harmonic closely matched the critical natural frequency of the bay. Figure 6b illustrates the response history of the same bay subjected to a 1.65 Hz walking activity after the floor model was added with the single-frequency dampers (TMDs option 3).

Also, plotted in Fig. 6 is the rolling RMS acceleration trace in which each a_{RMS} point was calculated from a set of acceleration values $a(t)$ as:

$$a_{RMS} = \sqrt{\frac{1}{T} \int_0^T a(t)^2 dt} \qquad (4)$$

in which the integration time T was taken as 1 s for response due to walking. The peak of the rolling RMS is referred to as the maximum transient vibration value (MTVV) which can be checked against the acceptance criteria recommended by the guidelines [3, 19]. For example, the MTVV found from Fig. 6 was 0.026 m/s² for the floor without dampers and 0.016 m/s² for the floor with dampers. It should be noted that the 1.70 Hz and 1.65 Hz pacing rates were found to be most critical to the bay without and with dampers, respectively (Fig. 7).

For each of the six investigated bays, a response spectrum associated with each TMD scenarios was constructed as presented in Figs. 7, 8 and 9. Each data point in the spectrum was derived from an appropriate time history analysis, similar to the one displayed in Fig. 6. The response spectrum shows the variation of the MTVV against the step frequency f_p. It can be seen that the response spectrum of the original
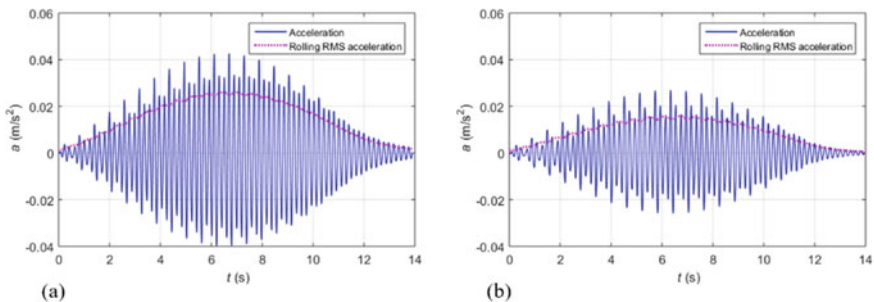

Fig. 6 Bay 1 acceleration time history: **a** without TMDs and **b** with TMDs option 3
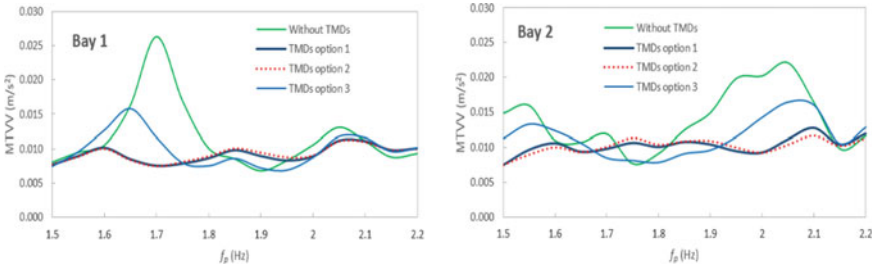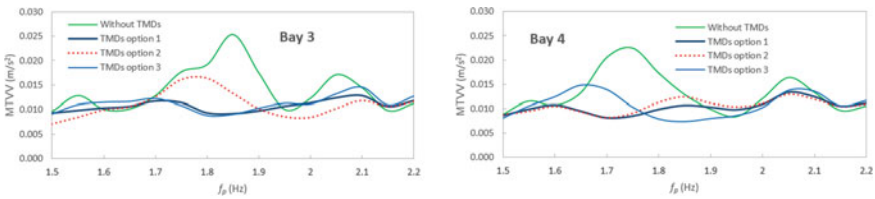
Fig. 7 Bays 1–2 response spectra
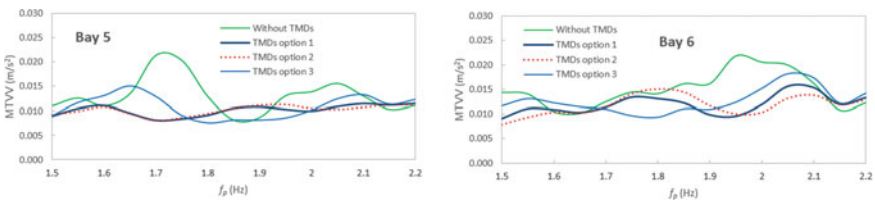

Fig. 8 Bays 3–4 response spectra

Fig. 9 Bays 5–6 response spectra

floor in the vicinity of resonance with high peak was flattened and lowered by the TMDs.

3.4 Evaluation of Floor Acceptability and Damper Effectiveness

The most critical step frequency which produced the maximum MTVV can be different across the floor without dampers and the floor with dampers as shown in Figs. 7, 8 and 9 and Table 3. This is because the natural frequencies of the floor changed after the floor was installed with dampers. Figure 10 presents a comparison of the maximum MTVV of the floor without dampers and that with dampers in three tuning scenarios. The maximum MTVV can be compared with tolerable thresholds

Table 3 Most critical step frequency f_p (Hz)

Scenario	Bay 1	Bay 2	Bay 3	Bay 4	Bay 5	Bay 6
Without TMDs	1.70	2.05	1.85	1.75	1.70	1.95
TMDs option 1	2.05	2.10	2.10	2.05	2.20	2.05
TMDs option 2	2.05	2.10	1.80	2.05	1.95	1.80
TMDs option 3	1.65	2.05	2.10	1.65	1.65	2.05
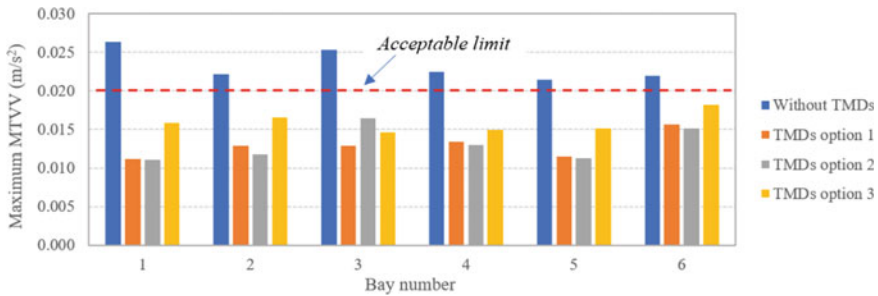
Fig. 10 Maximum response

to check the floor acceptability for human comfort. The limit of 0.02 m/s^2 is normally recommended for low probability of adverse comment in an office environment [4, 19].

Without dampers, the maximum MTVV found on the investigated floor zone was in the range 0.021–0.026 m/s^2, and all the six bays were deemed unsatisfactory for human comfort. The response level of the first bay, which was the most lively bay, can be decreased by 58% using either the four-frequency or two-frequency damper systems (TMDs options 1 and 2). The investigated floor zone equipped with one of these two damper systems was found to be in the range 0.011–0.016 m/s^2. For the floor with the single-frequency dampers (TMDs option 3), the maximum MTVV varied from 0.015 to 0.018 m/s^2 and a response reduction of up to 42% can be obtained. In other words, all the three damper options could enable the vibration levels of the floor bays to satisfy the acceptance criterion specified for a premium office.

4 Conclusion

A multi damper system has been proposed to control the walking-induced vibrations in multi bays of a long-span floor. Being compact and adding minimal weight to the existing structure, the dampers can be distributed within the raised floor space in the least intrusive manner. The effectiveness of three configurations of TMD tuning was examined. A reduction of up to 58% in acceleration response can be

obtained when the dampers were tuned to four frequencies covering the range of the critical natural frequencies of the bays under consideration. Approximately the same response mitigation can be achieved when the dampers were tuned to two frequencies which were the lower and upper bound of the natural frequency range of the bays. In the third tuning scenario, all dampers were tuned to a single frequency which was approximately the average of the critical natural frequencies of the six bays involved. The single-frequency damper system, which had the same weight as the two-frequency system and was 4% lighter than the four-frequency system, resulted in a lower reduction in response compared with the two other systems. The two-frequency damper system can therefore be considered most effective among the three options investigated. However, the single-frequency configuration was still be able to decrease the response of all six bays to the limit for comfort of occupancy, hence successfully enhancing the vibration serviceability of the case study floor.

References

1. Murray TM, Allen D, Ungar EE, Davis DB (2016) Design guide 11—vibrations of steel-framed structural systems due to human activity. American Institute of Steel Construction AISC, Chicago
2. Royvaran M, Avci O, Davis B (2021) An overview on floor vibration serviceability evaluation methods with a large database of recorded floor data. Dyn Civ Struct 2:91–101
3. Smith A, Hick S, Devine P (2009) Design of floors for vibration: a new approach—SCI publication P354. The Steel Construction Institute, Ascot
4. ISO 10137:2007 (2012) Bases for design of structures—serviceability of buildings and walkways against vibrations, 2nd edn. International Organization for Standardization, Geneva
5. Nguyen THA, Nguyen-Van H, Dao ND (2020) An investigation of human comfort criteria for footfall induced floor vibrations. IOP Conf Ser: Mater Sci Eng 869:052004
6. Setareh M (2020) Vibration serviceability evaluation of office building floors due to human movements. J Perform Constr Facil 34(4):04020068
7. Devin A, Fanning PJ (2019) Non-structural elements and the dynamic response of buildings: a review. Eng Struct 187:242–250
8. Nguyen HAT (2022) Relocation of walking path to resolve vibration problems in a lightweight floor. In: CIGOS 2021, emerging technologies and applications for green infrastructure, pp 471–479. Springer, Singapore
9. Ikeda Y, Yamamoto M, Furuhashi T, Kurino H (2019) Recent research and development of structural control in Japan. Jan Archit Rev 2(3):219–225
10. Den Hartog JP (2013) Mechanical vibrations. Dover Publication, New York
11. Tsai HC, Lin GC (1993) Optimum tuned-mass dampers for minimizing steady-state response of support-excited and damped systems. Earthquake Eng Struct Dynam 22:957–973
12. Nguyen HAT (2022) Optimum tuning of tuned mass dampers for acceleration control of damped structures. In: Tien Khiem N, Van Lien T, Xuan Hung N (eds) Modern mechanics and applications, LNME, pp 560–572. Springer, Singapore
13. Webster AC, Vaicaitis R (1992) Application of tuned mass dampers to control vibrations of composite floor systems. Eng J Am Inst Steel Constr 29(3):116–124
14. Setareh M, Ritchey J, Baxter A, Murray T (2006) Pendulum tuned mass dampers for floor vibration control. J Perform Constr Facil 20(1):64–73
15. Hudson EJ, Reynolds P, Nelson M, Christie N, Salcedo V (2016) Active control of concert-induced vibrations. In: Geotechnical and structural engineering congress, pp 1729–1741. American Society of Civil Engineers, Virginia

16. Liu P, Zhu HX, Moaveni B, Yang WG, Huang SQ (2019) Vibration monitoring of two long-span floors equipped with tuned mass dampers. Int J Struct Stab Dyn 19(09):1950101
17. Nguyen T, Gad E, Wilson J, Haritos N (2014) Mitigating footfall-induced vibration in long-span floors. Aust J Struct Eng 15(1):97–109
18. CSI (2017) Analysis reference manual for SAP2000, ETABS, SAFE and CSiBridge. Computers and Structures, Inc., Berkeley, CA
19. BS 6472-1:2008 (2008) Guide to evaluation of human exposure to vibration in buildings, Part 1: vibration sources other than blasting. British Standards Institution

Investigation of the Collapse of the Steel Space Truss Roof Induced by Wind Action

Tran-Hieu Nguyen [ID]**, Quoc-Cuong Nguyen, Nhu-Hoang Nguyen, Van-Cuong Nguyen, and Anh-Tuan Vu**

1 Introduction

In recent years, Vietnam has been seriously affected by natural disasters. In 2020, Typhoon Molave (known in Vietnam as Typhoon No. 9) swept through the central provinces of Vietnam, destroying more than 56,000 houses, collapsing several large-scale constructions, causing heavy damage to people and properties. On October 28, 2020, a part of the roof of coal storage collapsed due to the impact of the typhoon. The incident caused the loss of the life of workers and halted the production operation of the plant. In the context of climate change as well as unpredictable natural disasters, it is important to find out the causes of the collapse in order to propose measures to strengthen existing constructions as well as avoid repeating the above incident.

The literature review indicates that many studies on the collapse of constructions, especially large-span steel roof structures, have been conducted. For example, in 2010, Brencinh [1] investigated the causes of the collapse of an industrial steel shed. The study showed that a series of human mistakes as well as a lack of control procedures are the reasons for this incident. In 2013, Augenti and Parisi [2] carried out a buckling analysis of large-span planar trusses that are failed down during the erection phase. In this study, a three-dimensional numerical model that takes into account factors such as the geometry and material nonlinearities, the effect of purlins and temporary bracing was developed to evaluate the safety state of the structure. The results indicated that the temporary bracing does not ensure the overall stability of the structure under wind action.

T.-H. Nguyen (✉) · Q.-C. Nguyen · N.-H. Nguyen · A.-T. Vu
Hanoi University of Civil Engineering, Hanoi, Vietnam
e-mail: hieunt2@nuce.edu.vn

V.-C. Nguyen
CCU Ltd., Hanoi, Vietnam

Another study was implemented by Piroglu et al. in 2016 [3] to find out the cause of the partial collapse of a double-layer grid structure after exceptional snowfalls. In the same year, Fu and Parke [4] developed three-dimensional finite element models according to different collapse scenarios. Based on the obtained observations, some methods to reduce the risk of progressive collapse for this kind of structure were advised. Next, the influence of the structural behavior of MERO joints on the collapse of a long-span steel trusses roof in North Italy was carried out by Pieraccini et al. in 2017 [5]. Then, the buckling of tube bars of a space roof truss was investigated by Vatansever [6]. Moreover, seven failures that occurred from 2004 to 2017 were reviewed in [7], and the main causes of these failures were summarized.

In 2020, Tufekci et al. [8] conducted a numerical investigation of the failure of a steel roof truss in Turkey. In this study, the commercial finite element analysis software ABAQUS was used to simulate the behavior of the structure under severe weather conditions like strong wind or heavy rain with the aim of finding the main cause of the collapse. Recently, a study on the robustness of a double-layer space structure was carried out by Piana et al. [9]. By alternately removing the most stressed bars in the structure and monitoring the changes of the stress in the remaining bars, the behavior of the structure when occurring local damages is clarified.

A number of the collapse of large-span steel roof structures that have recently occurred in Vietnam can be listed as the failure of the roof of the 250-seat hall in 2019, the partial collapse of the steel space truss of coal storage in 2020, the buckling collapse of the steel rafters of an industrial building in the construction phase in 2021, etc. However, the understanding of the causes of these incidents is still very limited.

This study aims to find out the main reason for the collapse of the steel space truss under the heavy wind of Typhoon Molave in 2020. For this purpose, the study consists of two phases. Firstly, a site investigation is carried out, and observations are reported. In the second, a numerical model is developed to simulate the behavior of the structure under wind action. The results obtained from the numerical modeling are compared with the findings collected from the site investigation. Finally, a probable reason for the collapse is presented.

The rest of the article is organized as follows. Section 2 describes the details of the collapse. The findings collected from the site investigation are also reported in this section. Section 3 introduces the procedure to develop the numerical model. Next, obtained results and discussions are presented in Sect. 4. In the end, Sect. 5 concludes the article.

2 Description of the Collapse of the Roof Structure

2.1 Overview of the Roof Structure

The coal storage where the failure happen is located in a heavy industrial plant in central Vietnam. The coal storage consists of an outdoor yard and four vaulted sheds

arranged in parallel. The collapse has occurred at the largest vaulted shed with a span of 87 m and a height of 43 m. This vault is separated into five blocks in which two blocks at the ends (Block 1 and Block 5) have a length of 152 m, and three middle blocks (from Block 2 to Block 4) have a length of 144 m. Expansion joints with a length of 500 mm are arranged between two adjacent blocks.

The roof structure is a MERO-type double-layer grid with a depth of 2.8 m. The space truss consists of tubular members connected together through MERO joints. Each joint is a steel spherical ball linked to members via bolts. This kind of joint is widely used in double-layer grids due to its zero eccentricity as well as its ease of erection. Nine tubular sections used in this structure include D76 × 4; D88.9 × 4.5; D114.3 × 5; D139.7 × 6; D168.3 × 6.3; D193.7 × 8; D219 × 8; D219 × 12; and D244.5 × 20. Seven types of MERO nodes have diameters of 110, 140, 160, 180, 200, 220, and 240 mm, respectively. The bolt diameter varies from 16 to 56 mm. Members, balls, and sleeves are made from steel with the yield strength f_y = 345 MPa, except for cones made from steel with the yield strength f_y = 245 MPa. All bolts are grade 10.9 having the tensile strength f_{ub} = 1000 MPa and the yield strength f_{yb} = 900 MPa.

This structure is designed according to Vietnamese standards. In more detail, the load actions are determined based on the standard TCVN 2737:1995 [10] as follows: dead load DL = 16.5 daN/m^2 including the weights of profiled sheeting, purlins, sag rods, and cleats; live load for maintenance LL = 30 daN/m^2; dust load DST = 50 daN/m^2; mean wind pressure W_0 = 125 daN/m^2 (mean wind speed in 3 s, return period 20 years V_0 = 45.2 m/s); and territory category B; two actions caused by temperature changes T_1 = +30 °C and T_2 = −25 °C; the reference peak ground acceleration a_{gR} = 0.0519 g. The aerodynamic coefficients of the roof are calculated based on Diagram Number 4 of Table 6 in Ref. [10]. According to the meteorological report, the maximum value of the wind speed at the time of the incident reached 41 m/s, which is lower than the design value.

This structure is analyzed using the commercial software SAP2000 considering the perfect elastic behavior of the material and then checked the strength and displacement conditions according to TCVN 5575:2012 [11]. The diameters of MERO balls are determined using Eq. 5.3.3-1 and Eq. 5.3.3–2 of the standard JGJ 7-2010 [12]. Several critical joints are re-checked the stress condition using the finite element analysis software SIEMENS NX8.5.

2.2 The Collapse of the Roof Structure

At 11:30 (local time) on October 28, 2020, a part of the roof structure was collapsed due to the impact of Typhoon Molave. This typhoon has been recognized as the strongest typhoon in Vietnam in the last 20 years. The collapse partially occurred in Block 2, 3, and 4 as presented in Fig. 1. Two remaining blocks in the ends had local damages in some locations but still maintained overall stability. Three adjacent sheds were still safe after the typhoon. As can be observed in Fig. 1, the double-layer grids
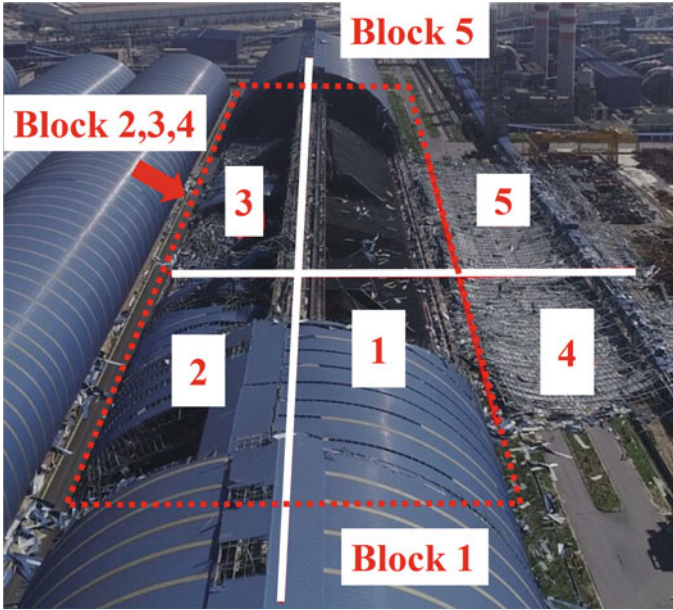
Fig. 1 View of the partial collapse

of Block 2, 3, and 4 were broken into two parts, in which the part on the windward side (Zone 2 and Zone 3) was failed down due to the impacts of the self-weight and the positive pressure of the wind, while the part on the leeward side (Zone 4 and Zone 5) was uplifted due to the suction pressure of the wind. Zone 1 did not fall down but it lost its bearing capacity.

A site survey was carried out some days after the collapse. At the time of the survey, the collapsed part was disassembled. Some photos taken during the site survey are presented in Fig. 2. It is clearly seen that in Block 1 and Block 5, the profiled sheet cladding is torn, and some tubular truss members were buckled (Fig. 2a); some connecting bolts were broken (Fig. 2b).

3 Numerical Modeling

In this section, a nonlinear finite element (FE) analysis is performed to assess the safety level of the double-layer grid structure. Only the collapsed part (Block 2, similar to Block 3 and Block 4) is simulated in the model. Two blocks at the ends of the construction are not considered in this study. The three-dimensional FE model containing 8122 members is developed using the software SAP2000 as shown in Fig. 3.
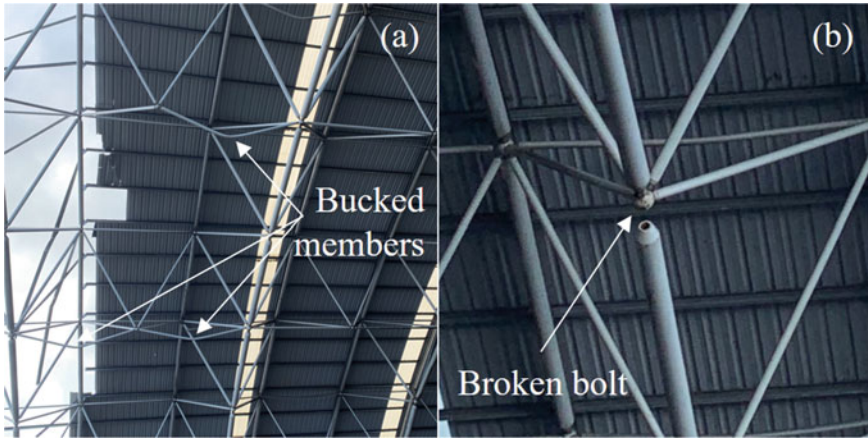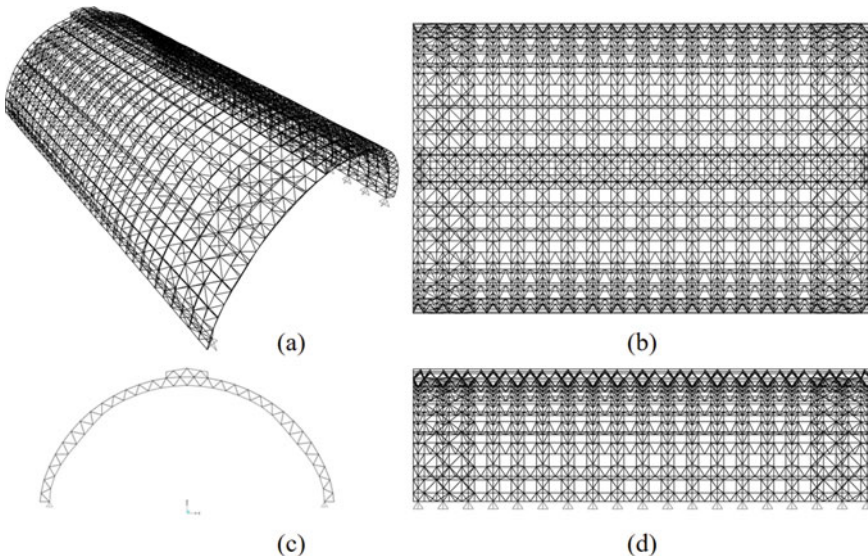
Fig. 2 Observations during the site survey

Fig. 3 Finite element model of the collapsed structure

The material properties of members are as follows: the modulus of elasticity E = 200,000 N/mm^2; the yield strength f_y = 345 N/mm^2, the ultimate strength f_u = 510 N/mm^2, Poisson's ratio v = 0.3, and the density ρ = 7850 kg/m^3. Tubular truss members are modeled as pinned frames which ensure that only axial forces exist inside the members. MERO balls are replaced by joint forces applied at nodes. The structure is pinned at base joints. The model is developed with the aim of investigating the collapse due to the wind action, therefore only the dead load (DL) and the
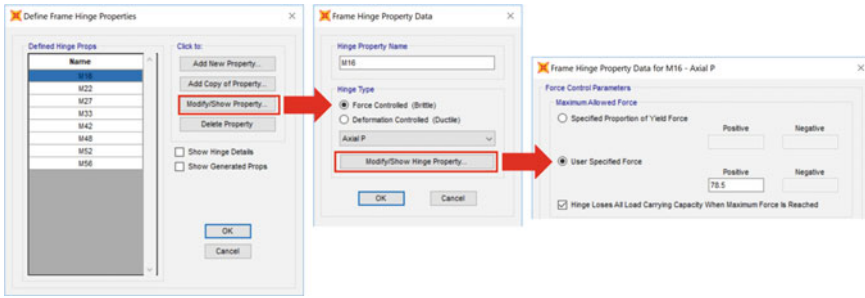
Fig. 4 Definition of *hinge*

transversal wind load (WX+) are introduced in the model, and other loads are not considered in this study.

Connecting bolts at the ends of truss members are presented in the model using the feature *Hinge* provided in the software SAP2000. Specifically, eight *Hinge* types are defined in the model corresponding to eight bolt diameters used in the structure. Figure 4 displays steps for defining *hinge* M16 for bolts with a diameter of 16 mm. All *hinge*s are set to force controlled (brittle) type with axial *P*. The maximum allowed force for each *hinge* type is specified as the design tensile strength of the corresponding bolt which is determined according to TCVN 5575:2012 [11] as follows:

$$[N]_{tb} = f_{tb} A_{bn} \tag{1}$$

in which: $[N]_{tb}$ is the design tensile strength of an individual bolt; f_{tb} is the design tensile strength of the bolt material ($f_{tb} = 500$ N/mm^2 for bolt Grade 10.9); A_{bn} is the net cross-sectional area of one bolt.

The option "*hinge loses all load carrying capacity when maximum force is reach*" is chosen to mimic the bolt fracture when the axial force exceeds the maximum allowable force. All members are then assigned the corresponding *hinge* at their two ends.

The initial geometrical imperfection of the structure is introduced in the model using the feature "*modify undeformed geometry*" as shown in Fig. 5. The shape of the initial geometrical imperfection is based on the eigenvector that is found from the modal analysis, while the magnitude of the imperfection equals the allowable displacement of the structure ($L/250 = 348$ mm).

Parameters of the nonlinear analysis are set as presented in Fig. 6. The geometric nonlinearity is taken into account by choosing the option "*P-delta plus large displacements*". In fact, the structure is subjected the wind action when it is subjecting its self-weight. To simulate sequential actions, the feature "*continue from state at end of nonlinear case*" is applied in which the analysis of the load case WX+ will be started from the initial stress state of the load case DL. The value of the load case WX+ is
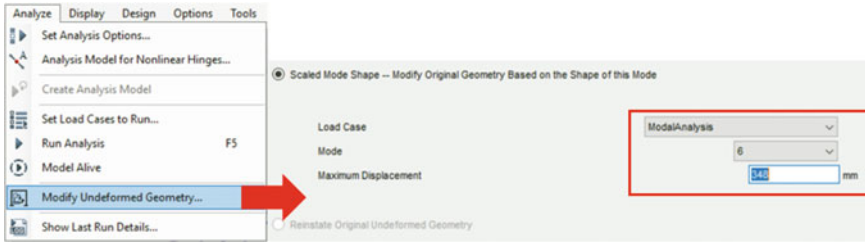
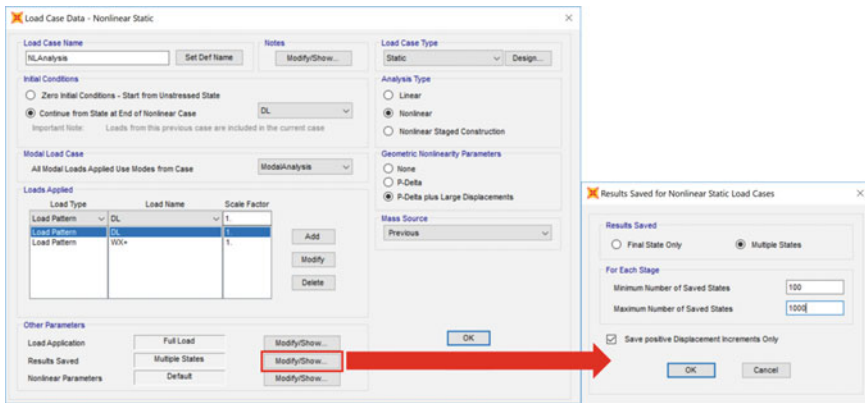Fig. 5 Introduction of the initial geometrical imperfection

Fig. 6 Parameters of nonlinear analysis

separated into 100 steps in the nonlinear analysis in which the results of every step are recorded for monitoring.

4 Results and Discussion

The nonlinear analysis is conducted using the personal computer having CPU Intel Core i5-5257 2.7 GHz and 8 Gb RAM. The result obtained from the nonlinear analysis is displayed in Fig. 7. *Hinge*s have appeared in some D76 × 4 members near the top of the shed. Additionally, Fig. 8 plots the increase of the axial force of Member 8801 per each step. At Step 70, the axial force equals 78.4 kN (very close to the maximum allowable force of the M16 *Hinge*) but at Step 71, the axial force decreases to 76.7 kN, indicating the appearance of *hinge*. In other words, the axial force of Member 8801 exceeds the tensile strength of the connecting bolts when the wind pressure reaches 71% of the design value.

The fracture of connecting bolts significantly changes the structural schematic of the double-layer grid, leading to the change of internal forces in comparison
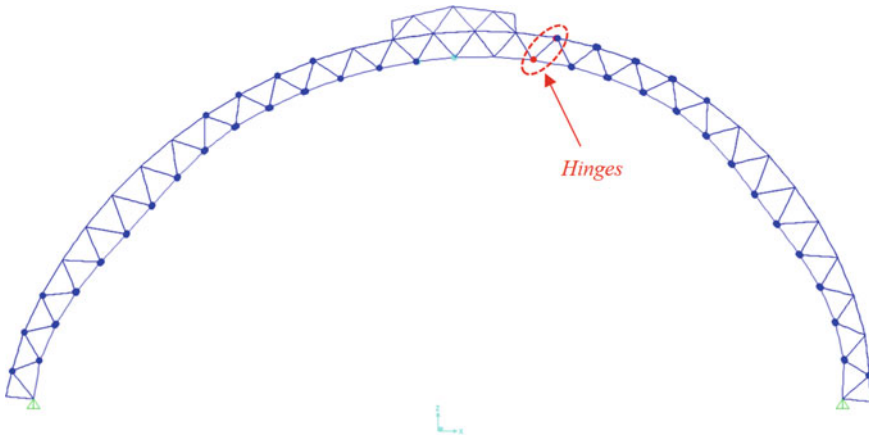
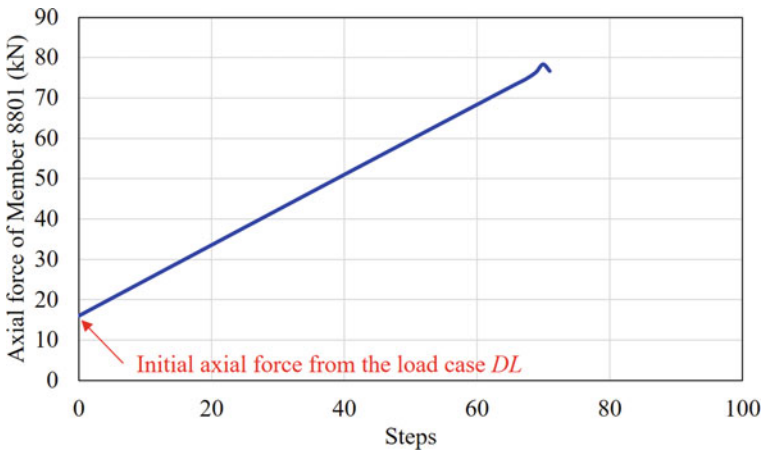**Fig. 7** Distribution of *hinge*s in the FE model

Fig. 8 Axial forces of Member 8801 per each step

with the initial design. Consequently, the structure can be broken into two parts at the location near the ventilation. The part on the windward side can be failed down while the remaining one can be uplifted as visualized in Fig. 9. The probable scenario is consistent with the real observation.

5 Conclusion

This article presents a study to find out the probable reason for the collapse of the coal shed due to the typhoon. Particularly, this research develops a nonlinear model using
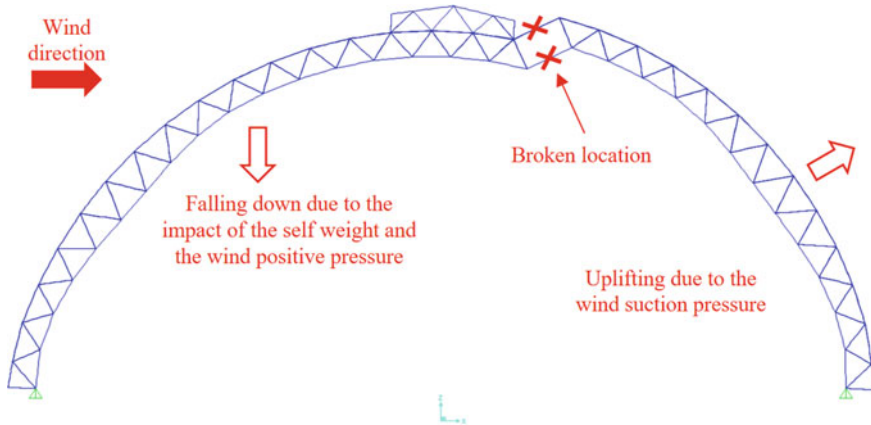
Fig. 9 Probable scenario of the collapse

the finite element analysis software SAP2000 with some advanced features such as hinge and nonlinear analysis. The obtained results show that in some members, the axial forces exceed the design tensile strength of the connecting bolts at their ends. This is probably the main cause of the collapse.

The study proposes a simulation procedure to identify the location of critical bolts in a double-layer grid structure using SAP2000. This software is widely used by structural engineers. The proposed procedure is highly applicable in practice.

In general, this study enlarges the understanding of the collapse of the double-layer grids, thereby proposing measurements to strengthen existing constructions as well as preventing repeat incidents.

References

1. Brencich A (2010) Collapse of an industrial steel shed: a case study for basic errors in computational structural engineering and control procedures. Eng Fail Anal 17(1):213–225
2. Augenti N, Parisi F (2013) Buckling analysis of a long-span roof structure collapsed during construction. J Perform Constr Facil 27(1):77–88
3. Piroglu F, Ozakgul K, Iskender H, Trabzon L, Kahya C (2014) Site investigation of damages occurred in a steel space truss roof structure due to ponding. Eng Fail Anal 36:301–313
4. Fu F, Parke GAR (2018) Assessment of the progressive collapse resistance of double-layer grid space structures using implicit and explicit methods. Int J Steel Struct 18(3):831–842
5. Pieraccini L, Palermo M, Trombetti T, Baroni F (2017) The role of ductility in the collapse of a long-span steel roof in North Italy. Eng Fail Anal 82:243–265

6. Vatansever C (2019) Investigation of buckled truss bars of a space truss roof system. Eng Fail Anal 106:104156
7. Kabando EK, Gong J (2019) An overview of long-span spatial grid structures failure case studies. Asian J Civ Eng 20(8):1137–1152
8. Tufekci M, Tufekci E, Dikicioglu A (2020) Numerical investigation of the collapse of a steel truss roof and a probable reason of failure. Appl Sci 10(21):7769
9. Piana G, De Biagi V, Chiaia B (2021) Robustness of an airport double layer space truss roof. Curved Layered Struct 8(1):36–46
10. Ministry of Science and Technology of the Socialist Republic of Vietnam: TCVN 2737:1995 (1995) Loads and actions. Design Standard, Hanoi
11. Ministry of Science and Technology of the Socialist Republic of Vietnam: TCVN 5575:2012 (2012) Steel structures. Design Standard, Hanoi
12. Ministry of Housing and Urban-Rural Construction of the People's Republic of China: JGJ 7-2010 (2010) Technical specification for space frame structures. Beijing

Deep Learning Damage Detection Using Time–Frequency Image Analysis

Dung Bui-Ngoc [ID]**, Hoa Tran-Ngoc** [ID]**, Lan Nguyen-Ngoc** [ID]**,
Hieu Nguyen-Tran** [ID]**, and Thanh Bui-Tien** [ID]

1 Introduction

Monitoring the life cycle of critical civil infrastructure is essential to ensure its structural integrity. Recently, researchers have paid more attention to the use of deep learning methods to solve damage detection problems. A neural network such as CNN-based models, which has the ability to learn hierarchical features, has shown promising results in dealing with different issues of SHM. In an SHM system, measured vibration data is usually recorded in the acceleration-time domain; however, this data can be converted into a time–frequency domain to identify damaged structures [1]. The vibration signal is transformed into a time–frequency domain by a short-term Fourier transform (STFT) and visualized on the image. Then, an efficient image classifier from the artificial intelligence program was used to detect damages in the structure. He et al. [2] took advantage of the comprehensive feed-forward architecture of a 2D-CNN classifier and combined it with the transfer learning technique to adjust the given model for damage detection. The learning transfer techniques allow it to export pre-trained general knowledge to a given field with big measurement data belonging to different segments. The damaged identification workflow consists of three basic steps. Initially, the initial vibration signal is fed to a spectral plate preprocessing unit to convert it into a time–frequency representation image and then to the input 2D-CNN models. The feature is then continuously transmitted to two fully connected levels, followed by going through the softmax activation function into the output level.

D. Bui-Ngoc · H. Nguyen-Tran
Faculty of Information Technology, University of Transport and Communications, Hanoi, Vietnam
e-mail: dnbui@utc.edu.vn

H. Tran-Ngoc · L. Nguyen-Ngoc · T. Bui-Tien (✉)
Faculty of Civil Engineering, University of Transport and Communications, Hanoi, Vietnam
e-mail: btthanh@utc.edu.vn

CNN has been used to identify structural damages by learning the vibration signal data [3, 4]. Recently, the vibration signals have been transformed into images, and the 2D CNN has been used to detect the damage on these images [5]. In [6], the signal time series is split into various segments and then converted to images; then, the deep neural network is used to automatically train and classify the abnormal in these images. The image localization method is also applied to the aerial vision sensors to detect the small fraction of interest on the images [7]. In this case, time-series data was split into sections and converted to a single dual-channel image, then applied CNN for training and abnormal detection [8]. The video measurement data can also be used to identify the high spatial resolution mode [9].

While CNN has been proved to be effective in solving many image-based object detection problems, there still exist some factors that may hinder its accuracy while dealing with damage detection. The first problem is the imbalance dataset, which is the lack of damage training data [8]. The second problem is that the features in the time-domain data are not clear enough to distinguish between the undamaged and damaged state. Moreover, the insufficiency in the visualization of frequency data poses a further challenge in distinguishing between these two states. In this paper, to overcome the above problems, we propose a method to enhance the features between normal and damage states by segmenting the time–frequency images using the graph method [10]. The segmented image helps increase the discrimination between bands in images, which helps avoid overfitting of the model. The accuracy of the experimental results has validated the efficiency of the method.

2 Methodology

2.1 Short-Time Fourier Transformation

Time-series signal is typically represented in the frequency domain through fourier transformation (FT). It is very effective at identifying sinusoidal components of a time-domain signal. However, the basic building blocks of the FT and complex exponentials oscillate over all of the time (between $-\infty$ and $+\infty$). For this reason, it is difficult for the FT to represent signals that are localized in time. This informal observation, in fact, reflects a fundamental property (uncertainty principle) of the fourier transform.

Meanwhile, the STFT has many advantages in compared with the fourier rans-form, such as its superiority in frequency and time localization properties. Thereby, the short-time fourier transform (STFT) is used to overcome this limitation of the fourier transform. STFT is considered to be a concatenation of fourier transforms of a windowed signal frame. We separate a long signal into various segments of equal length, followed by applying FT. The treated data will be used to generate spectro-grams in time–frequency analysis. While the fourier transform provides frequency

information for the whole time interval of the measured data, STFT is able to give information on the localized frequency of a signal varied over time.

The formulation for STFT based on basis functions is given in Eq. (1) as follows:

$$\text{STFT}(\tau, f) = \int_{-\infty}^{\infty} x_j(t)\psi(t - \tau)e^{-2\pi i f t} \ dt \tag{1}$$

With the time discretization, Eq. (1) is rewritten as follows:

$$\text{STFT}_{n,f} = \sum_{k=n}^{n+N-1} x_{k,j}\psi_{k-n}e^{-2\pi i f k} \tag{2}$$

where $x_j(t)$ is a signal from sensor j to be transformed, ψ is the window function, and N denotes the length of the segments. STFT visualization is represented by a spectrogram, which is a graphic representation of STFT magnitude over time [11]. A spectrogram of STFT also shows the squared value of STFT coefficients. This is why the energy in the time–frequency signal is considered to be equal to the energy in STFT spectrograms. In this paper, the proposed STFT technique can be used to convert a 1-D time-series into a 2D image of the respective time–frequency representation.

2.2 Two-Dimensional CNN

CNN is a deep neural network with a multilayer neural network consisting of two or more hidden layers. CNN is originally designed for image analysis or image recognition, and it has been widely used for different purposes such as object identification for images and videos, images classification, and so on [12]. The structure of CNNs consists of three main substructures: the convolutional layers, the pooling layers, and the fully connected layers. The input images are received by the passive layer of the input layer before getting passed to the convolutional layers. In CNN structure, the input data is represented as multidimensional arrays, and it can be used for any labeled data. The convolutional layer is the backbone component of a CNN structure. It extracts the high-level features from the input image by applying multiple different filters and capturing the characteristic features (feature maps). Each unit of feature map is created by convolving a so-called local receptive field, which consists of a small segment of input data. The back-propagation algorithm is then used to train these non-fixed filters. After the convolution layer comes the pooling layer. Several features can be extracted using convolutional operation; however, a large set of features can lead to overfitting of the data. To solve this issue, the pooling operation (subsampling layer) is applied to reduce the number of feature maps from the convolution operation. The processed features are then fed to the fully connected
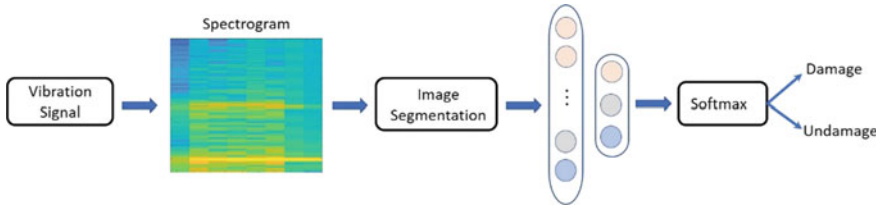
Fig. 1 Procedure of the CNN-based method for damage classification

layer, which consists of activation functions to perform the classification task. The fully connected layer will classify the image to its respective labels.

2.3 Proposed Methodology

The framework of the proposed methodology consists of two main steps, as shown in Fig. 1. Firstly, raw time-series signals are fed to the framework as input, followed by transforming the output-only signal into images presented as a spectrogram. These images are then segmented using the graph method. Secondly, the segmented images are fed to the 2D convolution neural network to extract the required features accordingly before passing through the softmax activation function for damage classification of damage or undamaged states.

In the first step, the time-domain input signal is segmented into several separated or overlapped frames by multiplying it with a window function. Then fast fourier transform (FFT) is applied to each frame to obtain the short-time fourier transform (STFT) segments. The log-spectrum in decibels is the most common visualization of STFT's spectra. It can be visualized with a heat-map known as a spectrogram, a so-called spectrogram-based image. After transforming these output-only vibration signals into images, it will take advantage of CNN's feature extraction and classification capabilities. In the second step, the images are fed to the convolution neural network to extract the desired features accordingly in order to classify the damage states.

Since the patterns of the images generated by STFT are insufficient to distinguish the undamaged and damaged state, the graph-based segmentation will be applied to enhance the intensity between bands, which will lead to improved detection results [10]. Considering the graph $G = (V, E)$, where V is the vertex set containing pixels in the image, E is the edge set constructed by connecting pairs of pixels. The edge weight function can be calculated as below:

$$w((v_i, v_j)) = |I(p_i) - I(p_j)| \tag{3}$$

where $I(p_i)$ is the intensity of pixel p_i.

For each time–frequency image, to enhance the difference between color bands, the image is segmented into three different channels, colored red, green, and blue, and get the intersection of three components. The weight w of an edge can be used as the distance between two points in the feature space, and each pixel is mapped to the feature point. Two regions in the image will be merged if a single low-weight edge is detected between them.

In the next step, the images are fed to the convolution neural network to extract the desired features accordingly in order to classify the damage and undamaged states. We constructed the CNN by adapting the ResNet. The CNN architecture contains the convolution layer, which consists of 32 filters, followed by 19 residual bottleneck layers. The ReLU is added for low computation. The kernel size is 3 × 3 for the model network, and the dropout and batch normalization was used during training.

3 Results

In this section, a case study of a simply supported bridge is used to consider the effectiveness of the proposed approach. The bridge is depicted as in Fig. 2.

Vang bridge is located at Km7+591, national road 47B, Yen Dinh district, Thanh Hoa Province, Viet Nam. The bridge was built and has been operating since 1995. The bridge includes four spans with the same length of 15 m. The cross-section consists of 4 T-shaped reinforced concrete beams with a distance of 115 cm. The height of the beam is 100 cm. Two abutments are buried ones, whereas the pier is of two-column bent.

Because four spans of the bridge are the same, to reduce the computational cost, only one span is chosen for damage detection. The bridge is divided into 31 elements as Fig. 3 using beam elements. Each element consists of 06° of freedom (DOFs) with translational, rotational displacements in x, y, and z directions.

FEM is then employed to generate data to train the network. Damage cases are created by reducing the stiffness values of different elements. Both undamaged and

(a)   (b)

Fig. 2 Vang bridge: **a** the top view of the bridge; **b** downstream side of the bridge

Fig. 3 Finite element model (FEM) of the bridge

damaged cases are taken into account. Totally, 145 scenarios comprising 29 undamaged and 116 damaged samples are generated. The initial outputs of FEM are accelerations in the time domain then converted into images with damaged and undamaged labels using spectrogram analysis of short-time fourier transform. The samples of the image according to the damaged and undamaged state are shown in Fig. 4.

The frequency images are segmented using graph-based method to enhance the difference between bands and states. The distances between feature points in this experiment are calculated by Euclidean distance. All the closeness points are then assigned to the cluster in the image. Figure 5 shows the segmented image corresponding to the 50% damage and undamaged image.

After the segmented images are generated, all of those images are then put on the CNN model to train it. About 80% of all the data are used for the training phase, while the remaining 20% are for testing. During the training process, the features
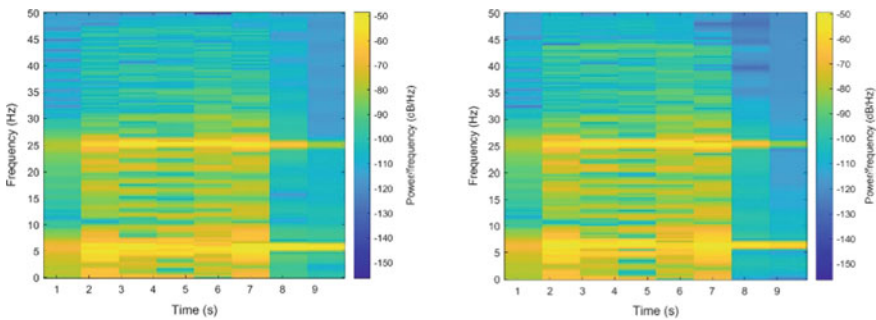

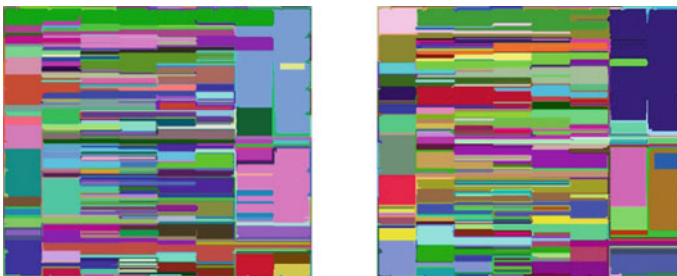**Fig. 4** The images with damaged (left) and undamaged (right) labels

Fig. 5 The images segmented with the damage (left) and undamaged (right) from the frequency image
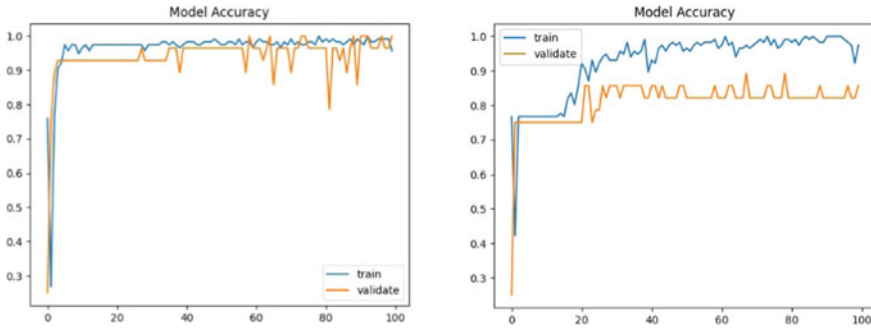
Fig. 6 Performance of training and validating of the time–frequency image (left) and segmented image (right)

and labels are given for all the time-series data of the training data set. The objective is to capture the liaison between features and class labels. The method was tested on the two types of data, the frequency images, and segmented images, for comparison. The performance of the training and testing process is shown in Fig. 6.

Twenty-eight samples are used for validation, including five samples for undamaged and 23 samples for damage. The level of accuracy is evaluated based on the test result. The ground truth notion of positive and negative detection is used to validate the accuracy of the proposed method. The confusion matrix for the proposed method is shown in Table 1. The accuracy level of the method is calculated as:

$$\text{Accuracy} = \frac{(\text{True Positive} + \text{True Negative})}{\left(\begin{array}{c}\text{True Positive} + \text{True Negative} \\ +\text{True Positive} + \text{True Negative}\end{array}\right)}$$

The obtained results shown that the accuracy of the proposed method for the frequency image is 97% in the training phase and 94% in the testing phase. According to the confusion matrix in Table 1 (left), this led to the overfitting because all the validate samples classified but the model cannot be performed to 100%. This problem is due to the lack of data as well as imbalance in the data. For the segmented image, the accuracy in training phase is 92% and testing phase is 79%. Also, as the confusion matrix in the Table 1 (right), there are 19 samples of damaged were detected, otherwise, 4 samples were misclassified. In the undamaged state, there are three samples

Table 1 Confusion matrix for frequency image (left) and segmented image (right)

Classification	Predicted			Predicted	
Actual	23	0	Actual	19	4
	0	5		2	3

of undamaged were detected and two samples was uncorrected. This suggested the method can be applied to the transformed vibration data.

4   Conclusions

In this paper, we proposed a novel damage identification method using an improved two-dimensional convolution neural network. The images converted from vibration data can be used as input for CNN to extract features from the given images. The image segmentation technique can also help to enhance distinguishing features. Experimental results show that the method is not only suitable but also effective for damaged detection. The results indicated that our proposed method is able to achieve high accuracy results in damaged detection with imbalanced data. This method is also promising in detecting the level of damage in the structure.

References

1. Pan H, Azimi M, Gui G, Yan F, Lin Z (2018) Vibration-based support vector machine for structural health monitoring. In: Conte J, Astroza R, Benzoni G, Feltrin G, Loh K, Moaveni B (eds) Experimental vibration analysis for civil structures. EVACES 2017. Lecture notes in civil engineering, vol 5. Springer, Cham. https://doi.org/10.1007/978-3-319-67443-8_14
2. He K, Zhang X, Ren S, Sun J (2016) Deep residual learning for image recognition. In: Proceedings of the IEEE conference on computer vision and pattern recognition (CVPR), pp 770–778. https://doi.org/10.1109/CVPR.2016.90
3. Abdeljaber O, Avci O, Kiranyaz MS, Boashash B, Sodano H, Inman DJ (2018) 1-D CNNs for structural damage detection: verification on a structural health monitoring benchmark data. Neurocomputing 275:1308–1317. https://doi.org/10.1016/j.neucom.2017.09.069
4. Nguyen-Tran H, Bui-Tien T, Wahab M, Bui-Ngoc D (2020) Damage detection in structural health monitoring using combination of deep neural networks. J Mater Eng Struct 7(4):619–626
5. Cha Y-J, Choi W, Buyukozturk O (2017) Deep learning-based crack damage detection using convolutional neural network. Comput-Aided Civ Inf 32:361–378
6. Yuequan B, Zhiyi T, Hui L, Yufeng Z (2019) Computer vision and deep learning–based data anomaly detection method for structural health monitoring. Struct Health Monit 18(2):1–21
7. Yeum CM, Choi J, Dyke SJ (2017) Autonomous image localization for visual inspection of civil infrastructure. Smart Mater Struct 26:035051
8. Tang Z, Chen Z, Bao Y, Li H (2019) Convolutional neural network-based data anomaly detection method using multiple information for structural health monitoring. Struct Control Health Monit 26:e2296
9. Yang YC, Dorn C, Mancini T et al (2017) Blind identification of full-field vibration modes from video measurements with phase-based video motion magnification. Mech Syst Signal Pr 85:567–590
10. Felzenszwalb PF, Huttenlocher DP (2004) Efficient graph-based image segmentation. Int J Comput Vision 59:167–181

11. Boashash B (2016) Time-frequency signal analysis and processing a comprehensive reference. Academic Press
12. LeCun Y, Boser B, Denker JS et al (1989) Handwritten digit recognition with a back-propagation network. In: Proceedings of the advances in neural information processing systems (NIPS), pp 396–404

Effect of Span-to-Depth Ratio on Strength and Deflection Reliability of Reinforced Concrete Beams

Huu Anh Tuan Nguyen

1 Introduction

Reliability is the ability of a structure to perform as expected during its lifecycle. In order to ensure the safety of a stucture current design codes and standards are based on semi-probabilistic approaches which use characteristic values and partial safety factors for materials and actions, or strength reduction factors and load factors [1–3]. Meanwhile, a full-probabilistic approach could provide an insight into the structure's performance. In reliability analysis, the state of a structure can be expressed as a function of uncertainty variables [4]:

$$g(X) = R - E \tag{1}$$

where R is the resistance (bearing capacity, allowable deflection or vibration, etc.), E is the load effect (stresses or internal forces, deflection or vibration response, etc.), X contains the basic variables representing the mechanical properties of materials, dimensions of members, various types of loads, etc. The difference between the probability density function of the resistance and that of the load allows determination of the probability of failure.

$$P_{\mathrm{f}} = P(g < 0) \tag{2}$$

The probability of failure P_{f} is hence equal to the cumulative distribution function of g corresponding to the limit state being exceeded. The level of reliability of a structure can be evaluated via the reliability index, β, which is commonly taken as the ratio of the mean to standard deviation of the limit state function. It is required

H. A. T. Nguyen (✉)
University of Architecture Ho Chi Minh City, HCMC, Ho Chi Minh City, Vietnam
e-mail: tuan.nguyenhuuanh@uah.edu.vn

331

that during the service life of a structure the probability of failure does not exceed the target value or the reliability index is greater than its target value. Recommended minimum values for the reliability index for various design situations can be found in building codes and standards such as the EN 1990 and ISO 2394 [5, 6]. For instance, the target reliability index β for structural members of residential and office buildings is taken as 3.8 for ultimate limit state and 1.5 for serviceability (irreversible) limit state for a reference period of 50 years.

Depending on the limit state function, a number of approaches such as the Cornell, Hasofer-Lind, and Rackwitz-Fiessler methods have been introduced to evaluate the reliability index. Being able to deal with any type of probability distribution of random variables and nonlinear limit state functions, the Monte Carlo simulation method has seen wide applications in many engineering problems. This method normally requires analysis of a large number of samples of random variables to achieve accurate predictions [4]. With regard to concrete structures, reliability-based methods have been used to model the deterioration process of concrete piles due to corrosion, predict the punching failure of flat slabs under accidental actions such as column removal, evaluate structural reliability of circular bridge columns subjected to vehicular impact and explosive blast loading, assess the shear strength of deep beams, and so on [7–10]. While studies have focused more on ultimate limit states relating to bearing capacity and stability, serviceability limit states relating to cracking, deflection, and vibrations [11–13] also need to be considered. Guidance has been provided by design standards and codes for calculating deflection of reinforced concrete beams and slabs, considering concrete cracking, tension stiffening, elastic–plastic properties of concrete and steel reinforcement, shrinkage, creep, and other time-dependent effects [1–3]. However, it was found that the ratio of long-term to short-term deflection of concrete structures can be significantly beyond the range of codes of practice [14]. Creep deformations predicted by design codes could be relatively lower than those measured on real structures [15].

Deflection control is of increasing interest as floor beams are being designed with a higher span-to-depth ratio or higher slenderness ratio to meet architectural requirements for aesthetics and use of space. This paper examines the effect of span-to-depth ratio on flexural strength and deflection reliability of a reinforced concrete beam. Shear design is outside the scope of this study. In particular, the limit state functions for the bending capacity and deflection of the beam are developed and statistical properties of random variables are identified. Monte Carlo simulations are performed to predict the probability of failure and reliability index of the beam for different span lengths and span-to-depth ratios. Comparisons are also made with the Eurocode 2 procedures which follow a semi-probabilistic or partial safety factors approach.

2   Methods

2.1   Beam Design Using Eurocode 2 [1, 16]

Ultimate Strength Design for Bending. Figure 1a shows the rectangular cross-section of a beam subjected to bending where b, h, d are the width, overall depth and effective depth of the section, A_s and A_{sc} correspond to the areas of the tension and compression reinforcement, and d_{sc} is the depth of the compression reinforcement, respectively.

Equation (3) is used to estimate the design bending capacity of the beam at the ultimate limit state, M_{Rd}, assuming the reinforcements have yielded, where a is the depth of the equivalent rectangular concrete stress block determined from the equilibrium Eq. (4). The design compressive strength of concrete, f_{cd}, and yield strength of reinforcement, f_{yd}, are $f_{cd} = 0.85 f_{ck}/\gamma_c$ and $f_{yd} = f_y/\gamma_s$ where f_{ck} and f_{yk} are the characteristic compressive strength of concrete and yield stress of reinforcement, $\gamma_c = 1.5$ and $\gamma_s = 1.15$ are the partial factors of safety for the concrete and reinforcement, respectively (Fig. 1b).

$$M_{Rd} = abf_{cd}(d - a/2) + A_{sc} f_{yd}(d - d_{sc}) \tag{3}$$

$$A_s f_{yd} = abf_{cd} + A_{sc} f_{yd} \tag{4}$$

At the ultimate limit state, the design moment M_{Ed} of the beam is calculated from the combination $1.35G_k + 1.5Q_k$ where G_k and Q_k are the characteristic values of the permanent and imposed load, 1.35 and 1.5 are the partial safety factors, respectively [5]. The required reinforcement areas can be found by letting $M_{Rd} = M_{Ed}$ in the expression (3). Also, the provided reinforcement areas should be within the limits specified by the code [1].

Serviceability Design for Deflection. The overall deflection is to be checked using the quasi-permanent combination $G_k + \psi_2 Q_k$ where ψ_2 is the factor for quasi-permanent value of the imposed action, taken as 0.3 for domestic, residential, and
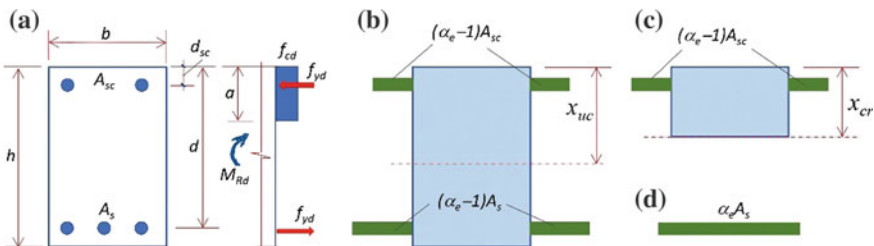

Fig. 1   RC Beam **a** cross-section, **b** stresses at ultimate limit state, **c** transformed section with concrete uncracked, **d** transformed section with concrete cracked

office areas [5]. The determination of long-term deflection requires estimation of the beam curvature considering creep and shrinkage effects.

An effective or "average" flexural curvature, $(1/r)_{\text{ef}}$, is to be calculated based on both the curvature for the fully cracked section, $(1/r)_{\text{cr}}$, and that for the uncracked section $(1/r)_{\text{uc}}$ as follows:

$$(1/r)_{\text{ef}} = \xi(1/r)_{\text{cr}} + (1 - \xi)(1/r)_{\text{uc}} \tag{5}$$

in which ξ is the coefficient taking account of tension stiffening. For sustained loads:

$$\xi = 1 - 0.5(M_{\text{cr}}/M_{\text{s}})^2 \tag{6}$$

where M_{cr} is the cracking moment of the section and M_{s} is the moment associated with the quasi-permanent combination. Each flexural curvature value is calculated as:

$$1/r = \frac{M_{\text{s}}}{E_{\text{c,ef}}I} \tag{7}$$

where I is the second moment of area of the section (cracked or uncracked as appropriate) and $E_{\text{c,ef}}$ is the effective modulus of concrete. The I values can be determined using equivalent transformed sections where the reinforcement area is converted into an equivalent concrete area via a modular ratio $\alpha_{\text{e}} = E_{\text{s}}/E_{\text{c,ef}}$ with E_{s} being the modulus of elasticity of the reinforcement [16]. Figures 1c–d show the uncracked and cracked transformed sections, respectively. The effective modulus of concrete which allows for the effect of creep is given by:

$$E_{\text{c,ef}} = \frac{E_{\text{c}}}{1 + \phi_{\text{cr}}} \tag{8}$$

in which E_{c} is the elastic modulus of concrete associated with the compressive strength; ϕ_{c} is the creep coefficient given by Eurocode 2 for a range of cement types, concrete classes, and concrete ages at the time of first loading, i.e., when construction props are removed, the load durations and notional member sizes.

The effective curvature due to shrinkage $(1/r_{\text{cs}})_{\text{ef}}$ is also calculated from the shrinkage curvatures of fully cracked section $(1/r_{\text{cs}})_{\text{cr}}$ and uncracked section $(1/r_{\text{cs}})_{\text{uc}}$ using the same combination rule of Eq. (5) where $1/r$ is substituted by $1/r_{\text{cs}}$ and each shrinkage curvature component (fully cracked and uncracked) is determined as:

$$1/r_{\text{cs}} = \varepsilon_{\text{cs}}\alpha_{\text{e}}S/I \tag{9}$$

It should be noted that I_{cr} and I_{uc} are used in Eq. (9) for $(1/r_{\text{cs}})_{\text{cr}}$ and $(1/r_{\text{cs}})_{\text{uc}}$, respectively, and S is the first moment of area of reinforcement about the centroid of the section (cracked or uncracked as appropriate). The value of free shrinkage strain ε_{cs} is obtained from Eurocode 2 depending on member dimensions, concrete ages,

and classes. The sum of $(1/r)_{ef}$ and $(1/r_{cs})_{ef}$ yields the total curvature from which the deflection can be calculated using general rules of structural mechanics. It is recommended that the final deflection of a beam or slab should not exceed span/250.

2.2 Reliability Analysis of Beam for Flexural Strength and Deflection

Description of Case Study Beam. Consider a simply supported beam with a span of L designed to carry a uniformly distributed permanent load G and imposed load Q. The permanent load of the beam was determined from the permanent load of the supported slab and the self-weight of the beam. The imposed load of the beam was calculated from the imposed load of the supported slab. For general office use, the characteristic value of the imposed load of the floor was taken as 2.5 kN/m^2. The loads were transferred from a 150-mm-thick concrete slab to the beam with a tributary width (beam spacing) of 4.5 m. The concrete has a characteristic compression strength of 25 MPa. The reinforcement has a characteristic yield stress of 500 MPa and elastic modulus of 200,000 MPa.

To study the effect of span-to-depth ratio on the reliability of the beam, span lengths of 7–10 m and span-to-depth ratios of 10–20 were examined. The beam's width was taken as 300 mm for $L/h = 10$–14 and 350–650 mm for $L/h = 15$–20. The following procedure was performed for each combination of L and L/h value:

- Firstly, the reinforcement area was calculated using the Eurocode 2 method presented earlier with the ultimate load combination $1.35G_k + 1.5Q_k$ and design strength f_{cd} and f_{yd} of the concrete and reinforcement materials. For flexural strength, all the investigated beams were designed according to the case of singly reinforced sections, so A_{sc} was excluded from Eqs. (3) and (4). Nominal reinforcement A_{sc} was then provided in the compression zone of the beam section.
- Subsequently, the flexural strength and deflection of the beam with provided reinforcement were evaluated using the probabilistic approach with random variables as detailed below.

Limit State Functions and Random Variables. The limit state functions for flexural strength and deflection of the beam are given by Eqs. (10) and (11), respectively where the model uncertainties factors θ_E and θ_R were included to express incompleteness and imprecision of the relevant theoretical models for load and resistance effects.

$$g_M(X) = M_R - M_E = \theta_R A_s f_y \left(d - \frac{0.5 A_s f_y}{0.85 b f_c} \right) - \theta_E \frac{(G + Q)L^2}{8} \qquad (10)$$

$$g_f(X) = f_R - f_E = \theta_R \frac{L}{250} - \theta_E \frac{5}{48} \left((1/r)_{ef} + (1/r_{cs})_{ef} \right) L^2 \qquad (11)$$

The statistical properties of basic random variables used in the reliability analysis are listed in Table 1 with normal, lognormal, and Gumbel distributions [17, 18]. The expression for flexural strength M_R in Eq. (10) was derived from Eqs. (3)–(4) and the curvatures for calculating the deflection f_E in Eq. (11) were determined using Eqs. (5)–(9). A load combination with full live load $(G + Q)$ was used for determining the moment M_E for strength check while a quasi-permanent combination $(G + 0.3Q)$ was employed for calculating the beam deflection f_E. For offices with a reference period of 50 years, the live load Q can be modeled by a Gumbel distribution with a mean value μ_Q of 0.6 times the characteristic value Q_k and coefficient of variation σ_Q/μ_Q of 0.35 as suggested by the European document EUR 29410 [17]. These values agree well with [18] which showed $\mu_Q/Q_k = 0.5$ and $\sigma_Q/\mu_Q = 0.386$ as a result of combining the coefficient of variation of the sustained and intermittent components of the live load.

Monte Carlo Simulation. A total of 44 Monte Carlo simulation cases, each with five million trials, were performed for beam spans of 7–10 m and span-to-depth ratios of 10–20. The following tasks were conducted in each simulation case:

- Using MATLAB built-in random number generators [19] to generate independent sample values for each of the basic variables with statistical properties given in Table 1. Figure 2 depicts an example of the probability density functions (PDFs) of the input variables.

Table 1 Statistical properties of random variables

| Name of variables	Symbol, X	Mean, μ_X	Standard deviation, σ_X	Distribution
Concrete compressive strength	f_c	$f_{ck} + 2\sigma_X$	$0.121\mu_X$	Lognormal
Yield stress of reinforcement	f_y	$f_{yk} + 2\sigma_X$	$0.053\mu_X$	Lognormal
Elastic modulus of reinforcement	E_s	E_s	$0.04\mu_X$	Normal
Overall depth of beam	h	h	8 mm	Normal
Width of beam	b	b	8 mm	Normal
Area of reinforcement	A_s, A_{sc}	A_s, A_{sc}	$0.02\mu_X$	Normal
Permanent load of beam	G	G_k	$0.1\mu_X$	Normal
Imposed load of beam	Q	$0.6Q_k$	$0.35\mu_X$	Gumbel
Load effect factor	θ_E	1	0.1	Normal
Resistance factor	θ_R	1	0.1	Normal
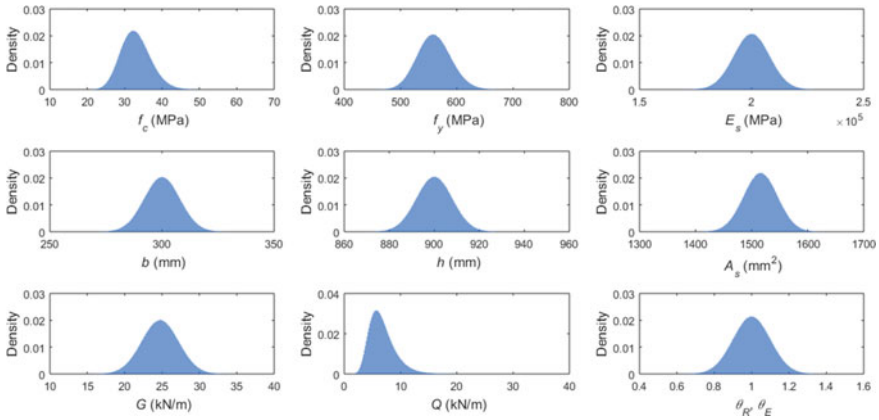
Fig. 2 PDFs of input parameters for $L = 9$ m and $L/h = 10$

- Evaluating the bending strength M_R, applied moment M_E, deflection limit f_R, deflection f_E, safety margins $(M_R - M_E)$ for strength, and $(f_R - f_E)$ for deflection control.
- Repeating the process for five million trials.
- Determining the failure probability P_f as the ratio of the number of trials with negative safety margin to the total number of trials.
- Identifying the reliability index β as the ratio of mean to standard deviation of the safety margin.

3   Results and Discussions

3.1   Beam Reinforcement and Deflection Based on Eurocode 2

Tables 2 and 3 present the required area of tensile reinforcement A_s and the relative displacement f_E/L, respectively, determined from Eurocode 2 procedures for different span lengths and span-to-depth ratios. For each span length, it can be seen that A_s increased with an increase in L/h and all the investigated L/h ratios from 10 to 20 resulted in an acceptable design in terms of ultimate strength. By contrast, the deflection requirement was violated, i.e., f_E/L exceeded 1/250, for L/h ratios greater than 13.

Table 2 Reinforcement area

L (m)	A_s (mm^2) for $L/h =$										
	10	11	12	13	14	15	16	17	18	19	20
7	1150	1280	1455	1612	1826	1959	2129	2289	2443	2627	2849
8	1329	1478	1647	1833	2091	2285	2451	2656	2848	3029	3241
9	1516	1685	1881	2107	2366	2551	2786	2983	3223	3451	3658
10	1710	1899	2123	2346	2651	2831	3054	3328	3558	3778	4099

3.2   Reliability Analysis Using Monte Carlo Simulation

For each Monte Carlo simulation case with five million trials, the probability density functions were produced for the resistance (moment capacity M_R, allowable deflection f_R), load effect (moment M_E, deflection f_E) as well as safety margin for bending strength and deflection control ($M_R - M_E, f_R - f_E$). For instance, the results for 9-m beam with $L/h = 10$ revealed an excellent reliability in both strength and deflection control (Fig. 3). The excellent reliability in strength was also observed in the much slender beam with $L/h = 15$ (Fig. 4a–b). By contrast, a very high probability of failure in deflection was detected in the slender beam with 70% of the trials showing negative values of the safety margin (Fig. 4c–d).

Tables 4, 5, 6 and 7 summarize the predicted values of failure probability and reliability index for all investigated cases. For beams with $L/h = 13$, the deflection calculated by the Eurocode 2 method was right equal to the limit of span/250 (Table 3). However, this L/h ratio could result in a failure probability of 31–35% as revealed by the probabilistic approach (Table 6). Although the shallowest beams with $L/h = 20$ can still be robust from a strength perspective with a failure probability of just 2 $\times 10^{-5}$, the probability of failure in deflection was extremely high at 99% (Tables 4 and 6).

4   Conclusion

The presented reliability-based evaluation has revealed a different trend of variation between strength reliability and deflection reliability in response to an increase in the span-to-depth ratio of reinforced concrete beams. Some conclusions can be drawn from the findings presented.

Even when the span-to-depth ratio doubled from 10 to 20, the same excellent reliability in flexural strength remained. The failure probability was found to be in the range of 1.4×10^{-5} to 4.7×10^{-5} which is below the target probability of 7.2×10^{-5} hence acceptable. The predicted reliability index was in the range of 4.0–4.3 which is greater than the target reliability index of 3.8 recommended for the ultimate limit state for a reference period of 50 years.

Table 3 Relative displacement

L (m)	f_E/L for $L/h =$										
	10	11	12	13	14	15	16	17	18	19	20
7	0.0026	0.0030	0.0035	0.0040	0.0045	0.0046	0.0051	0.0055	0.0059	0.0063	0.0069
8	0.0026	0.0030	0.0035	0.0039	0.0045	0.0047	0.0051	0.0055	0.0059	0.0063	0.0067
9	0.0026	0.0030	0.0035	0.0040	0.0045	0.0047	0.0051	0.0054	0.0058	0.0063	0.0066
10	0.0026	0.0031	0.0035	0.0040	0.0045	0.0046	0.0050	0.0054	0.0057	0.0061	0.0066
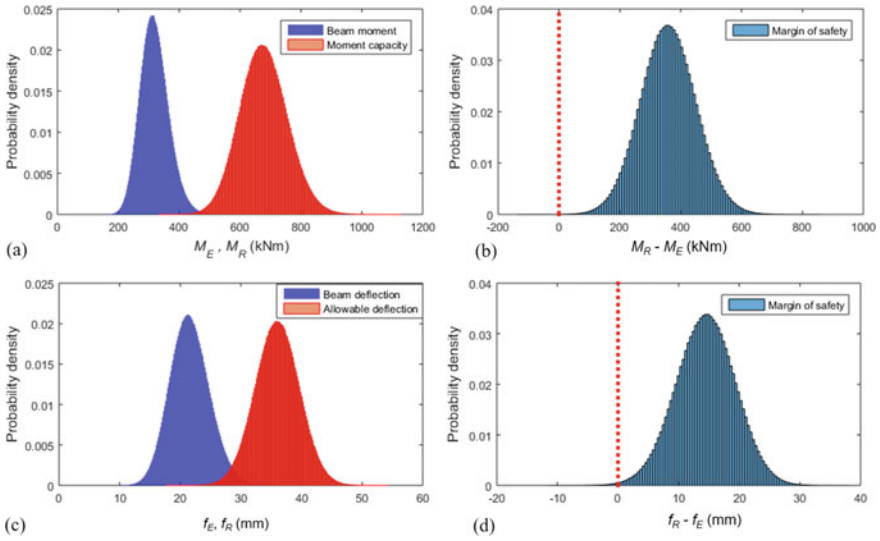
Fig. 3 $L = 9$ m, $L/h = 10$: PDFs of load effect, resistance and safety margin for **a, b** moment, **c, d** deflection
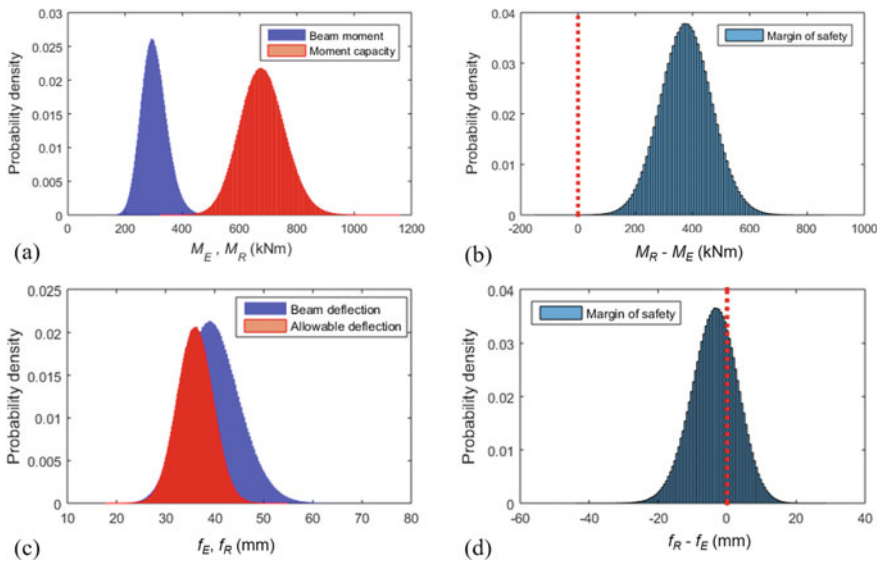
Fig. 4 $L = 9$ m, $L/h = 15$: PDFs of load effect, resistance and safety margin for **a, b** moment, **c, d** deflection

Table 4 Probability of failure (10^{-5}) in bending strength

L (m)	$10^5 P_f$ for L/h =										
	10	11	12	13	14	15	16	17	18	19	20
7	3.73	4.44	2.98	2.66	1.76	1.74	1.34	2.10	2.06	1.96	2.24
8	3.68	4.30	2.80	2.26	1.76	1.58	1.86	1.62	1.82	1.66	1.86
9	3.71	4.70	2.84	2.48	2.02	1.80	1.60	1.82	1.18	2.02	1.72
10	3.63	4.58	2.84	2.52	1.94	1.76	1.84	1.62	1.82	1.44	1.84

Table 5 Reliability index for bending strength

L (m)	β for L/h =										
	10	11	12	13	14	15	16	17	18	19	20
7	4.076	4.019	4.084	4.144	4.225	4.208	4.209	4.163	4.162	4.168	4.187
8	4.063	4.014	4.072	4.136	4.224	4.221	4.214	4.219	4.177	4.182	4.192
9	4.055	4.011	4.070	4.143	4.222	4.212	4.221	4.214	4.226	4.188	4.192
10	4.047	4.005	4.068	4.135	4.220	4.202	4.198	4.213	4.211	4.171	4.192

In contrast to the bending capacity, the target reliability index for serviceability relating to long-term deflection was violated with span-to-depth ratios of 12 and above. Negative values of reliability index could even be found with span-to-depth ratios of 14 and above, corresponding to a failure probability of more than 62%. In other words, there could be a high probability for a beam that is deemed perfect in terms of ultimate strength to have excessive deflections and hence unacceptable from a serviceability perspective. However, since the presented results were for simply supported beams, higher span-to-depth ratios might be allowed for a continuous beam which would be a future research object.

Table 6 Probability of failure in deflection control

L (m)	P_f for $L/h =$										
	10	11	12	13	14	15	16	17	18	19	20
7	0.0016	0.0189	0.1328	0.3377	0.6232	0.6897	0.8367	0.9209	0.9622	0.9849	0.9951
8	0.0017	0.0202	0.1102	0.3144	0.6201	0.7230	0.8407	0.9259	0.9674	0.9852	0.9942
9	0.0020	0.0222	0.1219	0.3517	0.6240	0.7029	0.8477	0.9202	0.9659	0.9860	0.9938
10	0.0023	0.0249	0.1349	0.3422	0.6317	0.6917	0.8219	0.9179	0.9598	0.9802	0.9936

Table 7 Reliability index for deflection control

L (m)	β for $L/h =$										
	10	11	12	13	14	15	16	17	18	19	20
7	3.046	2.126	1.116	0.400	−0.335	−0.513	−0.979	−1.377	−1.701	−2.033	−2.369
8	3.012	2.095	1.232	0.467	−0.326	−0.606	−0.994	−1.411	−1.766	−2.051	−2.342
9	2.966	2.052	1.170	0.363	−0.335	−0.548	−1.023	−1.376	−1.753	−2.076	−2.329
10	2.912	2.001	1.105	0.390	−0.354	−0.516	−0.924	−1.364	−1.689	−1.962	−2.327

References

1. EN 1992-1-1:2004 (2004) Eurocode 2—design of concrete structures, Part 1–1: general rules and rules for buildings. European Committee for Standardization, Brussels
2. ACI 318-19 (2019) Building code requirements for structural concrete and commentary. Concrete Institute, Michigan
3. AS 3600:2018 (2018) Concrete structures. Standards Australia Limited, Sydney
4. Melchers RE, Beck AT (2018) Structural reliability analysis and prediction. Wiley
5. EN 1990:2002 (2005) Eurocode—basis of structural design. European Committee for Standardization, Brussels
6. ISO 2394:2015 (2015) General principles on reliability for structures. International Standards Organization, Geneva
7. Mahmoodian M, Alani A (2014) Modeling deterioration in concrete pipes as a stochastic gamma process for time-dependent reliability analysis. J Pipeline Syst Eng Pract 5(1):04013008
8. Olmati P, Sagaseta J, Cormie D, Jones AEK (2017) Simplified reliability analysis of punching in reinforced concrete flat slab buildings under accidental actions. Eng Struct 130:83–98
9. Thomas RJ, Steel K, Sorensen AD (2018) Reliability analysis of circular reinforced concrete columns subject to sequential vehicular impact and blast loading. Eng Struct 168:838–851
10. Díaz RAS, Nova SJS, da Silva MCT, Trautwein LM, de Almeida LC (2020) Reliability analysis of shear strength of reinforced concrete deep beams using NLFEA. Eng Struct 203:109760
11. Nguyen T, Gad E, Wilson J, Lythgo N, Haritos N (2011) Evaluation of footfall induced vibration in building floor. In: Australian earthquake engineering society annual conference, pp 1–8. AEES
12. Nguyen T, Gad E, Wilson J, Haritos N (2014) Mitigating footfall-induced vibration in long-span floors. Aust J Struct Eng 15(1):97–109
13. Nguyen HAT (2022) Relocation of walking path to resolve vibration problems in a lightweight floor. In: Ha-Minh C, Tang AM, Bui TQ, Vu XH, Huynh DVK (eds) CIGOS 2021, emerging technologies and applications for green infrastructure. Lecture notes in civil engineering, vol 203. Springer, Singapore
14. Vakhshouri B, Nejadi S (2014) Limitations and uncertainties in the long-term deflection calculation of concrete structures. In: Vulnerability, uncertainty, and risk: quantification, mitigation, and management, pp 535–546. ASCE
15. Raphael W, Zgheib E, Chateauneuf A (2018) Experimental investigations and sensitivity analysis to explain the large creep of concrete deformations in the bridge of Cheviré. Case Stud Constr Mater 9:e00176
16. Mosley WH, Hulse R, Bungey JH (2012) Reinforced concrete design: to Eurocode 2. Macmillan International Higher Education, Hampshire, UK
17. Markova J, Sousa ML, Dimova S, Athanasopoulou A, Iannaccone S, Pinto A (2018) Reliability of structural members designed with the Eurocodes NDPs selected by EU and EFTA Member States, EUR 29410 EN. European Commission and Joint Research Centre, Luxembourg
18. Honfi D, Mårtensson A, Thelandersson S (2012) Reliability of beams according to Eurocodes in serviceability limit state. Eng Struct 35:48–54
19. MATLAB version 8.5.0 (R2015a) (2015) The MathWorks Inc, Natick, Massachusetts

Estimation Displacement of Diaphragm Wall Using Hardening Soil Versus Mohr–Coulomb Model

Thanh Sang-To, Minh Hoang-Le, Manh Vu-Tran, Magd Abdel Wahab, and Thanh Cuong-Le

1 Introduction

With the development of technology and Science Computer, many powerful methods are used to solve the complex problems in almost fields. One of them is the Finite Element (FE) method. Over the years, this method has gained an excellent reputation for dealing with the challenging problem in the real world effectively. It is complex and hard to calculate the whole construction process for a big project, and hence the FE method is an indispensable tool to support for engineers. Some FE methods such as Abaqus [1, 2] and/or PLAXIS [3, 4] are employed popularly. In order to assess the suitability of approaches, many studies have been conducted in recent decades. For excavation problem, estimation of the horizontal displacement of D.wall is an important section in this design problem. For this reason, some researchers, such as Tan et al. [5], Hongbing [6], Tan et al. [7], Huang et al. [8], make an effort to evaluate the behavior of soil and the concrete or steel structures. In the civil field, high-rise buildings play an important role in social, in which constructing building's basements [9, 10] is vital stage.

Two models, HS and MC, are used very popularly in soil mechanics. In this study, an investigation the effect of these two soil models on diaphragm wall displacement

T. Sang-To · M. Hoang-Le · T. Cuong-Le (✉)
Faculty of Civil Engineering, Ho Chi Minh City Open University, Ho Chi Minh City, Vietnam
e-mail: cuong.lt@ou.edu.vn

M. Vu-Tran
Unicons Investment Construction Company Limited, Floor 5-6-7, Coteccons Tower, 236/6 Dien Bien Phu Str., Ward 17, Binh Thanh District, Ho Chi Minh City, Vietnam

T. Sang-To · M. A. Wahab
Soete Laboratory, Faculty of Engineering and Architecture, Ghent University, Technologiepark Zwijnaarde 903, 9052 Zwijnaarde, Belgium

is conducted in detail. The obtained results are compared each other and then drawn some conclusions.

2 FE Model Using PLAXIS Software

In order to estimate the lateral displacement diaphragm wall, two soil models (i.e., MC and HS model) are employed. First of all, a brief description of the MC model required five primary parameters (see Table 1) is shown herein. One of the many advantages of this analyses is that an extension of Coulomb's friction law for the MC yield condition is conducted. Furthermore, by doing that, any plane within a material element is always obeyed the mentioned conditions. A full description of MC yield condition is shown by Smith and Griffiths [11]. In which, c (cohesion) and φ (friction angle) are the two factors that represented the plastic model characteristic. Figure 1 illustrates these conditions briefly in principal stress space. For dense soils, a model parameter, ψ (dilatancy angle), is used to simulate positive plastic volumetric strain increment.

Table 1 Parameters of MC model with their standard

Symbols	Unit	Description
E	kN/m^2	Young's modulus
ν	–	Poisson's ratio
c	kN/m^2	Cohesion
φ	(°)	Friction angle
ψ	(°)	Dilatancy angle

Fig. 1 The description of MC yield condition in principal stress space by a fixed hexagonal cone (with $c = 0$)
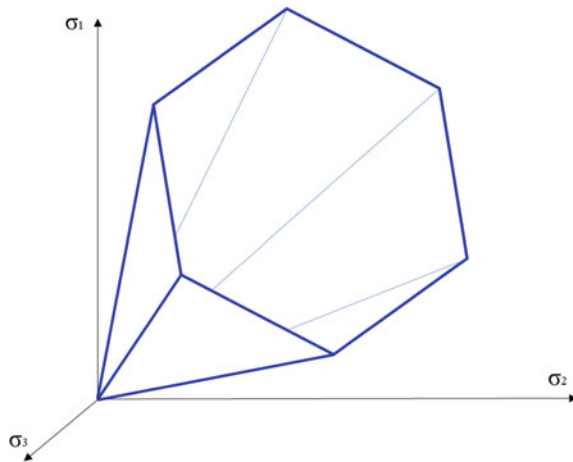
Table 2 Parameters of HS model

Symbols	Unit	Description
m	–	A power law to illustrate stress-dependent stiffness
E_{50}^{ref}	kN/m^2	The reference stiffness modulus
$E_{\text{oed}}^{\text{ref}}$	kN/m^2	The reference stiffness modulus
$E_{\text{ur}}^{\text{ref}}$	kN/m^2	The reference Young's modulus reloading
ν_{ur}	–	Possion's ratio

In the Hardening Soil model, it was the other way around, since the yield surface of a hardening plasticity model can expand due to plastic straining, and hence it is not fixed in principal stress space. In this model, there are the 2-distinct-types of hardening (i.e., compression hardening and shear hardening). In order to model irreversible plastic strains due to primary compression in oedometer loading and isotropic loading, this model employed the compression hardening. Whereas, to simulate irreversible strains because of primary deviatoric loading, shear hardening is adopted. Several basic parameters of the Hs model are presented in Table 2. The analyses is conducted based on the setting $E = E_{50}^{\text{ref}} = E_{\text{oed}}^{\text{ref}}$ and $E_{\text{ur}}^{\text{ref}} = 3E_{50}^{\text{ref}}$.

In this work, a simulation of basement constructed excavation for high-rise buildings is presented. The Geotechnical Engineering software, PLAXIS version 2020, is used to investigate for this problem. The data of this simulation are collected information from the soil investigation in district 3, Ho Chi Minh city, Vietnam. A brief description of the data is shown in Fig. 2 and Table 3. The stratigraphy of this analyses consists of seven layers up to 45 m deep, in which clay layers interspersed with two sand layer. The value of N_{spt} from 8 to 31. The density of the soil belongs a range of 19–20 kN/m^3 (Fig. 3). The investigations determinate the groundwater level was approximately 1 m below the surface. Figure 4 indicates the calculated mesh of this analysis using the FE method, the horizontal and vertical boundaries of the calculated mesh are, respectively, 50 and 220 m.

In this problem, we simulate a set of excavation phases of the high-rise building consisting of three basements and one underground water tank. Each floor height is about 3.25 m, and hence the total of excavation process is equal 13 m. The diaphragm wall is a reinforced concrete structure, 22 m deep. The basement slabs have an average thickness of 270 mm to 1000 mm. The whole excavation process is operated by semi-top-down construction method and presented the main excavation stages in detail as Table 4 and Fig. 3.

3 Results and Discussion

The main five excavation stages are simulated by ten phases in PLAXIS software. The effect of each excavation phase on the lateral displacement diaphragm wall is investigated in Fig. 5 in detail. For the displacement shape of D.wall, the results
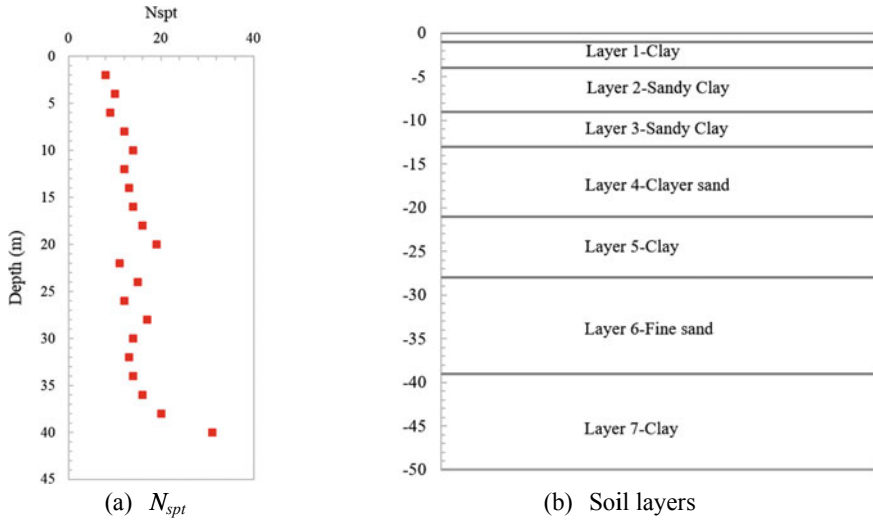
(a) N_{spt} (b) Soil layers

Fig. 2 The data of soil

Table 3 The engineering properties of the soil

Symbols		Layer							
		Fill	1	2	3	4	5	6	7
		Sand	Clay	Sandy clay	Sandy clay	Clayer sand	Clay	Fine sand	Clay
γ	kN/m^3	19	19	20	19	19	20	20	20
c	kN/m^2	5	19.3	28.5	21.3	10.3	33	2.8	45.5
φ	($^\circ$)	30	9.73	12.37	15.72	23	13.5	30	16.8
s_u	kN/m^2	–	20.1	27.6	81	–	138	–	306
E	kN/m^2	30E3	6030	8.28E3	40.5E3	62E3	69E3	62.8E3	153E3
ν	–	0.25	0.2	0.2	0.2	0.25	0.2	0.25	0.2
R_{inter}	–	0.5	0.8	0.8	0.8	0.8	0.8	0.8	0.8

obtained from the MC and HS analyses are quite similar generally. In addition, the maximum of lateral displacement of the MC and HS model are 31.1 mm and 30.2 mm, respectively.

The difference between of them is insignificant. The results reveal that both analyses provide a good estimation to predict the lateral displacement diaphragm wall in the preliminary stage. However, the fact that there are differences between the two models at specific stages. In detail, these maximum values at two first excavation stages of HS model are always smaller than the MC analyses. Meanwhile, the value of displacement at the toe of retaining wall analyzed by MC model is considerably larger than the HS in the phase 6 and 8. The use of the different stiffness parameter
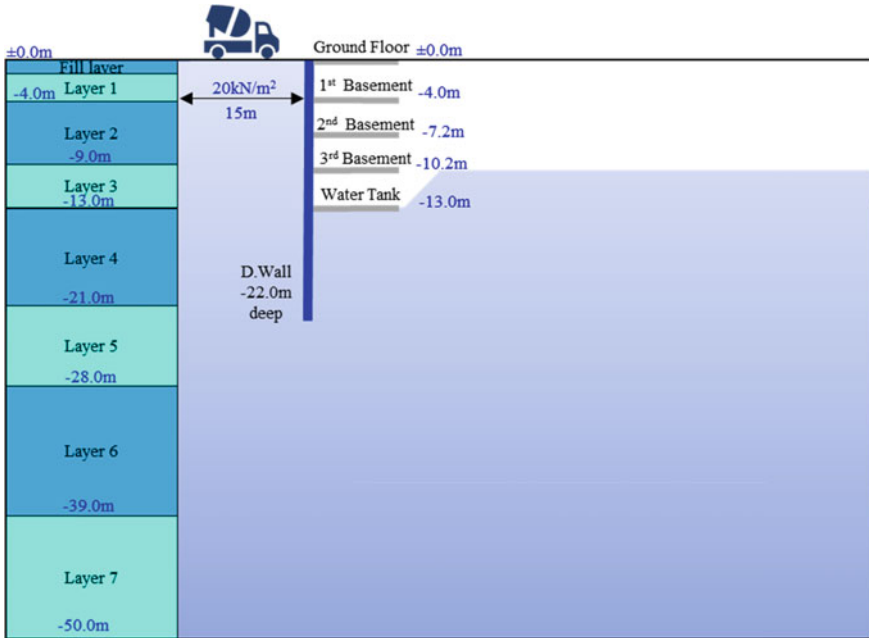
Fig. 3 Stratigraphy and geometric structure
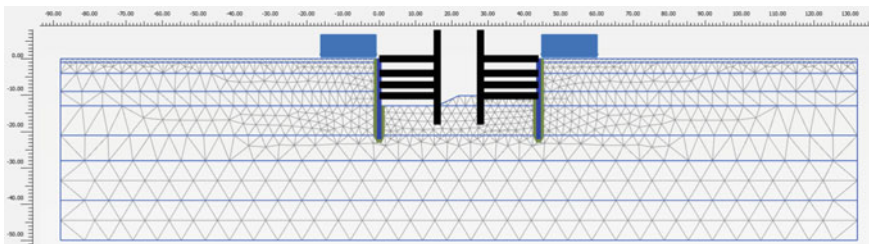
Fig. 4 The calculated mesh in PLAXIS

theoretically can explain the reasons for the difference of these displacements. Especially, the relationship between the stiffness parameter and stress obeys to a power law (m) in the HS model. In other words, the model implies for example the relationship as follows $E = E^{ref} (\sigma/p^{ref})^m$. By contrast, MC model commonly employs the stiffness parameter like a constant for each soil layer. Therefore HS analysis is more reasonable than the MC model to assess response between the retaining wall and soil in excavation problem. Nevertheless, one of the many advantages of the MC model is that it only requires five engineering properties of the soil, this led to easier using this model, and thus it suitable to adopt in preliminary prediction in the first assessment of a project.

Table 4 Construction sequence

Phases	Main excavation activity
1	Construct diaphragm wall
2	Excavate to level of underside of ground floor
3	Construct ground floor
4	Excavate to level of underside of the 1st basement
5	Construct the 1st basement slab
6	Excavate to level of underside of the 2nd basement
7	Construct the 2nd basement slab
8	Excavate to level of underside of the 3rd basement
9	Construct the 3rd basement slab
10	Excavate to level of underside of the underground water tank
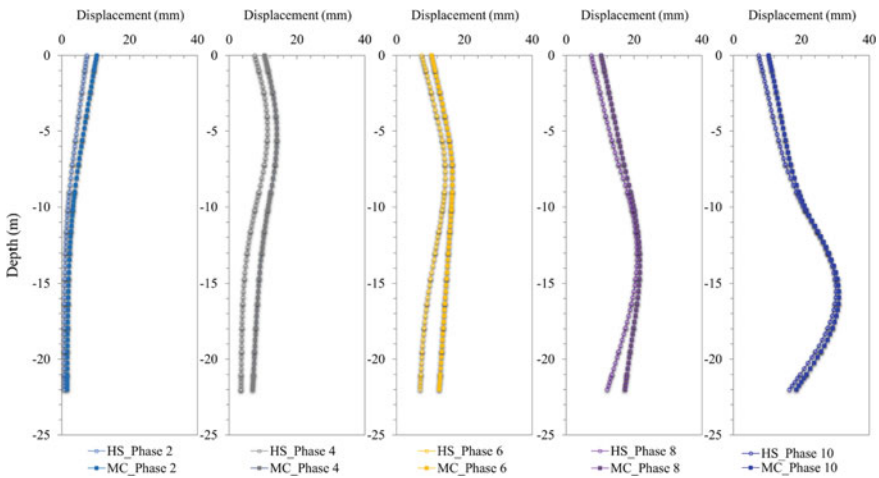
Fig. 5 Lateral displacement diaphragm wall

4 Conclusion

In this study, a detailed assessment of two model soil is presented. Each model has certain advantages and disadvantages. While HS model provides the excellent results for predicting the lateral displacement diaphragm wall, MC model is simple and easy to apply. Therefore the MC model is suitable for preliminary assessment of in the excavations problem, while HS is effective for detailed calculation simulation at actual construction stages. In sum, based on these analyzes we can see that FE method is a powerful tool to analyze and predict what happens in complex construction processes through MC and HS models. The results have provided an overview for

the evaluation of soil behavior and diaphragm wall in the excavation problem by these models.

References

1. Börgesson L (1996) ABAQUS. In: Stephansson O, Jing L, Tsang C-F (eds) Developments in geotechnical engineering, vol 79. Elsevier, pp 565–570
2. Helwany S (2007) Applied soil mechanics with ABAQUS applications. Wiley
3. Brinkgreve R, Kumarswamy S, Swolfs W, Waterman D, Chesaru A, Bonnier P (2016) PLAXIS 2016. PLAXIS bv, the Netherlands
4. Software PGE (2020)
5. Tan Y, Huang R, Kang Z, Bin W (2016) Covered semi-top-down excavation of subway station surrounded by closely spaced buildings in downtown Shanghai: building response. J Perform Constr Facil 30(6):04016040
6. Hongbing W (1998) Semi-top-down construction technology at the Jinanshi Station of Metro line no. 2 in Shanghai. Underground Space
7. Tan Y, Zhu H, Peng F, Karlsrud K, Wei B (2017) Characterization of semi-top-down excavation for subway station in Shanghai soft ground. Tunn Undergr Space Technol 68:244–261
8. Huang Z-h, Zhao X-s, Chen J-j, Wang J-h (2014) Numerical analysis and field monitoring on deformation of the semi-top-down excavation in Shanghai. In: New frontiers in geotechnical engineering, pp 198–207
9. Shen SL, Wang ZF, Cheng WC (2017) Estimation of lateral displacement induced by jet grouting in clayey soils. Géotechnique 67(7):621–630
10. Talha SB (2000) Deformation behaviour of a retaining wall for a deep basement excavation with semi-top down method, p 1049
11. Smith IM, Griffiths DV, Margetts L (2013) Programming the finite element method. Wiley

An Improved Particle Swarm Optimization Approach for Solving the Engineering Problems

Thi Thuy Linh-Nguyen, Hoang Le-Minh, and Thanh Cuong-Le

1 Introduction

Solving the optimization problems in real work is concerned robustly and requires more effort to develop a reliability approach. With the robust development of intelligent algorithms field, solving these problems is more flexible when there are multiple options available. Intelligent algorithms are often inspired by the observation about swarm's foraging in nature called meta-heuristic. Many meta-heuristic optimization methods have been developed, such as particle swarm optimization algorithm (PSO) [1], firefly algorithm (FA) [2], artificial bee colony (ABC) [3], grey wolf optimizer (GWO) [4], cat swarm optimization (CAT) [5], and Jaya optimization algorithm (JAYA) [6]. In the above algorithms, PSO is considered the most typical algorithm. It is widely applied in many fields, from economics to engineering, because of its simplicity and fast calculation time. The concept in PSO can be perceived as original, and it is a rich source of inspiration for researchers to propose new algorithms in the past two decades. The new swarm algorithms almost are established by proposing the different approaches through simulating swarm intelligence by mathematical models. PSO tries to assign these variables to agents in the population. The value of the objective function, which is characterized by these random variables, is then calculated to identify the best solution. Through each iteration, the process, which

T. T. Linh-Nguyen
Faculty of Civil Engineering, Ho Chi Minh City University of Technology—HUTECH, Ho Chi Minh City, Vietnam
e-mail: ntt.linh85@hutech.edu.vn

H. Le-Minh · T. Cuong-Le (✉)
Faculty of Civil Engineering, Ho Chi Minh City Open University, Ho Chi Minh City, Vietnam
e-mail: cuong.lt@ou.edu.vn

H. Le-Minh
e-mail: hoang.lm@ou.edu.vn

generates a new set of random variables through the position updating of each agent, is implemented continuously to update the new value of the objective function.

However, besides the advantages, the PSO still has limitations. For example, the accuracy of the PSO algorithm is not appreciated when compared to other algorithms.

Many innovative techniques have been introduced to overcome these limitations to improve the PSO's performance. Most techniques have the same trend: finding a new movement strategy through velocity updating. Wu et al. [7] presented a new method to improve the inertia weight in original PSO for solving alleviate power fluctuation of hybrid energy storage. Ouyang et al. [8] used a new technique with the more constrained condition to solve a particular problem. Higashi et al. [9] were presented the rules of the velocity and position updating using Gaussian mutation. The results show that unimodal and multimodal function was performed more effective in comparison with original PSO. Singh and Singh [10] was developed a new method for velocity updating through the share of space search information, namely HPSO. In this paper, we introduce a novel velocity updating strategy by adding the terms which is considered as the new method for expanding the new search space and more closer the local best and global best.

2 A Novel Efficient Approach for Improving PSO

In PSO algorithm, each particle is a solution candidate, and the group of particles create an initial swarm. To find the global best in optimization problems. The process of each particle's movement will iteration to explore the feasible region. This movement must ensure the condition that at the iteration movement $(k + 1)^{\text{th}}$, the process of position updating of each particle X_i must tend to be closer to the search regions of local best and global best; if the particle X_i is satisfied with this condition, it is a successful movement. By contrast, the particle X_i will explore a new search area to prepare for the next movement at step $(k + 2)^{\text{th}}$. The process of velocity and position updating of each particle X_i at the step $(k + 1)^{\text{th}}$ are shown in Eqs. (1) and (2).

$$V_i^{k+1} = wV_i^k + c_1r_1\left(L_{\text{best},i}^k - X_i^k\right) + c_2r_2\left(G_{\text{best}}^k - X_i^k\right) \tag{1}$$

$$X_i^{k+1} = X_i^k + V_i^k \tag{2}$$

where w is a scalar number named weight of velocity, and c_1 and c_2 are two parameters named learning factor. r_1, r_2 are random values which having the value in range [0, 1].

To increase the PSO's performance, in this work, we introduce a new strategy for velocity updating given in Eq. (3). Thus, Eq. (3) will replace Eq. (2) for calculating the velocity updating V_i^{k+1} at the $(k + 1)^{\text{th}}$ iteration. The flowchart of NEA-PSO is shown in Fig. 1.

$$V_i^{k+1} = w V_i^k + c_1 r_1 \left(L_{\text{best},i}^k - X_i^k (1 + f(k+1)\varepsilon_1 \zeta_1 R) \right)$$
$$+ c_2 r_2 \left(G_{\text{best}}^k - X_i^k (1 + f(k+1)\varepsilon_2 \zeta_2 R) \right) \tag{3}$$

In Eq. (3), $f(k+1) = 1 - \frac{\beta k}{K_{\max}}$ where k and $K_{\max}$ are current and max of iteration, respectively. The parameter β is to control the convergence rate, and this parameter can modify depending on the use's goal. ζ_1 and ζ_2 are denoted as the random parameters having value in range $[-1, 1]$, ε_1 and ε_2 are scale parameters, and in this study, we proposed $\varepsilon_1 = \varepsilon_2 = 0.01$.
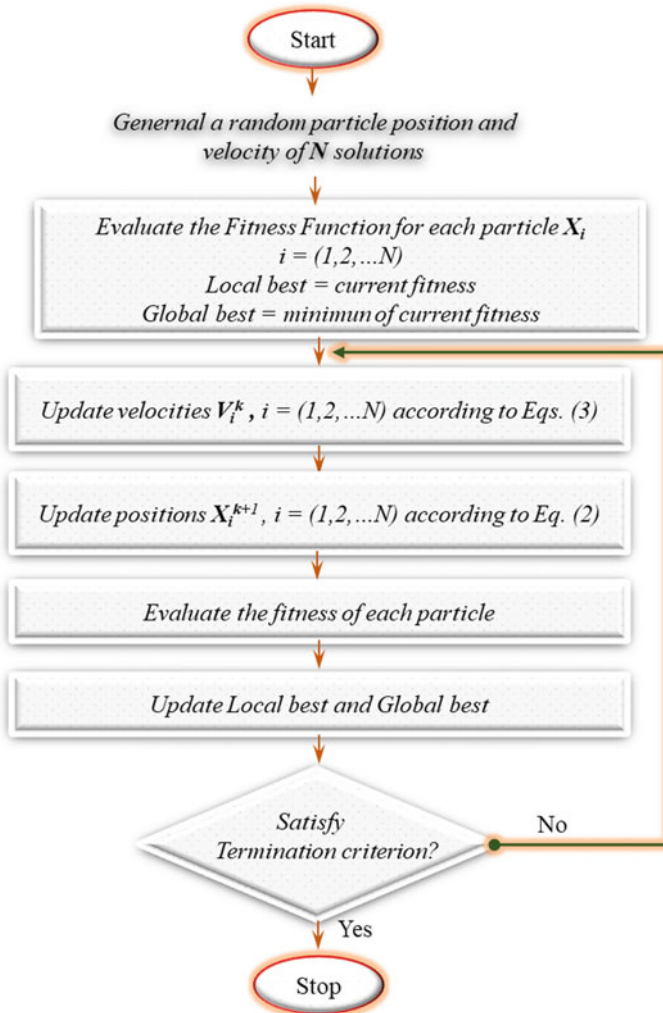
Fig. 1 Flowchart of NEA-PSO

R is considered as the search radius around the local best and global best.

This value depends on the upper (U_b) and lower (L_b) boundary conditions. In this research, *R* is expressed in Eq. (4).

$$R = \frac{(U_b - L_b)}{100} \tag{4}$$

It can be seen that the movement of each particle in NEA-PSO will be longer than that of PSO. Therefore, the convergence rate of NEA-PSO will be better promising than that of PSO. Two parameters ε_1 and ε_2 are proposed to control the expansion of the search space in NEA-PSO around each particle. This will help the NEA-PSO avoid missing potential search spaces. The strategy movement closing to local best and global best in NEA-PSO is controlled by a function $f(k+1) = 1 - \frac{\beta k}{K_{max}}$. The feature of this function is reduction linear as the number of iterations increases. At the iteration registers $f(k+1) = 0$, NEA-PSO will become the original PSO.

3 Numerical Examples

3.1 The First Example

To demonstrate the effectiveness of NEA-PSO. The first five benchmark test functions are used as the first example. Five functions are considered unimodal benchmark functions. For a fair comparison, both PSO and NEA-PSO algorithms have identical initial particles $N = 30$. The parameter $\beta = 0.2$ is assumed to achieve the fast convergence rate.

The coefficients of the algorithm are the same, and are described such as: The parameters learning $c_1 = c_2 = 2$, the weight of velocity w is denoted value in range [0.4, 0.9] and depend on each of iteration (Table 1).

Table 1 First five classical benchmark functions

Function	Solution space	f_{min}
$F_1 = \sum_{k=1}^{n} x_k^2$	$[-100, 100]^D$	0
$F_2 = \sum_{k=1}^{n} |x_k| + \prod_{k=1}^{n} |x_k|$	$[-100, 100]^D$	0
$F_3 = \sum_{k=1}^{n} \left(\sum_{j=1}^{i} x_j \right)^2$	$[-100, 100]^D$	0
$F_4 = \max\{|x_k|, 1 \le k \le n\}$	$[-100, 100]^D$	0
$F_5 = \sum_{k=1}^{n-1} \left[100(x_{k+1} - x_k^2) + (x_k - 1)^2 \right]$	$[-30, 30]^D$	0

Note that n is the dimension of function, f_{min} is the minimum value of the function, and S is a subset of R^n

The comparison results are shown in terms of the convergence rate of the objective function. Both two algorithms are run randomly ten times to evaluate the performance of each algorithm. The comparison results are shown in Fig. 2.

Based on the performance of the convergence trend and the accuracy level in Fig. 2, we can see that the NEA-PSO algorithm shows superiority at all of the functions. The new strategy movement of the NEA-PSO algorithm allows finding a better global position than PSO. Moreover, it was also registered a longer movement in comparison with PSO. It leads to that NEA-PSO was reached a convergence rate far faster.
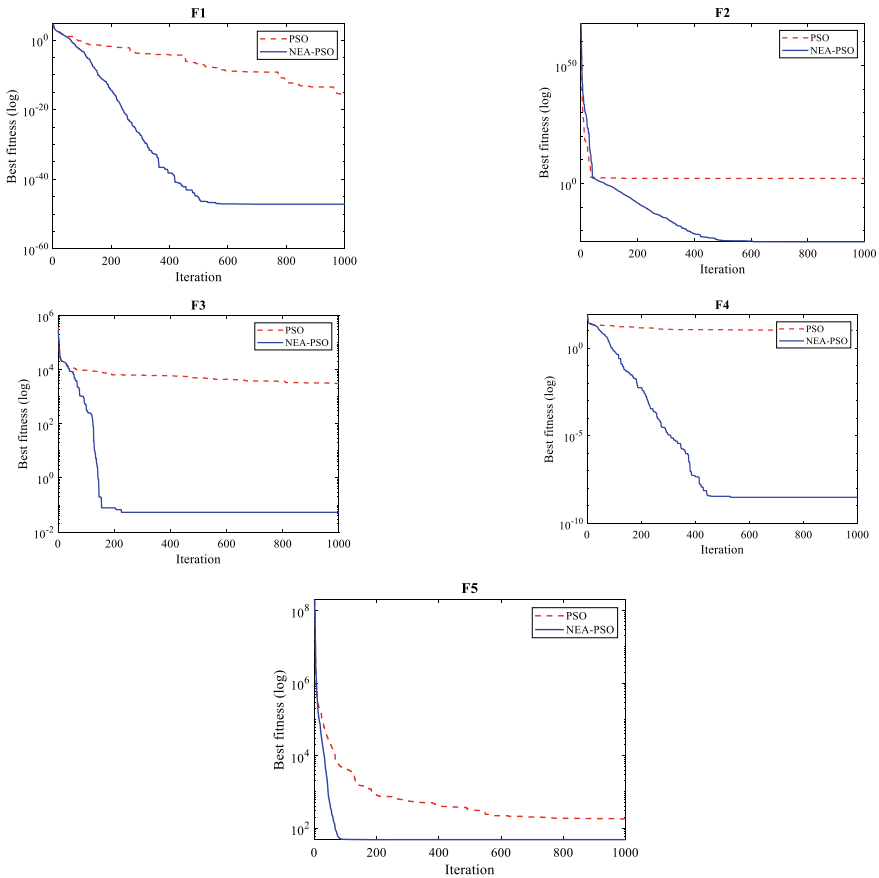
Fig. 2 Convergence trends of the five benchmark functions
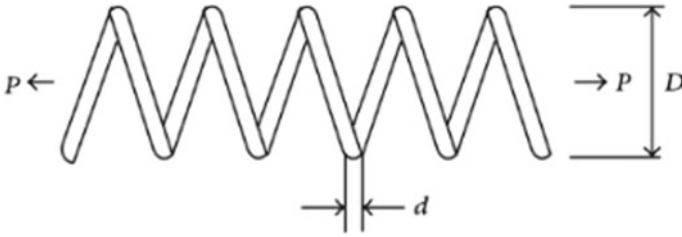
Fig. 3 Tension/compression spring design problem

3.2 The Second Example

The tension/compression spring is employed to illustrate the performance of NEA-PSO. This problem required determining the minimum mass of spring with three changeable d, D, and P given in Fig. 3. The dead penalty function technique is used as a robust tool together with NEA-PSO to solve the conditional constraints. The mathematical formulation of this problem was expressed as follows:

Give design variables: $x_1 = d$, $x_2 = D$, $x_3 = P$

Minimize: $f(x) = (x_3 + 2)x_2 x_1^2$

Subject to:

$$g_1(x) = 1 - \frac{x_2^3 x_3}{71785 x_1^4} \leq 0$$

$$g_2(x) = \frac{4x_2^2 - x_1 x_2}{12566(x_2 x_1^3 - x_1^4)} + \frac{1}{5108 x_1^2} - 1 \leq 0$$

$$g_3(x) = 1 - \frac{140.25 x_1}{x_2^2 x_3} \leq 0$$

$$g_4(x) = \frac{x_1 + x_2}{1.5} - 1 \leq 0$$

where

$$0.05 \leq x_1 \leq 2, \quad 0.25 \leq x_2 \leq 1.3, \quad 2 \leq x_3 \leq 15$$

The performance of NEA-PSO and PSO will be compared to the results released. Arora [11] used the usual mathematical method to solve this problem. Coello [12] solved this problem using GA algorithm. In this paper, parameter $R = 0.1$ is assumed for satisfaction with the boundary conditions for NEA-PSO. The comparison with the results obtained from Arora's and Coello's study is shown in Table 2. The results show that the NEA-PSO algorithm gives the best performance compared to the other methods.

Table 2 Performance of NEA-PSO compared to the other methods

Different methods	Design Variables			$f(x)$
	x_1	x_2	x_3	
Arora	0.053396	0.399180	9.185400	0.0127303
Coello	0.051480	0.351661	11.632201	0.01270478
In this work				
NEA-PSO	**0.052377**	**0.373456**	**10.3927**	**0.012697**
PSO	**0.05**	**0.3174280**	**14.027300**	**0.012719**

Bold indicates our presented results

4 Conclusions

This paper was presented a new improved technique for the velocity updating process in PSO algorithm. The new process allows creating more balance between the local best and global best position. Moreover, the ability finding the Gbest's position is also improved through short radian around the local and global position. By using a changeable parameter β that can be adjusted by the user, the convergence rate of NEA-PSO can be controlled depending on a particular problem. The proposed algorithm also shows the superiority of solving optimization problems with multiple constraint conditions. The NEA-PSO algorithm shows more flexibility and high reliability when solving real works through two numerical examples.

References

1. Kennedy J, Eberhart R (1995) Particle swarm optimization. In: Proceedings of ICNN'95-international conference on neural networks. IEEE
2. Yang X-S (2010) Firefly algorithm, stochastic test functions and design optimization. Int J Bio-inspired Comput 2(2):78–84
3. Karaboga D, Basturk B (2008) On the performance of artificial bee colony (ABC) algorithm. Appl Soft Comput 8(1):687–697
4. Mirjalili S, Mirjalili SM, Lewis A (2014) Grey Wolf optimizer. Adv Eng Softw 69:46–61
5. Chu S-C, Tsai P-W, Pan J-S (2006) Cat swarm optimization. In: Pacific Rim international conference on artificial intelligence. Springer
6. Rao R (2016) Jaya: a simple and new optimization algorithm for solving constrained and unconstrained optimization problems. Int J Ind Eng Comput 7(1):19–34
7. Wu T et al (2019) A capacity configuration control strategy to alleviate power fluctuation of hybrid energy storage system based on improved particle swarm optimization. Energies 12(4):642

8. Ouyang Z et al (2019) An improved particle swarm optimization algorithm for reliability-redundancy allocation problem with mixed redundancy strategy and heterogeneous components. Reliab Eng Syst Saf 181:62–74
9. Higashi N, Iba H (2003) Particle swarm optimization with Gaussian mutation. In: Proceedings of the 2003 IEEE Swarm intelligence symposium. SIS'03 (Cat. No. 03EX706). IEEE
10. Singh N, Singh S (2012) Personal best position particle swarm optimization. J Appl Comput Sci Math 12(6):69–76
11. Arora JS (2004) Introduction to optimum design. Elsevier
12. Coello CAC (2002) Theoretical and numerical constraint-handling techniques used with evolutionary algorithms: a survey of the state of the art. Comput Methods Appl Mech Eng 191(11–12):1245–1287

Application of Nonlinear Behaviour for Concrete Material in Numerical Simulation

Thi Thuy Linh-Nguyen, Hoang Le-Minh, T. Vu-Huu, and Thanh Cuong-Le

1 Introduction

The concrete damage is caused by (1) the formation of severe cracks at the tension zone and (2) by crushing at the compression zone. However, at the moment, concrete strength is measured mainly by the basic one-dimension (1D) confined compression or tension test, which cannot evaluate the real failure of concrete in the structure because the stress of concrete is a three-dimension (3D) stress state. The ABAQUS software can numerically simulate the concrete plastic damage model; the model employs the yield surface approach pioneered by Ref. [2] and finalized by Ref. [3]. Whereby the element stress is taken into consideration for all stress components to check the plastic state.

T. T. Linh-Nguyen
Faculty of Civil Engineering, Ho Chi Minh City University of Technology—HUTECH, Ho Chi Minh City, Vietnam
e-mail: ntt.linh85@hutech.edu.vn

H. Le-Minh · T. Cuong-Le (✉)
Faculty of Civil Engineering, Ho Chi Minh City Open University, Ho Chi Minh City, Vietnam
e-mail: cuong.lt@ou.edu.vn

H. Le-Minh
e-mail: hoang.lm@ou.edu.vn

T. Vu-Huu
Faculty of Civil Engineering, Vietnam Maritime University, 484 Lach Tray Str., Hai Phong, Vietnam
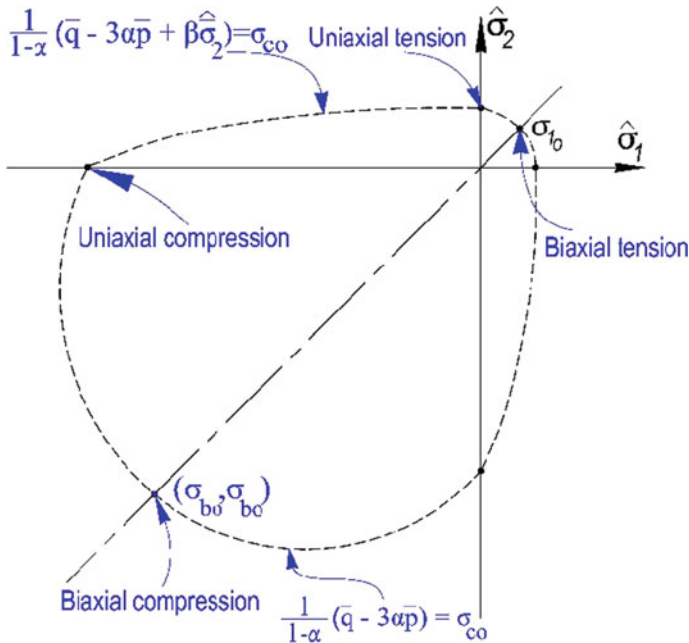
Fig. 1 Yield surface according to Eq. (3)

The yield surface equation, see Fig. 1, is

$$F = \frac{1}{1-\alpha}(q - 3\alpha p + \beta\langle\sigma_{max}\rangle - \gamma - \langle\sigma_{max}\rangle) - \overline{\sigma}_c = 0; \; \alpha = \frac{\left(\frac{f_{b0}}{f_{c0}}\right) - 1}{2\left(\frac{f_{b0}}{f_{c0}}\right) - 1} \quad (1)$$

$$\beta = \frac{\overline{\sigma}_c}{\overline{\sigma}_t}(1-\alpha) - (1+\alpha); \; \gamma = \frac{3(1 - K_c)}{2K_c - 1} \quad (2)$$

In which, $\langle\cdot\rangle$ Macaulay operation; p is the hydrostatic stress; q is the Von-Mises stress calculated with the principal stress $\sigma_1, \sigma_2, \sigma_3$, which are considered the effects of the compressive damage variable d_c and the tension damage variable d_t. Then, f_{b0} is the unconfined axial compression stress, f_{c0} is the confined axial compression stress, and σ_{max} is the maximum principal stress.

And, $\overline{\sigma}_c = \sigma_c(1 - d_c)$ are $\overline{\sigma}_t = \sigma_t(1 - d_t)$ are compression and tension stress. $K_c = \rho_{t0}/\rho_{c0}$ is the ratio of the compressive stress to the tension stress at the plastic surface, which is applied to determine the shape of the plastic plane in the plane of deflection stress (π plane). When, $K_c = 1$ corresponds to the yield surface proposed by Von-Mises, $K_c = 2/3$ is used to determine the yield surface of concrete materials according to ABAQUS, see Fig. 2.

Fig. 2 Plastic potential energy function in the stress plane $p - q$
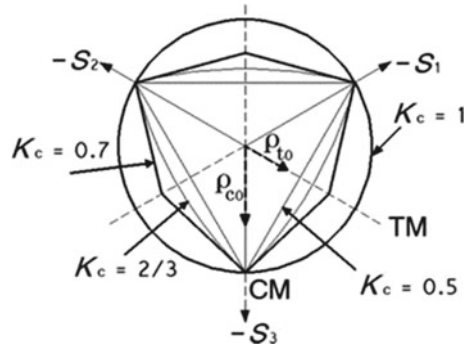
Table 1 Input parameters for the concrete plastic damage model

K_c	ψ (degree)	$\frac{f_{b0}}{f_{c0}}$	ε
0.7	35–40	1.16	0.1

The model describing the plastic behaviour of concrete is based on the independent plastic potential energy function G, which is as follows:

$$G(\sigma) = \sqrt{(\varepsilon \sigma_{t0} \tan \psi)^2 + q^2} - p \tan \psi \tag{3}$$

in which, $\varepsilon = 0.1$ is the definite deviation coefficient of the potential plastic surface from the yield surface, Then, σ_{t0} is the tension failure stress determined by the confined axial tension test. And, ψ is the angle between the intersection lines of the yield surface in terms of the p-plane (hydrostatic stress) and the q-plane (deviation stress) at a state of high normal stress. ABAQUS proposes $35° \leq \psi \leq 40°$. Other parameters of the yield surface are given in Table 1.

2 The Behaviour of Concrete in Axial Compression and Tension Test

The behaviour of concrete in axial compression or tension with lateral expansion (Poisson effect) in the phase of non-cracking is linear, so it does not depend on element size. When the concrete reaches the ultimate compressive or tensile stress, it approaches the compression softening phase or tension softening phase. In the finite element (FE) method, the mesh element sizes are key factors of the analysis. So, the effect of mesh size must be addressed in the process of simulation. We offer the computation for the values of material parameters according to Table 2 in this study to make the suggested model easier to set up and decrease the experimental procedure. Thus, the other concrete parameters can be directly calculated from the

Table 2 Equations for calculating the characteristics of the concrete base on the average compressive strength

Average compressive strength of the cylindrical sample	$f_{cm} = f_{ck} + 8$	Mpa
Average tensile strength of the cylindrical sample	$f_{tm} = \max\left(0.3 f_{ck}^{0.67}, 0.9 f_{sp}\right)$	Mpa
Tangent module	$E_{ci} = E_{c0}\alpha_E \left(\frac{f_{cm}}{10}\right)^{1/3}$	Gpa
Strain at the top of the sample when compressing	$\varepsilon_{tm} = 0.0007(f_{cm})^{0.31}$	
Fracture energy	$G_F = 73(f_{cm})^{0.18}$	N/m
Failure energy	$G_{ch} = \left(\frac{f_{cm}}{f_{tm}}\right)^2 G_F$	N/m

average compressive strength f_{cm} and the average tensile strength f_{tm} in the axial compression test.

2.1 Compression Behaviour of Concrete

The nonlinear behaviour of concrete at the confined axial compression can be divided into three states, see Fig. 3.
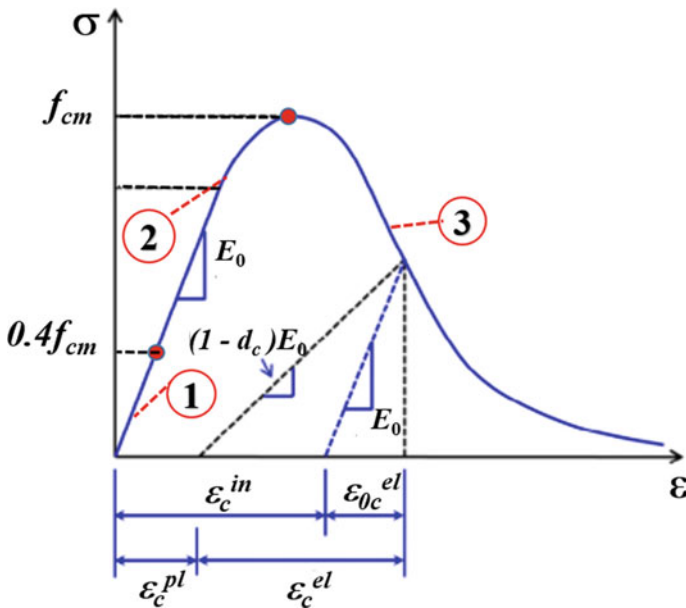
Fig. 3 Compressive behaviour of concrete
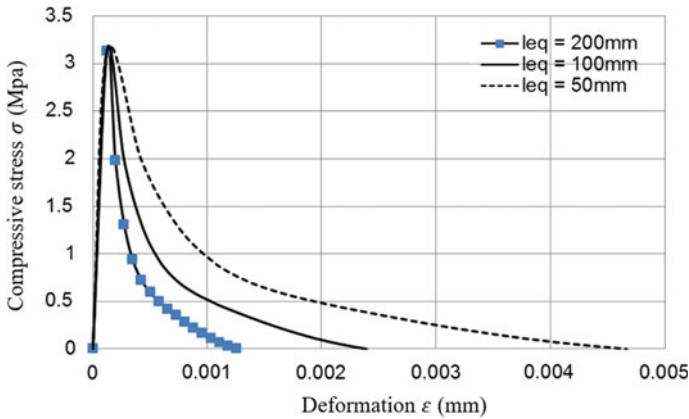
Fig. 4 Compressive behaviour of concrete with characteristic crack length l_{eq}

Stage 1: The stress–strain relationship of concrete is linear. The line segment ends at the $0.4 f_{cm}$ as [4] và EC2 (2002); then, the curve $\sigma_c^1 = E_0 \varepsilon_c$ is defined by secant moduli of concrete material, $E_{c0} = \left(0.8 + \frac{0.2 f_{cm}}{88}\right) E_{ci}$, see Fig. 4.

Stage 2: The stress–strain relationship of concrete is a curve defined by [4] hoặc EC2 (2002), as follow:

$$\sigma_c^2 = \frac{E_{ci} \frac{\varepsilon_c}{f_{cm}} - \left(\frac{\varepsilon_c}{\varepsilon_{ctm}}\right)^2}{1 + \left(E_{ci} \frac{\varepsilon_{tm}}{f_{cm}} - 2\right)\frac{\varepsilon_c}{\varepsilon_{tm}}} f_{cm} \tag{4}$$

in which, E_{ci} is the initial tangent module of concrete.

Stage 3: This stage represents the concrete strength decrease suggested by [5]. This model is appropriate for numerical models that rely on meshing.

$$\sigma_c^3 = \left(\frac{2 + \gamma_c f_{cm}\varepsilon_{tm}}{2 f_{cm}} - \gamma_c \varepsilon_c + \frac{\varepsilon_c^2 \gamma_c}{2\varepsilon_{tm}}\right)^{-1} \tag{5}$$

$$\gamma_c = \frac{\pi^2 f_{cm}\varepsilon_{tm}}{2\left[\frac{G_{ch}}{l_{eq}} - 0.5 f_{cm}\left(\varepsilon_{tm}(1 - b) + b\frac{f_{cm}}{E_0}\right)\right]^2} ; b = \frac{\varepsilon_c^{pl}}{\varepsilon_c^{ch}} \tag{6}$$

In which, l_{eq} is the characteristic crack length of the element that depends on the mesh size, type, crack propagation; b is the ratio of the plastic to inelastic deformation ε_c^{ch}, experimentally, $b = 0.9$; G_{ch} is the breaking energy from 10 to 25 kN/m according to [6]; ε_{tm} is the strain with respect to the average compressive strength f_{cm}. Figure 4 shows the uniaxial compression behaviour of concrete with $f_{cm} = 35$ Mpa witt respect to the different meshing sizes.
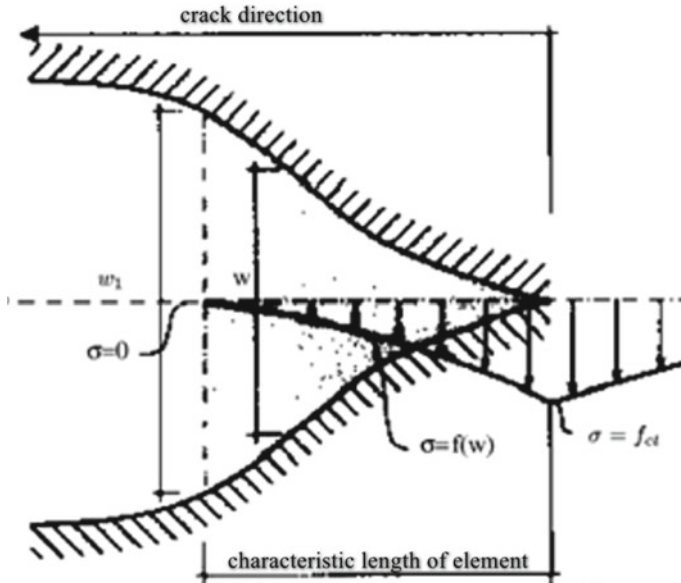
Fig. 5 Cracking model [8]

2.2 Tension Behaviour of Concrete

In the first stage, the behaviour of concrete has not been cracked. The stress–strain relation is linear and determined through the initial strain modulus of the concrete E_{ci}. The current behaviour does not depend on meshing. Then, in the tension softening state, cracks take place, and the stress–strain curve depends on meshing (i.e., the characteristic length of the element, l_e). Cracks form and expand until the concrete breaks. Because in FEM, l_{eq} occasionally causes the convergence problems, [7] proposed a stress-crack width relation that does not depend on meshing, see Fig. 5

$$\frac{\sigma_t(w)}{f_{tm}} = \left[1 + \left(c_1 \frac{w}{w_c}\right)^3\right] e^{-c_2 \frac{w}{w_c}} - \frac{w}{w_c}\left(1 + c_1^3\right) e^{-c_2} \tag{7}$$

$$w_c = 5.14 \frac{G_F}{f_{tm}} \tag{8}$$

in which, f_{tm} is the average tensile strength of concrete; w is the crack width at stress σ_t; w_c is the ultimate crack width depending on the fracture energy G_F.

In ABAQUS, the tension model of concrete can be established by the relation of stress and crack width or stress with cracking strain or the stress and strain. They are computed through the crack model suggested by [8], see Fig. 6, we have $\varepsilon_t^{ck} = w/l_{eq}$.
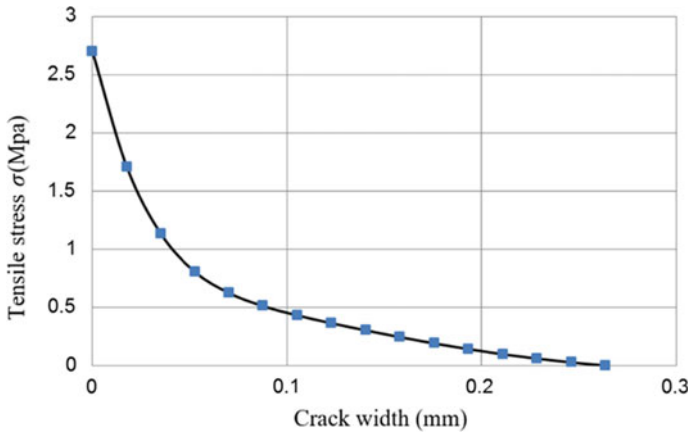
Fig. 6 Tensile stress-crack width ratio
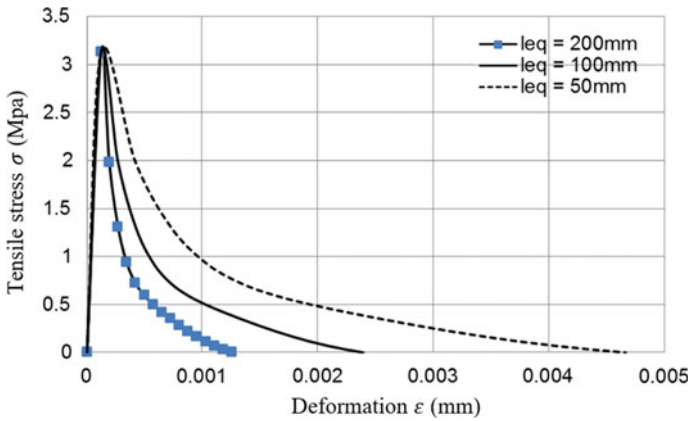
Fig. 7 Tensile stress-deformation ratio under the effect of l_{eq}

The strain at tension stress in the tension softening phase is calculated as follows:

$$\varepsilon_t^{cr} = (\varepsilon_t - \varepsilon_{tm}) = w/l_{eq} \Rightarrow \varepsilon_t = \varepsilon_{tm} + w/l_{eq} \qquad (9)$$

in which, ε_t is the strain of concrete corresponding to the tension softening phase at the stress σ_t. Thus, the strain in the tension softening phase of concrete can be determined by the characteristic crack length l_{eq}. The stress–strain behaviour in the tension depends on meshing, see Fig. 7.

2.3 Compression and Tension Softening Coefficients of Concrete

Softening coefficients in compression d_c and in tension d_t are established based on the stress–strain relation of concrete under compression and tension, see Fig. 9a, b. Therefore, in the softening phase, when loads are removed, the initial elastic stiffness decreases. In which, d_c and d_t are two characteristic coefficients for this stiffness decrease, $0 \leq d_c, d_t \leq 1$. The model (CDP) is based on the assumption of the plastic strain in the compressive and tensile behaviour of concrete. $\varepsilon_c^{\text{pl}}$ and $\varepsilon_t^{\text{pl}}$ can be calculated directly from the stress–strain curve with compression and tension softening known coefficients, as follows:

$$\varepsilon_c^{\text{pl}} = \varepsilon_c^{\text{ch}} - \frac{d_c}{1 - d_c} \frac{\sigma_c}{E_0}; \varepsilon_c^{\text{ch}} = \varepsilon_c - \frac{\sigma_c}{E_0} \tag{10}$$

$$\varepsilon_t^{\text{pl}} = \varepsilon_t^{\text{ck}} - \frac{d_t}{1 - d_t} \frac{\sigma_c}{E_0}; \varepsilon_t^{\text{ck}} = \varepsilon_t - \frac{\sigma_t}{E_0} \tag{11}$$

Typically, the softening coefficients are determined experimentally as [5], $d_c = 0.7$, $d_t = 0.1$. Alfarah et al. [1] proposes a method to calculate the softening coefficients d_c, d_t without experiments. In this research, the softening coefficients are calculated as follows:

$$a_c = 2(f_{\text{cm}}/f_{c0}) - 1 + 2\sqrt{(f_{\text{cm}}/f_{c0})^2 - (f_{\text{cm}}/f_{c0})} \tag{12}$$

$$a_t = 2(f_{\text{tm}}/f_{t0}) - 1 + 2\sqrt{(f_{\text{tm}}/f_{t0})^2 - (f_{\text{tm}}/f_{t0})} \tag{13}$$

$$b_c = \frac{f_{c0} l_{\text{eq}}}{G_{\text{ch}}} \left(1 + \frac{a_c}{2}\right) \tag{14}$$

$$b_t = \frac{f_{t0} l_{\text{eq}}}{G_F} \left(1 + \frac{a_t}{2}\right) \tag{15}$$

in which, f_{c0} and f_{t0} are the ultimate compressive and tensile strength of concrete before cracking, as Sect. 2.1, $f_{c0} = 0.4 f_{\text{cm}}$, $f_{t0} = f_{\text{tm}}$. The softening coefficients, d_c, d_t, are computed by Eqs. (16) and (17) as [1], see in Fig. 8.

$$d_c = 1 - \frac{1}{2 + a_c} \left[2(1 + a_c) \exp(-b_c \varepsilon_c^{\text{ch}}) - a_c \exp(-2b_c \varepsilon_c^{\text{ch}})\right] \tag{16}$$

$$d_t = 1 - \frac{1}{2 + a_t} \left[2(1 + a_t) \exp(-b_t \varepsilon_t^{\text{ck}}) - a_t \exp(-2b_t \varepsilon_t^{\text{ck}})\right] \tag{17}$$
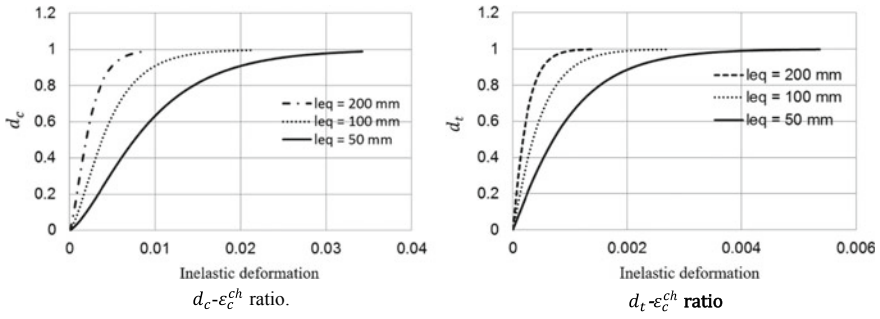
Fig. 8 Damage variable d_c and d_t
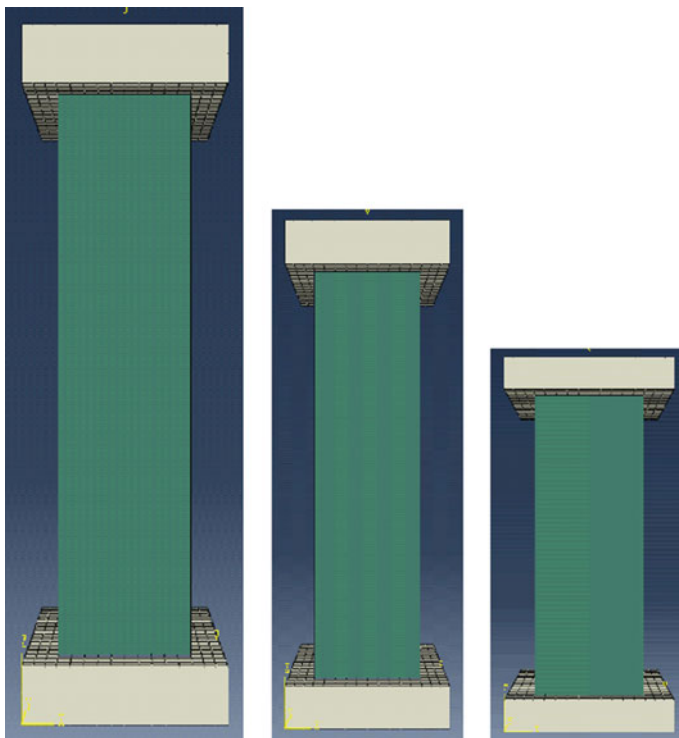
Fig. 9 Model test of [6] and [9] using ABAQUS

3 Characteristic Crack Length

The cracking energy $G_F = \int_0^{w_c} \sigma_t dw$ is the lower area of the tension curve of concrete in the compression softening /tension softening state. It represents a relation between the stress and crack opening, which causes no impact on the meshing. Consider a

single crack whose width corresponds to the cracking strain ε_{cr}. The value l_ed is a characteristic crack length to calculate the cracking strain such that $l_{ed}\varepsilon_{cr} = w$. The characteristic crack length l_{eq} can be taken as the square root of the shell-element area. In the case of solid-element, $l_{ed} = e$, in which, e is the element edge (ABAQUS Manual).

4 Numerical Examples

The first example of this study is a model to stimulate the concrete compression experience of [9] and [6]. Van Mier [9] and Vonk [6] conducted axial compression test with lateral expansion (Poisson effect) of different samples with the same cross section (100×100 mm) but various heights (200, 100 and 50 mm). The results show that the shortened samples have more resilient than the longer ones. The simulation is carried out with the element size equalling the length of the samples. It means that the mesh has only one element whose characteristic crack length l_{eq} in the simulation, see in Fig. 9.

The numerical results in Fig. 10 indicate that the parameters defining the yield surface in Table 1 and the method setting the tensile and compressive behaviour of concrete are reliable and compatible with the experimental results.
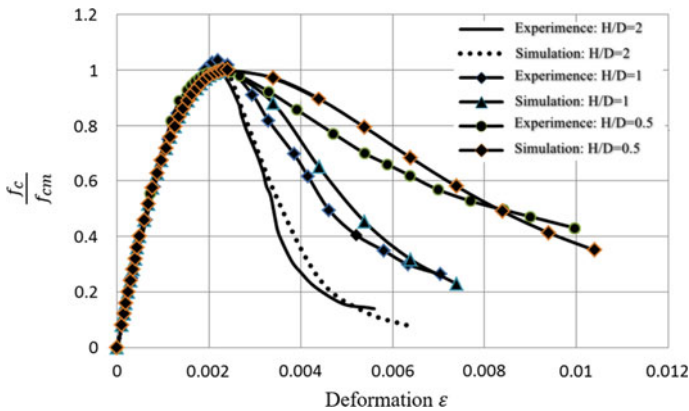
Fig. 10 Results obtained from ABAQUS compared to [9] and [6]
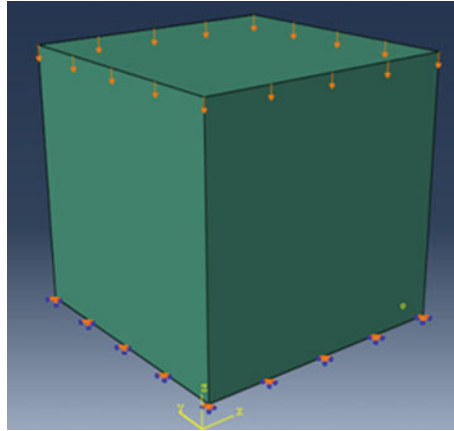
Fig. 11 Model test of [10] using ABAQUS

Our second test in this research is a model to simulate the compression softening test of [10]. The softening coefficients, d_c, d_t, are computed as the study of [1]. They are the exponential function and calculated for each compressive or tensile stress in the softening stages. In addition, d_c, d_t can be based on the [5], and they are constants with $d_c = 0.7$, $d_t = 0.1$. The softening coefficients are determined experimentally with the procedure of loading and unloading then reloading until the sample damages. Sinha et al. [10] conducted an experiment to determine the compressive softening coefficient d_c by a cube concrete sample with size $25 \times 125 \times 125$ mm, the average compressive strength of the sample $f_{cm} = 26$ (Mpa). The numerical simulation is set up as shown in Fig. 11. The sample element is meshed with real size; the characteristic crack length is taken as the ABAQUS Manual. The edge of the element $l_{eq} = 125$ mm.

The loading process is managed by a technique of displacement control for the loading–unloading–reloading with the increment of $\Delta = 0.06$ mm for one time increase of load as shown in Fig. 12. The concrete properties and the other parameters using in ABAQUS are based on [1], shown in Table 3. The comparison between numerical and experimental results shows that the compressive softening coefficient d_c is consistent to the experimental results, see Fig. 13. When the concrete works in the softening state, the stiffness decreases compared to the initial stiffness. The new stiffness of the element at the current stress is $E = E_{ci}(1 - d_c)$.
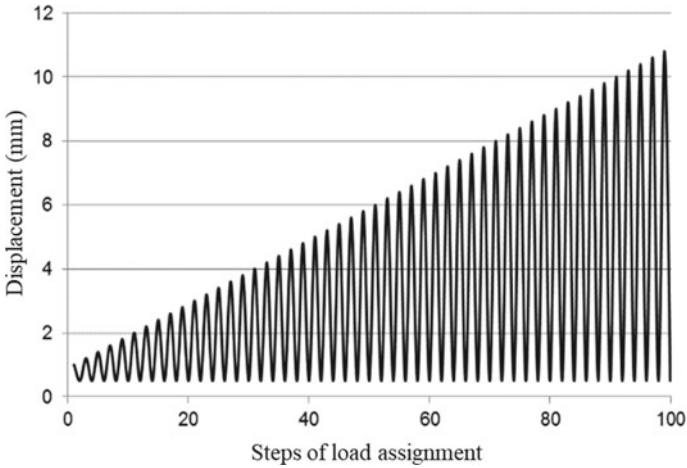
Fig. 12 Process of load assignment according to [10]

5   Conclusion

This paper introduces a model to simulate a nonlinear behaviour of concrete, and the compression and tension softening coefficient of concrete is calculated by the exponential function proposed by [1] to present the stiffness decrease of the concrete element in the softening stages. The comparison between experiment and numerical result in this paper shows that the application of concrete material model for the nonlinear analysis of concrete depends on the meshing sizes.

Table 3 Parameters are used to simulated the experiment of [10]

f_{cm} (Mpa)	E_{ci} (Mpa)	f_{tm} (Mpa)	G_{ch} (N/mm)	G_F (N/mm)	b	a_c	a_t	l_{eq} (mm)	b_c	b_t
26	29,564	2.06	20.894	0.131	0.8	7.873	1	125	306.425	2856.48
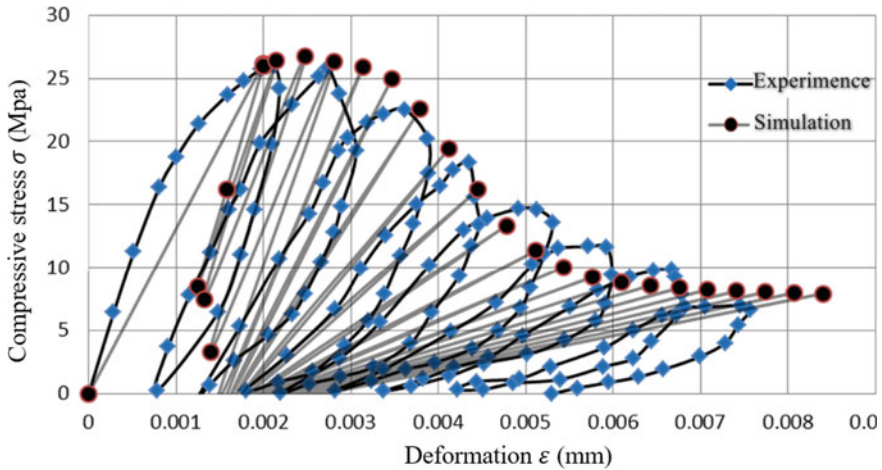
Fig. 13 Results obtained using ABAQUS compared to the experiment of [10]

References

1. Alfarah B, López-Almansa F, Oller S (2017) New methodology for calculating damage variables evolution in plastic damage model for RC structures. Eng Struct 132:70–86
2. Lubliner J et al (1989) A plastic-damage model for concrete. Int J Solids Struct 25(3):299–326
3. Lee J, Fenves GL (1998) Plastic-damage model for cyclic loading of concrete structures. J Eng Mech 124(8):892–900
4. Béton CE-Id (1993) CEB-FIP model code 1990: design code. Thomas Telford Publishing
5. Krätzig WB, Pölling R (2004) An elasto-plastic damage model for reinforced concrete with minimum number of material parameters. Comput Struct 82(15–16):1201–1215
6. Vonk RA (1992) Softening of concrete loading in compression. Ph.D. thesis
7. Cornelissen H, Hordijk D, Reinhardt H (1986) Experimental determination of crack softening characteristics of normalweight and lightweight. Heron 31(2):45–46
8. Hillerborg A (1983) Analysis of one single crack
9. Van Mier JG (2012) Concrete fracture: a multiscale approach. CRC press
10. Sinha B, Gerstle KH, Tulin LG (1964) Stress-strain relations for concrete under cyclic loading. J Proc

Particle Swarm Optimization (PSO) Algorithm Design of Feedforward Neural Networks (FFN) for Predicting the Single Damage Severity in 3D Steel Frame Structure

Thanh Cuong-Le and Hoang Le-Minh

1 Introduction

Structure damage can be predicted early, allowing for timely repair. Therefore, this problem has received more and more attention and research in recent years. Many methods have been proposed and proven for their effectiveness and suitability for the application. Model-based methods, which record changes in modal properties of the structure, such as natural frequencies and mode shapes, are widely applied for predicting the damage structures. Normally, there are two approaches to solve this problem. The first approach is based on inverse problem combined with the optimization algorithm to minimize the objective function, which is established from the differences between the mode shapes and frequencies registered at two states, damaged and undamaged structures [1–3]. And the second approach is relied on artificial neural networks, support vector machines, and deep learning [4, 5]. Over the past two decades, artificial neural networks (ANNs) techniques known have significant growth with their applications in many fields. The process of self-improvement of ANN uses back-propagation method, which is local search strategy using gradient descent to adapt the weights and biases in each layer. In this work, the process of back-propagation is replaced by PSO algorithm for optimization of the hyperparameters in FFN. There are also some research contribution based on optimization algorithm to improve FFN [6–8].

T. Cuong-Le (✉) · H. Le-Minh
Faculty of Civil Engineering, Ho Chi Minh City Open University, Ho Chi Minh City, Vietnam
e-mail: cuong.lt@ou.edu.vn

2 Particle Swarm Optimization (PSO)

Kennedy and Eberhart [9] proposed particle swarm optimization (PSO), which is a well-known optimization algorithm, and it is widely used in many fields. The background of PSO lies on two positions exploited at each iteration called the global best (G_{best}) and local best ($L_{\text{best},i}$). Based on these position, a movement strategy is established to ensure the balance between local best and global best. First of all, the velocity of each candidate solution X_i ($i = 1, 2, \ldots n$) at the step of movement $(t+1)$th will be updated. And the second, the new position of each candidate solution X_i ($i = 1, 2, \ldots n$) will be calculated based on its velocity. Thus, at the $(t + 1)$th iteration, the new position will be close to local best or global best. During their movement, the solution candidates can also expand the new search spaces through the two factors defined as learning factors c_1, c_2. The process of improvement of PSO is implemented through iterations. If we achieve a sufficiently large number of iterations, we will achieve convergence with an acceptable accuracy level.

The process of updating the new velocity and position of the PSO algorithm is described in Eqs. (1) and (2).

$$V_i^{t+1} = wV_i^t + c_1 r_1 (L_{\text{best},i} - X_i^t) + c_2 r_2 (G_{\text{best}} - X_i^t) \tag{1}$$

$$X_i^{t+1} = X_i^t + V_i^{t+1} \tag{2}$$

where r_1, r_2 are random vector registered the value in range [0, 1] and w is denoted as an inertia weight to control the velocity.

3 A Hybrid PSO-Feedforward Neural Networks (PSO-FFN)

A neural network will start with datasets including the two parts called input data and target data (known). Through FFN, the input data will pass through multiple hidden nodes, and the final layer in FFN will calculate the cohesive output based on the activation function. A feedforward neural network is a relatively simple artificial neural network in which the connections between nodes do not form a loop as shown in Fig. 1. They are called feedforward because information in the network only goes forward.

Neuron of each layer lth is considered as cohesive output from each neuron in previous layer $(l - 1)$th, and at the same time, it is also considered as input to the neurons in next layer $(l + 1)$th. This process will be straightforward to the last layer to produce the final cohesive output.

We define w_{jk}^l as the weight for the connection from the kth neuron in the $(l - 1)$th layer to jth neuron in the (l)th layer. And b_j^l is the bias of jth neuron in the (l)th
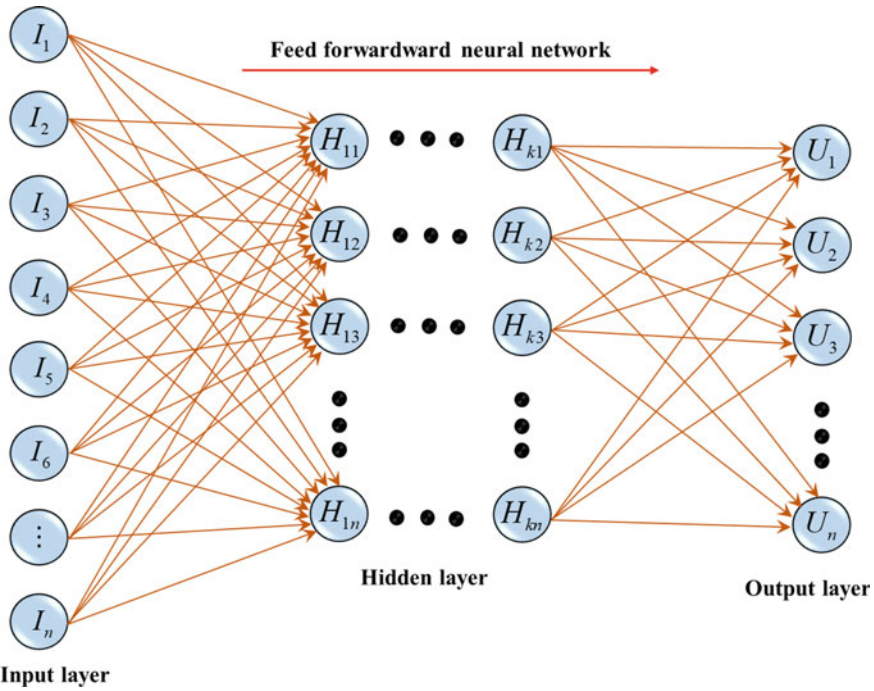
Fig. 1 Applications of feedforward neural networks

layer. With these notations, the activation f_j^l of jth neuron in the (l)th layer is given in Eq. (1)

$$a_j^l = f\left(\sum_k w_{jk}^l a_k^{l-1} + b_j^l\right) \qquad (3)$$

where the sum is defined over all neurons in the ($l - 1$)th layer. And $f = \frac{1}{1+e^{-x}}$ is sigmoid function. Based on the FNN, the final cohesive output will be determined at the last layer. Assume that $\widetilde{y}$ is the desired output (target). The loss function in DNN is calculated in Eq. (3)

$$\text{MSE} = \left(\frac{1}{n_{\text{row}} \times n_{\text{col}}}\right) \sum_{j=1}^{m} \left\| a^L - \widetilde{y} \right\|^2 \qquad (4)$$

where n_{row} and n_{col} are the number of rows and columns, respectively. And m is the number of training data. The process of neural network training is implemented through the weights and bias updating. And normally, this process is secured by back-propagation based on gradient descent. In this paper, we do not use this method; instead, PSO is employed to minimize the objective function as given in Eq. (3)
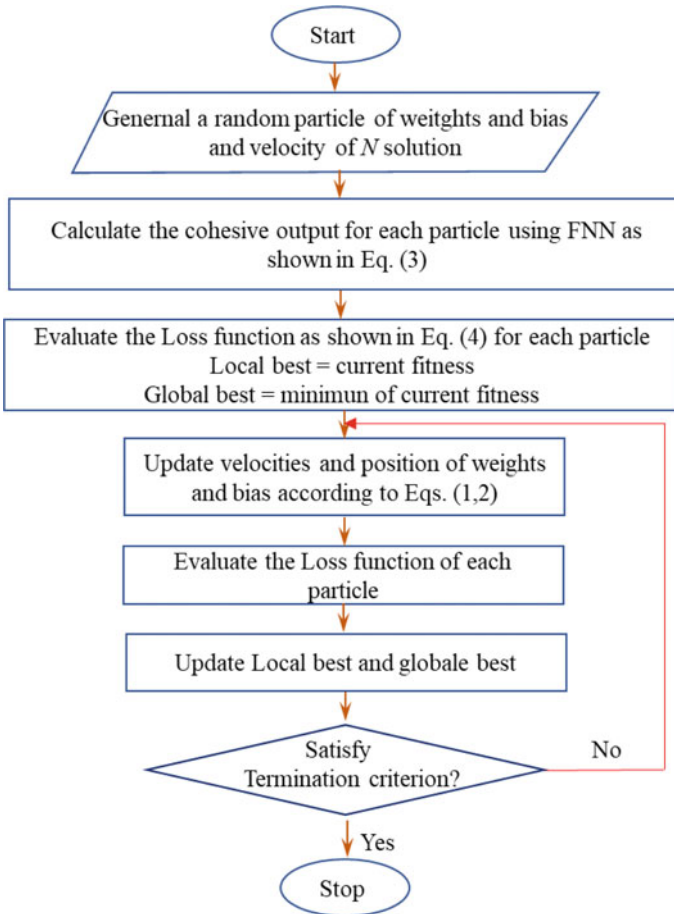
Fig. 2 Process of optimization the loss function in FNN using PSO

as shown in Fig. 2. The best solution obtained by PSO will be considered as the hyperparameters. Through these hyperparameter, we will establish a complete FFN for predicting damage severities elements in steel 2D frame.

4 Application PSO-FNN for Predicting the Damage Serverity of Columns in Steel 3D Frame Structure

This section mentions the application of PSO-FNN to determine the damage severity of columns in steel a 3D frame structure. Thus, a 3D steel frame having geometry with 3 m for two long sides and 3 m inner story height is shown in Fig. 3. The

Fig. 3 Geometry of 3D steel frame
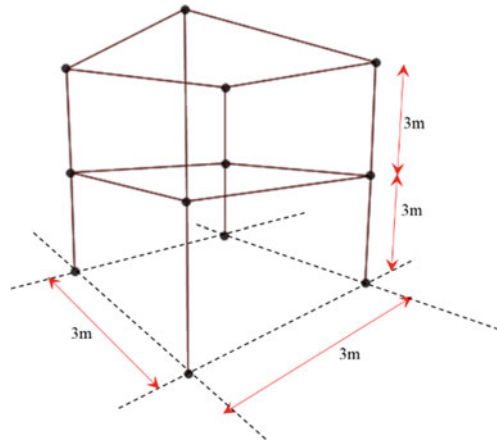
columns and beams are in the same section (H-300 × 10 + 125 × 6), which are denoted as H shape section with 300 mm height, 10 mm web thickness, 125 mm width of flange, and 6 mm flange thickness. A finite element (FE) model having 16 elements and 12 nodes, as shown in Fig. 4, is used to simulate the structure. The data training of FFN-PSO includes input datasets, which are defined as the mode shapes and frequencies obtained by FE analysis at the random damage cases. And these random damage cases are also considered as output datasets. To predict the single damage severities, column, whose label is 9, is selected. The process of FE model updating is used to create the training data by applying the random damage value distributed in range from 0.1 to 0.4. Then, these damage values will be assigned to the single column element 9 for story one to update the FE model. By this way, we create 200 data for training FFN-PSO including input datasets, which are extracted from FE model analysis with the first twelve frequencies and the first three mode shapes. And output datasets are random damage value of single column, which are defined as element 9.

The FFN-PSO uses three hidden layers to achieve a nonlinear relationship between input and cohesive output. The number of neurons in each hidden layer is 5, 3, and 5, respectively. Thus, the architect of FFN-PSO is rewritten in the notation [input 5 3 5 output]. The loss function (MSE) of FFN-PSO is shown in Fig. 5, and the difference between output using FFN-PSO and target is shown in Fig. 6. The results show that with the number of iterations $T = 5000$, the PSO can find the hyperparameters with an acceptable level of accuracy. At the last of iteration, FFN-PSO registers MSE = 10–3 and the regression $R = 0.95755$.

We conducted three tests given in Table 1 to evaluate the accuracy and generalizability of the FFN-PSO model. Thus, the random damage variables are assigned to column element 9 as reduction of stiffness. Then, based on FE analysis, the first twelve frequencies and the first three mode shapes are extracted. These data are considered as input datasets in FFN-PSO, and the cohesive output will be determined by the process of FFN as given in Eq. (3). The prediction results using FFN-PSO

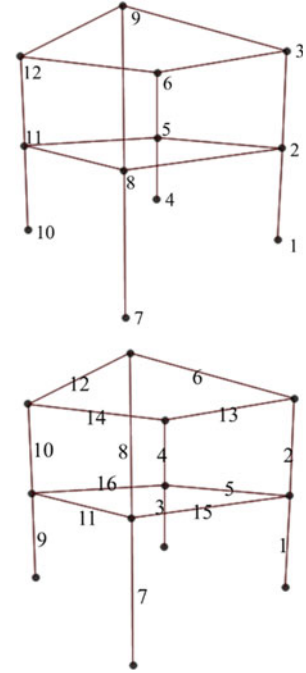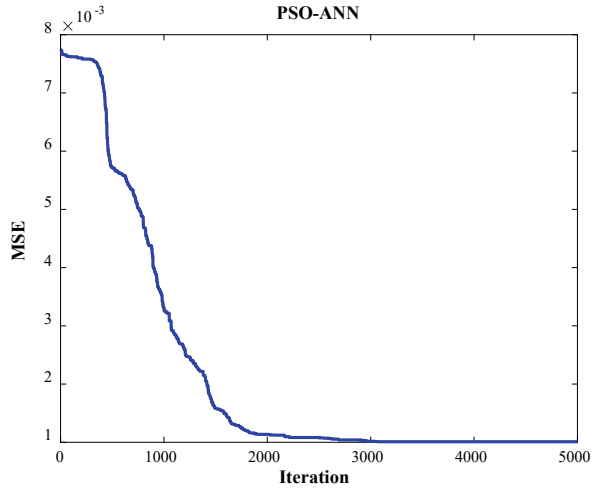**Fig. 4** Number of node labels and frame labels

Fig. 5 History of MSE value over the course of iterations

are presented in Table 2 and Fig. 7. Although there are errors between the predicted values and the true values, the accuracy level is acceptable with a good agreement. The largest error recorded is 0.025 for Case 3.

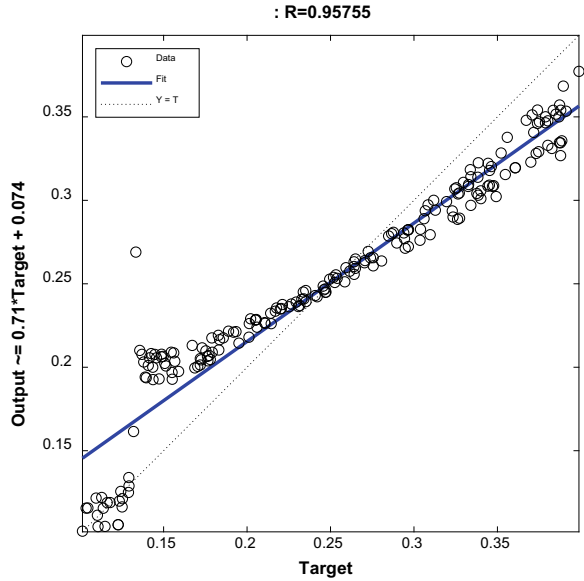**Fig. 6** Results of output value obtained by DNN vs target value

Table 1 Reduction stiffness in single element 9 for different elements

Case	Damaged elements	Reduction of stiffness (%)
Case 1	Element 9	$\alpha_1 = 32\%$
Case 2	Element 9	$\alpha_2 = 20\%$
Case 3	Element 9	$\alpha_3 = 18\%$

Table 2 Results of FFN-PSO for predicting the single damage for element 9

Case	Damaged elements	True value	Prediction value	Absolute error
Case 1	Element 9	0.32	0.322	0.002
Case 2	Element 9	0.2	0.218	0.018
Case 3	Element 9	0.18	0.205	0.025

5   Conclusion

In this paper, a method for hyperparameters optimization in a feedforward network defined by [input 5 3 5 output] is presented for predicting the single damage severity. After finding the best hyperparameter by PSO algorithm, the FFN-PSO is used to train a dataset, including input and target. These training datasets are obtained by the FE model updating. The results show that the FNN-PSO can predict exactly the damage severities in element 9 for a 3D steel frame. The results obtained in this study have proved that the application of optimization algorithms for optimizing the

Fig. 7 Damage
identification results for Case
1, Case 2, and Case 3 using
FFN-PSO
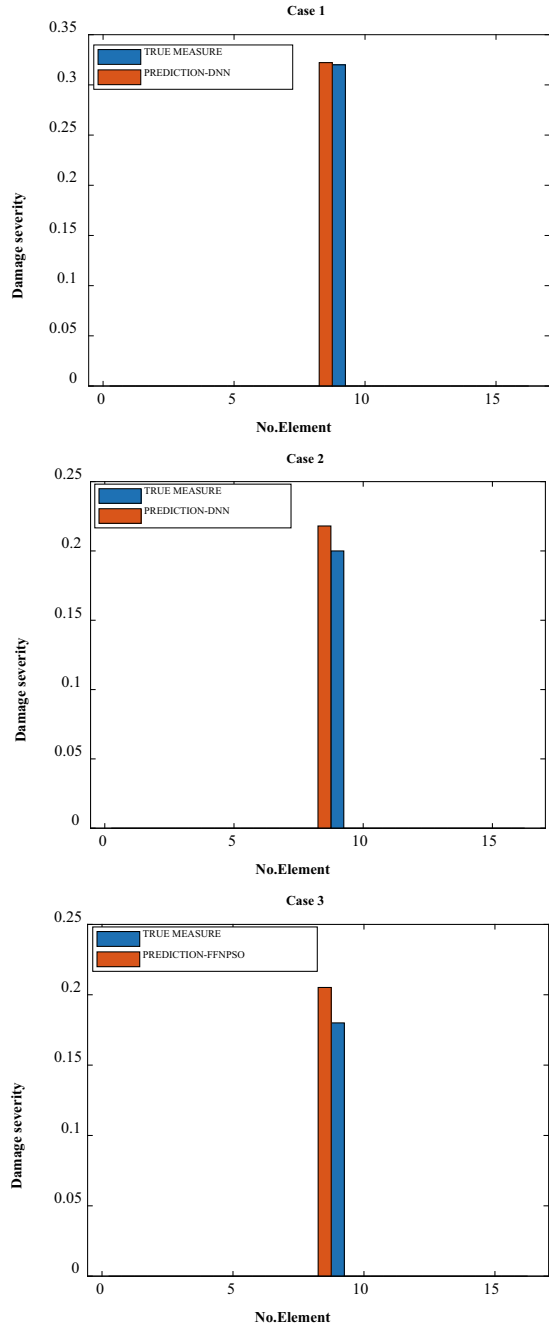
hyperparameters in the feedforward network is promising, and they can be used to improve the other complete networks such as ANN or DNN.

References

1. Minh H-L, Khatir S, Abdel Wahab M, Cuong-Le T (2021) An enhancing particle swarm optimization algorithm (EHVPSO) for damage identification in 3D transmission tower. Eng Struct 242:112412
2. Minh H-L, Khatir S, Rao RV, Abdel Wahab M, Cuong-Le T (2021) A variable velocity strategy particle swarm optimization algorithm (VVS-PSO) for damage assessment in structures. Eng Comput 1–30
3. Le Thanh C, Sang-To T, Hoang-Le H-L, Danh T-T, Khatir S, Wahab MA (2022) Combination of intermittent search strategy and an improve particle swarm optimization algorithm (IPSO) for damage detection of steel frame. Frattura ed Integrità Strutturale 16(59):141–152
4. Anaissi A, Khoa NLD, Wang Y (2018) Automated parameter tuning in one-class support vector machine: an application for damage detection. Int J Data Sci Anal 6(4):311–325
5. Lin Yz, Nie Zh, Ma Hw (2017) Structural damage detection with automatic feature-extraction through deep learning. Comput-Aided Civil Infrastruct Eng 32(12):1025–1046
6. Mendes R, Cortez P, Rocha M, Neves J (2002) Particle swarms for feedforward neural network training. In: Proceedings of the 2002 international joint conference on neural networks. IJCNN'02 (Cat. No. 02CH37290), vol 2. IEEE, pp 1895–1899
7. Meissner M, Schmuker M, Schneider G (2006) Optimized particle swarm optimization (OPSO) and its application to artificial neural network training. BMC Bioinform 7(1):1–11
8. Slowik A, Bialko M (2008) Training of artificial neural networks using differential evolution algorithm. In: 2008 conference on human system interactions. IEEE, pp 60–65
9. Kennedy J, Eberhart R (1995) Particle swarm optimization. In: Proceedings of ICNN'95-International conference on neural networks, vol 4. IEEE, pp 1942–1948

Predicting Damaged Truss Using Meta-Heuristic Optimization Algorithm

Thanh Sang-To, Minh Hoang-Le, Magd Abdel Wahab, and Thanh Cuong-Le

1 Introduction

The truss system is a vital component in many different kinds of structures. It has been widely employed in a lot of distinct fields, e.g. industry, high-tech agriculture, civil infrastructures, shipbuilding, auto production, etc. Because of fatigue, ageing, environmental effects, etc., truss systems may be reduced the level of security service substantially, which leads to accidents in the future. For this reason, not only is early damage prediction essential to maintain the integrity and safety of the structure, but also it means minimizing the maintenance cost. Thus, the construction of efficient and proper approaches to assess damage to truss structures is vital, which led to the attend of many scholars worldwide to solve this problem.

In recent decades, the development of the computer field, including hardware and software, allows us to process a number of huge calculations in a short time. In addition, artificial intelligence (AI), together with modern math theory, is more and more popular; simultaneously, they are proven effective in most fields. In which meta-heuristic optimization algorithms have several advantages, e.g. simple, easy for application, are used popularly. Many algorithms are well-known, such as particle swarm optimization (PSO) [1], genetic algorithm (GA) [2], cuckoo search (CS) [3] algorithm, grey wolf optimizer (GWO) [4] algorithm and bat algorithm (BA) [5]. All of them are employed to solve many various optimizations, in which a lot of damage structure problems were adopted these to search the best solution. For instance, Minh et al. [6] and Le Thanh et al. [7] employed PSO to detect damage for truss and frame

T. Sang-To · M. Hoang-Le · T. Cuong-Le (✉)
Faculty of Civil Engineering, Ho Chi Minh City Open University, Ho Chi Minh City, Vietnam
e-mail: cuong.lt@ou.edu.vn

M. A. Wahab
Soete Laboratory, Faculty of Engineering and Architecture, Ghent University, Technologiepark Zwijnaarde 903, 9052 Zwijnaarde, Belgium

385

system, respectively. Khatir et al. [8] adopted bat algorithm for forecasting damage beam. Ghannadi et al. [9] used GWO algorithm to deal with the optimization problem.

2 Methodology

In this study, meta-metaheuristics optimization algorithms combine with finite element (FE) analysis to predict position and severity damage structures. Based on mining the difference between actual damage and FE analysis frequencies, optimization algorithms are in charge to locate and measure the severity of damage element(s).

2.1 *Optimization Algorithms*

As we know that genetic algorithm is the well-known optimization and artificial intelligence (AI) field. This algorithm simulates theory evolution and is employed to solve many problems from politics to science, from agriculture to industry, and the most routine life activities. GA is described brief by three principles (namely selection, crossover and mutation).

On the other hand, particle swarm optimization (PSO) is an optimization algorithm simulated swarm behaviour. In comparison with GA, PSO is more simple and easy to run. The structure of PSO consists of two primary sections velocity (V) and location (X) each agent.

$$V_j^d(i+1) = \omega V_j^d(i) + c_1 \times rand \times \left[p_j^d(i) - X_j^d(i) \right]$$
$$+ c_2 \times rand \times \left[g^d(i) - X_j^d(i) \right]$$
$$X_j^d(i+1) = X_j^d(i) + V_j^d(i+1)$$

where ω, c_1 and c_2 are weight factors, while p and g are the best location of the member and swarm at the current, respectively.

Since these algorithms were proved the efficiency in many fields, hence they are adopted to assess structural health monitoring in this paper.

2.2 *The 21-Bar Truss*

A 21-bar truss is employed to investigate the damage scenarios. The location of nodes, bars and boundary conditions are shown in Fig. 1. The coordinate nodes are presented in Table 1. In addition, the material properties of all bars are the same,
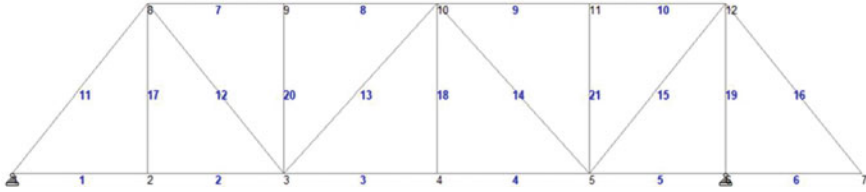
Fig. 1 Schematic of the 21-bar truss

Table 1 Location of point

Node	X (m)	Y (m)	Node	X (m)	Y (m)
1	0	0	7	50	0
2	8	0	8	8	10
3	16	0	9	16	10
4	25	0	10	25	10
5	34	0	11	34	10
6	42	0	12	42	10

namely Young's modulus $E = 205$ MPa, mass density $\rho = 7850$ kg/m^3 and across area $A = 7.0686$ E-04 m^2.

3 Results and Discussion

In this paper, we present three damage scenarios, including single-damage and multi-damage (from simple to complex), for structural health monitoring. Table 2 contains information about damage scenarios in detail. Each scenario is assessed by two cases (without noise and with noise 3%).

Table 2 Three damage scenarios

Scenarios	Damage bar(s)	Severity of damage (R)
The first scenario	Bar 01	$R = 35\%$
The second scenario	Bar 07	$R = 35\%$
	Bar 17	$R = 25\%$
The third scenario	Bar 05	$R = 10\%$
	Bar 10	$R = 15\%$
	Bar 14	$R = 20\%$
	Bar 20	$R = 30\%$

3.1   Scenario 1

See Figs. 2, 3 and 4.

(a) Noise-free   (b) Noise 3%
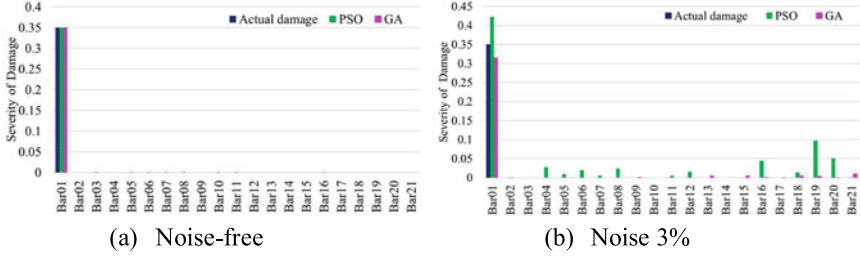
Fig. 2   Location and severity damage detection results for the first scenario

(a) Noise-free   (b) Noise 3%
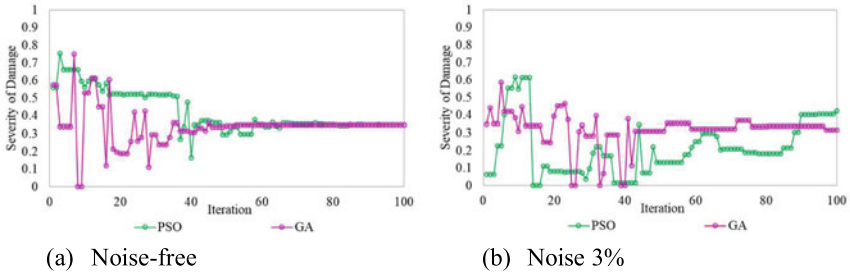
Fig. 3   History of the best solution

(a) Noise-free   (b) Noise 3%
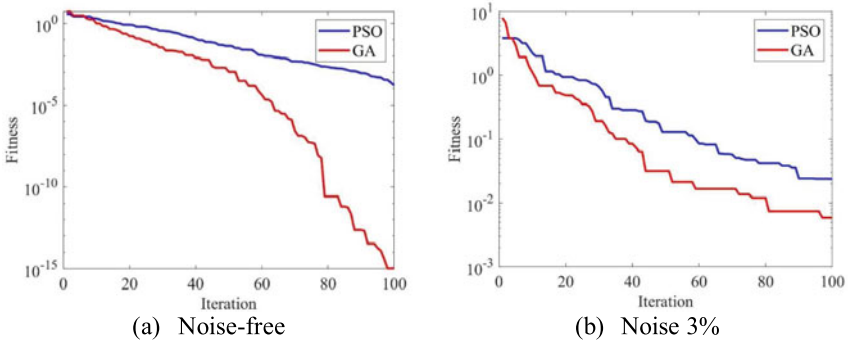
Fig. 4   Convergence curves for the first scenario

(a) Noise-free (b) Noise 3%
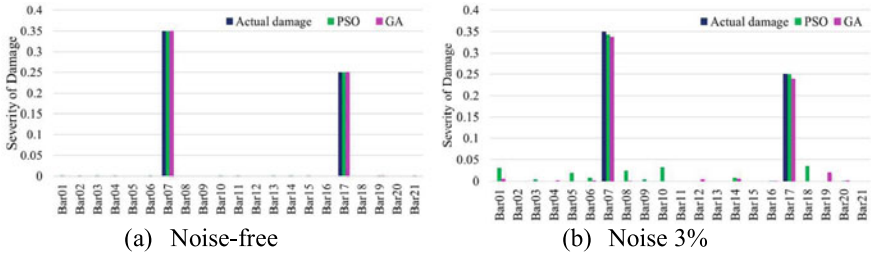
Fig. 5 Location and severity damage detection results for the second scenario

(a) Noise-free (b) Noise 3%
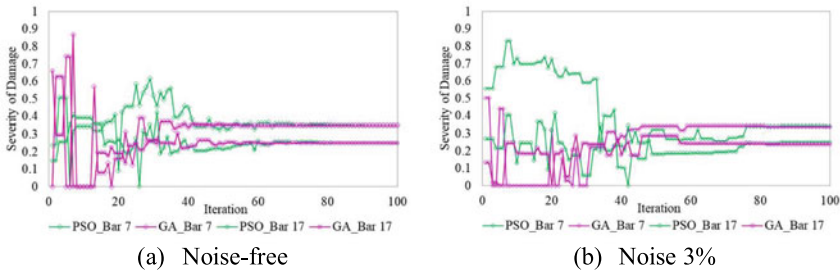
Fig. 6 History of the best solution

3.2 Scenario 2

See Figs. 5 and 6.

3.3 Scenario 3

The results reveal that both methods (using GA and PSO) provide the desired results for predicting damage structure in cases without noise, which is illustrated in Figs. 2a and 3a in detail. We can see that both algorithms get the desired results with only 60 iterations. Nevertheless, the results of forecasting damage using the PSO are affected significantly by noise cases. Indeed, the predicted result of the PSO is excessed by 20% in the single-damage case. In which the noise of total in all bars (expect bar 7 and 17) is 16.5% in the second scenario. In contrast, these errors when using the GA are only 8.9% and 4%, respectively, the first and second scenarios. For this reason, the convergence curves of the GA are better than the PSO (see Figs. 4 and 7) in most cases.

Once the challenge of the problem increased using in the four-damage case shown in the third scenario, the performance of the GA over the PSO is described clearly. Specifically, the noises of total are 30.8% and 9.65%, respectively, using the PSO and
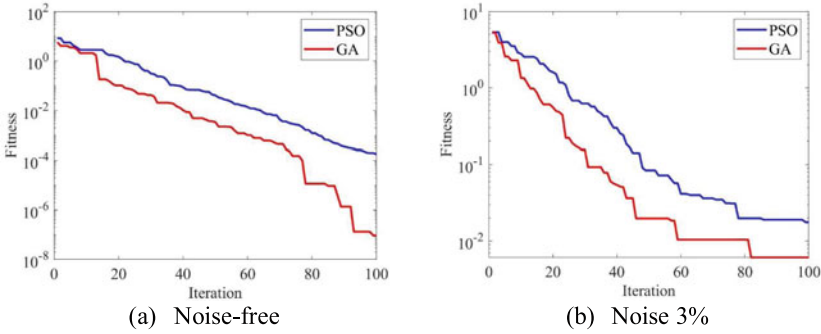
(a) Noise-free   (b) Noise 3%

Fig. 7 Convergence curves for scenario second

the GA for predicting damage the third scenario. Figures 8 and 9 show the location and severity damage detection results for this scenario with noise 3% as well as the history of the model updating. In the meantime, Fig. 10 presents convergence curves with noise 3% of the GA and the PSO. The results reveal that the GA employed to detect the damaged member(s) in this problem is reasonable rather than the PSO.
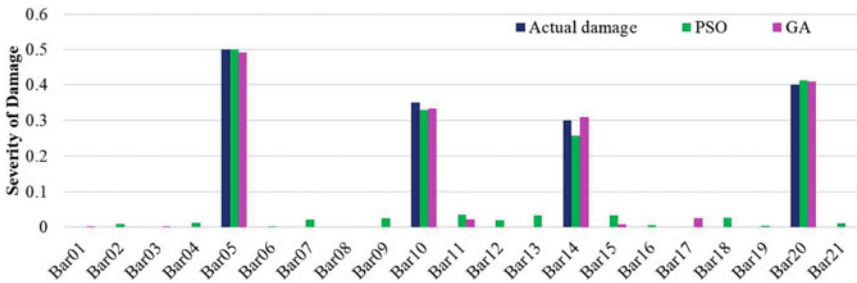
Fig. 8 Location and severity damage detection results for the third scenario with noise 3%

a   PSO with Noise 3%   b   GA with Noise 3%
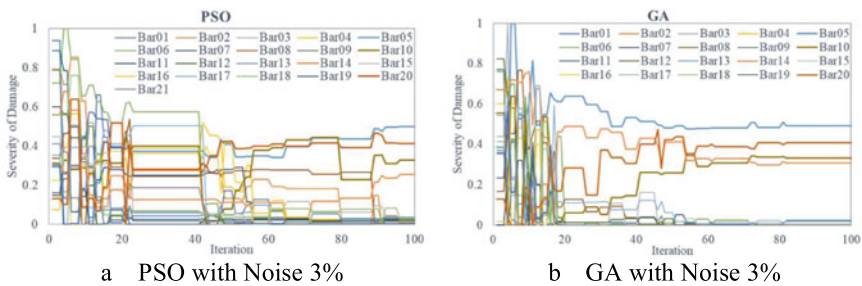
Fig. 9 History of the model updating

Fig. 10 Convergence curves with noise 3% for scenario third
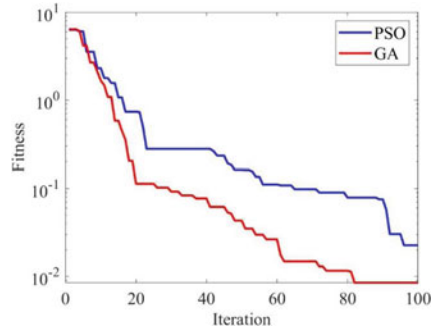
4 Conclusion

With three damage scenarios shown in this study, it can be seen that the optimization algorithm plays an essential role in structural health monitoring. A 21-bar truss with many damage cases, namely single-damage and multi-damage, is presented in detail. For global search, both algorithms are located well the position of damage bar(s) in single-damage cases, but it is noted that GA is always more accurate than PSO in these cases. In comparison with PSO, which are many errors when damage identification with measurement noise 3%, GA provides the more competitive results for damage identification for all scenarios. The obtained results proved that the GA is better than PSO to solve this problem.
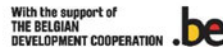
References

1. Kennedy J, Eberhart R (1995) Particle swarm optimization. In: Proceedings of ICNN'95-international conference on neural networks, vol 4. IEEE, pp 1942–1948
2. John H (1992) Holland genetic algorithms. Sci Am 267(1):44–50
3. Yang X-S, Deb S (2009) Cuckoo search via Lévy flights. In: 2009 World congress on nature & biologically inspired computing (NaBIC). IEEE, pp 210–214
4. Mirjalili S, Mirjalili SM, Lewis A (2104) Grey wolf optimizer. Adv Eng Softw 69:46–61. https://doi.org/10.1016/j.advengsoft.2013.12.007

5. Yang XS, Gandomi AH (2012) Bat algorithm: a novel approach for global engineering optimization. Eng Comput
6. Minh H-L, Khatir S, Wahab MA, Cuong-Le T (2021) An enhancing particle swarm optimization algorithm (EHVPSO) for damage identification in 3D transmission tower. Eng Struct 242:112412
7. Le Thanh C, Sang-To T, Hoang-Le H-L, Danh T-T, Khatir S, Wahab MA (2022) Combination of intermittent search strategy and an improve particle swarm optimization algorithm (IPSO) for damage detection of steel frame. Frattura ed Integrità Strutturale 16(59):141–152
8. Khatir S, Belaidi I, Serra R, Wahab MA, Khatir T (2016) Numerical study for single and multiple damage detection and localization in beam-like structures using BAT algorithm. J Vibroeng 18(1):202–213
9. Ghannadi P, Kourehli SS, Noori M, Altabey WA (2020) Efficiency of grey wolf optimization algorithm for damage detection of skeletal structures via expanded mode shapes. Adv Struct Eng 23(13):2850–2865

Forced Vibration of Delaminated Composite Beam with the Effect of Interfacial Contact

Hadjila Bournine

1 Introduction

Every structure is subject to degradation over time especially if it undergoes dynamic stress. The mechanisms may vary from a structure to another depending on its nature and working environment. Among the different faults that can appear in a multilayer composite structure comes the delamination or the disbanding of its different layers. It basically reflects the degradation of the resin used to hold the multiple layers together.

A number of authors have been looking into the dynamics of delaminated composites. Most of the models are based on the segmentation of the beam into undamaged and delaminated parts (Fig. 1) [1]. The earliest models were based on the assumption that delaminated segments must act according to a constraint or free model [1–3]. The constraint model meant that the delaminated parts do not separate or slide against each other whereas the free model meant that they vibrate separately and the authors assumed that they had the same mode shape [2, 3]. The authors of [3] added an axial load to the delaminated segments while most of the authors considered the axial displacement compatibility condition. Luo and Hanagud [4] considered the shear and rotation of section effects. Further, an interfacial contact model was introduced for the first time as an arbitrary stiffness normal to the delamination interface. Later on, The interface contact was further developed by Wang and Tong [5] into an interpenetration model characterized by a normal force made of a combination of a linear spring with a stiffness defined from the constitutive law of a normally loaded infinitesimal body and a Hertz like model. Further, An extended model that includes the tangential effects of delamination was proposed by Manoach et al. [6], it included a shear force as well as a damping parameter, in addition to the normal

H. Bournine (✉)
Université des Sciences et Technologie Houari Boumediene, Bab Ezzouar, Algeria
e-mail: hbournine@usthb.dz

Fig. 1 Beam with an
embedded delamination
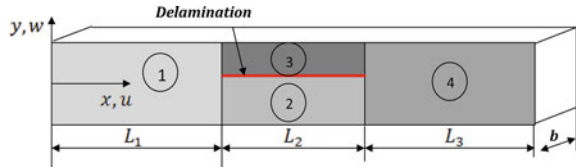
force proposed by Wang and Tong [5]. Other authors considered a simpler interface
contact behavior [7, 8] while the authors [7] considered the nonlinear behavior of a
beam under a varying normal interfacial force, in [7] both components of the contact
force were considered as arbitrary constants.

The energy dissipation through friction was considered by Manoach et al. [6] as an
equivalent to viscous damping whereas an energy dissipation approach is presented in
[9]. Forced vibration analysis remains very scarce, among the authors who considered
it, Kargarnovin et al. [10] with an analytical model whereas Infantes et al. [11] came
up with a numerical algorithm based on a finite element approach. Both papers
neglect the effect of the interfacial forces [10, 11].

In this paper, a generalized analytical model is developed that takes into consider-
ation secondary shear and inertial effects as well as longitudinal motion. In addi-
tion, the effect of the differential bending on the delaminated segments is also
included. The delaminated element undergoes an alternating cycle of opening and
closing modes which creates a discontinuous interfacial behavior. This discontinuity
is decomposed into a normal component and a tangential one. While the normal force
is modeled as a bilinear function based on the interpenetration constraint model the
tangential component interfacial contact is introduced as an equivalent damping term
due to friction.

The spatial part of the equation was defined analytically whereas the temporal
function was resolved numerically due to the weak nonlinearity presented by
the interfacial model. The natural frequencies are recalculated to account for the
alternating state of the interface.

2   Mathematical Formulation

2.1   *Geometric Representation*

In this work, a beam of length L with a rectangular uniform cross-section of thickness
h and depth b is considered. The delamination could appear between any two adjacent
layers at any depth (see Fig. 1).

2.2 Interaction at the Delamination Interface

The delaminated element undergoes an alternating cycle of opening and closing modes causing the appearance of interaction forces at the interface which leads to a continuous change in stiffness and damping over each vibration cycle.

The first interfacial interaction introduced was by Luo et al. [4], as they considered a piecewise linear spring for the normal force with an arbitrary stiffness that reduced into zero force during opening and a constant one during sticking. Later on, Wang et al. [5] worked on an interpenetration model characterized by a normal force made of a combination of a linear spring with a stiffness defined from the constitutive law of a normally loaded infinitesimal body and a Hertz-like model. An extended model that includes the tangential effects of delamination was proposed by Manoach et al. [6], it included a shear force as well as a damping parameter, in addition to the normal force proposed by Wang [5].

At the disbonding interface, the two segments involved are affected by each other normally and tangentially (see Fig. 2).

In this work, the normal force is a piecewise bilinear function [8] defined as follows:

$$q_n(x, t) = k_n(w_2(x, t) - w_3(x, t)) \tag{1}$$

with $k_n(x, t) = \begin{cases} \frac{2b}{\frac{h_2}{E_2} + \frac{h_3}{E_3}} & \text{for } (w_2 - w_3) < 0 \\ 0 & \text{for } (w_2 - w_3) \geq 0 \end{cases}$.

The tangential force has been proved to cause additional damping due to friction [9], therefore q_s is the distributed friction force which is modeled using a Coulomb law of friction defined as follows

$$q_s(x, t) = \begin{cases} 0 & \text{if } (w_2 - w_3) > 0 \\ k_s(h_2\gamma_2 + h_3\gamma_3) & \text{if } (w_2 - w_3) > 0 \,\&\, q_s(x, t) < \mu q_n(x, t) \\ \mu q_n(x, t)\mathrm{sgn}(\dot{w}) & \text{if } (w_2 - w_3) > 0 \,\&\, q_s(x, t) > \mu q_n(x, t) \end{cases} \tag{2}$$

Fig. 2 Interfacial acting forces
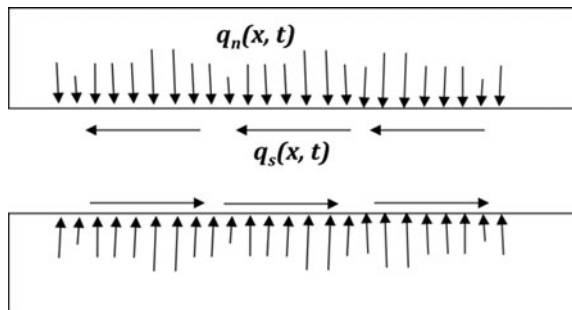
where μ is Coulomb's friction coefficient. It should be noted that sliding only occurs when the following condition is fulfilled [9]:

$$b\tau_{xz}(x,t) \geq \mu q_n(x,t) \tag{3}$$

As a result q_s is a bilinear function since it is a function of q_n.

2.3 The Governing Equation

As shown in Fig. 1, after delamination, a representative composite beam with width d, height h, and length L is decomposed into a combination of four beams connected at the delamination boundaries $x_1 = L_1$ and $x_2 = L_1 + L_2$, where L_1 and L_2 are the lengths of elements 1 and 2 (and 3), respectively (Fig. 1).

We denote by m, D, J, and S the mass per length, the cross-sectional bending stiffness, the cross-sectional moment of inertia, and cross-sectional shear stiffness, respectively and A is the cross-sectional area of each beam segment,

The equation of motion for each one of the undamaged beams (1 and 4) is given as [4]

$$\begin{cases} \frac{\partial}{\partial x}\left(D_i \frac{\partial \varphi_i}{\partial x}\right) + S_i(\gamma_i) - J_i \frac{\partial^2 w_i}{\partial t^2} = M_i \\ \frac{\partial(S_i \gamma_i)}{\partial x} - m_i \frac{\partial^2 w_i}{\partial t^2} + q_{ni}(x,t) = F_i \end{cases} \tag{4}$$

where the indices $i = 1, 2, 3$, and 4 refer to the beam segment, qni is the normal force at the delaminated interface which only exists for the delaminated parts ($i = 2$ and 3).

The blending slope w_i is related to the rotation of the cross section φ_i and the shear angle γ_i as follows

$$\frac{\partial w_i(x,t)}{\partial x} = \varphi_i(x,t) + \gamma_i(x,t). \tag{5}$$

In addition, the axial vibration (should be coupled with bending in the case of axial loading) for the damaged segments is introduced as follows

$$A_i \frac{\partial^2 u_i}{\partial x^2} - m_i \frac{\partial^2 u_i}{\partial t^2} = qi + N_i, \tag{6}$$

where $N_i = P_i + \text{sgn}(\dot{w}) \int_{x_1}^{x_2} q_s dx$ with q_s is the distributed tangential force acting along the delamination interface which only exists for the delaminated parts ($i = 2$ and 3) and P is the axial force due to the differential in length of the segments resulting from deflection which was defined in [1] as

$$P_2 = -\frac{E A_2}{L} \frac{h_3}{2} (\varphi_4(x_2) - \varphi_1(x_1)).$$

$$P_3 = \frac{E A_3}{L} \frac{h_2}{2} (\varphi_4(x_2) - \varphi_1(x_1)). \tag{7}$$

Combining Eqs. 4 and 5 the governing equations for the undamaged segments ($i = 1, 4$) under free vibration are as follows:

$$\frac{\partial^4 w_i}{\partial x^4} - \left(\frac{m_i}{S_i} + \frac{J_i}{D_i}\right) \frac{\partial^4 w_i}{\partial x^2 \partial t^2} + \frac{m_i}{D_i} \frac{\partial^2 w_i}{\partial t^2} + \frac{J_i}{D_i} \frac{m_i}{S_i} \frac{\partial^4 w_i}{\partial t^4} = 0 \tag{8}$$

$$A_i \frac{\partial^2 u_i}{\partial x^2} - m_i \frac{\partial^2 u_i}{\partial t^2} = 0 \tag{9}$$

whereas for the delaminated segments ($i = 2, 3$), taking into account delamination effects, they are summarized as follows:

$$\frac{\partial^4 w_i}{\partial x^4} - \left(\frac{m_i}{S_i} + \frac{J_i}{D_i}\right) \frac{\partial^4 w_i}{\partial x^2 \partial t^2} + \frac{m_i}{D_i} \frac{\partial^2 w_i}{\partial t^2} + \frac{J_i}{D_i} \frac{m_i}{S_i} \frac{\partial^4 w_i}{\partial t^4}$$
$$= \frac{k_n}{D_i} (w_2 - w_3) + \frac{J_i}{D_i} \frac{k_n}{S_i} \left(\frac{\partial^2 w_2}{\partial t^2} - \frac{\partial^2 w_3}{\partial t^2}\right) - \frac{k_n}{S_i} \left(\frac{\partial^2 w_2}{\partial x^2} - \frac{\partial^2 w_3}{\partial x^2}\right) \tag{10}$$

$$E_i A_i \frac{\partial^2 u_i}{\partial x^2} - m_i \frac{\partial^2 u_i}{\partial t^2} = P_i + \mathrm{sgn}(\dot{w}) \int_{x_1}^{x_2} q_s \, dx \tag{11}$$

It should be noted that the governing set of equations does not include viscous or friction damping. These terms need to be included in the temporal function reason why the friction force does not show in the equation is because it is an internal force for the whole structure, therefore a term to represent it can be added to the equation as an inherent damping term.

2.4 The Separation of Variables

For free vibration, one can assume the following separate solutions:

$u(x, t) = U(x)q(t)$ and $w(x, t) = W(x)q(t)$ with $q(t)$ a harmonic temporal function, i.e., $q(t) = Ae^{j\omega t}$ with $j = \sqrt{-1}$ and ω the natural frequency.

Using the harmonic temporal solution, the spatial part of the equation could be solved by the following sets of equations. The general solution for the axial motion governing equation is given as

$$X_i(x_i) = C_{i1} \sin(\gamma_i x_i) + C_{i2} \cos(\gamma_i x_i) \tag{12}$$

for $i = 1:4$, with $\gamma_i^2 = \frac{m_i \omega^2}{E_i A_i}$.

The sub-beams 2 and 3 are constantly under axial loading P due to the segment bending. Note that P is a constant function of x, therefore, the particular solution for beams 2 and 3 is given as follows

$$X_i(x_i) = C_{i1} \sin(\gamma_i x_i) + C_{i2} \cos(\gamma_i x_i) + \frac{N_i}{\gamma_i^2} \tag{13}$$

The flexural motion comes from solving the following set of ordinary differential equations

$$\frac{\partial^4 W_i}{\partial x^4} + \omega^2 \left(\frac{m_i}{S_i} + \frac{J_i}{D_i} \right) \frac{\partial^2 W_i}{\partial x^2} + \left(\omega^4 \frac{J_i}{D_i} \frac{m_i}{S_i} - \omega^2 \frac{m_i}{D_i} \right) W_i = 0 \tag{14a}$$

for $i = 1,4$ and

$$\frac{\partial^4 W_2}{\partial x^4} + \left(\omega^2 \left(\frac{m_2}{S_2} + \frac{J_2}{D_2} \right) + \frac{k_n}{S_2} \right) \frac{\partial^2 W_2}{\partial x^2}$$
$$+ \left(\left(\omega^4 \frac{J_2}{D_2} \frac{m_2}{S_2} - \omega^2 \frac{m_2}{D_2} \right) - k_n \left(\frac{1}{D_2} - \omega^2 \frac{J_2}{D_2} \frac{1}{S_2} \right) \right) W_2$$
$$= + \frac{k_n}{S_2} \left(\frac{\partial^2 W_3}{\partial x^2} \right) - \left(\frac{k_n}{D_2} - \omega^2 \frac{J_2}{D_2} \frac{k_n}{S_2} \right) W_3$$

$$\frac{\partial^4 W_2}{\partial x^4} + \left(\omega^2 \left(\frac{m_2}{S_2} + \frac{J_2}{D_2} \right) + \frac{k_n}{S_2} \right) \frac{\partial^2 W_2}{\partial x^2}$$
$$+ \left(\left(\omega^4 \frac{J_2}{D_2} \frac{m_2}{S_2} - \omega^2 \frac{m_2}{D_2} \right) - k_n \left(\frac{1}{D_2} - \omega^2 \frac{J_2}{D_2} \frac{1}{S_2} \right) \right) W_2$$
$$= + \frac{k_n}{S_2} \left(\frac{\partial^2 W_3}{\partial x^2} \right) - \left(\frac{k_n}{D_2} - \omega^2 \frac{J_2}{D_2} \frac{k_n}{S_2} \right) W_3 \tag{14b}$$

and

$$\frac{\partial^4 W_3}{\partial x^4} + \left(\omega^2 \left(\frac{m_3}{S_3} + \frac{J_3}{D_3} \right) - \frac{k_n}{S_3} \right) \frac{\partial^2 W_3}{\partial x^2}$$
$$+ \left(\left(\omega^4 \frac{J_3}{D_3} \frac{m_3}{S_3} - \omega^2 \frac{m_3}{D_3} \right) + k_n \left(\frac{1}{D_3} - \omega^2 \frac{J_3}{D_3} \frac{1}{S_3} \right) \right) W_3$$
$$= - \frac{k_n}{S_3} \left(\frac{\partial^2 W_2}{\partial x^2} \right) + \left(\frac{k_n}{D_3} - \omega^2 \frac{J_3}{D_3} \frac{k_n}{S_3} \right) W_2 \tag{14c}$$

Solving the equations' results in

$$\mathbf{W_i(x_i) = A_{i1}\cos(a_1 x_i) + A_{i2}\sin(a_1 x_i) + A_{i3}\cosh(b_1 x_i) + A_{i4}\sinh(b_1 x_i)} \tag{15}$$

with

$$(a_1)^2 = \frac{\omega^2}{2}\left(\frac{m_i}{S_i} + \frac{J_i}{D_i}\right) + \sqrt{\left(\frac{\omega^2}{2}\left(\frac{m_i}{S_i} + \frac{J_i}{D_i}\right)\right)^2 - \left(\omega^4 \frac{J_i}{D_i}\frac{m_i}{S_i} - \omega^2\frac{m_i}{D_i}\right)}$$

$$(b_1)^2 = -\frac{\omega^2}{2}\left(\frac{m_i}{S_i} + \frac{J_i}{D_i}\right) + \sqrt{\left(\frac{\omega^2}{2}\left(\frac{m_i}{S_i} + \frac{J_i}{D_i}\right)\right)^2 - \left(\omega^4 \frac{J_i}{D_i}\frac{m_i}{S_i} - \omega^2\frac{m_i}{D_i}\right)}$$

Or

$$W_i(\xi_i) = A_{i1}\cos(a_1 L_i\xi_i) + A_{i2}\sin(a_1 L_i\xi_i)$$
$$+ A_{i3}\cosh(b_1 L_i\xi_i) + A_{i4}\sinh(b_1 L_i\xi_i)$$

With $\xi_i = x_i/L_i$
The section rotation is defined as follows
$$\varphi_i(\xi_i) = A_{i1}\bar{a}_1\cos(a_1 L_i\xi_i) + A_{i2}\bar{a}_1\sin(a_1 L_i\xi_i)$$
$$+ A_{i3}\bar{b}_1\cosh(b_1 L_i\xi_i) + \bar{b}_1\sinh(b_1 L_i\xi_i)'$$

with $\quad \bar{a}_1 \quad = \quad \frac{a_1}{\omega^2\left(\frac{J_i}{D_i} - \frac{S_i}{D_i}\right)}\left(\left(\omega^2\frac{m_i}{S_i} + \frac{S_i}{D_i}\right) - a_1^2\right), \quad \bar{b}_1 \quad =$

$-\frac{b_1}{\omega^2\left(\frac{J_i}{D_i} - \frac{S_i}{D_i}\right)}\left(\left(\omega^2\frac{m_i}{S_i} + \frac{S_i}{D_i}\right) + b_1^2\right)$ .for $i = 1,4$. Whereas for $i = 2$ and 3, the solution resembles Eq. 15. When $K_n = 0$ and in the case of $K_n \neq 0$, the solution for the coupled equations is given as

$$W_i(x_2) = \sum_{j=1}^{8} A_{2j} v_{ij} \exp(\lambda_j x_2) \tag{16}$$

where $i = 2, 3$, A_{2j} are arbitrary constants to be defined from the continuity conditions and λ_j and v_{ij} are the Eigen values and vectors of the following reduced coupled differential equations

$$\begin{bmatrix} X_{20}' \\ X_{21}' \\ X_{22}' \\ X_{23}' \\ X_{30}' \\ X_{31}' \\ X_{32}' \\ X_{33}' \end{bmatrix} = \begin{bmatrix} 0 & 1 & 0 & 0 & 0 & 0 & 0 & 0 \\ 0 & 0 & 1 & 0 & 0 & 0 & 0 & 0 \\ 0 & 0 & 0 & 1 & 0 & 0 & 0 & 0 \\ -\beta_2 & 0 & -\alpha_2 & 0 & C_{21} & 0 & C_{22} & 0 \\ 0 & 0 & 0 & 0 & 0 & 1 & 0 & 0 \\ 0 & 0 & 0 & 0 & 0 & 0 & 1 & 0 \\ 0 & 0 & 0 & 0 & 0 & 0 & 0 & 1 \\ C_{31} & 0 & C_{32} & 0 & -\beta_3 & 0 & -\alpha_3 & 0 \end{bmatrix} \begin{bmatrix} X_{20} \\ X_{21} \\ X_{22} \\ X_{23} \\ X_{30} \\ X_{31} \\ X_{32} \\ X_{33} \end{bmatrix} \tag{17}$$

where $\mathbf{X_{ij}}$ is the jth derivative of $\mathbf{X_i}$ and $\alpha_2 = \left(\omega^2\left(\frac{m_2}{S_2} + \frac{J_2}{D_2}\right) + \frac{k_n}{S_2}\right)$,

$$\beta_2 = \left(\left(\omega^4\frac{J_2}{D_2}\frac{m_2}{S_2} - \omega^2\frac{m_2}{D_2}\right) - k_n\left(\frac{1}{D_2} - \omega^2\frac{J_2}{D_2}\frac{1}{S_2}\right)\right), \quad C_{22} = \frac{k_n}{S_2},$$

$$C_{21} = -\left(\frac{k_n}{D_2} - \omega^2 \frac{J_2}{D_2} \frac{k_n}{S_2}\right), \ \alpha_3 = \left(\omega^2 \left(\frac{m_3}{S_3} + \frac{J_3}{D_3}\right) - \frac{k_n}{S_3}\right),$$

$$\beta_3 = \left(\left(\omega^4 \frac{J_3}{D_3} \frac{m_3}{S_3} - \omega^2 \frac{m_3}{D_3}\right) + k_n \left(\frac{1}{D_3} - \omega^2 \frac{J_3}{D_3} \frac{1}{S_3}\right)\right),$$

$$\text{and } C_{32} = -\frac{k_n}{S_3} \text{ and } C_{31} = \left(\frac{k_n}{D_3} - \omega^2 \frac{J_3}{D_3} \frac{k_n}{S_3}\right).$$

The function for $\varphi_i(x_i)$ is easily recovered from deriving Eqs. (15) and (16) and replacing in Eq. (4).

2.5 The Continuity Conditions

Since the delaminated part is inherent to the beam a number of continuity conditions are naturally satisfied and in what follows, a summary of these conditions at $x = x_1$.

$$w_1(x_1) = w_2(x_1) = w_3(x_1), \ \varphi_1(x_1) = \varphi_2(x_1) = \varphi_3(x_1),$$

$$S_1\left(\frac{\partial w_1(x_1)}{\partial x} - \varphi_1(x_1)\right) = S_2\left(\frac{\partial w_2(x_1)}{\partial x} - \varphi_2(x_1)\right) + S_3\left(\frac{\partial w_3(x_1)}{\partial x} - \varphi_3(x_1)\right) \text{ and}$$

$$D_1 \frac{\partial \varphi_1(x_1)}{\partial x} = D_2 \frac{\partial \varphi_2(x_1)}{\partial x} + D_3 \frac{\partial \varphi_3(x_1)}{\partial x} - A_2 u_2{'}(x_1) + A_3 u_3{'}(x_1)$$

Seeing how

$$D_1 \frac{\partial \varphi_1(x_1)}{\partial x} = D_2 \frac{\partial \varphi_2(x_1)}{\partial x} + D_3 \frac{\partial \varphi_3(x_1)}{\partial x}$$

$$- \frac{E}{4L}\left(h_3^2 A_2 + h_2^2 A_3\right)(\varphi_4(x_2) - \varphi_1(x_1))$$

Continuity of the axial displacement is given by

$$u_2(x_1) = -\frac{(h_1 - h_2)}{2}\varphi_1 \text{ and } u_3(x_1) = \frac{(h_1 - h_3)}{2}\varphi_1.$$

An equivalent set of equations are applied at $x = x_2$ between the delaminated segments and the sub-beam 4.

3   The Model Simulation

A code to recreate the calculations was prepared using two sets of boundary conditions, double pined on both sides and a cantilever. The material characteristics were

chosen from [10] to ensure means to a comparison with previous work. The code to this calculation follows the following steps.

Step 1: Define the natural frequencies and mode shapes by solving for the boundary and continuity conditions.
Step 2: Calculate the Eigen values of the temporal problem and estimate the variation after dt.
Step 3: Simulate a forced input and recalculate the natural frequency.

4 Results and Discussion

The first element to observe is the natural frequencies. To verify the program, it was used to calculate the first three frequencies of a cantilever beam with a single delamination at $h2 = 0.6$ mm and $h3 = 0.2$ mm and compared to those presented in previous works and the results are summarized in Table 1. As can be clearly seen, there is a good agreement between these results and those presented in literature. For the first frequency, all three models are within less than 2% error margin. For higher modes, however, the error increases for all models, the current model improves tremendously the frequency prediction in comparison to the other models.

4.1 Interfacial Interaction

After plotting the mode shapes, it is interesting to visualize the interaction between the delaminated segments. Two examples are presented in Fig. 3. The first one depicts a frequency at which the interaction varies along the interface whereas the second one presents no interaction between the segments. The response in Fig. 3a is corrected using Eqs. 16 and 17, in doing so the frequency shifts automatically.

4.2 The Effect of the Axial Load Coupling

The effect of the coupled axial loading is the complex part of the model, therefore it is crucial to verify its added value. Tests with axial load and without it were carried

Table 1 Natural frequency (Hz) estimation comparison

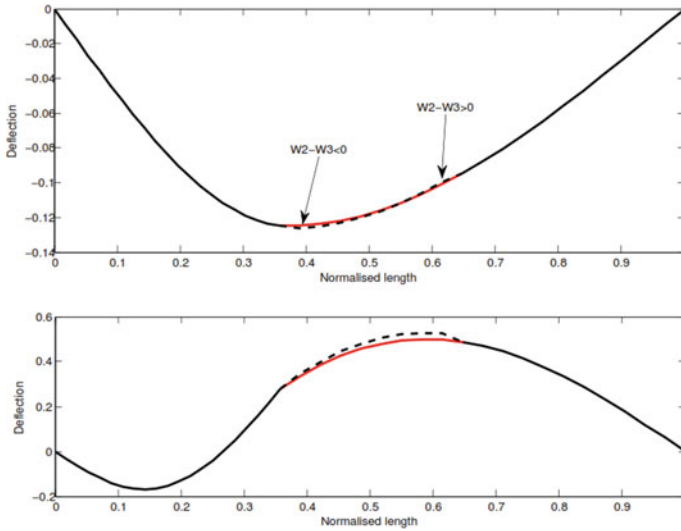| Mode	Present	Experimental [13]	Analytical [12]	Analytical [10]
1st	15.91	16	15.96	15.87
2nd	96.06	98	94.9	95.02
3rd	234.61	223	256.26	236.35

Fig. 3 Interfacial interaction at the delamination interface

out and as it turns out for the first Eigen value the effect is not major (Fig. 4a) while on the 2nd Eigen value and higher ones the effect is very visible (Fig. 4b), Even more so when the length of the delamination is increased.

5 Conclusions

The most obvious conclusion is that a delamination has a direct effect on the dynamics of a composite beam. The inclusion of the axial load mode coupling affects visibly the natural frequencies of the beam.

A further analysis will include the buckling of the delaminated part; therefore, the inclusion of the axial loading is essential to this model. Furthermore, this model is set to define the conditions for the delamination progression and its effect on the damping properties of the beam.
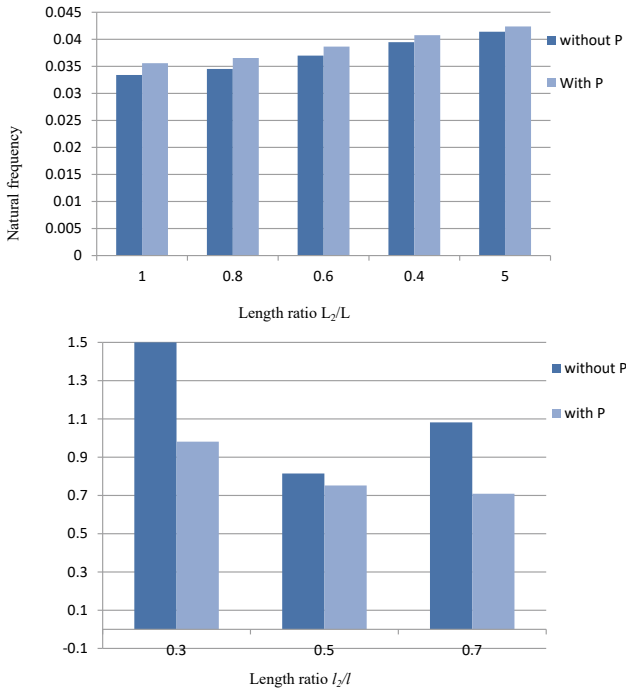
Fig. 4 The effect of the coupled axial loading as the through thickness disbanding position is varied

References

1. Mujumdar PM, Uryanarayan S (1988) Flexural vibrations of beams with delaminations. J Sound Vib 125(3):441–461
2. Della CN, Shu D (2005) Vibration of beams with double delaminations. J Sound Vib 282:919–935
3. Shu D, Della CN (2004) Free Vibration analysis of composite beams with two non-overlapping delaminations. Int J Mech Sci 46:509–529
4. Luo H, Hanagud S (2000) Dynamics of delaminated beams. Int J Solids Struct 37:1501–1519
5. Wang J, Tong L (2002) A study of the vibration of delaminated beams using a nonlinear anti-interpenetration constraint model. Compos Struct 57:483–488
6. Manoach E, Warminski J, Mitura A, Samborski S (2012) Dynamics of a composite Timoshenko beam with delamination. Mech Res Commun 46:47–53
7. Xue J, Xia F, Ye J et al (2017) Multiscale studies on the nonlinear vibration of delaminated composite laminates–global vibration mode with micro buckles on the interfaces. Sci Rep 7:4468
8. Bennati S, Fisicaro P, Taglialegne L, Valvo PS (2019) An elastic interface model for the delamination of bending-extension coupled laminates. Appl Sci 9(17):3560
9. Chaogan G, Chuwei Z (2018) Specific damping capacity calculation of composite plates with delamination based on higher-order Zig-Zag theory. J Vibroeng 20(8):2784–2795
10. Kargarnovin MH, Ahmadian MT, Jafari-Talookolaei RA (2013) Forced vibration of delaminated Timoshenko beams under the action of moving oscillatory mass. Shock Vib 20:79–96

11. Infantes M, Vidal P, Castro-Triguero R, Gallimard L, García-Macías A, Polit O (2021) Forced vibration analysis of composite beams based on the variable separation method. Mech Adv Mater Struct 28(6):618–634
12. Valoor MT, Chandrashekhara K (2000) Compos Sci Technol 60:1773–1779
13. Okafor A, Chandrashekhara K, Jiang YP (1996) Smart Mater Struct 5:338–347

Application of Slime Mould Optimization Algorithm on Structural Damage Identification of Suspension Footbridge

Lan Ngoc-Nguyen , **Samir Khatir** , **Huu-Quyet Nguyen** ,
Hieu Nguyen-Tran , **Dung Bui-Ngoc** , **Magd Abdel Wahab** ,
and **Thanh Bui-Tien**

1 Introduction

Recently, structural health monitoring (SHM) has been used widely in the long-term monitoring of civil transportation infrastructure such as bridges, dams, tunnels. SHM system helps to ensure not only the integrity but also the safety of the whole structure. Its ability to detect early damages further enables inspectors and engineers to perform structural maintenance more effectively at a lower cost. For years, enhancement of SHM has been the focus of many pieces of research [1–4], which have been able to provide improvement to the current system, especially its damage detection capability. The current development of modern technologies, especially in advanced optimization algorithms and artificial intelligence, has further helped to solve structural damage identification problems. Dang et al. [6] proposed the use of feature fusion and hybrid deep learning for damage detection of large-scale infrastructure. Different signal processing is used to extract damage features from raw sensory data before getting elaborated with hybrid deep learning 1-DCNN-LSTM. The results show that the proposed method not only has high accuracy in damage detection but also reduces computational costs significantly. Duong et al. [7] proposed a combination of transmissibility and machine learning algorithm to detect damage in truss bridge with a high level of accuracy in both damage quantification and damage localization. Teng et al. [8] proposed the use of convolution neural network (CNN) for damage identification of a steel frame. The research uses numerical data of modal

L. Ngoc-Nguyen · S. Khatir · H. Nguyen-Tran · M. A. Wahab
Soete Laboratory, Faculty of Engineering and Architecture, Ghent University, Ghent, Belgium

L. Ngoc-Nguyen · H.-Q. Nguyen · T. Bui-Tien (✉)
Faculty of Civil Engineering, University of Transport and Communications, Hanoi, Vietnam
e-mail: btthanh@utc.edu.vn

H. Nguyen-Tran · D. Bui-Ngoc
Faculty of Information Technology, University of Transport and Communications, Hanoi, Vietnam

strain for the training of the proposed CNN and obtains a 100% accuracy level in damage localization of different damage scenarios. Advanced optimization algorithms are also used to solve damage detection problems. Nguyen-Ngoc et al. [9] proposed a method that combined GA with ANN to detect damage on a truss bridge with a high level of efficiency. Tran et al. [10] used cuckoo search (CS) to improve the training parameters of ANN in damage detection of bridge and beam structures. The obtained results show that ANN-CS method not only helps to reduce computational time but also improves the accuracy in quantifying and localizing damage. Khatir et al. [11] introduced a novel damage indicator based on flexibility index to localize damage in truss structure. The damage indicator is then combined with atom search optimization (ASO) and salp swarm optimizer (SSA) to quantify the severity level of damage. Experimental validation shows that the proposed method is accurate and fast to predict the variation of damages.

In this paper, we introduced an application of slime mould algorithm (SMA) [12]—a novel optimization algorithm, to solve the damage detection problem of a suspension footbridge. SMA is a nature-inspired optimization that has shown superiority in optimization problems [13–15]. The efficiency of the proposed method is further compared with two other commonly used algorithms, genetic algorithm (GA) and cuckoo search (CS) for the level of efficiency.

2 Slime Mould Optimization Algorithm

2.1 Description

In 2020, Li et al. [12] introduced a novel nature-inspired metaheuristic algorithm called SMA. Slime mould is a unique type of eukaryotic organism that can exist not only as a single cell body but can also combine to form a multicell lifeform. One of the most interesting facts about slime mould is that it does not contain any brain cells; however, it is still able to not only identify the food source but also quantify the amount of food thanks to the forward and backward flows of its cytoplasm [16]. Based on those characteristics of slime mould, a mathematical model of SMA is constructed which consists mainly of two parts: approach food and wrap food + oscillation.

2.1.1 Approach Food

Food gives out the smell, which in turn becomes a source for the slime mould to get closer to. The contraction mode for food advancing is expressed in Eq. (1):

$$X_{t+1} = \begin{cases} X_b(t) + v_b \cdot (W \cdot X_A(t) - X_B(t)) & r < p \\ v_c \cdot X_t & r \geq p \end{cases} \tag{1}$$

where $\overrightarrow{X(t)}$ represents the position of the slime mould at the current iteration t, $\overrightarrow{X_b(t)}$ is the individual position with the most concentration of food smell within the reach of the slime, $\overrightarrow{X_A(t)}$, $\overrightarrow{X_B(t)}$ are two random individual positions chosen from the slime mould which has the weight of $\vec{W}$, $\vec{vc}$ is a linear parameter that decreases from 1 to 0, and $\vec{vb}$ is a parameter with a range of $[-a, a]$ with $a = \text{arctanh}\left(-\left(\frac{t}{\max_t}\right)+1\right)$.

The weight $\vec{W}$ of the slime mould is calculated in Eq. (2) as follows:

$$\overrightarrow{W(\text{SmellIndex}(i))} = \begin{cases} 1 + r \cdot \log\left(\frac{bF - S(i)}{bF - wF} + 1\right), & \text{condition} \\ 1 - r \cdot \log\left(\frac{bF - S(i)}{bF - wF} + 1\right), & \text{other} \end{cases} \tag{2}$$

With SmellIndex $= \text{sort}(S)$-sequence of fitness values enumerated, "condition" means the case where $S(i)$ ranks first half of the population, r is the random number between [0,1], wF and bF represent the worst and the best fitness obtained, respectively, within the current iteration.

2.1.2 Wrap Food + Oscillation

The location of slime mould during the food wrapping process is represented in Eq. (3):

$$X^* = \begin{cases} \text{rand}(UB - LB) + LB & \text{rand} < z \\ X_b(t) + v_b(W X_A(t) - X_B(t)) & r < p \\ v_c X(t) & r \geq p \end{cases} \tag{3}$$

where LB and UB are the lower and upper boundaries of the search and $r \in [0\ 1]$.

For oscillation, $\vec{vb}$ oscillates randomly between $[-a, a]$ and tends to 0 as the iteration increases. The pseudo-code of SMA is shown in Fig. 1.

3 Application Damage Detection of Na Xa Suspension Footbridge

3.1 Na Xa Suspension Footbridge

For validation of the proposed method, a case study on Na Xa Bridge in Vietnam was conducted. Na Xa is a suspension footbridge in the mountainous region of Vietnam. The bridge consists of one main span with a length of 78 m. Total length of the bridge is 125.83 m. The main cables systems consist of high tensile cables with a diameter of 56 mm. Abutment systems are made of reinforced concrete of M250 grade with the foundation placed on natural ground. The bridge gates are made of I-shaped

Pseudo-code of SMA algorithm

Inputs: Population size N, number of iterations n_iter, and position of slime mould X_i

while t<n_iter **do**

Calculate all slime mould's fitness

Calculate slime mould's weight W

for (each search of X_i) **do**

Update p, v_b, v_c;

Update positions;

Return bestFitness values and X_b

Fig. 1 Pseudo-code of SMA

steels and driven 1 m deep into the concrete. This bridge is a typical example of the suspension footbridge in the rural area of Vietnam. The overall view of the bridge and drawing are shown in Figs. 2 and 3.

3.2 Finite Element Model

A finite element model (FEM) of the bridge is constructed using MATLAB. The FEM model consists of 210 nodes according to various parts of the bridge: longitudinal beams, transverse beams, mains cables, tower, and the other components. The completed bridge structure includes 312 beam elements and link elements for cables accordingly. Boundary conditions of the bridge are fixed at both ends of the bridge, as well as at the main cable extension connected to the ground. Material properties of the bridge are given in Table 1.

Modal analysis of the FEM model was conducted using Stabil toolbox in MATLAB [17]. Stabil is a toolbox for structural analysis which has been used widely in structural researches [18] (Figs. 4 and 5). The first six natural frequencies of the bridge are obtained with the respective mode shapes as shown below (Table 2).

3.3 Damage Detection

In real-life structure, when a structural component is damaged due to various reasons such as fracture, corrosion, buckling, the modulus of elasticity of the component will
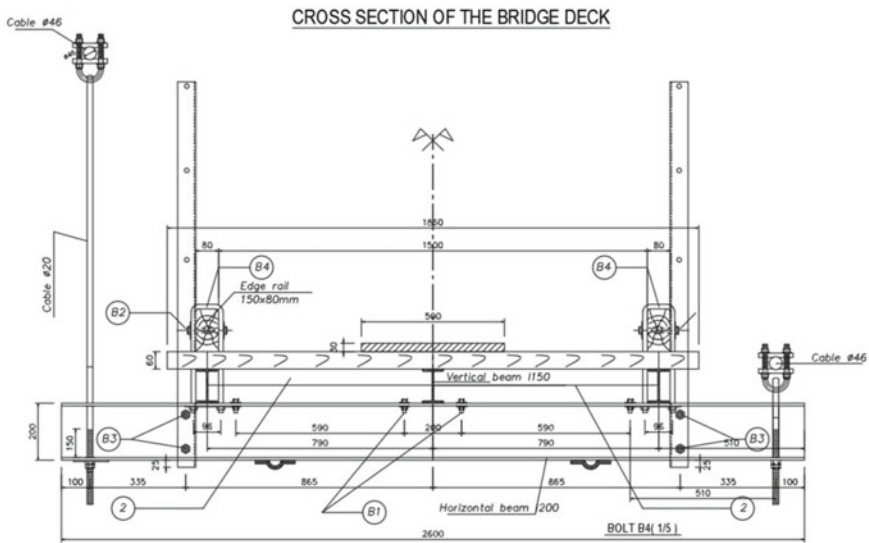
Fig. 2 Overall view of the bridge

Fig. 3 Cross-section composition of the bridge deck

Table 1 Material properties of the bridge's components

Components	Young's modulus (Pa)	Poisson ratio	Density (kg/m^3)
Main beam	2.1×10^{11}	0.3	7850
Cross beam	2.1×10^{11}	0.3	7850
Main cable	1.94×10^{11}	0.3	7850
Vertical suspender cable	1.94×10^{11}	0.3	7850
Bridge tower	2.1×10^{11}	0.3	7850

Fig. 4 FEM model of the bridge using MATLAB

also change accordingly. Thus, for the numerical model, damage can be simulated by adjusting the modulus of elasticity of the affected component. In this paper, to validate the efficiency of the proposed SMA, two damage scenarios are generated: in the first scenario, damage is introduced by reducing the stiffness of beam element no.1 in the FE model to 50%; in the second case, the stiffness of two beam elements no.7 and no.10 is reduced to 70% and 80% of its initial values. Figure 6 shows the location of the damaged beam within the structure.

Once the damage scenarios are generated, SMA is applied for the damage identification of the suspension bridge structure. To showcase its efficiency, SMA is compared with two other widely used optimization algorithms: genetic algorithm (GA) and cuckoo search (CS). For all the optimization algorithms, the same parameters of population = 400 and numbers of iteration = 100 are used. The results for damage identification are shown in Fig. 7.

From the results obtained, we see that in the first damage scenario, SMA is able to detect and locate damage correctly, CS and GA have multiple errors in identifying damage. In the second case, while in general all the three optimization algorithms have been able to correctly detect the location of damage, SMA performs
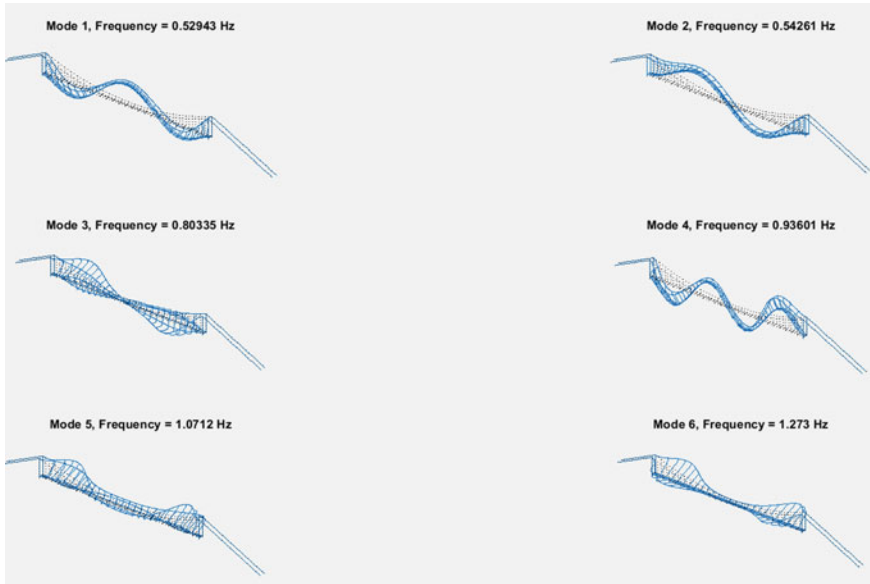
Fig. 5 Mode shape visualization of the first six modes

Table 2 Natural frequencies and mode shapes of the first six modes

Mode number	Frequency (Hz)	Mode shape
1	0.529	1st vertical bending
2	0.543	2nd vertical bending
3	0.803	Torsion
4	0.936	3rd vertical bending
5	1.071	Lateral bending + torsion
6	1.273	Torsion

more accurately in identifying the level of damage. This shows that ultimately SMA is a more effective method at not only locating the position of damage but also detecting the level of damage accordingly.

4   Conclusions

In this paper, we proposed a novel application of a recently developed optimization algorithm—SMA, to solve damage detection problem of a suspension foot-bridge. Damage scenarios are generated by adjusting the stiffness of the beam. The proposed method is then compared with other well-known algorithms GA and CS for their damage identification capability. The final results show that the proposed
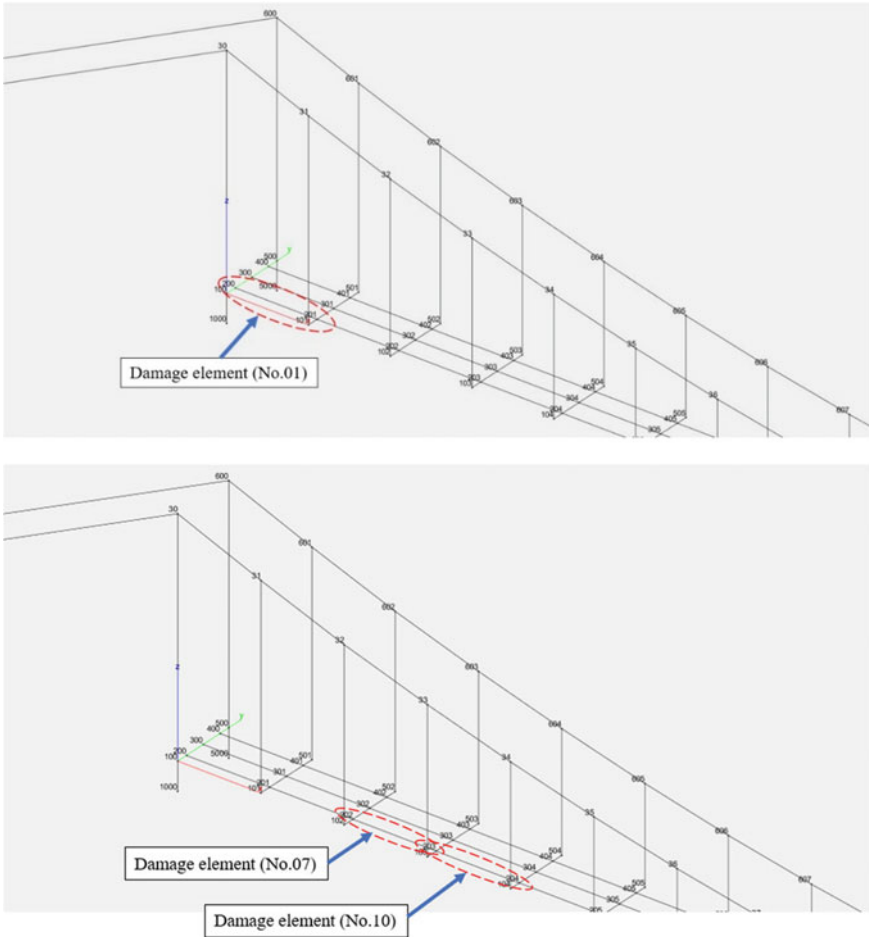
Fig. 6 Damage scenario 1 (upper) and damage scenario 2 (lower)

SMA outperformed GA and CS in terms of damage quantification and damage localization of the structure. Based on the results obtained in this paper, further research regarding this issue can be investigated, such as damage detection of bridge cables or application of SMA on other types of the bridge structure.
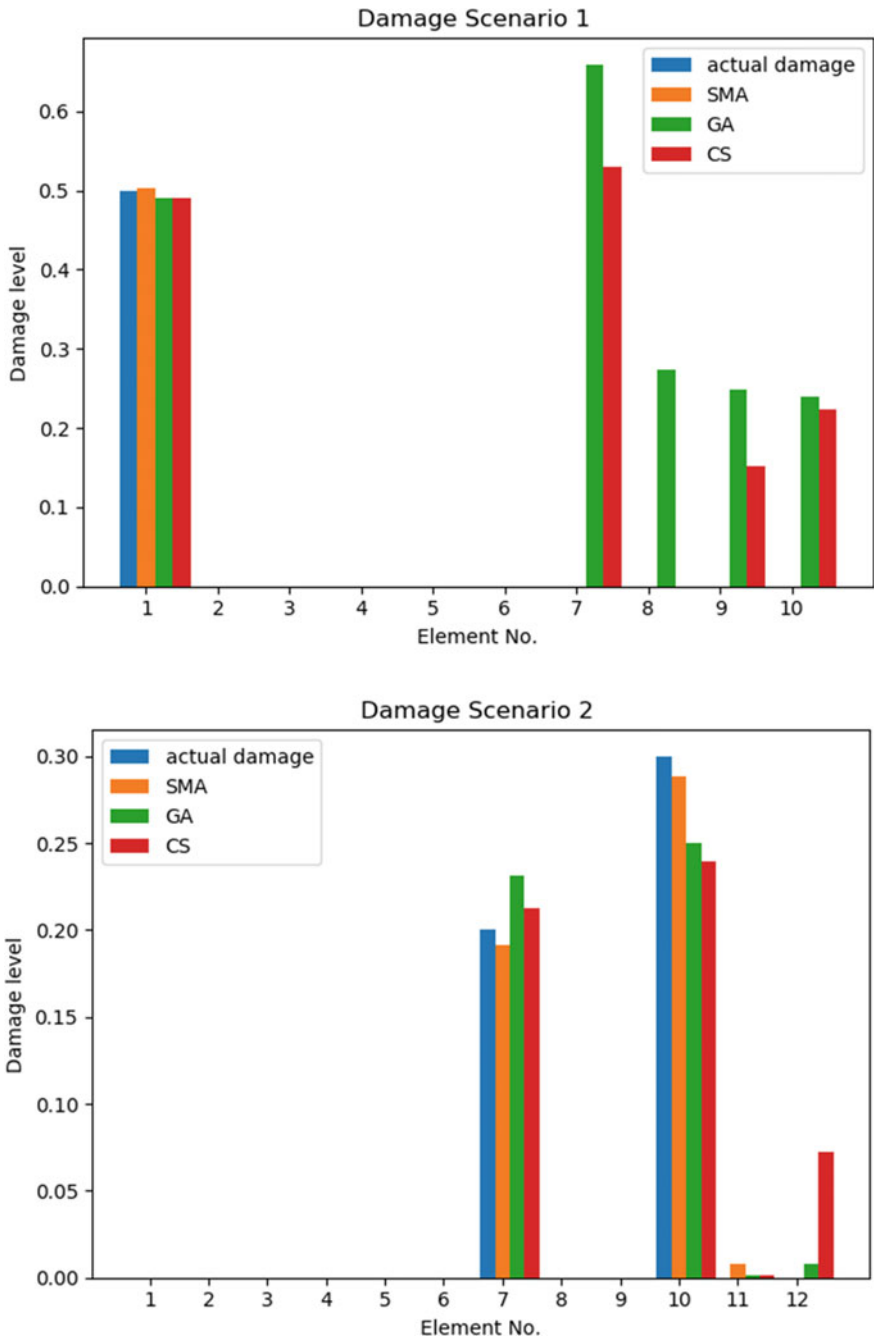
Fig. 7 Damage detection results for the two damage scenarios

References

1. Aldrin JC, Medina EA, Santiago J, Lindgren EA, Buynak CF, Knopp JS (2012) Demonstration study for reliability assessment of SHM systems incorporating model-assisted probability of detection approach. Americ Inst Phys Conf

2. Sohn H, Czarnecki JA, Farrar CR (2000) Structural health monitoring using statistical process control. J Struct Eng 126(11):1356–1363

3. Sinou JJ (2009) A review of damage detection and health monitoring of mechanical systems from changes in the measurement of linear and non-linear vibrations. In: Sapri RC (ed) Mechanical vibrations: measurement, effects and control. Nova Science Publishers, Inc., pp 643–702

4. Kong X, Cai CS, Hu J (2017) The state-of-the-art on framework of vibration-based structural damage identification for decision making. Appl Sci 7:497

5. Azimi M, Dadras A, Pekcan G (2020) Data-driven structural health monitoring and damage detection through deep learning: state-of-the-art review. Sensors 20.https://doi.org/10.3390/s20102778

6. Dang HV, Tran-Ngoc H, Nguyen TV, Bui-Tien T, De Roeck G, Nguyen HX (2021) Data-driven structural health monitoring using feature fusion and hybrid deep learning. IEEE Trans Autom Sci Eng 18(4):2087–2103

7. Duong N, Tran H, De Roeck G, Bui T, Abdel Wahab M (2020) Damage detection in truss bridges using transmissibility and machine learning algorithm: application to Nam O bridge. Smart Struct Syst

8. Teng S, Chen G, Liu G, Lv J, Cui F (2019) Modal strain energy-based structural damage detection using convolutional neural networks. Appl Sci 9:3376

9. Nguyen-Ngoc L, Tran-Ngoc H, Nguyen-Tran H, Nguyen-Duc B, Nguyen-Le-Minh D, Bui-Tien T, Wahab Magd A, Damaged detection in structures using artificial neural networks and genetic algorithms. In: Proceedings of the 3rd international conference on sustainability in civil engineering. Lecture Notes in civil engineering, vol 145. Springer, Singapore

10. Tran Hoa, Khatir S, De Roeck G, Bui-Tien T, Abdel Wahab M (2019) An efficient artificial neural network for damage detection in bridges and beam-like structures by improving training parameters using cuckoo search algorithm. Eng Struct. https://doi.org/10.1016/j.engstruct.2019.109637

11. Khatir S, Tiachacht S, Thanh Cuong L, Tran H, Mirjalili S, Wahab M (2021) A new robust flexibility index for structural damage identification and quantification. Eng Fail Anal 129:105714. https://doi.org/10.1016/j.engfailanal.2021.105714

12. Li S, Chen H, Wang M, Heidari AA, Mirjalili S (2020) Slime mould algorithm: a new method forstochastic optimization. Future Gener Comput Syst

13. Dhawale D, Kamboj VK, Anand P (2021) An effective solution to numerical and multi-disciplinary design optimization problems using chaotic slime mold algorithm. Eng Comput

14. Li L, Pan TS, Sun XX, Chu SC, Pan JS (2021) A novel binary slime mould algorithm with AU strategy for cognitive radio spectrum allocation. Int J Comput Intell Syst

15. Izci D, Ekinci S, Zeynelgil HL, Hedley J (2021) Performance evaluation of a novel improved slime mould algorithm for direct current motor and automatic voltage regulator systems. Transactions of the Institute of Measurement and Control
16. Beekman M, Latty T (2015) Brainless but multi-headed: decision making by the acellular slime mould physarum polycephalum. J Mol Biol 427(23):3734–3743
17. Dooms D, Jansen M, De Roeck G, Degrande G, Lombaert G, Schevenels M, François S (2010) StaBIL: a finite element toolbox for Matlab, 2.0 ed.; structural mechanics section of the Department of Civil Engineering, KU Leuven, Leuven, Belgium
18. François S, Schevenels M, Dooms D, Jansen M, Wambacq J, Lombaert G, Degrande G, De Roeck G (2021) Stabil: an educational Matlab toolbox for static and dynamic structural analysis. Comput Appl Eng Educ

The Application of a Hybrid Autoregressive and Artificial Neural Networks to Structural Damage Detection in Z24 Bridge

Hieu Nguyen-Tran , **Dung Bui-Ngoc** , **Lan Ngoc-Nguyen** , **Hoa Tran** , **Thanh Bui-Tien** , **Guido De Roeck** , **and Magd Abdel Wahab**

1 Introduction

Structural Health Monitoring (SHM) was designed by the civil engineering research community to evaluate the behavior of structures and to assess the properties of materials during the life cycle of structures. SHM involves the integration of many components, such as sensors, data transfer, computing power and processing. The two fundamental steps of SHM are collecting data from the sensor network affixed to the structure and processing the measured data to evaluate the condition of the structure [1].

Many algorithms have been developed to obtain damage-sensitive attributes from the measured data. From the measured response, modal analysis of the structure could be determined using the output-only approach. Those methods are based on the theory that physical parameters including mass, damping and stiffness have a direct impact on modal parameters of the structure [2]. Changes in physical properties may result in significant changes in modal properties. Traditional methods using a simulated model of the structure focused on the direct estimation of the physical properties of the structure, such as modal properties [3].

Recently, many researchers have made use of time series models to identify structural damage. The coefficients of the autoregressive model (AR) are used as an

H. Nguyen-Tran · L. Ngoc-Nguyen · H. Tran · M. A. Wahab
Soete Laboratory, Faculty of Engineering and Architecture, Ghent University, Ghent, Belgium

L. Ngoc-Nguyen · H. Tran · T. Bui-Tien (✉)
Faculty of Civil Engineering, University of Transport and Communications, Hanoi, Vietnam
e-mail: btthanh@utc.edu.vn

H. Nguyen-Tran · D. Bui-Ngoc
Faculty of Information Technology, University of Transport and Communications, Hanoi, Vietnam

G. De Roeck
Department of Civil Engineering, Katholieke Universiteit Leuven, Leuven, Belgium

417

effective damage-responsive property to detect structural damage. Sohn et al. [4] applied AR models to assess the vibration response of a bridge column. The authors performed statistical analysis of the AR model coefficients to categorize healthy and damaged states of the structure. This method was further enhanced and applied to monitor the health of a fast patrol boat with a surface effect [5]. Nair et al. [6] used the vibration signals of the ASCE reference structure as the autoregressive moving average time series for the model. The authors developed a damage-responsive property based on the first three AR components to categorize the healthy and damaged states of the structure. Besides that, many statistics and pattern recognition techniques, such as ANN, have been applied to classify damage-responsive characteristics [7]. ANN was also widely used for seismic damage detection using frequency domain data exclusively [8], although Nakamura et al. [9] proposed a direct analysis method for the historical seismic response data of a building. Khatir et al. [10] further improved the ANN using an Arithmetic Optimization Algorithm to locate and quantify damage, which proved to be more accurate than the traditional ANN method and the combined ANN-Balancing Composite Motion Optimization (BCMO). Saadatmorad et al. [11] introduced a novel method that used a multilayer perceptron neural network to detect beam-like structure damage. The result showed that the presented method could detect individual structural damages with good accuracy.

In this research, a novel hybrid structural damage detection method is proposed including the application of AR models to determine damage-responsive properties and the use of ANN to identify possible damages. The proposed method is applied to the case study of Z24 Bridge for validation of damage detection ability. The results show that the hybrid AR-ANN can detect damages of the structure accurately.

2 Methodology

2.1 Autoregressive

Autoregressive modeling (AR) is one of the good techniques used to analyze time series data. AR is often used to represent stationary time series processes. A stochastic process (random or stationary) is a statistical phenomenon consisting of a set of random variables arranged over time. The stationary process evolves over time according to the laws of probability. A time series plot represents the measurements of a variable performed over time. An AR model is defined as a time series model but with regressed values to the previous values of the same time series. In this research, the proposed AR models are output only, specifically autoregressive with extra input (ARX) models or pure AR formulations. For example, on y_{t-1}

$$y_t = \beta_0 + \beta_1 y_{t-1} + \varepsilon_t \tag{1}$$

The autoregression order is the number of instant previous values in the series data that are used to anticipate the present value. The first-order autoregression is the previous model, written as AR (1). The AR model used to calculate a time series y_t using y_{t-1}, y_{t-2} is shown in Eq. (2) as:

$$y_t = \beta_0 + \beta_1 y_{t-1} + \beta_2 y_{t-2} + \varepsilon_t \tag{2}$$

The model obtained is a second-order autoregression and it can be written as AR (2). The model can also be generalized for a kth order autoregression as AR(k), which is a multiple linear regression where the value of the series at a specific time t is a function of the preceding values $t - 1, t - 2, …, t - k$.

The autocorrelation function (ACF) is defined as the correlation coefficient between two data points in a time series. The ACF for a time series y_t is denoted as:

$$\text{Corr}(y_t, y_{t-k}) \tag{3}$$

where k is the delay the value of time interval considered. The autocorrelation offset 1 (i.e. when k is equal or higher than 1) is the correlation between values separated by the time interval considered. The autocorrelation delay k can also be expressed as the correlation between the values of the intervals k.

ACF is a means of measuring the linear relationship between two observations at a time interval. Assuming the AR (k) model given, the purpose is to measure only the linear relationship between y_i and y_{i-k}, and the partial autocorrelation function (PACF) is given as below:

$$\text{PACF}(y_i, y_{i-k}) = \frac{\text{Covariance}(y_i, y_{i-k}|y_{i-1}, y_{i-2}, \dots y_{i-k+1})}{\sigma_{y_i|y_{i-1}, y_{i-2},\dots y_{i-k+1}} \sigma_{y_{i-k}|y_{i-1}, y_{i-2},\dots y_{i-k+1}}} \tag{4}$$

PACF is used for identifying the autoregressive order. Specifically, partial auto-correlations which are different from 0 are indicated as lagged terms y, which in turns can be used to anticipate the value of y_t.

2.2 Artificial Neural Networks

Artificial neural networks (ANNs) have recently become a core research interest not only in computer sciences but also in all the others industrial fields. The (ANNs) models were inspired by human science, which studies the evolution of the neuroanatomy of human beings in problem-solving [12]. The fundamental of the ANNs consists of neurons which mimic the traits of the human biological neurons, divided into different layers. Normally, an ANN structure includes an input layer, one or more hidden layers and an output layer. A simplified model of an ANN is shown in Fig. 1.
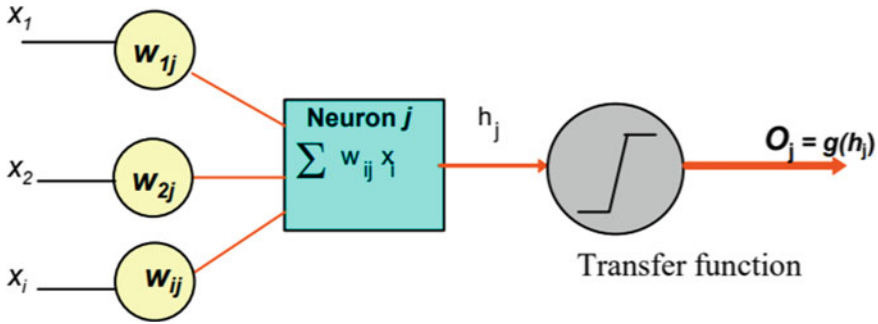
Fig. 1 Structure of ANNs

ANNs are based on the learning ability of the human brain by performing convoluted algorithms [13]. Previous layers are connected to the next one by connections that contain weights, which can have a positive or negative value. While neuron is activated by positive weights, it can also be constrained by negative weights. Figure 1 shows a typical ANN network structure where inputs parameters $x_1, x_2, \ldots, x_i$ are connected to the neuron j by sets of weights $(w_{1j}, w_{2j}, \ldots, w_{ij})$ on each connection. The received signals are then multiplied by the respective connection weights to obtain the output h_j. The output is then passed through a transfer function, normally denoted as the sigmoid function to produce the final output $O_{(j)}$. . The sigmoidal (logistic) function is defined as

$$O_{pj} = \frac{1}{1 + e^{-\text{net}_{pj}}} \tag{5}$$

where O_{pj} is the output of a neuron j given an input parameter p and a total of inputs to the ANN $(-\text{net}_{pj})$.

The backpropagation is a commonly used algorithm for training of a feed-forward neural network. The principle of backpropagation algorithm is to reduce the consecutive errors between the possible output and the target output of the backpropagation. The weights on each of the connections between neurons vary according to the magnitude of the initial error. The input data is then resent to create a new output and respective error. Transfer function is used in each neuron, and it is fully connected to the next level node. This process is cycled until the error reaches a minimum acceptable value. As a result, the final output is represented as model of the input at a specific point.
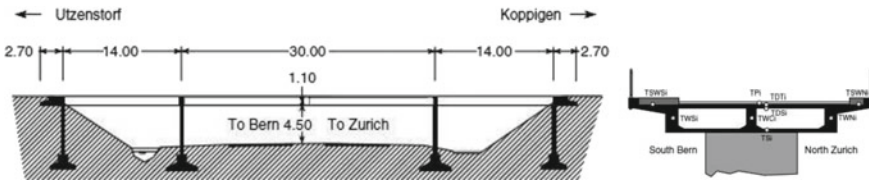
Fig. 2 Side view of the Z24 bridge

3 Applying the Method to Z24 Bridge

3.1 Z24 Bridge's Vibration Data

The proposed method is applied to the case of Z24 Bridge for validation. The vibration data used is taken from the Z24 Bridge measurement campaign within the System Identification to Monitor Civil Engineering Structures (SIMCES) project. The Swiss Z24 Bridge was a three-span prestressed reinforced concrete bridge with a width of 8.60 m and a total length of almost 60 m (see Fig. 2).

The bridge was located in the Swiss canton of Bern and connected Koppigen and Utzenstorf. Technical descriptions of the bridge were detailed in [14].

As part of the SIMCES project, different progressive damage scenarios were conducted on the bridge in the summer of 1998. Progressive damage scenarios were performed within a month (see Table 1). During the damage tests, a reference measurement of undamaged condition was first constructed. Then progressive damage measurement was taken after each step. Each scenario was conducted in 9 measured setups of 33 accelerometers in total. Temporal signals from 08 series of 8192 samples were collected at 100 Hz [15].

The undamaged data was collected on August 4, 1998, and then the bridge damaged on August 31, 1998. The aforementioned datasets for the 99 V sensor are shown in Figs. 3 and 4.

3.2 Obtained Results from the Proposed Method

The framework of the AR-ANN method is shown in Fig. 5.

Firstly, raw time series signals are used as input to the AR model (30) and transforms only the output signal into AR coefficients. Second, these coefficients are sent to the neural network for classification to determine the damage or healthy condition. In ANNs, the activation function used for the input and hidden layer is the ReLu function while the Softmax function is used for the activation function of the output layer (Fig. 6).

The training phase has a 75% share of all data and the others belong to the testing phase. During the training process, functions and labels of the time series are provided

Table 1 Z24's progressive damage tests in 1998 [15]

| Starting date	Scenario	Finishing date	Type of damage
4/8/1998	Undamaged condition	26/8/1998	Concrete spalling at soffit, 24 m^2
9/8/1998	Installation of pier settlement system	27/8/1998	Landslide of 1 m at abutment position
10/8/1998	Reducing pier's height, 20 mm	31/8/1998	Failure of concrete hinge
12/8/1998	Reducing pier's height, 40 mm	2/9/1998	Failure of 02 anchor heads
17/8/1998	Reducing pier's height, 80 mm	3/9/1998	Failure of 04 anchor heads
18/8/1998	Reducing pier's height, 95 mm	7/9/1998	Rupture of 2 tendons
19/8/1998	Lifting of pier, tilt of foundation	8/9/1998	Rupture of 4 tendons
20/8/1998	Introducing another reference condition	9/9/1998	Rupture of 6 tendons
25 August	Concrete spalling at soffit, 12 m^2		
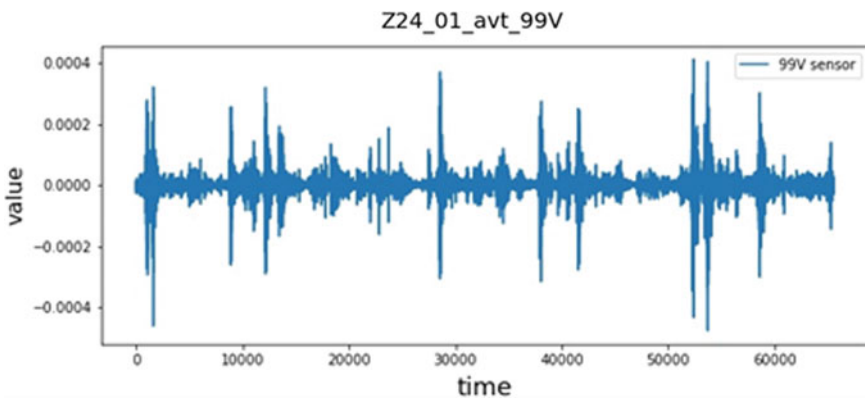
Fig. 3 Data of sensor 99 V on 4 August

in the training dataset. The goal is to identify the relationship between functions and class labels. The performance of the process of training and testing the network is shown in Fig. 7.

The accuracy of the prediction is assessed based on a test set, using the basic concept of positive and negative detection. The higher the precision score is, the more accurate the model could predict.

Accuracy score is an effective tool to calibrate the prediction success in the case where classes are very unbalanced. The convocation score represents the model's ability to correctly predict the positive aspects from the real ones. This contrasts with the accuracy, which measures the number of positive predictions made by the
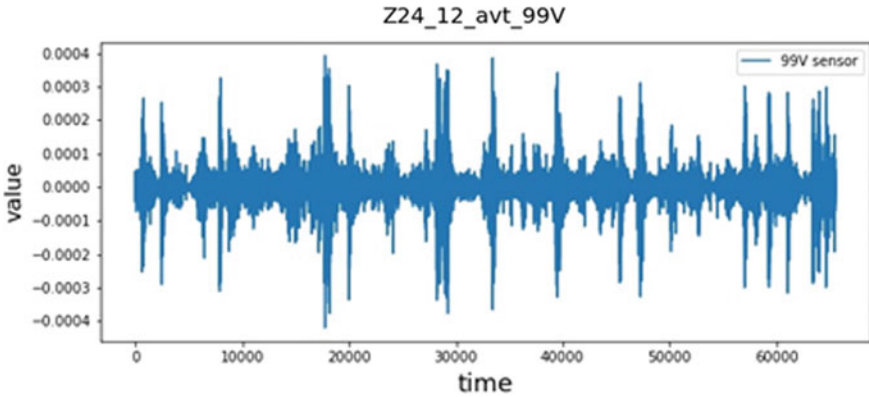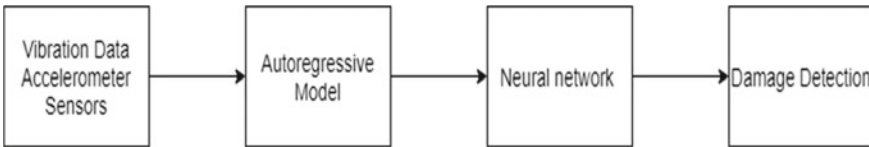
Fig. 4 Data of sensor 99 V on 31 August

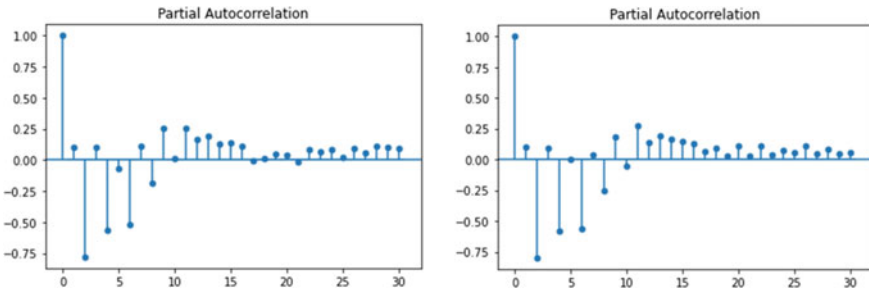**Fig. 5** Workflow of the hybrid AR and ANNs

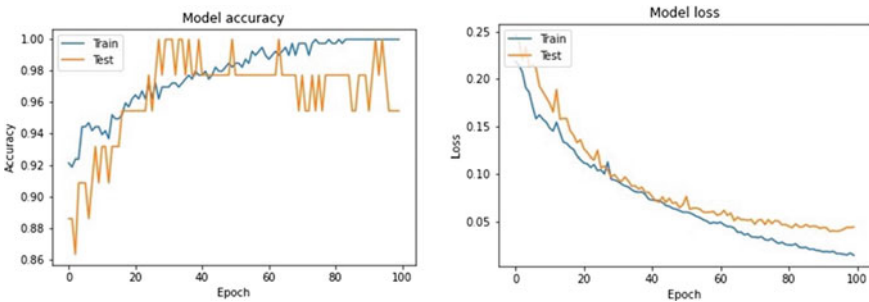**Fig. 6** Partial autocorrelation (PACF) of data from sensor 99 V on 4 and 31 August

Fig. 7 Accuracy and loss of training and testing

Table 2 Confusion matrix

	Undamage' (predicted)	Damaged' (predicted)
Undamage (actural)	True Positive (TP = 18)	False Negative (FN = 3)
Damaged (actural)	False Positive (FP = 2)	True Negative (TN = 21)

models out of all positive predictions. The F1 score is calculated based on the positive and negative detection values. It is often used as the only value that provides prominent information about the quality of the model's output. Mathematically, it can be represented as:

$$Accuracy\_ Score = \frac{(\text{True Positive } + \text{ True Negative})}{(\text{True Positive} + \text{False Negative} + \text{True Negative} + \text{False Positive})} \tag{6}$$

$$F1\_ Score = \frac{2 * \frac{\text{True Positive}}{(\text{True Positive} + \text{False Positive})} * \frac{\text{True Positive}}{(\text{True Positive} + \text{False Negative})}}{\left(\frac{\text{True Positive}}{(\text{True Positive} + \text{False Positive})} + \frac{\text{True Positive}}{(\text{True Positive} + \text{False Negative})}\right)} \tag{7}$$

The confusion matrix for the proposed method is given in Table 2. The accuracy of the proposed method is calculated as a percentage of correctly classified samples out of the total number of samples.

Based on the performance of the method, the accuracy of the method in the training phase is 99% and the test phase 95%. Furthermore, as a confusing matrix in Table 2, the total number of samples is 44, of which 18 are undamaged samples, otherwise 03 samples were misclassified. 21 damaged samples were found in a damaged condition and only 02 samples were not repaired. We obtain results for accuracy scores, accuracy scores, recall scores and F1 scores, which are 0.886, 0.9, 0.857 and 0.878, respectively. This suggests that a combination of autoregressive and ANN methods can be applied to the transformed vibration data.

4 Conclusions

In this paper, the authors have proposed a damage identification method using a hybrid autoregressive model and an ANNs network model. The coefficients of the AR model are efficient inputs for ANNs. Experimental results show that the method can be used to solve the damage detection problems. The final results obtained from the case study suggest that the proposed method has produced a high level of accuracy in damage detection of the structure. In the future research, this method can be further improved to not only classify damage in the structure but also quantify the damage level.

References

1. Farrar CF, Worden K (2007) An introduction to structural health monitoring. Philos Trans R Soc A 365(1851):303–315
2. Farrar CR, Doebling SW (1997) An overview of modal-based damage identification methods. DAMAS 97. Structural damage assessment using advanced signal processing procedures
3. Hoa TN, Samir K, Guido DR, Thanh B, Long N, MagdA W (2019) Stiffness identification of truss joints of the Nam O Bridge based on vibration measurements and model updating. ARCH 2019: proceedings of ARCH 2019, pp 264–272
4. Sohn H, Czarnecki JA, Farrar CR (2000) Structural health monitoring using statistical process control. J Struct Eng 126(11):1356–1363
5. Sohn H, Farrar CR, Hunter NK, Worden K (2001) Applying the lanl statistical pattern recognition paradigm for structural health monitoring to data from a surface-effect fast patrol boat. LA-13761-MS, Los Alamos National Laboratory, Los Alamos
6. Nair KK, Kiremidjian AS, Law KH (2006) Time series-based damage detection and localization algorithm with application to the asce benchmark structure. J Sound Vibr 291(1–2):349–368
7. Worden K, Manson G, Fieller NRJ (2000) Damage detection using outlier analysis. J Sound Vib 229(3):647–667
8. Zang C, Imregun M (2001) Structural damage detection using artificial neural networks and measured frf data reduced via principal component projection. J Sound Vib 242(5):813–827
9. Nakamura M, Masri SF, Chassiakos AG, Caughey AK (1998) A method for non-parametric damage detection through the use of neural networks. Earthq Eng Struct Dyn 27(997–1010)
10. Samir K, Samir T, Thanh Cuong Le, Ghandourah E, Mirjalili S, Wahab M (2021) An improved artificial neural network using arithmetic optimization algorithm for damage assessment in FGM composite plates. Compos Struct 273:114287. https://doi.org/10.1016/j.compstruct.2021.114287
11. Saadatmorad M, Jafari-Talookolaei RA, Pashaei M-H, Khatir S (2021) Damage detection on rectangular laminated composite plates using wavelet based convolutional neural network technique. Compos Struct 278:114656. https://doi.org/10.1016/j.compstruct.2021.114656
12. Yang GR, Wang X-J (2020) Artificial neural networks for neuroscientists: a primer. Neuron 107(6):1048–1070. ISSN: 0896-6273. https://doi.org/10.1016/j.neuron.2020.09.005
13. Alzubaidi L, Zhang J, Humaidi AJ et al (2021) Review of deep learning: concepts, CNN architectures, challenges, applications, future directions. J Big Data 8:53. https://doi.org/10.1186/s40537-021-00444-8
14. Reynders E, De Roeck G (2009) Continuous vibration monitoring and progressive damage testing on the Z24 bridge. In: Boller C, Chang FK, Fujino Y (eds) Encyclopedia of structural health monitoring. Wiley, New York, pp 2149–2158
15. Maeck J, Peeters B, De Roeck G, Damage identification on the Z24 bridge using vibration monitoring. Smart Mater Struct 10(3)